Научном већу Института за физику у Београду
Београд, 24. септембар 2020.

ПРЕДМЕТ:

Молба за покретање поступка за стицање звања виши научни сарадник

Молим Научно веће Института за физику у Београду да, у складу са Правилником о поступку и начину вредновања и квантитативном исказивању научно-истраживачких резултата истраживача, покрене поступак за мој избор у звање виши научни сарадник.

У прилогу достављам:

1. Мишљење руководиоца лабораторије са предлогом чланова комисије
2. Биографске податке
3. Преглед научне активности
4. Елементе за квалитативну оцену научног доприноса
5. Елементе за квантитативну оцену научног доприноса
6. Списак објављених радова и њихове копије
7. Податке о цитираности
8. Копију решења о претходном избору у звање
9. Додатне прилоге

С поштовањем,

др Јакша Вучичевић
научни сарадник,
Институт за физику у Београду

Научном већу Института за физику у Београду

Предмет: Мишљење руководиоца лабораторије о избору др Јакше Вучичевића у звање виши научни сарадник

Др Јакша Вучичевић је запослен у Лабораторији за примену рачунара у науци, у оквиру Националног центра изузетних вредности за изучавање комплексних система Института за физику у Београду. У истраживачком раду бави се темама везаним за транспорт наелектрисања и суперпроводност у јако корелисаним материјалима. С обзиром да испуњава све предвиђене услове у складу са Правилником о поступку, начину вредновања и квантитативном исказивању научноистраживачких резултата истраживача МПНТР, сагласан сам са покретањем поступка за избор др Јакше Вучичевића у звање виши научни сарадник.

За састав комисије за избор др Јакше Вучичевића у звање виши научни сарадник предлажем:

(1) др Дарко Танасковић, научни саветник, Институт за физику у Београду
(2) др Ненад Вукмировић, научни саветник, Институт за физику у Београду
(3) др Ђорђе Спасојевић, редовни професор Физичког факултета Универзитета у Београду

др Антун Балаж
научни саветник
Руководилац Лабораторије за примену рачунара у науци

2. БИОГРАФСКИ ПОДАЦИ КАНДИДАТА

Јакша Вучичевић је рођен 30. маја 1984. године у Београду. Матурирао је 2003. год. у Деветој београдској гимназији "Михаило Пупин", природно-математички смер, са просеком *одличан*. Студирао је 2003-2009. год. на Физичком факултету Универзитета у Београду, смер Примењена физика и информатика. Основне студије је завршио са просеком 9.05. Дипломски рад "Утицај асиметрије густине стања на особине Мотовог метал-изолатор прелаза" је написао под руководством др Дарка Танасковића, са Института за физику у Београду. У периоду 2009-2015. год. је био студент докторских студија на Физичком факултету Универзитета у Београду, смер Физика кондензованог стања материје и статистичка физика. Докторску тезу "Показатељи скривене кватне критичности у високо-температурном транспорту наелектрисања у близини Мотовог прелаза" је написао под руководством др Дарка Танасковића. Добитник је годишње студентске награде Института за физику у Београду 2016. год., за најбољу докторску тезу у претходној години.

Током 2010. године, као докторанд, J.B. је био стипендиста Министарства за науку. Од јануара 2011. је запослен на Институту за физику у Београду. Учествовао је на националном пројекту ОН171017 "Моделовање и нумеричке симулације комплексних вишечестичних система" Министартства просвете, науке и технолошког развоја у периоду 2011-2019. год. Као студент докторских студија учествовао је и на два билатерална пројекта са републиком Француском: "Тополошка стања и фазе у нискодимензионалним електронским системима", 2011-2012. год. под руководством др Милице Миловановић и др Марка Гербига (LPS Orsay), и "Квантно-критични транспорт у близини Мотовог метал-изолатор прелаза", 2012-2013. год. под руководством др Дарка Танасковића и др Марсела Розенберга (LPS Orsay).

Након докторирања, J.B. је провео две године (2015-2017) као постдок у групи др Оливијеа Парколеа у установи IPhT, CEA Saclay, Париз, Француска, и радио у блиској сарадњи са групом др Антоана Жоржа са College de France, такође у Паризу. Био је учесник пројекта "Quantitative approaches for strongly correlated quantum systems in equilibrium and far from equilibrium", *European Research Council (ERC) starting grant (O. Parcollet)*. У периоду 2016-2017. учествовао је и на билатералном пројекту Србије и републике Словеније "Јаке електронске корелације и суперпроводност" под руководством др Дарка Танасковића и др Јернеја Мравље-а.

Након повратка из Француске, 2017. J.B. је наставио рад на Институту за Физику у Београду. Тренутно је руководилац српске стране билатералног пројекта са републиком Немачком (DAAD) "Електронске корелације у оксидима са трансфером наелектрисања: функције одзива и дугодометна уређења" за период 2020-2021. године., у сарадњи са др Филипом Хансманом (Friedrich Alexander Universität Erlangen/Nürnberg). J.B. учествује и у пројекту NI4OS-Europe (National Initiatives for Open Science in Europe, Grant number 857645), финансираном од стране Европске комисије у оквиру програма Хоризонт 2020. На овом пројекту др Вучичевић ради на пројектном задатку под називом: LMDB, Distributed database of numerical results and codes pertaining to a large class of condensed matter theoretical models. Од августа 2020. J.B. је руководилац двогодишњег ПРОМИС пројекта Фонда за науку под називом "Хладни атоми, Хабардов модел и холографија: кључ за чудне метале".

Главна тема рада J.B. су ефекти јаких електронских корелација у системима чврстог стања. У досадашњем раду, J.B. се бавио феноменима као што су Мотов метал-изолатор прелаз и неконвенционална суперпроводност. Током боравка у француској J.B. се додатно специјализовао за развој нумеричких алгоритама за решење Хабардовог модела што му је од тада и централна линија рада. J.B. је објавио 13 публикација у међународним часописима (4 рада категорије М21а, 8 радова категорије М21, и 1 рад категорије М23). На основу базе

SCOPUS, радови су цитатирани 190 пута (172 не рачунајући ауто-цитате), а J.B. има h-index 8. J.B. има активну сарадњу са групама из Љубљане, Париза, Њујорка и Ерлангена (Немачка). J.B. је тренутно ментор једног студента на мастер студијама Физичког факултета у Београду и има сарадњу са истраживачком станицом Петница. J.B. је активан рецензент часописа Physical Review (Letters, B и E) са укупно 34 рецензије од октобра 2017. год.

3. ПРЕГЛЕД НАУЧНЕ АКТИВНОСТИ

Научно-истраживачки рад кандидата се може поделити у 3 дела:

1. истраживање особина транспорта наелектрисања у околини Мотовог метал-изтолатор прелаза
2. истраживање неконвенционалне суперпроводности
3. развој нумеричких метода за решење вишечестичног квантног проблема фермиона на решетки

3.1. Транспорт у околини Мотовог метал-изолатор прелаза

Мотов метал-изолатор прелаз је појава у системима чврстог стања где се отпорност система промени нагло и драстично при малој промени неког спољног параметра (притисак, температура или хемијски састав). Ова појава се опажа у низу материјала као што су разни оксиди ванадијума и капа-органски системи, а верује се да је релевантна и за купратне високотемпературне суперпроводнике. Представља последицу ефективно јаке кулонове интеракције између електрона у попупопуњеној валентној зони материјала. Први теоријски опис метал-изолатор прелаза је постигнут почетком 90-их, у оквиру решења Хабардовог модела помоћу теорије динамичког средњег поља (DMFT).

Квантно-критично скалирање

Током докторских студија, J.B. се фокусирао на прорачун отпорности у Хабардовом моделу, управо у околини Мотовог прелаза. У овој линији рада, J.B. и др Дарко Танасковић су имали блиску сарадњу са групом др Владимира Добросављевића са државног универзитета на Флориди, САД. У три публикације које су објавили у периоду 2011-2015. године, показано је да се отпорност на високим температурама понаша у складу са једноставним законом скалирања. Ово понашање наликује законима скалирања који важе у околини квантних критичних тачака (квантно-критично скалирање) у низу претходно добро изучених појава, укључујући и метал-изолатор прелаз у дводимензионом електронском гасу (нпр. остваренom на интерфејсу два полупроводника). Показано је да скалирање опстаје у широком делу фазног дијаграма Хабардовог модела, у околини оба типа Мотовог прелаза који се у том моделу опажа (прелаз услед јачине интеракције, и прелаз услед допирања). Ово понашање је подробно испитано и дати су аргументи да је то вид универзалног понашања везаног за сам фазни прелаз, које би се требало видети у експерименту независно од детаља структуре једињења.

Резултати ове линије рада су потврђени експериментално од стране групе K. Каноде из Јапана, што је објављено 2015. године у часопису Nature Physics. Они су извршили систематска мерења отпорности у неколико капа-органских материјала који испољавају Мотов прелаз и сматра се да су добро описани Хабардовим моделом. Заиста, независно од детаља структуре хемијског једињења, опсервирали су на високој температури квантно критично скалирање отпорности у складу са DMFT прорачунима приказаним у публикацијама кандидата.

Од нарочитог значаја је и што је установљено да су резултати прорачуна за Хабардов модел у складу са експерименталним опсервацијама у купратним једињењима у режиму лошег, тј. чудног метала. То је режим за који се сматра да је од изузетног значаја за разумевање високотемпературне суперпроводности у купратним једињењима. Овај режим карактерише линеарна зависност отпора од температуре, за шта недостаје дубље разумевање. Анализа учињена у раду кандидата је повезала нагиб линеарне отпорности са фундаменталним критичним експонентима Мотовог прелаза, што је резултовало публикацијом у врхунском часопису Physical Review Letters, чији је J.B. први аутор.

У овој линији рада, J.B. је доприносио имплементацијом нумеричких метода (DMFT и рачунање проводности), продукцијом и анализом резултата, као и писањем публикација.

Публикације кандидата из ове линије рада су:

1. **J. Vučičević**, D. Tanasković, M. Rozenberg, V. Dobrosavljević, "Bad-metal behavior reveals Mott quantum criticality in doped Hubbard models"
Phys. Rev. Lett. 114, 246402 (2015)

2. **J. Vučičević**, H. Terletska, D. Tanasković, V. Dobrosavljević, "Finite temperature crossovers and the quantum Widom line near the Mott transition"
Phys. Rev. B 88, 075143 (2013)

3. H. Terletska, **J. Vučičević**, D. Tanasković, V. Dobrosavljević, "Quantum Critical Transport Near the Mott Transition "
Phys. Rev. Lett. 107, 026401 (2011)

Неуређеност и јаке интеракције

Од раније је познато да неуређеност у материјалима негативно утиче на њихову проводност, и да јака неуређеност може довести до локализације електрона, што је фаза позната као Андерсон изолатор. Међутим није било у потпуности разјашњено на који начин се ово понашање модификује у присуству јаких интеракција између електрона.

На изучавању неуређеног Хабардовог модела, кандидат је радио у сарадњи са др Дарком Танасковићем, и групама др Владимира Добросављевића и др Марије Каролине О. Агуиар (Бело Хоризонте, Бразил). У раду објављеном 2015. год., испитан је одговарајући фазни дијаграм. Испоставља се да се ефекти јаких интеракција и неуређености међусобно поништавају, и да је систем најметалнији када су енергијске скале неуређености и интеракција блиске. При великим интеракцијама и великој неуређености, описана је и мешана фаза Мотовог и Андерсоновог изолатора.

У овој линији рада, кандидат је развио сет C++ кодова који имплементирају метод типичног медијума (TMT) за решење неуређеног Хабардовог модела. Кодови које је развио кандидат су и даље у употреби, што се наводи и у захвалници скорашњег препринта arXiv:2008.09714.

Рад кандидата из ове линије рада је:

1. H. Braganca, M. C. O. Aguiar, **J. Vučičević**, D. Tanasković, V. Dobrosavljević, "Anderson localization effects near the Mott metal-insulator transition"
Phys. Rev. B 92, 125143 (2015)

Отпорност у две димензије и вертекс корекције

У оквиру DMFT теорије, проводност за Хабардов модел се може израчунати без додатних апроксимација. Међутим, у случају дводимензионалне решетке (квдаратна, троугласта), DMFT је само приближан метод, а са систематским поправкама DMFT-а, настаје и потреба за корекцијама израза за проводност (такозване "вертекс" корекције). Међутим, урачунавање вертекс корекција у отпорности за Хабардов модел представља вишедеценијски изазов, и досадашњи покушаји нису дали дефинитиван одговор на питање величине ових корекција. На основу физичарске интуиције, даване су различите процене, а често се сматрало да су вертекс корекције занемариве на високој температури где је соптствена енергија електрона локална.

У периоду 2017-2020. год. кандидат је сарађивао са др Дарком Танасковићем, групом из Института Јозеф Стефан из Љубљане као и др Нилсом Венцелом (Flatiron Institute, Њујорк, САД) на проблему одређивања доприноса вертекс корекција у случају дводимензионалне решетке. Поређењем резултата неколико најмодернијих нумеричких метода успешно су рашчлањени различити доприноси оптичкој проводности. Установљено је да незанемарљиве вертекс корекције опстају и до највиших температура, док неки други ефекти као што су коначност решетке и нелокалне корелације играју секундарну улогу. На тај начин, показано је да је резултат прорачуна егзактне дијагонализације на решетки величине 4x4 (FTLM) практично егзактан резултат за Хабардов модел у термодинамичком лимиту и температурама већим од око десетог дела ширине енергетске зоне.

Овај резултат је нарочито значајан у светлу скорашњих експеримената са хладним атомима у оптичким решеткама, који симулирају Хабардов модел. У експерименту објављеном у часопису Science (P. T. Brown et. al., Science 363, 379 (2019)) поређена је измерена отпорност са DMFT и FTLM теоријама и закључено је да се две теорије не слажу, и да се резултат мерења слаже боље са FTLM теоријом. Међутим, остало је неразјашњено која од две теорије је ближа егзактном резултату, и одакле потиче разлика између тих теорија. У раду кандидата, ово питање је сада разјашњено, што је од изузетне важности за успостављање провере будућих експеримената на хладним атомима.

У најскоријем раду кандидата, систематски прорачуни из ове линије рада су проширени и на случај троугласте решетке. Документовано је да је сопствена енергија електрона на троугластој решетки локалнија него на квадратној, и потврђена је физичка интуиција да је то индикатор мањег значаја вертекс корекција за отпорност, иако су оне квантитативно незанемарљиве и у случају троугласте решетке. Показано је и да, неочекивано, на троугластој решетки термодинамичке величине спорије конвергијрају са величином решетке. Ови резултати имају важне импликације везано за избор нумеричких метода и теоријске студије у будућности.

У овој линији рада, J.B. је допринео имплементацијом неколико најмодернијих нумеричких метода (CDMFT, DCA, CTINT), као и анализом резултата и писањем публикација.

Ова линија рада је до сада резултовала са две публикације:

1. A. Vranić, **J. Vučičević**, J. Kokalj, J. Skolimowski, R. Žitko, J. Mravlje, D. Tanasković, "Charge transport in the Hubbard model at high temperatures: triangular versus square lattice"
Phys. Rev. B 102, 115142 (2020)

2. **Jaksa Vučičević**, Jure Kokalj, Rok Žitko, Nils Wentzell, Darko Tanasković, Jernej Mravlje, "Conductivity in the square lattice Hubbard model at high temperatures: importance of vertex corrections"
Phys. Rev. Lett. 123, 036601 (2019)

3.2. Неконвенционална суперпроводност

Суперпроводност у двослоју графена

Графен је последњих година привлачио пуно пажње као систем са многим изузетним својствима, и великим бројем могућности за потенцијалне примене. Једна од важних и недовољно истражених питања је могућност остварења неконвенционалне суперпроводности у оваквим системима, нарочито у случају двослоја графена где постоји ненулта густина стања на Ферми нивоу.

У периоду 2011-2012. год. кандидат је сарађивао са др Милицом Миловановић (Институт за физику у Београду) и Марком Гербигом (LPS, Orsay, Француска) на истраживању суперпроводне нестабилности у двослоју графена, услед ефективних антиферомагнетих интеракција. Показано је да такве нестабилности постоје, али да функција спаривања значајно зависи од попуњености енергетске зоне. Нађено је да је спаривање мешаног типа, али да је доминантно типа $d+id$, и да опстаје првенствено на умереном допингу.

Кандидат је у овој линији рада допринео имплементацијом решења једначина средњег поља, продукцијом и анализом резултата и писањем публикације.

Публикација кандидата у овој линији рада је:

1. **J. Vučičević**, M. O. Goerbig, M. V. Milovanovic, "d-wave superconductivity on the honeycomb bilayer"
Phys. Rev. B 86, 214505 (2012)

Суперпроводност у Хабардовом моделу

Многи сматрају да је Хабардов модел на квадратној решетки минимални модел за опис високотемпературне суперпроводности у купратним једињењима. У Хабардовом моделу, узрок суперпроводности је одбојна Кулонова интеракција. Као и у купратима, спаривање је *d*-типа, што значи да се спарују електрони на различитим чворовима решетке. Третирање овакве суперпроводности је изузетан изазов за теорију јер захтева рад у вишечестичном формализму и опис нелокалних корелација; то значи да се не могу користити теорије средњег поља као што је BCS теорија, али ни DMFT теорија у оригиналној формулацији. Минималном теоријом суперпроводности у Хабардовом моделу се последњих декада сматрала кластер DMFT теорија, која захтева велике рачунарске ресурсе, а може описати само краткодометно спаривање електрона.

У раду кандидата у оквиру групе др Оливијеа Парколеа током 2016-2017. године, развијен је TRILEX метод за третирање суперповодности *d*-типа у Хабардовом моделу. Овај метод је сличан оригиналној DMFT теорији по рачунској захтевности, али омогућава опис и дугодометног спаривања. Разрађена су и систематска поједностављења ове теорије која се могу користити у режиму слабије интеракције. Теорија је искоришћена да се испита фазни дијаграм Хабардовог модела и добијени су резултати у складу сад другим методима и општом феноменологијом купрата. Додатно, испитане су спектралне особине у суперпроводној фази упоредо са "pseudogap" фазом и опажена је изузетна сличност између те

две фазе. Такође, систематски је испитана висина критичне температуре за суперпроводност у функцији константи прескока решетке и пронађен је један конкретан избор параметара за коју је висина критичне температуре нарочито висока, у режиму како слабих тако и јаких интеракција.

У овој линији рада, кандидат је допринео извођењем TRILEX једначина у Намбу формализму, имплементацијом методе, продукцијом и анализом резултата као и писањем публикације.

Публикација кандидата из ове линије рада је:

1. **Jakša Vučičević**, Thomas Ayral, Olivier Parcollet, "TRILEX and *GW*+EDMFT approach to *d*-wave superconductivity in the Hubbard model"
Phys. Rev. B 96, 104504 (2017)

Суперпроводни сценарио платоа 5/2 у фракционом квантном Холовом ефекту

Током 2018. године, кандидат је сарађивао са др Милицом Миловановић на истраживању могућих основних стања електронског гаса у јаком магнетном пољу које одговара фактору попуњености 5/2 у фракционом квантном Холовом ефекту. Основно стање у том случају се очекује да садржи спаривање електрона истог спина, *p* типа. У оквиру апроксимације једног Ландау нивоа са масеним чланом који слама честица-рупа симетрију и на тај начин описује ефекат присуства осталих Ландау нивоа, показано је да основно стање заиста има нестабилност ка спаривању. Описане су нестабилности ка трију врста спаривања, које одговарају вишечестичним стањима честица-рупа-симетричном Пфафијану, као и Пфафијану и анти-Пфафијану који су међусобно симетрични до на предзнак масеног члана. Налази ове поједностављене теорије су у складу са софистицираним нумеричким симулацијама из литературе.

Кандидат је у овој линији рада допринео имплементацијом самоусаглашене једначине средњег поља, продукцијом нумеричких резултата и писањем одговарајућег дела публикација.

Публикације кандидата из ове линије рада су:

1. L. Antonić, **J. Vučičević**, M. V. Milovanović, "Paired states at 5/2: PH Pfaffian and particle-hole symmetry breaking"
Phys. Rev. B 98, 115107 (2018)

2. M.V. Milovanović, S. Djurdjević, **J. Vučičević**, L. Antonić, "Pfaffian paired states for half-integer fractional quantum Hall effect"
Modern Physics Letters B 34, 2030004 (2020)

3.3. Нумеричке методе за решење интерагујућим фермиона на решетки

Проблем интерагујућих фермиона на решетки је један од најтежих у свој теоријској физици. У корену проблема је експоненцијално растући простор стања квантних вишечестичних система са величином тих система. Директна решења методима егзактне дијагонализације Хамилтонијана су ограничена на мале системе до око 16 чворова решетке. То није задовољавајуће за разматрања на ниској температури и у присуству средње- или дуго-дометних корелација. Решење се обично тражи помоћу метода заснованим на Монте Карло сумацији бесконачних редова који су добијени некаквим развојем партиционе функције или

опсервабли од интереса. Овакве методе могу бити јако моћне, али се и често наилази на непремостив проблем "фермионског знака" (проблем осцилаторних подинтегралних функција). Чак и када га је могуће превазићи, преостаје и проблем аналитичког продужења које уноси неконтролисану систематску грешку у резултате за динамичке (тј. фреквентно зависне) опсервабле. Последњих деценија у току је изузетан напор физичарске заједнице да се фомулишу методи базирани на Монте Карло сумацијама који су и контролисани и заобилазе проблеме знака и аналитичког продужења.

Рубтсов Монте Карло (CTINT), TRILEX и метод угњеждених кластера

Један од најуспешнијих Монте Карло приступа решењу модела решетке је Рубтсов алгоритам (CTINT). Међутим, као и други слични алгоритми, решење постаје рачунски неизводиво за велике решетке, на ниској температури, и у одсуству честица-рупа симетрије. Иако је оваквим приступом могуће третирати веће решетке него егзактном дијагонализацијом, и даље остају присутни ефекти коначности решетке који су непожељни. Један систематски приступ је да се коначна решетка решава у присуству некаквог самоусаглашеног медијума који уноси у систем ефекте остатка бесконачне решетке (приступ "урођеног кластера", quantum embedding, QE). Самоусаглашеност медијума се може остварити на различите начине, па на основу тога разликујемо неколико различитих QE метода (у том смислу, DMFT се може сматрати најједноставнијим QE методом).

Током постдокторског усавршавања 2015-2017. године у групи др Оливијеа Парколеа, кандидат је радио на развоју и имплементацији TRILEX методе за решење Хабардовог модела. TRILEX метода је по духу слична DMFT методи, али иде корак даље у комплексности објекта који се апроксимира рачуном на коначној решетки. Док се у DMFT приступу и његовим директним генерализацијама апроксимира сопствена енергија електрона, у TRILEX методу се апроксимира иредуцибилни електрон-бозон вертекс, тј. фреквентно и просторно зависна амплитуда расејања електрона о флуктуације густине наелектрисања и спина. Ово омогућава да се заобиђе ограничење DMFT методе и њених уопштења у којима је сопствена-енергија или локална или краткодомента величина или, пак, величина дисконтинуална у простору импулса. У TRILEX методу, сопствена енергија може бити произвољног домета, и континуална је у простору импулса. Ово долази по цени потребе да урођени кластер садржи временски зависне интеракције. За ово је било потребно уопштити Рубтсов алгоритам који се користи за решење урођеног кластера.

Током 2015-2016. год., кандидат је уопштио једначине Рубтсов алгоритма на случај временски зависних интеракција, формулисао неколико додатних унапређења везаних за ефикасност калкулације и имплементирао одговарајуће измене у постојећој C++ имплементацији CTINT. Програмски код на коме је кандидат радио је део TRIQS бибилотеке који се и данас активно користи и цитира се у дугом низу публикација. Од 2017. рад на том коду је преузео др Нилс Венцел са Flatiron института у Њујорку.

Као што је већ поменуто под ставком **3.2.**, кандидат је током 2016-2017. развио и уопштење TRILEX метода у Намбу простору што омогућава третман супрпроводности у Хабардовом моделу.

Такође у периоду 2016-2017. године, кандидат је развио дуго чекано уопштење метода угњеждених кластера (NCS). NCS је оригинално формулисан још давне 1995. године (A. Schiller and K. Ingersent, Phys. Rev. Lett. **75**, 113 (1995)) и прво је уопштење DMFT метода за дводоимензионалне решетке. Осовна идеја NCS је да се уместо једно урођеног кластера решава више њих самоусаглашено, и да се сопствена-енергија реконструише линеарном комбинацијом вредности добијених у тим кластерима тако да се сваки дијаграм урачуна

тачно једном. На тај начин избегавају се проблеми других уопштења DMFT која укључују или вештачко сламање транслаторне симетрије, или дисконтинуалност сопствене енергије у импулсном простору. Оригинално, метод је формулисан само за кластере величине 2 чвора, а пуно уопштење на кластере произвољне величине и облика није било могуће. Уз помоћ алгоритама симболичке алгебре, кандидат је успео да формулише општи NCS метод, за кластере произвољне величине и облика. Метод је имплементирао и подробно истестирао у поређењу са преосталим QE методима. Резултати ове велике систематске студије су открили суштинско ограничење метода који се заснивају на апроксимацијама Латинџер-Ворд функционала слободне енергије. Овај недостатак NCS теорије се испољава у режиму јаких интеракција, и у сличном облику је тада први пут примећен и у другим методима, првенствено методу DCA+. Ово је мотивисало даљи рад, и довело до публикације Phys. Rev. B **101**, 195114 (2020) где су потврђени налази рада кандидата и предложена одговарајућа унапређења методе DCA+.

Рад кандидата на развоју CTINT и QE метода се може сматрати важним помаком у методологији и важном основом за даљи развој у изузетно активној области, што потврђују и цитати у скорашњем прегледном раду Rev. Mod. Phys. **90** 025003 (2018).

Публикације кандидата из ове линије рада су:

1. **Jakša Vučičević**, Nils Wentzell, Michel Ferrero, Olivier Parcollet, "Practical consequences of Luttinger-Ward functional multivaluedness for cluster DMFT methods"
Phys. Rev. B 97, 125141 (2018)

2. Thomas Ayral, **Jaksa Vučičević**, Olivier Parcollet ,"The Fierz convergence criterion: a controlled approach to strongly-interacting systems with small embedded clusters"
Phys. Rev. Lett. 119, 166401 (2017)

3. **Jakša Vučičević**, Thomas Ayral, Olivier Parcollet,"TRILEX and *GW*+EDMFT approach to *d*-wave superconductivity in the Hubbard model"
Phys. Rev. B 96, 104504 (2017)

Дијаграматски Монте Карло у домену реалне фреквенције

Дијаграматски Монте Карло методи су класа алгоритама у којима се врши прорачун појединачних Фајнманових дијаграма у интеракционом развоје неке физичке величине. Овај метод има предност да може директно третирати термодинамички лимит, али је ограничен на релативно ниске вредности константе интеракције. Ипак, од скора је показано да се овај метод може одговарајуће уопштити тако да омогући приступ и режиму јачих интеракција и већу ефикасност. Ово је довело да обновљеног интересовања за дијаграматски Монте Карло. Међутим, као и у свим методима у Мацубара формализму, остаје проблем аналитичког продужења.

Од 2018. год. кандидат се бави формулацијом дијаграматског Монте Карла у домену реалне фреквенције, што омогућава да се избегне потреба за аналитичким продужењем. Могућност да се оваква реформулација постигне је препозната независно и првобитно објављена у публикацији групе др Џејмса Леблана (Њуфаундленд, Канада) 2018. год. У сарадњи са др Мишел Ферером (College de France, Париз), кандидат је развио прву имплементацију дијаграматског Монте Карла у домену реалне фреквенце, што је вероватно први потпуно контролисани прорачун спектралне функције у Хабардовом моделу у нетривијалном режиму параметара и близу термодинамичког лимита.

Основа за овај рад је алгоритам симболичке алгебре који егзактно решава вишеструке интерне суме по Мацубара фреквенцијама које фигуришу у доприносима сваког појединачног дијаграма. Решења аналитичког дела су често изрази који у меморији рачунара заузимају читаве мегабајте, а њихова нумеричка евалуација представља велики изазов и захтева употребу низа напредних алгоритамских и програмерских техника, везано за тачност и ефикасност.

У последњих годину дана, кандидат је додатно уопштио и унапредио овај метод, употребом раније непознатог аналитичког решења вишеструких интеграла по имагинарном времену који фигуришу у одговарајуће формулисаним Фајнмановим дијаграмима (публикација је у припреми).

Публикација кандидата из ове линије рада је:

1. **Jakša Vučičević,** Michel Ferrero, "Real-frequency Diagrammatic Monte Carlo at Finite Temperature"
Phys. Rev. B 101, 075113 (2020)

4. ЕЛЕМЕНТИ ЗА КВАЛИТАТИВНУ ОЦЕНУ НАУЧНОГ ДОПРИНОСА КАНДИДАТА

4.1 Квалитет научних резултата

4.1.1 Научни ниво и значај резултата, утицај научних радова

Др Јакша Вучичевић је у свом досадашњем раду објавио 13 радова у међународним часописима са ISI листе, од којих 4 у категорији М21а, 8 у категорији М21, и 1 у категорији М23. У периоду након одлуке Научног већа о предлогу за стицање претходног научног звања, др Јакша Вучичевић је објавио 8 радова у међународним часописима са ISI листе од којих 2 у категорији М21а, 5 у категорији М21 и 1 у категорији М23. Као пет најзначајнијих радова кандидата могу се узети (број цитата на основу базе Scopus):

1. **J. Vučičević** and M. Ferrero, "Real-frequency diagrammatic Monte Carlo at finite temperature", Phys. Rev. B 101, 075113 (2020)
Цитиран 2 пута

2. **J. Vučičević**, J. Kokalj, R. Žitko, N. Wentzell, D. Tanasković, J. Mravlje, “Conductivity in the Square Lattice Hubbard Model at High Temperatures: Importance of Vertex Corrections”, Phys. Rev. Lett. 123, 036601 (2019)
Цитиран 5 пута

3. **J. Vučičević**, N. Wentzell, M. Ferrero, and O. Parcollet, "Practical consequences of the Luttinger-Ward functional multivaluedness for cluster DMFT methods", Phys. Rev. B 97, 125141 (2018)
Цитиран 14 пута

4. **J. Vučičević**, D. Tanasković, M. J. Rozenberg, and V. Dobrosavljević, "Bad-Metal Behavior Reveals Mott Quantum Criticality in Doped Hubbard Models", Phys. Rev. Lett. 114, 246402 (2015)
Цитиран 35 пута

5. H. Terletska, **J. Vučičević**, D. Tanasković, and V. Dobrosavljević, “Quantum Critical Transport

near the Mott Transition”,
Phys. Rev. Lett. 107, 026401 (2011)
Цитиран 54 пута

Радови 4. и 5. су били део докторске дисертације кандидата. У раду 5. је уведен појам квантне критичности Мотовог прелаза и успостављено квантно критично скалирање вредности отпора на високим темпратурама у оквиру DMFT теорије за полупопуњени Хабардов модел. Налази теорије су потврђени након тога у експериментима на капа-органским системима, а концепт квантне критичности Мотовог прелаза је преузет и испитиван у низу теоријских радова, што потврђује висока цитираност рада. Рад 4. је уопштење теорије из рада 5. на случај допираног Хабардовог модела, где је показано слагање са мерењима на чувеном високотемпературном суперпроводнику LSCO.

Рад 3. је написан током боравка кандидата на постдокторском усавршавању у Француској. Теорија представљена у том раду је више од две деценије чекано уопштење метода угњеждених кластера на кластере произвољног облика и величине. У раду је представљено и систематско поређење постојећих метода за решење Хабардовог модела, што ће користити као основа за даљи развој теоријских апроксимација. У раду је откривен инхерентни недостатак Лутинџер-Ворд функционала као основе за контролисане апроксимације са задовољеним законима одржања, махом коришћене већ 50 година. Конкретно, показан је недостатак теорије DCA+, што је накнадно потврђено, и што је довело до нових предлога за унапређње те теорије.

У раду 2., установљено је нумерички егзактно решење за проводност Хабардовог модела на високим температурама. Ово је изузетно важно за интерпретацију скорашњег експеримента на хладним атомима у оптичкој решетки (P. T. Brown et. al., Science 363, 379 (2019)). Такође, у раду је дат одговор на вишедеценијско питање важности вертекс корекција за проводност Хабардовог модела у две димензије. Очекује се да ће методологија и подробна анализа резултата које су приказане у раду имати важан утицај на будућа теоријска испитивања.

У раду 1., развијен је први дијаграматски Монте Карло метод на бази Мацубара формализма, који не захтева аналитичко продужење и даје потпуно контролисан резултат за спектралне особине (и потенцијално друге динамичке опсервабле). Ово је значајан методолошки искорак који се очекује да ће у будућности омогућити боље разумевање спектралних особина купрата, као и самог Хабард модела и његових експерименталних реализација у експериментима са хладним атомима у оптичкој решетки.

4.1.2 Позитивна цитираност научних радова кандидата

Подаци о цитирању радова кандидата на дан 16. 9. 2020. су сумирани у наредној табели:

База података	Број цитата	Број цитата без самоцитата	h-index
Scopus	190	172	8
Web of Science	181	164	8

Радови кандидата су цитирани у часописима Reviews of Modern Physics, Science, Nature Physics, Nature Materials, Nature Photonics, Reports on Progress in Physics и многим другим.

4.1.3 Параметри квалитета часописа

Процена квалитета часописа у којима је кандидат објављивао се може учинити на основу импакт фактора. Импакт фактор (ИФ) се мења из године у годину па ниже наводимо најбољу вредност из периода до две године уназад од када је рад објављен. Подвученим се означава број радова након одлуке Научног већа о предлогу за стицање претходног научног звања.

1. 4 рада (2+2) у часопису Physical Review Letters (категорија М21а)
(ИФ: 1 рад 7.622, 1 рад 7.728, 1 рад 8.839, 1 рад 9.227)

2. 8 радова (5+3) у часопису Physical Review B (категорија М21)
(ИФ: 1 рад 3.774, 1 рад 3.767, 3 рада 3.736, 3 рада 3.836)

3. 1 рад (1+0) у часопису Modern Physics Letters B (категорија М23)
(ИФ: 1.224)

Укупан фактор утицаја радова кандидата је 64,897, а у периоду након одлуке Научног већа о предлогу за стицање претходног научног звања тај фактор је 38.27.

Часопис Physical Review Letters је нарочито цењен у области физике кондензованог стања материје, а најцитиранији је часопис у свој физици.

Додатни библиометријски показатељи у вези са објављеним радовима кандидата након одлуке Научног већа о предлогу за стицање претходног научног звања дати су у доњој табели. Она садржи импакт факторе (ИФ) радова, М бодове радова по српској категоризацији научноистраживачких резултата, као и импакт фактор нормализован по импакту цитирајућег чланка (СНИП) (користимо најбољу вредност из периода до две године уназад од објаве рада). У табели су дате укупне вредности, као и вредности свих фактора усредњених по броју чланака и по броју аутора по чланку, за радове објављене у категоријама

	ИФ	М	СНИП
Укупно	38.27	63	11.49
Усредњено по чланку	4.784	7.875	1.436
Усредњено по аутору	10.708	18.226	3.230

4.1.4 Степен самосталности и степен учешћа у реализацији радова у научним центрима у земљи и иностранству

Кандидат је водећи аутор 7 радова, други аутор 4 рада, а трећи аутор 2 рада.

На радовима који су објављени у периоду након избора у претходно звање, кандидат је водећи аутор 4 рада, други аутор 2, и трећи аутор једног рада.

У периоду након доктората, кандидат је у свим публикацијама доприносио имплементацијом нумеричких метода и/или продукцијом резултата, а активно је учествовао на формулисању тема радова, одабиру методологије, а често и предводио имплементацију и анализу резултата и поређење са експериментима. Кандидат је имао важну улогу у конципирању и писању већине публикација.

Нарочито у скорашњој линији рада везаној за дијаграматски Монте Карло, кандидат је самостално осмислио метод и у потпуности га имплементирао и истестирао, самостално

продуковао резултате и написао публикацију, док је коаутор Мишел Фереро имао саветодавну улогу. Кандидат наставља да предводи ову линију рада.

У скорије време, кандидат предводи три линије рада у оквиру ПРОМИС пројекта Фонда за науку којег је руководилац, са сарадницима Михаилом Чубровићем, Аном Худомал, Вељком Јанковићем и Иваном Васић. Кандидат такође предводи сарадњу са Роком Житком са института Јозеф Стефан у Љубљани у коју је укључен и студент мастер студија Павле Стипсић.

У току боравка на постдокторском усавршавању у Француској, нарочито се истиче допринос кандидата у раду на методи угњеждених кластера (NCS). Кандидат је самостално открио симболичку технику којим се може уопштити NCS, самостално имплементирао велики број метода које се у том раду користе, и самостално испродуковао највећи део резултата који су у раду приказани. Такође, кандидат је дао централни допринос у анализи добијених резултата и резултата из литературе доневши хипотезу о вези неуспеха појединих теорија и дивергенције иредуцибилног вертекса и предложивши начин да се та хипотеза провери.

У истом периоду, кандидат је предводио истраживање везано за суперпроводност у Хабардовом моделу, и предложио највећи број прорачуна и анализа које су у тој публикацији приказане.

4.1.5 Награде

Кандидат је добитник Студентске награде Института за физику у Београду 2016. године за најбољу докторску дисертацију урађену током претходне године.

Прилог: извештај комисије за доделу Студентске награде Института за физику у Београду 2016. год.

4.2 Ангажованост у формирању научних кадрова

Кандидат др Јакша Вучичевић је од октобра 2019. ментор Павла Стипсића, студента мастер студија на Физичком факултету Универзитета у Београду.

Прилог: извештај са седнице ННВ Физичког факултета

Током 2017-2019. кандидат је помагао у раду докторанда Willem-Victor van Gerven Oei-ја што се може закључити и из захвалнице у његовом раду W. -V. van Gerven Oei, D. Tanasković, J. Phys.: Condens. Matter 32 325601 (2020) и захвалнице у његовој тези која је тренутно на увиду јавности.

Прилог: насловна страна и захвалница докторске тезе Willem-Victor van Gerven Oei-ја.

Кандидат је одржао два предавања у оквиру предмета Модерна физика за студенте треће године основних студија на Физичком факултету у Београду на тему нумеричких метода у вишечестичној квантној физици, 2017 и 2019 године.

Кандидат је одржао једно предавање на семинару физике у Истраживачкој станици Петница, и био је ментор два полазника (Богдана Поповића и Богдана Рајкова).

4.3 Нормирање броја коауторских радова, патената и техничких решења

Сви радови кандидата спадају у категорију у категорију радова са нумеричким симулацијама који се признају са пуним бројем М бодова до пет коаутора.

Број М бодова које је кандидат остварио након одлуке Научног већа о предлогу за стицање претходног научног звања је 63, а након нормализације са бројем коаутора тај број постаје 59.04. Нормирање не утиче значајно на број бодова, а кандидат свакако има већи број бодова од захтеваног.

4.4 Руковођење пројектима, потпројектима и пројектним задацима

Од 2018. год. кандидат руководи потпројектом “Транспорт наелектрисања, суперпроводност и динамика решетке у јако корелисаним материјалима” у оквиру Центра изузетних вредности за изучавање комплексних система Института за физику у Београду. Тренутно ангажовани на потпројекту су др Дарко Танасковић, др Милош Радоњић, докторанд Willem-Victor van Gerven Oei и студент мастер студија Павле Стипсић.

Прилог: потврда руководиоца пројекта о руковођењу потпројектом.

Кандидат руководи српском страном билатералног пројекта са републиком Немачком (DAAD) "Електронске корелације у оксидима са трансфером наелектрисања: функције одзива и дугодометна уређења" за период 2020-2021. године.

Прилог: листа одобрених пројеката

Кандидат руководи ПРОМИС пројектом Фонда за науку "Хладни атоми, Хабардов модел и холографија: кључ за чудне метале" за период 2020-2021. год. На пројекту су ангажовани Михаило Чубровић, Ивана Васић и Ана Худомал.

Прилог: email обавештење о финансирању пројекта и листа одобрених пројеката.

4.5 Активност у научним и научно-стручним друштвима

Кандидат је рецензент у следећим научним часописима: Physical Review Letters, Physical Review B, Physical Review E. Од октобра 2017. урадио је 34 рецензије.

Прилог: потврда уредништва часописа

4.6 Утицајност научних резултата

Утицајност научних резултата кандидата је наведена у одељцима **3** и **4.1** овог документа. Пун списак радова је дат у одељку **6**, а подаци о цитираности са интернет странице базе Scopus су дати након списка свих радова кандидата.

4.7 Конкретан допринос кандидата у реализацији радова у научним центрима у земљи и иностранству

Кандидат је значајно допринео сваком раду у чијој припреми је учествовао.

Од 8 радова објављених у периоду након одлуке Научног већа Института за физику о предлогу за стицање претходног научног звања, 7 је урађено у сарадњи са колегама из иностранства (Француска, САД, Словенија, Црна Гора), а 4 су урађена у сарадњи са колегама

из земље. Др Вучичевић је имао кључни допринос у публикацијама на којима је први аутор (4 рада) и други аутор (3 рада).

Кандидат је увек учествовао у избору теме и методологије, често самостално имплементирао методе и продуковао резултате, а дао је више пута и централни допринос у анализи и интерпретацији резултата као и поређењу са експериментима и радовима из литературе. Учествовао је у писању сваке публикације и често био задужен за конципирање манускрипта. Детаљан опис доприноса за неке од појединачних публикација је дат у секцији **4.1.4.**

4.8 Уводна предавања на конференцијама и друга предавања

У периоду након одлуке Научног већа о предлогу за стицање претходног звања, кандидат је одржао 2 предавања по позиву на међународним конфененцијама.

1. "Introducing the LMDB project", TRIQS meeting, 14-15. јун 2018. год., College de France, Париз, Француска.

Прилог: распоред конференције и списак учесника.

2. "Conductivity in the Hubbard model", СФКМ, 7-11. октобар 2019. год., Београд.

Прилог: списак предавача по позиву са интернет сајта конференције

Кандидат је у истом периоду одржао и 4 семинара на Институту за физику:

1. "Beyond DMFT - capturing low temperature physics of the cuprates", 21. децембар 2016.

2. "C++ and Python - modern programming techniques", 28. фебруар 2017.

3. "Monte Carlo methods for general lattice fermions", 3. март 2017.

4. "Lattice Model Database (LMDB)", 5. јул 2018.

Др Вучичевић је одржао и предавање на Природно-математичком факултету у Новом Саду у оквиру радног састанка СПРУН 7.0:

"Оптимизација дијаграматски Монте Карло методе за решење интерагујућих модела решетке: симболички алгоритми и аритметика високе прецизности", 26. децембар 2019.

5. ЕЛЕМЕНТИ ЗА КВАНТИТАТИВНУ ОЦЕНУ НАУЧНОГ ДОПРИНОСА КАНДИДАТА

Остварени резултати у периоду након одлуке Научног већа о предлогу за стицање претходног научног звања:

Категорија	М бодова по раду	Број радова	Укупно М бодова	Нормирани број М бодова
M21a	10	2	20	18.333
M21	8	5	40	37.714
M23	3	1	3	3

Поређење са минималним квантитативним условима за избор у звање виши научни сарадник:

Минимални број М бодова		Оствaррено М бодова, без нормирања	Остварено М бодова, са нормирањем
Укупно	50	63	59.047
M10+M20+M31+M32+M33+M41+M42+M90	40	63	59.047
M11+M12+M21+M22+M23	30	63	59.047

Према бази података Scopus (Web of Science) на дан 16. септембра 2020. године, радови кандидата су цитирани укупно 190 (181) пута, односно 172(164) пута не рачунајући самоцитате. Према обе базе, Хиршов индекс кандидата је 8.

6. СПИСАК РАДОВА ДР ЈАКШЕ ВУЧИЧЕВИЋА

6.1 Радови у међународним часописима изузетних вредности (M21a)

Радови објављени након претходног избора у звање

1. "Conductivity in the square lattice Hubbard model at high temperatures: importance of vertex corrections "
Аутори: **Jaksa Vučičević**, Jure Kokalj, Rok Žitko, Nils Wentzell, Darko Tanasković, Jernej Mravlje
Phys. Rev. Lett. 123, 036601 (2019)
(најбољи ИФ 2017-2019: 9.227)

2. "The Fierz convergence criterion: a controlled approach to strongly-interacting systems with small embedded clusters"
Аутори: Thomas Ayral, **Jaksa Vučičević**, Olivier Parcollet
Phys. Rev. Lett. 119, 166401 (2017)
(најбољи ИФ 2015-2017: 8.839)

Радови објављени пре претходног избора у звање

1. "Bad-metal behavior reveals Mott quantum criticality in doped Hubbard models"
Аутори: **J. Vučičević**, D. Tanasković, M. Rozenberg, V. Dobrosavljević
Phys. Rev. Lett. 114, 246402 (2015)
(најбољи ИФ 2013-2015: 7.728)

2. "Quantum Critical Transport Near the Mott Transition "
Аутори: H. Terletska, **J. Vučičević**, D. Tanasković, V. Dobrosavljević
Phys. Rev. Lett. 107, 026401 (2011)
(најбољи ИФ 2009-2011: 7.622)

6.2 Радови у врхунским међународним часописима (M21)

Радови објављени након претходног избора у звање

1. "Charge transport in the Hubbard model at high temperatures: triangular versus square lattice"
Аутори: A. Vranić, **J. Vučičević**, J. Kokalj, J. Skolimowski, R. Žitko, J. Mravlje, D. Tanasković
Phys. Rev. B 102, 115142 (2020)
(најбољи ИФ 2018-2019: 3.736)

2. "Real-frequency Diagrammatic Monte Carlo at Finite Temperature"
Аутори: **Jakša Vučičević,** Michel Ferrero
Phys. Rev. B 101, 075113 (2020)
(најбољи ИФ 2018-2019: 3.736)

3. "Paired states at 5/2: PH Pfaffian and particle-hole symmetry breaking"
Аутори: L. Antonić, **J. Vučičević**, M. V. Milovanović
Phys. Rev. B 98, 115107 (2018)
(најбољи ИФ 2016-2018: 3.836)

4. "Practical consequences of Luttinger-Ward functional multivaluedness for cluster DMFT methods"
Аутори: **Jakša Vučičević**, Nils Wentzell, Michel Ferrero, Olivier Parcollet
Phys. Rev. B 97, 125141 (2018)
(најбољи ИФ 2016-2018: 3.836)

5. "TRILEX and *GW*+EDMFT approach to *d*-wave superconductivity in the Hubbard model"
Аутори: **Jakša Vučičević**, Thomas Ayral, Olivier Parcollet
Phys. Rev. B 96, 104504 (2017)
(најбољи ИФ 2015-2017: 3.836)

Радови објављени пре претходног избора у звање

1. "Anderson localization effects near the Mott metal-insulator transition"
Аутори: H. Braganca, M. C. O. Aguiar, **J. Vučičević**, D. Tanasković, V. Dobrosavljević
Phys. Rev. B 92, 125143 (2015)
(најбољи ИФ 2013-2015: 3.736)

2. "Finite temperature crossovers and the quantum Widom line near the Mott transition"
Аутори: **J. Vučičević**, H. Terletska, D. Tanasković, V. Dobrosavljević
Phys. Rev. B 88, 075143 (2013)
(најбољи ИФ 2011-2013: 3.767)

3. "d-wave superconductivity on the honeycomb bilayer"
Аутори: **J. Vučičević**, M. O. Goerbig, M. V. Milovanovic
Phys. Rev. B 86, 214505 (2012)
(најбољи ИФ 2010-2012: 3.774)

6.3 Радови у међународним часописима (М23)

Радови објављени након претходног избора у звање

1. "Pfaffian paired states for half-integer fractional quantum Hall effect"
Аутори: M.V. Milovanović, S. Djurdjević, **J. Vučičević**, L. Antonić
Modern Physics Letters B 34, 2030004 (2020)
(најбољи ИФ 2018-2020: 1.224)

Citation report for 12 results from Web of Science Core Collection between 1996 and 2021 Go

You searched for: **AUTHOR:** (vucicevic j*) **...More**

This report reflects citations to source items indexed within Web of Science Core Collection. Perform a Cited Reference Search to include citations to items not indexed within Web of Science Core Collection.

Export Data: Save to Excel File

Total Publications	*h*-index	Sum of Times Cited	Citing articles
12 Analyze	8	181	138 Analyze
2001 – 2020	Average citations per item: 15.08	Without self citations: 164	Without self citations: 130 Analyze

Sum of Times Cited per Year

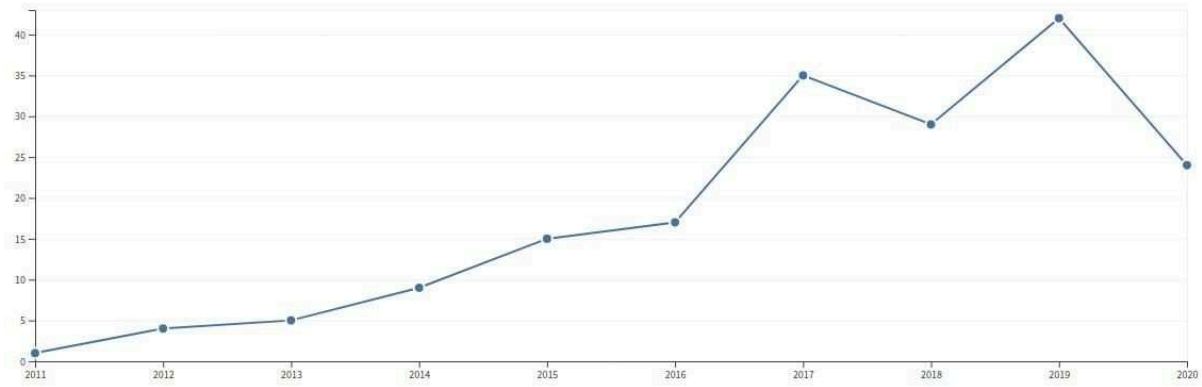

Sort by: Times Cited Date More

How are these totals calculated?

Use the checkboxes to remove individual items from this Citation Report

or restrict to items published between 1996 and 2021 Go

		2017 ◄	2018	2019	2020	2021 ►	Total	Average Citations per Year
		35	29	42	24	0	181	18.10
1.	**Quantum Critical Transport near the Mott Transition** By: Terletska, H.; Vucicevic, J.; Tanaskovic, D.; et al. PHYSICAL REVIEW LETTERS Volume: 107 Issue: 1 Article Number: 026401 Published: JUL 5 2011	12	5	5	5	0	51	5.10
2.	**Bad-Metal Behavior Reveals Mott Quantum Criticality in Doped Hubbard Models** By: Vucicevic, J.; Tanaskovic, D.; Rozenberg, M. J.; et al. PHYSICAL REVIEW LETTERS Volume: 114 Issue: 24 Article Number: 246402 Published: JUN 18 2015	8	4	10	3	0	34	5.67
3.	**Finite-temperature crossover and the quantum Widom line near the Mott transition** By: Vucicevic, J.; Terletska, H.; Tanaskovic, D.; et al. PHYSICAL REVIEW B Volume: 88 Issue: 7 Article Number: 075143 Published: AUG 28 2013	8	3	6	3	0	26	3.25
4.	**Practical consequences of the Luttinger-Ward functional multivaluedness for cluster DMFT methods** By: Vucicevic, J.; Wentzell, N.; Ferrero, M.; et al. PHYSICAL REVIEW B Volume: 97 Issue: 12 Article Number: 125141 Published: MAR 23 2018	0	5	6	4	0	15	5.00
5.	**d-wave superconductivity on the honeycomb bilayer** By: Vucicevic, J.; Goerbig, M. O.; Milovanovic, M. V. PHYSICAL REVIEW B Volume: 86 Issue: 21 Article Number: 214505 Published: DEC 7 2012	4	0	0	0	0	15	1.67

6. **Fierz Convergence Criterion: A Controlled Approach to Strongly Interacting Systems with Small Embedded Clusters** By: Ayral, Thomas; Vucicevic, Jaksa; Parcollet, Olivier PHYSICAL REVIEW LETTERS Volume: 119 Issue: 16 Article Number: 166401 Published: OCT 16 2017	0	4	5	0	0	9	2.25
7. **Anderson localization effects near the Mott metal-insulator transition** By: Braganca, Helena; Aguiar, M. C. O.; Vucicevic, J.; et al. PHYSICAL REVIEW B Volume: 92 Issue: 12 Article Number: 125143 Published: SEP 24 2015	2	3	1	2	0	9	1.50
8. **Paired states at 5/2: Particle-hole Pfaffian and particle-hole symmetry breaking** By: Antonic, L.; Vucicevic, J.; Milovanovic, M. V. PHYSICAL REVIEW B Volume: 98 Issue: 11 Article Number: 115107 Published: SEP 5 2018	0	0	6	2	0	8	2.67
9. **TRILEX and GW plus EDMFT approach to d-wave superconductivity in the Hubbard model** By: Vucicevic, J.; Ayral, T.; Parcollet, O. PHYSICAL REVIEW B Volume: 96 Issue: 10 Article Number: 104504 Published: SEP 5 2017	1	5	2	0	0	8	2.00
10. **Conductivity in the Square Lattice Hubbard Model at High Temperatures: Importance of Vertex Corrections** By: Vucicevic, J.; Kokalj, J.; Zitko, R.; et al. PHYSICAL REVIEW LETTERS Volume: 123 Issue: 3 Article Number: 036601 Published: JUL 19 2019	0	0	1	3	0	4	2.00
11. **Real-frequency diagrammatic Monte Carlo at finite temperature** By: Vucicevic, J.; Ferrero, Mi PHYSICAL REVIEW B Volume: 101 Issue: 7 Article Number: 075113 Published: FEB 12 2020	0	0	0	2	0	2	2.00
12. **Pfaffian paired states for half-integer fractional quantum Hall effect** By: Milovanovic, M., V; Djurdjevic, S.; Vucicevic, J.; et al. MODERN PHYSICS LETTERS B Volume: 34 Issue: 21 Article Number: 2030004 Published: JUL 30 2020	0	0	0	0	0	0	0.00

Select Page | Save to Excel File

Sort by: Times Cited | Date | More

12 records matched your query of the 48,820,467 in the data limits you selected.

Citation overview

Back to author details Export Print

This is an overview of citations for this author. Author *h*-index : 8 View *h*-graph

12 Cited Documents from"Vučičević, Jaksa" + Add to list

Author ID:57196122467

Date range: 2016 to 2020 Exclude self citations of selected author Exclude self citations of all authors Exclude citations from books Update

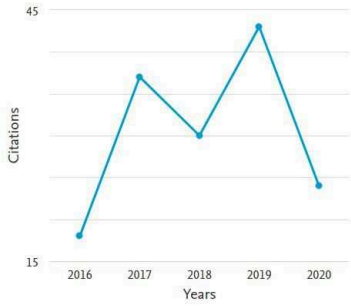

Sort on: Date (newest)

Page Remove

	Documents	Citations	<2016	2016	2017	2018	2019	2020	Subtotal	>2020	Total
		Total	38	18	37	30	43	24	152	0	190
1	Pfaffian paired states for half-integer fractional quantum H...	2020							0		0
2	Real-frequency diagrammatic Monte Carlo at finite temperatur...	2020						2	2		2
3	Conductivity in the Square Lattice Hubbard Model at High Tem...	2019					1	4	5		5
4	Paired states at 5/2: Particle-hole Pfaffian and particle-ho...	2018					6	1	7		7
5	Practical consequences of the Luttinger-Ward functional mult...	2018				5	6	3	14		14
6	Fierz Convergence Criterion: A Controlled Approach to Strong...	2017				4	5		9		9
7	TRILEX and GW +EDMFT approach to d -wave superconductivity i...	2017			1	5	2		8		8
8	Anderson localization effects near the Mott metal-insulator ...	2015		1	2	3	1	2	9		9
9	Bad-Metal Behavior Reveals Mott Quantum Criticality in Doped...	2015	2	7	9	4	10	3	33		35
10	Finite-temperature crossover and the quantum Widom line near...	2013	6	2	9	3	7	4	25		31
11	D-wave superconductivity on the honeycomb bilayer	2012	11		4	1			5		16
12	Quantum critical transport near the mott transition	2011	19	8	12	5	5	5	35		54

Display: 20 results per page 1 Top of page

Citation overview

Self citations of selected authors are excluded. ×

Back to author details Export Print

This is an overview of citations for this author. Author h-index : 7 View h-graph

12 Cited Documents from"Vučičević, Jaksa" + Add to list

Author ID:57196122467

Date range: 2016 to 2020 Exclude self citations of selected author Exclude self citations of all authors Exclude citations from books Update

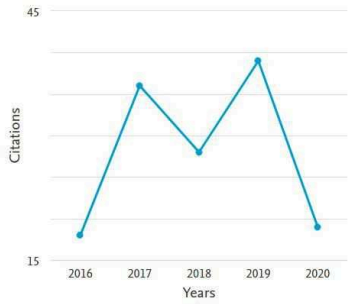

Sort on: Date (newest)

Page Remove

	Documents	Citations	<2016	2016	2017	2018	2019	2020	Subtotal	>2020	Total
		Total	32	18	36	28	39	19	140	0	172
1	Pfaffian paired states for half-integer fractional quantum H...	2020							0		0
2	Real-frequency diagrammatic Monte Carlo at finite temperatur...	2020						2	2		2
3	Conductivity in the Square Lattice Hubbard Model at High Tem...	2019					1	3	4		4
4	Paired states at 5/2: Particle-hole Pfaffian and particle-ho...	2018					6		6		6
5	Practical consequences of the Luttinger-Ward functional mult...	2018				5	5	3	13		13
6	Fierz Convergence Criterion: A Controlled Approach to Strong...	2017				3	4		7		7
7	TRILEX and GW +EDMFT approach to d -wave superconductivity i...	2017				4	2		6		6
8	Anderson localization effects near the Mott metal-insulator ...	2015		1	2	3	1	2	9		9
9	Bad-Metal Behavior Reveals Mott Quantum Criticality in Doped...	2015	1	7	9	4	9	2	31		32
10	Finite-temperature crossover and the quantum Widom line near...	2013	4	2	9	3	7	3	24		28
11	D-wave superconductivity on the honeycomb bilayer	2012	11		4	1			5		16
12	Quantum critical transport near the mott transition	2011	16	8	12	5	4	4	33		49

Display: 20 results per page 1 Top of page

Република Србија
МИНИСТАРСТВО ПРОСВЕТЕ,
НАУКЕ И ТЕХНОЛОШКОГ РАЗВОЈА
Комисија за стицање научних звања

Број:660-01-00011/534
30.03.2016. године
Б е о г р а д

На основу члана 22. става 2. члана 70. став 5. Закона о научноистраживачкој делатности ("Службени гласник Републике Србије", број 110/05 и 50/06 – исправка и 18/10), члана 50. став 1. Закона о изменама и допунама Закона о научноистраживачкој делатности ("Службени гласник Републике Србије", број 112/15) члана 2. става 1. и 2. тачке 1 – 4.(прилози) и члана 38. Правилника о поступку и начину вредновања и квантитативном исказивању научноистраживачких резултата истраживача ("Службени гласник Републике Србије", број 38/08) и захтева који је поднео

Институт за физику у Београду

Комисија за стицање научних звања на седници одржаној 30.03.2016. године, донела је

ОДЛУКУ
О СТИЦАЊУ НАУЧНОГ ЗВАЊА

Др Јакша Вучичевић
стиче научно звање
Научни сарадник

у области природно-математичких наука - физика

О Б Р А З Л О Ж Е Њ Е

Институт за физику у Београду

утврдио је предлог број 1289/1 од 22.09.2015. године на седници Научног већа Института и поднео захтев Комисији за стицање научних звања број 1322/1 од 01.10.2015. године за доношење одлуке о испуњености услова за стицање научног звања ***Научни сарадник***.

Комисија за стицање научних звања је по претходно прибављеном позитивном мишљењу Матичног научног одбора за физику на седници одржаној 30.03.2016. године разматрала захтев и утврдила да именовани испуњава услове из члана 70. став 5. Закона о научноистраживачкој делатности ("Службени гласник Републике Србије", број 110/05 и 50/06 – исправка и 18/10), члана 2. става 1. и 2. тачке 1 – 4.(прилози) и члана 38. Правилника о поступку и начину вредновања и квантитативном исказивању научноистраживачких резултата истраживача ("Службени гласник Републике Србије", број 38/08) за стицање научног звања ***Научни сарадник,*** па је одлучила као у изреци ове одлуке.

Доношењем ове одлуке именовани стиче сва права која му на основу ње по закону припадају.

Одлуку доставити подносиоцу захтева, именованом и архиви Министарства просвете, науке и технолошког развоја у Београду.

ПРЕДСЕДНИК КОМИСИЈЕ
Др Станислава Стошић-Грујичић,
научни саветник

МИНИСТАР
Др Срђан Вербић

УНИВЕРЗИТЕТ У БЕОГРАДУ
ИНСТИТУТ ЗА ФИЗИКУ БЕОГРАД
Прегревица 118, 11080 Земун - Београд, Србија
Телефон: +381 11 3713000, Факс: +381 11 3162190, www.ipb.ac.rs
ПИБ: 100105980, Матични број: 07018029, Текући рачун: 205-66984-23

Научном већу Института за физику

Извештај жирија за доделу Годишње награде за научни рад и Студентске награде Института за физику за 2016. годину

I) Годишња награда за научни рад

За Годишњу награду за научни рад Института за физику за 2016. годину предложена су четири кандидата:

1. **др Бранислав Саздовић**, научни саветник (предлагачи: др Бранислав Цветковић, виши научни сарадник, др Бојан Николић, виши научни сарадник, и др Љубица Давидовић, научни сарадник),
2. **др Марија Митровић Данкулов**, научни сарадник (предлагачи: др Александар Белић, научни саветник и др Милован Шуваков, виши научни сарадник),
3. **др Владимир Стојановић**, виши научни сарадник (предлагачи: др Жељка Никитовић, научни саветник и др Зоран Распоповић, виши научни сарадник), и
4. **др Магдалена Ђорђевић**, виши научни сарадник (предлагач: др Лидија Живковић, научни саветник).

Након детаљне квалитативне и квантитативне анализе научног доприноса кандидата током претходне две календарске године, а посебно узимајући у обзир квалитет објављених радова и њихов импакт на научну област, односно проблематику којој припадају, стваралачки удео кандидата у оствареним резултатима, удео Института у оствареним резултатима, као и број радова и њихове категорије у смислу Правилника о поступку и начину вредновања, и квантитативном исказивању научноистраживачких резултата Министарства надлежног за науку, **жири је донео једногласну одлуку да се Годишња награда за научни рад Института за физику за 2016. годину додели**

др Магдалени Ђорђевић
за значајан допринос разумевању кварк-глуонске плазме и развој модела динамичких губитака енергије.

Образложење:
Сви предложени кандидати имају импресиван научни опус и током претходне две календарске године су објавили нове и значајне резултате у међународним научним часописима и представили их на међународним конференцијама.

УНИВЕРЗИТЕТ У БЕОГРАДУ
ИНСТИТУТ ЗА ФИЗИКУ БЕОГРАД
Прегревица 118, 11080 Земун - Београд, Србија
Телефон: +381 11 3713000, Факс: +381 11 3162190, www.ipb.ac.rs
ПИБ: 100105980, Матични број: 07018029, Текући рачун: 205-66984-23

Др Бранислав Саздовић је проучавао Т-дуализацију бозонске струне у равном и слабо закривљеном простору и разматрао Т-дуализацију као трансформацију симетрије у дуплираном простору. Применом канонске методе извео је релацију за некомутативност координата затворене струне у најопштијем случају слабо закривљеног простора. Показао је да се Т-дуализација може репрезентовати у дуплираном простору као пермутација одређених подскупова иницијалних и Т-дуалних координата. У свом истраживању др Саздовић је дао и комплетну анализу трансформације дилатонског поља, која захтева квантни третман. Током претходне две календарске године, др Бранислав Саздовић је објавио укупно 5 радова у међународним часописима категорије М21.

Др Марија Митровић Данкулов се бавила проучавањем различитих колективних феномена у социјалним и техно-социјалним системима, као и развојем теорије комплексних мрежа. Она је у току 2014. и 2015. године објавила четири рада у међународним часописима категорије М21а (часописи који су према ИФ рангирани у својој области наука међу првих 10% часописа). У питању су публикације у изузетним часописима *Nature*, *Nature Communications* и *Scientific Reports*. Њен рад *Growing time lags threatens Nobel* објављен је у часопису *Nature* 2014. године и привукао је велику пажњу светских медија, како оних посвећених науци (*Phys.org, Scientific American*), тако и оних који се баве општим темама (*USA Today, SPIEGEL ONLINE, Business Standard*). О пажњи коју је привукао рад говори и његов Altmetric индекс који га сврстава у 5% чланака који су привукли највећу пажњу икада. Др Марија Митровић Данкулов је у својим радовима по први пут одредила минималан скуп тополошких особина које одређују структуру реалних комплексних мрежа и дефинисала начин квантификације њихове разлике од случајних мрежа. Такође је употребила методе статистичке физике и теорије комплексних мрежа за проучавање феномена настанка колективног знања у социјалним заједницама.

Др Владимир Стојановић се бавио проучавањем Таунсендовог пражњења и ударним процесима на високом односима енергије и густине плазме, као и изучавањем транспорта у смешама основног гаса са радикалима, при чему је посебну пажњу посветио проучавању транспортних коефицијената за расејање електрона у угљеник тетрафлуориду уз присуство различитих радикала. Др Стојановић се бавио и проучавањем транспортних и брзинских коефицијената јона у неутралном гасу који су од интереса за моделирање нискотемпературних плазми у употреби у медицини, као и прорачуном пресека и транспортних параметара за позитивне и негативне јоне у нискотемпературним плазмама. Током претходне две календарске године, др Владимир Стојановић је објавио 9 радова у међународним часописима, од тога 2 категорије М21, 2 категорије М22, 3 категорије М23 и 2 категорије М24.

Др Магдалена Ђорђевић се бавила проучавањем кварк-глуонске плазме, новог стања материје које настаје при великим густинама енергије и које се успешно формира при експериментима са сударима масивних језгара у ЦЕРН-у (LHC експерименти са течким јонима) и Brookhaven National Laboratory (RHIC експеримент). Др Ђорђевић је развила модел динамичких губитака енергије, који представља тренутно најнапреднији формализам за проучавање особина кварк-глуон плазме, и применила га на проучавање експерименталних резултата са LHC и RHIC. Ово је по први пут омогућило поређење широког опсега есперименталних података са теоријским предвиђањима која потичу од једног модела, и скупа парметара фиксираних на стандардне вредности из литературе. Анализа помоћу развијеног формализма и нумеричке процедуре је омогућила да др Магдалена Ђорђевић реши загонетку тешких кваркова у LHC-ју, што је објављено у

часопису P*hysical Review Letters*, на коме је она једини аутор. Ова загонетка у RHIC експериментима представља класичан, до тада нерешен проблем, а односи се на слично потискивање производње пиона (лаких честица) и електрона који настају распадом тешких честица. Слична загонетка се јавља и у LHC експериментима, и односи се на потискивање производње лаких хадрона и D мезона (тешких хадрона), при чему интуитивно тумачење указује на нарушавање QCD принципа у кварк-глуон плазми. За загонетку у RHIC експерименту, др Ђорђевић је показала да је последица комбинације ефеката проузрокованих губицима енергије, фрагментационих функција и распада честица у електроне. У *Physical Review Letters* раду је формулисала и решила загонетку тешких кваркова у LHC експериментима, при чему је показала да су експериментални резултати последица још једноставније феноменологије, тј. директна последица неочекиване комбинације ефеката проузрокованих губицима енергије и фрагментационих функција. Њени резултати су показали да се загонетке тешких кваркова могу у потпуности објаснити у оквиру пертурбативне хромодинамике.
Др Магдалена Ђорђевић је током претходне две календарске године објавила 10 радова у међународним часописима, од тога 6 категорије М21а, 1 категорије М21 и 3 категорије М22. Од тога су 7 оригинални научни радови (М21а и М21), а 3 су прегледни радови по позиву. Она је у 2015. години била и финалиста конкурса за ERC (European Research Council) Starter грант, при чему је њено дотадашње истраживање оцењено највишим оценама од стране референција и панела.

Закључак:
На основу свега наведеног, иако су сва четири кандидата дала значајне научне доприносе у свом раду током претходне две календарске године, истичући посебно радове др Марије Митровић Данкулов објављене у часописима *Nature* и *Nature Communications*, **сматрамо да** се научни резултати др Магдалене Ђорђевић посебно истичу по свом изузетном квалитету и значају, да доприносе повећању међународног угледа Института за физику, и да због тога **Годишњу награду за научни рад Института за физику за 2016. годину треба доделити др Магдалени Ђорђевић**.

II) Студентска награда

За Студентску награду Института за физику за 2016. годину предложено је пет кандидата:

1. **др Александар Матковић** (предлагач: др Радош Гајић, научни саветник),
2. **др Гордана Вуковић** (предлагач: др Мира Аничић Урошевић, научни сарадник),
3. **др Јакша Вучичевић** (предлагач: др Дарко Танасковић, виши научни сарадник),
4. **др Милка Јаковљевић** (предлагач: др Горан Исић, научни сарадник), и
5. **др Марија Марјановић** (предлагач: др Љиљана Симић, научни саветник).

Након детаљне анализе докторских теза и научних доприноса кандидата, а посебно узимајући у обзир квалитет теза и објављених радова и њихов импакт на научну област, односно проблематику којој припадају, стваралачки удео кандидата у

УНИВЕРЗИТЕТ У БЕОГРАДУ
ИНСТИТУТ ЗА ФИЗИКУ БЕОГРАД
Прегревица 118, 11080 Земун - Београд, Србија
Телефон: +381 11 3713000, Факс: +381 11 3162190, www.ipb.ac.rs
ПИБ: 100105980, Матични број: 07018029, Текући рачун: 205-66984-23

остваренim резултатима, удео Института у остваренim резултатима, као и број радова и њихове категорије у смислу Правилника о поступку и начину вредновања, и квантитативном исказивању научноистраживачких резултата Министарства надлежног за науку, **жири је донео једногласну одлуку да се Студентска награда Института за физику за 2015. годину додели**

др Јакши Вучичевићу
за докторску тезу под називом *"Signatures of Hidden Quantum Criticality in the High-temperature Charge Transport Near the Mott Transition".*

Образложење:
Жири констатује да су докторске тезе свих предложених кандидата изузетно високог квалитета. Сви кандидати су били изузетни студенти, а основне, мастер и докторске студије су завршили у сличном временском року, при чему се истиче др Гордана Вуковић која је студије завршила у рекордно кратком року. Сви кандидати имају значајан број објављених радова у квалитетним међународним часописима, а своје резултате су представили на бројним међународним и домаћим конференцијама.

Др Александар Матковић је докторску дисертацију под називом *Investigating the optical properties of graphene with spectroscopic ellipsometry* одбранио на Физичком факултету Универзитета у Београду, под руководством др Радоша Гајића. У својој дисертацији он се бавио мерењем оптичких особина графена у видљивом и ултраљубичастом делу спектра. Оптичке особине графена су измерене примењујући технике нулирајуће и спектроскопске елипсометрије.

Др Гордана Вуковић је докторску дисертацију под називом *Biomonitoring of urban air pollution (particulate matter, trace elements and polycyclic aromatic hydrocarbons) using mosses Sphagnum girgensohnii Russow and Hypnum cupressiforme Hedw* одбранила на Хемијском факултету Универзитета у Београду под руководством др Мире Аничић Урошевић. Њена дисертација је обухватала истраживање активног биомониторинга односно могућности коришћења трансплантираних маховина као индикатора квалитета ваздуха. Наиме, тестирала је различите параметре који утичу на примену ове методе у комплексним условима градске средине: врста маховине, припрема трансплanта, време експозиције маховина и висина експозиције над подлогом.

Др Јакша Вучичевић је докторску дисертацију под називом "*Signatures of Hidden Quantum Criticality in the High-temperature Charge Transport Near the Mott Transition*" одбранио на Физичком факултету Универзитета у Београду, под руководством др Дарка Танасковића. Докторска дисертација др Јакше Вучичевића је у области теоријске физике кондензоване материје и бави се проучавањем транспортних особина у близини Мотовог метал-изолатор прелаза из перспективе квантних фазних прелаза. Показано је да се особине Мотовог метал-изолатор прелаза у високо-температурном режиму између метала и изолатора поклапају са особинама које проистичу из претпоставке постојања квантне критичне тачке, упркос фазном прелазу првог реда и региону коегзистенције металне и изолаторске фазе којима је квантна критична тачка замаскирана.

Др Милка Јаковљевић је докторску дисертацију под називом *Проучавање плазмонских наноструктура коришћењем спектроскопске елипсометрије* одбранила на Електротехничком факултету Универзитета у Београду, под руководством др Радоша Гајића и др Горана Исића. Она се у својој дисертацији бави проучавањем

УНИВЕРЗИТЕТ У БЕОГРАДУ
ИНСТИТУТ ЗА ФИЗИКУ | БЕОГРАД
Прегревица 118, 11080 Земун - Београд, Србија
Телефон: +381 11 3713000, Факс: +381 11 3162190, www.ipb.ac.rs
ПИБ: 100105980, Матични број: 07018029, Текући рачун: 205-66984-23

локализованих површинских плазмона који се јављају у инфрацрвеном спектру тзв. прекинутих прстенова, који привлаче пажњу због тога што представљају компактне оптичке антене са израженим магнетним диполним моментом који се не среће у одзиву хомогених материјала у блиском инфрацрвеном спектру и вишим фреквенцијама. Значајна пажња у дисертацији је посвећена елипсометријском проучавању геп плазмон поларитона у метал-изолатор-метал структурама на бази злата и силицијум диоксида.

Др Марија Марјановић је докторску дисертацију под називом *Search for strongly produced Supersymmetric particles with the ATLAS detector and interpretation in the pMSSM model* одбранила на Универзитету Paris-Saclay у Француској. Ова дисертација је урађена под заједничким руководством dr Sophie Henrot-Versille (Orsay LAL) и др Марије Врањеш Милосављевић (Институт за физику, Универзитет у Београду), а реализована је у оквиру споразума о заједничком руководству над докторским дисертацијама између Универзитета Paris-Saclay и Универзитета у Београду. У својој дисертацији, др. Марија Марјановић се бави трагањем за суперсиметричним (SUSY) честицама, чије постојање је предвиђено Минималним суперсиметричним проширењем Стандардног модела. Проучавање фонских процеса са хадронским распадом тау лептона је најважнији допринос дисертације у овој анализи.

Закључак:
Имајући у виду разноликост истраживачких тема и области, разнородност доприноса кандидата, као и квалитет докторских теза и радова проистеклих из њих, било је изузетно тешко одабрати добитника овогодишње Студентске награде. Ипак, **жири се одлучио да награду додели др Јакши Вучичевићу**, због значаја главног научног резултата његове тезе. Теоријска предвиђања из његове тезе су истраживачи из Јапана недавно и експериментално потврдили у раду објављеном у часопису *Nature Physics*. Поред тога, посебно желимо да истакнемо и тезу др Гордане Вуковић која је урађена у рекордно кратком року, а представља систематичан и изузетно значајан допринос из области биомониторинга квалитета ваздуха.

На крају бисмо поново желели да истакнемо да су све овогодишње докторске тезе изузетно високог квалитета и да то видимо као велики успех предложених кандидата, њихових ментора и Института за физику. Посебно скрећемо пажњу да су сви кандидати наставили веома успешно са радом и након одбране својих докторских теза, и да су у међувремену објавили нове и значајне резултате.

Надамо се још јачој и бројнијој конкуренцији следеће године и свим кандидатима честитамо на изврсним научним резултатима, а добитницима на освојеним наградама.

Београд, 25. април 2016. год.

др Антун Балаж
научни саветник, Институт за физику

др Ненад Вукмировић
виши научни сарадник, Институт за физику

др Саша Дујко
научни саветник, Институт за физику

УНИВЕРЗИТЕТ У БЕОГРАДУ
ИНСТИТУТ ЗА ФИЗИКУ | БЕОГРАД
ИНСТИТУТ ОД НАЦИОНАЛНОГ ЗНАЧАЈА ЗА РЕПУБЛИКУ СРБИЈУ
Прегревица 118, 11080 Земун - Београд, Република Србија
Телефон: +381 11 3713000, Факс: +381 11 3162190, www.ipb.ac.rs
ПИБ: 100105980, Матични број: 07018029, Текући рачун: 205-66984-23

УНИВЕРЗИТЕТ У БЕОГРАДУ
ИНСТИТУТ ЗА ФИЗИКУ | БЕОГРАД
ИНСТИТУТ ОД НАЦИОНАЛНОГ ЗНАЧАЈА ЗА РЕПУБЛИКУ СРБИЈУ
www.ipb.ac.rs

0801 Број 779/1

Датум 22. 09. 2020

ПОТВРДА О РУКОВОЂЕЊУ ПОТПРОЈЕКТОМ

Овим потврђујем да научни сарадник **др Јакша Вучичевић,** за кога се покреће избор у звање виши научни сарадник, у оквиру Лабораторије за примену рачунара у науци Националног центра изузетних вредности за изучавање комплексних система Института за физику у Београду, руководи потпројектом: „Транспорт наелектрисања, суперпроводност и динамика решетке у јако корелисаним материјалима“. На поменутом потпројекту су ангажовани следећи истраживачи: др Јакша Вучичевић, др Милош Радоњић, др Дарко Танасковић и Willem-Victor van Gerven Oei.

др Антун Балаж
научни саветник
Руководилац Центра за изучавање комплексних система Института за физику у Београду

webmail

Mail Address Book Settings Logout

Folders

- Inbox
- Drafts
- Sent
- Junk
- Trash
- **inbox-20200221**
- Personal

Subject **Key2SM – Obaveštenje o finansiranju Projekta u okviru programa PROMIS**
From Fond za nauku - Programi
To jaksa.vucicevic@ipb.ac.rs
Date 2020-03-03 00:22

PROMIS-Final Evaluation-Key2SM.pdf (15 KB)

Poštovani dr Vučičević,

Obaveštavamo Vas da je predlog projekta koji ste podneli u okviru ovog javnog poziva Programa za izvrsne projekte mladih istraživača (u daljem tekstu: PROMIS) **odobren za finansiranje**.

Programski odbor za evaluaciju projekata, u skladu sa članom 26. stav 3. Akta o ciljevima, načinu realizacije i uslovima finansiranja projekata u okviru Programa za izvrsne projekte mladih istraživača, je formirao rang listu predloga projekata koji su zadovoljili oba stepena evaluacije i koji će biti finansirani u okviru raspoloživih sredstava PROMIS-a. Naučni savet Fonda za nauku je dao pozitivno mišljenje na tu listu, a Upravni odbor je usvojio kao konačnu listu Projekata kojima se odobrava finansiranje sredstvima Fonda za nauku Republike Srbije u okviru ovog javnog poziva programa PROMIS.

U prilogu Vam dostavljamo rezultat evaluacije Vašeg Projekta.

Konačnu listu Projekata odobrenih za finansiranje u okviru PROMIS-a možete pogledati na sajtu Fonda za nauku Republike Srbije na sledećem linku: PROMIS- konačna rang lista projekata odobrenih za finansiranje

U narednom koraku ćemo Vas kontaktirati radi pripreme i potpisivanja ugovora o finansiranju projekta.

Svečanost povodom dodele projekata će biti organizovana dana 11.03.2020. godine u 11:00 časova u Narodnom pozorištu, o čemu ćete biti dodatno obavešteni u narednom mailu.

Čestitamo Vama i projektnom timu na odobrenom projektu i radujemo se budućoj saradnji!

S poštovanjem,

Fond za nauku Republike Srbije

Masarikova 5, Beograd

Message 2 of 20

Fond za nauku Republike Srbije
Konačna lista Predloga projekata odobrenih za finansiranje u okviru
Programa za izvrsne projekte mladih istraživača (PROMIS)

Akronim	Šifra	Naziv projekta	Rukovodilac projekta (PI)	Naučno-istraživačka organizacija (NIO)	Budžet	Rezultat
BIANCO	6061817	BIOMARKERS OF NEUROACTIVE COMPOUNDS IN THE AQUATIC ENVIRONMENT: INTEGRATION INTO ADVERSE OUTCOME PATHWAY FRAMEWORK	Sonja Kaišarević	Prirodno-matematički fakultet, Univerzitet u Novom Sadu	€ 110,571.39	85.67
BioITGenoSelect	6066512	A BIOINFORMATICS APPROACH TO DAIRY CATTLE BREEDING USING GENOMIC SELECTION	Ljuba Štrbac	Poljoprivredni fakultet, Univerzitet u Novom Sadu	€ 169,763.96	88.62
BioSolAfla	6064541	BIOPROCESS SOLUTION FOR THE PRODUCTION OF BIOCONTROL AGENT AGAINST AFLATOXIGENIC ASPERGILLUS SPECIES	Jovana Grahovac	Tehnološki fakultet Novi Sad, Univerzitet u Novom Sadu	€ 170,000.00	85.19
BOWIE	6060916	BLOWING IN THE WIND	Marko Stalevski	Astronomska opservatorija	€ 168,225.62	86.33
BREATHE	6039613	REAL-TIME DETECTION AND QUANTIFICATION OF BIOAEROSOLS RELEVANT FOR HUMAN AND PLANT HEALTH	Branko Šikoparija	Institut BioSens - Istraživačko-razvojni institut za informacione tehnologije biosistema	€ 171,064.50	92.19
CASCH-MOF	6066708	CARBON CAPTURE BY SELF-DRYING SCHIFF BASE MOFS	Marko Rodić	Prirodno-matematički fakultet, Univerzitet u Novom Sadu	€ 193,601.44	86.24
CD-HEM	6066886	COMPUTATIONAL DESIGN OF HIGH ENERGETIC MATERIALS: CASE OF CHELATE COMPLEXES	Dušan Veljković	Hemijski fakultet, Univerzitet u Beogradu	€ 46,859.94	85.24
CLOUDS	6062228	CLASSIFICATION OF LARGE OBJECTS - ULTRAFILTERS AND DIRECTED SETS	Boriša Kuzeljević	Prirodno-matematički fakultet, Univerzitet u Novom Sadu	€ 61,484.08	86.81
CryoPlum	6062279	CONSERVATION AND PLUM POX VIRUS ERADICATION FROM SERBIAN AUTOCHTHONOUS PLUM GENOTYPES USING CRYOTECHNIQUES	Darko Jevremović	Institut za voćarstvo Čačak	€ 105,065.27	85.19
DecodExpo	6066532	DECODING THE ROLE OF EXPOSOME IN ENDOCRINE HEALTH	Aleksandra Buha Đorđević	Farmaceutski fakultet, Univerzitet u Beogradu	€ 186,522.28	88.10
DEStiny	6060592	NATURAL DEEP EUTECTIC SOLVENTS FOR GREEN AGRI-FOOD SOLUTIONS	Aleksandra Mišan	Naučni institut za prehrambene tehnologije, Univerzitet u Novom Sadu	€ 163,694.35	85.04
DETOX	6062573	COMMON PHTHALATE DEHP AND WOMEN'S REPRODUCTIVE HEALTH RISK ASSESSMENT: MECHANISTIC AND CHRONIC LOW-DOSE EXPOSURE STUDIES.	Kristina Pogrmić-Majkić	Prirodno-matematički fakultet, Departman za biologiju i ekologiju, Univerzitet u Novom Sadu	€ 189,421.58	87.90
DiaBoNet	6064549	EFFECTS OF DIABETES MELLITUS ON OSTEOCYTIC, NEURAL AND VASCULAR NETWORKS IN BONE: IMPLICATIONS FOR INCREASED FRACTURE SUSCEPTIBILITY AT THE PROXIMAL FEMUR	Petar Milovanović	Medicinski fakultet, Univerzitet u Beogradu	€ 199,171.79	86.57
DyRes_System	6062556	DYNAMICS RESILIENCE AS A MEASURE FOR RISK ASSESSMENT OF THE COMPLEX WATER, INFRASTRUCTURE AND ECOLOGICAL SYSTEMS: MAKING A CONTEXT.	Milan Stojković	Institut za vodoprivredu Jaroslav Černi	€ 199,532.93	86.17
FLIM	6066876	FEMALE LEADERSHIP IN MUSIC: A CROSS-GENRE RESEARCH OF WOMEN'S ROLES, AGENCY AND COLLABORATIVE MUSIC-MAKING PRACTICES IN SERBIA	Iva Nenić	Fakultet muzičke umetnosti, Univerzitet umetnosti u Beogradu	€ 86,419.47	86.14
ForNextCobot	6062528	MECHANICAL IMPEDANCE ESTIMATION AND PLANNING FOR THE NEXT GENERATION COLLABORATIVE ROBOTS	Kosta Jovanović	Elektrotehnički fakultet, Univerzitet u Beogradu	€ 155,215.45	87.07
Gramulsen	6057070	GRAPHENE-BASED WEARABLE MULTIPARAMETER SENSOR	Marko Spasenović	Institut za hemiju, tehnologiju i metalurgiju, Institut od nacionalnog značaja, Univerzitet u Beogradu	€ 171,357.63	85.34
HEMMAGINERO	6066079	HEMOGLOBIN-BASED SPECTROSCOPY AND NONLINEAR IMAGING OF ERYTHROCYTES AND THEIR MEMBRANES AS EMERGING DIAGNOSTIC TOOL	Aleksandar Krmpot	Institut za fiziku u Beogradu, Univerzitet u Beogradu	€ 199,285.55	86.67
HiSuperBat	6062667	HIGH-CAPACITY ELECTRODES FOR AQUEOUS RECHARGEABLE MULTIVALENT-ION BATTERIES AND SUPERCAPACITORS: NEXT STEP TOWARDS A HYBRID MODEL	Milica Vujković	Fakultet za fizičku hemiju, Univerzitet u Beogradu	€ 180,689.98	85.67
HUMANE	6061921	HYDROXYUREA-MEDIATED ACTIVATION OF NITRIC OXIDE SYNTHASE IN ERYTHROID PROGENITORS	Milica Tošić	Institut za medicinska istraživanja, Univerzitet u Beogradu	€ 116,041.26	85.14

Fond za nauku Republike Srbije
Konačna lista Predloga projekata odobrenih za finansiranje u okviru Programa za izvrsne projekte mladih istraživača (PROMIS)

Akronim	Šifra	Naziv projekta	Rukovodilac projekta (PI)	Naučno-istraživačka organizacija (NIO)	Budžet	Rezultat
HYBIS	6066223	HYBRID BRAIN COMPUTER INTERFACE FOR CONTROL OF SENSORY-MOTOR COUPLING IN POST- STROKE REHABILITATION	Andrej Savić	Elektrotehnički fakultet, Univerzitet u Beogradu	€ 119,559.72	89.16
IAPS	6062629	INTEGRATED AGRO-METEOROLOGICAL PREDICTION SYSTEM	Mirjam Vujadinović Mandić	Poljoprivredni fakultet, Univerzitet u Beogradu	€ 180,503.78	87.83
iDUCOMBSENS	6066816	AN INTEGRATED DUAL-COMB GAS SENSOR	Marko Krstić	Elektrotehnički fakultet, Univerzitet u Beogradu	€ 149,173.86	85.00
IN-DEPTH	6059147	AN EVOLUTIONARY INSIGHT INTO MOLECULAR DIVERSITY OF EMERGING PATHOGENS IN SERBIA THROUGH PHYLOGENETIC APPROACH	Irena Arandjelović	Institut za mikrobiologiju i imunologiju, Medicinski fakultet, Univerzitet u Beogradu	€ 189,867.80	85.19
InfoBomat	6066966	INTRAMAMMARY ETHNO-VETERINARY FORMULATION IN PREVENTION AND TREATMENT OF BOVINE MASTITIS FOR OPTIMIZATION OF ANTIMICROBIAL TREATMENT	Zorana Kovačević	Poljoprivredni fakultet, Univerzitet u Novom Sadu	€ 88,807.21	87.29
Key2SM	6066160	COLD ATOMS, HUBBARD MODEL AND HOLOGRAPHY: KEY TO STRANGE METALS	Jakša Vučičević	Institut za fiziku u Beogradu, Univerzitet u Beogradu	€ 199,827.18	87.47
LABLUNG	6066974	MECHANISTIC INSIGHT INTO THE ANTI-INFLAMMATORY AND ANTIOXIDATIVE EFFECTS OF LACTIC ACID BACTERIA IN IN VITRO MODELS OF CHRONIC LUNG DISEASES	Marija Stanković	Institut za molekularnu genetiku i genetičko inženjerstvo, Univerzitet u Beogradu	€ 147,524.84	85.00
LEAPSyn-SCI	6039663	LATE EMBRYOGENESIS ABUNDANT PROTEINS: STRUCTURAL CHARACTERISATION AND INTERACTION WITH A-SYNUCLEIN	Marija Vidović	Institut za multidisciplinarna istraživanja, Univerzitet u Beogradu	€ 178,110.44	85.33
MaKiPol	6066089	MATHEMATICAL METHODS IN THE KINETIC THEORY OF POLYATOMIC GAS MIXTURES: MODELLING, ANALYSIS AND COMPUTATION	Milana Čolić	Prirodno-matematički fakultet, Univerzitet u Novom Sadu	€ 52,537.96	85.00
MEMORYST	6058808	FROM BRAIN WAVES TO MEMORY BOOST: MEMORY ENHANCEMENT BY PERSONALIZED FREQUENCY-MODULATED NONINVASIVE BRAIN STIMULATION	Jovana Bjekić	Institut za medicinska istraživanja, Univerzitet u Beogradu	€ 168,490.00	89.90
MiFaDriCa	6066923	IDENTIFICATION OF CNV-MIRNAS AS GENETIC DRIVERS AND RISK FACTORS FOR CONGENITAL ANOMALIES OF THE KIDNEY AND URINARY TRACT (CAKUT)	Ivan Jovanović	Vinča Institut za nuklearne nauke, Institut od nacionalnog značaja, Univerzitet u Beogradu	€ 196,566.95	85.10
MoDeCo2000	6067004	MORTAR DESIGN FOR CONSERVATION - DANUBE ROMAN FRONTIER 2000 YEARS AFTER	Emilija Nikolić	Arheološki institut Beograd	€ 199,657.08	87.84
MYCOCLIMART	6066613	DEVELOPMENT OF CLIMATE SMART FORESTRY (CSF) CONCEPT IN THE REPUBLIC OF SERBIA THROUGH MYCORRHIZAL MODULATION OF POLYAMINE METABOLISM IN PEDUNCULATE OAK (QUERCUS ROBUR L.) TREES	Marko Kebert	Institut za nizijsko šumarstvo i životnu sredinu, Univerzitet u Novom Sadu	€ 194,419.63	87.81
Nano-MDSC-Thera	6062673	NOVEL IMMUNOTHERAPEUTIC APPROACHES FOR AUTOIMMUNE DISEASES BASED ON MYELOID DERIVED SUPPRESSOR CELLS INDUCED BY NANOMATERIALS	Sergej Tomić	Institut za primenu nuklearne energije, Univerzitet u Beogradu	€ 199,727.74	86.62
PHANTER	6066764	BACTERIOPHAGES AND ANTIBIOTICS INTERACTIONS – A MISSING LINK TOWARD PHAGE THERAPEUTIC APPLICATION	Petar Knežević	Prirodno-matematički fakultet, Univerzitet u Novom Sadu	€ 198,794.62	86.38
PHYCAT	6062285	PROTEIN HYDROGEL FOR CANCER THERANOSTICS	Ana Popović-Bijelić	Fakultet za fizičku hemiju, Univerzitet u Beogradu	€ 134,759.68	87.14
POLYGREEN	6062612	TOWARDS A "GREEN" AND SUSTAINABLE POLYMER INDUSTRY: FULLY BIOBASED UNSATURATED POLYESTER RESINS	Pavle Spasojević	Fakultet tehničkih nauka u Čačku, Univerzitet u Kragujevcu	€ 169,706.55	87.47
PRECAST	6060755	PREDICTION OF CANCER TREATMENT EFFECTIVENESS WITH STIMULI-RESPONSIVE NANOMATERIALS	Nikola Knežević	Institut Biosens - Istraživačko-razvojni institut za informacione tehnologije biosistema	€ 199,999.77	85.10
PROTECTA	6066210	PROMISING NATURAL ALTERNATIVES FOR THE CULTURAL HERITAGE SAFEGUARD: A FORCE OF NATURE	Nikola Unković	Biološki fakultet, Univerzitet u Beogradu	€ 140,329.97	85.62
PsyCise	6066800	UTILITY OF PLASMA DRUG LEVEL MONITORING AND CYP2C19/CYP2D6 GENOTYPING IN DOSE PERSONALIZATION OF ANTIDEPRESSANTS AND ANTIPSYCHOTICS	Marin Jukić	Farmaceutski fakultet, Univerzitet u Beogradu	€ 199,872.88	88.71

Fond za nauku Republike Srbije
Konačna lista Predloga projekata odobrenih za finansiranje u okviru Programa za izvrsne projekte mladih istraživača (PROMIS)

Akronim	Šifra	Naziv projekta	Rukovodilac projekta (PI)	Naučno-istraživačka organizacija (NIO)	Budžet	Rezultat
PV-Waals	6062710	NANOMETER THIN PHOTOVOLTAICS BASED ON PLASMONICALLY ENHANCED VAN DER WAALS HETEROSTRUCTURES	Goran Isić	Institut za fiziku u Beogradu, Univerzitet u Beogradu	€ 200,000.00	88.33
RACOLNS	6062361	REGIONAL ABSOLUTE CHRONOLOGY OF THE LATE NEOLITHIC IN SERBIA	Miroslav Marić	Balkanološki Institut SANU	€ 164,470.03	85.00
RatioCAT	6062244	RATIONAL DESIGN OF MULTIFUNCTIONAL ELECTRODE INTERFACES FOR EFFICIENT ELECTROCATALYTIC HYDROGEN PRODUCTION	Igor Pašti	Fakultet za fizičku hemiju, Univerzitet u Beogradu	€ 94,886.10	91.33
RECLAIM	6062225	THE POLITICS OF REPRESENTATION: PERFORMANCES AND DEMOCRATIC LEGITIMACY OF REPRESENTATIVE CLAIMS IN SERBIA	Jelena Lončar	Fakultet političkih nauka, Univerzitet u Beogradu	€ 94,960.66	88.67
REPANCAN	6056979	DRUG REPURPOSING IN PANCREATIC DUCTAL ADENOCARCINOMA	Jelena Grahovac	Institut za onkologiju i radiologiju Srbije	€ 194,075.79	85.71
ReTRA	6062634	REVIVING TRADITIONAL BREADMAKING PROCESSES THROUGH INNOVATIVE APPROACHES	Miroslav Hadnađev	Naučni institut za prehrambene tehnologije u Novom Sadu, Univerzitet u Novom Sadu	€ 175,399.30	91.29
RIBIDF	6066818	RESEARCH AND DEVELOPMENT OF IONIC BIO FLUIDS	Siniša Bikić	Fakultet tehničkih nauka, Univerzitet u Novom Sadu	€ 99,231.78	85.83
ROLERS	6060866	THE ENIGMATIC ROLE OF EPSTEIN-BARR VIRUS INFECTION IN RHEUMATOID ARTHRITIS AND SYSTEMIC LUPUS ERYTHEMATOSUS: WHICH VIRAL MARKER COULD SUGGEST TRIGGERING OF AUTOIMMUNE DISEASES?	Ana Banko	Medicinski fakultet, Univerzitet u Beogradu	€ 131,051.15	89.10
SENSOGENE	6052315	CANCER BIOSENSORS BASED ON GENE REGULATORY ELEMENTS	Aleksandra Nikolić	Institut za molekularnu genetiku i genetičko inženjerstvo, Univerzitet u Beogradu	€ 113,697.39	85.43
SERBHIWE	6066205	HONEY BEES OF SERBIA, WILD VS. MANAGED COLONIES THROUGH THE EYES OF POPULATION GENETICISTS	Slobodan Davidović	Institut za biološka istraživanja "Siniša Stanković", Institut od nacionalnog značaja za Republiku Srbiju, Univerzitet u Beogradu	€ 111,679.17	85.38
SerbRightWing	6062708	THE SERBIAN RIGHT-WING PARTIES AND INTELLECTUALS IN THE KINGDOM OF YUGOSLAVIA, 1934-1941	Dragan Bakić	Balkanološki institut SANU	€ 93,566.35	85.24
STOLKit	6060914	A TOOLKIT FOR RISK ASSESSMENT INTEGRATION IN MODELING A MANAGEMENT STRATEGY FOR STOLBUR PHYTOPLASMA ASSOCIATED DISEASES IN SUSTAINABLE AGRICULTURE	Milana Mitrović	Institut za zaštitu bilja i životnu sredinu	€ 25,261.66	85.00
StrainedFeSC	6062656	STRAIN EFFECTS IN IRON CHALCOGENIDE SUPERCONDUCTORS	Nenad Lazarević	Institut za fiziku u Beogradu, Univerzitet u Beogradu	€ 199,789.40	85.00
SYMBIOSIS	6066997	CONTROLLABLE DESIGN OF EFFICIENT ENZYME@MOF COMPOSITES FOR BIOCATALYSIS	Tamara Todorović	Hemijski fakultet, Univerzitet u Beogradu	€ 129,524.02	85.04
TRACEPIGEN	6060876	TRACKING SYSTEMIC THERAPY RESISTANCE OF LUNG AND COLORECTAL CANCER THROUGH TARGETED NGS ANALYSIS OF GENETIC AND EPIGENETIC VARIANTS IN LIQUID BIOPSIES	Miljana Tanic	Institut za onkologiju i radiologiju Srbije	€ 199,986.22	90.04
TreeVita	6066697	UNDERSTANDING QUERCUS ROBUR L. VITALITY LOSS USING STABLE CARBON ISOTOPES RATIO (Δ13C), DROUGHT AND REMOTELY SENSED INDICES AND DEVELOPMENT OF STRATEGIES FOR ADAPTATION TO CHANGING CLIMATE CONDITIONS	Dejan Stojanović	Institut za nizijsko šumarstvo i životnu sredinu, Univerzitet u Novom Sadu	€ 192,666.87	89.96
WARMED	6066747	DEVELOPMENT OF NO-BASED APPROACHES FOR GUIDED WHITE ADIPOSE TISSUE BROWNING. CAN WE TACKLE METABOLIC DISEASES BY HEATING UP/COOLING DOWN THE FAT?	Aleksandra Janković	Institut za biološka istraživanja "Siniša Stanković", Institut od nacionalnog značaja za Republiku Srbiju, Univerzitet u Beogradu	€ 159,512.67	85.14
WasteWaterForce	6066881	WASTE WATER TREATMENT REINFORCEMENT– ADVANCED PROCESSES USING GREEN AND COST-EFFECTIVE MATERIALS	Djurdja Kerkez	Prirodno-matematički fakultet, Departman za hemiju, biohemiju i zaštitu životne sredine, Univerzitet u Novom Sadu	€ 165,254.49	84.96
YEH	6062589	YUGOSLAVIA'S COMPARATIVE HISTORICALEXPERIENCE WITH THE POLICIES OF ALLIANCE-MAKING AND NEUTRALITY/NONALIGNMENT	Srđan Mićić	Institut za noviju istoriju Srbije	€ 66,924.24	87.16

Министарство просвете, науке и технолошког развоја Републике Србије

и Немачка служба за академску размену - ДААД

Ministry of Education, Science and Technological Development of the Republic of

Serbia and Deutcher Akademischer Austauschdienst - DAAD

Пројектни циклус / *Project years* 2020-2021

	Srpski rukovodilac projekta i srpska institucija ***Serbian applicant and Serbian institution***	***Nemački rukovodilac projekta i nemačka institucija*** ***German applicant and German institution***	***Naziv projekta*** ***Project title***
1.	Др Јелена ЗАГОРАЦ, научни саветник Институт за нуклеарне науке „Винча“, У Београд	Research Scientist Vesna SROT Max Planc Institute for Solid state Research, Stuttgart	ZnO/ZnS хетероструктуре, од теорије до експеримента *ZnO/ZnS heterostructures from theory to the experiment*
2.	Др Бојан ДУДУК, научни саветник Институт за пестициде и заштиту животне средине, У Београд	Prof. Dr. Michael KUBE University of Hohenheim	Диференцијација и упоредна молекуларна анализа фитоплазми из шаргарепе у Србији и Немачкој *Differentiation and Comparative Molecular Analyses of Phytoplasmas infecting Carrots in Serbia and Germany*
3.	Др Данијела МАКСИМОВИЋ	Prof. Dr. Evamarie HEY-HAWKINS	Савремени приступ терапији меланома базиран на инхибицији

	ИВАНИЋ, научни саветник Институт за биолошка истраживања „Синиша Станковић“, У Београд	University of Leipzig	циклоксигеназе *An Advanced Option for Melanoma Treatment by Targeting Cyclooxygenase 2*
4.	Др Ана ПРОТИЋ Фармацеутски факултет, У Београд	Prof. Dr. Urlike HOLZGRABE University of Würzburg	Хемометријски приступ испитивњу одговора *Corona Charged Aerosol* детектора у фармацеутској анализи *Chemometrically supported study of Charged Aerosol Detector*
5.	Др Наташа САМАРЏИЋ Факултет техничких наука, У Нови Сад	Full Professor Ronald TETZLAFF Technical University of Dresden	Мемристори: од фабрикације до дизајна интегрисаних кола *Memristors: from fabrication to IC design*
6.	Др Владислав ВОЛАРЕВИЋ Факултет медицинских наука, У Крагујевац	PhD Marietta HERMANN University of Würzburg	Улога IL-33/ST2 сигналног пута у зарастању костију *The role of IL-33/ST2 pathway in bone healing*
7.	Др Мирослав СОКИЋ,	Dr.- Ing. Habil Srećko STOPIĆ	Развој напредне технологије за

	научни саветник Институт за технологију нуклеарних и других минералних сировина, У Београд	RWTH Aachen University	рециклажу штампаних плоча у оквиру концепта циркуларне економије *Advanced recycling technologies of end of life products (EOL) within the*
8.	Др Игор ПОПОВ, виши научни сарадник Институт за мултидисциплинарна истраживања, УБеоград	PhD Gianaurelio CUNIBERTI Technical University of Dresden	Контролисана модификација електронских особина танких филмова дихалкогенида прелазних метала за примене у соларним ћелијама – комбиновани теоријско-експериментални приступ *Engineering of TMDCs for solar cells*
9.	Др Ранка СТАНКОВИЋ Рударско-геолошки факултет, У Београд	Dr. Jelena MITROVIĆ University of Passau	Међујезичко препознавање говора мржње *Cross-Lingual Hate Speach Detection*
10.	Др Марија МИРКОВИЋ, научни сарадник	Senior. Sc. Sanjay MATHUR	Биокоњуговане магнетне наночестице дизајниране за

	Институт за нуклеарне науке „Винча“, У Београд	University of Köln	мултимодалну терапију канцера *Bioconjugated Magnetic Nanoparticles Designed for Multimodal Cancer*
11.	Др Annemarie SORESCU – МАРИНКОВИЋ, виши научни сарадник Балканолошки институт САНУ	PhD Aleksandra SAMUROVIĆ University of Jena	Језички пејзаж културне области Баната: дијахрона и синхрона перспектива *Liguistic Landscape of the Cultural Region Banat in Diachrony and Sinchrony perspective*
12.	Проф. Др Снежана САВИЋ Фармацеутски факултет, У Београд	Privatdozent Dominique LUNTER University of Tübingen	Иновативне наноформулације за испоруку лекова у мозак/кожу *Innovative nanoformulations for brain/skin delivery*
13.	Др Александар КРМПОТ, виши научни сарадник Институт за физику, У Београд	Postdoctoral beamline scientist Rui PAN DESY Hamburg	Осликавање и временски разложена спектроскопија у терахерцној, блиској инфрацрвеној и видљивој области за будуће биомедицинске примене *Imaging and time resolved spectroscopy of hemoglobin and red blood cells*
14.	Проф. др Жарко ЋОЈБАШИЋ, Машински факултет,	Prof. Dr. Manfred ZEHN TU Berlin	Биомедицинско инжењерство засновано на вештачкој интелигенцији и

	У Ниш		напредној методи коначних елемената (Next Level BME) *Artificial intelligence and Advanced FEM Based Biomedical Eng.*
15.	Др Наташа ЂУРИШИЋ МЛАДЕНОВИЋ Технолошки факултет, У Нови Сад	Dr. Alberto BEZAMA UFY Leipzig	Промена утицаја РЕгионалних БИоекономских система на животну средину и друштво (РЕБИС) Assessing environmental and social impacts of Regional Bioeconomy
16.	Др Сандра ВОЈНОВИЋ, виши научни сарадник Институт за молекуларну генетику и генетичко инжењерство, У Београд	PhD Tobias GULDER Technical University of Dresden	Оптимизација структуре секундарних метаболита ради побољшања њихове антифугалне активности *Development of efficient antifungals based on microbial secondary*
17.	Др Катарина ВОЈИСАВЉЕВИЋ, виши научни сарадник	Dr. Nicolae BARSAN	Гасни сензори на бази наноструктурних полупроводних метал-оксида за медицинску дијагностику путем

	Институт за мултидисциплинарна истраживања, У Београд	University of Tübingen	анализе даха *Nanostructured semiconducting metal-oxides as gas sensors for medical diagnostics by breath analysis*
18.	Др Милица ПОЈИЋ, научни саветник Научни институт за прехрамбене технологије, У Нови Сад	Dr. Oliver SCHLÜTER ATB Potsdam	Потенцијал хладне плазме у наклијавању семена индустријске конопље *Non-thermal plasma potential in the hemp seed sprouting*
19.	Др Марко СПАСЕНОВИЋ, виши научни сарадник Научни институт за хемију технологију и металургију, У Београд	Univ.-Prof. Dr. Rer. Nat. Georg DUESBERG UB w Munich	Танки филмови платина –диселенида као гасни сензори *Thin films of liquid phase exfoliated TMDs for gas sensing*
20.	Др Магдалена СТЕВАНОВИЋ, научни саветник Институт техничких наука САНУ	Prof. Dr.-Ing. habil Aldo R. BOCCACCINI University of Erlangen	Биокомпатибилни терапеутици на бази скафолда биоактивног стакла и полимерних честица за регенерацију ткива и

			ћелијску терапију Biocompatible engineered therapeutics based on bioactive glass scaffolds
21.	Проф. др Јелена ЂОРЂЕВИЋ Биолошки факултет, У Београд	Prof. Dr. Agnes GORLACH TU Munich	Улога реактивних кисеоничких врста у хипоталамичкој контроли гојазности *Role of reactive oxygen species in the hypothalamic control of obesity*
22.	Др Урош ЛАЧЊЕВАЦ, виши научни сарадник Институт за мултидисциплинарна истраживања, Београд	Ph.D. Patrick SCHMUKI University of Erlangen	TiO2 нанотубуларни низови декорисани наночестицама метала платинске групе за примену у електролизи TiO2 nanotube arrays decorated with platinum group metal nanoparticles for electro catalysis applications
23.	Др Александра ЈАНКОВИЋ, виши научни сарадник Институт за биолошка истраживања „Синиша Станковић“,	Dr.rer.nat. Dubravka VUČIĆEVIĆ MDC Berlin	Детекција биомаркера рака дојке код жена у пременопаузи – утицај гојазности *Detection of breast cancer biomarkers in*

	У Београд		*premenopausal women*
24.	Проф. др Гордана ЋИРИЋ МАРЈАНОВИЋ Факултет за физичку хемију, У Београд	PhD Urich KORTZ JU Bremen	Пероксо-полиоксометалати: синтеза, структура и Раман студија *Peroxo-Polyoxometalates: Synthesis, Structure and Raman Study*
25.	Др Јакша ВУЧИЋЕВИЋ, научни сарадник Институт за физику, У Београд	Dr. Philipp HANSMANN Max Planc Institute for Chemical Physics of Solids, Dresden	Електронске корелације у оксидима са трансфером наелектрисања: функције одзива и дугодометна одређења *Electronic correlations in charge transfer oxides*

AMERICAN PHYSICAL SOCIETY
EDITORIAL OFFICE
1 Research Road • Ridge, NY 11961• http://journals.aps.org/
(631) 591-4000

Physical Review Letters • Physical Review • Reviews of Modern Physics • Physics

Michael Thoennessen
Editor in Chief

September 17, 2020

Dr. Jaksa Vucicevic
Institut za Fiziku Beograd
Univerzitet u Beogradu
Pregrevica 118
11080 Zemun
SERBIA

Dear Dr. Vucicevic,

This is to confirm that you have served as a referee for *Physical Review B, Physical Review E* and *Physical Review Letters*, journals of the American Physical Society, since October 2017. Our files indicate that you have so far provided us with 34 reviews.

Our journals are leading international journals in basic physics research. Physics researchers around the world submit roughly 40,000 manuscripts to us annually. To evaluate these submissions, we rely on the advice of expert reviewers such as yourself, whose expertise has been established by, for example, a strong record of publication in the field and the frequent citation of their work in various research journals. Referees are asked to assess the correctness, importance, interest, and clarity of presentation of manuscripts in their fields of physics or related sciences. The editors rely on this advice in making decisions about whether to publish manuscripts, reject them, or request changes in them. You and our other experts provide such advice as a service to the scientific community that, eventually, contributes to the intellectual and economic prosperity of the country. The enclosed Advice for Referees gives an idea of what we request of reviewers.

We hope that this information is helpful to you and that we will be able to count on your advice and assistance in the future.

Yours sincerely,

Michael Thoennessen
Enclosures

TRIQS meeting schedule

Thursday		Friday	
PMC	**COFFEE**	*PMC*	**COFFEE**
Salle 4	Olivier: An overview of recent developments in TRIQS Nils: Installation, benchmarks, CT-INT developments Discussions	*Amphi Budé*	Daniel B: Tensor product state solver Xiaodong: DMFT study of cuprates with MPS based impurity solver Manuel: MPS impurity solver
PMC	**LUNCH**	*PMC*	**LUNCH**
Salle 4	Antoine: About CCQ Minjae: Sign problem in CT-INT Manuel: Recent developments of the maximum entropy approach Evgeny: TRIQS interface to CASTEP	*Salle 5*	Jaksa: Introducing the LMDB project Thomas: Recent development with TRILEX, etc. Hugo: A library of two-particle response function tools
PMC	**COFFEE**	*PMC*	**COFFEE**
Salle 4	Short presentations: Alice, Daniel M, François, Jernej, Leonid, Thomas	*Salle 5*	Short presentations: Marcel, Markus, Michael, Philipp, Robert

Venue

We can meet on Thursday morning, at 9:30, at the Condensed Matter Chair of Collège de France, 11 Place Marcelin Berthelot, 75231 Paris. For those of you who know the place, you can just walk in. For those who haven't been at Collège before, there is a welcome desk on the right after the main entrance. You can ask them to give me or our secretary (Françoise Salagnac) a call and we will come to get you. If there is a problem, call me on my cell phone : +33 6 87 79 77 11.

Participants

— Olivier Parcollet, CCQ, Flatiron Institute, New York, USA
— Antoine Georges, CCQ, Flatiron Institute, New York, USA
— Hugo Strand, CCQ, Flatiron Institute, New York, USA
— Manuel Zingl, CCQ, Flatiron Institute, New York, USA
— Minjae Kim, Collège de France, Paris, France
— Thomas Schaefer, Collège de France, Paris, France
— Alice Moutenet, Collège de France, Paris, France
— Giacomo Mazza, Collège de France, Paris, France
— Leonid Pourovskii, Ecole Polytechnique, Palaiseau, France
— Michel Ferrero, Ecole Polytechnique, Palaiseau, France
— Nils Wentzell, CEA Saclay, France
— Marco Schiro, CEA Saclay, France
— Francesco Peronaci, CEA Saclay, France
— Markus Aichhorn, TU Graz, Austria
— Robert Triebl, TU Graz, Austria
— Daniel Bauernfeind, TU Graz, Austria
— Jaksa Vucicevic, University of Belgrade, Serbia
— Jernej Mravlje, Jozef Stefan Institute, Ljubljana, Slovenia
— Thomas Ayral, Atos Quantum Lab, Les Clayes-sous-Bois, France
— Pablo Cornaglia, Centro Atómico Bariloche, Argentina
— Cedric Weber, King's College, London, UK
— Evgeny Plekhanov, King's College, London, UK
— François Jamet, King's College, London, UK
— Philipp Hansmann, Max Planck Stuttgart, Germany
— Daniel Mantadakis, Max Planck Stuttgart, Germany
— Xiaodong Cao, Max Planck Stuttgart, Germany
— Marcel Klett, Max Planck Stuttgart, Germany
— Michael Schmid, Max Planck Stuttgart, Germany

Belgrade, 7-11th October 2019

Symposium on Condensed Matter Physics

Invited Speakers

Invited Speakers at National Symposium on Condensed Matter Physics

- Marco Aprili, PS-CNRS Université Paris-Sud, France
- Stefano Baroni, Scuola Internazionale Superiore di Studi Avanzati, Italy
- Wolfgang Belzig, University of Konstanz, Germany
- Emil Božin, Brookhaven National Laboratory, USA
- Harald Brune, Ecole Polytechnique Fédérale de Lausanne, Switzerland
- Liviu Chioncel, University of Augsburg, Germany
- Gyula Eres, Oak Ridge National Laboratory, USA
- Laszlo Forro, Ecole Polytechnique Fédérale de Lausanne, Switzerland
- Rudi Hackl, Walther Meissner Institute, Germany,
- Igor Herbut, Simon Fraser University, Canada
- Kurt Hingerl, Johannes Kepler University, Linz, Austria
- Liv Hornekaer, Aarhus University, Denmark
- Zoran Ikonić, Univsity of Leeds, UK
- Vladimir Juričić, Nordita, KTH Royal Institute of Technology and Stockholm University, Sweden
- Miloš Knezevic, Berlin Institute of Technology, Germany
- Hechang Lei, Renmin University
- Marjana Ležaić, Forschungszentrum Jülich, Germany
- Zoran Mišković, University of Waterloo, Canada

Conference photo

Latest news

Conference photo
October 8, 2019
Please join us at Wednesday at 13.30h in front of the SASA building for conference photo.

Changes in the program
October 6, 2019
Please note changes in the program for Monday morning session and Tuesday afternoon session.

Book of Abstracts is online
October 2, 2019
Book of abstracts is online!

- Danilo Nikolić, UniversitätKonstanz,Konstanz,Germany
- Francois Peeters, University of Antwerp, Belgium
- Maria Peressi, University of Trieste, Italy
- Cedomir Petrovic, Brookhaven National Laboratory, USA
- Hyejin Ryu, Korea Institute of Science and Technology
- Milan Radović, Paul Scherrer Institute, Switzerland
- Nicolas Regnault, Ecole Normale Supérieure Paris, France
- Rastko Sknepnek, University of Dundee, UK
- Frank Steglich, MPICPfS Dresden and Zhejiang University
- Bosiljka Tadić, Jožef Štefan Institute, Slovenia
- Jack Tuszynski, University of Alberta, Canada
- Dieter Vollhardt, University of Augsburg, Germany
- Rok Zitko, Jožef Štefan Institute, Slovenia
- Qingming Zhang, Lanzhou University and Institute of Physics, Chinese Academy of Science
- Vladimir Damljanović, Institute of Physics Belgrade
- Marija Mitrović-Dankulov, Institute of Physics Belgrade
- Saša Dmitrović, Faculty of Physics, University of Belgrade
- Vladimir Đoković, Institute of Nuclear Sciences Vinca, Belgrade
- Igor Franović, Institute of Physics Belgrade
- Sanja Janićievć, Institute of Physics Belgrade
- Zorica Konstantinović, Institute of Physics Belgrade
- Nenad Lazarević, Institute of Physics Belgrade
- Aleksandar Matković, Institute of Physics, Montanuniversität Leoben, Austria
- Ivana R. Milošević, Institute of Physics Belgrade
- Ivanka Milošević, Faculty of Physics, University of Belgrade
- Milica Milovanović, Institute of Physics Belgrade
- Jovan Odavić, Institut für Theorieder Statistischen Physik, RWTH Aachen University
- Marko Petrović, Department of Physics & Astronomy, University of Delaware
- Igor Popov, Institute for Multidisciplinary Research, Belgrade
- Miloš Radonjić, Institute of Physics Belgrade
- Milan Rajković, Institute of Nuclear Sciences Vinca, Belgrade
- Marko Spasenović, Institute of Chemistry, Technology and Metallurgy (IHTM),
- Đorđe Spasojević, Faculty of Physics, University of Belgrade
- Borislav Vasić, Institute of Physics Belgrade
- Jakša Vučičević, Institute of Physics Belgrade

PROGRAM IN ONLINE!

September 20, 2019

Preliminary schedule for SCMP conference is online!

Participation fee in cash

August 15, 2019

Everyone having issues with payment from abroad can pay participation fee in cash at conference opening (payment confirmation will be provided on-site).

Conference Poster

A SiteOrigin Theme

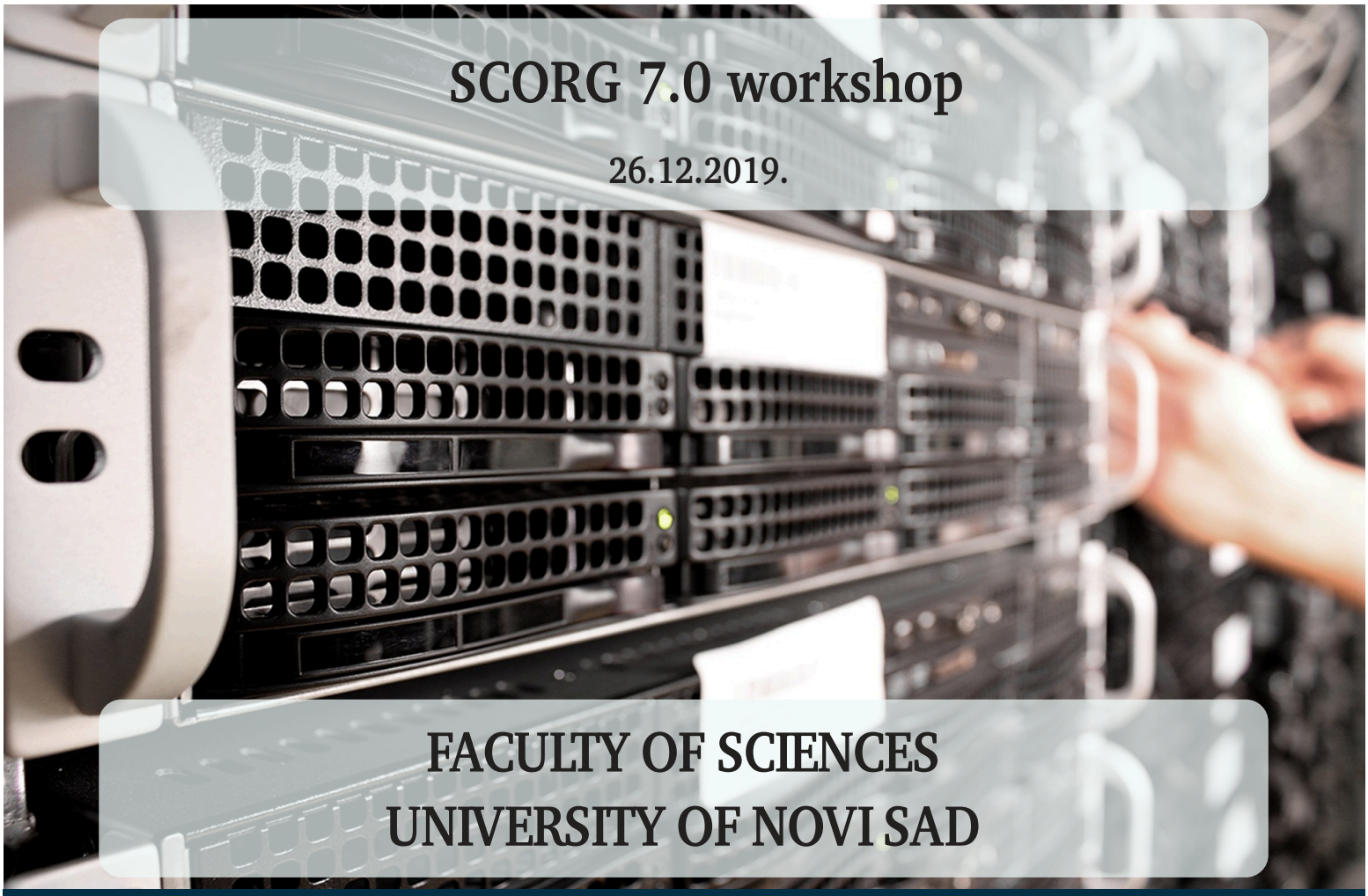

SCORG 7.0 workshop

26.12.2019.

FACULTY OF SCIENCES
UNIVERSITY OF NOVI SAD

Presentation session: RC3 - new wing (DMI), 2nd floor

10:00-10:30
Welcome coffee

10:30-10:50
Introduction

Dr Srđan Škrbić
Faculty of Sciences, University of Novi Sad

10:50-11:10
Synergy between normal and missing-feature classification in deep convolutional neural networks

Nemanja Milošević
Faculty of Sciences, University of Novi Sad

11:10-11:30
Optimization of diagrammatic Monte Carlo for interacting lattice models: symbolic algorithms and multiple precision arithmetic

Dr Jakša Vučičević
Institute of Physics Belgrade

11:30-11:50
Migrating HPC Applications to Cloud - Experiences from the CloudiFacturing Project

Dr Miloš Ivanović
Faculty of Science, University of Kragujevac

11:50-12:10
Market fragmentation and consolidation in adaptive agent models

Dr Aleksandra Alorić
Institute of Physics Belgrade

12:10-12:30
Multi-scale modelling in designing anti-cancer nanomedicine drug delivery Systems

Dr Igor Balaž
Faculty of Sciences, University of Novi Sad

UNIVERSITY OF NOVI SAD, FACULTY OF SCIENCES,
DEPARTMENT OF MATHEMATICS AND INFORMATICS,
TRG DOSITEJA OBRADOVICA 4, NOVI SAD

www.scorg.pmf.uns.ac.rs
srdjan.skrbic@dmi.uns.ac.rs

З А П И С Н И К

са VII седнице Изборног и Наставно-научног већа одржане у среду 24. јуна 2020. године

Седници присуствује 42 члана Изборног и Наставно-научног већа, присутних у амфитеатру и преко Zoom апликације.

Оправдано одсутни: проф. др Татјана Вуковић
проф. др Владимир Милосављевић
проф. др Марија Димитријевић Ћирић
проф. др Владимир Ђурђевић
проф. др Душан Поповић
доц. др Катарина Вељовић
доц. др Саша Дмитровић
доц. др Мирјана Сарван
др Биљана Николић

Неоправдано одсутни: проф. др Милан Дамњановић
проф. др Иван Дојчиновић
доц. др Владимир Миљковић

Декан Факултета проф. др Иван Белча отворио је седницу у 11:10 часова и предложио следећи

Д н е в н и р е д

1. Усвајање Записника са VI седнице Изборног и Наставно-научног већа Физичког факултета.

Изборно веће

2. Разматрање предлога катедара у вези са избором наставника Физичког факултета и то:
   a) Катедре за физику атома, молекула, јонизованих гасова, плазме и квантну оптику за избор једног доцента за ужу научну област Физика јонизованих гасова и плазме.
   b) Катедара Института за метеорологију за избор једног доцента за ужу научну област Физика облака
3. Усвајање извештаја Комисије за избор једног редовног професора за ужу научну област Физика честица и поља (*унапређење др Марије Димитријевић Ћирић*)
4. Покретање поступка за избор Милице Васиљевић у звање истраживач сарадник за ужу научну област Физика јонизованог гаса и плазме.
5. Давање сагласности Физичког факултета на ангажовање наставника у школској 2020/21 и то:
   a) ангажовање др Браниславе Вучетић (Мисаиловић) за извођење наставе из предмета Физика А и Б на Војној Академији Министарства одбране
   b) ангажовање проф. др Дејана Јанца за извођење наставе из предмета Ваздухопловна метеорологија на Војној Академији Министарства одбране
   c) ангажовање проф. др Срђана Буквића за извођење наставе из предмета Методе мерења на Природно математичком факултету Универзитета у Бањој Луци
   d) ангажовање доц. др Зорана Поповића за извођење наставе из предмета Програмирање у физици 1 и 2 и Квантна механика 1 и 2 на Природно математичком факултету Универзитета у Бањој Луци
   e) ангажовање проф. др Марије Димитријевић Ћирић из предмета Квантна теорија поља и Физика елементарних честица на Природно-математичком факултету Универзитета у Нишу

Наставно-научно веће

6. Одређивање Комисије за оцену испуњености услова и оправданост предложене теме за израду докторске дисертације за:
   a) АНУ МИЛОСАВЉЕВИЋ, дипломираног математичара, мастер физичара, која је пријавила докторску дисертацију под називом: "ЕЛЕКТРОН-ФОНОН И СПИН-ФОНОН ИНТЕРАКЦИЈА У

СУПЕРПРОВОДНИЦИМА НА БАЗИ ГВОЖЂА И КВАЗИ-2D МАТЕРИЈАЛИМА ИЗУЧАВАНА МЕТОДОМ РАМАНОВЕ СПЕКТРОСКОПИЈЕ"

7. Усвајање Извештаја Комисије за оцену испуњености услова и оправданост предложене теме за израду докторске дисертације и одређивање ментора за:
   a) ВИЛЕМА ВИКТОРА ВАН ГЕРВЕНА, дипломираног физичара, који је пријавио докторску дисертацију под називом: „МАГНЕТНЕ НЕЧИСТОЋЕ У СУПЕРПРОВОДНИЦИМА: СТАЊА УНУТАР ЕНЕРГИЈСКОГ ПРОЦЕПА У КВАНТНИМ ТАЧКАМА И ЕФЕКТИ ПЕРИОДИЧНИХ ЛОКАЛНИХ МОМЕНАТА“ (Magnetic impurities in superconductors: subgap states in quantum dots and effects of periodic local moments)
8. Одређивање Комисије за преглед и оцену докторске дисертације за:
   a) КАТАРИНУ ЂОРЂЕВИЋ, дипломираног физичара, која је предала докторску дисертацију под називом: "ПРИМЕНА НЕУРОНСКИХ МРЕЖА У ФОТОАКУСТИЧКОЈ АНАЛИЗИ СИЛИЦИЈУМА n-ТИПА У ФРЕКВЕНТНОМ ДОМЕНУ“
9. Усвајање пријављене теме за израду мастер рада, одређивање руководиоца и Комисије за одбрану рада за:
   a) МИЛЕНУ ЈОВИЋ, студента мастер студија смера Метеорологија, која је пријавила мастер рад под називом: „ВЛАЖНА ДЕПОЗИЦИЈА АЕРОСОЛА КРИСТАЛИМА ЛЕДА“
   b) ТАМАРУ РАДОВАНОВИЋ, студента мастер студија смера Метеорологија, која је пријавила мастер рад под називом: „ПРОЦЕНА АНОМАЛИЈЕ У СЕЗОНСКОМ ЦИКЛУСУ АТМОСФЕРСКЕ КОНЦЕНТРАЦИЈЕ CO_2 ТОКОМ ПЕРИОДА 2019 - 2020“
   c) ДАНУ ЦМИЉАНОВИЋ, студента мастер студија смера Метеорологија, која је пријавила мастер рад под називом: „УТИЦАЈ БУДУЋИХ ПРОМЕНА ТЕМПЕРАТУРЕ И ВЛАЖНОСТИ НА ТОПЛОТНИ КОМФОР“
   d) МИЛИЦУ БРАНКОВИЋ, студента мастер студија смера Теоријска и експериментална физика, која је пријавила мастер рад под називом: „ОСОБИНЕ СПИНСКИХ ЛАВИНА У НЕУРЕЂЕНИМ ТРАКАСТИМ ФЕРОМАГНЕТНИМ СИСТЕМИМА“
   e) ПАВЛА СТИПСИЋА, студента мастер студија смера Теоријска и експериментална физика, који је пријавио мастер рад под називом: „УТИЦАЈ МАГНЕТНОГ ПОЉА НА ПРОВОДНОСТ У ХАБАРДОВОМ МОДЕЛУ“
   f) ЈОВАНУ МИЛИЈАНОВИЋ, студента мастер студија смера Општа физика, која је пријавила мастер рад под називом: „ПРОБЛЕМ ДЕФИНИСАЊА ПОЈМА ТЕЖИНЕ У НАСТАВИ“
   g) АЛЕКСАНДРУ ЈЕЛИЋ, студента мастер студија смера Општа физика, која је пријавила мастер рад под називом: „АНАЛИЗА ПОСТИГНУЋА УЧЕНИКА У РЕШАВАЊУ ГРАФИЧКИХ ЗАДАТАКА У НАСТАВИ ФИЗИКЕ“
   h) СТЕВАНА ПЕЦИЋА, студента мастер студија смера Примењена и компјутерска физика, који је пријавио мастер рад под називом: "МОНТЕ КАРЛО ДОЗИМЕТРИЈА И РЕДУКЦИЈА ВАРИЈАНСЕ ЗА РОТАЦИОНО СИМЕТРИЧНЕ СЛУЧАЈЕВЕ"
10. Усвајање правилника усаглашених са изменама и допунама закона и других прописа и то:
    - Правилника о издавачкој делатности Физичког факултета,
    - Правилника о раду библиотека Физичког факултета и
    - Правилника о уџбеницима Физичког факултета.
11. Утврђивање предлога Савету Факултета за усвајање докумената и прописа и то:
    - измена и допуна Статута Физичког факултета - усаглашавање са Статутом Универзитета у Београду,
    - Стратегије за обезбеђивање квалитета - у процедури самовредновања,
    - измена и допуна Правилника о организацији и систематизацији радних места Физичког факултета - усаглашавање са актуелним бројем извршилаца,
    - Именовање Савета послодаваца Физичког факултета (допуњен предлозима чланова Наставно-научног већа са седнице одржане 26. фебруара 2020).
12. Питања наставе, науке и финансија.
13. Захтеви за одобрење одсуства.
14. Усвајање извештаја са службених путовања.
15. Дописи и молбе упућене Наставно-научном већу.
16. Обавештења. Текућа питања. Питања и предлози.

Пошто је усвојен предложени Дневни ред, прешло се на

1. тачку

Усвојен је Записник са VI седнице Изборног и Наставно-научног већа Физичког факултета.

Изборно веће

2. тачка

На предлог катедара, Изборно веће је донело одлуку о расписивању конкурса за избор наставника Физичког факултета и то:

a) Катедре за физику атома, молекула, јонизованих гасова, плазме и квантну оптику за избор једног доцента за ужу научну област Физика јонизованих гасова и плазме.
Комисија: др Милорад Кураица, редовни професор ФФ
др Братислав Обрадовић, редовни професор ФФ
др Миливоје Ивковић, научни саветник ИФ

b) катедара Института за метеорологију за избор једног доцента за ужу научну област Физика облака
Комисија: др Дејан Јанц, ванредни професор ФФ
др Владан Вучковић, ванредни професор ФФ
др Мирјана Румл, редовни професор Пољопривредног факултета

3. тачка

Поводом Извештаја Комисије за избор једног редовног професора за ужу научну област Физика честица и поља, а након тајног гласања у коме су учествовали редовни професори Факултета, са 17 гласова ЗА (од укупно 23 колико чини изборно тело) утврђен је предлог о избору др Марије Димитријевић Ћирић у звање редовног професора за ужу научну област Физика честица и поља.

4. тачка

Покренут је поступак за избор Милице Васиљевић у звање истраживач сарадник за ужу научну област Физика јонизованог гаса и плазме.

Комисија: др Ђорђе Спасојевић, редовни професор ФФ
др Никола Коњевић, професор емеритус ФФ
др Иван Виденовић, ванредни професор ФФ
др Гордана Мајсторовић, редовни професор Војне академије

5. тачка

Изборно веће Физичког факултета дало је сагласност на ангажовање наставника у школској 2020/21 и то:

a) др Браниславе Вучетић (Мисаиловић) за извођење наставе из предмета Физика А и Физика Б на Војној Академији Министарства одбране
b) проф. др Дејана Јанца за извођење наставе из предмета Ваздухопловна метеорологија на Војној Академији Министарства одбране
c) проф. др Срђана Буквића за извођење наставе из предмета Методе мерења на Природно математичком факултету Универзитета у Бањој Луци
d) доц. др Зорана Поповића за извођење наставе из предмета Програмирање у физици 1 и 2 и Квантна механика 1 и 2 на Природно математичком факултету Универзитета у Бањој Луци
e) проф. др Марије Димитријевић Ћирић из предмета Квантна теорија поља и Физика елементарних честица на Природно-математичком факултету Универзитета у Нишу

Наставно-научно веће

6. тачка

Одређена је Комисија за оцену испуњености услова и оправданост предложене теме за израду докторске дисертације за:

a) АНУ МИЛОСАВЉЕВИЋ, дипломираног математичара, мастер физичара, која је пријавила докторску дисертацију под називом: "ЕЛЕКТРОН-ФОНОН И СПИН-ФОНОН ИНТЕРАКЦИЈА У СУПЕРПРОВОДНИЦИМА НА БАЗИ ГВОЖЂА И КВАЗИ-2D МАТЕРИЈАЛИМА ИЗУЧАВАНА МЕТОДОМ РАМАНОВЕ СПЕКТРОСКОПИЈЕ"
   Комисија: *др Ненад Лазаревић, виши научни сарадник ИФ*
   др Зоран Поповић, научни сарадник ИФ
   др Божидар Николић, ванредни професор ФФ
   др Зорица Поповић, доцент ФФ

7. тачка

Усвојен је Извештај Комисије за оцену испуњености услова и оправданост предложене теме за израду докторске дисертације и одређен ментор за:

a) ВИЛЕМА ВИКТОРА ВАН ГЕРВЕНА, дипломираног физичара, који је пријавио докторску дисертацију под називом: „МАГНЕТНЕ НЕЧИСТОЋЕ У СУПЕРПРОВОДНИЦИМА: СТАЊА УНУТАР ЕНЕРГИЈСКОГ ПРОЦЕПА У КВАНТНИМ ТАЧКАМА И ЕФЕКТИ ПЕРИОДИЧНИХ ЛОКАЛНИХ МОМЕНАТА“ (Magnetic impurities in superconductors: subgap states in quantum dots and effects of periodic local moments)
   Ментор: *др Дарко Танасковић, научни саветник ИФ*

8. тачка

Одређена је Комисија за преглед и оцену докторске дисертације за:

a) КАТАРИНУ ЂОРЂЕВИЋ, дипломираног физичара, која је предала докторску дисертацију под називом: "ПРИМЕНА НЕУРОНСКИХ МРЕЖА У ФОТОАКУСТИЧКОЈ АНАЛИЗИ СИЛИЦИЈУМА n-ТИПА У ФРЕКВЕНТНОМ ДОМЕНУ“
Комисија: др Драган Маркушев, научни саветник ИФ
др Слободанка Галовић, научни саветник ИНН Винча
др Горан Попарић, редовни професор ФФ
др Мићо Митровић, редовни професор ФФ
др Едиб Добарџић, ванредни професор ФФ

9. тачка

Усвојена је пријављена тема за израду мастер рада, одређен руководилац и Комисије за одбрану рада за:

a) МИЛЕНУ ЈОВИЋ, студента мастер студија смера Метеорологија, која је пријавила мастер рад под називом: „ВЛАЖНА ДЕПОЗИЦИЈА АЕРОСОЛА КРИСТАЛИМА ЛЕДА“
Комисија: др Владан Вучковић, ванредни професор ФФ, руководилац рада
др Драгана Вујовић, ванредни професор ФФ
др Дејан Јанц, ванредни професор ФФ

b) ТАМАРУ РАДОВАНОВИЋ, студента мастер студија смера Метеорологија, која је пријавила мастер рад под називом: „ПРОЦЕНА АНОМАЛИЈЕ У СЕЗОНСКОМ ЦИКЛУСУ АТМОСФЕРСКЕ КОНЦЕНТРАЦИЈЕ CO_2 ТОКОМ ПЕРИОДА 2019 - 2020“
Комисија: др Владимир Ђурђевић, ванредни професор ФФ, руководилац рада
др Ивана Тошић, редовни професор ФФ
др Лазар Лазић, редовни професор ФФ

c) ДАНУ ЦМИЉАНОВИЋ, студента мастер студија смера Метеорологија, која је пријавила мастер рад под називом: „УТИЦАЈ БУДУЋИХ ПРОМЕНА ТЕМПЕРАТУРЕ И ВЛАЖНОСТИ НА ТОПЛОТНИ КОМФОР“
Комисија: др Владимир Ђурђевић, ванредни професор ФФ, руководилац рада
др Драгана Вујовић, ванредни професор ФФ
др Лазар Лазић, редовни професор ФФ

d) МИЛИЦУ БРАНКОВИЋ, студента мастер студија смера Теоријска и експериментална физика, која је пријавила мастер рад под називом: „ОСОБИНЕ СПИНСКИХ ЛАВИНА У НЕУРЕЂЕНИМ ТРАКАСТИМ ФЕРОМАГНЕТНИМ СИСТЕМИМА“
Комисија: др Светислав Мијатовић, научни сарадник ФФ, руководилац рада
др Ђорђе Спасојевић, редовни професор ФФ
Драгутин Јовковић, истраживач ФФ

e) ПАВЛА СТИПСИЋА, студента мастер студија смера Теоријска и експериментална физика, који је пријавио мастер рад под називом: „УТИЦАЈ МАГНЕТНОГ ПОЉА НА ПРОВОДНОСТ У ХАБАРДОВОМ МОДЕЛУ“
Комисија: др Јакша Вучићевић, научни сарадник ИФ, руководилац рада
др Ђорђе Спасојевић, редовни професор ФФ
др Божидар Николић, ванредни професор ФФ

f) ЈОВАНУ МИЛИЈАНОВИЋ, студента мастер студија смера Општа физика, која је пријавила мастер рад под називом: „ПРОБЛЕМ ДЕФИНИСАЊА ПОЈМА ТЕЖИНЕ У НАСТАВИ“
Комисија: др Саша Ивковић, доцент ФФ, руководилац рада
др Братислав Обрадовић, редовни професор ФФ
др Никола Цветановић, ванредни професор Саобраћајног факултета

g) АЛЕКСАНДРУ ЈЕЛИЋ, студента мастер студија смера Општа физика, која је пријавила мастер рад под називом: „АНАЛИЗА ПОСТИГНУЋА УЧЕНИКА У РЕШАВАЊУ ГРАФИЧКИХ ЗАДАТАКА У НАСТАВИ ФИЗИКЕ“
Комисија: др Андријана Жекић, ванредни професор ФФ, руководилац рада
др Мићо Митровић, редовни професор ФФ
др Саша Ивковић, доцент ФФ

h) СТЕВАНА ПЕЦИЋА, студента мастер студија смера Примењена и компјутерска физика, који је пријавио мастер рад под називом: "МОНТЕ КАРЛО ДОЗИМЕТРИЈА И РЕДУКЦИЈА ВАРИЈАНСЕ ЗА РОТАЦИОНО СИМЕТРИЧНЕ СЛУЧАЈЕВЕ"
Комисија: др Милош Вићић, редовни професор ФФ, руководилац рада
др Иван Белча, редовни професор ФФ
др Јован Пузовић, редовни професор ФФ

10. тачка

Наставно-научно веће је усвојило правилнике усаглашене са изменама и допунама закона и других прописа и то:

- Правилник о издавачкој делатности Физичког факултета,
- Правилник о раду библиотека Физичког факултета и
- Правилник о уџбеницима Физичког факултета.

11. тачка

Утврђен је предлог Савету Факултета за усвајање докумената и прописа и то:

- измене и допуне Статута Физичког факултета - усаглашавање са Статутом Универзитета у Београду,
- Стратегије за обезбеђивање квалитета - у процедури самовредновања,
- измене и допуне Правилника о организацији и систематизацији радних места Физичког факултета - усаглашавање са актуелним бројем извршилаца,

- Именовање Савета послодаваца Физичког факултета, допуњен предлозима чланова Наставно-научног већа са седнице одржане 26. фебруара 2020, као и предлогом да се за члана Савета послодаваца именује и директор Математичке гимназије и директор фирме ЦИНИ из Чачка.

12. тачка

Поводом пријаве програма мастер студија при Универзитету у Београду - Оптика и фотоника за биомедицину, у коме је предвиђено учешће наставника и сарадника неколико институција из Београда и Новог Сада, развила се дискусија у којој је учествовало више чланова Већа. Након гласања, са 41 гласом ЗА и 1 гласом ПРОТИВ, донета је одлука да проф. др Милорад Кураица у име Физичког факултета са креаторима предлога програма мастер студија договори учешће факултета у формирању овог мастер програма, као и да се нашим наставницима одобри учешће у програму , с обзиром да је област студија из наше матичности. У међувремену ће декан Факултета тражити одлагање гласања по овом питању на Већу групација и Сенату Универзитета.

13. тачка

Питања наставе

Продекан за наставу, доц. др Славица Малетић, обавестила је чланове Већа да је почела пријава за упис на I годину основних студија физике и метеорологије. Ове године заинтересовани кандидати могу пријаве да подносе и online.

На захтев студената, а према препоруци Универзитета у Београду, донета је одлука о оргазовању додатног испитног рока у септембру.

Продекан је, такође обавестила чланове Већа да ће ускоро бити расписан интерни конкурс за ангажовање у настави студената докторских и мастер студија. Планира се да конкурс буде отворен до 15. септембра 2020, а да услови конкурса буду исти као и претходне године.

Продекан за наставу је позвала шефове катедри да одрже састанке катедри и да пошаљу планирани распоред наставника и сарадника по предметима за јесењи семестра 2020/21. године.

Питања науке

Продекан за науку, проф. др Стеван Стојадиновић, обавестио је чланове Већа да је почела пријава пројеката за програм ИДЕЈА. Продекан ће наставницима и сарадницима послати упутства за пријаву и корисне информације, а заказаће и састанак са заинтересованима који имају неке недоумице. Факултет ће пружити потребну помоћ и подршку при пријављивању, а декан ће свима који желе потписати сагласност за учешће на конкурсу.

14. тачка

Наставно-научно веће је одобрило плаћена одсуства:

a) проф. др Милану Дамњановићу у периоду од 6. до 11. јула 2020. године ради учешћа на конференцији 17th Int. Conference on Nanosciences & Nanotechnologies која се одржава у Солуну, Грчка
b) проф. др Иванки Милошевић у периоду од 6. до 11. јула 2020. године ради учешћа на конференцији 17th Int. Conference on Nanosciences & Nanotechnologies која се одржава у Солуну, Грчка
c) др Јовици Јововићу у периоду од 24. до 28. августа 2020. године ради учешћа на конференцији 30th SPIG која се одржава у Шапцу, Србија
d) др Милошу Скочићу у периоду од 24. до 28. августа 2020. године ради учешћа на конференцији 30th SPIG која се одржава у Шапцу, Србија
e) Никодину Недићу у периоду од 24. до 28. августа 2020. године ради учешћа на конференцији 30th SPIG која се одржава у Шапцу, Србија.

Наставно-научно веће је одобрило и неплаћено одсуство Милици Васиљевић у периоду од 15. јула до 15. октобра 2020. године ради студијског боравка на EPFL у Лозани, Швајцарска.

15. тачка

Наставно-научно веће је усвојио извештај са службеног путовања проф. др Владимира Милосављевића који је у периоду од 3. до 12. марта 2020. године боравио на Универзитету у Даблину, Ирска.

Седница је завршена у 12:10 часова.

Београд, 1.7.2020.

ДЕКАН ФИЗИЧКОГ ФАКУЛТЕТА
Проф. др Иван Белча, с.р.

University of Belgrade
Faculty of Physics

Willem-Victor van Gerven

MAGNETIC IMPURITIES IN SUPERCONDUCTORS: SUBGAP STATES IN QUANTUM DOTS AND EFFECTS OF PERIODIC LOCAL MOMENTS

Doctoral Dissertation

Belgrade, 2020

Thesis defense committee

Thesis advisor, Committee member:
Dr. Darko Tanasković
Research Professor
Institute of Physics Belgrade
University of Belgrade

Committee member:
Dr. Đorđe Spasojević
Full Professor
Faculty of Physics
University of Belgrade

Committee member:
Dr. Zorica Popović
Assistant Professor
Faculty of Physics
University of Belgrade

Committee member:
Dr. Antun Balaž
Research Professor
Institute of Physics Belgrade
University of Belgrade

Acknowledgments

This thesis was completed at the Scientific Computing Laboratory, National Center of Excellence for the Study of Complex Systems, Institute of Physics Belgrade under supervision of Dr. Darko Tanasković. The funding was provided by the Institute of Physics Belgrade, through the grant by the Ministry of Education, Science, and Technological Development of the Republic of Serbia.

First and foremost I want to express my sincerest gratitude to Dr. Aleksandar Belić and Dr. Aleksandar Bogojević for their hospitality and willingness to accept me as a part of the Institute of Physics Belgrade (IPB) family. Without their generosity it would not have been possible for me to build a life in Serbia, a country which soon became my home and which I have come to love.

For his patience and careful guidance I want to thank my adviser Dr. Darko Tanasković. He has taught me to thoroughly look at the problem at hand and not jump into any quick conclusions. His proofreading, commentary and critique substantially raised the level of any of my work.

Most sincerely I wish to thank Dr. Antun Balaž and everybody at the Scientific Computing Laboratory for welcoming me as a PhD student and making me feel part of the scientific endeavor. I want to thank my other colleagues at IPB—in particular Dr. Saša Lazović and Dr. Marija Mitrović Dankulov and the other people from the IPB Innovation Centre—for their friendly input and valuable learning experiences. I wish to thank the IPB staff for their support and friendliness.

A big thank you goes out to Dr. Jakša Vučičević for very fruitful collaboration, many stimulating discussions and valuable insights (*'aha Erlebnisse'*) during the second half of my PhD.

I wish to thank Dr. Rok Žitko for his hospitality during my fruitful stays at the Institut Jožef Stefan in Ljubljana, and many stimulating discussions and insightful and patient guidance.

I want to express my gratitude to Dr. Marcello Civelli at the *Université Paris-Sud 11* for his generous help and kind hospitality.

Without a doubt my most sincere gratefulness goes out to my wife Ekaterina, whom has given me unimaginable support and unshaken belief in my ability. Without her this work could not have been written. I wish to thank my parents Wim van Gerven and Oei Swan Ien for their years of support and upbringing, which bears fruit and gives life.

Charge transport in the Hubbard model at high temperatures: Triangular versus square lattice

A. Vranić,[1] J. Vučičević,[1] J. Kokalj,[2,3] J. Skolimowski,[3,4] R. Žitko,[3,5] J. Mravlje,[3] and D. Tanasković[1]

[1]*Institute of Physics Belgrade, University of Belgrade, Pregrevica 118, 11080 Belgrade, Serbia*
[2]*University of Ljubljana, Faculty of Civil and Geodetic Engineering, Jamova 2, Ljubljana, Slovenia*
[3]*Jožef Stefan Institute, Jamova 39, SI-1000 Ljubljana, Slovenia*
[4]*International School for Advanced Studies (SISSA), Via Bonomea 265, I-34136 Trieste, Italy*
[5]*University of Ljubljana, Faculty of Mathematics and Physics, Jadranska 19, Ljubljana, Slovenia*

(Received 3 June 2020; revised 7 August 2020; accepted 2 September 2020; published 21 September 2020)

High-temperature bad-metal transport has been recently studied both theoretically and in experiments as one of the key signatures of strong electronic correlations. Here we use the dynamical mean field theory and its cluster extensions, as well as the finite-temperature Lanczos method to explore the influence of lattice frustration on the thermodynamic and transport properties of the Hubbard model at high temperatures. We consider the triangular and the square lattices at half-filling and at 15% hole doping. We find that for $T \gtrsim 1.5t$ the self-energy becomes practically local, while the finite-size effects become small at lattice size 4×4 for both lattice types and doping levels. The vertex corrections to optical conductivity, which are significant on the square lattice even at high temperatures, contribute less on the triangular lattice. We find approximately linear temperature dependence of dc resistivity in doped Mott insulator for both types of lattices.

DOI: 10.1103/PhysRevB.102.115142

I. INTRODUCTION

Strong correlation effects in the proximity of the Mott metal-insulator transition are among the most studied problems in modern condensed matter physics. At low temperatures, material-specific details play a role, and competing mechanisms can lead to various types of magnetic and charge density wave order, or superconductivity [1–5]. At higher temperatures, physical properties become more universal, often featuring peculiarly high and linear-in-temperature resistivity (the bad-metal regime) [6–12] and gradual metal-insulator crossover obeying typical quantum critical scaling laws [13–17].

There are a number of theoretical studies of transport in the high-T regime based on numerical solutions of the Hubbard model [10,12,13,18,19], high-T expansion [20], and field theory [21–23]. Finding numerically precise results is particularly timely having in mind a very recent laboratory realization of the Hubbard model using ultracold atoms on the optical lattice [24]. This system enables fine tuning of physical parameters in a system without disorder and other complications of bulk crystals, which enables a direct comparison between theory and experiment. In our previous work (Ref. [25]) we have performed a detailed analysis of single- and two-particle correlation functions and finite-size effects on the square lattice using several complementary state-of-the-art numerical methods, and established that a finite-temperature Lanczos method (FTLM) solution on the 4×4 lattice is nearly exact at high temperatures. The FTLM, which calculates the correlation functions directly on the real-frequency axis, is recognized [25] as the most reliable method for calculating the transport properties of the Hubbard model at high temperatures. The dependence of charge transport and thermodynamics on the lattice geometry has not been examined in Ref. [25] and it is the subject of this work.

Numerical methods that we use are (cluster) dynamical mean field theory (DMFT) and FTLM. The DMFT treats an embedded cluster in a self-consistently determined environment [26]. Such a method captures long-distance quantum fluctuations, but only local (in single-site DMFT), or short-range correlations (in cluster DMFT) [27]. The results are expected to converge faster with the size of the cluster than in the FTLM, which treats a finite cluster with periodic boundary conditions [28]. FTLM suffers from the finite-size effects in propagators as well as in correlations. The conductivity calculation in DMFT is, however, restricted just to the bubble diagram, while neglecting the vertex corrections. Approximate calculation of vertex corrections is presented in few recent works [29–34]. This shortcoming of DMFT is overcome in FTLM where one calculates directly the current-current correlation function which includes all contributions to the conductivity. Also, the FTLM calculates conductivity directly on the real-frequency axis, thus eliminating the need for analytical continuation from the Matsubara axis which can, otherwise, lead to unreliable results (see Supplemental Material of Ref. [25]). Both DMFT and FTLM methods are expected to work better at high temperatures [35] when single- and two-particle correlations become more local, and finite-size effects less pronounced. Earlier work has shown that the single-particle nonlocal correlations become small for $T \gtrsim t$ for both the triangular and the square lattices [25,36,37].

In this paper we calculate the kinetic and potential energy, specific heat, charge susceptibility, optical and dc conductivity in the Hubbard model on a triangular lattice and make a comparison with the square-lattice results. We consider strongly correlated regime at half-filling and at 15% hole doping. In

agreement with the expectations, we find that at high temperatures, $T \gtrsim 1.5t$, the nonlocal correlations become negligible and the results for thermodynamic quantities obtained with different methods coincide, regardless of the lattice type and doping. At intermediate temperatures, $0.5t \lesssim T \lesssim 1.5t$, the difference between DMFT and FTLM remains rather small. Interestingly, we do not find that the thermodynamic quantities are more affected by nonlocal correlations on the square lattice in this temperature range, although the self-energy becomes more local on the triangular lattice due to the magnetic frustration. On the other hand, the vertex corrections to optical conductivity remain important even at high temperatures for both lattice types, but we find that they are substantially smaller in the case of a triangular lattice. For the doped triangular and square lattice the temperature dependence of resistivity is approximately linear for temperatures where the finite-size effects become negligible and where the FTLM solution is close to exact.

The paper is organized as follows. In Sec. II we briefly describe different methods for solving the Hubbard model. Thermodynamic and charge transport results are shown in Sec. III, and conclusions in Sec. IV. The Appendix contains a detailed comparison of the DMFT optical conductivity obtained with different impurity solvers, a brief discussion of the finite-size effects at low temperatures, and an illustration of the density of states in different transport regimes.

II. MODEL AND METHODS

We consider the Hubbard model given by the Hamiltonian

$$H = -t \sum_{\langle i,j\rangle,\sigma} c^{\dagger}_{i\sigma} c_{j\sigma} + U \sum_{i} n_{i\uparrow} n_{i\downarrow} - \mu \sum_{i\sigma} n_{i\sigma}, \qquad (1)$$

where t is the hopping between the nearest neighbors on either triangular or square lattice. $c^{\dagger}_{i\sigma}$ and $c_{i\sigma}$ are the creation and annihilation operators, U is the onsite repulsion, $n_{i\sigma}$ is the occupation number operator, and μ is the chemical potential. We set $U = 10t$, $t = 1$, lattice constant $a = 1$, $e = \hbar = k_B = 1$ and consider the paramagnetic solution for $p = 1 - n = 1 - \sum_{\sigma} n_{\sigma} = 0.15$ hole doping and at half-filling.

We use the FTLM and DMFT with its cluster extensions to solve the Hamiltonian. FTLM is a method based on the exact diagonalization of small clusters (4×4 in this work). It employs the Lanczos procedure to obtain approximate eigenstates and uses sampling over random starting vectors to calculate the finite-temperature properties from the standard expectation values [28]. To reduce the finite-size effects, we further employ averaging over twisted boundary conditions.

The (cluster) DMFT equations reduce to solving a (cluster) impurity problem in a self-consistently determined effective medium. We consider the single-site DMFT, as well as two implementations of cluster DMFT: cellular DMFT (CDMFT) [38,39] and dynamical cluster approximation (DCA) [27]. In DMFT the density of states is the only lattice-specific quantity that enters into the equations. In CDMFT we construct the supercells in the real space and the self-energy obtains short-ranged nonlocal components within the supercell. In DCA we divide the Brillouin zone into several patches and the number of independent components of the self-energy equals the number of inequivalent patches. The DCA results on 4×4 and

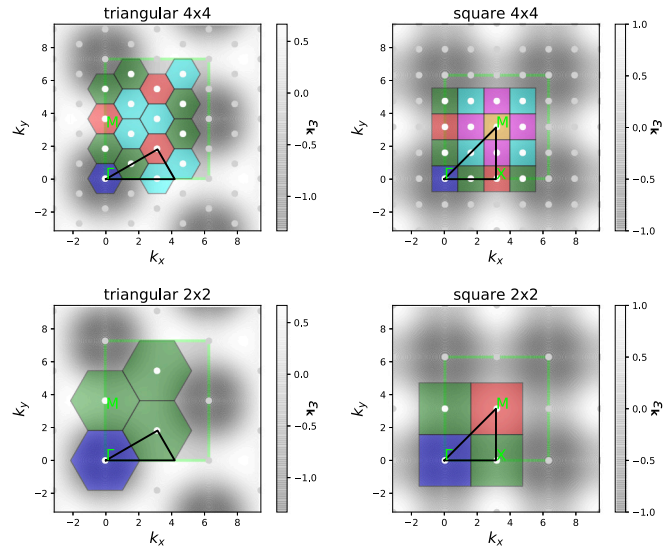

FIG. 1. DCA patches in the Brillouin zone. The irreducible Brillouin zone is marked by the black triangle. The dispersion relation is shown in gray shading. Note the position of the Γ point in the center of the first Brillouin zone which is not marked in this figure.

2×2 clusters are obtained by patching the Brillouin zone in a way that obeys the symmetry of the lattice, as shown in Fig. 1. As the impurity solver we use the continuous-time interaction expansion (CTINT) quantum Monte Carlo (QMC) algorithm [40,41]. In the single-site DMFT we also use the numerical renormalization group (NRG) impurity solver [42–45].

The (cluster) DMFT with QMC impurity solver (DMFT-QMC) gives the correlation functions on the imaginary (Matsubara) frequency axis, from which static quantities can be easily evaluated. The kinetic energy per lattice site is equal to

$$E_{\mathrm{kin}} = \frac{1}{N} \sum_{\mathbf{k}} \varepsilon_{\mathbf{k}} n_{\mathbf{k}\sigma} = \frac{2}{N} \sum_{\mathbf{k}} \varepsilon_{\mathbf{k}} G_{\mathbf{k}}(\tau = 0^{-}), \qquad (2)$$

where for the triangular lattice $\varepsilon_{\mathbf{k}} = -2t[\cos k_x + 2\cos(\frac{1}{2}k_x)\cos(\frac{\sqrt{3}}{2}k_y)]$ and for the square lattice $\varepsilon_{\mathbf{k}} = -2t(\cos k_x + \cos k_y)$ (gray shading in Fig. 1). The noninteracting band for the triangular lattice goes from $-6t$ to $3t$ with the van Hove singularity at $\varepsilon = t$. The potential energy is equal to

$$E_{\mathrm{pot}} = Ud = \frac{1}{N} T \sum_{\mathbf{k}, i\omega_n} e^{i\omega_n 0^{+}} G_{\mathbf{k}}(i\omega_n) \Sigma_{\mathbf{k}}(i\omega_n), \qquad (3)$$

where $d = \langle n_{i\uparrow} n_{i\downarrow} \rangle$ is the average double occupation. In DCA the cluster double occupation is the same as on the lattice, and we used the direct calculation of d in the cluster solver to cross check the consistency and precision of the numerical data. In CDMFT we calculated E_{pot} from periodized quantities G and Σ, where the periodization is performed on the self-energy and then the lattice Green's function is calculated from it. The total energy is $E_{\mathrm{tot}} = E_{\mathrm{kin}} + E_{\mathrm{pot}}$. The specific heat $C = dE_{\mathrm{tot}}/dT|_n$ is obtained by interpolating $E_{\mathrm{tot}}(T)$ and then taking a derivative with respect to temperature. C is shown only in the DMFT solution where we had enough points

at low temperatures. The charge susceptibility $\chi_c = \partial n/\partial\mu$ is obtained from a finite difference using two independent calculations with μ that differs by a small shift $\delta\mu = 0.1t$. In the FTLM, C and χ_c are calculated without taking the explicit numerical derivative since the derivation can be done analytically from a definition of the expectation values,

$$C = C_\mu - \frac{T\zeta^2}{\chi_c} = \frac{1}{N}\frac{1}{T^2}\left[\langle H^2\rangle - \langle H\rangle^2 - \frac{(\langle HN_e\rangle - \langle H\rangle\langle N_e\rangle)^2}{\langle N_e^2\rangle - \langle N_e\rangle^2}\right], \quad (4)$$

which is directly calculated in FTLM. Here, $C_\mu = \frac{1}{N}\frac{1}{T^2}[\langle(H-\mu N_e)^2\rangle - \langle H-\mu N_e\rangle^2]$, $\zeta = \frac{1}{N^2}\frac{1}{T^2}[\langle(H-\mu N_e)N_e\rangle - \langle H-\mu N_e\rangle\langle N_e\rangle]$, $\chi_c = \frac{1}{N}\frac{1}{T}(\langle N_e^2\rangle - \langle N_e\rangle^2)$, and $N_e = \sum_{i\sigma} n_{i\sigma}$ is the operator for the total number of electrons on the lattice.

We calculate the conductivity using DMFT and FTLM. Within the DMFT the optical conductivity is calculated from the bubble diagram as

$$\sigma(\omega) = \sigma_0 \iint d\varepsilon\, d\nu\, X(\varepsilon)A(\varepsilon,\nu)A(\varepsilon,\nu+\omega) \times \frac{f(\nu) - f(\nu+\omega)}{\omega}, \quad (5)$$

where $X(\varepsilon) = \frac{1}{N}\sum_{\mathbf{k}} \left(\frac{\partial\varepsilon_k}{\partial k_x}\right)^2 \delta(\varepsilon - \varepsilon_k)$ is the transport function, $A(\varepsilon,\nu) = -\frac{1}{\pi}\mathrm{Im}[\nu + \mu - \varepsilon - \Sigma(\nu)]^{-1}$, and f is the Fermi function. For the square lattice $\sigma_0 = 2\pi$ and for triangular $\sigma_0 = 4\pi/\sqrt{3}$. For the calculation of conductivity in DMFT-QMC we need the real-frequency self-energy $\Sigma(\omega)$, which we obtain by Padé analytical continuation of the DMFT-QMC $\Sigma(i\omega_n)$. In the DMFT with NRG impurity solver (DMFT-NRG) we obtain the correlation functions directly on the real-frequency axis, but this method involves certain numerical approximations (see Appendix A).

In order to put into perspective the interaction strength $U = 10t$ and the temperature range that we consider, in Fig. 2 we sketch the paramagnetic (cluster) DMFT phase diagram for the triangular and square lattices at half-filling adapted from Refs. [46,47] (see also Refs. [36,37,48–54]). In the DMFT solution (blue lines) the critical interaction for the Mott metal-insulator transition (MIT) is $U_c \sim 2.5D$, where the half-bandwidth D is $4.5t$ and $4t$ for the triangular and the square lattice, respectively. The phase diagram features the region of coexistence of metallic and insulating solution below the critical end point at $T_c \approx 0.1t$. In this work we consider the temperatures above T_c. We set $U = 10t$, which is near U_c for the MIT in DMFT, but well within the Mott insulating part of the cluster DMFT and FTLM phase diagram.

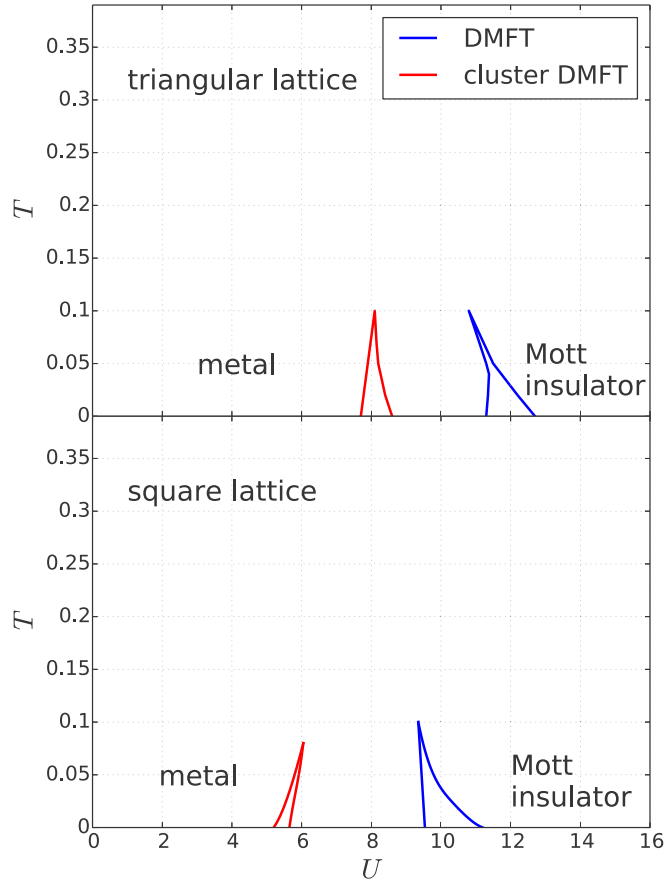

FIG. 2. Sketch of the paramagnetic phase diagram at half-filling, adapted from Refs. [46,47]. There is a region of the coexistence of metallic and insulating solution below the critical end point at T_c. The critical interaction is smaller in the cluster DMFT solution. Above T_c there is a gradual crossover from a metal to the Mott insulator. In this work we consider $T > T_c$ and $U = 10t$.

III. RESULTS

We will first present the results for the thermodynamic properties in order to precisely identify the temperature range where the nonlocal correlations and finite-size effects are small or even negligible. In addition, from the thermodynamic quantities, e.g., from the specific heat, we can clearly identify the coherence temperature above which we observe the bad-metal transport regime. We then proceed with the key result of this work by showing the contribution of vertex corrections to the resistivity and optical conductivity.

Before going into this detailed analysis, and in order to obtain a quick insight into the strength of nonlocal correlations, we compare in Fig. 3 the self-energy components in the cluster DMFT solution at two representative temperatures. We show the imaginary part of the DCA 4×4 self-energy at different patches of the Brillouin zone according to the color scheme of Fig. 1. The statistical error bar of the Im Σ results presented in Fig. 3 we estimate by looking at the difference in Im Σ between the last two iterations of the cluster DMFT loop. We monitor all **K** points and the lowest three Matsubara frequencies. At lower temperature (bottom row), this difference is smaller than 0.05 (0.01) for the square (triangular) lattice, respectively. At higher temperature (upper row), these values are both 10 times lower and the error bar is much smaller than the size of the symbol. At $T = 0.4t$ the differences in the self-energy components are more pronounced on the square than on the triangular lattice, which goes along the general expectations that the larger connectivity ($z = 6$) and the frustrated magnetic fluctuations lead to the more local self-energy. At $T \sim 1.5t$ all the components of the self-energy almost coincide for both lattices. We note that for the triangular

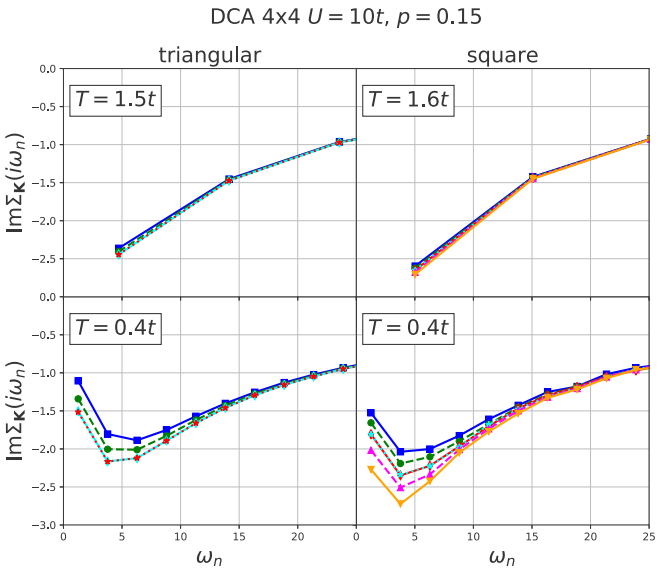

FIG. 3. Imaginary part of the self-energy at the Matsubara frequencies at different patches of the Brillouin zone for several temperatures for $p = 0.15$ hole doping. The position of the patches is indicated by the same colors as in Fig. 1. The solid lines are guide to the eye.

lattice the components of the self-energy marked by red and cyan colors are similar, but they do not coincide completely. There are four independent patches in this case. For the square lattice the red and cyan components of the self-energy are very similar, while we have six independent patches.

A. Thermodynamics

1. $p = 0.15$

We first show the results for hole doping $p = 0.15$. The results for the triangular lattice are shown in the left column of Fig. 4, and the results for the square lattice in the right column. Different rows correspond to the kinetic energy per lattice site E_{kin}, potential energy E_{pot}, total energy E_{tot}, specific heat $C = dE_{\mathrm{tot}}/dT|_n$, and charge susceptibility χ_c. The DMFT results are shown with blue solid lines and FTLM with red dashed lines. The red circles correspond to DCA 4×4, light green to DCA 2×2, green to CDMFT 2×2, and magenta to the CDMFT 2×1 result.

The FTLM results are shown down to $T = 0.2t$. The FTLM finite-size effects in thermodynamic quantities are small for $T \gtrsim 0.2t$ (see Appendix B). The DMFT results are shown for $T \geqslant 0.05t$ and cluster DMFT for $T \geqslant 0.2t$. Overall, the (cluster) DMFT and FTLM results for 15% doping look rather similar. The kinetic and potential energy do not differ much on the scale of the plots, and the specific heat looks similar.

The Fermi-liquid region, with $C \propto T$, is restricted to very low temperatures. For the triangular lattice we find a distinct maximum in $C(T)$ at $T \approx 0.4t$ in FTLM, and at $T \approx 0.3t$ in DMFT. This maximum is a signature of the coherence-incoherence crossover, when the quasiparticle peak in the density of states gradually diminishes and the bad-metal regime starts. The increase in the specific heat for $T \gtrsim 2t$ is

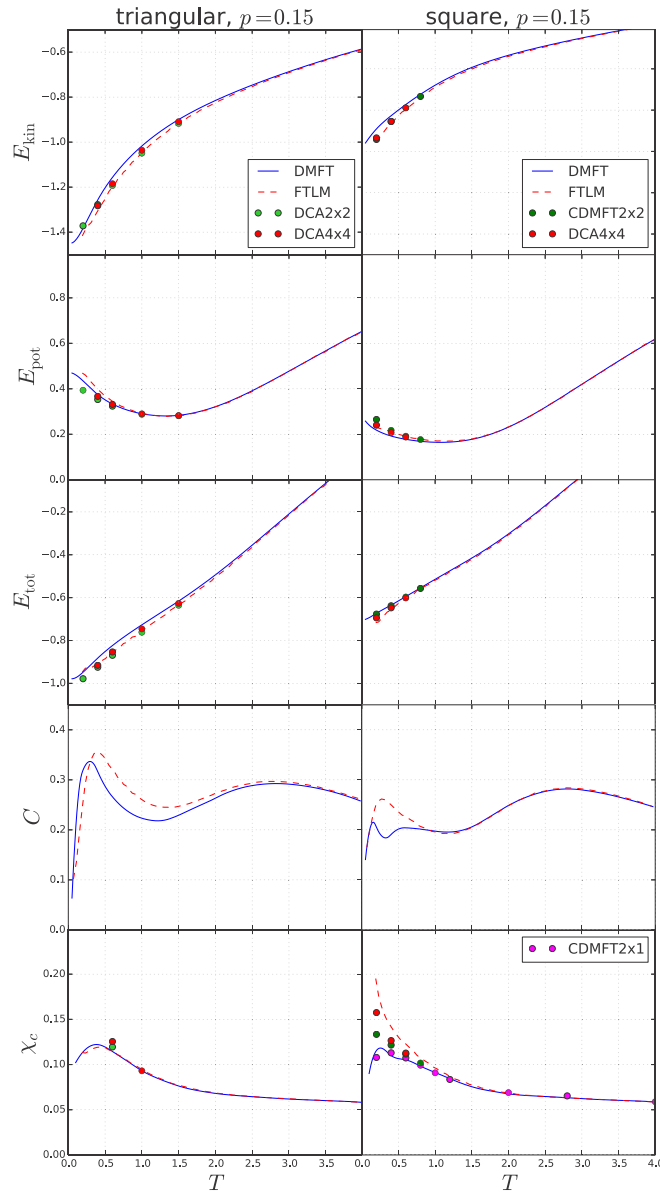

FIG. 4. Kinetic, potential, total energy, specific heat, and charge susceptibility as a function of temperature for the triangular and the square lattice at 15% doping.

caused by the charge excitations to the Hubbard band. The specific heat of the square lattice looks qualitatively the same. [A very small dip in the DMFT specific heat near $T = 0.4t$ for the square lattice may be an artifact of the numerics, where C is calculated by taking a derivative with respect to temperature of the interpolated $E_{\mathrm{tot}}(T)$.] We note that the specific heat, shown here for the fixed particle density, is slightly different than the one for the fixed chemical potential $C_\mu = dE_{\mathrm{tot}}/dT|_\mu$, as in Refs. [28,51,55].

For the square lattice all thermodynamic quantities obtained with different methods practically coincide for $T \gtrsim t$. This means that both the nonlocal correlations and the finite-size effects have negligible effect on thermodynamic quantities. For $T \lesssim t$ the DMFT and FTLM results start to differ. Interestingly, for the triangular lattice there is a small

difference in the DMFT and FTLM kinetic energy up to higher temperatures $T \sim 1.5t$. The FTLM and DCA 4×4 results coincide for $T \gtrsim t$, implying the absence of finite-size effects in the kinetic energy for both lattice types. We also note that the agreement of the CDMFT and DMFT solutions for the total energy on the square lattice at low temperatures is coincidental, as a result of a cancellation of differences in $E_{\rm kin}$ and $E_{\rm pot}$.

The intersite correlations in the square lattice lead to an increase in the charge susceptibility at low temperatures (bottom panel in Fig. 4). Here, the FTLM and DCA 4×4 results are in rather good agreement. For the triangular lattice we found a sudden increase of χ_c at low temperatures in the DCA results (see Appendix B) but not in FTLM. These DCA points are not shown in Fig. 4 since we believe that they are an artifact of the particular choice of patching of the Brillouin zone. In order to keep the lattice symmetry, we had only four (in DCA 4×4) and two (in DCA 2×2) independent patches in the Brillouin zone for triangular lattice (Fig. 1). The average over twisted boundary conditions in FTLM reduces the finite-size error (see Appendix B), and hence we believe that the FTLM result for χ_c is correct down to $T = 0.2t$. We note that an increase of χ_c cannot be inferred from the ladder dual-fermion extension of DMFT [37] either. Still, further work would be needed to precisely resolve the low-T behavior of charge susceptibility for the triangular lattice.

2. $p = 0$

We now focus on thermodynamic quantities at half-filling (Fig. 5). In this case, the results can strongly depend on the method, especially since we have set the interaction to $U = 10t$, which is near the critical value for the Mott MIT in DMFT, while well within the insulating phase in the cluster DMFT and FTLM. The results with different methods almost coincide for $T \gtrsim 2t$ and are very similar down to $T \sim t$. The difference between the cluster DMFT and FTLM at half-filling is small, which means that the finite-size effects are small down to the lowest shown temperature $T = 0.2t$. Therefore, the substantial difference between the FTLM and single-site DMFT solutions at half-filling is mostly due to the absence of nonlocal correlations in DMFT.

The specific heat at half-filling is strongly affected by nonlocal correlations and lattice frustration. For triangular lattice the low-temperature maximum in $C(T)$ has different origin in the DMFT and FTLM solutions. The maximum in the FTLM is due to the low-energy spin excitations in frustrated triangular lattice, while in DMFT it is associated with the narrow quasiparticle peak since the DMFT solution becomes metallic as $T \to 0$. Our DMFT result agrees very well with the early work from Ref. [36] for $T \gtrsim t$. At lower temperatures there is some numerical discrepancy which we ascribe to the error due to the imaginary-time discretization in the Hirsch-Fye method used in that reference. For the square lattice the DMFT and FTLM solutions are both insulating. The maximum in the FTLM $C(T)$ is due to the spin excitations at energies $\sim 4t^2/U = 0.4t$, and it is absent in the paramagnetic DMFT solution which does not include dynamic nonlocal correlations. The increase in $C(T)$ at higher temperatures is due to the charge excitations to the upper Hubbard band.

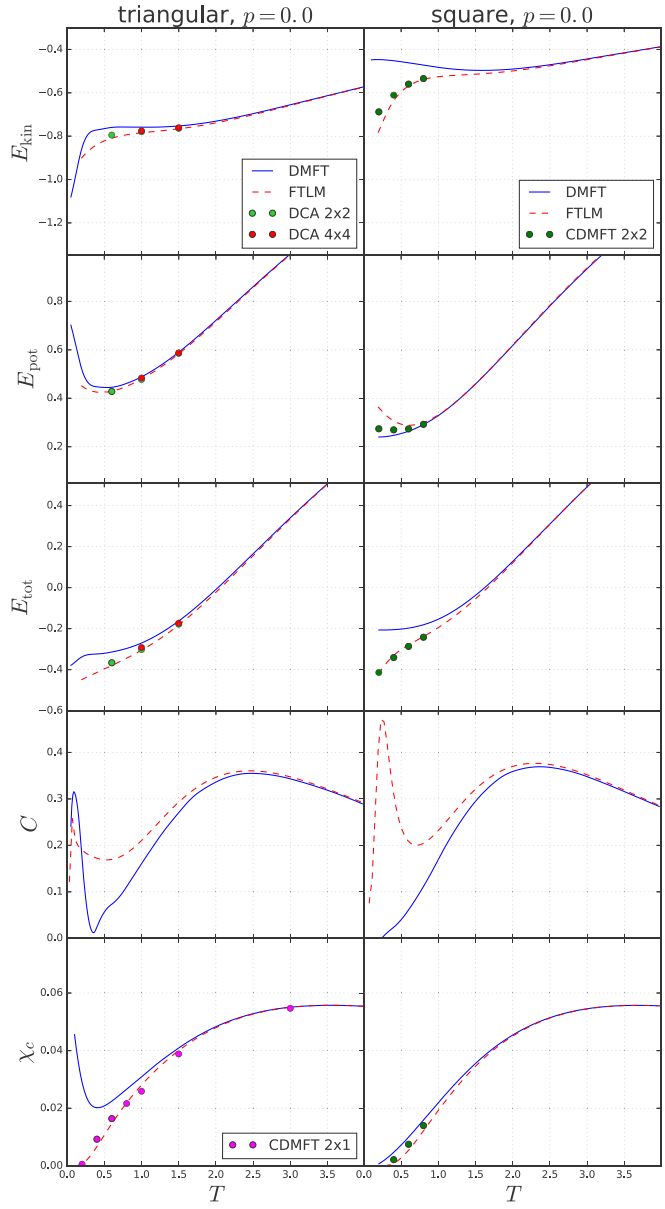

FIG. 5. Kinetic, potential, total energy, specific heat, and charge compressibility as a function of temperature for the triangular and the square lattice at half-filling.

B. Charge transport

The analysis of thermodynamic quantities has shown that the FTLM results for static quantities are close to exact down to $T \sim 0.5t$ or even $0.2t$. For charge transport we show the results for higher temperatures $T \gtrsim t$ since the finite-size effects are more pronounced in the current-current correlation function at lower temperatures.

An indication of the finite-size effects in optical conductivity can be obtained from the optical sum rule

$$\int_0^\infty d\omega\, \sigma(\omega) = \frac{\pi}{4V_{u.c.}}(-E_{\rm kin}), \tag{6}$$

where $V_{u.c}$ is equal to 1 and $\frac{\sqrt{3}}{2}$ for the square and triangular lattice, respectively. The deviation from the sum rule in FTLM

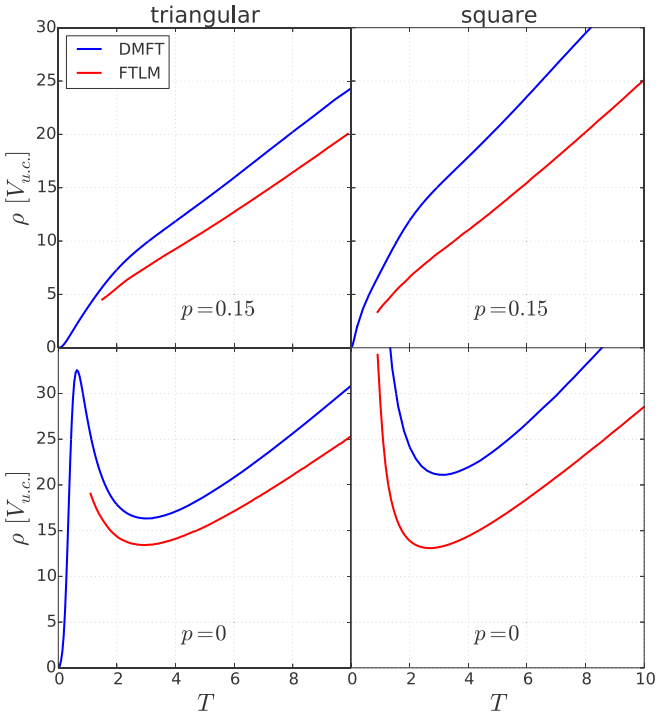

FIG. 6. Resistivity as a function of temperature.

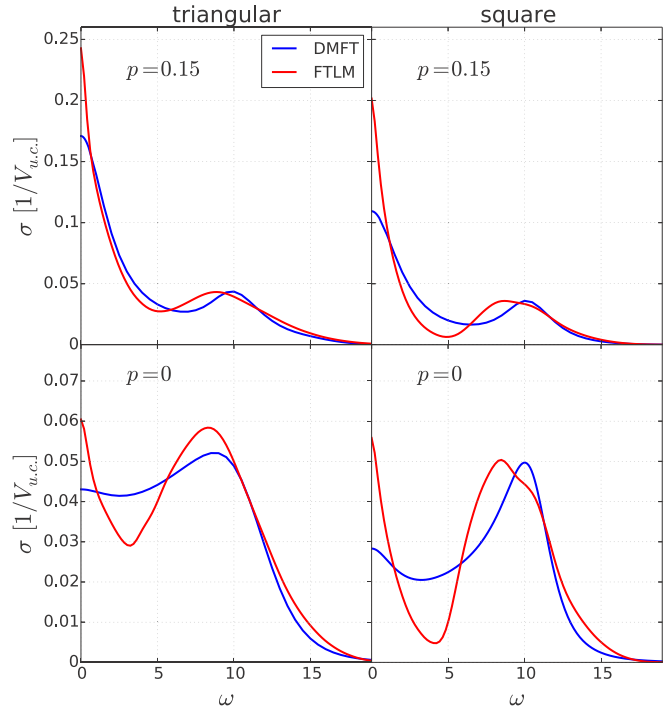

FIG. 7. Optical conductivity at $T = 1.4$.

can be ascribed to the finite charge stiffness and δ function at zero frequency in optical conductivity [28]. The FTLM result for dc resistivity, shown by the red lines in Fig. 6, corresponds the temperature range where the weight of the δ-function peak at zero frequency (charge stiffness) [28] is smaller than 0.5% of the total spectral weight. The other finite-size effects are small and the FTLM resistivity is expected to be close to the exact solution of the Hubbard model. The remaining uncertainty, due to the frequency broadening, is estimated to be below 10% (see Supplemental Material in Ref. [25]). Smallness of the finite-size effects for the square lattice at $T \gtrsim t$ was also confirmed from the current-current correlation function calculated on the 4×4 and 8×8 lattices using CTINT QMC (see Ref. [25]). For doped triangular lattice we show the conductivity data for $T \gtrsim 1.5t$ since below this temperature the weight of the charge stiffness δ function is larger than 0.5% of the total weight, which indicates larger finite-size effects.

The DMFT resistivity is shown in Fig. 6 by the blue lines. It is obtained using the NRG impurity solver. Numerical error of the DMFT-NRG method is small, as we confirmed by a comparison with the DMFT-QMC calculation followed by the Padé analytical continuation (see Appendix A). We note that we do not show the conductivity data in the DCA since in this approximation we cannot reliably calculate the conductivity beyond the bubble term. At high temperatures the bubble-term contribution in cluster DMFT does not differ from the one in single-site DMFT since the self-energy becomes local [25].

Since the FTLM resistivity in Fig. 6 is shown only for temperatures when both the nonlocal correlations and the finite-size effects are small, the difference between the DMFT and FTLM resistivity is due to the vertex corrections. Their contribution corresponds to the connected part of the current-current correlation function whereas the DMFT conductivity is given by the bubble diagram. A detailed analysis of vertex corrections for the square lattice is given in our previous work (Ref. [25]). Here, our main focus is on the comparison of the importance of vertex corrections for different lattices: the numerical results show that the vertex corrections to conductivity are less important in the case of the triangular lattice.

In the doped case, the FTLM solution gives the resistivity which is approximately linear in the entire temperature range shown in Fig. 6. This bad-metal linear-T temperature dependence is one of the key signatures of strong electronic correlations. The resistivity is here above the Mott-Ioffe-Regel limit which corresponds to the scattering length one lattice spacing within the Boltzmann theory. The Mott-Ioffe-Regel limit can be estimated as [6] $\rho_{\mathrm{MIR}} \sim \sqrt{2\pi} \approx 2.5$.

At half-filling and low temperatures the result qualitatively depends on the applied method. For the half-filled triangular lattice at $U = 10t$ the DMFT solution gives a metal, whereas the nonlocal correlations lead to the Mott insulating state. Still, similar as for thermodynamic quantities, the numerically cheap DMFT gives an insulatinglike behavior and a rather good approximation down to $T \sim 0.5t$.

The optical conductivity, shown in Fig. 7 for $T = 1.4t$, provides further insight into the dependence of the vertex correction on the lattice geometry. The DMFT-QMC conductivity is calculated using Eq. (5) with $\Sigma(\omega)$ obtained by the Padé analytical continuation of $\Sigma(i\omega_n)$ (see Appendix A for a comparison with DMFT-NRG). In the DMFT solution, the Hubbard peak is determined by the single-particle processes and it is centered precisely at $\omega = U$. The vertex corrections in FTLM shift the position of the Hubbard peak to lower frequencies. The total spectral weight is the same in FTLM and DMFT solution since it obeys the sum rule of Eq. (6), while the kinetic energies coincide. The Ward identity for

vertex corrections [25,31]

$$\Lambda^{\text{conn}}(i\nu=0) = -2T\frac{1}{N}\sum_{\mathbf{k}} v_{\mathbf{k}} \sum_{i\omega_n} G^2_{\mathbf{k}}(i\omega_n)\partial_{k_x}\Sigma_{\mathbf{k}}(i\omega_n) \quad (7)$$

also implies that the vertex corrections do not affect the sum rule if the self-energy is local. Here, $\Lambda(i\nu)$ is the current-current correlation function and $\Lambda(i\nu=0) = \frac{1}{\pi}\int d\omega\,\sigma(\omega)$.

The results clearly show the much stronger effect of vertex corrections on the square lattice on all energy scales. In addition to a very different $\omega \to 0$ (dc) limit, we observe the more significant reduction of the Drude-like peak width and a larger shift of the Hubbard peak on the square lattice, with a more pronounced suppression of the optical weight at intermediate frequencies. We note that a broad low-frequency peak in conductivity is due to incoherent short-lived excitations characteristic of the bad-metal regime. The structure of the density of states in different transport regimes is discussed in Appendix C.

IV. CONCLUSION

In summary, we have performed a detailed comparison of the thermodynamic and charge transport properties of the Hubbard model on a triangular and square lattice. We identified the temperatures when the finite-size effects become negligible and the FTLM results on the 4×4 cluster are close to exact. In the doped case, for both lattice types, the resistivity is approximately linear in temperature for $T \gtrsim 1.5t$. In particular, we found that the contribution of vertex corrections to the optical and dc conductivity is smaller in the case of a triangular lattice, where it leads to ∼20% decrease in dc resistivity as compared to the bubble term. The vertex corrections also leave a fingerprint on the position of the Hubbard peak in the optical conductivity, which is shifted from $\omega = U$ to slightly lower frequencies.

On general grounds, higher connectivity and/or magnetic frustration should lead to more local self-energy and smaller vertex corrections in the case of triangular lattice, as it is observed. However, the precise role of these physical mechanisms and possible other factors remains to be established. Another important open question is to find an efficient approximate scheme to evaluate the vertex corrections, which would be sufficiently numerically cheap to enable calculations of transport at lower temperatures and in real materials. These issues are to be addressed in the future, but we are now better positioned as we have established reliable results that can serve as a reference point.

With this work we also made a benchmark of several state-of-the-art numerical methods for solving the Hubbard model and calculating the conductivity at high temperatures. This may be a useful reference for calculations of conductivity using a recent approach that calculates perturbatively the correlation functions directly on the real-frequency axis [56–59], thus eliminating a need for analytical continuation, while going beyond the calculation on the 4×4 cluster.

ACKNOWLEDGMENTS

J.M. acknowledges useful discussions with F. Krien. A.V., J.V., and D.T. acknowledge funding provided by the Institute of Physics Belgrade, through the grant by the Ministry of Education, Science, and Technological Development of the Republic of Serbia. J.K., R.Ž., and J.M. are supported by the Slovenian Research Agency (ARRS) under Programs No. P1-0044, No. J1-1696, and No. J1-2458. Numerical simulations were performed on the PARADOX supercomputing facility at the Scientific Computing Laboratory of the Institute of Physics Belgrade. The CTINT algorithm has been implemented using the TRIQS toolbox [60].

APPENDIX A: COMPARISON OF THE DMFT-NRG AND DMFT-QMC CONDUCTIVITY

Here, we compare the DMFT results for the dc resistivity and optical conductivity obtained with two different impurity solvers. The optical conductivity $\sigma(\omega)$ is calculated according to Eq. (5). The dc resistivity is equal to $\rho = \sigma^{-1}(\omega \to 0)$.

Within DMFT-NRG solver the self-energy is obtained directly on the real-frequency axis. There are three sources of errors in this approach: discretization errors, truncation errors, and (over)broadening errors. The method is based on the discretization of the continuum of states in the bath; the ensuing discretization errors can be reduced by performing the calculation for several different discretization meshes with interleaved points and averaging these results. It has been shown [45] that in the absence of interactions, the discretization error can be fully eliminated in a systematic manner. For an interacting problem, the cancellation of artifacts is only approximate, but typically very good, so that this is a minor source of errors. The truncation errors arise because in the iterative diagonalization one discards high-energy states after each set of diagonalizations. For static quantities this error is negligible, but it affects the dynamical (frequency-resolved) quantities because they are calculated from contributions linking kept and discarded states [61–63]. Finally, the raw spectral function in the form of δ peaks needs to be broadened in order to obtain the smooth spectrum. If the results are overbroadened, this can result in a severe overestimation of resistivity, and this is typically the main source of error in the NRG for this quantity. Fortunately, the resistivity is calculated as an integrated quantity, thus, the broadening kernel width can be systematically reduced [20,64]. The lower limit is set by the possible convergence issues in the DMFT self-consistency cycle due to jagged aspect of all quantities, where the actual limit value is problem dependent. In the NRG results reported in this work, it was possible to use very narrow broadening kernel. By studying the dependence of the $\rho(T)$ curves on the kernel width, we estimate that the presented results have at most a few percent error even at the highest temperatures considered.

The DMFT-QMC gives the self-energy $\Sigma(i\omega_n)$ at the Matsubara frequencies and the analytical continuation is necessary to obtain $\Sigma(\omega)$. The statistical error in QMC makes the analytical continuation particularly challenging. However, at high temperatures the CTINT QMC algorithm is very efficient. Running a single DMFT iteration for 10 minutes on 128 cores and using 20 or more iterations, we obtained the self-energies with the statistical error $|\delta\Sigma(i\omega_0)| \approx 5\times10^{-4}$ and $|\delta G(i\omega_0)| \approx 2\times10^{-5}$ at the first Matsubara frequency at $T = t$. Such a small statistical error makes the Padé analytical continuation possible for temperatures $T \lesssim 2t$.

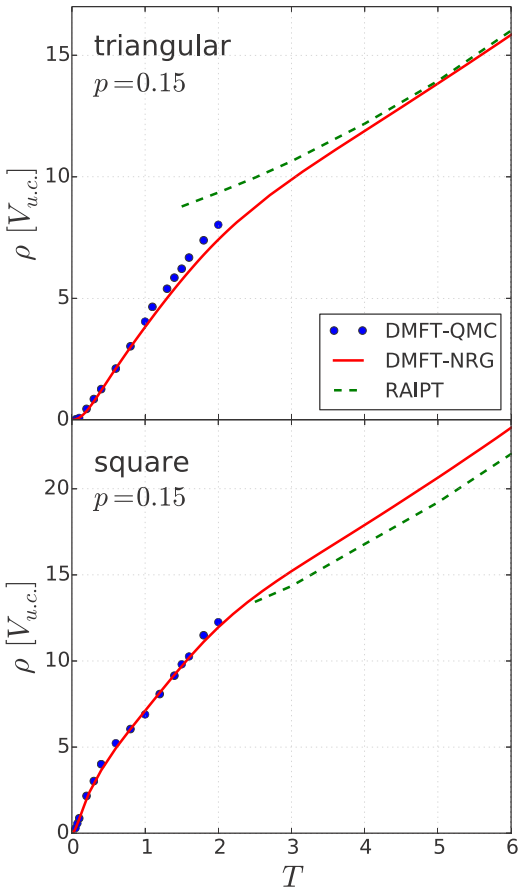

FIG. 8. DMFT-QMC (blue dots) and DMFT-NRG (red lines) resistivity as a function of temperature. The analytical continuation of the self-energy is performed with the Padé method. At high temperatures the DMFT-NRG result agrees rather well with the RAIPT (green dashed lines).

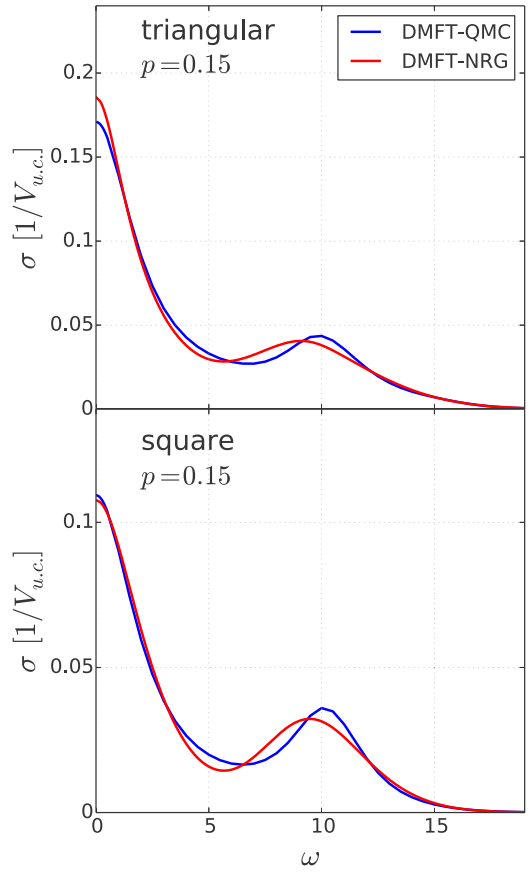

FIG. 9. DMFT-QMC and DMFT-NRG optical conductivity at $T = 1.4$.

We have checked that Padé continuation gives similar results for $\Sigma(\omega)$ when performed on $\Sigma(i\omega_n)$ taken from last few DMFT iterations. We than used $\Sigma(i\omega_n)$ averaged over the last five iterations to further reduce the noise in $\Sigma(i\omega_n)$, before performing the Padé analytical continuation subsequently used in the calculation of the conductivity. We also obtained $G(\omega)$ directly by the Padé analytical continuation of $G(i\omega_n)$, and checked that the result is consistent with the one calculated as $G(\omega) = \int d\varepsilon\, \rho_0(\varepsilon)[\omega + \mu - \varepsilon - \Sigma(\omega)]^{-1}$. These cross checks have confirmed that Padé analytical continuation is rather reliable.

Figure 8 shows the temperature dependence of resistivity calculated with the DMFT-NRG (red lines) and DMFT-QMC (blue dots). For the square lattice we find excellent agreement between the two methods. For the triangular lattice we find some discrepancy for $T \sim 1.5t$, which is likely due to the approximations in DMFT-NRG. We also find that the real-axis iterative perturbation theory [65–67] (RAIPT) agrees rather well with the DMFT-NRG solution for $T \gtrsim 2t$.

It is also interesting to note how the lattice geometry can influence the range of the Fermi liquid $\rho \propto T^2$ behavior in the DMFT solution. In the DMFT equations the lattice structure enters only through the noninteracting density of states. We observe $\rho \propto T^2$ behavior up to much lower temperatures on the square lattice. In this case, $\rho \propto T^2$ region is hardly visible on the scale of the plot, while $\rho \propto T^2$ up to $T \sim 0.3t$ on the triangular lattice. This observation is in agreement with the extension of the $C \propto T$ region in $C(T)$, which is restricted to lower temperatures in the case of a square lattice (Fig. 4).

A comparison of the DMFT-NRG (red lines) and DMFT-QMC (blue lines) optical conductivity at $T = 1.4t$ is shown in Fig. 9. The overall agreement is very good. We, however, find a small discrepancy at $\omega \sim 10t$. The DMFT-QMC result has the Hubbard peak in $\sigma(\omega)$ centered exactly at $\omega = U$, whereas it is shifted to slightly lower frequency in the DMFT-NRG solution. This shift is an artifact of numerical approximations in DMFT-NRG. A position of the Hubbard peak at $U = 10t$ is another manifestation of the precision of analytical continuation of the QMC data.

APPENDIX B: FINITE-SIZE EFFECTS IN CHARGE SUSCEPTIBILITY

In Fig. 10 we show the charge susceptibility obtained with different methods. The single-site DMFT result agrees very well with the 4×4 FTLM after averaging over the twisted boundary conditions. We show χ_c averaged over $N_{\rm tbc} = 1,\ 4,\ 16,\ 64$, and 128 clusters with different boundary conditions. χ_c obtained with a single setup of boundary conditions deviates at low temperatures from the averaged values. The DCA results for $T \lesssim 0.5t$ are also inconsistent.

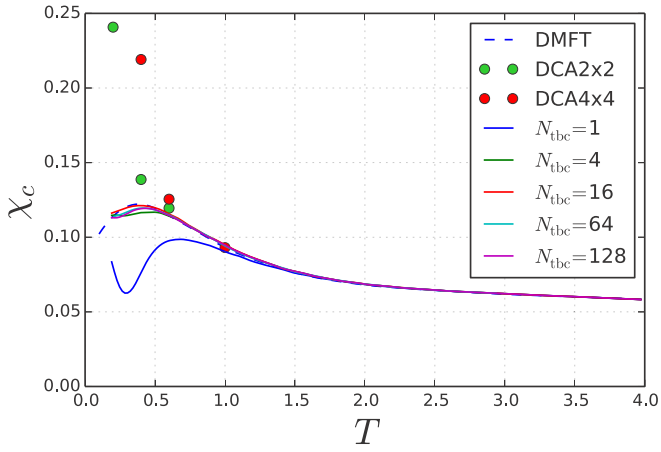

FIG. 10. Charge susceptibility as a function of temperature for the triangular lattice at $p = 0.15$ hole doping.

We believe that this is an artifact of the particular choice of the Brillouin zone patches. In DCA 4×4 and 2×2 we have just four and two independent patches in the Brillouin zone for triangular lattice, respectively.

APPENDIX C: DMFT DENSITY OF STATES

Here, we illustrate the density of states in different transport regimes in the DMFT solution. The results in Fig. 11 are obtained with the QMC solver followed by the Padé analytical continuation. We have checked that the density of states agrees with the DMFT-NRG result.

In the Fermi-liquid regime at low temperatures there is a peak in the density of states around the Fermi level. In the doped case the coherence-decoherence crossover is at temperature $T \sim 0.3$, as we established from the specific-heat data (see Fig. 4) and from the condition that the resistivity reaches the Mott-Ioffe-Regel limit (see Sec. III B). In agreement with earlier work [10,12], we see that at $T \sim 0.3$ there is a peak in the density of states even though long-lived quasiparticles are absent. At even higher temperatures (here shown $T = 1.4$), deeply in the bad-metal regime, the peak at the density of states at the Fermi level is completely washed out.

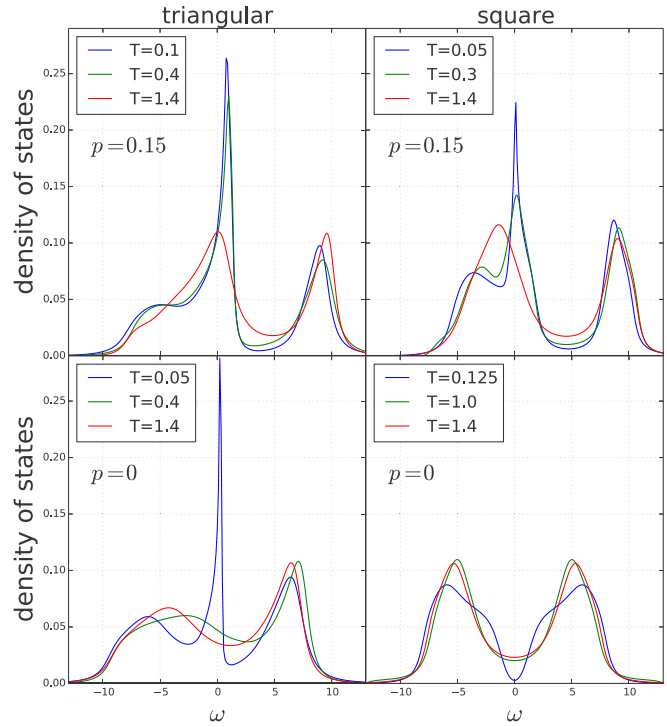

FIG. 11. Density of states in the Fermi liquid at low temperatures and in the bad-metal regime at high temperatures.

At half-filling the result is very sensitive to the exact position of parameters on the U-T phase diagram (see Fig. 2). For the triangular lattice at $U = 10$ the solution is metallic even at low temperature which leads to the formation of narrow quasiparticle peak at the Fermi level. This peak is quickly suppressed by thermal fluctuations which is accompanied by a sudden increase in the resistivity. For the square lattice at $U = 10$ the system is insulating above for $T \gtrsim 0.03$, while the Mott gap gradually gets filled as the temperature increases. We note that the low-temperature peak in optical conductivity in Fig. 7 is not connected to the existence of quasiparticles. It is just a consequence of a finite spectral density at the Fermi level (the absence of an energy gap), as expected in the bad-metal regime.

[1] S. A. Kivelson, I. P. Bindloss, E. Fradkin, V. Oganesyan, J. M. Tranquada, A. Kapitulnik, and C. Howald, Rev. Mod. Phys. **75**, 1201 (2003).

[2] B. J. Powell and R. H. McKenzie, Rep. Prog. Phys. **74**, 056501 (2011).

[3] K. Miyagawa, A. Kawamoto, Y. Nakazawa, and K. Kanoda, Phys. Rev. Lett. **75**, 1174 (1995).

[4] Y. Shimizu, K. Miyagawa, K. Kanoda, M. Maesato, and G. Saito, Phys. Rev. Lett. **91**, 107001 (2003).

[5] V. Dobrosavljević, N. Trivedi, and J. M. Valles, Jr., *Conductor-Insulator Quantum Phase Transitions* (Oxford University Press, Oxford, 2012).

[6] O. Gunnarsson, M. Calandra, and J. E. Han, Rev. Mod. Phys. **75**, 1085 (2003).

[7] N. E. Hussey, K. Takenaka, and H. Takagi, Philos. Mag. **84**, 2847 (2004).

[8] M. M. Qazilbash, K. S. Burch, D. Whisler, D. Shrekenhamer, B. G. Chae, H. T. Kim, and D. N. Basov, Phys. Rev. B **74**, 205118 (2006).

[9] M. M. Qazilbash, J. J. Hamlin, R. E. Baumbach, L. Zhang, D. J. Singh, M. B. Maple, and D. N. Basov, Nat. Phys. **5**, 647 (2009).

[10] X. Deng, J. Mravlje, R. Žitko, M. Ferrero, G. Kotliar, and A. Georges, Phys. Rev. Lett. **110**, 086401 (2013).

[11] W. Xu, K. Haule, and G. Kotliar, Phys. Rev. Lett. **111**, 036401 (2013).

[12] J. Vučičević, D. Tanasković, M. J. Rozenberg, and V. Dobrosavljević, Phys. Rev. Lett. **114**, 246402 (2015).

[13] H. Terletska, J. Vučičević, D. Tanasković, and V. Dobrosavljević, Phys. Rev. Lett. **107**, 026401 (2011).
[14] J. Vučičević, H. Terletska, D. Tanasković, and V. Dobrosavljević, Phys. Rev. B **88**, 075143 (2013).
[15] T. Furukawa, K. Miyagawa, H. Taniguchi, R. Kato, and K. Kanoda, Nat. Phys. **11**, 221 (2015).
[16] H. Eisenlohr, S.-S. B. Lee, and M. Vojta, Phys. Rev. B **100**, 155152 (2019).
[17] B. H. Moon, G. H. Han, M. M. Radonjić, H. Ji, and V. Dobrosavljević, arXiv:1911.02772.
[18] J. Kokalj, Phys. Rev. B **95**, 041110(R) (2017).
[19] E. W. Huang, R. Sheppard, B. Moritz, and T. P. Devereaux, Science **366**, 987 (2019).
[20] E. Perepelitsky, A. Galatas, J. Mravlje, R. Žitko, E. Khatami, B. S. Shastry, and A. Georges, Phys. Rev. B **94**, 235115 (2016).
[21] S. Hartnoll, Nat. Phys. **11**, 54 (2015).
[22] S. A. Hartnoll, A. Lucas, and S. Sachdev, *Holographic Quantum Matter* (MIT Press, Cambridge, MA, 2018).
[23] P. Cha, A. A. Patel, E. Gull, and E.-A. Kim, arXiv:1910.07530.
[24] P. T. Brown, D. Mitra, E. Guardado-Sanchez, R. Nourafkan, A. Reymbaut, C.-D. Hébert, S. Bergeron, A.-M. S. Tremblay, J. Kokalj, D. A. Huse, P. Schauß, and W. S. Bakr, Science **363**, 379 (2019).
[25] J. Vučičević, J. Kokalj, R. Žitko, N. Wentzell, D. Tanasković, and J. Mravlje, Phys. Rev. Lett. **123**, 036601 (2019).
[26] A. Georges, G. Kotliar, W. Krauth, and M. J. Rozenberg, Rev. Mod. Phys. **68**, 13 (1996).
[27] T. A. Maier, M. Jarrell, T. Prushke, and M. H. Hettler, Rev. Mod. Phys. **77**, 1027 (2005).
[28] J. Jaklič and P. Prelovšek, Adv. Phys. **49**, 1 (2000).
[29] N. Lin, E. Gull, and A. J. Millis, Phys. Rev. B **80**, 161105(R) (2009).
[30] N. Lin, E. Gull, and A. J. Millis, Phys. Rev. B **82**, 045104 (2010).
[31] D. Bergeron, V. Hankevych, B. Kyung, and A.-M. S. Tremblay, Phys. Rev. B **84**, 085128 (2011).
[32] T. Sato, K. Hattori, and H. Tsunetsugu, Phys. Rev. B **86**, 235137 (2012).
[33] T. Sato and H. Tsunetsugu, Phys. Rev. B **94**, 085110 (2016).
[34] A. Kauch, P. Pudleiner, K. Astleithner, P. Thunström, T. Ribic, and K. Held, Phys. Rev. Lett. **124**, 047401 (2020).
[35] A. Georges, Ann. Phys. (Berlin) **523**, 672 (2011).
[36] K. Aryanpour, W. E. Pickett, and R. T. Scalettar, Phys. Rev. B **74**, 085117 (2006).
[37] G. Li, A. E. Antipov, A. N. Rubtsov, S. Kirchner, and W. Hanke, Phys. Rev. B **89**, 161118(R) (2014).
[38] G. Kotliar, S. Y. Savrasov, G. Pálsson, and G. Biroli, Phys. Rev. Lett. **87**, 186401 (2001).
[39] G. Biroli and G. Kotliar, Phys. Rev. B **65**, 155112 (2002).
[40] A. N. Rubtsov and A. I. Lichtenstein, J. Exp. Theor. Phys. Lett. **80**, 61 (2004).
[41] E. Gull, A. J. Millis, A. I. Lichtenstein, A. N. Rubtsov, M. Troyer, and P. Werner, Rev. Mod. Phys. **83**, 349 (2011).
[42] K. G. Wilson, Rev. Mod. Phys. **47**, 773 (1975).
[43] H. R. Krishna-murthy, J. W. Wilkins, and K. G. Wilson, Phys. Rev. B **21**, 1003 (1980).
[44] R. Bulla, T. A. Costi, and T. Pruschke, Rev. Mod. Phys. **80**, 395 (2008).
[45] R. Žitko and T. Pruschke, Phys. Rev. B **79**, 085106 (2009).
[46] H. T. Dang, X. Y. Xu, K.-S. Chen, Z. Y. Meng, and S. Wessel, Phys. Rev. B **91**, 155101 (2015).
[47] H. Park, K. Haule, and G. Kotliar, Phys. Rev. Lett. **101**, 186403 (2008).
[48] H. Lee, G. Li, and H. Monien, Phys. Rev. B **78**, 205117 (2008).
[49] T. Shirakawa, T. Tohyama, J. Kokalj, S. Sota, and S. Yunoki, Phys. Rev. B **96**, 205130 (2017).
[50] J. Merino, B. J. Powell, and R. H. McKenzie, Phys. Rev. B **73**, 235107 (2006).
[51] J. Kokalj and R. H. McKenzie, Phys. Rev. Lett. **110**, 206402 (2013).
[52] T. Schäfer, F. Geles, D. Rost, G. Rohringer, E. Arrigoni, K. Held, N. Blümer, M. Aichhorn, and A. Toschi, Phys. Rev. B **91**, 125109 (2015).
[53] E. G. C. P. van Loon, M. I. Katsnelson, and H. Hafermann, Phys. Rev. B **98**, 155117 (2018).
[54] C. Walsh, P. Sémon, D. Poulin, G. Sordi, and A.-M. S. Tremblay, Phys. Rev. B **99**, 075122 (2019).
[55] J. Bonča and P. Prelovšek, Phys. Rev. B **67**, 085103 (2003).
[56] J. Vučičević and M. Ferrero, Phys. Rev. B **101**, 075113 (2020).
[57] A. Taheridehkordi, S. H. Curnoe, and J. P. F. LeBlanc, Phys. Rev. B **99**, 035120 (2019).
[58] A. Taheridehkordi, S. H. Curnoe, and J. P. F. LeBlanc, Phys. Rev. B **101**, 125109 (2020).
[59] A. Taheridehkordi, S. H. Curnoe, and J. P. F. LeBlanc, Phys. Rev. B **102**, 045115 (2020).
[60] O. Parcollet, M. Ferrero, T. Ayral, H. Hafermann, P. Seth, and I. S. Krivenko, Comput. Phys. Commun. **196**, 398 (2015).
[61] R. Peters, T. Pruschke, and F. B. Anders, Phys. Rev. B **74**, 245114 (2006).
[62] A. Weichselbaum and J. von Delft, Phys. Rev. Lett. **99**, 076402 (2007).
[63] R. Žitko, Phys. Rev. B **84**, 085142 (2011).
[64] R. Žitko, D. Hansen, E. Perepelitsky, J. Mravlje, A. Georges, and B. S. Shastry, Phys. Rev. B **88**, 235132 (2013).
[65] H. Kajueter and G. Kotliar, Phys. Rev. Lett. **77**, 131 (1996).
[66] M. Potthoff, T. Wegner, and W. Nolting, Phys. Rev. B **55**, 16132 (1997).
[67] L.-F. Arsenault, P. Sémon, and A.-M. S. Tremblay, Phys. Rev. B **86**, 085133 (2012).

Brief Review

Modern Physics Letters B
2030004 (23 pages)

DOI: 10.1142/S0217984920300045

World Scientific
www.worldscientific.com

Pfaffian paired states for half-integer fractional quantum Hall effect

M. V. Milovanović*,‡, S. Djurdjević†,§ and J. Vučičević*,¶

*Scientific Computing Laboratory,
Center for the Study of Complex Systems,
Institute of Physics Belgrade, University of Belgrade,
Pregrevica 118, Belgrade 11080, Serbia
†Faculty of Natural Sciences and Mathematics,
University of Montenegro, Džordža Vašingtona bb,
Podgorica 81000, Montenegro
‡milica.milovanovic@ipb.ac.rs
§stevandj@ucg.ac.me
¶jaksa.vucicevic@ipb.ac.rs

L. Antonić

Department of Physics, Technion, Haifa 32000, Israel
luka.antonic@campus.technion.ac.il

Received 1 June 2020
Accepted 8 June 2020
Published 3 July 2020

In this review, the physics of Pfaffian paired states, in the context of fractional quantum Hall effect, is discussed using field-theoretical approaches. The Pfaffian states are prime examples of topological (p-wave) Cooper pairing and are characterized by non-Abelian statistics of their quasiparticles. Here we focus on conditions for their realization and competition among them at half-integer filling factors. Using the Dirac composite fermion description, in the presence of a mass term, we study the influence of Landau level mixing in selecting a particular Pfaffian state. While Pfaffian and anti-Pfaffian are selected when Landau level mixing is not strong, and can be taken into account perturbatively, the particle–hole (PH) Pfaffian state requires non-perturbative inclusion of at least two Landau levels. Our findings, for small Landau level mixing, are in accordance with numerical investigations in the literature, and call for a non-perturbative approach in the search for PH Pfaffian correlations. We demonstrated that a method based on the Chern–Simons field-theoretical approach can be used to generate characteristic interaction pseudo-potentials for Pfaffian paired states.

Keywords: Fractional quantum Hall effect; half-integer filling factor; Pfaffian paired states.

‡Corresponding author.

1. Introduction

The fractional quantum Hall effect (FQHE)[1] is a strongly correlated phenomenon of electrons that is observed when they are confined to two dimensions and subjected to a strong magnetic field perpendicular to the two-dimensional plane, in which electrons live and interact. At special filling factors, i.e. ratios between the number of electrons and the number of flux quanta piercing the two-dimensional plane, experiments reveal highly entangled topological states of electrons with fractionally quantized Hall conductance, for intervals of magnetic field (or density). Almost exclusively the denominator of these fractions is an odd number, which can be traced and connected to the fermionic statistics of electrons. A surprise came when an even-denominator FQHE, at filling factor $5/2$, was discovered.[2] This introduced a new paradigm in our understanding of (even-denominator) FQHE states: they may be Bardeen–Cooper–Schrieffer (BCS) paired states of underlying quasiparticles. If we neglect the role of spin in high magnetic fields, the most natural choice for a pairing in a fixed Landau level (LL) is the unconventional, p-wave pairing of spinless quasiparticles proposed in Ref. 3. The resulting state, Moore–Read state is also called Pfaffian due to the necessary antisymmetrization of a collection of pairs of quasiparticles — identical fermions, which do not possess any additional characteristic like spin.

The underlying quasiparticles at even-denominator fractions beside the possibility of having the BCS pairing correlations in a paired state, may in principle exist in its parent, Fermi-liquid-like (FLL) state.[4] Indeed such a state was probed and detected at filling factor $1/2$,[5] and firstly theoretically described in Ref. 6. The theoretical assessment of even-denominator FLL state(s) may lead also to further understanding of the physics of the BCS pairing of underlying quasiparticles. An important direction in this effort is the understanding of the FLL state that occurs at a half-integer (denominator 2) filling of the system, and, at the same time, in an artificial circumstance of a precisely half-filled LL. Namely, a LL is singled out and half-filled. This mathematical limit of the physical system is highly relevant for the understanding of the real system. Our understanding of FQHE phenomena and real circumstances of FQHE experiments call for the concept of the projection to a single LL. Very often the physics of FQHE is confined to a single LL, and we can neglect the LL mixing — the influence of other LLs. Thus if the system is at half(-integer) filling, it nearly possesses the particle–hole (PH) symmetry — the symmetry under exchange of electrons and holes that a half-filled LL has. The Halperin–Lee–Read (HLR) theory[6] of the FLL state at half-filling does not possess this symmetry (because it is a theory that does not include a projection to a fixed LL), but a phenomenological, effective theory with Dirac quasiparticles, proposed in Ref. 7 is manifestly invariant under exchange of electrons and holes, and describes the artificial system of electrons that is confined to a single LL.

On the other hand, the Pfaffian paired state is not invariant under exchange of electrons and holes. When the PH symmetry operation is applied to the

Pfaffian, a new topological state is generated, Pfaffian's conjugated partner, known as anti-Pfaffian.[8,9] Here we may ask whether a state exists, that is a collection of p-wave Cooper pairs and respects the PH symmetry. Indeed one may argue that the Dirac theory of the half-filled LL offers a distinct possibility[7] known as PH Pfaffian (PH symmetric Pfaffian). Before the proposal of the Dirac theory, studies that were examining possibilities of additional, negative-flux pairing, in which angular momentum of p-wave has opposite sign with respect to the one in Pfaffian, also proposed the PH Pfaffian.[10,11]

While the relevance of Pfaffian and especially anti-Pfaffian for the explanation of the FQHE at 5/2 is firmly established in numerical experiments confined to a fixed LL with LL mixing (perturbatively) included via additional, three-body interactions,[12] we do not have a support for PH Pfaffian when numerical experiments are confined to a fixed LL.[13] But a recent experiment[14] on thermal Hall conductance is consistent with a PH Pfaffian scenario at 5/2. That the PH Pfaffian correlations and topological order may be relevant even in the absence of the PH symmetry (as is the case in experiments) may be shown by careful examination of various experimental probes as discussed in Ref. 15.

Thus the question is whether for sufficiently strong LL mixing, that cannot be treated perturbatively (as it is done in all numerical experiments confined to a single LL), we can reach a regime in a uniform system when PH Pfaffian correlations prevail. Or, is disorder needed to install the effective PH Pfaffian correlations?[16,17] In any case LL mixing may play decisive role in selecting a specific kind of Pfaffian state in experiments. In the following sections, Secs. 3 and 4, we will review our work[18,19] that used Dirac and Chern–Simons (CS) field-theoretical description to examine the role of LL mixing and explore pairing at half-integer fillings, in general.

In Sec. 2, we will review the Dirac theory of the FLL state of underlying quasiparticles — composite fermions at a half-filled LL, and select and describe a version of the theory that is best fitted for a description of Pfaffian paired states. The mass term in this theory mimics LL mixing (for small LL mixing has the role of those additional (three-body) interactions in the electron representation), and the limiting behavior of large mass may be identified with the usual HLR picture of the FLL state of FQHE at half-filling.

In Sec. 3, within this version of the Dirac theory, we will probe the question of topological pairing instabilities in a mean-field approximation (as usual in topological explorations when we assume that topological characterization is immune to the neglect of fluctuations). Instabilities will originate from the minimal coupling term, i.e. the coupling with the CS gauge field, and we will be disregarding the remaining influence of the Coulomb interaction, which has a pair-breaking effect. Our interest will be to find which kind of Pfaffian will prevail at certain LL mixing, if we assume a pairing instability.

In Sec. 4, we will discuss which model Hamiltonians for electrons, i.e. effective interaction pseudo-potentials (PPs) in fixed LLs lead to Pfaffian states. Using CS field-theoretical description we recover dominant, already known PPs for

Pfaffian and anti-Pfaffian in a fixed LL, and discuss the necessity to include non-perturbatively at least one more LL to establish PH Pfaffian correlations, and list pertinent PPs.[19] Section 5 is reserved for a discussion and conclusions.

2. Theoretical Approaches to the Physics at a Half-Integer Filling

2.1. *Wave-function approach*

The basic explanation of the FQHE rests on the Laughlin wave function — the ground state wave function for the most prominent effect at filling 1/3.[20] The wave function captures the basic correlations of electrons in a constrained space of an isolated LL. To introduce the Laughlin wave function, we start with the single-particle Hamiltonian,

$$H = \frac{(\mathbf{p} - \mathbf{A})^2}{2m_{\mathrm{e}}}\,, \tag{1}$$

of a particle in a constant magnetic field, $\mathbf{B} = B\mathbf{z}$, with $A_x = -(B/2)y$ and $A_y = (B/2)x$, in a rotationally symmetric gauge. We fixed $c = 1$, $e = 1$, and $\hbar = 1$. The physics of FQHE is largely confined to a fixed LL and in the case of filling factor 1/3, to the lowest LL (LLL). In the rotationally symmetric gauge and in the LLL, the appropriate basis is given by the following single particle wave functions,

$$\Psi_n(\mathbf{r}) = \frac{1}{\sqrt{2\pi l_B^{2+2n} 2^n n!}} z^n \exp\left\{-\left(\frac{1}{4l_B^2}\right)|z|^2\right\}\,, \tag{2}$$

where $l_B = \sqrt{\frac{\hbar c}{eB}}$, and $n = 0, 1, 2\ldots$ is the guiding center angular momentum number. Apart from the exponential factor, these wave functions depend only on the coordinate $z = x+iy$, i.e. they make a holomorphic description, when we neglect the factor which is the same for each $\Psi_n(\mathbf{r})$. Thus many-body wave functions of frozen spin electrons become polynomials in the z coordinate(s) in the LLL, as in the following expression,

$$\Psi(\mathbf{r}_1, \mathbf{r}_2, \ldots, \mathbf{r}_{N_e}) = P(z_1, z_2, \ldots, z_N) \exp\left\{-\left(\frac{1}{4l_B^2}\right)\sum_{i=1}^{N_e}|z_i|^2\right\}\,. \tag{3}$$

The Laughlin wave function at filling factor 1/3 is specified by the Laughlin–Jastrow choice for P,

$$P_{L-J}(z_1, z_2, \ldots, z_{N_e}) = \prod_{i<j}(z_i - z_j)^m\,, \tag{4}$$

with $m = 3$. In this polynomial, the highest power of any z_i; $i = 1, 2, \ldots, N_e$ is $N_m = m(N_e - 1)$ and this number also specifies the number of (single-particle) states available to the system, i.e. the number of flux-quanta piercing the system, $N_\phi = N_m + 1$. Thus the ratio N_e/N_ϕ becomes 1/3 in the thermodynamic limit when $m = 3$.

For monotonically decreasing with distance repulsive interactions like Coulomb, we may expect an extreme capacity of the wave-function to minimize the interaction energy. Namely, as a function of a fixed electron coordinate, the wave function has all (N_m) zeros on the other electrons, $m = 3$ per electron, though only one zero is required by Fermi statistics. Equivalently, we may say that the zero on any other electron is of the m^{th} order as we study the limiting behavior when a fixed electron approaches any other in (4).

Following the same logic, we may attempt the same construction at filling factor 1/2, but, because $m = 2$ in (4), in this case, we need additional factors that will ensure that the wave function is antisymmetric. These additional factors should not contribute or change the value of N_m in the thermodynamic limit (mN), and thus, as additional factors in the total wave function, may be considered as its "neutral part" — the part that does not see the macroscopic flux. (The Laughlin–Jastrow part (4) would represent the charged part.) The neutral part may describe a collection of fermionic quasiparticles (that do not see any macroscopic flux, i.e. external magnetic field), and they may be in the first approximation non-interacting (make a FLL state), or they may come in BCS pairs (make a bosonic condensate and possibly a gapped state). Indeed experiment and theory are equivocal that the state at filling factor 1/2 (in GaAs structures) is a FLL state of underlying quasiparticles, and the state at filling factor 5/2 (in GaAs[2]) is effectively a gapped state of half-filled second LL of frozen-spin (spinless) electrons, in which quasiparticles may pair. The exact topological nature of the paired state at filling factor 5/2 is still under debate.

But we may say that the most theoretically appealing (the most simple and natural BCS pairing) guess for the gapped state at the half-integer filling factors (in various experimental set-ups) is proposed in Ref. 3, and goes under name Moore–Read state or Pfaffian (state). The Pfaffian wave function in the LLL is

$$\Psi_{\text{Pf}} = \sum_{\sigma} \operatorname{sgn}\sigma \left\{ \frac{1}{(z_{\sigma(1)} - z_{\sigma(2)})} \cdots \frac{1}{(z_{\sigma(N_e-1)} - z_{\sigma(N_e)})} \right\} \prod_{k<l} (z_k - z_l)^2 \,, \qquad (5)$$

where the sum is over all permutations of N_e objects where N_e is an even number. We omitted the exponential factors and the expression is unnormalized. In mathematics, if $A = \{a_{ij}\}$ is $N \times N$ antisymmetric matrix, and N is even, its Pfaffian is

$$\operatorname{pf}(a_{ij}) = \operatorname{pf}(A) = \frac{1}{2^{N/2}(N/2)!} \sum_{\sigma \in S_N} \operatorname{sgn}\sigma \prod_{i=1}^{N/2} a_{\sigma(2i-1)\sigma(2i)} \,, \qquad (6)$$

and $\operatorname{pf}(A)^2 = \det(A)$. In more physical terms, we see that the sum in the Moore–Read wave function describes the antisymmetrization of a collection of Cooper pairs, where each pair wave function, $g(\mathbf{r})$, where $\mathbf{r}$ is the relative coordinate of a pair, can be described as

$$g(\mathbf{r}) \sim \frac{1}{z} \,. \qquad (7)$$

This special algebraic decay is the hallmark of the Pfaffian (Moore–Read) wave function, and expresses a special kind of topological, long-range entanglement in this function that represents a p-wave pairing. The construction is given in the LLL, but can be easily generalized and considered in the second LL, i.e. in any isolated LL.

The highest power of any z_i in the Pfaffian wave function is $N_m = 2N_e - 3$, i.e. $N_m = 2N_e - \mathcal{S}$, where $\mathcal{S} = 3$ is so-called shift — a topological number that characterizes a state of a FQHE system on a curved background, such as a sphere. If a state is PH symmetric, the shift should be invariant under the PH exchange. We require $N_e + N_h = N_m + 1$, i.e. the number of electrons, N_e, plus the number of holes, N_h, should be equal to the number of available single-particle states. Thus the state that we get by applying the PH transformation on Pfaffian, is a distinct state, anti-Pfaffian, with shift equal to -1. This anti-Pfaffian state, that has distinct topological features with respect to Pfaffian, was firstly described in Refs. 8 and 9.

We may wonder whether we may still have a p-wave pairing (the smallest angular momentum pairing of spinless electrons) in a many-body wave function that is invariant under PH exchange. It is not hard to see that in this case we must have $N_m = 2N_e - 1$, and this implies some kind of a microscopic negative flux or simply reversed p-wave pairing as in

$$g_{\rm ph}(\mathbf{r}) \sim \frac{1}{z^*}\,. \tag{8}$$

The naive guess would be that by doing the projection to the LLL, in the first approximation, we have

$$g_{\rm ph}(\mathbf{r}) \sim z\,. \tag{9}$$

But, because for any set of complex numbers z_i, $i = 1, 2, \ldots, N, ; N$ even, and $N > 2$,

$$\mathrm{pf}(z_i - z_j) = 0\,, \tag{10}$$

this does not lead to a non-trivial state in the LLL. Thus the question is whether a half-filled isolated LL with special interactions can support a gapped state with PH symmetry, i.e. PH (symmetric) Pfaffian. In the case of Pfaffian and anti-Pfaffian, special interactions exist in an isolated LL[21] (and they do not respect the PH symmetry). Furthermore, the negative flux pairing expression in (8) calls for inclusion of other LLs, and maybe only with significant LL mixing, when the PH symmetry is broken, we can stabilize the pairing correlations in (8). Even in this case, we will call this exotic state PH Pfaffian.

2.2. *Field-theoretical approach*

2.2.1. *Quasiparticles in the FQHE and the HLR theory at half-filling*

We may separate the phase part from the rest of the Laughlin wave function at filling factor $1/m$, where $m = 3$, or from the Laughlin–Jastrow part of a ground

state wave function at half-filling, when $m = 2$, and, then, define a decomposition into two parts of any many-electron wave-function, $\Psi_{\rm e}$, as

$$\Psi_{\rm e}(\mathbf{r}_1, \mathbf{r}_2, \ldots, \mathbf{r}_{N_e}) = \prod_{i<j} \frac{(z_i - z_j)^m}{|z_i - z_j|^m} \Psi_{\rm qp}(\mathbf{r}_1, \mathbf{r}_2, \ldots, \mathbf{r}_{N_e})\,. \tag{11}$$

The wave function $\Psi_{\rm qp}(\mathbf{r}_1, \mathbf{r}_2, \ldots, \mathbf{r}_{N_e})$ represents a wave function of quasiparticles after the unitary transformation defined by the phase factor: in the Laughlin ($m = 3$) case quasiparticles are bosons, and at half-filling ($m = 2$) they are fermions. This defines a CS transformation, or what we will refer to as a Zhang's construction of quasiparticles.[22] In the field-theoretical terms, quasiparticles induce field $\mathbf{a}$ — they are the sources of an artificial (internal) magnetic field b that also acts as an additional field on quasiparticles,

$$\rho_{\rm qp} = -\frac{1}{m} \frac{\nabla \times \mathbf{a}}{2\pi} = -\frac{1}{m} b\,. \tag{12}$$

In (12) $\rho_{\rm qp}$ is the quasiparticle density. We will discuss the CS field-theoretical approach to the system at half-filling, i.e. the HLR theory with more mathematical details below. Here we will note that in a mean-field picture the internal field will cancel the external field. As a first approximation to the half-filling problem, we will find that the ground state in the quasiparticle representation is simply a Slater-determinant of free waves that are filling a Fermi sphere in the inverse space in two dimensions, i.e. it represents a gas of fermionic quasiparticles. (The amplitude part of the Laughlin–Jastrow factor can be recovered in the field-theoretical approach by the random phase approximation (RPA) treatment of the density harmonic fluctuations.)

Therefore, in the Zhang's quasiparticle construction to each electron at position w is attached the following phase factor:

$$\prod_i \frac{|z_i - w|^m}{(z_i - w)^m}\,, \tag{13}$$

a flux tube. The ensuing quasiparticle sees two gauge fields: external and internal — it is a quasiparticle that possesses charge, and the density of quasiparticles is equal to the density of electrons.

On the other hand in the Read's construction[23] of quasiparticles, we start with the notion of fluxes (flux quanta or vortices) that can be introduced by external field in the system, and can be described by the following construction,

$$\prod_i (z_i - w)^m\,, \tag{14}$$

i.e. by insertion of m Laughlin quasiholes. We can make this object neutral by adding a unit of charge, more precisely an electron, to it, and in this way define the Read's quasiparticles as neutral objects, number of which is proportional to the number of external field flux quanta piercing the system. This view is in a way a dual approach (equivalent description of the same theory from a different

point of view) that was initially applied to bosonic systems where the description in terms of elementary particles — bosons was traded for the description in terms of excitations — vortices.[24]

In any case both approaches take into account the precise commensuration between the number of electrons and the number of flux quanta in a system at a fixed filling factor, in our case 1/2.

The CS approach at 1/2, based on the Zhang's construction of quasiparticles, begins with the following Lagrangian (density),

$$\mathcal{L} = \Psi^*_{\rm cf}(i\partial_t - A_0 - a_0)\Psi_{\rm cf} - \frac{\Psi^*_{\rm cf}(\mathbf{p} - \mathbf{A} - \mathbf{a})^2\Psi_{\rm cf}}{2m} - \frac{1}{2}\frac{1}{4\pi}a\partial a\,. \tag{15}$$

In (15), $\Psi_{\rm cf}$ represents a fermionic (Grassmann quasiparticle) field, and the CS term is defined by $a\partial a \equiv \epsilon^{\mu\nu\lambda}a_\mu\partial_\nu a_\lambda$, $\mu, \nu, \lambda = 0, 1, 2$ (denote one time and two spatial coordinates), the summation over repeated indices is understood, and $a_\mu = (a_0, \mathbf{a})$ is a three-vector. The cf stands for composite fermions, a general name for underlying quasiparticles.

Considering the classical equations of motion, from $\frac{\delta\mathcal{L}}{\delta a_0} = 0$, we get

$$-\Psi^*_{\rm cf}\Psi_{\rm cf} - \frac{1}{2}\frac{\nabla\times\mathbf{a}}{2\pi} = 0\,. \tag{16}$$

(Above $\nabla\times\mathbf{a}$ denotes the z component of the vector, and can be considered as a scalar in this two-dimensional theory.) In the mean-field, when we assume that the density of quasiparticles is uniform, the internal field, $\frac{\nabla\times\mathbf{a}}{2\pi}$, exactly cancels the uniform external field at half-filling,

$$\frac{\nabla\times\mathbf{A}}{2\pi} = 2\overline{\Psi^*_{\rm e}\Psi_{\rm e}} = 2\overline{\Psi^*_{\rm cf}\Psi_{\rm cf}}\,, \tag{17}$$

where $\overline{\Psi^*_{\rm e}\Psi_{\rm e}}$ stands for the uniform electron density.

The Lagrangian in (15) is the basis or starting point for the HLR theory, which describes the physics at 1/2 as a FLL state of (fermionic) quasiparticles. We may notice, from the form of the Lagrangian, that the electron density–current vector is equal to the one of quasiparticles,

$$-\frac{\delta\mathcal{L}}{\delta A^\mu} = j^\mu_{\rm e} = j^\mu_{\rm cf}\,. \tag{18}$$

2.2.2. *Dirac quasiparticle description of half-filled LL and at half-filling*

In this section, we will first review the Dirac theory for a half-filled LL proposed in Ref. 7 and then consider its extension in the presence of a mass term that is relevant for the general case (with LL mixing) at half-filling.

We start with an isolated LL (of classical electrons) that is half-filled. It has the PH symmetry — the symmetry under exchange of electrons and holes. The low-energy physics of a zeroth LL of Dirac electrons in the weak coupling limit should correspond to the low-energy physics of isolated LL (of classical electrons).[7]

Thus we consider the Dirac problem in an external (magnetic) field, which is a background field (no dynamics):

$$\mathcal{L}_D = i\overline{\Psi}\gamma^\mu D_\mu^A \Psi + \text{interactions} = i\overline{\Psi}(\gamma^0 D_t + \boldsymbol{\gamma}\cdot\mathbf{D})\Psi + \text{interactions} \tag{19}$$

where $D_t = \frac{\partial}{\partial t} + iA_0$ and $\mathbf{D} = \boldsymbol{\nabla} - i\mathbf{A}$, and $\gamma^\mu,\ \mu = 0, 1, 2$ are 2×2 gamma matrices for the Dirac description in two spacial dimensions, and Ψ is a two-component Grassmann field.

The Dirac system is a neutral system and there is no Hall conductance. To make up for this, i.e. to continue to discuss an isolated LL (of classical electrons), which has $1/(4\pi)$ of the units $(e^2/\hbar)$ of Hall conductance, we consider

$$\mathcal{L}_A = i\overline{\Psi}\gamma^\mu D_\mu^A \Psi - \frac{A\partial A}{8\pi} + \text{interactions}. \tag{20}$$

If we define the density–current of electrons as

$$j^\mu_{\text{el}} = -\frac{\delta\mathcal{L}}{\delta A^\mu}\,, \tag{21}$$

it follows that for densities,

$$\rho_{\text{el}} = \rho_{\text{D}} + \frac{\boldsymbol{\nabla}\times\mathbf{A}}{4\pi}\,. \tag{22}$$

Because, $\overline{\rho}_{\text{D}}$ (average density of the Dirac system) $= 0$, we have a non-zero density of electrons

$$\frac{\overline{\rho}_{\text{el}}}{B} = \frac{1}{2}\,, \tag{23}$$

where $B = \frac{\boldsymbol{\nabla}\times\mathbf{A}}{2\pi}$ is the uniform external magnetic field. Also

$$\mathbf{j}_{\text{el}} = \mathbf{j}_{\text{D}} + \hat{\epsilon}\frac{\mathbf{E}}{4\pi}\,, \tag{24}$$

where $\hat{\epsilon}$ is a 2×2 matrix, $\epsilon_{xy} = -\epsilon_{yx} = 1$, $\epsilon_{xx} = \epsilon_{yy} = 0$. Thus, with $\overline{\rho}_{\text{D}} = 0$ and $\mathbf{j}_{\text{D}} = 0$, we are at half-filling, and the Hall conductance is equal to $\frac{1}{4\pi}(\frac{e^2}{\hbar})$.

Following Ref. 7, in a dual picture, we postulate a new Lagrangian, $\mathcal{L}$, with new dual Dirac field χ:

$$\mathcal{L} = i\overline{\chi}\gamma^\mu D_\mu^a \chi + a\frac{\partial A}{4\pi} - \frac{A\partial A}{8\pi} + \cdots \tag{25}$$

where $\cdots$ denotes higher order terms. (We will ignore these higher order terms below and consider classical equations of motion in the framework of the linear response theory.) Why would we expect this Lagrangian in a dual picture? We provide an analysis with more details below, but here we may note that the Dirac (two-component) formalism is expected also in a dual picture, because it makes possible that the PH symmetry is manifestly included as demonstrated in Ref. 7. Also note that the dual fermion is not directly coupled to the external field, and, as we show below, the Lagrangian describes a Dirac system at a finite density, in agreement with our expectation that the system is in a FLL state of quasiparticles. For further details on the dual approach see Refs. 25 and 26.

(i) It seems that χ's represent Read's quasiparticles. Indeed, if we consider the following equation of motion,

$$0 = \frac{\delta \mathcal{L}}{\delta a_0} = -\rho_\chi + \frac{\nabla \times \mathbf{A}}{4\pi}\,, \tag{26}$$

we can conclude that the density of χ depends on the number of flux quanta. On the other hand,

$$\rho_{\rm el} = -\frac{\delta \mathcal{L}}{\delta A_0} = -\frac{\boldsymbol{\nabla} \times \mathbf{a}}{4\pi} + \frac{\boldsymbol{\nabla} \times \mathbf{A}}{4\pi}\,, \tag{27}$$

and, at half-filling, in the mean-field approximation, $\boldsymbol{\nabla} \times \mathbf{a} = 0$. Thus, χ's do not experience any uniform, non-zero gauge field, $b = \frac{\boldsymbol{\nabla} \times \mathbf{a}}{2\pi}$, that couples χ's indirectly to the external field. Therefore, χ's are, in the first approximation, neutral objects, but with the Dirac's singularity in the inverse space at $\mathbf{k} = 0$. In this way, they have a non-analytical feature that we do not expect from a description that is based on Read's quasiparticles. We find that the effective theories based on the description with the Dirac's quasiparticle are very useful when considering the pairing physics, as they capture the time-reversal and parity breaking (that is essential for the pairing physics) as we will explain later in this section.

(ii) We expect that the effective theory of a half-filled LL should describe a Fermi-liquid of quasiparticles (if we do not consider the BCS instability). Indeed, in the mean-field approximation, in the first approximation, the internal field (b) is zero, and the theory describes a Dirac Fermi-liquid.

(iii) If we vary $\mathbf{a}$ in $\mathcal{L}$ we find

$$\mathbf{j}_{\rm D} = \hat{\epsilon}\frac{\mathbf{E}}{4\pi}\,. \tag{28}$$

Also,

$$\mathbf{j}_{\rm el} = -\frac{\delta \mathcal{L}}{\delta \mathbf{A}} = \hat{\epsilon}\frac{\mathbf{E} - \mathbf{e}}{4\pi}\,, \tag{29}$$

where $\mathbf{e}$ is the electric field due to the potential a^μ. Next, we assume that even in the presence of disorder, the PH symmetry is respected, and in the linear response we have,

$$\mathbf{j}_{\rm D} = \hat{\sigma}^{\rm D}\mathbf{e}\,, \tag{30}$$

where $\sigma^{\rm D}_{xx} = \sigma^{\rm D}_{yy} \neq 0$ represents a longitudinal conductance, and $\sigma^{\rm D}_{xy} = \sigma^{\rm D}_{yx} = 0$ (the Hall conductance is zero). The zero Hall conductance is an expression of the PH symmetry and a property of Dirac fermions. These three equations, (28), (29), and (30), combined lead to the conclusion that the Hall conductance of electrons is $\frac{1}{2}(\frac{e^2}{h})$, which we expect to be the case in the theory of the system with classical electrons that respects the PH symmetry.[27]

It is important to notice that $\sigma^{\rm D}_{xy} = \sigma^{\rm D}_{yx} = 0$ is not an only natural "choice" for the response of the non-interacting Dirac system (conus) to a perturbation due to a gauge (internal a^μ) field. To get the Hall conductance, we assume the presence of the mass term in the non-interacting Dirac description,

$$\mathcal{L}_{\rm D} = i\overline{\chi}\gamma^\mu D^a_\mu \chi - m\overline{\chi}\chi\,. \tag{31}$$

The $\sigma^{\rm D}_{xy}$ can be found by integration of Berry curvature in the inverse ($\mathbf{k}$) space,[27,28] by choosing a specific gauge for eigenstates, and integrating over occupied states. In this way, we can get contributions (in units $e^2/\hbar$):

$$\mathrm{sgn}(m)\frac{1}{4\pi}\left(1 - \frac{|m|}{\sqrt{k_F^2 + m^2}}\right), \tag{32}$$

from the positive-energy states that are filled for $0 \leq |\mathbf{k}| < k_F$, and

$$-\mathrm{sgn}(m)\frac{1}{4\pi}\,, \tag{33}$$

from the negative-energy states. There are two natural ways to take into account these two contributions: (1) to add them,

$$\sigma^{\rm D}_{xy} = -\frac{m}{\sqrt{k_F^2 + m^2}}\,, \tag{34}$$

i.e. adopt a "dimensional regularization," or (2) to consider only the contribution from the positive energy solutions:

$$\sigma^{\rm D}_{xy} = \mathrm{sgn}(m)\frac{1}{4\pi}\left(1 - \frac{|m|}{\sqrt{k_F^2 + m^2}}\right), \tag{35}$$

i.e. adopt a "Pauli–Villars regularization." It is obvious that in order to get an appropriate response in the Dirac theory (of the half-filled LL) we need to assume and apply the dimensional regularization in the field-theoretical treatment.

We can also conclude that by choosing an appropriate singular gauge (phase) transformation on the negative energy eigenstates, we can switch from the dimensional regularization to the Pauli–Villars regularization (and vice versa). This transformation can be understood as an adoption of a new quasiparticle picture and a new Lagrangian (here without higher order terms):

$$\mathcal{L} = i\overline{\chi}^{\rm qp}\gamma^\mu D^a_\mu \chi^{\rm qp} - \frac{a\partial a}{8\pi} + a\frac{\partial A}{4\pi} - \frac{A\partial A}{8\pi}\,. \tag{36}$$

To find the same response as before, we have to adopt Pauli–Villars regularization (when integrating out fermions and generating quadratic terms in a) with a positive mass to cancel the second term in $\mathcal{L}$. Physically we indeed switched to a new quasiparticle picture of Zhang's type. To see that let's consider the full theory with a positive ($m > 0$) mass term:

$$\mathcal{L} = i\overline{\chi}^{\rm qp} D_a \chi^{\rm qp} - m\overline{\chi}^{\rm qp}\chi^{\rm qp} - \frac{a\partial a}{8\pi} + a\frac{\partial A}{4\pi} - \frac{A\partial A}{8\pi}\,. \tag{37}$$

(i) From the equations of motion,

$$0 = \frac{\delta \mathcal{L}}{\delta a^\mu} = -j_\chi^{\mathrm{qp},\mu} - \frac{\partial a}{4\pi} + \frac{\partial A}{4\pi}\,, \tag{38}$$

and

$$j_{\mathrm{el}}^\mu = -\frac{\delta \mathcal{L}}{\delta A^\mu} = \frac{\partial A}{4\pi} - \frac{\partial a}{4\pi}\,, \tag{39}$$

it follows that, $j_{\mathrm{el}}^\mu = j_\chi^{\mathrm{qp},\mu}$, as usual in the CS theory, i.e. the theory directly relates to the Zhang's quasiparticle construction.

(ii) If we let $m \to \infty$ the effective Lagrangian becomes the HLR after the shift $a^\mu \to a^\mu + A^\mu$.[29]

We can conclude that the Lagrangian in (37), with $m = 0$, describes the physics of an isolated (PH symmetric) LL using the Zhang's quasiparticle picture. The introduction of non-zero m represents LL mixing, i.e. a measure of the inclusion of other LLs, so that for large m we can recover the HLR theory that does not reduce the effective physics of the electron system to a single LL.

3. Pfaffian Paired States at Half-Integer Filling

In this section, we will adopt the Dirac quasiparticle picture that is given by the Lagrangian in (37) for a FQHE system at a half-integer filling factor. Thus, the starting Lagrangian is

$$\mathcal{L} = i\overline{\chi}\gamma^\mu D_\mu^a \chi - m\overline{\chi}\chi - \frac{m}{|m|}\frac{a\partial a}{8\pi} + a\frac{\partial A}{4\pi} - \frac{A\partial A}{8\pi}\,, \tag{40}$$

where for simplicity we omitted qp letters when writing χ fields with respect to (37), but we should be aware that for any probes (perturbative expansions) the Pauli–Villars regularization is understood. We generalized the Lagrangian in (37) for both signs of mass m (to cancel the additional contribution due to the assumed Pauli–Villars regularization, the first term in (35)). It follows that

$$j_\chi^\mu = -\frac{m}{|m|}\frac{\partial a}{4\pi} + \frac{\partial A}{4\pi}\,, \tag{41}$$

and

$$j_{\mathrm{el}}^\mu = -\frac{\partial a}{4\pi} + \frac{\partial A}{4\pi}\,, \tag{42}$$

as a generalization of (38) and (39) to both signs of mass. Exactly at half-filling, i.e. when in a uniform, constant magnetic field we have on average one electron per two flux quanta, we may solve (41) in the Coulomb gauge, $\boldsymbol{\nabla}\cdot\mathbf{a} = 0$. The solutions are[22]

$$a_x(\mathbf{r}) = 2\frac{m}{|m|}\int d\mathbf{r}' i\frac{y - y'}{|\mathbf{r} - \mathbf{r}'|^2}\delta\rho_\chi(\mathbf{r}')\,, \tag{43}$$

and

$$a_y(\mathbf{r}) = -2\frac{m}{|m|}\int d\mathbf{r}' i\frac{x-x'}{|\mathbf{r}-\mathbf{r}'|^2}\delta\rho_\chi(\mathbf{r}')\,, \tag{44}$$

and $\delta\rho_\chi(\mathbf{r}') = \chi^\dagger(\mathbf{r}')\chi(\mathbf{r}') - \bar{\rho}$, where $\bar{\rho}$ is a constant (external flux density). We would like to analyze the effect on pairing of the interaction term,

$$V_{\text{int}} = -\mathbf{a}\overline{\chi}\boldsymbol{\gamma}\chi\,. \tag{45}$$

In the following, representation of γ matrices,

$$\gamma^0 = \sigma_3, \quad \gamma^1 = i\sigma_2, \quad \gamma^2 = -i\sigma_1\,, \tag{46}$$

where $\sigma_i, i = 1,2,3$ are Pauli matrices, we have

$$V_{\text{int}} = -\mathbf{a}\chi^+\boldsymbol{\sigma}\chi\,. \tag{47}$$

In this representation, we have the following expression for the interaction:

$$V_{\text{int}} = -i2\frac{m}{|m|}\int d\mathbf{r}'\delta\rho_\chi(\mathbf{r}')\chi^\dagger(\mathbf{r})\begin{bmatrix} 0 & \dfrac{\bar{z}-\bar{z}'}{|\mathbf{r}-\mathbf{r}'|^2} \\ -\dfrac{z-z'}{|\mathbf{r}-\mathbf{r}'|^2} & 0 \end{bmatrix}\chi(\mathbf{r})\,. \tag{48}$$

On the other hand, the presence of the mass term in the Dirac system leads to the following eigenproblem,

$$\begin{bmatrix} m-\epsilon & k_- \\ k_+ & -m-\epsilon \end{bmatrix}\chi(\mathbf{k}) = 0\,, \tag{49}$$

where $k_- = k_x - ik_y$ and $k_+ = k_x + ik_y$. The positive eigenvalue, $\epsilon = \sqrt{|\mathbf{k}|^2 + m^2} \equiv E_\mathbf{k}$, corresponds to the following eigenstate,

$$\chi_E = \begin{bmatrix} m + E_\mathbf{k} \\ k_+ \end{bmatrix}\frac{1}{\sqrt{2E_\mathbf{k}(E_\mathbf{k}+m)}}\,. \tag{50}$$

As we consider relevant only (positive energy) states around k_F, we will keep only these states in the expansion over $\mathbf{k}$-eigenstates of field $\chi(\mathbf{r})$, and, further, only consider the BCS pairing channel in V_{int}. Thus (in the second-quantized notation)

$$\chi(\mathbf{r}) = \frac{1}{\sqrt{2V}}\sum_\mathbf{k}\exp\{i\mathbf{k}\cdot\mathbf{r}\}\chi_E(\mathbf{k})a_\mathbf{k} + \cdots\,, \tag{51}$$

and

$$\begin{aligned} V_{\text{int}}^{\text{BCS}} = \frac{m}{|m|}\frac{2\pi}{8V}\sum_{\mathbf{k},\mathbf{p}} a_\mathbf{k}^\dagger a_\mathbf{p} a_{-\mathbf{k}}^\dagger a_{-\mathbf{p}} \times \frac{1}{E_\mathbf{k}E_\mathbf{p}(m+E_\mathbf{k})(m+E_\mathbf{p})} \\ \times\{(m+E_k)(m+E_p) + k_-p_+\} \\ \times\begin{bmatrix} m+E_k, & -k_- \end{bmatrix}\begin{bmatrix} 0 & \dfrac{1}{k_+-p_+} \\ -\dfrac{1}{k_--p_-} & 0 \end{bmatrix}\begin{bmatrix} m+E_p \\ -p_+ \end{bmatrix}. \end{aligned} \tag{52}$$

We used: $\int d\mathbf{r}\frac{1}{z}\exp\{i\mathbf{kr}\} = i\frac{2\pi}{k_+}$. We may rewrite this expression (taking into account the antisymmetry of the fermionic operators) as

$$V_{\text{int}}^{\text{BCS}} = \sum_{\mathbf{k},\mathbf{p}} V_{\mathbf{kp}} a_{\mathbf{k}}^\dagger a_{\mathbf{p}} a_{-\mathbf{k}}^\dagger a_{-\mathbf{p}}\,, \tag{53}$$

where

$$\begin{aligned} V_{\mathbf{kp}} = \frac{2\pi}{8V}\frac{1}{E_k \cdot E_p} \\ \times \left[-4|m|kp\frac{i\sin(\theta_p-\theta_k)}{|\mathbf{k}-\mathbf{p}|^2} - \frac{m}{|m|}(E_k+E_p+2m)(E_k-m)(E_p-m)\right. \\ \left.\times \frac{\exp\{i2(\theta_p-\theta_k)\}-1}{|\mathbf{k}-\mathbf{p}|^2}\right]. \end{aligned} \tag{54}$$

Now we will adopt the mean-field BCS approximation, in an expectation that the topological characterization of pairing instabilities, will stay unchanged under this approximation. In the following, we will review the relevant parts of the BCS mean-field theory. We will follow the notation of Ref. 30. The effective Hamiltonian is

$$K_{\text{eff}} = \sum_{\mathbf{k}} \left\{ \xi_k a_{\mathbf{k}}^\dagger a_{\mathbf{k}} + \frac{1}{2}(\Delta_{\mathbf{k}}^* a_{-\mathbf{k}} a_{\mathbf{k}} + \Delta_{\mathbf{k}} a_{\mathbf{k}}^\dagger a_{-\mathbf{k}}^\dagger) \right\}, \tag{55}$$

and in our case $\xi_k = E_k - \mu$, with $E_k = \sqrt{|\mathbf{k}|^2 + m^2}$. The Bogoliubov transformation is

$$\alpha_{\mathbf{k}} = u_{\mathbf{k}} a_{\mathbf{k}} - v_{\mathbf{k}} a_{-\mathbf{k}}^\dagger\,, \tag{56}$$

with

$$\begin{aligned} \frac{v_{\mathbf{k}}}{u_{\mathbf{k}}} = \frac{-(\mathcal{E}_k - \xi_k)}{\Delta_{\mathbf{k}}^*}, \quad |u_{\mathbf{k}}|^2 = \frac{1}{2}\left(1 + \frac{\xi_k}{\mathcal{E}_k}\right), \\ |v_{\mathbf{k}}|^2 = \frac{1}{2}\left(1 - \frac{\xi_k}{\mathcal{E}_k}\right), \end{aligned} \tag{57}$$

and $\mathcal{E}_k = \sqrt{\xi_k^2 + |\Delta_{\mathbf{k}}|^2}$.

On the other hand, if we start with a Cooper channel interaction and do the BCS mean-field decomposition with $b_{\mathbf{k}}^\dagger = a_{\mathbf{k}}^\dagger a_{-\mathbf{k}}^\dagger$

$$\sum_{\mathbf{k},\mathbf{p}} V_{\mathbf{kp}}\, b_{\mathbf{k}}^\dagger\, b_{\mathbf{p}} = \sum_{\mathbf{k},\mathbf{p}} V_{\mathbf{kp}} \langle b_{\mathbf{k}}^\dagger \rangle b_{\mathbf{p}} + \sum_{\mathbf{k},\mathbf{p}} V_{\mathbf{kp}} b_{\mathbf{k}}^\dagger \langle b_{\mathbf{p}} \rangle - \sum_{\mathbf{k},\mathbf{p}} V_{\mathbf{kp}} \langle b_{\mathbf{k}}^\dagger \rangle \langle b_{\mathbf{p}} \rangle\,, \tag{58}$$

and specify $u_{-\mathbf{k}} = u_{\mathbf{k}} = u_{\mathbf{k}}^*$ and $v_{-\mathbf{k}} = -v_{\mathbf{k}}$, then

$$\begin{aligned} \frac{\Delta_{\mathbf{p}}^*}{2} &= \sum_{\mathbf{k}} V_{\mathbf{kp}} \langle a_{\mathbf{k}}^\dagger a_{-\mathbf{k}}^\dagger \rangle \\ &= \sum_{\mathbf{k}} V_{\mathbf{kp}} \langle (u_{\mathbf{k}} \alpha_{\mathbf{k}}^\dagger + v_{\mathbf{k}}^* \alpha_{-\mathbf{k}})(-v_{\mathbf{k}}^* \alpha_{\mathbf{k}} + u_{\mathbf{k}} \alpha_{-\mathbf{k}}^\dagger) \rangle\,, \end{aligned} \tag{59}$$

i.e.

$$\frac{\Delta^*_{\mathbf{p}}}{2} = \sum_{\mathbf{k}} V_{\mathbf{kp}} v^*_k u_k = \sum_{\mathbf{k}} V_{\mathbf{kp}} (-) \frac{\Delta^*_{\mathbf{k}}}{2\,\mathcal{E}_k} \,. \tag{60}$$

In our case $V_{\mathbf{kp}}$ is given in (54). The numerical solutions of the BCS self-consistent equation, when the parameter k_F is kept fixed, but mass m is varied, for channels $l = 1, 3, -1$, with $\Delta^*_{\mathbf{k}} = |\Delta_{\mathbf{k}}| \exp\{il\theta_{\mathbf{k}}\}$ are described in Fig. 1. We find that $\Delta^*_{\mathbf{k}} = |\Delta_{\mathbf{k}}| \exp\{-il\theta_{\mathbf{k}}\}$, $l = 1, 3, -1$ are solutions if we switch gauge for the eigenstates of the Dirac equation, i.e. instead of (50) we take

$$\chi_E = \begin{bmatrix} k_- \\ E_{\mathbf{k}} - m \end{bmatrix} \frac{1}{\sqrt{2E_{\mathbf{k}}(E_{\mathbf{k}} - m)}} \,. \tag{61}$$

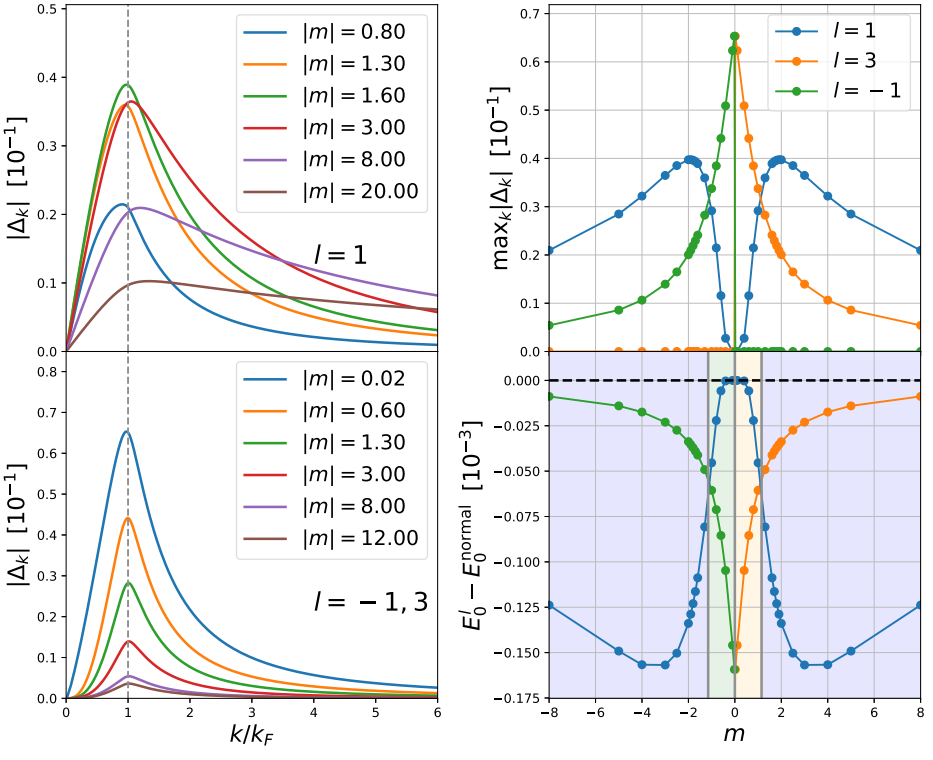

Fig. 1. (Color online) The solution of the self-consistent BCS problem. Left column: radial direction k-dependent pairing amplitude for various values of m. Channel $l = 1$ solution (PH Pfaffian) only depends on $|m|$, while $l = 3$ (anti-Pfaffian) and $l = -1$ (Pfaffian) channel solutions are symmetric with the sign-flip of m. Upper right panel: dependence of the maximum of the pairing amplitude on m (always found at the Fermi level k_F). Lower right panel: total energy of the different pairing solutions compared to the normal state energy. Gray vertical lines denote the transition between different channels. Color in the background corresponds to the energetically favorable channel at the given m: a measure of LL mixing. The color of lines: Pfaffian: green, anti-Pfaffian: orange, PH Pfaffian: blue. Reprinted with permission from Ref. 18 © the American Physical Society.

Thus we get two sets of solutions, because the effective theory does not possess the knowledge of the direction of the external magnetic field. Despite this, we have a clear prediction that for small m, LL mixing, depending on the sign of m we have Pfaffian or anti-Pfaffian, and for large m the PH Pfaffian solution is possible. Thus, in principle, the PH Pfaffian is possible in this effective theory of quasiparticle pairing. The nature of this state, whether it is gapped or gapless state of electrons, needs further investigations (though we see that the Bogoliubov quasiparticle spectrum is gapped).

These predictions on topological pairing, when the LL mixing (mass m) is small, are in accordance with numerical experiments (a) in the second LL, because for $m = 0$ there is a Schrodinger cat superposition of Pfaffian and anti-Pfaffian,[31,32] and depending on the LL mixing (sign of PH breaking mass) we have Pfaffian or anti-Pfaffian, and (b) in the LLL, where a PH Pfaffian wave function has a large overlap with the composite fermion Fermi-liquid wave function,[13,33] in accordance with Fig. 1 where the PH Pfaffian-like state is continuously connected to the excited composite fermion Fermi-liquid state at $m = 0$ and cannot represent a gapped state in an isolated LL.

The dimensionless m in the theory is a measure of the PH symmetry breaking and LL mixing, although the precise relation between m and

$$\kappa = \frac{\frac{e^2}{\epsilon_r l_B}}{\hbar\omega_c}\,, \tag{62}$$

i.e. the ratio between the characteristic interaction energy and cyclotron energy, known as a LL mixing coefficient, we do not know. In (62), ϵ_r is the dielectric constant of the background material, $\hbar\omega_c = \frac{\hbar eB}{m_{\rm b}c}$, and $m_{\rm b}$ is the electron band mass. As we keep the density, $\rho = \frac{\nu}{2\pi l_B^2} = \frac{1}{2}\frac{1}{2\pi l_B^2}$, i.e. k_F fixed, from the mathematical limit of the PH symmetric case when $m = 0$, we reach various systems (experimental settings) by changing the interaction strength (dielectric constant ϵ_r). Thus m, in principle, can be connected with κ, which can be considerable in experiments. (According to Ref. 41 the parameter κ is given by $2.6/\sqrt{B}$, $14.6/\sqrt{B}$, $16.7/\sqrt{B}$, $22.5/\sqrt{B}$, in n-doped GaAs, p-doped GaAs, n-doped ZnO, and n-doped AlAs, with B measured in Tesla.)

4. Model Interactions for Pfaffian Paired States

It is important to know model interactions for model wave functions in order to probe their stability and nature. In the case of bosons, the Pfaffian state at filling factor 1 is

$$\Psi^b_{\rm Pf} = \sum_\sigma \operatorname{sgn}\sigma \left\{ \frac{1}{(z_{\sigma(1)} - z_{\sigma(2)})} \cdots \frac{1}{(z_{\sigma(N_e-1)} - z_{\sigma(N_e)})} \right\} \times \prod_{k<l} (z_k - z_l)\,. \tag{63}$$

The model interaction for which this state is an exact, densest state of zero energy[34] is

$$H = v \sum_{\langle ijk \rangle} \delta^2(z_i - z_j)\delta^2(z_i - z_k)\,, \tag{64}$$

where $v > 0$ and the sum is over all distinct triples of particles. Thus if three bosons meet (come as close as possible) this will cost repulsive energy. In the case of fermions at filling factor 1/2, the Pfaffian model interaction is a generalization of the boson interaction to the one that, if three fermions come as close as possible, again, only this will cost energy. The lowest angular momentum wave function of three electrons in the LLL can be described as

$$\Psi(\mathbf{r}_1, \mathbf{r}_2, \mathbf{r}_3) \sim \sum_{\sigma} \operatorname{sgn} \sigma z^2_{\sigma(1)} z^1_{\sigma(2)} z^0_{\sigma(3)} \exp\left\{-\frac{1}{4l_B}(|z_1|^2 + |z_2|^2 + |z_3|^2)\right\}. \tag{65}$$

We may conclude that if $M(\text{angular momentum}) = 3$ for three electrons this will cost interaction energy. Indeed, it can be argued, just as in the case of the Laughlin state and two-body PPs,[35] that in the case of Pfaffian we need to specify only a truncated series of three-body PPs with definite three-body angular momenta. At filling factor 1/2, only non-zero three-body PP is the one for $M = 3$. (For bosons, at filling factor 1, the only non-zero three-body PP is for $M = 0$.)

These model interactions are highly artificial if we want to model and probe real physical systems. In the FQHE, we can always specify the base LL from which most of correlations originate, but should also consider the effects of LL mixing. Beside the Coulomb (two-body) interaction at a half-integer filling factor, we may take into account perturbatively the effects of LL mixing, by considering special three-body interactions.[37–41] In this way we may find a characteristic series of three-body PPs for Pfaffian state, when considering the specific problem of the second LL and associated LL mixing contribution. A PP is a certain characteristic energy, V_M, associated with a three-body state at total angular momentum M. (The dimension of the subspace of a fixed angular momentum for three particles may be larger than one for higher M, and V_M may be a matrix.) In the case of Pfaffian, the dominant, first three values of three-body PPs, for $M = 3, 5, 6$ are negative and $\frac{V_{M=5}}{V_{M=3}} \sim 0.4$ and $\frac{V_{M=6}}{V_{M=3}} \sim 0.7$.[41] We may ask what would be a characteristic series for PH Pfaffian, if we assume that the PH Pfaffian state or phase exists, and expect that some kind of three-body interaction will be relevant also in this case.

To answer this question we may consider again the CS formalism, not directly connected with considerations in Sec. 3. We will recall[34] the effective derivation of the Pfaffian physics, by a part of the kinetic term in the non-relativistic CS description. (Thus these considerations will not relate to the solution in Sec. 3, in the large m limit, when we take into account the complete kinetic term.) We will use this formal derivation to propose a method for recovering model interactions for Pfaffian and PH Pfaffian. (By using the PH exchange we can reach a model interaction also for anti-Pfaffian.)

To get (formally) the Pfaffian pairing solution we may consider the kinetic energy part of the (non-relativistic) CS approach in (15), i.e. the part of the Hamiltonian given by

$$\mathcal{H} = \frac{\Psi^{+}_{\rm cf}(\mathbf{p}-\mathbf{A}-\mathbf{a})^2\Psi_{\rm cf}}{2m}\,, \tag{66}$$

with $\mathbf{B} = B\mathbf{z}$, with $A_x = -(B/2)y$ and $A_y = (B/2)x$, as before, and

$$a_x(\mathbf{r}) = 2\int d\mathbf{r}' i\frac{y-y'}{|\mathbf{r}-\mathbf{r}'|^2}\delta\rho_{\rm cf}(\mathbf{r}')\,, \tag{67}$$

and

$$a_y(\mathbf{r}) = -2\int d\mathbf{r}' i\frac{x-x'}{|\mathbf{r}-\mathbf{r}'|^2}\delta\rho_{\rm cf}(\mathbf{r}')\,, \tag{68}$$

as before, in the Coulomb gauge $\boldsymbol{\nabla}\cdot\mathbf{a} = 0$, and $\delta\rho_{\rm cf} = \Psi^{+}_{\rm cf}\Psi_{\rm cf} - \overline{\rho}$, where $\overline{\rho}$ is the average density. We consider the following part of the implied interaction,

$$V_{\rm a} = -\mathbf{a}\mathbf{j}_{\rm cf}\,, \tag{69}$$

with

$$\mathbf{j}_{\rm cf} = \frac{1}{2m}[\Psi^{+}_{\rm cf}(\mathbf{p}\Psi_{\rm cf}) - (\mathbf{p}\Psi^{+}_{\rm cf})\Psi_{\rm cf}]\,, \tag{70}$$

more specifically its Cooper channel part.

After simple steps,[19] we arrive at the Cooper channel part,

$$V^{\rm C}_{\rm int} = \frac{4\pi}{m}\frac{1}{V}\sum_{\mathbf{k},\mathbf{p}}|\mathbf{k}||\mathbf{p}|\frac{i\sin(\theta_k-\theta_p)}{|\mathbf{p}-\mathbf{k}|^2}a^{\dagger}_{\mathbf{k}}a_{\mathbf{p}}a^{\dagger}_{-\mathbf{k}}a_{-\mathbf{p}}\,. \tag{71}$$

Note that in this case (following the mean-field equations and derivation in Ref. 30, or in Ref. 19) we find that the Cooper pair wave function behaves as,

$$\lim_{|\mathbf{r}|\to\infty} g(\mathrm{r}) \sim \frac{1}{z}\,. \tag{72}$$

This implies the Pfaffian construction (after the unitary CS transformation into the electron representation), if we recall that the choice of $\mathbf{A}$ in (66) implies a holomorphic Laughlin–Jastrow factor (more precisely a phase factor after the unitary CS transformation) that is associated with the usual description of the Pfaffian state in (5). If we had an extra minus sign in (71), this would lead to the antiholomorphic pairing, i.e. the PH Pfaffian pairing.

To derive the model interactions for Pfaffian and PH Pfaffian, we assume that we can use an effective non-relativistic CS description to describe the pairing of underlying quasiparticles (composite fermions). On the basis of the previous consideration ((69) and (71)), we consider an effective Hamiltonian,

$$H^{\rm ef}_{\rm BCS} = \frac{1}{2m}\Psi^{\dagger}_{\rm cf}(\mathbf{p})^2\Psi_{\rm cf} + \lambda\delta\mathbf{a}\mathbf{j}_{\rm cf}\,, \tag{73}$$

where $\delta\mathbf{a} = \mathbf{A} + \mathbf{a}$, and the coupling λ is negative in the Pfaffian case and positive in the PH Pfaffian case. Thus we assumed that a complete (non-relativistic) CS

description that includes all effects of interactions can be reduced to the effective form if a pairing occurs. By using the non-relativistic CS description we take into account PH symmetry breaking necessary to stabilize these pairing states.

If we apply the CS transformation in reverse,[19] going from the composite fermion representation to an electron one, we arrive at the following effective Hamiltonian for electrons,

$$H^{\rm el}_{\rm BCS} = \frac{1}{2m}\Psi^\dagger(\mathbf{p}-\mathbf{A})^2\Psi - \frac{1}{2m}(\delta\mathbf{a})^2\Psi^\dagger\Psi + (1+\lambda)\delta\mathbf{a}\mathbf{J}_{\rm el} + (1+\lambda)\frac{1}{m}(\delta\mathbf{a})^2\Psi^\dagger\Psi\,, \tag{74}$$

where

$$\mathbf{J}_{\rm el} = \frac{-i}{2m}\Psi^\dagger(\nabla + i\mathbf{A})\Psi - [(\nabla + i\mathbf{A})\Psi]^\dagger\Psi\,, \tag{75}$$

is the (gauge invariant) electron current.

We concentrate on the effective three-body (electron) interaction that is present in the Hamiltonian,

$$V^3_{\rm BCS}(\lambda) = (1/2+\lambda)\frac{1}{m} : (\mathbf{a})^2\Psi^\dagger\Psi : \,. \tag{76}$$

The three-body interaction in coordinate representation is

$$V(\mathbf{r}_1,\mathbf{r}_2,\mathbf{r}_3) = (1/2+\lambda)\frac{4}{m}\frac{(\mathbf{r}_3-\mathbf{r}_1)(\mathbf{r}_3-\mathbf{r}_2)}{|\mathbf{r}_3-\mathbf{r}_1|^2|\mathbf{r}_3-\mathbf{r}_2|^2}\,. \tag{77}$$

To describe the relevant matrix elements for LL(s), we will choose our base LL to be the LLL, which is the most natural choice when we consider a CS description; the very CS transformation is based on the Laughlin–Jastrow correlations in the LLL. Thus, for example, we will relate the effective PPs that we know for the Pfaffian state, based on the perturbation theory, in the second LL, with here calculated PPs, based on the CS description, in the LLL.

To describe relevant three-body PPs (V_M) in the LLL, we introduce rescaled matrix elements, $\Delta_{M=2k+3l}$,

$$V_M = \int d\mathbf{r}_1 \int d\mathbf{r}_2 \int d\mathbf{r}_3 V(\mathbf{r}_1,\mathbf{r}_2,\mathbf{r}_3)|\Psi_{k,l}(\mathbf{r}_1,\mathbf{r}_2,\mathbf{r}_3)|^2 = (1/2+\lambda)\cdot 4/m\cdot\Delta_{M=2k+3l}\,,$$

where $\Psi_{k,l}$ are normalized, fully antisymmetric wave functions for three electrons,[42] classified by integers $k \geq 0; l \geq 1$, and the total angular momentum of the state is $M = (2k+3l)$. The calculated Δ_M are shown in the Table 1.

The matrix elements are illustrated by their rescaled values $\frac{m}{4}V_M = (1/2+\lambda)\cdot\Delta_{M=2k+3l}$, in the cases when $\lambda = -1$ and $\lambda = 0$ in Fig. 2. What is remarkable is that according to the Table 1, $\frac{V_{M=5}}{V_{M=3}} = 0.5$, and $\frac{V_{M=6}}{V_{M=3}} = 0.7$, and are quite close to the ratios of the relevant matrix elements from the perturbation theory in the second LL, ~ 0.4, and ~ 0.7, respectively, that favor the Pfaffian physics.[43]

Thus the CS description is able to capture the sign — a negative one of necessary PPs when $\lambda < -1/2$, and their relative magnitude for relevant, those first three PPs in the Pfaffian case. Therefore, we are encouraged to probe the PH Pfaffian case

Table 1. Matrix elements in the LLL. Reprinted with permission from Ref. 19 © the American Physical Society.

M	3	5	6	7	8	9	
Δ_M	1/24	1/48	7/240	1/80	2/105	221/10080	$1/(240\sqrt{21})$
						$1/(240\sqrt{21})$	1/120
$\frac{\Delta_M}{\Delta_{M=3}}$	1	0.5	0.7	0.3	~ 0.475	~ 0.526	~ 0.022
						~ 0.022	0.2

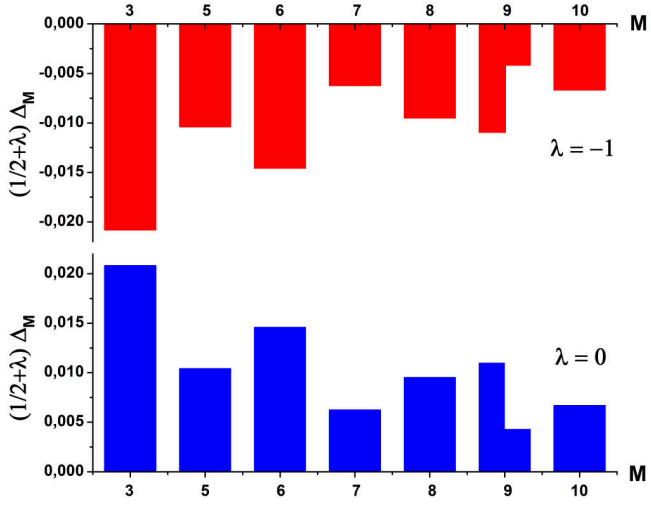

Fig. 2. (Color online) Matrix elements of three body PPs in the LLL for $\lambda = -1$ (above) and $\lambda = 0$ (bottom). (We plotted two values, diagonal matrix elements in the two-dimensional subspace, in the case when $M = 9$.) Reprinted with permission from Ref. 19 © the American Physical Society.

for certainly $\lambda > 0$. (We can identify the $\lambda = 0$ case with composite fermion Fermi liquid case.) But we have to be aware that in the effective description by $H^{\rm el}_{\rm BCS}$, the estimate that we can make for LL mixing parameter (in general the ratio of characteristic interaction energy and cyclotron energy) is $|\lambda+1/2|$, and that for any considerable $\lambda \gtrsim 1/2$ for which PH Pfaffian correlations are relevant, we have to include higher LL(s) (i.e. not only the base LL — the LLL in the CS description). Thus in the PH Pfaffian case, we have to include (three-body) PPs for at least one more LL. The calculated PPs (more precisely their rescaled $(m/4)V_M$ values) for two LLs when $\lambda = 1$ are illustrated in Fig. 3. While calculating these PPs, we had to include the natural cut-off l_B in the field-theoretical description, to suppress divergences in the second LL. We can conclude from Fig. 3 that in the case of PH Pfaffian, there is an abrupt decrease in the positive values of three-body PPs at $M = 7$ in the base (LLL) level and also at $M = 5$, when two of three electrons are in the higher (second) LL. This can be compared with the usual (truncated) model for Pfaffian with only non-zero, positive potential $V_{M=3}$; there is no three fermion state

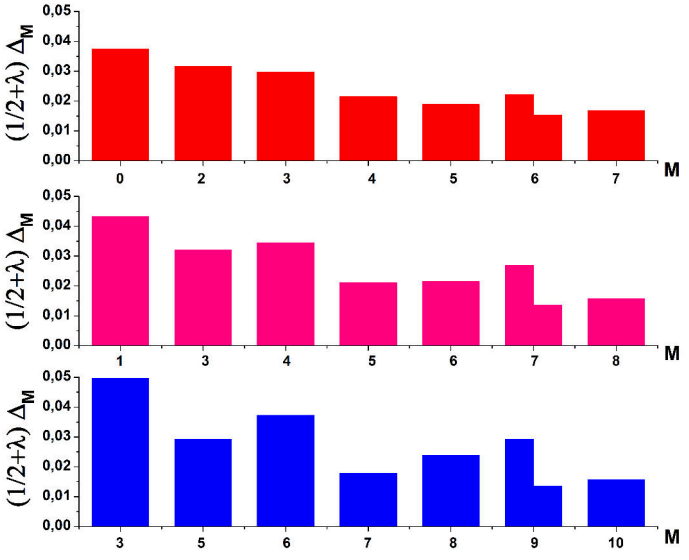

Fig. 3. (Color online) Three-body PP matrix elements for $\lambda = 1$ (PH Pfaffian case) in the second LL (top), for states with two particles in the second LL and one in the LLL (middle), and (all three) in the LLL (bottom). Reprinted with permission from Ref. 19 © the American Physical Society.

with $M = 4$, and the V_5 PP that is connected with the characteristic three-body angular momentum for Pfaffian in the LLL, $M = 5$, is zero.[36] In the case of the PH Pfaffian, the characteristic angular momentum is $M = 7$ in the LLL, and thus the abrupt decrease(s) in the values of three-body PPs that we may associate with the PH Pfaffian pairing correlations. The (almost) monotonic decrease of PPs when all three particles are in the second LL suggests that the space of two LLs may be necessary, but also sufficient for the realization of the PH Pfafian correlations. The important question, which needs further investigation, is whether these correlations are associated with a gapped state. The most recent suggestion for the realization of PH Pfaffian is in Ref. 44.

5. Conclusions and Outlook

In this review, we have demonstrated that the CS field-theoretical approach can be useful and informative in the description of Pfaffian and anti-Pfaffian states — well-established candidate states for the explanation of gapped states at half-integer filling factors in the FQHE. It can capture the pairing nature of these states, when the basic gauge-field constraints are taken into account in a generalized Dirac effective description of the problem. The effective Dirac description originates from the physics inside a base LL, which, when isolated (in the case of the Coulomb problem) possesses PH symmetry. To stabilize Pfaffian or anti-Pfaffian, we have to break this symmetry by a mass (of definite sign) term in the Dirac theory.

The physics of an isolated base LL in the Dirac effective description suggests a possible existence of a PH symmetric Pfaffian state.[7] We find that this solution is relevant only when a significant PH breaking (mass) is included in the Dirac description. Considering a non-relativistic limit of the description we find that interaction parameters that describe the influence from the higher (second) LL must be non-perturbatively included in a model interaction for PH Pfaffian (beside the ones from the base (lowest) LL). This may be helpful in the effort to stabilize and detect PH Pfaffian correlations in numerical experiments.

Acknowledgments

This research was supported by the Ministry of Education, Science, and Technological Development of the Republic of Serbia under Project ON171017, and by the Ministry of Science of Montenegro under Project SFS013454.

References

1. D. C. Tsui, H. L. Stormer and A. C. Gossard, *Phys. Rev. Lett.* **59** (1987) 1776.
2. R. Willett, J. P. Eisenstein, H. L. Stormer, D. C. Tsui, A. C. Gossard and J. H. English, *Phys. Rev. Lett.* **59** (1987) 1776.
3. G. Moore and N. Read, *Nucl. Phys. B* **360** (1991) 362.
4. S. H. Simon, in *Composite Fermions*, ed. O. Heinonen (World Scientific, Singapore, 1998), p. 91.
5. R. L. Willett, R. R. Ruel, K. W. West and L. N. Pfeiffer, *Phys. Rev. Lett.* **71** (1993) 3846.
6. B. I. Halperin, P. A. Lee and N. Read, *Phys. Rev. B* **47** (1993) 7312.
7. D. T. Son, *Phys. Rev. X* **5** (2015) 031027.
8. S.-S. Lee, S. Ryu, C. Nayak and M. P. A. Fisher, *Phys. Rev. Lett.* **99** (2007) 236807.
9. M. Levin, B. I. Halperin and B. Rosenow, *Phys. Rev. Lett.* **99** (2007) 236806.
10. T. Jolicoeur, *Phys. Rev. Lett.* **99** (2007) 036805.
11. P. T. Zucker and D. E. Feldman, *Phys. Rev. Lett.* **117** (2016) 096802.
12. E. H. Rezayi, *Phys. Rev. Lett.* **119** (2017) 026801.
13. R. V. Mishmash, D. F. Mross, J. Alicea and O. I. Motrunich, *Phys. Rev. B* **98** (2018) 081107(R).
14. M. Banerjee, M. Heiblum, V. Umansky, D. E. Feldman, Y. Oreg and A. Stern, *Nature* **559** (2018) 205.
15. K. K. W. Ma and D. E. Feldman, *Phys. Rev. B* **100** (2019) 035302.
16. D. F. Mross, Y. Oreg, A. Stern, G. Margalit and M. Heiblum, *Phys. Rev. Lett.* **121** (2018) 026801.
17. C. Wang, A. Vishwanath and B. I. Halperin, *Phys. Rev. B* **98** (2018) 045112.
18. L. Antonić, J. Vučičević and M. V. Milovanović, *Phys. Rev. B* **98** (2018) 115107.
19. S. Djurdjević and M. V. Milovanović, *Phys. Rev. B* **100** (2019) 195303.
20. R. B. Laughlin, *Phys. Rev. Lett.* **50** (1983) 1395.
21. E. H. Rezayi and F. D. M. Haldane, *Phys. Rev. Lett.* **84** (2000) 4685.
22. S.-C. Zhang, *Int. J. Mod. Phys. B* **6** (1992) 25.
23. N. Read, *Semicond. Sci. Technol.* **9** (1994) 1859; N. Read, *Surf. Sci.* **361** (1996) 7.
24. D. H. Lee and M. P. A. Fisher, *Phys. Rev. Lett.* **63** (1989) 903.
25. N. Seiberg, T. Senthil, C. Wang and E. Witten, *Ann. Phys.* **374** (2016) 395.

26. T. Senthil, D.T. Son, C. Wang and C. Xu, *Phys. Rep.* **827** (2019) 1.
27. A. C. Potter, M. Serbyn and A. Vishwanath, *Phys. Rev. X* **6** (2016) 031026.
28. D. Xiao, M.-C. Chang and Q. Niu, *Rev. Mod. Phys.* **82** (2010) 1959.
29. C. Wang, N. R. Cooper, B. I. Halperin and A. Stern, *Phys. Rev. X* **7** (2017) 031029.
30. N. Read and D. Green, *Phys. Rev. B* **61** (2000) 10267.
31. M. R. Peterson, K. Park and S. Das Sarma, *Phys. Rev. Lett.* **101** (2008) 156803.
32. H. Wang, D. N. Sheng and F. D. M. Haldane, *Phys. Rev. B* **80** (2004) 241311(R).
33. A. C. Balram, M. Barkeshli and M. S. Rudner, *Phys. Rev. B* **98** (2018) 035127.
34. M. Greiter, X. G. Wen and F. Wilczek, *Nucl. Phys. B* **374** (1982) 567.
35. F. D. Haldane, in *The Quantum Hall Effect*, eds. R. Prange and S. M. Girvin (Springer-Verlag, New York, 1987), p. 303; F. D. M. Haldane, *Phys. Rev. Lett.* **51** (1983) 605.
36. S. H. Simon, E. H. Rezayi and N. R. Cooper, *Phys. Rev. B* **75** (2007) 195306.
37. W. Bishara and C. Nayak, *Phys. Rev. B* **80** (2009) 121302(R).
38. M. R. Peterson and C. Nayak, *Phys. Rev. B* **87** (2013) 245129.
39. S. H. Simon and E. H. Rezayi, *Phys. Rev. B* **87** (2013) 155426.
40. R. E. Wooten, J. H. Macek and J. J. Quinn, *Phys. Rev. B* **88** (2013) 155421.
41. I. Sodemann and A. H. MacDonald, *Phys. Rev. B* **87** (2013) 245425.
42. R. B. Laughlin, *Phys. Rev. B* **27** (1983) 3383.
43. K. Pakrouski, M. R. Peterson, T. Jolicoeur, V. W. Scarola, C. Nayak and M. Troyer, *Phys. Rev.* **X5** (2015) 021004.
44. C. Sun, K. K. W. Ma and D. Feldman, arXiv:2003.14227 (2020).

Real-frequency diagrammatic Monte Carlo at finite temperature

J. Vučičević[1] and M. Ferrero[2,3]

[1]*Scientific Computing Laboratory, Center for the Study of Complex Systems, Institute of Physics Belgrade, University of Belgrade, Pregrevica 118, 11080 Belgrade, Serbia*

[2]*CPHT, CNRS, Ecole Polytechnique, Institut Polytechnique de Paris, Route de Saclay, 91128 Palaiseau, France*

[3]*Collège de France, 11 place Marcelin Berthelot, 75005 Paris, France*

(Received 3 September 2019; revised manuscript received 15 January 2020; accepted 21 January 2020; published 12 February 2020)

Diagrammatic expansions are a central tool for treating correlated electron systems. At thermal equilibrium, they are most naturally defined within the Matsubara formalism. However, extracting any dynamic response function from a Matsubara calculation ultimately requires the ill-defined analytical continuation from the imaginary- to the real-frequency domain. It was recently proposed [A. Taheridehkordi *et al.*, Phys. Rev. B **99**, 035120 (2019)] that the internal Matsubara summations of any interaction-expansion diagram can be performed analytically by using symbolic algebra algorithms. The result of the summations is then an analytical function of the complex frequency rather than Matsubara frequency. Here we apply this principle and develop a diagrammatic Monte Carlo technique which yields results directly on the real-frequency axis. We present results for the self-energy $\Sigma(\omega)$ of the doped 32×32 cyclic square-lattice Hubbard model in a nontrivial parameter regime, where signatures of the pseudogap appear close to the antinode. We discuss the behavior of the perturbation series on the real-frequency axis and in particular show that one must be very careful when using the maximum entropy method on truncated perturbation series. Our approach holds great promise for future application in cases when analytical continuation is difficult and moderate-order perturbation theory may be sufficient to converge the result.

DOI: 10.1103/PhysRevB.101.075113

I. INTRODUCTION

Interacting lattice fermions are one of the central subjects in condensed matter theory. Especially in two dimensions, a full many-body solution for even the simplest models (e.g., the Hubbard model) is a formidable task. In recent decades, great progress has been achieved using Monte Carlo algorithms for the summation of various diagrammatic expansions. The main advantage of this approach is that the approximations can be controlled; i.e., convergence of the results with respect to the control parameters can be systematically verified. The control parameters of the calculations are most commonly the lattice size and the maximal perturbation order. Some algorithms [1–16] are very efficient for small systems but have not yet reached very large lattice sizes, while others [17–24] can address the thermodynamic limit directly but are limited in the number of perturbation orders that can be computed.

In thermal equilibrium, expansions are naturally formulated within the Matsubara formalism, with all the propagators defined in imaginary time/frequency. Therefore, to obtain dynamic response functions, one needs to perform the analytical continuation from the imaginary- to the real-frequency domain. This procedure is notoriously ill defined and becomes especially difficult when the Matsubara axis data contain statistical noise, as is the case with all Monte Carlo results. The problem is further exacerbated with increasing temperature. As the discrete imaginary Matsubara frequencies spread out and move away from the real axis, the statistical noise chips away more and more information from the Matsubara data. The most common way of analytically continuing a noisy result is the maximum entropy method (MEM) [25,26], but it requires "the default model," an *a priori* qualitative knowledge of the real-frequency spectrum that may not always be available; it is difficult to control and estimate the error bars of any such procedure.

Analytical continuation is a common hurdle in finite-temperature calculations, and it came up recently in the study of transport in the optical lattice realizations of the Hubbard model [16,27]. It turns out that the direct-current resistivity is particularly difficult to extract from the imaginary-axis current-current correlation function. But even the self-energy is often interpreted only on the imaginary axis [24], as analytical continuation is considered ultimately unreliable. This particularly hinders the progress in the study of the pseudogap phase and superconductivity in the cuprates, where one would like to compare the momentum-resolved spectral function to experiments [28,29]. The ability to reliably calculate the spectral function becomes even more important in view of the recent photoemission measurements (ARPES) in the cold-atom realizations of the Hubbard model [30].

There are alternative routes that avoid analytical continuation altogether (Keldysh formalism [7–14,31], exact diagonalization techniques [16,32–34]), but those have so far been limited to impurity models or small lattice sizes. It is therefore of primary importance to try to develop methods that avoid the analytical continuation, but are not limited by lattice size.

As was recently proposed [35], an opportunity lies in symbolic algebra algorithms. One can implement a recursive transformation to perform analytically all the internal Matsubara frequency summations for any interaction-expansion

diagram, for any quantity. The result of the Matsubara frequency summations is an analytical expression for the contribution of a given diagram to the given dynamic quantity, in the whole of the complex-frequency plane, rather than just in the discrete set of points along the imaginary axis. The general idea is, however, not entirely new; at perturbation order 2, the Matsubara summations for the self-energy diagrams can be carried out by hand, which leads to the well-known real-axis iterative perturbation theory (RAIPT) [36–38]. Similarly, the bubble diagrams can be easily rewritten in terms of real frequencies, which has applications in the *GW* method [39–41] and the calculation of optical conductivity within the Kubo formalism [42–44]. In the context of diagrammatic Monte Carlo, however, obtaining the analytical expression for each diagram of interest is only a part of the problem. In fact, there are several immediate obstacles in applying the algorithmic Matsubara summations in a calculation of quantities at perturbation order $\geqslant 3$.

Here we address these problems and successfully develop and test a diagrammatic Monte Carlo technique that yields results directly on the real-frequency axis, yet can treat very large systems. We present solutions for the momentum-resolved self-energy for a doped 32×32 Hubbard lattice, in a nontrivial parameter regime where results are almost converged at order 5. Our results show that in this regime precursor signatures of the pseudogap are visible in the real-frequency antinodal self-energy. We also show that the truncation of the perturbation series leads to noncausal features that challenge the use of MEM to obtain real-frequency data from Matsubara axis results.

II. MODEL

We solve the Hubbard model on the square lattice

$$H = -t \sum_{\sigma,\langle i,j\rangle} c^\dagger_{\sigma i} c_{\sigma j} + U \sum_i n_{\uparrow i} n_{\downarrow i} - \mu \sum_{\sigma,i} n_{\sigma i}, \qquad (1)$$

where $c^\dagger_{\sigma i}/c_{\sigma i}$ create/annihilate an electron of spin σ at the lattice site i. The hopping amplitude between the nearest neighbors is denoted t, and we set $D = 4t$ as the unit of energy. The density operator is $n_{\sigma i} = c^\dagger_{\sigma i} c_{\sigma i}$, the chemical potential μ, and the on-site Hubbard interaction U. We restrict ourselves to paramagnetic solutions with full lattice symmetry.

III. METHOD

A. Symbolic algorithm

Following similar steps to those in Ref. [35], we first define the Hartree-shifted bare Green's function of the model $G^{\mathrm{HF}}_{0,\mathbf{k}}(i\omega) = [i\omega - \varepsilon(\mathbf{k})]^{-1}$, where we absorbed the chemical potential and the Hartree shift in the dispersion $\varepsilon(\mathbf{k})$, i.e.,

$$\varepsilon(\mathbf{k}) = -\mu + U n_\sigma - 2t(\cos k_x + \cos k_y), \qquad (2)$$

where $\mathbf{k} = (k_x, k_y)$ is the momentum. For the sake of clarity we omit the integer index n in the fermionic Matsubara frequency, $i\omega \equiv i\omega_n = i(2n+1)\pi T$, where T is temperature. We reserve the subscript in $i\omega$ for denoting different Matsubara variables. We denote n_σ the density per spin evaluated in the interacting problem.

The self-energy Σ can be written as a series in the interaction amplitude U,

$$\Sigma_{\mathbf{k}}(i\omega) = \sum_{N=1}^{\infty} (-U)^N \sum_{\alpha=1}^{\mathcal{N}_N} \mathcal{D}^{N,\alpha}_{\mathbf{k}}(i\omega), \qquad (3)$$

where N is the perturbation order, $\mathcal{N}_N$ is the number of distinct diagrams in the given expansion, α enumerates the diagrams, and $\mathcal{D}^{N,\alpha}_{\mathbf{k}}$ is the contribution of αth diagram in the Nth order. If the diagrams are written in terms of the Hartree-shifted bare propagator there is no need for tadpole insertions in the topology of the diagrams (see Appendix A 8).

The contribution of a general diagram to the bare series for self-energy written in terms of $G^{\mathrm{HF}}_{0,\mathbf{k}}(i\omega_n)$ is given by

$$\mathcal{D}^{N,\alpha}_{\mathbf{k}}(i\omega) = (-1)^{N_b} \sum_{\substack{\mathbf{k}_1 \ldots \mathbf{k}_M \\ i\Omega_1 \ldots i\Omega_M}} \prod_\gamma \frac{1}{\sum_{(s,j)\in\mathcal{K}_\gamma} s\, i\Omega_j - \varepsilon\left(\sum_{(s,j)\in\mathcal{K}_\gamma} s\, \mathbf{k}_j\right)}. \qquad (4)$$

$N_b \equiv N_b^{N,\alpha}$ is the number of fermionic loops (bubbles) in the given diagram: each bubble carries one independent fermionic frequency and momentum. Each interaction carries a bosonic frequency $i\nu \equiv i\nu_n = 2n\pi T$ and momentum, but some are not independent due to conservation laws. We denote M the total number of independent degrees of freedom, each consisting of a frequency and momentum $(i\Omega_j, \mathbf{k}_j)$, where $i\Omega$ can be either fermionic or bosonic. There are $2N-1$ Green's functions in each diagram, indexed by γ. Each Green's function depends on a certain subset of the internal degrees of freedom and possibly the external variables, indexed $j \in [0, M]$ (we take $\mathbf{k}_0 \equiv \mathbf{k}$, $i\Omega_0 \equiv i\omega$), and each entering with a sign $s = \pm 1$ in the corresponding sums. The Green's function γ is fully defined by a set of sign/index pairs $\mathcal{K}_\gamma \equiv \mathcal{K}^{N,\alpha}_\gamma$. The Green's functions may not be unique; i.e., it is possible that $\mathcal{K}_\gamma = \mathcal{K}_{\gamma'}$. For the discussion of the Feynman rules leading to the general expression Eq. (4), we refer the reader to the classic textbook Ref. [45]. For a worked-out example of Eq. (4) in the 4th order of perturbation, see Appendix A 3.

As a function of any given internal Matsubara frequency $i\Omega_c$, and for a fixed choice of the remaining internal and external degrees of freedom, the contribution to self-energy from any given diagram (N, α) has the form of a product of poles,

$$\mathcal{D}_{\mathbf{k}}(i\omega) = (-1)^{N_b} \sum_{\substack{\mathbf{k}_1 \ldots \mathbf{k}_M \\ \{i\Omega_j\}_{j\neq c}}} P \sum_{i\Omega_c} \prod_\gamma \frac{1}{(i\Omega_c - z_\gamma)^{m_\gamma}}, \qquad (5)$$

where P and z_γ implicitly depend on the rest of the internal and external variables, and here we assume that γ goes only over the unique Green's functions that depend on the given $i\Omega_c$, and $m_\gamma \in \mathbb{N}$ is the number of appearances of the γth Green's function in the diagram. Using the partial fraction expansion, and an analytic expression for the derivative of a product of an arbitrary number of poles (see Appendix A 1),

we can perform the transformation

$$\prod_{\gamma}\frac{1}{(z-z_\gamma)^{m_\gamma}}=\sum_{\gamma}\sum_{r=1}^{m_\gamma}\frac{1}{(z-z_\gamma)^{r}}\times(-1)^{m_\gamma-r}\sum_{\mathcal{C}\{p_{\gamma'\neq\gamma}\in\mathbb{N}_0\}:\sum_{\gamma'\neq\gamma}p_{\gamma'}=m_\gamma-r}\prod_{\gamma'\neq\gamma}\frac{(m_{\gamma'}+p_{\gamma'}-1)!}{p_{\gamma'}!(m_{\gamma'}-1)!}\frac{1}{(z_\gamma-z'_\gamma)^{m_{\gamma'}+p_{\gamma'}}}. \quad (6)$$

Here $\mathcal{C}\ldots$ denotes all combinations of a non-negative-integer p per pole $\gamma'\neq\gamma$, such that the total sum of p's is equal to $m_\gamma-r$. Therefore, after selecting one internal Matsubara variable, the full expression can be rewritten as a sum of poles in that Matsubara variable. Then, one may proceed to perform the Matsubara summation of each term using

$$\sum_{i\Omega}\frac{1}{(i\Omega-z)^r}=-\frac{\eta}{(r-1)!}\partial^{r-1}n_\eta(z) \quad (7)$$

with $\eta=\pm1$ for bosonic/fermionic Matsubara frequency. n_η is the Bose/Fermi distribution function. Here we can immediately get rid of the complex part of z because

$$\partial^r_\omega n_\eta(\omega+i\Omega_{\eta'})=\eta'\partial^r_\omega n_{\eta'\cdot\eta}(\omega), \quad (8)$$

where $\eta'=-1$ or $+1$ denotes whether $i\Omega_{\eta'}$ is fermionic or bosonic Matsubara frequency, respectively. Note that the derivatives $\partial^r n$ can be expressed analytically for the purpose of precise numerical evaluation (details in Appendix A 4).

Now the remaining Matsubara variables appear only in the denominators of fractions which can again be interpreted as poles with respect to these variables, and the procedure can be applied recursively until we have gotten rid of all the Matsubara variables. For a detailed example of the symbolic algorithm and an illustration of Eq. (5), see Appendix A 3.

The final result has the form of a sum of poles on the real axis

$$\mathcal{D}_{\mathbf{k}}(z)=(-1)^{N_\mathrm{b}}\sum_{\mathbf{k}_1\ldots\mathbf{k}_M}\sum_{\kappa}\frac{A_\kappa}{(z-\omega_\kappa)^{m_\kappa}} \quad (9)$$

with $\omega_\kappa=\sum_\gamma s^\kappa_\gamma\varepsilon(\sum_{(s,j)\in\mathcal{K}^\kappa_\gamma}s\,\mathbf{k}_j)$, which is a series of terms equal up to the sign $s^\kappa_\gamma=\pm1$ to the dispersion ε, evaluated at various possible linear combinations of the internal/external momenta, as they appear in the Green's functions (indexed γ). The series can be of any length $\leqslant 2N-1$ and include an arbitrary subset of γ's. The amplitude for each (unique) pole $(\omega_\kappa, m_\kappa)$ is given by a large sum of terms of the general form

$$A_\kappa=\sum_\varsigma\frac{a_\varsigma}{b_\varsigma}\prod_\zeta\frac{1}{\omega_{\zeta\varsigma}^{m_{\zeta\varsigma}}}\prod_\varrho\partial^{r_{\varrho\varsigma}}n_{\eta_\varrho}(\omega_{\varrho\varsigma}). \quad (10)$$

a, b are integers, m positive integers. $\omega_{\zeta\varsigma}$ and $\omega_{\varrho\varsigma}$ have the same general form as ω_κ, but do not necessarily coincide with any of the ω_κ's, and may differ from one another. The products over ζ and ϱ may be of various lengths including 0. ω's (and thus A_κ's) are implicitly dependent on the internal and external momenta.

The symbolic forms for A_κ and ω_κ need be obtained only once for any given diagram, independently of the choice of the lattice geometry, parameters of the Hamiltonian, or temperature. See Appendix A 2 for numbers of poles ω_κ and terms in A_κ at various perturbation orders.

B. Application in diagrammatic Monte Carlo

Evaluating the prefactor A_κ numerically is not straightforward for several reasons.

First, the terms in A_κ containing at least one ratio $1/\omega^m$ or a bosonic $\partial^r n_\eta(\omega)$ will diverge if the corresponding ω goes to zero. For any finite lattice this will occur regularly during the Monte Carlo sampling, but even in the thermodynamic limit, ω can approach arbitrarily close to zero. Our solution for this problem is to add small shifts to a certain choice of ε's appearing in ω. This is done at the symbolic level, in a way that $|\omega|$ can never be smaller than a given value that we set to be $\sim10^{-10}$ to 10^{-6} depending on the perturbation order. Note that even this will cause the terms in A_κ to be very large by absolute value (order as large as 10^{30}), yet they will cancel to produce contributions to A_κ of order $\lesssim 1$. This greatly exceeds the capability of standard precision arithmetic which handles only around $\sim$16 digits. We have found the solution in using multiple precision floating point types which can store more digits and allow for subtraction of large numbers, as required in our algorithm. The additional approximation made by numerical shifts can be controlled, and we have checked on several examples that the result is insensitive to the precise choice of the numerical parameters (size of the shifts and the choice of the floating point precision). Surely, the shifts can be always made smaller if the precision is made greater, but this has an adverse effect on performance. For more details see Appendix A6.

Next, one needs to perform the remaining sums over momenta, numerically. For smaller lattices it is possible to do the full summation, but otherwise we employ a flat-weight Monte Carlo (see Appendix B; for an alternative algorithm useful in the case of local self-energy, see Appendix A 7). In each step, we select randomly the internal momenta $\mathbf{k}_1\ldots\mathbf{k}_M$, evaluate all A_κ, and permanently store the triplets $(\omega_\kappa, m_\kappa, A_\kappa)$. We perform "on the fly" integration for any reappearing values of ω_κ. Even for modest lattice sizes, the number of possible values of ω_κ will be very large. To avoid immense outputs, we project $\varepsilon(\mathbf{k})$ on a uniform energy grid, so that linear combinations of ε's and thus ω_κ's always fall on the same uniform grid. The small shifts discussed in the previous paragraph also fall on a uniform grid of a much smaller step, so there will generally be several values of ω_κ concentrated around each point in the "big" ε grid. This way, the number of different values of ω_κ one can obtain is determined by the resolution of the energy grid, i.e., the step $\Delta\varepsilon$. Again, this is a well-controlled approximation, and one can easily push the resolution so that the approximation is negligible compared to statistical noise. See Appendix A 5 for details.

Note also that it is essential for performance to store the different values of $\omega_\kappa, \omega_{\zeta\varsigma}, \omega_{\varrho\varsigma}$ and the corresponding $\partial^r n_\eta(\omega)$, and reuse them whenever possible during the Monte Carlo sampling.

The Monte Carlo run is then performed for a given choice of the external momentum, temperature, lattice geometry, and the Hartree-shifted chemical potential $\mu-Un_\sigma$ (the doping can be determined *a posteriori*). Once enough measurements

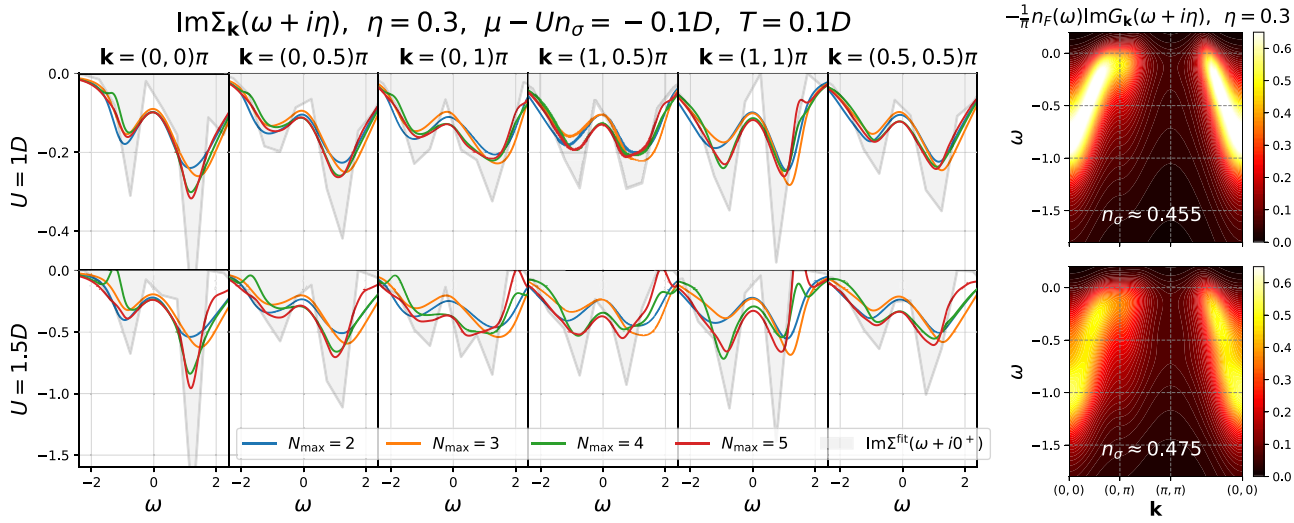

FIG. 1. Calculation for the 32×32 Hubbard lattice at two values of U, $T=0.1D$, and $\mu-Un_\sigma=0.1D$. These parameters correspond to densities per spin indicated in the rightmost panels, i.e., dopings $\delta(U=1)\approx9\%$ and $\delta(U=1.5)\approx5\%$. Left: Imaginary part of the self-energy $\mathrm{Im}\,\Sigma(\omega+i\eta)$, at a distance $\eta=0.3D$ from the real axis, for various $\mathbf{k}$ vectors. Different lines correspond to different maximal perturbation orders in the calculation, $N_{\max}$. Gray-shaded curve is the piecewise-trapezoid fit at $\eta=i0^+$, obtained with resolution $\Delta\omega=1.6\eta$. Right: The corresponding filled part of the spectral function, broadened with η, and interpolated in $\mathbf{k}$ space. The result is obtained with 5.12×10^7 Monte Carlo steps per diagram.

of $(\omega_\kappa, m_\kappa, A_\kappa)$ have been collected, the result for $\Sigma_{\mathbf{k}}(z)$ for any z and any U can be obtained using Eq. (9) and then Eq. (3) (with $i\omega\to z$). However, the result is a discrete set of poles on the real axis, and requires regularization, similarly to exact diagonalization techniques. If it were just the simple poles on a dense uniform energy grid with a step $\Delta\varepsilon$, one could easily interpret $\mathrm{Im}\,\Sigma_{\mathbf{k}}(\omega+i0^+)$ as continuous, but known with a finite resolution, simply through $\mathrm{Im}\,\Sigma_{\mathbf{k}}(\omega_\kappa+i0^+)=-\pi A_\kappa/\Delta\varepsilon$. An analogous scheme could be performed even for higher-order poles on a uniform grid, order by order [46].

The problem is that the poles are not only on a uniform grid, but rather cluster around the grid points, due to the small numerical shifts discussed previously. It is also impossible to separate poles according to their order because multiple poles can combine to effectively form a single higher-order pole. This makes it very difficult to construct a binning scheme that would reinterpret the result directly on the real axis. A better strategy is to use broadening, i.e., evaluate the self-energy slightly away from the real axis, $\Sigma(\omega+i\eta)$. In our calculation, statistical noise dominates close to the real axis; thus we take η just large enough so that $\Sigma(\omega+i\eta)$ is a smooth function of ω.

To recover the desired $\omega+i0^+$ result, one can perform a fit based on the obtained $\Sigma(\omega+i\eta)$ and the Hilbert transform

$$\Sigma(\omega+i\eta)=-\frac{1}{\pi}\int d\varepsilon\frac{\mathrm{Im}\,\Sigma^{\mathrm{fit}}(\varepsilon)}{(\omega+i\eta)-\varepsilon}. \tag{11}$$

This procedure becomes trivial with $\eta\to0$; it treats all frequencies on equal footing and is much better defined than $\Sigma(i\omega_n)\to\Sigma(\omega+i0^+)$ whenever η is small. Let us emphasize that the only limitation in taking a small η is the numerical noise: when the statistical error bars are small, the procedure is very reliable, numerically stable, and does not require additional input (such as the default model for MEM). This is illustrated in the Appendix B, where the algorithm is benchmarked against the numerical renormalization group (NRG) [47] for the solution of an Anderson impurity model [48].

IV. RESULTS

We have benchmarked our method carefully on several simple examples (see Appendix B). We now consider a 32×32 cyclic Hubbard lattice at temperature $T=0.1D$ and $\mu-Un_\sigma=-0.1D$ (hole doping). In this case we benchmark our method against 8th-order Σ Det [22,23] in imaginary frequency and find excellent agreement (see Appendix B 5).

In Fig. 1 we show the results for $\mathrm{Im}\,\Sigma(\omega+i\eta)$ close to the real axis (finite $\eta<\pi T$, lower than the first fermionic Matsubara frequency). Closer than this, stronger noisy features start to appear. Let us emphasize that the statistical noise is far more pronounced on the real axis; i.e., convergence on the imaginary axis does not necessarily imply convergence on the real axis. Different lines represent calculations with different maximal perturbation orders $N_{\max}$, at 6 characteristic $\mathbf{k}$ points and 2 values of U. The shaded region is a piecewise trapezoid $\mathrm{Im}\,\Sigma^{\mathrm{fit}}(\omega+i0^+)$ obtained with resolution $\Delta\omega=1.6\eta$.

At $U=1D$ fifth-order diagrams contribute very little and the result is practically converged with respect to $N_{\max}$. At $U=1.5D$, the result is not fully converged by order 5, but is apparently close to convergence. We observe several noncausal features $\mathrm{Im}\,\Sigma_{\mathbf{k}}(\omega)>0$. At large negative ω, this happens at $\mathbf{k}=(0,0)$ at order 4, but is then fixed by order 5. At large positive ω, the problem appears at order 5, and is likely to be fixed by higher orders in perturbation. These noncasual features do not appear to be artifacts of the statistical noise but rather a result of the truncation of the perturbation series.

This calls for great caution in the use of MEM. Indeed, MEM performed with built-in causality is bound to miss any such features and may compensate for them in an uncontrolled way.

It is interesting that in most cases $\mathrm{Im}\,\Sigma(\omega)$ features two broad peaks with a dip around $\omega = 0$. However, at $U = 1.5D$ around $\mathbf{k} = (0, \pi)$, a third peak appears close to $\omega = 0$. We interpret this peak as a precursor for the pseudogap behavior: as temperature further decreases at this doping (around 5%), the peak may approach $\omega = 0$ and induce a larger, insulating-like self-energy as observed in imaginary-time calculations, e.g., Ref. [24].

Finally, the panels on the right present the filled part of the corresponding **k**-resolved spectral functions. These plots are relevant for recent spectral function measurements in optical lattice realizations of the Hubbard model [30]. One can observe that the spectral function preserves the general form of the noninteracting limit, but spans a bigger energy range and becomes more incoherent (wider lines of lesser intensity) as interaction is increased.

V. CONCLUSIONS AND PROSPECTS

We have resolved the main conceptual issues regarding the application of algorithmic Matsubara summations in the context of diagrammatic Monte Carlo. This includes the precision and efficiency concerns in the evaluation of the pole amplitudes, as well as the extraction of the real-axis results. There is a possibility for further optimization which will likely allow us to push the method to higher perturbation orders in the future.

We demonstrate that our method is readily useful in the study of the single-particle spectra in the intermediate-coupling regime of the Hubbard model, which has been the subject of recent publications [30,49,50]. Finally, our method holds great promise for future work in the cases where analytical continuation is particularly difficult. These include, for example, high temperature and calculations of the current-current correlation function $\Lambda(\omega)$ [16]. Our approach even allows for a straightforward restriction to a selected window of energies; if one is interested in dc resistivity, one may calculate $\Lambda(\omega)$ only at very low frequency and that way gain an important speedup.

ACKNOWLEDGMENTS

We are grateful to Rok Žitko for providing NRG data. The exact-diagonalization results were obtained using the PyED code, written by Hugo Strand [51]. The continuous-time interaction expansion algorithm [1,2] was developed using the TRIQS [52] library. Computations were performed on the PARADOX supercomputing facility (Scientific Computing Laboratory of the Institute of Physics Belgrade) and ALPHA cluster (Collège de France) as well as using HPC resources from GENCI (Grant No. A0050510609). We thank Mihailo Čubrović for his help with the preparation of the manuscript. J.V. acknowledges funding provided by the Institute of Physics Belgrade, through the grant by the Ministry of Education, Science, and Technological Development of the Republic of Serbia.

APPENDIX A: FORMALISM DETAILS

1. Derivation of Eq. (6)

The partial fraction expansion employs the residue theorem, and the textbook expression reads

$$\prod_\gamma \frac{1}{(z-z_\gamma)^{m_\gamma}} = \sum_\gamma \sum_{r=1}^{m_\gamma} \frac{1}{(z-z_\gamma)^r} \frac{1}{(m_\gamma - r)!} \lim_{z\to z_\gamma} \partial_z^{m_\gamma - r} \prod_{\gamma' \neq \gamma} \frac{1}{(z-z_{\gamma'})^{m_{\gamma'}}}. \tag{A1}$$

The derivative of a product of poles can be expressed in the following way:

$$\partial_z^n \prod_\gamma \frac{1}{(z-z_\gamma)^{m_\gamma}} = (-1)^n n! \sum_{\mathcal{C}\{p_\gamma \in \mathbb{N}_0 : \sum_\gamma p_\gamma = n} \prod_\gamma \frac{(m_\gamma + p_\gamma - 1)!}{p_\gamma!(m_\gamma - 1)!} \frac{1}{(z-z_\gamma)^{m_\gamma + p_\gamma}}. \tag{A2}$$

Here the sum goes over all combinations $\mathcal{C}$ of a choice of a non-negative-integer p per pole γ, such that their sum is n.

Putting together the equations Eq. (A1) and Eq. (A2), one obtains Eq. (6).

The derivation of Eq. (A2) relies on performing $\partial_z[f(z)g(z)] = [\partial_z f(z)]g(z) + f(z)[\partial_z g(z)]$ and $\partial_z \frac{1}{(z-z_\gamma)^{m_\gamma}} = -m_\gamma \frac{1}{(z-z_\gamma)^{m_\gamma+1}}$, recursively. Having these in mind, it is clear that the final result will consist of a number of terms, each term being a product of the original poles, some with increased orders. In each term, we will have acted with the derivative upon each pole γ a certain number of times $p_\gamma \geqslant 0$, so as to use up all the derivatives, i.e., $\sum_\gamma p_\gamma = n$. For each pole that is acted upon at least once, this leads to $\partial_z^{p_\gamma} \frac{1}{(z-z_\gamma)^{m_\gamma}} = (-1)^{p_\gamma} m_\gamma (m_\gamma + 1)\ldots(m_\gamma + p_\gamma - 1) \frac{1}{(z-z_\gamma)^{m_\gamma + p_\gamma}}$. Hence the overall sign $\prod_\gamma (-1)^{p_\gamma} = (-1)^n$. However, we can apply derivatives in any order, so there is also a combinatorial factor corresponding to permutation of multisets $n!/(\prod_\gamma p_\gamma!)$ (number of distinct anagrams of an n-long word consisting of unique letters indexed by γ, each appearing p_γ times in the word).

Let us check and illustrate Eq. (A2) on a simple example, where one can carry out the derivatives by hand. Say

$$\partial_z^3 \frac{1}{z-z_1}\frac{1}{(z-z_2)^2} = -6\left(4\frac{1}{z-z_1}\frac{1}{(z-z_2)^5} + 3\frac{1}{(z-z_1)^2}\frac{1}{(z-z_2)^4} + 2\frac{1}{(z-z_1)^3}\frac{1}{(z-z_2)^3} + \frac{1}{(z-z_1)^4}\frac{1}{(z-z_2)^2}\right). \tag{A3}$$

We can immediately identify the prefactor $(-1)^n n! = (-1)^3 3! = -6$. Also, we see there are 4 terms corresponding to 4 possible choices of (p_1, p_2) such that $p_1 + p_2 = n = 3$, respectively,

$$\mathcal{C} = \{(0,3), (1,2), (2,1), (3,0)\}. \tag{A4}$$

TABLE I. Numbers of poles and terms in the symbolic expression obtained by analytical Matsubara summations.

N	N_{poles}	$N^{\text{typ}}_{\text{poles}}$	N_{terms}	$N^{\text{typ}}_{\text{terms}}$
2	1	1	4	4
3	2	2	12–14	13
4	3–4	3.5	16–70	29.7
5	4–8	5.6	32–482	97.9
6	5–14	8.9	32–5092	296.2

Now the prefactors $\prod_\gamma (m_\gamma + p_\gamma - 1)!/[p_\gamma!(m_\gamma - 1)!]$ can be evaluated for each combination

$$\begin{aligned}
(0,3): &\frac{(1+0-1)!}{0!0!}\frac{(2+3-1)!}{3!1!} = \frac{1}{1}\frac{4!}{3!} = 4,\\
(1,2): &\frac{(1+1-1)!}{1!0!}\frac{(2+2-1)!}{2!1!} = \frac{1}{1}\frac{3!}{2!} = 3,\\
(2,1): &\frac{(1+2-1)!}{2!0!}\frac{(2+1-1)!}{1!1!} = \frac{2!}{2!}\frac{2!}{1} = 2,\\
(3,0): &\frac{(1+3-1)!}{3!0!}\frac{(2+0-1)!}{0!1!} = \frac{3!}{3!}\frac{1}{1} = 1,
\end{aligned} \tag{A5}$$

all of which we can readily identify on the right-hand side of Eq. (A3).

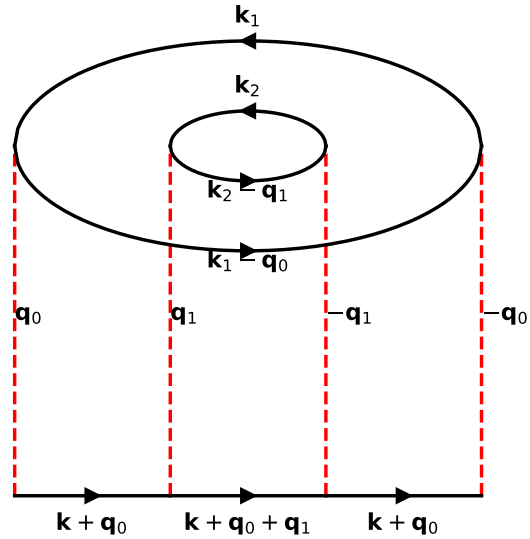

FIG. 2. An example of a momentum-labeled 4th-order diagram on the lattice.

2. Numbers of poles and terms per diagram

Equation (9) in the main text is the final result of Matsubara summations for a given diagram. It is a sum of a a certain number N_{poles} of distinct poles $(\omega_\kappa, m_\kappa)$, each with N_{terms} distinct terms in the amplitude A_κ. We tabulate in Table I the range and the geometrical average (typical value) of these numbers for each perturbation order N.

3. Results of symbolic algebra

We present here an example of the analytic expression for the contribution of a self-energy diagram. We choose the 4th-order diagram presented in Fig. 2. We start from the expression of the form Eq. (4):

$$\begin{aligned}
\mathcal{D}_{\mathbf{k}}(i\omega) &= (-1)^2 \sum_{\mathbf{k}_1,\mathbf{k}_2} \sum_{\mathbf{q}_0,\mathbf{q}_1} \sum_{i\omega_1,i\omega_2} \sum_{i\nu_0,i\nu_1} \\
&\quad \times G^{\text{HF}}_{\mathbf{k}+\mathbf{q}_0}(i\omega + i\nu_0) G^{\text{HF}}_{\mathbf{k}+\mathbf{q}_0+\mathbf{q}_1}(i\omega + i\nu_0 + i\nu_1) G^{\text{HF}}_{\mathbf{k}+\mathbf{q}_0}(i\omega + i\nu_0) G^{\text{HF}}_{\mathbf{k}_1}(i\omega_1) G^{\text{HF}}_{\mathbf{k}_1-\mathbf{q}_0}(i\omega_1 - i\nu_0) G^{\text{HF}}_{\mathbf{k}_2}(i\omega_2) G^{\text{HF}}_{\mathbf{k}_2-\mathbf{q}_1}(i\omega_2 - i\nu_1) \\
&= (-1)^2 \sum_{\mathbf{k}_1,\mathbf{k}_2} \sum_{\mathbf{q}_0,\mathbf{q}_1} \sum_{i\omega_1,i\omega_2} \sum_{i\nu_0,i\nu_1} \\
&\quad \times \left(\frac{1}{i\omega + i\nu_0 - \varepsilon_{\mathbf{k}+\mathbf{q}_0}}\right)^2 \frac{1}{i\omega + i\nu_0 + i\nu_1 - \varepsilon_{\mathbf{k}+\mathbf{q}_0+\mathbf{q}_1}} \frac{1}{i\omega_1 - \varepsilon_{\mathbf{k}_1}} \frac{1}{i\omega_1 - i\nu_0 - \varepsilon_{\mathbf{k}_1-\mathbf{q}_0}} \frac{1}{i\omega_2 - \varepsilon_{\mathbf{k}_2}} \frac{1}{i\omega_2 - i\nu_1 - \varepsilon_{\mathbf{k}_2-\mathbf{q}_1}}.
\end{aligned} \tag{A6}$$

Here we have already imposed momentum conservation, which leaves only two internal bosonic frequencies/momenta to be summed over (independent momenta carried by fermions and vertices are denoted in Fig. 2). For the sake of notational brevity, here, as well as in the rest of this Appendix, we take $\varepsilon_{\mathbf{k}} \equiv \varepsilon(\mathbf{k})$.

The first step in performing the analytical Matsubara frequency summations is to choose one internal Matsubara frequency, and then isolate the factors (poles) which depend on it. Say we choose $i\nu_0$. We can regroup the factors conveniently:

$$\begin{aligned}
&\mathcal{D}_{\mathbf{k}}(i\omega) \\
&= (-1)^2 \sum_{\mathbf{k}_1,\mathbf{k}_2} \sum_{\mathbf{q}_0,\mathbf{q}_1} \sum_{i\omega_1,i\omega_2} \sum_{i\nu_1} \\
&\times \frac{1}{i\omega_1 - \varepsilon_{\mathbf{k}_1}} \frac{1}{i\omega_2 - \varepsilon_{\mathbf{k}_2}} \frac{1}{i\omega_2 - i\nu_1 - \varepsilon_{\mathbf{k}_2-\mathbf{q}_1}} \sum_{i\nu_0} \frac{1}{\left[i\nu_0 - (-i\omega + \varepsilon_{\mathbf{k}+\mathbf{q}_0})\right]^2} \frac{1}{i\nu_0 - (-i\omega - i\nu_1 + \varepsilon_{\mathbf{k}+\mathbf{q}_0+\mathbf{q}_1})} \frac{-1}{i\nu_0 - (i\omega_1 - \varepsilon_{\mathbf{k}_1-\mathbf{q}_0})}.
\end{aligned} \tag{A7}$$

Now the expression has the form of a product of poles with respect to $i\nu_0$ [Eq. (5)], where the rest can be considered a prefactor (denoted P). The product of poles can be then transformed using the main transformation Eq. (6):

$$
\begin{aligned}
&\mathcal{D}_{\mathbf{k}}(i\omega) \\
&= (-1)^2 \sum_{\mathbf{k}_1,\mathbf{k}_2} \sum_{\mathbf{q}_0,\mathbf{q}_1} \sum_{i\omega_1,i\omega_2} \sum_{i\nu_1} \frac{1}{i\omega_1 - \varepsilon_{\mathbf{k}_1}} \frac{1}{i\omega_2 - \varepsilon_{\mathbf{k}_2}} \frac{1}{i\omega_2 - i\nu_1 - \varepsilon_{\mathbf{k}_2-\mathbf{q}_1}} \\
&\quad \times \left\{ \frac{1}{\left[i\omega_1 - \varepsilon_{\mathbf{k}_1-\mathbf{q}_0} - (-i\omega + \varepsilon_{\mathbf{k}+\mathbf{q}_0})\right]^2} \frac{1}{i\omega_1 - \varepsilon_{\mathbf{k}_1-\mathbf{q}_0} - (-i\omega - i\nu_1 + \varepsilon_{\mathbf{k}+\mathbf{q}_0+\mathbf{q}_1})} \sum_{i\nu_0} \frac{-1}{i\nu_0 - (i\omega_1 - \varepsilon_{\mathbf{k}_1-\mathbf{q}_0})} \right. \\
&\quad + \frac{1}{\left[-i\omega - i\nu_1 + \varepsilon_{\mathbf{k}+\mathbf{q}_0+\mathbf{q}_1} - (-i\omega + \varepsilon_{\mathbf{k}+\mathbf{q}_0})\right]^2} \frac{-1}{-i\omega - i\nu_1 + \varepsilon_{\mathbf{k}+\mathbf{q}_0+\mathbf{q}_1} - (i\omega_1 - \varepsilon_{\mathbf{k}_1-\mathbf{q}_0})} \sum_{i\nu_0} \frac{1}{i\nu_0 - (-i\omega - i\nu_1 + \varepsilon_{\mathbf{k}+\mathbf{q}_0+\mathbf{q}_1})} \\
&\quad - \left[\left(\frac{1}{-i\omega + \varepsilon_{\mathbf{k}+\mathbf{q}_0} - (-i\omega - i\nu_1 + \varepsilon_{\mathbf{k}+\mathbf{q}_0+\mathbf{q}_1})} \right)^2 \frac{-1}{-i\omega + \varepsilon_{\mathbf{k}+\mathbf{q}_0} - (i\omega_1 - \varepsilon_{\mathbf{k}_1-\mathbf{q}_0})} \right. \\
&\quad \left. + \frac{1}{-i\omega + \varepsilon_{\mathbf{k}+\mathbf{q}_0} - (-i\omega - i\nu_1 + \varepsilon_{\mathbf{k}+\mathbf{q}_0+\mathbf{q}_1})} \left(\frac{-1}{-i\omega + \varepsilon_{\mathbf{k}+\mathbf{q}_0} - (i\omega_1 - \varepsilon_{\mathbf{k}_1-\mathbf{q}_0})} \right)^2 \right] \sum_{i\nu_0} \frac{1}{i\nu_0 - (-i\omega + \varepsilon_{\mathbf{k}+\mathbf{q}_0})} \\
&\quad \left. + \frac{1}{-i\omega + \varepsilon_{\mathbf{k}+\mathbf{q}_0} - (-i\omega - i\nu_1 + \varepsilon_{\mathbf{k}+\mathbf{q}_0+\mathbf{q}_1})} \frac{-1}{-i\omega + \varepsilon_{\mathbf{k}+\mathbf{q}_0} - (i\omega_1 - \varepsilon_{\mathbf{k}_1-\mathbf{q}_0})} \sum_{i\nu_0} \frac{1}{\left[i\nu_0 - (-i\omega + \varepsilon_{\mathbf{k}+\mathbf{q}_0})\right]^2} \right\}. \qquad \text{(A8)}
\end{aligned}
$$

We can now evaluate the Matsubara frequency summations per $i\nu_0$, using Eq. (7) and then Eq. (8). Then, the denominators can be simplified at the symbolic level:

$$
\begin{aligned}
\mathcal{D}_{\mathbf{k}}(i\omega) &= (-1)^2 \sum_{\mathbf{k}_1,\mathbf{k}_2} \sum_{\mathbf{q}_0,\mathbf{q}_1} \sum_{i\omega_1,i\omega_2} \sum_{i\nu_1} \frac{1}{i\omega_1 - \varepsilon_{\mathbf{k}_1}} \frac{1}{i\omega_2 - \varepsilon_{\mathbf{k}_2}} \frac{1}{i\omega_2 - i\nu_1 - \varepsilon_{\mathbf{k}_2-\mathbf{q}_1}} \\
&\quad \times \left\{ \frac{1}{\left(i\omega + i\omega_1 - \varepsilon_{\mathbf{k}_1-\mathbf{q}_0} - \varepsilon_{\mathbf{k}+\mathbf{q}_0}\right)^2} \frac{1}{i\omega + i\nu_1 + i\omega_1 - \varepsilon_{\mathbf{k}_1-\mathbf{q}_0} - \varepsilon_{\mathbf{k}+\mathbf{q}_0+\mathbf{q}_1}} (-)^3 n_F(-\varepsilon_{\mathbf{k}_1-\mathbf{q}_0}) \right. \\
&\quad + \frac{1}{\left(-i\nu_1 + \varepsilon_{\mathbf{k}+\mathbf{q}_0+\mathbf{q}_1} - \varepsilon_{\mathbf{k}+\mathbf{q}_0}\right)^2} \frac{-1}{-i\omega - i\omega_1 - i\nu_1 + \varepsilon_{\mathbf{k}+\mathbf{q}_0+\mathbf{q}_1} + \varepsilon_{\mathbf{k}_1-\mathbf{q}_0}} (-)^2 n_F(\varepsilon_{\mathbf{k}+\mathbf{q}_0+\mathbf{q}_1}) \\
&\quad - \left[\left(\frac{1}{i\nu_1 + \varepsilon_{\mathbf{k}+\mathbf{q}_0} - \varepsilon_{\mathbf{k}+\mathbf{q}_0+\mathbf{q}_1}} \right)^2 \frac{-1}{-i\omega - i\omega_1 + \varepsilon_{\mathbf{k}+\mathbf{q}_0} + \varepsilon_{\mathbf{k}_1-\mathbf{q}_0}} \right. \\
&\quad \left. + \frac{1}{i\nu_1 + \varepsilon_{\mathbf{k}+\mathbf{q}_0} - \varepsilon_{\mathbf{k}+\mathbf{q}_0+\mathbf{q}_1}} \left(\frac{-1}{-i\omega - i\omega_1 + \varepsilon_{\mathbf{k}+\mathbf{q}_0} + \varepsilon_{\mathbf{k}_1-\mathbf{q}_0}} \right)^2 \right] (-)^2 n_F(\varepsilon_{\mathbf{k}+\mathbf{q}_0}) \\
&\quad \left. + \frac{1}{i\nu_1 + \varepsilon_{\mathbf{k}+\mathbf{q}_0} - \varepsilon_{\mathbf{k}+\mathbf{q}_0+\mathbf{q}_1}} \frac{-1}{-i\omega - i\omega_1 + \varepsilon_{\mathbf{k}+\mathbf{q}_0} + \varepsilon_{\mathbf{k}_1-\mathbf{q}_0}} (-)^2 \partial n_F(\varepsilon_{\mathbf{k}+\mathbf{q}_0}) \right\}. \qquad \text{(A9)}
\end{aligned}
$$

The procedure can now be repeated for the next choice of the Matsubara variable.

We now present the final result of the symbolic algorithm for the diagram presented in Fig. 2. The diagram contributes one second-order pole and two simple poles. The number of terms in the amplitudes for each pole is 16, 24, and 16, respectively. To display the expression easily, we only show several representative terms in the amplitude of each pole:

$$
\begin{aligned}
\mathcal{D}_{\mathbf{k}}(z) &= (-1)^2 \sum_{\mathbf{k}_1,\mathbf{k}_2} \sum_{\mathbf{q}_0,\mathbf{q}_1} \left\{ \frac{1}{(z + \varepsilon_{\mathbf{k}_1} - \varepsilon_{\mathbf{k}_1-\mathbf{q}_0} - \varepsilon_{\mathbf{k}+\mathbf{q}_0})^2} \right. \\
&\quad \times \left[n_F\left(\varepsilon_{\mathbf{k}_2-\mathbf{q}_1}\right) n_F\left(\varepsilon_{\mathbf{k}_1-\mathbf{q}_0}\right) n_F\left(\varepsilon_{\mathbf{k}+\mathbf{q}_0+\mathbf{q}_1}\right) \frac{1}{\varepsilon_{\mathbf{k}_2} - \varepsilon_{\mathbf{k}+\mathbf{q}_0+\mathbf{q}_1} - \varepsilon_{\mathbf{k}_2-\mathbf{q}_1} + \varepsilon_{\mathbf{k}+\mathbf{q}_0}} n_F\left(\varepsilon_{\mathbf{k}+\mathbf{q}_0}\right) \right. \\
&\quad + n_F\left(\varepsilon_{\mathbf{k}_2-\mathbf{q}_1}\right) n_F\left(\varepsilon_{\mathbf{k}_1-\mathbf{q}_0}\right) n_B\left(\varepsilon_{\mathbf{k}_2} - \varepsilon_{\mathbf{k}_2-\mathbf{q}_1}\right) \frac{1}{\varepsilon_{\mathbf{k}_2} - \varepsilon_{\mathbf{k}+\mathbf{q}_0+\mathbf{q}_1} - \varepsilon_{\mathbf{k}_2-\mathbf{q}_1} + \varepsilon_{\mathbf{k}+\mathbf{q}_0}} n_F\left(\varepsilon_{\mathbf{k}+\mathbf{q}_0}\right) \\
&\quad - n_F\left(\varepsilon_{\mathbf{k}_2-\mathbf{q}_1}\right) n_F\left(\varepsilon_{\mathbf{k}_1}\right) n_F\left(\varepsilon_{\mathbf{k}+\mathbf{q}_0+\mathbf{q}_1}\right) \frac{1}{\varepsilon_{\mathbf{k}_2} - \varepsilon_{\mathbf{k}+\mathbf{q}_0+\mathbf{q}_1} - \varepsilon_{\mathbf{k}_2-\mathbf{q}_1} + \varepsilon_{\mathbf{k}+\mathbf{q}_0}} n_F\left(\varepsilon_{\mathbf{k}+\mathbf{q}_0}\right) \\
&\quad \left. \left. - n_F\left(\varepsilon_{\mathbf{k}_2}\right) n_F\left(\varepsilon_{\mathbf{k}_1-\mathbf{q}_0}\right) n_B\left(\varepsilon_{\mathbf{k}_2} - \varepsilon_{\mathbf{k}_2-\mathbf{q}_1}\right) \frac{1}{\varepsilon_{\mathbf{k}_2} - \varepsilon_{\mathbf{k}+\mathbf{q}_0+\mathbf{q}_1} - \varepsilon_{\mathbf{k}_2-\mathbf{q}_1} + \varepsilon_{\mathbf{k}+\mathbf{q}_0}} n_F\left(\varepsilon_{\mathbf{k}+\mathbf{q}_0}\right) + \cdots \right] \right.
\end{aligned}
$$

$$
\begin{aligned}
&+\frac{1}{z+\varepsilon_{\mathbf{k}_1}-\varepsilon_{\mathbf{k}_1-\mathbf{q}_0}-\varepsilon_{\mathbf{k}+\mathbf{q}_0}}\\
&\times\Big[n_F\left(\varepsilon_{\mathbf{k}_2-\mathbf{q}_1}\right)n_F\left(\varepsilon_{\mathbf{k}_1-\mathbf{q}_0}\right)n_F\left(\varepsilon_{\mathbf{k}+\mathbf{q}_0+\mathbf{q}_1}\right)\frac{1}{\varepsilon_{\mathbf{k}_2}-\varepsilon_{\mathbf{k}+\mathbf{q}_0+\mathbf{q}_1}-\varepsilon_{\mathbf{k}_2-\mathbf{q}_1}+\varepsilon_{\mathbf{k}+\mathbf{q}_0}}\partial n_F\left(\varepsilon_{\mathbf{k}+\mathbf{q}_0}\right)\\
&+n_F\left(\varepsilon_{\mathbf{k}_2-\mathbf{q}_1}\right)n_F\left(\varepsilon_{\mathbf{k}_1}\right)n_F\left(\varepsilon_{\mathbf{k}+\mathbf{q}_0+\mathbf{q}_1}\right)n_B\left(\varepsilon_{\mathbf{k}_1}-\varepsilon_{\mathbf{k}_1-\mathbf{q}_0}\right)\frac{1}{(\varepsilon_{\mathbf{k}_2}+\varepsilon_{\mathbf{k}+\mathbf{q}_0}-\varepsilon_{\mathbf{k}+\mathbf{q}_0+\mathbf{q}_1}-\varepsilon_{\mathbf{k}_2-\mathbf{q}_1})^2}\\
&-n_F\left(\varepsilon_{\mathbf{k}_2}\right)n_F\left(\varepsilon_{\mathbf{k}_1-\mathbf{q}_0}\right)n_F\left(\varepsilon_{\mathbf{k}+\mathbf{q}_0+\mathbf{q}_1}\right)\frac{1}{\varepsilon_{\mathbf{k}_2}-\varepsilon_{\mathbf{k}+\mathbf{q}_0+\mathbf{q}_1}-\varepsilon_{\mathbf{k}_2-\mathbf{q}_1}+\varepsilon_{\mathbf{k}+\mathbf{q}_0}}\partial n_F\left(\varepsilon_{\mathbf{k}+\mathbf{q}_0}\right)\\
&-n_F\left(\varepsilon_{\mathbf{k}_2}\right)n_F\left(\varepsilon_{\mathbf{k}_1}\right)n_B\left(\varepsilon_{\mathbf{k}_2}-\varepsilon_{\mathbf{k}_2-\mathbf{q}_1}\right)\frac{1}{(\varepsilon_{\mathbf{k}_2}-\varepsilon_{\mathbf{k}+\mathbf{q}_0+\mathbf{q}_1}-\varepsilon_{\mathbf{k}_2-\mathbf{q}_1}+\varepsilon_{\mathbf{k}+\mathbf{q}_0})^2}n_F\left(\varepsilon_{\mathbf{k}+\mathbf{q}_0}\right)+\cdots\Big]\\
&+\frac{1}{z+\varepsilon_{\mathbf{k}_2}+\varepsilon_{\mathbf{k}_1}-\varepsilon_{\mathbf{k}+\mathbf{q}_0+\mathbf{q}_1}-\varepsilon_{\mathbf{k}_2-\mathbf{q}_1}-\varepsilon_{\mathbf{k}_1-\mathbf{q}_0}}\\
&\times\Big[n_F\left(\varepsilon_{\mathbf{k}_2-\mathbf{q}_1}\right)n_F\left(\varepsilon_{\mathbf{k}_1-\mathbf{q}_0}\right)n_F\left(\varepsilon_{\mathbf{k}+\mathbf{q}_0+\mathbf{q}_1}\right)\frac{1}{(-\varepsilon_{\mathbf{k}_2}+\varepsilon_{\mathbf{k}+\mathbf{q}_0+\mathbf{q}_1}+\varepsilon_{\mathbf{k}_2-\mathbf{q}_1}-\varepsilon_{\mathbf{k}+\mathbf{q}_0})^2}\\
&\times n_F\left(-\varepsilon_{\mathbf{k}_2}+\varepsilon_{\mathbf{k}+\mathbf{q}_0+\mathbf{q}_1}+\varepsilon_{\mathbf{k}_2-\mathbf{q}_1}\right)\\
&+n_F\left(\varepsilon_{\mathbf{k}_2-\mathbf{q}_1}\right)n_F\left(\varepsilon_{\mathbf{k}_1-\mathbf{q}_0}\right)n_F\left(\varepsilon_{\mathbf{k}+\mathbf{q}_0+\mathbf{q}_1}\right)n_B\left(\varepsilon_{\mathbf{k}_1}-\varepsilon_{\mathbf{k}_1-\mathbf{q}_0}\right)\frac{1}{(-\varepsilon_{\mathbf{k}_2}-\varepsilon_{\mathbf{k}+\mathbf{q}_0}+\varepsilon_{\mathbf{k}+\mathbf{q}_0+\mathbf{q}_1}+\varepsilon_{\mathbf{k}_2-\mathbf{q}_1})^2}\\
&-n_F\left(\varepsilon_{\mathbf{k}_2}\right)n_F\left(\varepsilon_{\mathbf{k}_1-\mathbf{q}_0}\right)n_F\left(\varepsilon_{\mathbf{k}+\mathbf{q}_0+\mathbf{q}_1}\right)\frac{1}{(-\varepsilon_{\mathbf{k}_2}+\varepsilon_{\mathbf{k}+\mathbf{q}_0+\mathbf{q}_1}+\varepsilon_{\mathbf{k}_2-\mathbf{q}_1}-\varepsilon_{\mathbf{k}+\mathbf{q}_0})^2}\\
&\times n_F\left(-\varepsilon_{\mathbf{k}_2}+\varepsilon_{\mathbf{k}+\mathbf{q}_0+\mathbf{q}_1}+\varepsilon_{\mathbf{k}_2-\mathbf{q}_1}\right)+\cdots\Big]\Big\}. \qquad \text{(A10)}
\end{aligned}
$$

4. Calculation of Fermi/Bose function derivatives

In the numerical evaluation of the amplitudes of the poles [A_κ; Eq. (9) and Eq. (10)], we use the general expression for the derivatives of the Fermi/Bose distribution function,

$$\partial_\omega^r n_\eta(\omega) = -\beta^r \sum_{k=0}^{r} \frac{(-)^{k+1} f_{r,k} e^{k\beta\omega}}{(e^{\beta\omega}-\eta)^{k+1}} \qquad \text{(A11)}$$

with $f_{r,k} \in \mathbb{N}_0$ tabulated here:

$r\backslash k$	0	1	2	3	4	5	6
0	1						
1	0	1					
2	0	1	2				
3	0	1	6	6			
4	0	1	14	36	24		
5	0	1	30	150	240	120	
6	0	1	62	540	1560	1800	720

5. Dispersion on an equidistant grid

We present here in detail the numerical trick that we use to avoid unmanageable outputs from the Monte Carlo summation. For a given lattice size (in our case 32×32), we approximate $\varepsilon_{\mathbf{k}}$ so that it takes on values only from a given set Ξ of equidistant numbers spanning the bandwidth (in our case the number of points is $N_\Xi = 151$). The new approximate dispersion therefore has the property

$$\tilde{\varepsilon}_{\mathbf{k}} \in \Xi, \forall \mathbf{k} \qquad \text{(A12)}$$

with

$$\Xi = \{\min_{\mathbf{k}}\varepsilon_{\mathbf{k}} + j\Delta\varepsilon\}_{j=0}^{N_\Xi - 1} \qquad \text{(A13)}$$

and

$$\Delta\varepsilon = \frac{\max_{\mathbf{k}}\varepsilon_{\mathbf{k}} - \min_{\mathbf{k}}\varepsilon_{\mathbf{k}}}{N_\Xi - 1}, \qquad \text{(A14)}$$

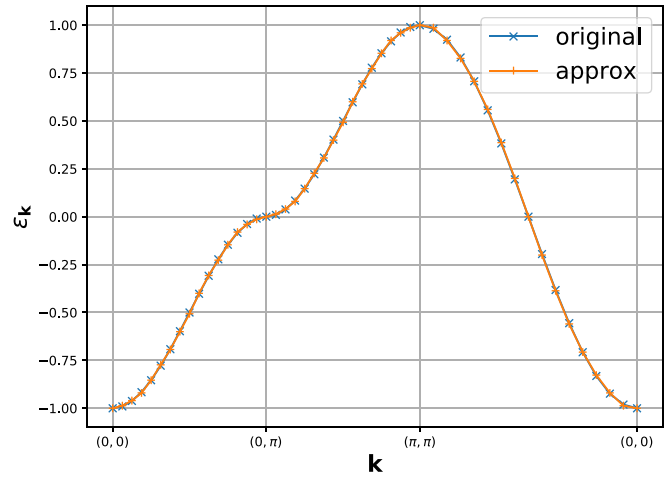

FIG. 3. Approximation of the dispersion used to avoid unmanageable outputs.

and is determined simply by choosing the closest value to the original dispersion:

$$\tilde{\varepsilon}_{\mathbf{k}} \equiv \text{closest}(\Xi, \varepsilon_{\mathbf{k}}). \tag{A15}$$

With a sufficiently dense grid Ξ, the approximation becomes negligible. We present the approximate $\tilde{\varepsilon}_{\mathbf{k}}$ we used in our calculations in comparison to the exact dispersion in Fig. 3.

6. Multiple precision algebra and regulators

To illustrate the need for multiple precision algebra, we focus here on the simplest example, which is the second-order diagram. The Matsubara summations here can be easily carried out by hand:

$$\begin{aligned}
&\mathcal{D}_{\mathbf{k}}(i\omega) \\
&= (-1)\sum_{i\omega',i\nu}\sum_{\mathbf{k}',\mathbf{q}} G^{\mathrm{HF}}_{0,\mathbf{k}'}(i\omega')G^{\mathrm{HF}}_{0,\mathbf{k}'+\mathbf{q}}(i\omega'+i\nu)G^{\mathrm{HF}}_{0,\mathbf{k}-\mathbf{q}}(i\omega-i\nu) \\
&= (-1)\sum_{i\omega',i\nu}\sum_{\mathbf{k}',\mathbf{q}} \frac{1}{i\omega'-\varepsilon_{\mathbf{k}'}}\frac{1}{i\omega'+i\nu-\varepsilon_{\mathbf{k}'+\mathbf{q}}}\frac{1}{i\omega-i\nu-\varepsilon_{\mathbf{k}-\mathbf{q}}} \\
&= \sum_{\mathbf{k}',\mathbf{q}} \frac{n_F(\varepsilon_{\mathbf{k}'})n_B(\varepsilon_{\mathbf{k}'+\mathbf{q}}-\varepsilon_{\mathbf{k}'}) + n_F(\varepsilon_{\mathbf{k}'})n_F(-\varepsilon_{\mathbf{k}-\mathbf{q}}) - n_F(\varepsilon_{\mathbf{k}'+\mathbf{q}})n_B(\varepsilon_{\mathbf{k}'+\mathbf{q}}-\varepsilon_{\mathbf{k}'}) - n_F(\varepsilon_{\mathbf{k}'+\mathbf{q}})n_F(-\varepsilon_{\mathbf{k}-\mathbf{q}})}{i\omega-\varepsilon_{\mathbf{k}'+\mathbf{q}}-\varepsilon_{\mathbf{k}-\mathbf{q}}+\varepsilon_{\mathbf{k}'}}.
\end{aligned} \tag{A16}$$

We see that the final result has four terms in total, and that the two terms featuring n_B diverge as $\mathbf{q}\to 0$, or equivalently as $t\to 0$, i.e., $\varepsilon_{\mathbf{k}}\to 0$, $\forall\mathbf{k}$. Nevertheless, the contribution of the diagram is *finite* as the following limit is well defined:

$$\lim_{\varepsilon\to 0}\left[n_F(0)n_B(\varepsilon) - n_F(\varepsilon)n_B(\varepsilon)\right] = \tfrac{1}{4}. \tag{A17}$$

However, in numerical implementation one cannot simply let $\varepsilon\to 0$ in the above expression as n_B becomes ill defined. We find the solution in adding small shifts in the symbolic expression. At second order, it suffices to associate a small shift ϵ to $\varepsilon_{\mathbf{k}'}$:

$$\begin{aligned}
\mathcal{D}_{\mathbf{k}}(i\omega) \approx \sum_{\mathbf{k}',\mathbf{q}} &\frac{1}{i\omega-\varepsilon_{\mathbf{k}'+\mathbf{q}}-\varepsilon_{\mathbf{k}-\mathbf{q}}+\varepsilon_{\mathbf{k}'}+\epsilon} \\
\times\big[&n_F(\varepsilon_{\mathbf{k}'}+\epsilon)n_B(\varepsilon_{\mathbf{k}'+\mathbf{q}}-\varepsilon_{\mathbf{k}'}-\epsilon) + n_F(\varepsilon_{\mathbf{k}'}+\epsilon)n_F(-\varepsilon_{\mathbf{k}-\mathbf{q}}) - n_F(\varepsilon_{\mathbf{k}'+\mathbf{q}})n_B(\varepsilon_{\mathbf{k}'+\mathbf{q}}-\varepsilon_{\mathbf{k}'}-\epsilon) - n_F(\varepsilon_{\mathbf{k}'+\mathbf{q}})n_F(-\varepsilon_{\mathbf{k}-\mathbf{q}})\big].
\end{aligned} \tag{A18}$$

That solves the problem as n_B will no longer be ill defined even when $\mathbf{q}=0$. However, depending on the size of ϵ and β, the two problematic terms may become large. Consider $\epsilon = 10^{-20}$ and $\beta = 1$. In that case the terms featuring n_B can become as big as 10^{20}. The subtraction of two numbers of size 10^{20} that are different only by $\frac{1}{4}$ will fail if performed in standard (double) precision, as it handles only up to $\sim$16 digits. While in the case of the second-order diagram one can clearly use a larger ϵ and avoid any problems, at higher perturbation orders there will be products of several diverging n_B, multiplied also with expressions of the type $1/0$, and ever larger shifts would be needed; increasing the numerical shifts would eventually start introducing noticeable systematic error. The solution is then to use larger floating point data types that can store more digits. In our implementation we use the GNU Multiple Precision Arithmetic (GMP) C++ library and its Python wrapper GMPY2 and use floating point type of 350 bits, and we keep the shifts perturbation-order dependent, $\sim 10^{-12+N}$.

7. Monte Carlo application to local self-energy

We also devise an algorithm to treat directly the local self-energy. This algorithm relies on rewriting the diagrams in real space. In notation analogous to Eq. (4), the contribution of a general real-space diagram has the following form:

$$\begin{aligned}
&\mathcal{D}_{\mathbf{i}_0\mathbf{i}_N}(i\omega) = (-1)^{N_b}\sum_{\mathbf{i}_1\ldots\mathbf{i}_{N-1}}\sum_{i\Omega_1\ldots i\Omega_M} \\
&\int d\varepsilon_1\ldots d\varepsilon_{2N-1}\prod_{\gamma}\frac{\rho_{\mathbf{r}(\gamma;\mathbf{i}_0\ldots\mathbf{i}_N)}(\varepsilon_\gamma)}{\sum_{(s,j)\in\mathcal{K}_\gamma} si\Omega_j-\varepsilon_\gamma},
\end{aligned} \tag{A19}$$

where $\mathbf{i}_i$ denote the lattice sites where the interaction vertices are positioned (the first and last are the external site indices). The energy integrals come from the Hilbert transform

$$G_{\mathbf{r}}(i\omega) = -\frac{1}{\pi}\int d\epsilon\frac{\mathrm{Im}G_{\mathbf{r}}(\varepsilon+i0^+)}{i\omega-\varepsilon} \tag{A20}$$

and

$$\begin{aligned}
\rho_{\mathbf{r}}(\varepsilon) &= -\frac{1}{\pi}\mathrm{Im}G_{\mathbf{r}}(\varepsilon+i0^+) \\
&= -\frac{1}{\pi}\mathrm{Im}\sum_{\mathbf{k}} e^{i\mathbf{k}\cdot\mathbf{r}}G_{\mathbf{k}}(\varepsilon+i0^+) \\
&= \sum_{\mathbf{k}} e^{i\mathbf{k}\cdot\mathbf{r}}\delta_{\varepsilon,\varepsilon_{\mathbf{k}}} \\
&= 2\sum_{0<k_x,k_y<\pi}\left[\cos(\mathbf{k}\cdot\mathbf{r})+\cos(\mathbf{k}\sigma^z\mathbf{r})\right]\delta_{\varepsilon,\varepsilon_{\mathbf{k}}},
\end{aligned} \tag{A21}$$

where $\mathbf{k}\sigma^z\mathbf{r} = k_x r_x - k_y r_y$. The above can be evaluated numerically to high precision. It is important to note that

$$\int d\varepsilon\rho_{\mathbf{r}=(0,0)}(\varepsilon) = 1, \tag{A22}$$

$$\int d\varepsilon\rho_{\mathbf{r}\neq(0,0)}(\varepsilon) = 0. \tag{A23}$$

Now note that only ρ actually depends on the choice of lattice sites. We rewrite the expression in a way that is more revealing:

$$\mathcal{D}_{\mathbf{i}_0\mathbf{i}_N}(i\omega) = (-1)^{N_b} \sum_{i\Omega_1..i\Omega_M} \int d\varepsilon_1 \dots d\varepsilon_{2N-1} \prod_\gamma \times \frac{1}{\sum_{(s,j)\in\mathcal{K}_\gamma} si\Omega_j - \varepsilon_\gamma} \sum_{\mathbf{i}_1\dots\mathbf{i}_{N-1}} \rho_{\mathbf{r}(\gamma;\mathbf{i}_0\dots\mathbf{i}_N)}(\varepsilon_\gamma). \quad \text{(A24)}$$

For a given choice of ε's and $\mathbf{i}$'s, this is formally the same as what we had in Eq. (4) in the main text. A completely analogous symbolic algebra algorithm can be used to resolve the Matsubara summations, but the results will be different. The difference from the $\mathbf{k}$-space case is that all the ε's are now independent, which will lead to different analytical expressions for each diagram. The final expressions will, however, have the same general form [Eq. (9) and Eq. (10) in the main text], yet slightly simplified: now one obtains only simple poles because no two Green's functions are identical, i.e., $m_\gamma = 1, \forall\gamma$. In fact, even in the $\mathbf{k}$-space case, higher-order poles appear only in dressed diagrams; a skeleton series would not have this feature. After the analytical summation of the Matsubara frequencies, the remaining expression to be evaluated has the form

$$\mathcal{D}_{\mathbf{i}_0\mathbf{i}_N}(z) = (-1)^{N_b} \int d\varepsilon_1 \dots d\varepsilon_{2N-1} \sum_\kappa \frac{A_\kappa}{z-\omega_\kappa} \times \prod_\gamma \sum_{\mathbf{i}_1\dots\mathbf{i}_{N-1}} \rho_{\mathbf{r}(\gamma;\mathbf{i}_0\dots\mathbf{i}_N)}(\varepsilon_\gamma), \quad \text{(A25)}$$

where A and ω implicitly depend on $\varepsilon_1 \dots \varepsilon_{2N-1}$. The remaining variables to be summed over now include both the energies ε and the lattice sites $\mathbf{i}$. Note, however, that A and ω do *not* depend on the $\mathbf{i}$'s, so recalculating them for each configuration of $\mathbf{i}$'s would be inefficient. We are immediately inclined to use $\prod_\gamma \sum_{\mathbf{i}_1\dots\mathbf{i}_{N-1}} \rho_{\mathbf{r}(\gamma;\mathbf{i}_0\dots\mathbf{i}_N)}(\varepsilon_\gamma)$ as the weight for Monte Carlo over the space of ε's. We recall the general expression

$$\frac{\int f(x)w(x)dx}{\int w(x)dx} = \frac{\sum_{x\in \mathrm{MC}(|w|)} f(x)\mathrm{sgn}[w(x)]}{\sum_{x\in \mathrm{MC}(|w|)} \mathrm{sgn}[w(x)]}, \quad \text{(A26)}$$

where MC($|w|$) is the Markov chain constructed with respect to $|w|$ as the weight. Therefore it is necessary that the overall integral of our weight function is known and nonzero. However, this will only be the case if $\mathbf{i}_0 = \mathbf{i}_N$. First, the integrals over our proposed weight decouple:

$$\int d\varepsilon_1 \dots d\varepsilon_{2N-1} \prod_\gamma \sum_{\mathbf{i}_1\dots\mathbf{i}_{N-1}} \rho_{\mathbf{r}(\gamma;\mathbf{i}_0\dots\mathbf{i}_N)}(\varepsilon_\gamma) = \sum_{\mathbf{i}_1\dots\mathbf{i}_{N-1}} \prod_\gamma \int d\varepsilon_\gamma \rho_{\mathbf{r}(\gamma;\mathbf{i}_0\dots\mathbf{i}_N)}(\varepsilon_\gamma). \quad \text{(A27)}$$

We see that the only contribution comes from the choice $\mathbf{i}_0 = \mathbf{i}_1 = \dots = \mathbf{i}_N$ in which case $\mathbf{r}(\gamma;\mathbf{i}_0\dots\mathbf{i}_N) = (0,0), \forall\gamma$, and so each integral over energy equals 1, and the total integral of the weight is also equal 1. Otherwise, if $\mathbf{i}_0 \neq \mathbf{i}_N$, there will always be at least one nonlocal $\rho_{\mathbf{r}}(\varepsilon)$ involved, the integral of which is 0. Therefore, the proposed weight has total integral zero for any nonlocal self-energy component and cannot be used in this purpose. Nevertheless, one can use it for calculating the local self-energy. Furthermore, in a local problem, e.g., Anderson impurity [48], this scheme can be used straightforwardly without the summations over lattice sites. We use it in our Anderson impurity benchmark below.

8. Diagram topologies

In Fig. 4 we present all the topologies of the interaction-expansion diagrams up to order 5. Full lines are the Hartree-shifted bare propagators, and the dashed lines are interactions. All the drawn diagrams went into calculation of the self-energy in Fig. 1.

APPENDIX B: BENCHMARK

Here we benchmark our method in the following cases:

(i) atomic limit against analytic result;

(ii) 4-site Hubbard chain against exact diagonalization (ED) [51];

(iii) 4×4 lattice against numerically exact Rubtsov algorithm, continuous-time interaction-expansion quantum Monte Carlo (CTINT) [1,2,52];

(iv) single Anderson impurity problem against the approximative NRG [47];

(v) 32×32 lattice against imaginary-time diagrammatic Monte Carlo, Σ Det, up to 8th order in perturbation theory [22,23].

1. Atomic limit

We start by benchmarking our method in the case of the half-filled Hubbard atom. It corresponds to setting $t = 0$, $\mu = U/2$ (and $n_\sigma = 0.5$ in the definition of the Hartree-shifted bare propagator). As there is no longer $\mathbf{k}$ dependence in the dispersion, the $\mathbf{k}$ sums now reduce to a single term, and each diagram needs to be evaluated only once, for $\varepsilon_{\mathbf{k}} = 0$. As explained in Appendix A 6, this cannot be done straightforwardly because it would lead to divergent terms in the analytical expression, namely of the form $n_B(0)$ and $1/0$ [see Eq. (10) and the example Eq. (A10)]. The numerical treatment boils down to adding small shifts to a certain number of ε's at the symbolic level so that zeros are avoided in the arguments of n_B and denominators of fractions, and only then letting the original ε's go to zero (say, $\varepsilon_{\mathbf{k}_2-\mathbf{q}_1} \to \varepsilon_{\mathbf{k}_2-\mathbf{q}_1} + \zeta$, $\varepsilon_{\mathbf{k}_1} \to \varepsilon_{\mathbf{k}_1} + 2\zeta$, and so on, simultaneously across all terms in a given diagram; the shifts are integer multiples of ζ which we set depending on perturbation order $\zeta = 10^{-12+N}$; the choice of ε's to be shifted is nonunique). This will *a priori* lead to systematic numerical error and here we check whether the numerical treatment is satisfactory (the atomic limit is the worst case scenario in this respect).

First, we recall the analytical expression for the self-energy beyond the Hartree shift:

$$\Sigma^{(\mathrm{HF})}(i\omega_n) = \frac{U^2}{4}\frac{1}{i\omega_n}. \quad \text{(B1)}$$

It can be shown that this expression corresponds to the second-order diagram in the U series written down in terms of the Hartree-shifted bare propagator. The contribution of higher orders is zero "order by order," but individual higher-order diagrams are not necessarily zero. Therefore, it is a stringent

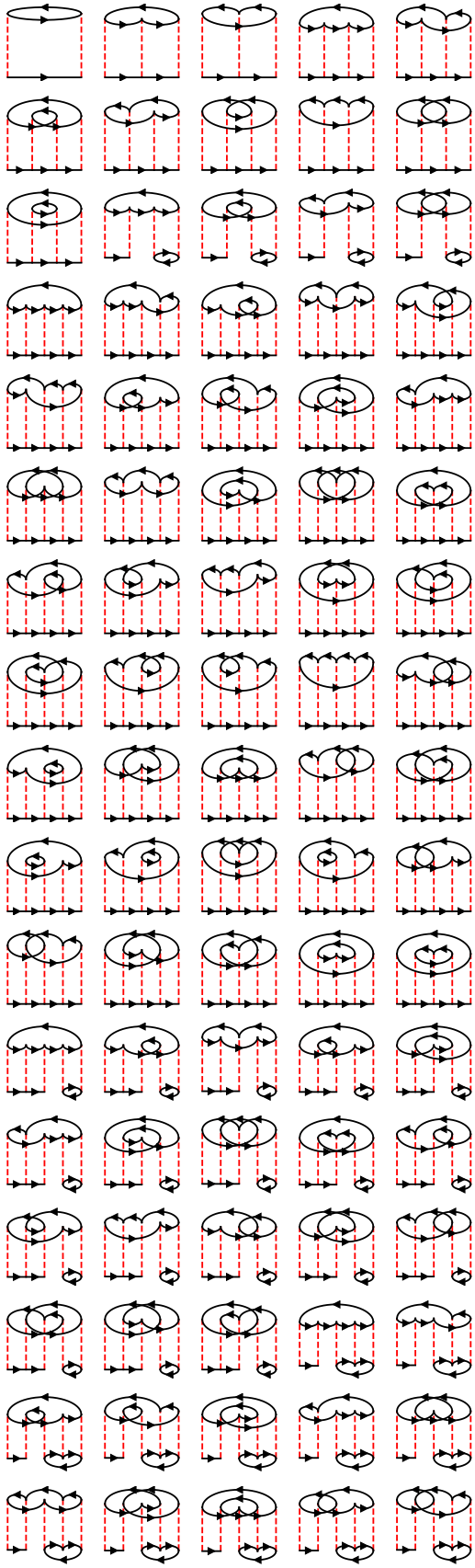

FIG. 4. Hartree-shifted self-energy series up to 5th order. The numbers of diagrams per order are 1, 2, 12, 70, 515, . . . starting from the second order, respectively.

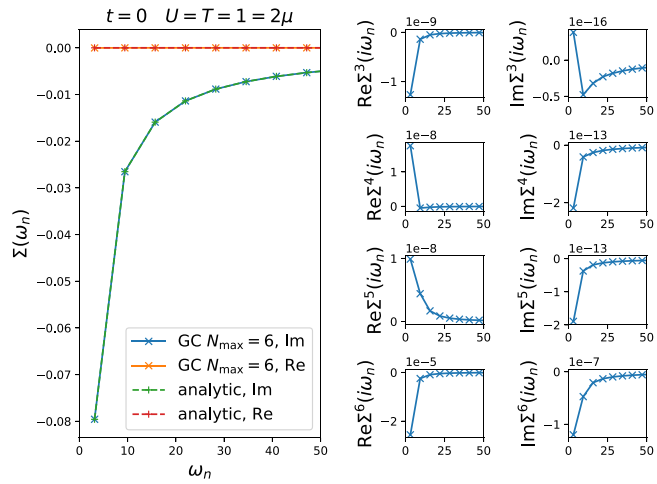

FIG. 5. Benchmark in the case of an isolated Hubbard atom at half filling. Big panel: Our method (GC) is compared to the analytical expression. Smaller panels on the right: Self-energy contributions order by order; the only contribution comes from the second-order diagram.

check of our method to show that the higher orders truly cancel.

We present the results in Fig. 5. We evaluate all the diagrams up to and including the 6th order, at a fixed $U = T = 1$. The total series is in excellent agreement with the analytical result (big panel). On the smaller panels on the right, we examine the contributions order by order (Σ^N denotes contribution at order N). Indeed, the only contribution comes from the second-order diagram, while the contributions of higher orders are negligible. However, the numerical error grows with approaching the real axis, and with growing order. The real part of self-energy coming from the 6th-order diagrams already reaches 10^{-5}. This is expected, as we use bigger numerical shifts in higher-order diagrams. Alternatively, one would need to drastically increase the floating-point precision in the evaluation of higher-order diagrams, which is not suitable for lattice computations, so we do not consider this approach; rather, we keep the floating-point precision fixed across orders.

In the atomic limit, the real-frequency self-energy cannot be reliably extracted from our method. This is, however, a somewhat pathological case where the self-energy is a single simple pole at $\omega = 0$. Due to numerical shifts and cutting the series at finite order, our numerical self-energy here is composed of multiple poles of various orders at various small frequencies $\sim\zeta$. Very close to the real axis, these numerical artifacts become apparent, and the method is of little use.

2. 4-site Hubbard chain

Next, we benchmark our method in the case of the half-filled 4-site cyclic Hubbard chain at temperature $T = 0.2D = 0.8t$ (note that the actual half-bandwidth in this case is $2t$). This small system can be solved using exact diagonalization (ED). In our method, the **k** summations go over only 4 points and can be performed fully, so we denote our method GC

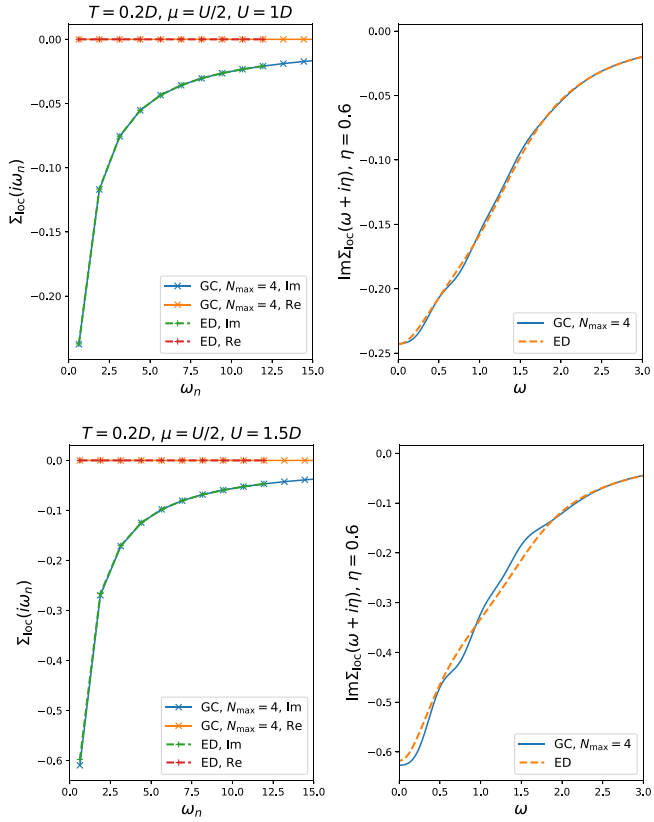

FIG. 6. Benchmark in the case of the 4-site cyclic Hubbard chain at half filling.

(gray code). In this case we go up to order 4 [due to particle-hole (PH) symmetry, the order 5 does not contribute, but order 6 we cannot fully sum].

We present our result in Fig. 6. The agreement is excellent at $U = 1D$, yet at $U = 1.5D$ higher orders become important.

Similarly to the atomic limit, the self-energy in the 4-site chain is composed of a relatively small number of poles on the real axis, and does not form a smooth frequency spectrum. On the other hand, having that $\varepsilon_{\mathbf{k}}$ takes on only three distinct values $(-0.5, 0, 0.5)$, our method can yield poles only at frequencies which are integer multiples of $1/2$ (plus/minus small numerical shifts). The immediate question is then, How does one recover the correct self-energy even with an infinite self-energy series? One would expect the poles in self-energy to appear at various different frequencies and even move continuously with increasing U, yet our analytical expression seemingly does not support that. The answer is that all the higher-order poles ultimately merge into (shifted) simple poles through

$$\sum_{k=1}^{\infty} \frac{a^{k-1}}{z^k} = \frac{1}{z-a} \tag{B2}$$

and that way recover the correct physical result. Note, however, that the principle part of the Laurent series Eq. (B2) cut at a finite order no longer resembles a simple pole at $\eta \lesssim a$, irrespective of the maximum order in the series. Therefore, it makes no sense to look at $\Sigma(\omega + i\eta)$ results at small η. One reasoning is that we should take η proportional to the

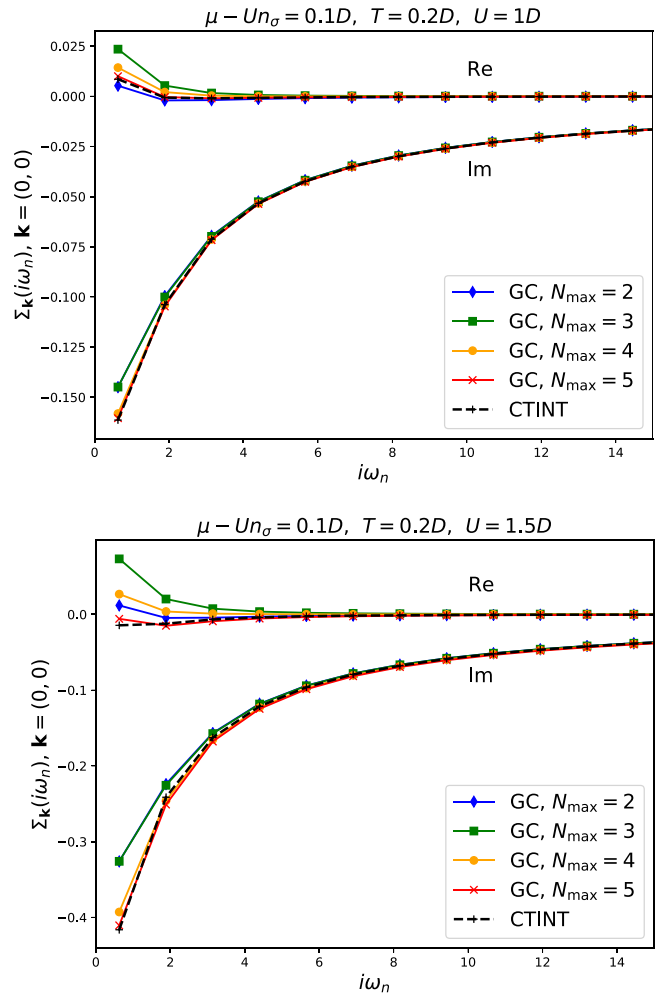

FIG. 7. Benchmark of the method in the case of 4×4 cyclic Hubbard cluster.

distance between the poles we get, which is in this case 0.5. We therefore compare our result to ED at $\eta = 0.6$ which is just below the first Matsubara frequency πT and find similarly good agreement to that on the imaginary axis.

Again, our method cannot be used to reliably extract discrete spectra on the real axis. Fitting the result at $\eta = 0.6$ to a causal and piecewise constant spectrum on the real axis does reproduce the correspondingly binned ED result, but the detailed pole structure cannot be inferred.

3. 4 × 4 lattice

We now turn to the 4×4 cyclic Hubbard cluster. This system cannot easily be solved with ED, so we use the Rubtsov algorithm continuous-time interaction expansion Monte Carlo (CTINT) which is numerically exact. However the comparison can now only be made on the imaginary axis. In our method, full $\mathbf{k}$ summations can be performed up to order 5.

In Fig. 7 we show the results at $\mu - Un_\sigma = 0.1D$, $T = 0.2D$, $\mathbf{k} = (0, 0)$. Additionally, we show the GC results for different perturbation-order cutoffs $N_{\rm max} = 2 \ldots 5$. At $U = 1D$ the agreement is excellent and the perturbation series

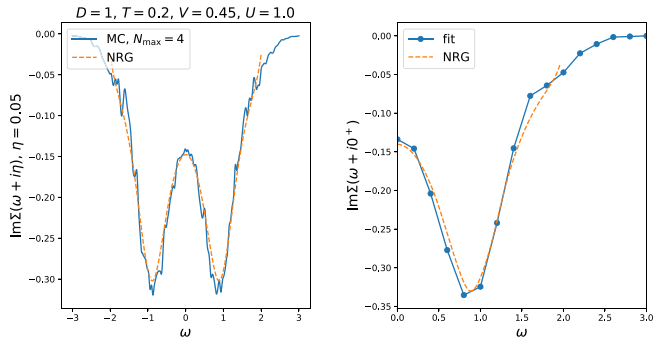

FIG. 8. Benchmark of our method in the case of the single-impurity Anderson model with a semicircular bath.

seems converged at order 5. At $U = 1.5D$ the agreement is solid, but 5th order still makes a sizable contribution.

As for the real-frequency spectrum, there is a similar problem as in the 4-site chain case: dispersion now assumes only the values $(\pm 1, \pm 0.5, 0)$, and again one obtains poles only at integer multiples of 0.5 plus an integer multiple of $\mu - Un_\sigma$. Although discrete, the exact self-energy spectrum is expected to be much denser, and any kind of fit to the $\eta \sim 0.5$ result is likely to miss details of it. Our method is suitable only for continuous spectra, as we will show in the following sections.

4. Anderson impurity

To test our method in the continuous spectrum case, we start with the simplest possible model: the Anderson impurity model with a semicircular bath. We consider only the PH-symmetric case. The Hartree-shifted bare propagator is given by

$$G_0^{\mathrm{HF}}(z) = \frac{1}{z - \Delta(z)} \tag{B3}$$

and the hybridization function

$$\Delta(z) = V^2 \int d\varepsilon \frac{\rho(\varepsilon)}{z - \varepsilon}, \tag{B4}$$

$$\rho(\varepsilon) = \theta(D - |\varepsilon|) 2\sqrt{D^2 - \varepsilon^2}/(\pi D^2), \tag{B5}$$

where V^2 sets the norm, and D sets the width of $\mathrm{Im}\Delta(\omega)$.

This model can be solved approximately using numerical renormalization group (NRG). NRG yields the self-energy directly on the real axis.

In our method, we utilize the real-space algorithm introduced in Appendix A 7, with the important simplification that there are no sums over lattice sites. We discretize the energy (200 points between -1 and 1), and perform Monte Carlo integration for the ε integrals using the product $\prod_\gamma \rho(\varepsilon_\gamma)$ as the weight.

A priori, now we should be able to approach the real axis to around $\eta \sim 1/100$. However, the statistical error now also plays the role, and we find that $\mathrm{Im}\,\Sigma(\omega + i\eta)$ becomes noisy below $\eta \sim 0.05D$. Nevertheless, this should be sufficient to resolve all the details of the spectrum. We compare our results to NRG at $\eta = 0.05$ and find excellent agreement (Fig. 8). Note that we do not impose PH symmetry, but the result is PH-symmetric apparently within the level of noise in the curve. Next, we fit our result at $\eta = 0.05D$ to a PH-symmetric piecewise-trapezoid spectrum on the real axis with resolution $\sim$0.1 and compare to the NRG result on the real axis. The agreement is excellent, and the resolution is sufficient to capture all the features in $\mathrm{Im}\,\Sigma(\omega + i0^+)$.

5. 32 × 32 lattice

Finally, we benchmark our method in the 32×32 Hubbard lattice case. The best available result is that of the

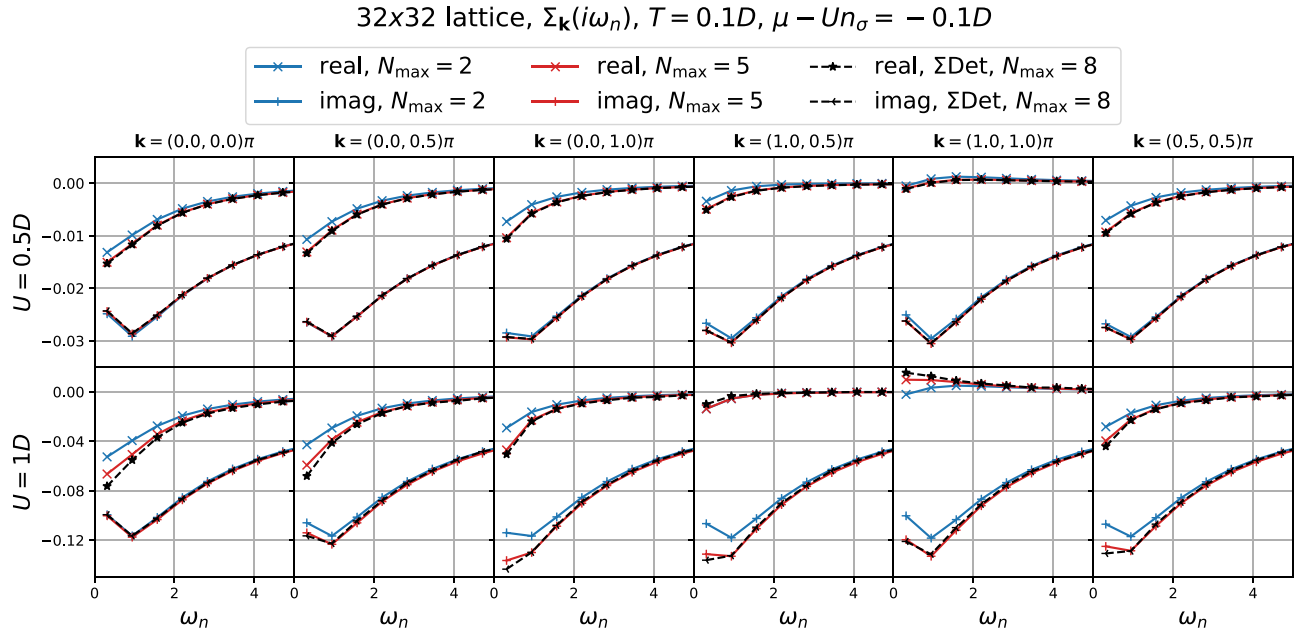

FIG. 9. Matsubara self-energy on the 32×32 Hubbard lattice: benchmark against the Σ Det method at 8th order.

imaginary-time Σ Det diagrammatic Monte Carlo calculation, performed up to 8th order. We compare the two methods on the Matsubara axis in Fig. 9.

At $U = 0.5D$ the agreement is excellent, and the calculation is clearly converged by order 5, but clearly not by order 2.

At $U = 1D$ higher orders still contribute, and there is a bit of discrepancy at low frequency. From the real-frequency results (Fig. 1 in the main text), however, it is clear that the self-energy is qualitatively converged, although some corrections are expected with inclusion of higher orders.

We do not benchmark using $U = 1.5$ data, as in that case the higher orders are expected to contribute more, and results are not expected to coincide.

[1] A. N. Rubtsov and A. I. Lichtenstein, J. Exp. Theor. Phys. Lett. **80**, 61 (2004).
[2] A. N. Rubtsov, V. V. Savkin, and A. I. Lichtenstein, Phys. Rev. B **72**, 035122 (2005).
[3] P. Werner, A. Comanac, L. de' Medici, M. Troyer, and A. J. Millis, Phys. Rev. Lett. **97**, 076405 (2006).
[4] P. Werner and A. J. Millis, Phys. Rev. B **74**, 155107 (2006).
[5] E. Gull, P. Werner, O. Parcollet, and M. Troyer, Europhys. Lett. **82**, 57003 (2008).
[6] E. Gull, A. J. Millis, A. I. Lichtenstein, A. N. Rubtsov, M. Troyer, and P. Werner, Rev. Mod. Phys. **83**, 349 (2011).
[7] R. E. V. Profumo, C. Groth, L. Messio, O. Parcollet, and X. Waintal, Phys. Rev. B **91**, 245154 (2015).
[8] A. Moutenet, P. Seth, M. Ferrero, and O. Parcollet, Phys. Rev. B **100**, 085125 (2019).
[9] C. Bertrand, O. Parcollet, A. Maillard, and X. Waintal, Phys. Rev. B **100**, 125129 (2019).
[10] C. Bertrand, S. Florens, O. Parcollet, and X. Waintal, Phys. Rev. X **9**, 041008 (2019).
[11] G. Cohen, D. R. Reichman, A. J. Millis, and E. Gull, Phys. Rev. B **89**, 115139 (2014).
[12] G. Cohen, E. Gull, D. R. Reichman, and A. J. Millis, Phys. Rev. Lett. **112**, 146802 (2014).
[13] G. Cohen, E. Gull, D. R. Reichman, and A. J. Millis, Phys. Rev. Lett. **115**, 266802 (2015).
[14] A. Boag, E. Gull, and G. Cohen, Phys. Rev. B **98**, 115152 (2018).
[15] E. Eidelstein, E. Gull, and G. Cohen, arXiv:1907.08570.
[16] J. Vučičević, J. Kokalj, R. Žitko, N. Wentzell, D. Tanasković, and J. Mravlje, Phys. Rev. Lett. **123**, 036601 (2019).
[17] N. V. Prokof'ev and B. V. Svistunov, Phys. Rev. Lett. **81**, 2514 (1998).
[18] N. Prokof'ev and B. Svistunov, Phys. Rev. Lett. **99**, 250201 (2007).
[19] K. V. Houcke, E. Kozik, N. Prokof'ev, and B. Svistunov, Phys. Procedia **6**, 95 (2010).
[20] E. Bourovski, N. Prokof'ev, and B. Svistunov, Phys. Rev. B **70**, 193101 (2004).
[21] R. Rossi, Phys. Rev. Lett. **119**, 045701 (2017).
[22] A. Moutenet, W. Wu, and M. Ferrero, Phys. Rev. B **97**, 085117 (2018).
[23] F. Šimkovic and E. Kozik, Phys. Rev. B **100**, 121102(R) (2019).
[24] W. Wu, M. Ferrero, A. Georges, and E. Kozik, Phys. Rev. B **96**, 041105(R) (2017).
[25] A. Macridin, S. P. Doluweera, M. Jarrell, and Th. Maier, arXiv:cond-mat/0410098.
[26] R. Levy, J. LeBlanc, and E. Gull, Comput. Phys. Commun. **215**, 149 (2017).
[27] E. W. Huang, R. Sheppard, B. Moritz, and T. P. Devereaux, Science **366**, 987 (2019).
[28] P. Staar, T. Maier, and T. C. Schulthess, Phys. Rev. B **89**, 195133 (2014).
[29] E. Gull and A. J. Millis, Phys. Rev. B **91**, 085116 (2015).
[30] P. T. Brown, E. Guardado-Sanchez, B. M. Spar, E. W. Huang, T. P. Devereaux, and W. S. Bakr, Nat. Phys. **16**, 26 (2020).
[31] H. Aoki, N. Tsuji, M. Eckstein, M. Kollar, T. Oka, and P. Werner, Rev. Mod. Phys. **86**, 779 (2014).
[32] M. Rigol, T. Bryant, and R. R. P. Singh, Phys. Rev. Lett. **97**, 187202 (2006).
[33] J. Kokalj, Phys. Rev. B **95**, 041110(R) (2017).
[34] P. T. Brown, D. Mitra, E. Guardado-Sanchez, R. Nourafkan, A. Reymbaut, C.-D. Hébert, S. Bergeron, A.-M. S. Tremblay, J. Kokalj, D. A. Huse, P. Schauß, and W. S. Bakr, Science **363**, 379 (2018).
[35] A. Taheridehkordi, S. H. Curnoe, and J. P. F. LeBlanc, Phys. Rev. B **99**, 035120 (2019).
[36] H. Kajueter and G. Kotliar, Phys. Rev. Lett. **77**, 131 (1996).
[37] M. Potthoff, T. Wegner, and W. Nolting, Phys. Rev. B **55**, 16132 (1997).
[38] N. Dasari, W. R. Mondal, P. Zhang, J. Moreno, M. Jarrell, and N. S. Vidhyadhiraja, Eur. Phys. J. B **89**, 202 (2016).
[39] F. Onufrieva and P. Pfeuty, Phys. Rev. B **65**, 054515 (2002).
[40] F. Onufrieva and P. Pfeuty, Phys. Rev. Lett. **102**, 207003 (2009).
[41] F. Onufrieva and P. Pfeuty, Phys. Rev. Lett. **109**, 257001 (2012).
[42] H. Terletska, J. Vučičević, D. Tanasković, and V. Dobrosavljević, Phys. Rev. Lett. **107**, 026401 (2011).
[43] J. Vučičević, H. Terletska, D. Tanasković, and V. Dobrosavljević, Phys. Rev. B **88**, 075143 (2013).
[44] J. Vučičević, D. Tanasković, M. J. Rozenberg, and V. Dobrosavljević, Phys. Rev. Lett. **114**, 246402 (2015).
[45] R. D. Mattuck, *A Guide to Feynman Diagrams in the Many-Body Problem*, 2nd ed. (Dover Publications, Inc., New York, 1992).
[46] $(m+1)$th-order poles contribute to the mth ω derivative of $\Sigma(\omega + i0^+)$ through $\partial_\omega^m A(\omega + i0^+) = -\frac{(-1)^m m!}{\pi} \int_{-\infty}^{\infty} d\varepsilon \frac{\mathrm{Im}A(\varepsilon + i0^+)}{(\omega + i0^+ - \varepsilon)^{m+1}}$.
[47] R. Žitko and T. Pruschke, Phys. Rev. B **79**, 085106 (2009).
[48] A. C. Hewson, *The Kondo Problem to Heavy Fermions*, Cambridge Studies in Magnetism (Cambridge University Press, Cambridge, UK, 1993).
[49] F. Šimkovic, IV, J. P. F. LeBlanc, A. J. Kim, Y. Deng, N. V. Prokof'ev, B. V. Svistunov, and E. Kozik, Phys. Rev. Lett. **124**, 017003 (2020).
[50] A. J. Kim, F. Simkovic, IV, and E. Kozik, arXiv:1905.13337.
[51] H. U. Strand, PYED: Exact Diagonalization for Finite Quantum Systems, https://github.com/HugoStrand/pyed.
[52] O. Parcollet, M. Ferrero, T. Ayral, H. Hafermann, I. Krivenko, L. Messio, and P. Seth, Comput. Phys. Commun. **196**, 398 (2015).

Conductivity in the Square Lattice Hubbard Model at High Temperatures: Importance of Vertex Corrections

J. Vučičević,[1] J. Kokalj,[2,3] R. Žitko,[3,4] N. Wentzell,[5] D. Tanasković,[1] and J. Mravlje[3]
[1]*Scientific Computing Laboratory, Center for the Study of Complex Systems, Institute of Physics Belgrade, University of Belgrade, Pregrevica 118, 11080 Belgrade, Serbia*
[2]*University of Ljubljana, Faculty of Civil and Geodetic Engineering, Jamova 2, Ljubljana, Slovenia*
[3]*Jozef Stefan Institute, Jamova 39, SI-1000 Ljubljana, Slovenia*
[4]*University of Ljubljana, Faculty of Mathematics and Physics, Jadranska 19, Ljubljana, Slovenia*
[5]*Center for Computational Quantum Physics, Simons Foundation Flatiron Institute, New York, New York 10010, USA*

(Received 20 November 2018; revised manuscript received 31 May 2019; published 19 July 2019)

Recent experiments on cold atoms in optical lattices allow for a quantitative comparison of the measurements to the conductivity calculations in the square lattice Hubbard model. However, the available calculations do not give consistent results, and the question of the exact solution for the conductivity in the Hubbard model remained open. In this Letter, we employ several complementary state-of-the-art numerical methods to disentangle various contributions to conductivity and identify the best available result to be compared to experiment. We find that, at relevant (high) temperatures, the self-energy is practically local, yet the vertex corrections remain rather important, contrary to expectations. The finite-size effects are small even at the lattice size 4×4, and the corresponding Lanczos diagonalization result is, therefore, close to the exact result in the thermodynamic limit.

DOI: 10.1103/PhysRevLett.123.036601

Theoretical study of transport in condensed matter systems with strong interactions is very difficult. In many cases there are no long-lived quasiparticles and the conventional Boltzmann theory of transport provides little insight. Progress can only be made using bona fide many-body approaches to simplified lattice models or effective field theories where approximations are made in a controlled manner. [1–9] Even then, as only a few specifics of a real system enter the model, the comparison to relevant experiments can only be made at a qualitative level. This changed very recently when Ref. [10] reported a measurement of transport in a quantum simulator of the fermionic Hubbard model in two dimensions (2D). The experiment is performed on cold lithium atoms in an optical lattice, a controllable setup free from disorder, phonons, and other complications of realistic materials. It is well justified to compare at the quantitative level such experimental result for conductivity with the Hubbard model calculations.

Reference [10] found that two state-of-the-art methods, namely, the finite-temperature Lanczos method (FTLM) and the dynamical mean field theory (DMFT) give conductivities that differ by up to a factor $\frac{3}{2}$, and only FTLM shows a solid agreement with the experiment. At high temperatures $T \gtrsim t$ relevant to these observations (for instance, in cuprates where the hopping parameter $t \approx 0.3$ eV the corresponding temperature is well above the melting temperature), one expects the correlation lengths to be short and the approximations made in the two methods to apply. Our aim is to reveal the physical origin of this discrepancy and to establish a numerically exact solution in the regime $T/t \gtrsim 1$ relevant for optical lattice experiments, as well as other narrow band systems, such as organic superconductors [11], low temperature phase of TaS_2 [12], twisted bilayer graphene [13], and monolayer transition metal dichalcogenides [14], such as $1T$-$NbSe_2$ [15].

It is useful to recall that the mentioned numerical methods belong to two distinct general approaches: (A) one solves an isolated finite cluster of lattice sites, as representative of the thermodynamic limit [7,8,16]; (B) one solves an effective, self-consistently determined "embedded" cluster, which provides propagators of infinite range, yet limits the range of electronic correlations [17–25]. The diagrammatic content of the self-energy in the two approaches is sketched in Fig. 1(a). Approach B captures longer distance quantum fluctuations and, therefore, is assumed to converge more quickly with cluster size at the price of an iterative solution of the (embedded) cluster, as opposed to the "single-shot" calculation in approach A. FTLM solves a 4×4 isolated cyclic cluster and belongs to A. DMFT is an embedded cluster calculation (B) with the cluster size one, and therefore, it approximates the self-energy by a purely local quantity.

Therefore, there are three possible sources of discrepancy between the DMFT and FTLM results for resistivity: (i) nonlocal correlations which are encoded in the nonlocal corrections to self-energy, present in FTLM but beyond the DMFT approximation; (ii) quantum fluctuations at

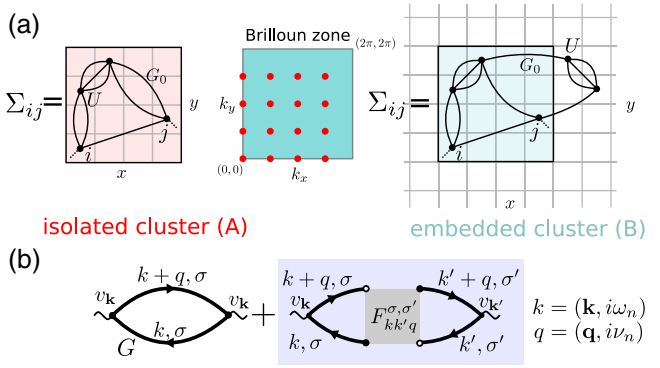

FIG. 1. (a) Illustration of the type of self-energy diagrams that are captured by isolated cluster and embedded cluster (in particular cellular DMFT), and the respective difference in the Brillouin zone (discrete vs continuous). (b) Separation of a susceptibility into the bubble and the vertex corrections part.

distances beyond the linear size of the FTLM cluster; DMFT captures them through an effective fermionic bath; (iii) vertex corrections, included within FTLM but neglected within DMFT where one calculates only the bubble contribution. We recall that the two-particle correlation functions can be split into the disconnected part ("the bubble") and the connected part ("vertex corrections"), as shown in Fig. 1(b). The bubble captures only the single-particle scattering off the medium, described by the self-energy which enters the full Green's function. The collective excitations come from the particle-hole scattering, and are present only in the vertex corrections. Whereas the contribution of the connected part is always important for charge susceptibility [26–28], in the large dimensionality limit the vertex corrections to conductivity cancel [29] (the full vertex F loses $\mathbf{k}\mathbf{k}'$ dependence and the current vertex is odd $v_{-\mathbf{k}} = -v_{\mathbf{k}}$, unlike the charge vertex which is even). In finite dimensions, however, the vertex corrections do contribute to conductivity as discussed previously in several approximative approaches at low temperatures [30–36]. Based on the Ward identity, one could think that when the correlations are approximately local, the vertex corrections become negligible [30,32]. We show that this expectation is not satisfied [37] and that, despite the nonlocal self-energy being practically negligible at $T \gtrsim 0.3D$, the vertex corrections still amount to a sizable shift in dc resistivity. Additionally, we show that long-distance quantum fluctuations have little effect on dc conductivity, thus, a 4×4 isolated-cluster calculation is sufficient to obtain exact results for the bulk model.

Model.—We consider the Hubbard model on the square lattice

$$H = -t \sum_{\sigma,\langle i,j\rangle} c^{\dagger}_{\sigma i} c_{\sigma j} + U \sum_{i} n_{\uparrow i} n_{\downarrow i} - \mu \sum_{\sigma,i} n_{\sigma i}, \qquad (1)$$

where $c^{\dagger}_{\sigma i}/c_{\sigma i}$ creates or annihilates an electron of spin σ at the lattice site i. The hopping amplitude between the nearest neighbors is denoted t, and we set $D = 4t$ as the unit of energy. We also take lattice spacing $a = 1$, and $\hbar = e = 1$. The density operator is $n_{\sigma i} = c^{\dagger}_{\sigma i} c_{\sigma i}$, the chemical potential μ, and the on-site Hubbard interaction U. Throughout the Letter, we keep $U = 2.5D$, which corresponds to the (doped) Mott insulator regime, and assume paramagnetic solutions with full lattice symmetry.

Formalism.—The conductivity is defined in terms of the current-current correlation function

$$\Lambda^{xx}_{\mathbf{q}}(i\nu_n) \equiv \sum_i e^{-i\mathbf{q}\cdot\mathbf{r}_i} \int d\tau e^{i\nu_n \tau} \langle j^x_i(\tau) j^x_{i=0}(0)\rangle, \qquad (2)$$

where τ is imaginary time, $i\nu_n = 2in\pi T$ is the bosonic Matsubara frequency, $\mathbf{r}_i = (x_i, y_i)$ denotes the real-space vector of the site i. The current operator j is defined as $j^x_i = -it \sum_{\sigma} c^{\dagger}_{\sigma i} c_{\sigma,\mathrm{n.n.}(i;x)} + \mathrm{H.c.}$ where $\mathrm{n.n.}(i;x)$ denotes the nearest neighbor in the x direction. We are interested in longitudinal, uniform conductivity $\sigma^{xx}_{\mathbf{q}=0}(\omega)$, so we adopt a shorthand notation $\Lambda(i\nu_n) \equiv \Lambda^{xx}_{\mathbf{q}=0}(i\nu_n)$ and $\sigma(\omega) \equiv \sigma^{xx}_{\mathbf{q}=0}(\omega)$. The optical conductivity is given by [38] $\sigma(\omega) = -(i/\omega)[\Lambda(\omega) - \Lambda(\omega = 0)]$, where $\Lambda(\omega)$ is the analytical continuation of $\Lambda(i\nu_n)$ to the real axis, i.e., the inverse of the Hilbert transform

$$\Lambda(i\nu) = \frac{1}{\pi} \int d\omega \frac{\mathrm{Im}\Lambda(\omega)}{\omega - i\nu} = \frac{1}{\pi} \int d\omega \frac{\omega \mathrm{Re}\sigma(\omega)}{\omega - i\nu}. \qquad (3)$$

The second equality in Eq. (3) is due to $\mathrm{Im}\Lambda(\omega = 0) = 0$. The direct-current (dc) conductivity is defined as $\sigma_{\mathrm{dc}} = \mathrm{Re}\sigma(\omega = 0) = \mathrm{Im}\Lambda'(\omega = 0)$, and the dc resistivity is then $\rho_{\mathrm{dc}} = 1/\sigma_{\mathrm{dc}}$.

In order to better identify and understand the importance of various processes for the transport, we also calculate the charge susceptibility $\chi_c = d\langle n\rangle/d\mu$, which corresponds to the charge-charge correlation function [39]. Both χ_c and Λ can be separated into the bubble and the vertex corrections part [40], Fig. 1. In all quantities, the superscript "disc" denotes the bubble contribution, and the superscript "conn," the vertex corrections part.

Methods A.—We solve an isolated cyclic 4×4 cluster using the FTLM [41,42] method and both 4×4 and 8×8 using quantum Monte Carlo calculations [the continuous-time interaction-expansion algorithm (CTINT) [20,43]] Both methods yield numerically exact solutions of the representative finite-size model. In FTLM, we calculate $\sigma(\omega)$, while CTINT yields $\Lambda(i\nu_n)$, as well as the self-energy $\Sigma_{ij}(i\omega_n)$ and the Green's function $G_{ij}(i\omega_n)$ [44]. Note that both CTINT and FTLM allow for a direct calculation of the full current-current correlation function, and that we need not evaluate the full vertex function F at any stage of the calculation.

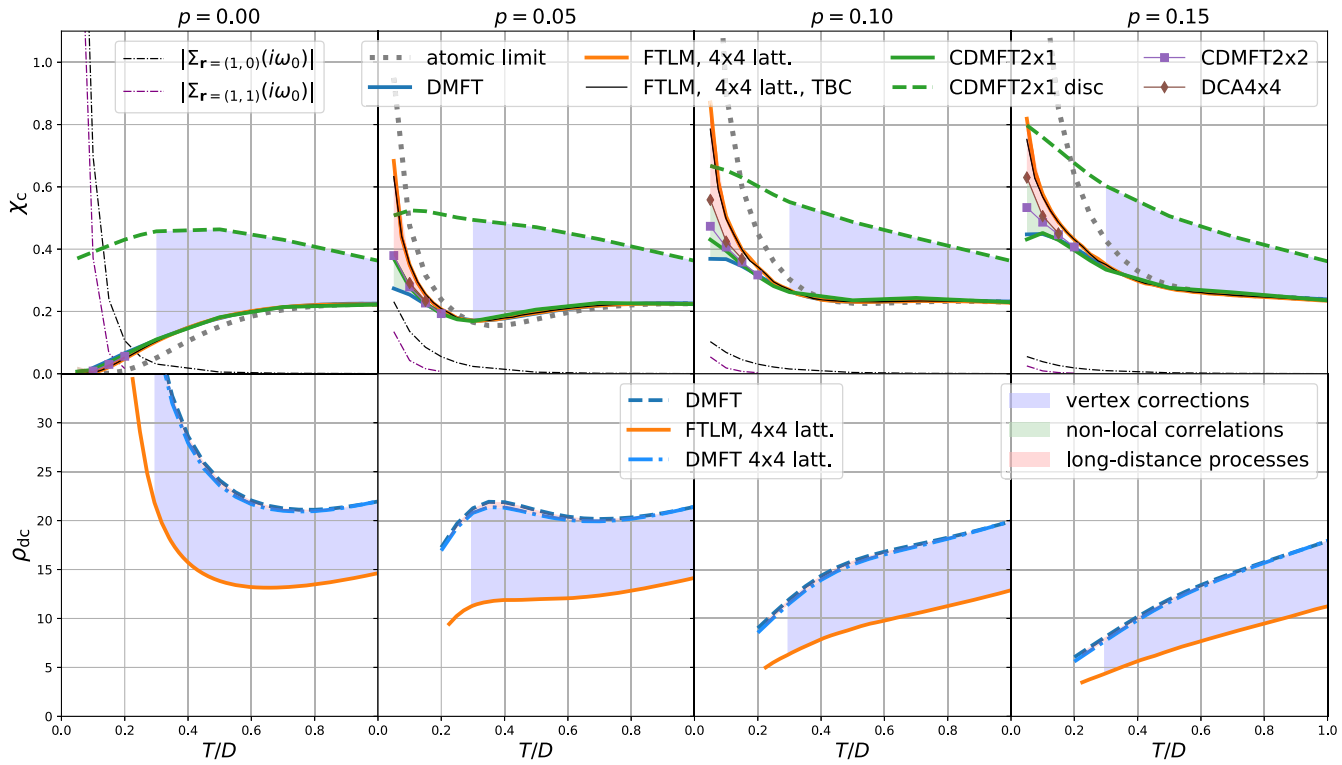

FIG. 2. Charge susceptibility (upper) and dc resistivity (lower) as a function of temperature, at different levels of doping. The color between the curves denotes the physical origin of the difference. Dashed curves denote just the bubble contribution, solid lines the full result.

In the isolated cluster calculations, one faces several finite-size effects stemming from the finite range of the bare electronic propagator [41,42]. Most importantly, this not only limits the range of electronic correlations, but also affects the diagrammatic content of short range correlations: diagrams with distant interaction vertices are not captured (Fig. 1). One may see this equivalently in the $\mathbf{k}$ space as a discretization of the Brillouin zone, which affects the internal momentum summations in all self-energy and full vertex diagrams.

Methods B.—We solve the embedded clusters of size 2×1 and 2×2 within the cellular DMFT (CDMFT) scheme [45] and the 4×4 cluster within the dynamical cluster approximation (DCA) scheme [46], both using CTINT. (Unlike the isolated cluster case, the bare propagator entering CTINT here takes into account the effective medium.) The single-site DMFT calculations (cluster size $N_c = 1$) are done using both the CTINT and the approximative real-frequency numerical renormalization group method as impurity solvers.

In CDMFT, an electron can travel infinitely far between two scatterings, but a self-energy insertion in the corresponding diagrammatic expansion can only be of limited range (see Fig. 1). In DCA, the approximation is made in reciprocal space and amounts to allowing the electron to visit $\mathbf{k}$ states otherwise not present in the finite cluster [24].

Results.—The top panels of Fig. 2 show the temperature dependence of χ_c for several values of doping $p = 1 - \langle n \rangle$. One sees that, in the high-temperature regime $T \gtrsim 0.3D$, the results of different methods (solid curves) all agree and tend toward the atomic limit, as expected for a thermodynamic quantity.

At lower temperatures, the nonlocal correlations show up. Away from half-filling, FTLM and DCA yield a charge susceptibility that increases with lowering temperature, yet in DMFT, it saturates, instead. The enhancement of charge susceptibility at low T comes from the antiferromagnetic fluctuations [7]. The difference between the DCA and the DMFT is used to characterize the importance of nonlocal correlations (green shading). They also manifest themselves in the growth of nonlocal self-energy at low T (thin dashed-dotted lines). The DCA and the FTLM results do not completely coincide; the difference (pink shading) comes from the longer-distance quantum fluctuations. The discretization of the Brillouin zone in FTLM can be somewhat ameliorated by the twisted-boundary conditions (TBC) scheme [47]. As expected, TBC is closer to DCA (black line), but one needs a better method to capture the full effect of longer-range processes.

We have also separately evaluated the bubble contribution χ^{disc} to χ_c (dashed lines) and observe that it is substantially larger than the full result χ_c.

The bottom panels of Fig. 2 show the temperature dependence of resistivity ρ_{dc} as calculated from the bubble term in the DMFT (dashed line) and the full result from FTLM (solid line). Strikingly, even in the temperature range $T \gtrsim 0.3D$ where the behavior of χ_c collapsed to that of the atomic limit, the DMFT and FTLM are shown to yield significantly different results with a lower value of resistivity found in the FTLM.

To understand the origin of this difference, we take a closer look at the data at $T = 0.5$, $p = 0.1$ that we show in Fig. 3. In panel (a) we compare the self-energies found in the DMFT, CDMFT 2×1, and the CTINT calculation for the isolated 4×4 and 8×8 clusters. Not only is the nearest neighbor self-energy (top) found to be 2 orders of magnitude smaller than the local one (bottom), but also the local parts of the self-energies show excellent agreement. Thus, neither nonlocal correlations (neglected in DMFT) nor long-range processes (neglected in 4×4) play an important role for the self-energy at this temperature.

Might long-range processes play a more important role for the conductivity? One can readily investigate the role of long-range processes for the bubble part of the conductivity. This is done by calculating the conductivity in the DMFT formulated for the 4×4 lattice, which amounts to discretizing the Brillouin zone [in both the self-consistency condition and internal bubble summation, Fig. 1(b)]. Figure 3(b) compares the optical conductivity obtained in this way (denoted by DMFT 4×4) to the infinite lattice DMFT result and to the FTLM one. The DMFT and the DMFT 4×4 are close: the long-range processes clearly do not account for the discrepancy between the DMFT and the FTLM either. Therefore, the difference between the DMFT and FTLM conductivities mostly comes from the vertex corrections.

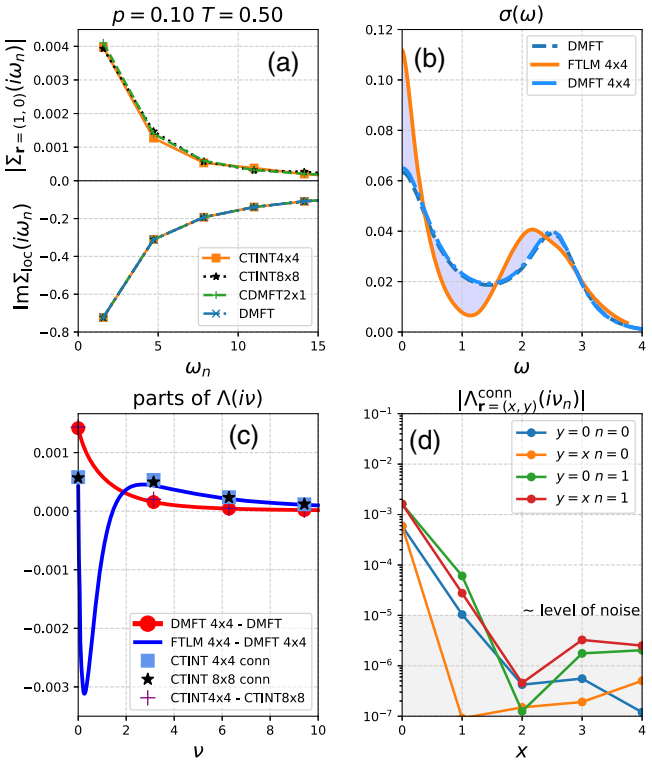

FIG. 3. All panels: $p = 0.1$, $T = 0.5D$. a) Benchmark of self-energy and inspection of its leading non-local component. b) Comparison of the optical conductivity between various methods. c) See text. d) Real-space resolution of the vertex corrections along two spatial directions (CTINT 8×8 result).

To further verify this result, we have also evaluated the current-current correlation function $\Lambda(i\nu_n)$ in CTINT 4×4, and deduced the connected part by $\Lambda^{\text{conn}}(i\nu_n) = \Lambda(i\nu_n) - \Lambda^{\text{disc}}(i\nu_n)$, which is shown by the blue squares in Fig. 3(c). These points fall on the blue line which is obtained by the Hilbert transform to the imaginary axis [Eq. (3)] of the difference in $\sigma(\omega)$ between the FTLM and the DMFT 4×4 [see Supplemental Material (SM) [48] for details and other p, T]. Note that the magnitude of Λ^{conn} at the Matsubara frequencies is rather small, consistent with the Ward identity $\Lambda^{\text{conn}}(i\nu = 0) \sim \sum_{\mathbf{k}} v_{\mathbf{k}} \sum_{i\omega_n} G^2_{\mathbf{k}}(i\omega_n) \partial_{k_x} \Sigma_{\mathbf{k}}(i\omega_n)$, that associates $\Lambda^{\text{conn}}(i\nu_0)$ with $\partial_{k_x} \Sigma_{\mathbf{k}}$ (see SM [48] for further discussion). The conductivity is, however, determined by the slope, $-\partial_\nu \text{Re}\Lambda(i\nu)|_{\nu=0^+} = \sigma(\omega = 0) = \sigma_{\text{dc}}$, and the contribution from Λ^{conn} is not small but comparable to the bubble term. The slope of the red line which corresponds to the difference between the DMFT 4×4 and DMFT is small, reflecting the practically negligible finite-size effects in the bubble.

The shape of Λ^{conn} is difficult to reconstruct with analytical continuation from noisy data at the Matsubara frequencies (see SM [48]), which we circumvented by using FTML.

Might the impact of vertex corrections change if larger systems are considered? The added longer distance components of $\Lambda^{\text{conn}}_{\mathbf{r}}$ could be sizeable, and even the short distance components might change due to improved diagrammatic content captured by the bigger cluster. We have performed the CTINT 8×8 computation to address this question. In Fig. 3(c), we compare $\Lambda^{\text{conn}}(i\nu_n)$ between 4×4 and 8×8 clusters (blue squares and black stars) and observe that they are equal within the statistical error bars (about the size of the square symbol). As for the longer distance components, we analyze the vertex corrections term as a function of real-space vector $\Lambda^{\text{conn}}_{\mathbf{r}}(i\nu_n)$ and present the results in Fig. 3(d). Indeed, the values drop rapidly with distance, and the range of Λ^{conn} is clearly captured by the 4×4 cluster. Furthermore, the difference in the full Λ between 4×4 and 8×8 clusters (purple crosses) appears to coincide with the finite size effects in the bubble (red line and dots) obtained entirely independently with DMFT.

Small finite-size effects are also indicated from a comparison of the frequency moments of FTLM $\sigma(\omega)$ in the high-T limit with the exact values from Ref. [8], where

we find an excellent agreement within $\lesssim 0.2\%$ (see SM [48]).

It is important to note that apart from reducing the dc resistivity, the vertex corrections have a characteristic effect on the frequency dependence of optical conductivity [see Fig. 3(b) and SM [48]]. The high-frequency peak in $\sigma(\omega)$ obtained from DMFT is centered at precisely $\omega = U = 2.5D$. This peak describes single-particle transitions between the Hubbard bands. The inclusion of vertex corrections brings about multiparticle excitations which move this peak towards lower frequencies, as noted previously in a slightly different context (see Refs. [49–51]).

Conclusions.—In the high-temperature $T \gtrsim t$, (doped) Mott insulator regime of the Hubbard model, the single-particle self-energy is almost local, yet the vertex corrections to dc resistivity persist. This finding applies to the optical lattice investigation in Ref. [10], and explains why the DMFT results disagree with the experiment. On the other hand, we demonstrate that the long-distance quantum fluctuations play a negligible role, and thus, the 4×4 isolated cluster becomes representative of the thermodynamic limit. Therefore, the corresponding FTLM result is close to exact, and is an important benchmark for the experiment in Ref. [10] and future cold atoms experiments.

We cannot access, with the same confidence, the regime below $T \sim t$. In principle, determinantal quantum Monte Carlo algorithms allow access to larger lattices and, thus, lower temperatures (see Ref. [8]), but the analytical continuation presents a possible source of systematic error which is difficult to detect and estimate (see SM [48] for a detailed analysis using the implementation of the maximum entropy method taken from Ref. [52]). Our results highlight the need for developing real-frequency diagrammatic methods, like the one proposed recently in Ref. [53].

Finally, our results suggest that proper account of the vertex corrections is needed at all temperatures. The discrepancies between the experimental observations and the DMFT, such as those observed in the case of hcp-Fe [54] or in Sr_2RuO_4 [55] should not be interpreted only in terms of nonlocal correlations. Very recently [36], this conclusion has been shown to be valid even at much weaker coupling and in various other models.

We acknowledge useful discussions with V. Dobrosavljević, A. Georges, F. Krien, and A. M. Tremblay, and contributions of A. Vranić and J. Skolimowski at the early stage of this project. J. K., R. Ž., and J. M. are supported by the Slovenian Research Agency (ARRS) under Program No. P1-0044 and Project No. J1-7259. J. V and D. T. are supported by the Serbian Ministry of Education, Science and Technological Development under Project No. ON171017. Numerical calculations were partially performed on the PARADOX supercomputing facility at the Scientific Computing Laboratory of the Institute of Physics Belgrade. The CTINT algorithm has been implemented using the TRIQS toolbox [56].

[1] H. Terletska, J. Vučičević, D. Tanasković, and V. Dobrosavljević, Phys. Rev. Lett. **107**, 026401 (2011).
[2] X. Deng, J. Mravlje, and R. Žitko, M. Ferrero, G. Kotliar, and A. Georges, Phys. Rev. Lett. **110**, 086401 (2013).
[3] W. Xu, K. Haule, and G. Kotliar, Phys. Rev. Lett. **111**, 036401 (2013).
[4] J. Vučičević, D. Tanasković, M. J. Rozenberg, and V. Dobrosavljević, Phys. Rev. Lett. **114**, 246402 (2015).
[5] N. Pakhira and R. H. McKenzie, Phys. Rev. B **91**, 075124 (2015).
[6] E. Perepelitsky, A. Galatas, J. Mravlje, R. Žitko, E. Khatami, B. S. Shastry, and A. Georges, Phys. Rev. B **94**, 235115 (2016).
[7] J. Kokalj, Phys. Rev. B **95**, 041110(R) (2017).
[8] E. W. Huang, R. Sheppard, B. Moritz, and T. P. Devereaux, arXiv:1806.08346.
[9] S. A. Hartnoll, A. Lucas, and S. Sachdev, *Holographic Quantum Matter* (MIT Press, Cambridge, MA, 2018).
[10] P. T. Brown, D. Mitra, E. Guardado-Sanchez, R. Nourafkan, A. Reymbaut, C.-D. Hébert, S. Bergeron, A.-M. S. Tremblay, J. Kokalj, D. A. Huse, P. Schauß, and W. S. Bakr, Science **363**, 379 (2019).
[11] B. J. Powell and R. H. McKenzie, Rep. Prog. Phys. **74**, 056501 (2011).
[12] K. Rossnagel and N. V. Smith, Phys. Rev. B **73**, 073106 (2006).
[13] Y. Cao, V. Fatemi, A. Demir, S. Fang, S. L. Tomarken, J. Y. Luo, J. D. Sanchez-Yamagishi, K. Watanabe, T. Taniguchi, E. Kaxiras, R. C. Ashoori, and P. Jarillo-Herrero, Nature (London) **556**, 80 (2018).
[14] J. N. Coleman *et al.*, Science **331**, 568 (2011).
[15] Y. Nakata, K. Sugawara, R. Shimizu, Y. Okada, P. Han, T. Hitosugi, K. Ueno, T. Sato, and T. Takahashi, NPG Asia Mater. **8**, e321 (2016).
[16] N. Trivedi, R. T. Scalettar, and M. Randeria, Phys. Rev. B **54**, R3756 (1996).
[17] G. Biroli and G. Kotliar, Phys. Rev. B **65**, 155112 (2002).
[18] T. A. Maier, M. Jarrell, Th. Pruschke, and M. Hettler, Rev. Mod. Phys. **77**, 1027 (2005).
[19] G. Kotliar, S. Y. Savrasov, K. Haule, V. S. Oudovenko, O. Parcollet, and C. A. Marianetti, Rev. Mod. Phys. **78**, 865 (2006).
[20] E. Gull, A. J. Millis, A. I. Lichtenstein, A. N. Rubtsov, M. Troyer, and P. Werner, Rev. Mod. Phys. **83**, 349 (2011).
[21] J. P. F. LeBlanc *et al.*, Phys. Rev. X **5**, 041041 (2015).
[22] T. Ayral and O. Parcollet, Phys. Rev. B **94**, 075159 (2016).
[23] T. Ayral, J. Vučičević, and O. Parcollet, Phys. Rev. Lett. **119**, 166401 (2017).
[24] J. Vučičević, N. Wentzell, M. Ferrero, and O. Parcollet, Phys. Rev. B **97**, 125141 (2018).
[25] G. Rohringer, H. Hafermann, A. Toschi, A. A. Katanin, A. E. Antipov, M. I. Katsnelson, A. I. Lichtenstein, A. N. Rubtsov, and K. Held, Rev. Mod. Phys. **90**, 025003 (2018).

[26] H. Hafermann, E. G. C. P. van Loon, M. I. Katsnelson, A. I. Lichtenstein, and O. Parcollet, Phys. Rev. B **90**, 235105 (2014).

[27] R. Nourafkan, M. Côté, and A.-M. S. Tremblay, Phys. Rev. B **99**, 035161 (2019).

[28] F. Krien, E. G. C. P. van Loon, M. I. Katsnelson, A. I. Lichtenstein, and M. Capone, Phys. Rev. B **99**, 245128 (2019).

[29] A. Khurana, Phys. Rev. Lett. **64**, 1990 (1990).

[30] N. Lin, E. Gull, and A. J. Millis, Phys. Rev. B **80**, 161105 (R) (2009).

[31] N. Lin, E. Gull, and A. J. Millis, Phys. Rev. B **82**, 045104 (2010).

[32] D. Bergeron, V. Hankevych, B. Kyung, and A.-M. S. Tremblay, Phys. Rev. B **84**, 085128 (2011).

[33] T. Sato, K. Hattori, and H. Tsunetsugu, Phys. Rev. B **86**, 235137 (2012).

[34] N. Lin, E. Gull, and A. J. Millis, Phys. Rev. Lett. **109**, 106401 (2012).

[35] T. Sato and H. Tsunetsugu, Phys. Rev. B **94**, 085110 (2016).

[36] A. Kauch, P. Pudleiner, K. Astleithner, T. Ribic, and K. Held, arXiv:1902.09342.

[37] The irreducible vertex in the ph-channel is $\Gamma_{\mathrm{ph},\alpha\beta\gamma\delta} = \{\delta\Sigma_{\delta\gamma}[G]/(\delta G_{\alpha\beta})\}|_{G=G[G_0,\Sigma]}$, so even if a component of Σ is zero, it still depends on all components of the Green's function, and its derivative is not necessarily zero.

[38] P. Coleman, *Introduction to Many-Body Physics* (Cambridge University Press, Cambridge, England, 2015).

[39] Charge susceptibility is the uniform, zero-frequency component of the charge-charge correlation function $\chi_c \equiv \chi_{\mathbf{q}=0}(i\nu_n = 0) \equiv \sum_i \int d\tau \langle [n_i(\tau) - \langle n\rangle][n_{i=0}(0) - \langle n\rangle]\rangle$ where $n_i = n_{\uparrow i} + n_{\downarrow i}$ is the total charge operator.

[40] The bubble part is expressed in terms of the full Green's function G as $(\chi, \Lambda^{xx})^{\mathrm{disc}}_{\mathbf{q}}(i\nu_m) = -T\sum_{i\omega_n,\mathbf{k},\sigma} v^2_{\mathbf{k}} G_{\sigma,\mathbf{k}+\mathbf{q}}(i\omega_n + i\nu_m) G_{\sigma,\mathbf{k}}(i\omega_n)$ with the vertex factor $v_{\mathbf{k}} = 1$ in the case of χ, and $v_{\mathbf{k}} = [(\partial\varepsilon_{\mathbf{k}})/(\partial k_x)] = 2t \sin k_x$ in the case of Λ^{xx} on the square lattice. Here, $\varepsilon_{\mathbf{k}}$ denotes the bare dispersion, $i\omega_n = i(2n+1)\pi T$ is the fermionic Matsubara frequency.

[41] J. Jaklič and P. Prelovšek, Adv. Phys. **49**, 1 (2000).

[42] J. Jaklič and P. Prelovšek, Phys. Rev. B **52**, 6903 (1995).

[43] A. N. Rubtsov and A. I. Lichtenstein, J. Exp. Theor. Phys. Lett. **80**, 61 (2004).

[44] In FTLM one can calculate the self-energy as well, but it is beyond the generality of our implementation.

[45] G. Kotliar, S. Y. Savrasov, G. Pálsson, and G. Biroli, Phys. Rev. Lett. **87**, 186401 (2001).

[46] M. H. Hettler, A. N. Tahvildar-Zadeh, M. Jarrell, T. Pruschke, and H. R. Krishnamurthy, Phys. Rev. B **58**, R7475 (1998).

[47] D. Poilblanc, Phys. Rev. B **44**, 9562 (1991).

[48] See Supplemental Material at http://link.aps.org/supplemental/10.1103/PhysRevLett.123.036601 for detailed analysis and supporting data.

[49] B. Cunningham, M. Grüning, P. Azarhoosh, D. Pashov, and M. van Schilfgaarde, Phys. Rev. Mater. **2**, 034603 (2018).

[50] M. Gatti, F. Bruneval, V. Olevano, and L. Reining, Phys. Rev. Lett. **99**, 266402 (2007).

[51] J. Vidal, S. Botti, P. Olsson, J.-F. Guillemoles, and L. Reining, Phys. Rev. Lett. **104**, 056401 (2010).

[52] R. Levy, J. LeBlanc, and E. Gull, Comput. Phys. Commun. **215**, 149 (2017).

[53] A. Taheridehkordi, S. H. Curnoe, and J. P. F. LeBlanc, Phys. Rev. B **99**, 035120 (2019).

[54] L. V. Pourovskii, J. Mravlje, M. Ferrero, O. Parcollet, and I. A. Abrikosov, Phys. Rev. B **90**, 155120 (2014).

[55] X. Deng, K. Haule, and G. Kotliar, Phys. Rev. Lett. **116**, 256401 (2016).

[56] O. Parcollet, M. Ferrero, T. Ayral, H. Hafermann, P. Seth, and I. S. Krivenko, Comput. Phys. Commun. **196**, 398 (2015).

Supplemental Material: Conductivity in the square lattice Hubbard model at high temperatures: importance of vertex corrections

J. Vučičević,[1] J. Kokalj,[2,3] R. Žitko,[3,4] N. Wentzell,[5] D. Tanasković,[1] and J. Mravlje[3]

[1] *Scientific Computing Laboratory, Center for the Study of Complex Systems, Institute of Physics Belgrade, University of Belgrade, Pregrevica 118, 11080 Belgrade, Serbia*

[2] *University of Ljubljana, Faculty of Civil and Geodetic Engineering, Jamova 2, Ljubljana, Slovenia*

[3] *Jozef Stefan Institute, Jamova 39, SI-1000, Ljubljana, Slovenia*

[4] *University of Ljubljana, Faculty of Mathematics and Physics, Jadranska 19, Ljubljana, Slovenia*

[5] *Center for Computational Quantum Physics, Simons Foundation Flatiron Institute, New York, NY 10010 USA*

Here we present a detailed analysis of the numerical results that we perform to disentangle the different contributions to the optical conductivity and identify the source of discrepancy between DMFT and FTLM. The analysis is performed on the imaginary axis where we can obtain the results from CTINT. Note that at high temperature, the Matsubara frequencies are far apart and the values of $\Lambda(i\nu_n)$ are insensitive to the details of $\sigma(\omega)$. We illustrate this in Fig. S1 where we show that, on the Matsubara axis, the FTLM and DMFT $\Lambda(i\nu_n)$ results are almost indistinguishable. However, the discrepancy is *not* below the level of noise in our numerics and we are able to reconstruct this difference from three different contributions, namely the finite-size effects, non-local self-energy effects and vertex corrections, all obtained independently using combinations of other methods. However, in the present context, we find the CTINT method useful only as a tool for benchmarking, since the analytical continuation from the imaginary to the real axis introduces a systematic error, and a precise σ_{dc} value is difficult to extract from $\Lambda(i\nu_n)$. In Section I we present our imaginary axis analysis of the results, and in Section II we discuss the difficulty of analytical continuation. Then, in Section III we benchmark our FTLM result against analytically computed frequency moments of the optical conductivity. In Section IV we discuss the details of the pole-broadening procedure used in FTLM.

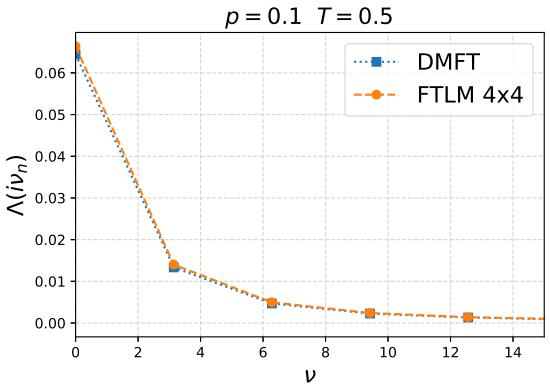

FIG. S1. Current-current correlation function $\Lambda(i\nu_n)$ in FTLM and DMFT (the dashed and dotted lines are guides to the eye).

I. DETAILED BENCHMARK

In Fig. S2 we show the detailed comparison and cross-checks between the different methods in 12 doping-temperature (p, T) points in the Hubbard model phase diagram at $U = 2.5D = 10t$. The continuous lines are obtained by the Hilbert transform from the real-axis to the continuous imaginary variable $\sigma(\omega) \to \Lambda(i\nu)$, and then taking the difference between the different methods, as written in the legend. The question we are addressing in the main text and that is considered in further detail here is the physical origin of the difference difference between DMFT and FTLM 4×4, presented on Fig. S2 by the orange lines.

We can readily inspect the effect of finite cluster size on the bubble Λ^{disc}. This is given by the red line which presents the difference between DMFT 4×4 and DMFT. Red circles are obtained independently on the Matsubara axis without any analytical continuation, directly from DMFT data (DMFT here is performed with CTINT solver), and present an additional cross-check of our analytical continuation of the self-energy which was used to obtain $\sigma(\omega)$ in DMFT. We note that the statistical noise coming from CTINT in the single-site DMFT solution is very small, and the Padé analytical continuation of $\Sigma(i\omega_n)$ can be successfully performed. The optical conductivities agree closely (within few percent) between QMC and the numerical renormalization group (NRG) solution.

We can also compare the red line with the difference between the full Λ from CTINT 8×8 and 4×4 (purple crosses). The agreement is solid: it appears that the only difference between the 8×8 and 4×4 clusters is the finite-size effects in the bubble Λ^{disc}, and that the finite-size effects disappear entirely already at cluster size 8×8. Note, however, that finite-size effects mostly pertain to the overall integral of $\sigma(\omega)$ (i.e. $\Lambda(i\nu = 0)$),

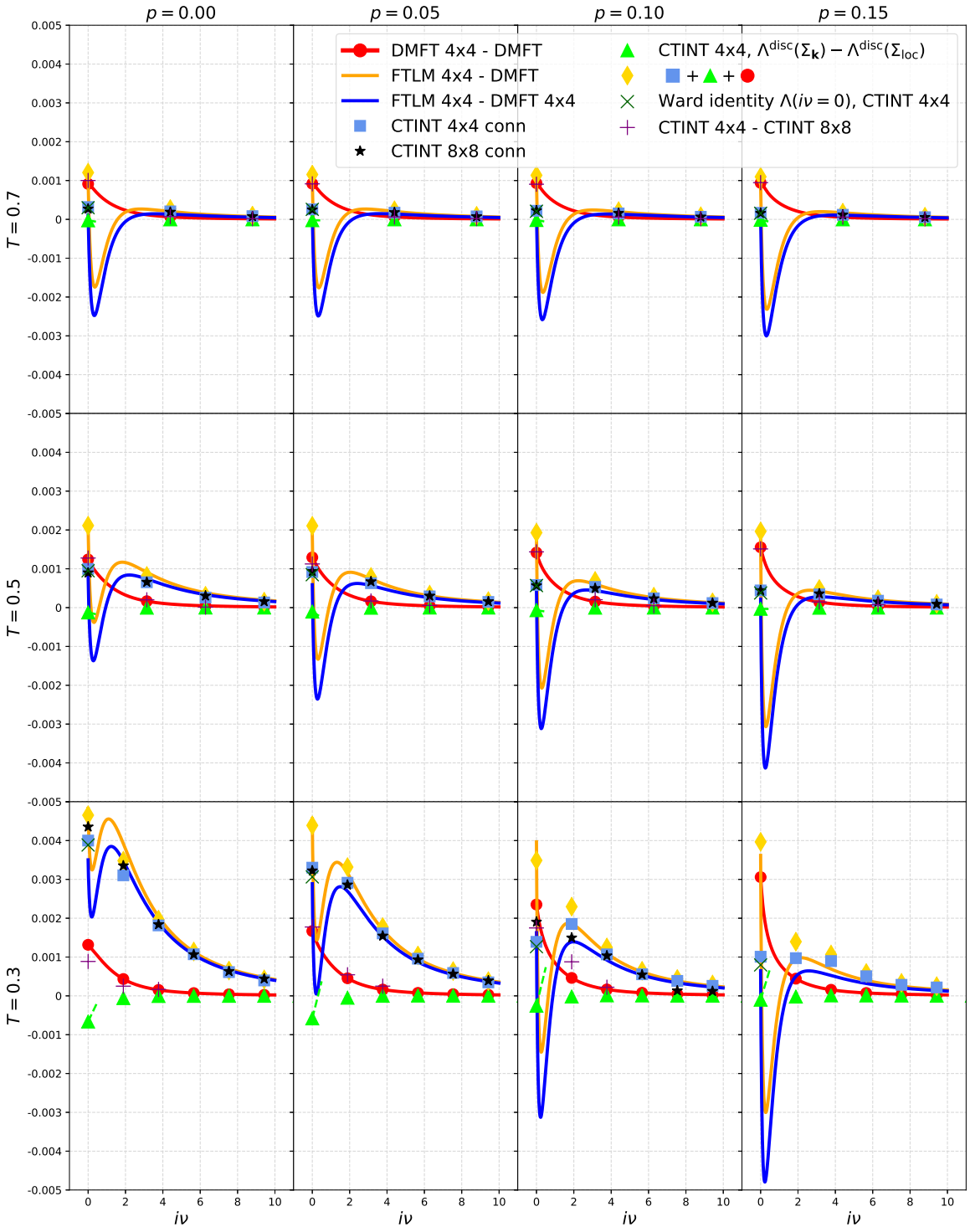

FIG. S2. Comparison of various parts of the current-current correlation functions $\Lambda(i\nu)$ on the imaginary axis (see text).

and have little impact on $\sigma_{\rm dc}$.

The blue line presents the difference between FTLM 4×4 and DMFT 4×4, which is by construction the orange line minus the red line, i.e. the difference between DMFT and FTLM 4×4, up to the finite-size effects in the bubble.

The blue squares and black stars are the vertex corrections $\Lambda^{\rm conn}$ as obtained from CTINT 4×4 and 8×8: at $T\geq0.5D$ their agreement is excellent, and even at the lowest temperature it is likely within the statistical error bars of the method. At the lowest temperature there is some discrepancy but mostly due to increased statistical error in CTINT. The problem particularly pronounced at the biggest doping, where our CTINT 8×8 calculation suffers from the sign problem and failed to converge properly in the available computational time (384 `cpu*days` per point).

We have inspected also the self-energies and found excellent agreement between CTINT 8×8 and 4×4 (see Fig.3a in main text, other data not shown). We observe that the range of $\Sigma_{\mathbf{r}}$ is at most 2 lattice spacings, which means that the longer distance components that are captured by the 8×8 cluster are unlikely to have a measurable effect on any observable.

We cross check our results by calculating $\Lambda^{\rm conn}(i\nu=0)$ from the Ward identity[1].

$$\Lambda^{\rm conn}(i\nu=0)=-2T\sum_{\mathbf{k}}v_{\mathbf{k}}\sum_{i\omega_n}G^2_{\mathbf{k}}(i\omega_n)\partial_{k_x}\Sigma_{\mathbf{k}}(i\omega_n)$$

and present it using the dark-green cross. Here we have constructed $\Sigma_{\mathbf{k}}(i\omega_n)$ on the lattice (64×64 grid Brillouin zone) using the Fourier transform of the short-distance $\Sigma_{\mathbf{r}}$ components available on the 4×4 cluster, which also allowed us to take the derivative analytically. Again, the agreement with the corresponding blue square and black star is within the roughly estimated statistical error of CTINT at all temperatures.

In most cases the blue line (difference between FTLM 4×4 and DMFT 4×4) passes through the blue squares (vertex correction from CTINT 4×4). However, at $i\nu=0$ there appears to be a systematic deviation, and the blue line passes below the blue square. This we can link to the effect of non-local self-energy on the bubble which we calculate from the CTINT 4×4 results and present as green color triangles. Indeed, the green triangles are mostly negligible except at $\nu=0$ where they are slightly negative.

We check our decomposition by summing the green triangles, blue squares and red circles, and comparing them to the orange line. Within statistical error bars, the total difference between FTLM4×4 and DMFT appears to come from 1) finite-size effects in the bubble, 2) effects of non-local self-energy in the bubble and 3) vertex corrections.

Note, however, that the effects of non-local self-energy on the bubble are small and visible only at the lowest temperature, and related only to the overall integral of $\sigma(\omega)$, i.e. the kinetic energy. The only measurable effect on $\sigma(\omega=0)=-\partial_\nu\Lambda(i\nu)|_{\nu\to0^+}$ appears to come from the vertex corrections. We additionally cross check this by analytically continuing $\Sigma_{\mathbf{r}\neq0}$ from CTINT 4×4 and using it together with DMFT $\Sigma_{\rm loc}(\omega)$ that we already have on the real-axis from NRG solver, to construct $\Sigma_{\mathbf{k}}(\omega)$ and calculate $\sigma^{\rm disc}(\omega=0)$. The difference from the pure DMFT result is negligible in relative terms except at $p=0$ and lowest T where $\sigma_{\rm dc}$ becomes very small. We present the corresponding slope in $\Lambda(i\nu)$ with green color dashed lines and see that it is much smaller that the slope of the blue line, and even in the opposite direction.

Based on the above analysis we conclude that at $T\gtrsim0.3D$, finite-size effects and the effect of non-local self-energy on $\sigma^{\rm disc}_{\rm dc}$ become negligible, and that the vertex corrections $\sigma^{\rm conn}_{\rm dc}$ are already well converged with respect to the cluster size at the size 4×4. This builds confidence that our FTLM 4×4 is close to exact solution of the bulk Hubbard model.

II. UNCERTAINTIES IN THE ANALYTICAL CONTINUATION OF $\Lambda(i\nu_n)$

In this section we thoroughly test the Maximum Entropy analytical continuation (MaxEnt) of the Matsubara current-current correlation function $\Lambda(i\nu_n)\to\sigma(\omega)$. We find that the result is strongly biased towards the model function used in MaxEnt continuation, and therefore discard the CTINT results for $\sigma(\omega)$ in favor of FTLM 4×4 which requires no analytical continuation.

In Fig. S3 we compare $\sigma(\omega)$ and $\Lambda(i\nu)$ between FTLM and DMFT. As a function of continuous imaginary variable, $\Lambda(i\nu)$ is displayed by a line, and the Matsubara frequencies are indicated with crosses. Note that only the values at the Matsubara frequencies $\Lambda(i\nu_n)$ serve as the input for MaxEnt. We see that most of the difference between FTLM and DMFT is encoded between the first two Matsubara frequencies in $\Lambda(i\nu)$. In particular, the dc conductivity is given by $\sigma_{\rm dc}=-\partial_\nu\Lambda(i\nu)|_{\nu\to0^+}$, which is hard to estimate based on $\Lambda(i\nu_n)$. Although there is a one-to-one correspondence between any given function on the real axis and its Hilbert transform on the imaginary axis, any amount of noise in $\Lambda(i\nu_n)$ and a truncation of Matsubara frequencies is likely to lead to loss of critical information necessary to distinguish between two similar $\sigma(\omega)$.

Fig. S4 shows the optical conductivity obtained by the analytical continuation of the current-current correlation function $\Lambda(i\nu_n)$ from CTINT. We use the implementation of the Maximum Entropy method from

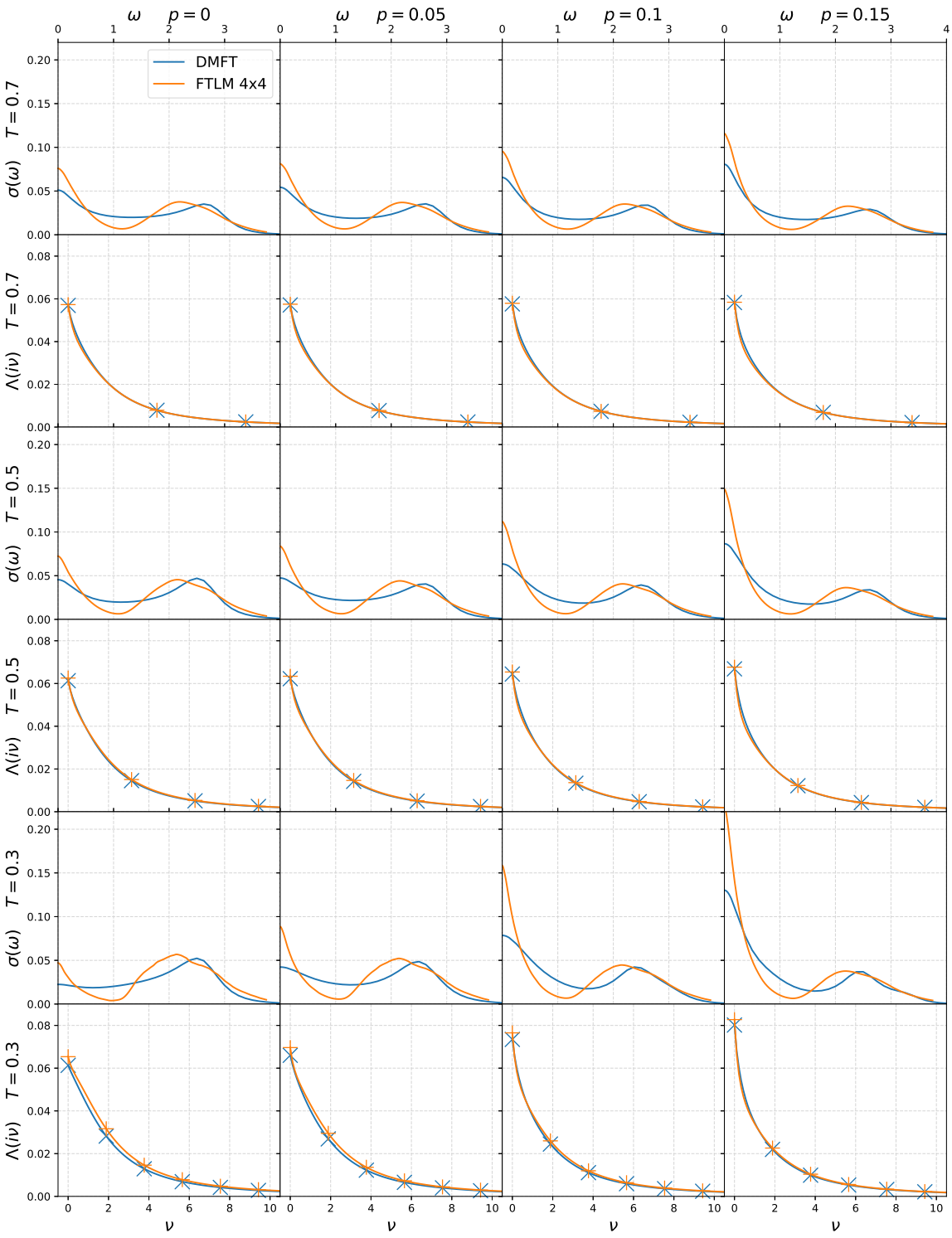

FIG. S3. Optical conductivity and current-current correlation function (see text).

Ref. 2. We put the error bar $d\Lambda(i\nu_n) = 10^{-4}$. Below this value the MaxEnt $\sigma(\omega)$ starts to acquire noisy and manifestly wrong features, due to overfitting. This value of 10^{-4} also agrees with the deviation in $\Lambda(i\nu_n)$ between CTINT 4×4 and FTLM, attributed to the statistical noise in CTINT. We perform annealing similar to Ref. 3: we apply MaxEnt at temperature $T = 0.5D$, using either FTLM (left column) or DMFT (middle column) $\sigma(\omega)$ at $T = 0.7$ as the default model. MaxEnt is then done at $T = 0.3D$, using the result of previous MaxEnt as the default model. The right column in Fig. S4 shows the resulting dc resistivities.

We see that the result of the analytical continuation strongly depends on the initial model function at high temperature. Furthermore, when the initial model is given by FTLM, the result at $T = 0.3$ still tends to deviate towards the DMFT solution. The reason for this is that the Drude-like peak in DMFT is broader than in FTLM, and the MaxEnt generally tends to make the spectrum smoother. This means that even with the correct default model at the highest temperature, the error bar introduced by annealing can easily erase any information about the vertex corrections and produce a result comparable to just the bubble contribution that one can safely obtain from DMFT(NRG). When the initial default model is taken to be DMFT, the error bar goes up to 50 percent, and the results typically resemble the DMFT solution.

Instead of choosing as the default model the FTLM results, which are computationally expensive to obtain (around one month on 32 cores with 80 GB of RAM for single choice of boundary conditions), it may appear reasonable to try and start the annealing using the high-T expansion[4] result at the highest temperature. However, as shown in Ref. 3 even high-T expansion is not trivial to calculate, and can only yield $\sigma(t)$ results up to $t \approx 1$ (t here is real time). In Fig. S5 we illustrate how the short time conductivity holds little information about $\sigma_{\rm dc}$ as $\sigma_{\rm dc} \sim \int dt {\rm Re}\sigma(t)$. The error made in the high-T expansion then propagates in MaxEnt, and can lead to wrong results.

Finally, it should be noted that with increasing temperature, Matsubara frequencies spread out, leaving less and less information to be extracted from even a slightly noisy $\Lambda(i\nu_n)$. We conclude that doing MaxEnt on CTINT 8×8 even with the corresponding FTLM 4×4 default model would not bring any information other than what is already contained in FTLM. Our analysis highlights the importance of developing methods that calculate the current-current correlation function directly on the real frequency axis.

III. COMPARISON WITH THE MOMENTS FROM THE HIGH-TEMPERATURE EXPANSION

In the high-T limit with $\sigma(\omega) \propto 1/T$, the frequency moments $\mu_k = \frac{1}{2\pi}\int_{-\infty}^{\infty}\sigma(\omega)\omega^k d\omega$ can be calculated reliably or even analytically[3,4] as the expectation values of certain commutators between the Hamiltonian and the current operator. Despite the difficult to reconstruct $\sigma(\omega)$, and in particular $\sigma_{\rm dc}$ from such moments with high confidence[3], the moments still provide a firm test of the numerical approaches.

By using the real frequency $\sigma(\omega)$ obtained with FTLM, we calculate frequency moments in the high-T limit for $U = 1.5D$ and $p = 0.2$. Such moments can be compared to the exact values reported in Ref. 3. We find that our FTLM moments μ_k for $k = 0 - 8$, which have main contributions from $\sigma(\omega)$ in the regime $|\omega| \lesssim 4D$ (i.e. up to ω about $2D$ above the upper edge of the Hubbard band), deviate from the exact moments by $\lesssim 0.2\%$. Some lower moments show even smaller deviation (see Table S1), which suggest FTLM correctly reproduces high-T behavior with small finite size effects. Our higher moments ($k \gtrsim 10$) show systematic larger deviation from the exact results due to high frequency cutoff at $\omega > 5D$ in our FTLM results.

$T \to \infty$ values of the FTLM moments are obtained by fitting T dependence of $2T\mu_k$ to $a + b/T^2$ in the temperature range between $5D$ and $10D$. The numerical uncertainties given in brackets in the Table S1 are obtained as a standard deviation in the fitting procedure.

k	$2T\mu_k$ (exact)	$2T\mu_k$ (FTLM)
0	0.96	0.96001(9)
2	16.5888	16.554(4)
4	879.206	879.4(2)
6	71350.4	71525(20)
8	$7.95719 \cdot 10^6$	$7.963(2) \cdot 10^6$

TABLE S1. Exact frequency moments $2T\mu_k$ taken from Ref. 3 and the moments from integrating FTLM $\sigma(\omega)$ (here the units of $t = D/4 = 1$ are used). The numbers in the brackets are estimates of numerical uncertainty for the last digits. Small deviations of FTLM moments from exact values suggest small finite size effects in the high-T limit.

IV. BROADENING IN FTLM

Optical conductivity calculated with FTLM on a finite cluster is strictly a set of delta functions in frequency space. The number of such delta functions grows with the number of many-body states, leading to a high density for the used cluster sizes. Still, the delta functions

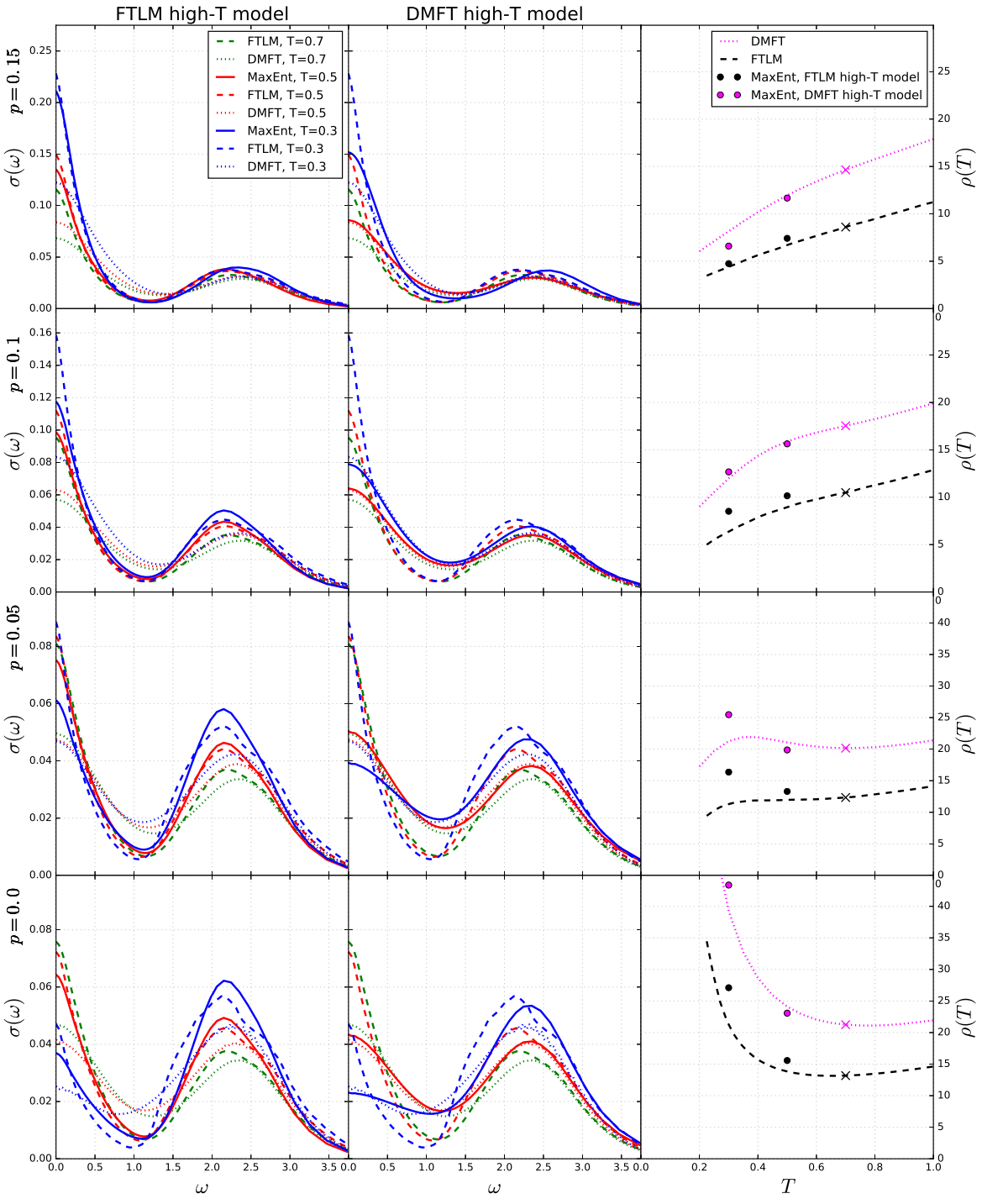

FIG. S4. Optical conductivity obtained by MaxEnt analytical continuation of the CTINT $\Lambda(i\nu_n)$ (solid lines in the first and the second column). The annealing method is used, where the initial model function, used for MaxEnt at $T = 0.5$, is the FTLM (first column), and DMFT (second column) at $T = 0.7$. At $T = 0.3$ the model function is the MaxEnt result from $T = 0.5$. The dashed (dotted) lines are FTLM (DMFT) data. The right column shows the MaxEnt resistivities, $\rho = 1/\sigma(\omega = 0)$, in comparison with FTLM and DMFT $\rho(T)$ curves. The four rows correspond to different doping levels $p = 0.15, 0.1, 0.05, 0$. The crosses are the dc resistivity corresponding to the initial model function.

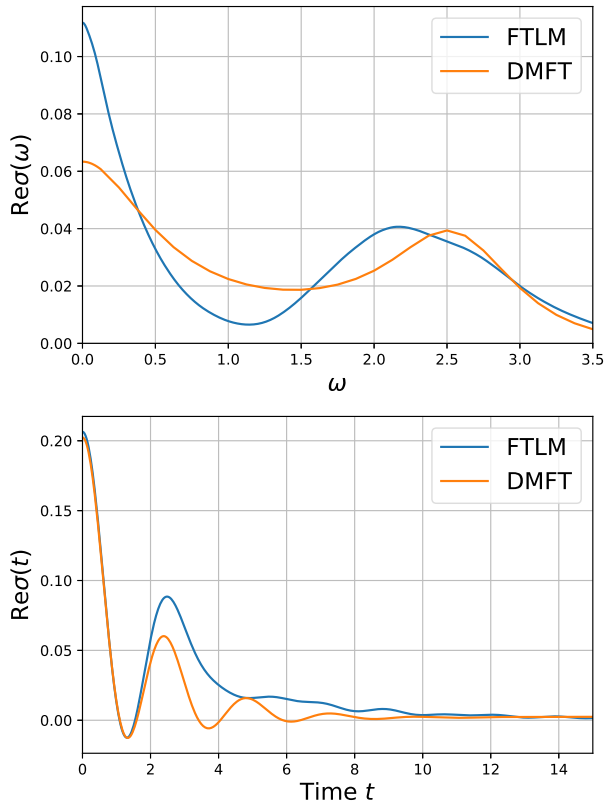

FIG. S5. Optical conductivity and its Fourier transform at $p = 0.1$, $T = 0.5D$. The dc conductivity has contributions from up to $t \sim 10$. DMFT and FTLM practically coincide at $t < 1$.

need to be broadened to get a smooth spectra, representative of the thermodynamic limit. The value of the broadening needs to be appropriate: sufficiently large to remove the finite-size artifacts, but not large enough to over-broaden the real features of the spectrum[5,6].

In our case we use Gaussian broadening, with the broadening parameter chosen as the parameter for which $\sigma_{\rm dc}$ is not changing or shows smallest change with broadening, a choice to which we refer as the optimal one. See Fig. S6. This prescription works also for finite and high frequencies, where the delta functions are denser and the spectra are smooth even with smaller broadening parameter. The used optimal broadening parameter is substantially smaller than the width of the Drude peak and we estimate the broadening uncertainty of $\rho_{\rm dc}$ within FTLM to be below 10%.

It is worth noting that that with increasing broadening the $\sigma_{\rm dc}$ drops monotonically. Since in all cases $\sigma_{\rm dc}$ in DMFT is lower, there must always be a certain broadening level that reproduces the DMFT result for $\sigma_{\rm dc}$, but not simultaneously $\sigma(\omega)$ at all frequencies. We have checked that the broadening level needed to reproduce $\sigma_{\rm dc}$ from DMFT is about 10 times the optimal one, and becomes comparable to the width of the Drude peak. This choice of broadening leads to severe modification in the shape of $\sigma(\omega)$, especially of the high-frequency peak which is otherwise well determined already by a fine binning of delta functions or with a tiny broadening. Therefore, we exclude such large broadening from consideration.

Finally, we note that for the calculation of $\Lambda(i\nu_n)$ from $\sigma(\omega)$ obtained by FTLM with Hilbert transform, Eq. (3) in the main text, no broadening is needed due to integration and that even if the broadened $\sigma(\omega)$ is used, $\Lambda(i\nu_n)$ change by the order of 10^{-5}, which is smaller than the symbol size in Fig. 3 (main text) and in Fig. S2 and is also below the CTINT noise level.

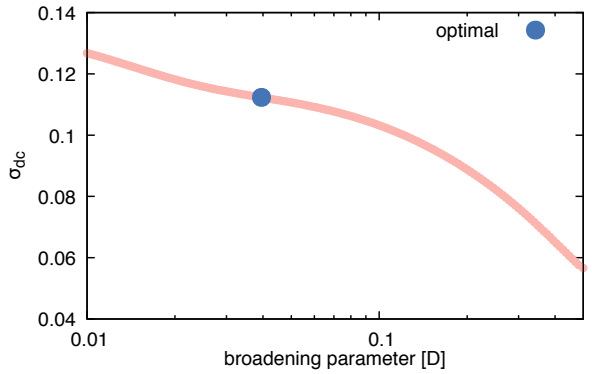

FIG. S6. Representative dependence of $\sigma_{\rm dc}$ from FTLM on the broadening parameter and the optimal parameter according to the minimal change of $\sigma_{\rm dc}$ with broadening. Data are for $p = 0.1$ and $T = 0.5D$.

[1] D. Bergeron, V. Hankevych, B. Kyung, and A.-M. S. Tremblay, Phys. Rev. B **84**, 085128 (2011).
[2] R. Levy, J. LeBlanc, and E. Gull, Computer Physics Communications **215**, 149 (2017).
[3] E. W. Huang, R. Sheppard, B. Moritz, and T. P. Devereaux, arXiv:1806.08346 (2018).
[4] E. Perepelitsky, A. Galatas, J. Mravlje, R. Žitko, E. Khatami, B. S. Shastry, and A. Georges, Phys. Rev. B **94**, 235115 (2016).
[5] J. Jaklič and P. Prelovšek, Adv. Phys. **49**, 1 (2000).
[6] J. Jaklič and P. Prelovšek, Phys. Rev. B **52**, 6903 (1995).

Paired states at 5/2: Particle-hole Pfaffian and particle-hole symmetry breaking

L. Antonić,[1] J. Vučičević,[2] and M. V. Milovanović[2]
[1]*Faculty of Physics, University of Belgrade, 11001 Belgrade, Serbia*
[2]*Scientific Computing Laboratory, Center for the Study of Complex Systems, Institute of Physics Belgrade, University of Belgrade, Pregrevica 118, 11080 Belgrade, Serbia*

(Received 2 August 2018; published 5 September 2018)

We study Cooper pairing in the Dirac composite fermion (CF) system. The presence of the mass term in the Dirac CF description (which may simulate Landau level mixing), i.e., breaking of particle-hole (PH) symmetry in this system, is a necessary condition for the existence of a PH Pfaffian-like topological state. In the scope of the random-phase approximation (RPA) and hydrodynamic approach, we find some signatures of pairing at finite frequencies. Motivated by this insight, we extend our analysis to the case of a different but still Dirac quasiparticle (CF) representation, appropriate in the presence of a mass term, and discuss the likelihood of PH Pfaffian and Pfaffian pairings in general. On the basis of gauge field effects, we find for a small Dirac mass, an anti-Pfaffian or Pfaffian instability depending on the sign of mass, while for large mass (Landau level mixing), irrespective of its sign, we find a PH Pfaffian-like instability.

DOI: 10.1103/PhysRevB.98.115107

I. INTRODUCTION

The fractional quantum Hall effect (FQHE) [1] is a remarkable effect of electrons confined to two dimensions. In the presence of a strong, perpendicular to the plane magnetic field, the phase space of the strongly correlated system is further confined into Landau levels (LLs) and quantized. At special fillings of LLs, when the system is described by special ratios of the number of electrons per number of flux quanta, highly entangled states of FQHE are established. In experiments, the effect is seen by measuring the fractionally quantized Hall conductance, which stays constant, at the particular value of fractional filling factor, as the magnetic field or density is varied.

The Laughlin state [2] with its generalizations describes the effect at odd denominator filling factors. A surprise came with the experimental detection of FQHE at filling factor 5/2, i.e., half-filling of the second LL (SLL) [3]. The Cooper pairing was invoked to explain the effect. Assuming spinless (frozen spin) electrons, at half-filling of active (second) LL, in the regime of experiments, the most natural BCS pairing function in the real space, which can be associated with an antisymmetric matrix, is a Pfaffian wave function [4]. Thus we expect Cooper pairing due to phase-space constraints—gauge field effects in a field theory description, in the presence of the repulsive Coulomb interaction.

However, the realization of the pairing correlations even for spinless fermions is not unique. We may envision a theoretical construct, an isolated half-filled LL with the exact particle-hole symmetry that can be explored in numerical experiments. The early pairing proposal—Pfaffian or Moore-Read state [4]—does not possess the particle-hole symmetry, and, under particle-hole exchange the Pfaffian transforms into an anti-Pfaffian state [5,6]. The Pfaffian and anti-Pfaffian equally participate in the ground state of the half-filled SLL with Coulomb interaction [7]. The system with the particle-hole symmetry requires for its field-theoretical description a special Dirac composite fermion (DCF) representation of constitutive classical electrons and their strong correlations [8]. On the basis of this representation a proposal was made for a special Pfaffian that respects the particle-hole symmetry, the so-called PH Pfaffian [8].

Arguments were given in Refs. [9–13] that the PH Pfaffian in the particle-hole symmetric setting, i.e., half-filled LL is an unstable, critical state. Arguments based on numerics were first given in Ref. [12]. Nevertheless, the PH Pfaffian type of pairing seems relevant from the experimental point of view, as argued in Ref. [14], despite LL mixing (absence of the particle-hole symmetry) and disorder effects.

Inspired by the recent experiment described in Ref. [15] that measured the thermal Hall conductance of the paired state at filling 5/2, and found that the measured value is consistent with the conductance of PH Pfaffian, we would like to check if a PH Pfaffian-like state may be realized in the absence of the PH symmetry, i.e., in the presence of LL mixing, but without disorder. The possibility for PH Pfaffian physics due to disorder effects is considered in Refs. [14,16–18], see also Ref. [19], while in Ref. [20], a proposal is made that the result of the experiment may be still consistent with the anti-Pfaffian state, due to an insufficient equilibration of edge modes. Very recently, this proposal is criticized in Ref. [21].

In this work we discuss the effective Cooper pairing channel of the system at half-filling in the scope of the DCF theory with a mass term. The mass term of the DCF theory represents a term that breaks the particle-hole symmetry of electrons confined in an LL and represents an LL mixing.

The paper is organized as follows. In Sec. II, we review arguments for the criticality of the PH Pfaffian in a particle-hole symmetric setting, and argue why a symmetry-breaking mass in the DCF theory is necessary to stabilize the PH Pfaffian. In Sec. III, we discuss the effective Cooper pairing

channel in the DCF theory in the presence of a mass term, and recover only some finite frequency pairing correlations. This is followed by a discussion in Sec. IV, which uses a different form of the DCF theory to analyze the Cooper pairing of modified CFs, in which a usual BCS problem emerges from a gauge field description of constraints. The Pfaffian family solutions of the problem are described and conclusions can be found in Sec. V.

II. PH PFAFFIAN AS A CRITICAL STATE IN A HALF-FILLED LANDAU LEVEL

A. PH Pfaffian as a critical state in a (particle-hole symmetric) half-filled Landau level

In this section, we will review arguments given in Ref. [11] for the critical nature of the PH Pfaffian state, and, in addition, relate the PH Pfaffian physics in a half-filled Landau level to the critical behavior and transition between Pfaffian and anti-Pfaffian [5], and discuss how general the arguments for the critical nature of PH Pfaffian are.

In the following, we will denote by a PH Pfaffian state, a FQHE state, at filling factor $1/2$ (half-filled Landau level) with Pfaffian (p-wave pairing) correlations that is invariant under particle-hole (PH) transformation. The correlations are expected to be in the opposite sense of rotation with respect to the one set by external magnetic field. [This is corroborated by available constructions based (a) on the Laughlin-Jastrow ansatz, Eqs. (1) and (2) below, at the PH symmetric filling factor on sphere, and (b) on the DCF theory.] On the other hand, we will denote by P$\tilde{\text{H}}$ Pfaffian, a state with Pfaffian correlations in the opposite sense of rotation with respect to the one set by an external magnetic field that may or may not have the PH symmetry. The P$\tilde{\text{H}}$ Pfaffian is a generalization of PH Pfaffian. A Pfaffian state with the PH symmetry was mathematically defined as an s-wave pairing instability of an effective description by Dirac composite fermions at half-filling. That is known in the literature as the Son's proposal for the PH (symmetric) Pfaffian [8].

Based on a mean-field analysis, we will argue that the PH Pfaffian and its P$\tilde{\text{H}}$ Pfaffian extensions, in the presence of the PH symmetry (i.e., in a system with PH symmetric Hamiltonian), describe *critical* states and thus they can not describe gapped topological phase(s) in half-filled LLs.

First, we will examine the underlying physics behind the states with the so-called negative flux insertion, either macroscopically (the number of the inserted negative flux quanta is of the order of the size of the system) as in Ref. [22], or microscopically (the number of the inserted negative flux quanta is of the order of one) as in Ref. [14], that induces p-wave pairing in the opposite sense of the rotation with respect to the one set by the external field. These states can be described as P$\tilde{\text{H}}$ Pfaffian states. As long as we are not sure of the fate of the PH symmetry in these constructions we will consider them as P$\tilde{\text{H}}$ Pfaffians. Here we should note that for the states in Eqs. (1) and (2) below, which we classify as the P$\tilde{\text{H}}$ Pfaffian constructions, recent numerical investigations demonstrate high degrees of the PH symmetry [12,13].

A negative flux Pfaffian (a P$\tilde{\text{H}}$ Pfaffian), which is also a lowest LL (LLL) wave function, was introduced in Ref. [22] as

$$\Psi_{TJ} = P_{\text{LLL}}\Big[\mathcal{S}\Big\{\prod(z_{i1}^* - z_{j1}^*)^2 \times \prod(z_{i2}^* - z_{j2}^*)^2\Big\} \times \prod(z_k - z_l)^3\Big], \tag{1}$$

where $\{z_i = x_i + iy_i, i = 1, \ldots, N_e\}$ are the electron coordinates, we omitted the Gaussian factors, P_{LLL} projects to the lowest LL, and the symmetrizer $\mathcal{S}$ symmetrizes between two groups, 1 and 2, in which the particles are equally distributed. This is a state with the number of flux quanta equal to $N_\phi = 3N_e - 3 - 2(N_e/2 - 1) = 2N_e - 1$, i.e., with a PH symmetric shift. An algebraic procedure introduced in Ref. [23] may be followed to generate possible edge states, i.e., a sector, if the system is incompressible. Namely, the proposition applied in the procedure is that if we consider bulk quasihole coherent state constructions, we can use them to generate edge states of an incompressible state. The method proved successful in the Pfaffian case especially so because, in that case, the edge states can be defined as those that make energy zero subspace of a model interaction for which the ground state—Pfaffian model wave function—is also a zero-energy state. In the case of the state in (1), we are not aware of the existence of a model interaction, and, furthermore, we do not know if the state is incompressible. Nevertheless, we may examine which states well-known, well-motivated quasiparticle bulk constructions can generate as low-momentum states. If the state is incompressible, these states we expect will make the edge sector. The analysis was done in Ref. [24], and the states recovered in this way, under the assumption of the incompressibility, would make a counterpropagating Majorana edge branch, together with the charged boson edge branch. The analysis missed a neutral copropagating neutral boson, whose states can be described as insertions in the antiholomorphic part of the wave function, of holomorphic differences of symmetric polynomials belonging to two groups of particles under a symmetrizer. (The antiholomorphic differences, i.e., their linearly independent combinations under symmetrization, make the states of the counterpropagating Majorana edge branch.)

Next to the construction in (1) we can consider a P$\tilde{\text{H}}$ Pfaffian state:

$$\Psi_{ZF} = P_{\text{LLL}}\left[Pf\left\{\frac{1}{(z_i^* - z_j^*)}\right\}\prod(z_k - z_l)^2\right], \tag{2}$$

which was introduced in Ref. [14]. Here,

$$Pf\left\{\frac{1}{(z_i^* - z_j^*)}\right\} \sim \sum_P \text{sgn}\, P \prod_{i=1}^{N/2} \frac{1}{(z_{P(2i-1)}^* - z_{P(2i)}^*)}. \tag{3}$$

In this case, an analysis of the edge states can include only antiholomorphic Majorana (neutral fermion) constructions described in the Moore-Read (holomorphic Pfaffian) case in Ref. [23]. Thus next to the charged boson we have only a single counterpropagating Majorana.

At this stage, it is interesting to note that in one of the papers that introduced the anti-Pfaffian physics, in Ref. [5], two out of three states that may appear at the transition

between Pfaffian and anti-Pfaffian, have the same edge physics as described here for the states in (1) and (2).

In the following, we will demonstrate that the states in (1) and (2), which may describe electrons in half-filled LLs, are in fact critical states, i.e., gapless and unstable states. For that we will consider a simplified (mean field) version of the Son's theory—the DCF theory [8]—that describes the Fermi-liquid-like state of Dirac CFs, in a half-filled, i.e., PH symmetric, Landau level. Thus we consider a massless Dirac fermion, at finite density, with s-wave pairing among spinor components, and neglect the presence of the gauge field, i.e., its fluctuations around zero value. In the chirality basis, i.e., in the basis of Dirac eigenstates without pairing, see Ref. [11] for details, we can express the pairing term. which pairs spinor components a and b as

$$\Psi_a(\mathbf{k})\Psi_b(-\mathbf{k}) = -\frac{1}{2}\frac{k_+}{k}[\Psi_+(\mathbf{k})\Psi_+(-\mathbf{k}) + \Psi_-(\mathbf{k})\Psi_-(-\mathbf{k})], \quad (4)$$

where $k \equiv |\mathbf{k}|$ and $k_+ = k_x + ik_y$. The fermion fields Ψ_+ and Ψ_- represent definite chirality (eigenstates of $\frac{\vec{\sigma}\cdot\vec{k}}{k}$) particle (positive energy) and hole (negative energy) states. As the relevant low-energy physics is around a finite chemical potential, for the description of the pairing physics we may use the following low-energy, decoupled from higher modes, BCS Hamiltonian,

$$H_{\rm BCS} = \sum_{\mathbf{k}}(k-\mu)\Psi_+^\dagger(\mathbf{k})\Psi_+(\mathbf{k}) + \sum_{\mathbf{k}}\left\{\frac{1}{2}\frac{k_+}{k}\Delta_s\Psi_+(\mathbf{k})\Psi_+(-\mathbf{k}) + \text{H.c.}\right\}. \quad (5)$$

We arrived to the usual form of the p-wave spinless fermion pairing Hamiltonian as can be found in Ref. [25] except that here we have linearly dispersing fermions, and not a fully specified Δ_s function in the pairing part. With respect to the notation of Ref. [25], the pairing function can be identified as

$$\Delta_{\mathbf{k}}^* = -\frac{k_+}{k}\Delta_s. \quad (6)$$

The algebra of the Bogoliubov problem (Ref. [25]) leads to the following expression for the Cooper pair wave function:

$$g_{\mathbf{r}} = \frac{1}{V}\int d\mathbf{k}\exp(i\mathbf{kr})\frac{-(E_{\mathbf{k}}-\xi_{\mathbf{k}})}{\Delta_{\mathbf{k}}^*}, \quad (7)$$

where $\xi_{\mathbf{k}} = k-\mu$, and $E_{\mathbf{k}}^2 = \xi_{\mathbf{k}}^2 + |\Delta_{\mathbf{k}}|^2$. We are interested in the long-distance behavior, and thus the behavior of $\Delta_{\mathbf{k}}$ for small momenta around $k=0$. For $\mu > 0$, finite chemical potential and density of the system that we consider here, the long distance behavior is determined by the behavior of $\Delta_{\mathbf{k}}$, i.e., Δ_s [see Eq. (6)] for small $\mathbf{k}$. In the small k limit, we are motivated to consider two cases:

$$(a)\ \lim_{k\to 0}\Delta_s \to \text{const.}, \quad \text{when} \quad g_{\mathbf{r}} \sim \frac{1}{z|z|} \quad (8)$$

and

$$(b)\ \lim_{k\to 0}\Delta_s \sim k \equiv |\mathbf{k}|, \quad \text{when} \quad g_{\mathbf{r}} \sim \frac{1}{z}. \quad (9)$$

For the usual choice of the direction of the magnetic field $\vec{B} = B\,\hat{e}_z$, $B<0$ (instead of $B>0$ as is implicit in the DCF theory because the density of Dirac CFs is proportional to B) we would have in (49) and (9), instead of z, in fact z^*. Thus, in the long-distance limit, when we can neglect the projection to a definite LL, the case (9) corresponds to wave functions in (1) and (2), because [26]

$$\mathcal{S}\left\{\prod(z_{i1}^*-z_{j1}^*)^2\times\prod(z_{i2}^*-z_{j2}^*)^2\right\} = Pf\left\{\frac{1}{(z_i^*-z_j^*)}\right\}\times\prod(z_k^*-z_l^*), \quad (10)$$

and thus the pairing with the Cooper pair wave function, $g_{\mathbf{r}} \sim \frac{1}{z^*}$, is present in both wave functions. Thus we can conclude that in order to reproduce the pairing encoded in the wave functions (1) and (2) we need nonanalytic behavior in the small k limit, $\lim_{k\to 0}\Delta_s \sim k \equiv |\mathbf{k}|$.

Thus, for the states in Eqs. (1) and (2), we cannot have a Landau-Ginzburg type of description (together with the fermionic part, see below), as we would expect to have for a well-defined, stable pairing phase. A question may be raised, whether in this argument for the critical nature of these states, we are allowed to use the region around $|\mathbf{k}|=0$ to describe the pairing instabilities of Dirac CFs, with the understanding that the Dirac description is only well-defined near $|\mathbf{k}| = k_F$. However, a complete theory (description) of a pairing instability involves both regions; the one around $|\mathbf{k}| = k_F$ and the one around $|\mathbf{k}|=0$, associated with the long-wavelength, low-energy description with a bosonic variable (an order parameter $\Delta_{\mathbf{k}}$ in the mean-field description) associated with the pairing.

On the other hand, the introduction of an analytical s-wave pairing in the DCF theory would lead to the following Lagrangian density:

$$\mathcal{L} = i\bar{\chi}\gamma^\mu(\partial_\mu + ia_\mu)\chi + (ig\tilde{\Delta}_s(\mathbf{r})\chi\sigma_y\chi + \text{H.c.}) + |(\partial_\mu - 2ia_\mu)\tilde{\Delta}_s|^2 - u|\tilde{\Delta}_s|^2 - \frac{v}{2}|\tilde{\Delta}_s|^4. \quad (11)$$

The theory is invariant under CP (charge conjugation + parity) transformation

$$CP\chi(\mathbf{r})(CP)^{-1} = \sigma_x\chi(\mathbf{r}'), \quad (12)$$

where $\mathbf{r} = (x,y)$ and $\mathbf{r}' = (x,-y)$, though the pairing term up to a gauge transformation. This invariance corresponds to the invariance under the PH transformation of real electrons [8]; the introduced s-wave pairing constitutes the Son's proposal for the PH Pfaffian. With the usual s-wave pairing behavior, $\lim_{k\to 0}\Delta_s \to$ Const., and neglecting the influence of gauge field, as before, we can arrive to the following characteristic long-distance behavior:

$$g_{\mathbf{r}} \sim \frac{1}{z|z|}\left(\text{i.e.,}\frac{1}{z^*|z|}\right), \quad (13)$$

which should enter the Pfaffian part of the PH Pfaffian,

$$\Psi_{\rm PH} = P_{\rm LLL}\left[Pf\left\{\frac{1}{(z_i^*-z_j^*)|z_i-z_j|}\right\}\prod(z_k-z_l)^2\right]. \quad (14)$$

We will list two reasons why this state can be considered only as a gapless (critical) state. (a) If we attempt to generate an edge Majorana sector using $\Psi_{\rm PH}$, and the method of Ref. [23], we will not be able to separate (bulk) charge modes from the usual Majorana counterpropagating edge modes, because this is possible only for the peculiar form of the Cooper pair wave function with $g_{\mathbf{r}} \sim \frac{1}{z^*}$. (b) The universal, long-distance behavior $g_{\mathbf{r}} \sim \frac{1}{z^*|z|}$ is also a characteristic behavior of the critical system of classical (nonrelativistic) fermions at the transition from weak to strong coupling as described in Ref. [25].

Though we commented in the beginning that we are applying the mean-field approach and neglect gauge field fluctuations, our approach is in fact quite general, and can reach conclusions that are not biased. Namely, once we assume PH Pfaffian pairing instabilities, by the very assumption of the pairing order parameters of the underlying Dirac composite fermions, we expect, due to the Anderson-Higgs mechanism, that the gauge field (that couples to the fermions) will be expelled from the low-energy physics, and therefore our assumption and approach concerning the nature of PH Pfaffian is justified. The arguments, in this section, are given in the long-distance limit, when the magnetic length can be neglected with respect to distances considered and thus the projection to the LLL in Eqs. (1), (2), and (14) can be omitted. The limit characterizes the universal, low-energy physics, which we argue is gapless, and this should be valid even when the projection is included and the system is characterized as a whole in a half-filled LL.

Thus the state with a manifest PH symmetry, the PH Pfaffian in the half-filled LL, can be only a critical state. This state may correspond to the (third) state that characterizes the transition between Pfaffian and anti-Pfaffian state in Ref. [5]. According to the analysis of Ref. [5] we may expect that this state is the lowest energy state at the transition between Pfaffian and anti-Pfaffian state, i.e., a "real" critical state, while other two states, in (1) and (2), may represent excited states at the point of the transition with an exact particle-hole symmetry. [The two states in (1) and (2), correspond to the other two states of the same reference, due to their edge spectrum.]

B. Particle-hole symmetry breaking and the criticality of PH Pfaffian

It is interesting to introduce a mass, i.e., a particle-hole symmetry breaking term in the previously discussed description of the pairing instabilities in a fixed Landau level. We will assume the analytic ($\lim_{k\to 0}\Delta_s \sim$ const) description, discussed in the previous section. At the particle-hole symmetric point, m(mass) $= 0$. Away from this point, for $\Delta_s = 0$, we have a simple Dirac description of the Hamiltonian with the following 2×2 matrix,

$$H = \begin{bmatrix} m & k_- \\ k_+ & -m \end{bmatrix}, \tag{15}$$

for the following choice for gamma matrices $\gamma^0 = \sigma_3$, $\gamma^1 = i\sigma_2$, and $\gamma^2 = -i\sigma_1$, and we set the Dirac velocity, $v_F = 1$. In this case,

$$\Psi_+(\mathbf{k}) = \frac{1}{\sqrt{2E(E+m)}}[(m+E)\Psi_a(\mathbf{k}) + k_-\Psi_b(\mathbf{k})] \tag{16}$$

and

$$\Psi_-(\mathbf{k}) = \frac{1}{\sqrt{2E(E-m)}}[(m-E)\Psi_a(\mathbf{k}) + k_-\Psi_b(\mathbf{k})], \tag{17}$$

where $E \equiv \sqrt{|\mathbf{k}|^2 + m^2}$. We find that

$$\begin{aligned}\Psi_a(\mathbf{k})\Psi_b(-\mathbf{k}) = &-\frac{k_+}{2E}\Psi_+(\mathbf{k})\Psi_+(-\mathbf{k}) \\ &-\frac{m}{E}\frac{k_+}{|\mathbf{k}|}\Psi_+(\mathbf{k})\Psi_-(-\mathbf{k}) \\ &+\frac{k_+}{2E}\Psi_-(\mathbf{k})\Psi_-(-\mathbf{k}).\end{aligned} \tag{18}$$

We immediately see that in this case, with respect to the Eq. (4), we do not have nonanaliticity for $\mathbf{k} = 0$ (if Δ_s is a constant in that limit). Thus, for $m \neq 0$, we have a description similar to the ordinary p wave in Ref. [25], that reproduces Pfaffian pairing in the opposite direction with respect to the one set by the external magnetic field, as discussed in the previous section, but with a mixing term $\sim\Psi_+(\mathbf{k})\Psi_-(-\mathbf{k})$.

A straightforward solution of the Bogoliubov (BCS) problem gives a BCS ground state, where Ψ_+ degrees of freedom pair as $g_{\mathbf{r}} \sim \frac{1}{z}$, while interband correlations are described with $g_{\mathbf{r}} \sim \frac{1}{z|z|}$. Thus the implied ground-state wave function in the effective long-wavelength description is

$$\Psi_{PHL} = Pf\left\{\frac{1}{(z_i^* - z_j^*)}\right\}\prod(z_k - z_l)^2. \tag{19}$$

This leads to the conclusion that the particle-hole symmetry breaking mass term may stabilize the PH Pfaffian -like state in (19). This is a very interesting, counterintuitive conclusion, which was originally suggested in Ref. [11], in the context of singlet and triplet pairings of spinor components, in the presence of a mass term. Here we showed that the same conclusion can be reached by considering only the s-wave (singlet) pairing [Eq. (18)] in the presence of a mass term.

Although this simple scenario seems quite plausible, the numerical investigations of the second Landau level (SLL) (for which we expect that is dominated by the Pfaffian physics) imply that the physics around the particle-hole symmetric point is dominated by a nonuniversal influence of the short-range part of the Coulomb interaction, which is hard to capture by field theoretical means. Namely, the investigation in Ref. [7] clearly shows the (Schroedinger cat) mixing of Pfaffian and anti-Pfaffian at the particle-hole symmetric point, and their relevance for the nearby physics. The most recent investigations in Refs. [12,13] point out that the state in Eq. (2) is likely an excited state in the half-filled SLL (compare with our identification above), and has very high overlap with the composite Fermi liquid (CFL) wave function [27,28]. Thus, although the DCF theory seems a very good description of the half-filled LLL, it has to be modified to capture the nonuniversal physics in the SLL. But, by modifying the Coulomb interaction in the SLL, one may increase the overlap of the exact ground state with the state in (2) or stabilize the CFL

state [13]. Thus a relevant question may be whether a mass term in the DCF theory may induce pairing irrespective of the details of the projected to an LL Coulomb interaction. Therefore we are motivated to study the DCF theory in the presence of a mass term in order to see if this may induce pairing correlations and a pairing instability of the PH Pfaffian kind [Eq. (19)].

III. THE DIRAC COMPOSITE FERMION THEORY WITH A PARTICLE-HOLE SYMMETRY BREAKING TERM

In this section, we will consider the usual formulation of the DCF theory, with a mass term, in the RPA approximation in order to find the effective Cooper channel and examine pairing correlations. A different formulation of the same theory we will discuss in the next section.

A. The Dirac composite fermion theory with a particle-hole symmetry breaking term: an introduction

We start by examining the DCF theory in the presence of PH symmetry breaking mass term. The generalized Lagrangian can be found in Ref. [29] and is given by the following expression,

$$\mathcal{L} = i\bar{\psi}\gamma^{\mu}(\partial_{\mu} + ia_{\mu})\psi + \frac{1}{4\pi}adA + \frac{1}{8\pi}AdA - m\bar{\psi}\psi, \tag{20}$$

where χ is the Dirac CF field, a_{μ} is an emergent $U(1)$ gauge field, the Chern-Simons terms are abbreviated as $\epsilon^{\mu\nu\lambda}A_{\mu}\partial_{\nu}A_{\lambda} \equiv A\partial A$, $\mu = 0, x, y$, and we have omitted the Coulomb interaction and higher order terms. As a consequence, we have the following equations, by differentiating with resect to A_{μ},

$$J_e = \frac{dA}{4\pi} + \frac{da}{4\pi}, \tag{21}$$

where J_e is the electron density current, and, by differentiating with resect to a_{μ},

$$J_{\psi} = \frac{dA}{4\pi}, \tag{22}$$

where J_{ψ} is the Dirac composite fermion density current. As discussed in Ref. [29], transport coefficients like the Hall conductance can be found from the implied form of currents,

$$\mathbf{j}_e = \frac{1}{4\pi}\hat{\epsilon}(\mathbf{E} - \mathbf{e}) \tag{23}$$

and

$$\mathbf{j}_{\psi} = \frac{1}{4\pi}\hat{\epsilon}\mathbf{E}, \tag{24}$$

where $\hat{\epsilon}$ is the unit antisymmetric tensor with components $\epsilon^{ii} = 0, \epsilon^{xy} = -\epsilon^{yx} = 1$, together with the relationship that we have to extract from the theory,

$$\mathbf{j}_{\psi} = \frac{1}{4\pi}\hat{\sigma}_D\mathbf{e}, \tag{25}$$

where $\hat{\sigma}_D$ represents the Dirac composite fermion conductance tensor. To find $\hat{\sigma}_D$, we need to find the polarization tensor $\Pi_{\mu\nu}$,

$$j^{\psi}_{\mu} = \Pi_{\mu\nu}\, a^{\nu}, \tag{26}$$

which may be identified in the RPA treatment of the theory: the expansion of the effective action to second order in a^{ν}, after the integration of fermion fields in the functional formalism, or directly calculating

$$\Pi^{\mu\nu} = -itr[\gamma^{\mu}S_F(x, y)\gamma^{\nu}S_F(y, x)], \tag{27}$$

where

$$iS_F(x, y) = \langle T[\psi(x)\bar{\psi}(y)]\rangle, \tag{28}$$

i.e., the composite fermion propagator (T is the time ordering and the expectation value is with respect to the ground state of noninteracting fermions). In calculating (27), we encounter (ultraviolet) divergences, which come from the presence of the infinite sea of negative energy solutions. There are two ways to regularize the theory: (a) dimensional and (b) Pauli-Villars regularization. The physical meaning of these two possibilities, when considering Berry curvature contributions of the positive and negative energy band to the Hall conductance, is that in the dimensional regularization we combine (add) the contributions, while in the Pauli-Villars regularization we consider the contribution only from the positive band. (For the Berry curvature contributions of the two bands see Ref. [29].) The dimensional regularization at the neutrality point [μ(chemical potential) = 0], and in the presence of a mass gives an unphysical prediction for the Hall conductance ($=\frac{1}{2}\frac{e^2}{h}$), i.e., a half integral quantum Hall effect of noninteracting fermions. But at a finite chemical potential, and in the absence of mass the Hall conductance is zero. This result or consequence is at the basis of the DCF theory (that is defined at a finite chemical potential), which results in the precise value of the Hall conductance of electrons $= \frac{1}{2}\frac{e^2}{h}$, dictated by the particle-hole symmetry, even in the presence of disorder. Thus the dimensional regularization is the assumed regularization in the DCF theory. On the other hand, the Pauli-Villars regularization gives a so-called parity anomaly, a half of the unit of the Hall conductance even in the absence of a mass. Later, we will explore the role of the Pauli-Villars regularization, when we consider a smooth connection between the DCF theory and the HLR theory [30]. Thus this type of regularization is important when we switch the quasiparticle representation from the one based on the Read's construction [31] (the DCF theory) to the one based on the usual Chern-Simons construction [32] (the HLR theory [33]).

We obtained the polarization tensor $\Pi^{\mu\nu}(\mathbf{k}, \omega)$, in the hydrodynamic approximation, i.e., when $|\mathbf{k}| \ll k_F$, in the presence of the mass term. The results can be found in Appendix A.

B. The Cooper channel in the Dirac composite fermion theory with a particle-hole symmetry breaking term

In this section, we will extend the approach applied in Refs. [9,10] to the case with the particle-hole symmetry breaking mass term. Namely, in Ref. [9], in order to study the possibilities for pairing within the DCF theory, the Coulomb interaction was considered as an additional term in the theory

described by Eq. (20) with $m = 0$. An effective Coulomb interaction was found by a projection of fermion operators to the low-energy sector around $|\mathbf{k}| = k_F$ of positive energy solutions. The BCS interaction or Cooper channel of the effective interaction for the p-wave (PH Pfaffian) pairing was found to be repulsive and in no way conducive for the pairing. The investigations in Refs. [9,10] included, at the RPA level, modifications of the effective interaction due to the fluctuations of the gauge field (a_μ), but the conclusion was the same. In this section, we would like to find out the effective Cooper channel, within the RPA approach, in the presence of a mass term.

To investigate the possibility for a stable pairing phase, we will look for the expression of the effective interaction in the imaginary time formalism, but fix T(temperature) $= 0$. In the Euclidean space-time, we have

$$\mathcal{L}_E = \bar{\psi}_E \gamma^0 \left(\partial_\tau + a_E^0\right)\psi_E + \bar{\psi}_E(-i\gamma)(\nabla + i\mathbf{a}_E)\psi_E - \mu\bar{\psi}_E\gamma^0\psi_E + m\bar{\psi}_E\psi_E, \tag{29}$$

where we consider the situation with a constant magnetic field and, thus, the Fermi system at a finite chemical potential μ. We can get (29) from (20) by a naive analytical continuation $\tau = it$. We may introduce Euclidean gamma matrices $\gamma_E = \gamma_0$ and $\vec{\gamma}_E = (-i)\vec{\gamma}$, but to make an easier contact with previous calculations and literature, we will keep a Minkowski set: $\gamma_0 = \sigma_3$ and $\vec{\gamma} = i\vec{\sigma}$. We introduce the gauge field propagator by the functional integration over fermionic degrees of freedom,

$$\int \mathcal{D}\bar{\psi}_E \mathcal{D}\psi_E \exp\left\{-\int d\tau d\mathbf{x}[\mathcal{L}_E]\right\} = \exp\left\{-\int dx \int dy \frac{\bar{\mathcal{D}}^{-1}_{\mu\nu}}{2}(x-y)a^\mu(x)a^\nu(y)\right\}. \tag{30}$$

Therefore

$$\bar{\mathcal{D}}^{-1}_{\mu\nu}(x-y) = \mathrm{tr}[\gamma_\mu G_E(x,y)\gamma_\nu G_E(y,x)], \tag{31}$$

where

$$G_E(x,y) = -\langle T_\tau[\psi_E(x)\bar{\psi}_E(y)]\rangle, \tag{32}$$

and x and y are points in the Euclidean space-time. We present explicit expressions for $\bar{\mathcal{D}}^{-1}_{\mu\nu}$, in the hydrodynamic approximation, in Appendix B.

With the addition of the Coulomb interaction to $\mathcal{L}_E$ [Eq. (29)], its contribution to the propagator of the vector potential a_i, $i = x, y$ can be found by considering

$$\delta\mathcal{L}_E = \frac{\int d\mathbf{q}\int d\omega}{(2\pi)^3}\frac{1}{2}\left(\frac{\mathbf{q}\times\mathbf{a}(-\mathbf{q})}{4\pi}\right)\frac{2\pi e^2}{\epsilon_r q}\left(\frac{\mathbf{q}\times\mathbf{a}(\mathbf{q})}{4\pi}\right). \tag{33}$$

To get the effective interaction among fermions, at the RPA level, we integrate out gauge fields in the transverse gauge ($\vec{\nabla}\cdot\vec{a} = 0$). If we define the fermion density-current as

$$\frac{\delta\mathcal{L}_E}{\delta a_E^\mu} = \mathcal{J}^\mu, \tag{34}$$

for the effective four-fermion interaction, we get

$$V_{\mathrm{int}}(x-y) = -\tfrac{1}{2}\mathcal{D}_{\mu\nu}(x-y)\mathcal{J}^\mu(x)\mathcal{J}^\mu(y), \tag{35}$$

where by $\mathcal{D}_{\mu\nu}$ we denoted the gauge-field propagator with the Coulomb interaction contribution. The propagator $\mathcal{D}_{\mu\nu}$ can be found in Appendix B.

To find the second quantized expressions for the currents and the interaction, we use the following expansion for the fermionic operator,

$$\Psi_E(\mathbf{x}) = \sum_{\mathbf{k}}\begin{bmatrix} ik_- \\ E-m\end{bmatrix}\frac{1}{\sqrt{2E(E-m)}}\exp\{i\mathbf{kx}\}\,c_{\mathbf{k}} + \cdots, \tag{36}$$

where we did not write the negative energy contribution. To describe the Cooper channel we project all momenta to the Fermi circle, i.e., $k_\pm = k_x \pm ik_y = k_F\exp\{\pm i\theta\}$. Starting from the defining expression

$$\mathcal{J}_0(x) = \bar{\Psi}_E(x)\gamma_0\Psi_E(x) = \Psi_E^\dagger(x)\Psi_E(x), \tag{37}$$

we find an effective expression for the density operator,

$$\mathcal{J}_0(\mathbf{k}_1-\mathbf{k}_2) = \exp\left\{i\frac{(\theta_2-\theta_1)}{2}\right\}\left[\cos\left\{\frac{(\theta_2-\theta_1)}{2}\right\} + i\frac{m}{\mu}\sin\left\{\frac{(\theta_2-\theta_1)}{2}\right\}\right]c^\dagger_{\mathbf{k}_2}c_{\mathbf{k}_1}. \tag{38}$$

Defining the transverse part of the current operator by

$$\mathcal{J}_T(\mathbf{k}_1-\mathbf{k}_2) = i\hat{q}\times\bar{\Psi}_E(\mathbf{k}_1)\vec{\gamma}\Psi_E(\mathbf{k}_2), \tag{39}$$

where $\mathbf{q} = \mathbf{k}_1 - \mathbf{k}_2$ $\hat{q} = \frac{\mathbf{q}}{|\mathbf{q}|}$, we find the effective expression to be

$$\mathcal{J}_T(\mathbf{k}_1-\mathbf{k}_2) = i\frac{k_F}{\mu}\exp\left\{i\frac{(\theta_2-\theta_1)}{2}\right\}\times\frac{\sin\left\{\frac{(\theta_2-\theta_1)}{2}\right\}}{\left|\sin\left\{\frac{(\theta_2-\theta_1)}{2}\right\}\right|}c^\dagger_{\mathbf{k}_2}c_{\mathbf{k}_1}. \tag{40}$$

Note the presence of the sine function which ensures the hermiticity of the operator $[\mathcal{J}_T^\dagger(\mathbf{q}) = \mathcal{J}_T(-\mathbf{q})]$. This part is missing in Ref. [9].

If we denote the components of $\mathcal{D}^{-1}$ by

$$\mathcal{D}^{-1}(\mathbf{q},\omega) = \begin{bmatrix}\hat{\Pi}_{00} & \hat{\Pi}_{0T} \\ \hat{\Pi}_{0T} & \hat{\Pi}_{TT}\end{bmatrix}, \tag{41}$$

the effective interaction potential is

$$V_{\mathrm{int}}(\mathbf{q},\omega) = -\frac{1}{[\hat{\Pi}_{00}\hat{\Pi}_{TT} - (\hat{\Pi}_{0T})^2]}[\hat{\Pi}_{TT}\mathcal{J}_0(-\mathbf{q})\mathcal{J}_0(\mathbf{q}) + \hat{\Pi}_{00}\mathcal{J}_T(-\mathbf{q})\mathcal{J}_T(\mathbf{q}) - 2\hat{\Pi}_{0T}\mathcal{J}_0(-\mathbf{q})\mathcal{J}_T(\mathbf{q})]. \tag{42}$$

We can find the effective Cooper channel, by taking expressions for the components of the gauge field propagator (B3)–(B5) with $k_0 = i\omega$, where ω is real, inserting the components in the expression for the effective interaction in (42), and choosing momenta to describe a Cooper pair scattering.

Before a closer look at the effective Cooper channel, we may note that always $\hat{\Pi}_{00}(i\omega,\mathbf{k}) < 0$ and $\hat{\Pi}_{TT}(i\omega,\mathbf{k}) > 0$. In the static limit ($\omega = 0$), we have $\hat{\Pi}_{00}(0,\mathbf{k}) = -\frac{\mu}{2\pi}$, $\hat{\Pi}_{TT}(0,\mathbf{k}) = \alpha\frac{|\mathbf{k}|}{(4\pi)^2}$, and $\hat{\Pi}_{0T}(0,\mathbf{k}) = 0$. In this case, the

Cooper channel is

$$V_{\rm int}^{\rm Cooper}(\mathbf{q}=\mathbf{p}-\mathbf{k},\omega=0) = \left\{-\frac{1}{\hat{\Pi}_{00}(0,\mathbf{q})}\left[\cos\frac{(\theta_{\mathbf{k}}-\theta_{\mathbf{p}})}{2}+i\frac{m}{\mu}\sin\frac{(\theta_{\mathbf{k}}-\theta_{\mathbf{p}})}{2}\right]^2 + \frac{1}{\hat{\Pi}_{TT}(0,\mathbf{q})}\left(\frac{k_F}{\mu}\right)^2\right\}\exp\{i(\theta_{\mathbf{k}}-\theta_{\mathbf{p}})\}c_{\mathbf{k}}^{\dagger}c_{\mathbf{p}}c_{-\mathbf{k}}^{\dagger}c_{-\mathbf{p}}. \tag{43}$$

In the scope of the hydrodynamic approximation, i.e., $\theta_{\mathbf{k}}\approx\theta_{\mathbf{p}}$, we find repulsive behavior and no cause for a Cooper instability even in the massive case.

The second limit we want to consider is a finite frequency limit $\omega\gg\alpha_F|\mathbf{k}|$. We have $\hat{\Pi}_{00}(\omega,\mathbf{k})\approx-\frac{\mu}{4\pi}\frac{(\alpha_F|\mathbf{k}|)^2}{\omega^2}\sim 0$, $\hat{\Pi}_{TT}(\omega,\mathbf{k})\approx\frac{\mu}{4\pi}+\alpha\frac{|\mathbf{k}|}{(4\pi)^2}$, and $\hat{\Pi}_{0T}(\omega,\mathbf{k})\approx-\frac{1}{4\pi}\frac{m}{\mu}|\mathbf{k}|$. The effective Cooper channel can be described with two terms: (a) density-current part,

$$V_{\rho J}^{\rm Cooper}(\mathbf{q}=\mathbf{p}-\mathbf{k},\omega) = \frac{4\pi}{m}i\frac{\sin\frac{(\theta_{\mathbf{k}}-\theta_{\mathbf{p}})}{2}}{\left|\sin\frac{(\theta_{\mathbf{k}}-\theta_{\mathbf{p}})}{2}\right|^2}\left[\cos\frac{(\theta_{\mathbf{k}}-\theta_{\mathbf{p}})}{2}+i\frac{m}{\mu}\sin\frac{(\theta_{\mathbf{k}}-\theta_{\mathbf{p}})}{2}\right] \times\exp\{i(\theta_{\mathbf{k}}-\theta_{\mathbf{p}})\}c_{\mathbf{k}}^{\dagger}c_{\mathbf{p}}c_{-\mathbf{k}}^{\dagger}c_{-\mathbf{p}}; \tag{44}$$

(b) density-density part,

$$V_{\rho\rho}^{\rm Cooper}(\mathbf{q}=\mathbf{p}-\mathbf{k},\omega) = \left(\frac{4\pi\mu}{m}\right)^2\frac{\frac{k_F^2}{4\pi\mu}+\frac{\alpha}{(4\pi)^2}(2k_F)\left|\sin\frac{(\theta_{\mathbf{k}}-\theta_{\mathbf{p}})}{2}\right|}{(2k_F)^2\left|\sin\frac{(\theta_{\mathbf{k}}-\theta_{\mathbf{p}})}{2}\right|^2} \times\left[\cos\frac{(\theta_{\mathbf{k}}-\theta_{\mathbf{p}})}{2}+i\frac{m}{\mu}\sin\frac{(\theta_{\mathbf{k}}-\theta_{\mathbf{p}})}{2}\right]^2 \times\exp\{i(\theta_{\mathbf{k}}-\theta_{\mathbf{p}})\}c_{\mathbf{k}}^{\dagger}c_{\mathbf{p}}c_{-\mathbf{k}}^{\dagger}c_{-\mathbf{p}}. \tag{45}$$

In the density-density part, we have extremely singular repulsive interaction present at finite frequencies, i.e., a repulsive singular interaction that describes the physics of excited states. We do not see any cause for a real Cooper instability, except that in the density-current part we can recognize some pairing correlations. This motivates a search for a different quasiparticle representation in which the pairing correlations may be better captured and exposed.

IV. PAIRING CORRELATIONS WITHIN A DIFFERENT QUASIPARTICLE REPRESENTATION

In this section, we will consider a different formulation of the DCF theory with a mass term. This will enable us, on the level of equations of motion, to deduce the effective Cooper channel of different Dirac quasiparticles from the ones discussed in the preceding section. The channel, derived from purely gauge field effects, supports the Pfaffian family of instabilities, and we will examine the ensuing phase diagram as a function of the Dirac mass.

We may also consider the addition of the mass term to the Dirac composite fermion theory by adopting the following form of the Lagrangian [30]:

$$\mathcal{L}=i\bar{\chi}\gamma^{\mu}(\partial_{\mu}+ia_{\mu})\chi+\frac{1}{4\pi}adA+\frac{1}{8\pi}AdA -\frac{m}{|m|}\frac{1}{8\pi}ada-m\bar{\chi}\chi. \tag{46}$$

Note the presence of the Chern-Simons term for gauge field a^{μ}. In this case (to recover the identical results for the response with respect to the previous formulation), we have to adopt the Pauli-Villars way of regularizing the theory. Why we discuss this, to say, a redundant formulation? It is important to notice that with a simple redefinition of the gauge field in (46), and in the large mass limit, we can recover the HLR or anti-HLR [35] theory depending on the sign of mass [30]. See Appendix D for details.

By differentiating with resect to A_{μ} the Lagrangian density in (46), we get

$$J_e=\frac{dA}{4\pi}+\frac{da}{4\pi}, \tag{47}$$

where J_e is the electron density-current, and, by differentiating with resect to a_{μ},

$$J_{\chi}=\frac{dA}{4\pi}-\frac{m}{|m|}\frac{da}{4\pi}, \tag{48}$$

where J_{χ} is the Dirac composite fermion density-current. Thus the Dirac composite fermion density-current in this case is determined, on the classical level, by the fluctuations of the gauge field, just as in usual Chern-Simons theories [32,33]. These theories are based on the quasiparticle (composite fermion) constructions via "flux tube"—unitary transformations of the original electrons, and not with "vortex"—Laughlin quasihole constructions [31] of quasiparticles. The usual Chern-Simons theories (at the RPA level) can recover the Jastrow-Laughlin correlations [32] as a part of magnetoplasmon (cyclotron energy) dynamics, while in the "vortex" constructions they are, in a way, frozen and built in quasiparticles. This distinction may be important when discussing the presence of pairing correlations. In the DCF limit, at the RPA level, both formulations give the same response, because they describe the response of "vortex" construction, using different regularization schemes. However, at the classical level [Eqs. (22) and (48)], their predictions may differ, because the distinction between the quasiparticle perspectives is preserved. Thus, although, at the RPA level, we find the absence of pairing correlations for "vortex" constructions (Sec. III), the fact that some pairing correlations are present in the high-energy, i.e., the high-frequency sector in the density-current part of the interaction, gives us an expectation that by adopting different quasiparticle representation, we may recover the pairing correlations in the low-frequency or static limit.

The problem, as described by Eq. (48), is formally identical to the problem discussed in Ref. [34] in the context of the graphene Dirac electrons in FQHE regime. Following the analysis of Ref. [34], for a fixed valley, definite spin, Dirac electrons, of the gauge field a^{μ} induced interaction between current and density of Dirac particles in the presence of a mass term, we can arrive at the effective form of the pairing channel, Eq. (25) in Ref. [34].

Let us discuss the details that lead to the p-wave pairing channel or attractive interaction for a definite, negative sign of the mass, $m < 0$. The equality in Eq. (48) will lead to the following integral expression for the gauge field a^μ, $a = a_x + i a_y$,

$$a(\mathbf{r}) = 2 \int d\mathbf{r}' i \frac{z - z'}{|\mathbf{r} - \mathbf{r}'|^2} \delta\rho_\chi(\mathbf{r}'), \tag{49}$$

where $\delta\rho_\chi(\mathbf{r}')$ represents the fermion density with respect to the constant value given by the fixed strength of the external magnetic field that we assume. In the following, we will analyze the statistical interaction defined as the one between the current of Dirac fermions and the field $a_i; i = x, y$:

$$V_{st} = \bar{\chi} \gamma^i a_i \chi. \tag{50}$$

We work in the following representation of γ matrices:

$$\gamma^0 = \sigma_3, \quad \gamma^1 = i\sigma_2, \quad \gamma^2 = -i\sigma_1. \tag{51}$$

In this representation, we have the following expression for the statistical interaction:

$$V_{st} = -i2 \int d\mathbf{r}' \delta\rho_\chi(\mathbf{r}') \chi^\dagger(\mathbf{r}) \begin{bmatrix} 0 & \frac{\bar{z} - \bar{z}'}{|\mathbf{r} - \mathbf{r}'|^2} \\ -\frac{z - z'}{|\mathbf{r} - \mathbf{r}'|^2} & 0 \end{bmatrix} \chi(\mathbf{r}), \tag{52}$$

and $\delta\rho_\chi(\mathbf{r}') = \chi^\dagger(\mathbf{r}')\chi(\mathbf{r}') - \bar{\rho}$, where $\bar{\rho}$ is a constant (external flux density). The constant part gives no contribution to V_{st}.

On the other hand, the presence of the mass term in the Dirac system leads to the following eigenproblem,

$$\begin{bmatrix} m - \epsilon & k_- \\ k_+ & -m - \epsilon \end{bmatrix} \chi(\mathbf{k}) = 0, \tag{53}$$

where a positive eigenvalue $\epsilon = \sqrt{|\mathbf{k}|^2 + m^2} \equiv E_\mathbf{k}$, corresponds to the following eigenstate:

$$\chi_E = \begin{bmatrix} m + E_\mathbf{k} \\ k_+ \end{bmatrix} \frac{1}{\sqrt{2E_\mathbf{k}(E_\mathbf{k} + m)}}. \tag{54}$$

As we consider relevant only (positive energy) states around k_F, we will keep only these states in the expansion over $\mathbf{k}$ eigenstates of field $\chi(\mathbf{r})$, and, further, only consider the BCS pairing channel in V_{st}. Thus

$$\chi(\mathbf{r}) = \frac{1}{\sqrt{2V}} \sum_\mathbf{k} \exp\{i\mathbf{k}\mathbf{r}\} \chi_E(\mathbf{k}) a_\mathbf{k} + \cdots, \tag{55}$$

and

$$\begin{aligned} V_{st}^{\mathrm{BCS}} = {} & \frac{2\pi}{8V} \sum_{\mathbf{k},\mathbf{p}} a_\mathbf{k}^\dagger a_\mathbf{p} a_{-\mathbf{k}}^\dagger a_{-\mathbf{p}} \frac{1}{E_\mathbf{k} E_\mathbf{p} (m + E_\mathbf{k})(m + E_\mathbf{p})} \\ & \times [m + E_k \quad k_-] \begin{bmatrix} 0 & \frac{1}{k_+ - p_+} \\ -\frac{1}{k_- - p_-} & 0 \end{bmatrix} \begin{bmatrix} m + E_p \\ p_+ \end{bmatrix} \\ & \times [(m + E_k)(m + E_p) + k_- p_+]. \end{aligned} \tag{56}$$

We used $\int d\mathbf{r} \frac{1}{z} \exp\{i\mathbf{k}\mathbf{r}\} = i\frac{2\pi}{k_+}$. The terms with the coefficient $k_- p_+$ give a p-wave channel contribution (for spinless fermions),

$$\begin{aligned} & \frac{k_- p_+}{|\mathbf{k} - \mathbf{p}|^2} \{(2m + E_k + E_p)(m + E_k)(m + E_p) \\ & \quad - |p|^2 (m + E_k) - |k|^2 (m + E_p)\}. \end{aligned} \tag{57}$$

These terms give the following contribution:

$$\begin{aligned} V_p^{\mathrm{BCS}} = {} & m \frac{2\pi}{2V} \sum_{\mathbf{k},\mathbf{p}} a_\mathbf{k}^\dagger a_\mathbf{p} a_{-\mathbf{k}}^\dagger a_{-\mathbf{p}} \\ & \times \exp\{-i(\theta_k - \theta_p)\} \frac{|k||p|}{E_\mathbf{k} \cdot E_\mathbf{p} |\mathbf{k} - \mathbf{p}|^2}, \end{aligned} \tag{58}$$

where we see that because of the assumed sign of the mass, $m < 0$, we have an attractive pairing channel. We will discuss in more detail the effective interaction and possible pairing solutions below, but in the following we will make a few general comments. We see from Eq. (58) that only for nonzero mass we can have pairing. Also the chirality of the induced p-wave pairing can be identified. Notice the different phase factors in V_p^{BCS} with respect to Ref. [34]. That comes from a different overall phase in eigenstates that we used in the fermion field expansion in Eq. (55) and the one used in Ref. [34]. Both representations lead to a special chirality pairing function $g(\mathbf{r})$:

$$\lim_{|r| \to \infty} g(\mathbf{r}) \sim f(|\mathbf{r}|) \frac{|z|}{z}. \tag{59}$$

The function $f(|\mathbf{r}|)$ depends on the details of the small $\mathbf{k}$ behavior of the order parameter. The self-consistent equation for the pairing function, $\Delta_\mathbf{k}^* = 2\mathcal{E}_\mathbf{k} \langle a_\mathbf{k}^\dagger a_{-\mathbf{k}}^\dagger \rangle$, where $\mathcal{E}_\mathbf{k}^2 = (E_\mathbf{k} - \mu)^2 + |\Delta_\mathbf{k}|^2$, implied by Eq. (58), with the assumption that $|\Delta_k|$ is the largest around $|\mathbf{k}| = k_F$, gives us the small $\mathbf{k}$ behavior, $\Delta_\mathbf{k}^* \sim k_+$, and thus $g(\mathbf{r}) \sim \frac{1}{z}$. However, again we have to take into account that the assumed direction of the external magnetic field in the Son's formalism is $\vec{B} = B\,\vec{e}_z$, $B > 0$, because the uniform Dirac composite fermion density is $\bar{\rho}_\chi = \vec{\nabla} \times \vec{A} = B > 0$. For the usual setup, with $B < 0$, the analysis implies $g(\mathbf{r}) \sim \frac{1}{z^*}$, i.e., Pfaffian pairing of the opposite chirality with respect to the one given by the external field. The same conclusions, i.e., an attractive pairing channel with special PH Pfaffian chirality pairing hold true for $m > 0$ as can be easily checked. Thus, for large enough mass, we may expect that the interaction term due to the gauge field [Eq. (58)] can lead to the PH Pfaffian-like pairing instability, but for very large m, the pairing interaction is suppressed. [For large m, in the scope of the HLR theories as shown in Appendix D, any pairing (Pfaffian and anti-Pfaffian) correlations that come from the current-density interaction are obstructed by a three-body interaction, and do not give a clear scenario that comes from the constrained dynamics of the system.]

A more careful examination of the Cooper channel interaction in Eq. (58), which we may begin by angular integration in a BCS self-consistent equation, shows that the pairing interaction is extremely singular and would overcome any repulsive, short-range or Coulomb, interaction. Also the interaction in Eq. (58) does not correspond exactly to the statistical interaction that is usually connected with the Pfaffian physics as described in Ref. [36]. Thus we need to examine more carefully all the terms that follow from Eq. (56). A complete discussion can be found in Appendix C. The picture that emerges from the detailed analysis in Appendix C is very simple: for large $|m|$, irrespective of the sign of mass, we may expect a PH Pfaffian-like state, but for small $|m|$, depending on its sign,

we have anti-Pfaffian, for $m > 0$, and Pfaffian state for $m < 0$. Due to considerable numerical support for anti-Pfaffian under LL mixing in the SLL [37], we may identify the case with the positive mass to the one of the SLL. Furthermore, the identification of Pfaffian and anti-Pfaffian for opposite sign of m, i.e., particle-hole symmetry breaking that is not large is consistent with the numerics (in the SLL) [7].

However, we should be aware of the absence of pairing in the LLL, and that our analysis based on the gauge field description only, is not sufficient for the explanation of the physics in the LLL. We need to include Coulomb repulsive interactions among electrons. This inclusion in the Chern-Simons theories, especially the DCF theory is not an easy task, because a part of the influence of the interactions is built in the gauge dynamics. We may try to include a bare Coulomb interaction with densities that correspond to those of the Dirac quasiparticles [of the theory in the Eq. (46)] as a consequence of Eqs. (47) and (48). The singular behavior of the Coulomb law can suppress any pairing correlations that follow from the gauge field description and constraints. Thus we need to include the interactions in a way that reflects the physics of a fixed LL to explain the dichotomy of the physics in the LLL and SLL, i.e., a Fermi-liquid-like state, and topological paired state, respectively, i.e., to include more intra-Landau level physics in the DCF theory. The way to achieve that is to include a term that represents the interaction of the effective dipoles of the Read's construction with an electric field as discussed in Refs. [38,39]. As explained in Ref. [39], the inclusion of this physics amounts to a change in the expression of the Coulomb interaction of the form

$$\frac{\alpha}{|\mathbf{q}|} \to \frac{\alpha}{|\mathbf{q}| + \frac{m^*}{2B}\alpha|\mathbf{q}|^2}, \tag{60}$$

where we assumed a static case, i.e., no external fields except for the uniform, constant magnetic field B, and m^* represents an effective parameter (mass) in the long distance limit. In the following, we briefly recapitulate how we can reach the modified interaction in (60). First, we note that in a functional formulation we can introduce a scalar field ϕ that decouples the Coulomb term in the inverse space as

$$\begin{aligned}\delta\mathcal{L}_c &= -\frac{2\pi\alpha}{|\mathbf{q}|}\delta\rho(-\mathbf{q})\delta\rho(\mathbf{q}) \\ &\to \phi(-\mathbf{q})\delta\rho(\mathbf{q}) + \frac{|\mathbf{q}|}{2\pi\alpha}\phi(-\mathbf{q})\phi(\mathbf{q}).\end{aligned} \tag{61}$$

The scalar represents a potential that a particle experiences due to other particles. On the other hand, Galilean invariance allows an extra term in the kinetic part of the DCF theory [38],

$$\delta\mathcal{L}_u = i u_i \chi^\dagger \partial_i \chi, \tag{62}$$

where u_i is the local drift velocity, $u_i = \epsilon_{ij}\frac{\partial_i\phi}{B}$, $i = x, y$. This term represents an interaction between the (local) electric field and dipoles of the composite fermion quasiparticles, which are propotional to quasiparticle momenta [38]. If we introduce a mass parameter, m^*, to relate the momenta of quasiparticles to their (local) velocity $\mathbf{u}$, we may represent (62), in the inverse space, as

$$\delta\mathcal{L}_u = \frac{m^*|\mathbf{u}|^2\bar{\rho}}{2} = m^*\frac{\bar{\rho}}{2B^2}|\mathbf{q}|^2\phi(-\mathbf{q})\phi(\mathbf{q}), \tag{63}$$

where $\bar{\rho} = \frac{1}{2\pi l_B^2}$ with $l_B = 1/k_F$, the magnetic length, is the density of the system. Integrating field ϕ in the functional representation of the theory, with $\delta\mathcal{L}_u$ and $\delta\mathcal{L}_c$ included, we reach (60). Thus the BCS channel in Eq. (C3) with a modified Coulomb interaction in Eq. (60) may represent a good starting point for the investigation of the pairing instabilities at half-filling in the presence of the PH symmetry breaking mass m.

The role of the modified Coulomb interaction is crucial for the existence of paired states. For m^* finite, we have to deal with a singular repulsive interaction at this level of approximation, which will preclude any pairing as is the case in the LLL. For m^* infinite, the effects of the interaction will be obliterated, and we will have the pairing scenario as is the case in the SLL. Moreover, in this case, for $|m|$ (LL mixing) large, we may expect the PH Pfaffian-like state, which is stabilized with $|m|$ in a uniform system and a consequence of the constrained gauge field description. Nevertheless, we should note that the PH Pfaffian effective (attractive) interaction scales as $\sim\frac{k_F}{|m|}$ (with respect to those of Pfaffian and anti-Pfaffian for small $|m|$), and thus it is suppressed in magnitude with large $|m|$.

We may ask ourselves what is the physical meaning of the m^* infinite limit in the SLL. In this case, the local drift velocity should go to zero and thus the potential that other particles make for a given one is flat, i.e., the correlation hole does not exist and particles are free to pair. That this indeed may be the case in the SLL, we have indications from numerical experiments that find larger size of hole excitations in the SLL than in the LLL in the FQHE regime at filling factors $1/3$ and $7/3$ [40,41].

The numerical solutions of the BCS self-consistent equation:

$$\Delta^*_{\mathbf{p}} = -\sum_{\mathbf{k}} V_{\mathbf{kp}}\frac{\Delta^*_{\mathbf{k}}}{\mathcal{E}_{\mathbf{k}}}, \tag{64}$$

for channels $l = 1, 3, -1$, with $\Delta^*_{\mathbf{k}} = |\Delta_{\mathbf{k}}|e^{il\theta_{\mathbf{k}}}$, are described in Fig. 1. Details concerning Eq. (64) and its solutions can be found in Appendix E. The parameter m in Fig. 1 is measured in units of energy, $(\hbar v_F)k_F$, and this dimensionless quantity along x axis on the right-hand side of Fig. 1, can be described in the following way. First, we rewrite the quantity with the Fermi velocity and explicit physical constants:

$$m \to \frac{m_D v_F^2}{\hbar v_F k_F} = \frac{m_D v_F}{\hbar} l_B = \sqrt{\frac{c}{\hbar e}} v_F \frac{m_D}{\sqrt{B}}, \tag{65}$$

where m_D is the mass of DCFs, $l_B = \sqrt{\frac{\hbar c}{eB}}$ is the magnetic length, and $k_F = \frac{1}{l_B}$. On the other hand, the coefficient of the LL mixing is the ratio of the characteristic Coulomb energy and cyclotron energy:

$$\frac{V_c}{\hbar\omega_c} = \frac{e^2}{l_B}\frac{m_e c}{eB} = \frac{e\sqrt{ec}}{\hbar\sqrt{\hbar}}\frac{m_e}{\sqrt{B}}, \tag{66}$$

where m_e is the mass of electron. Thus the plotted (dimensionless) parameter m may be identified with LL mixing if $m_D = \frac{e^2}{\hbar v_F}m_e$, i.e., the mass of DCF is the electron mass multiplied with a "fine-structure constant" of DCFs, $\frac{e^2}{\hbar v_F}$, characterizing the relative strength of the Coulomb interaction. The

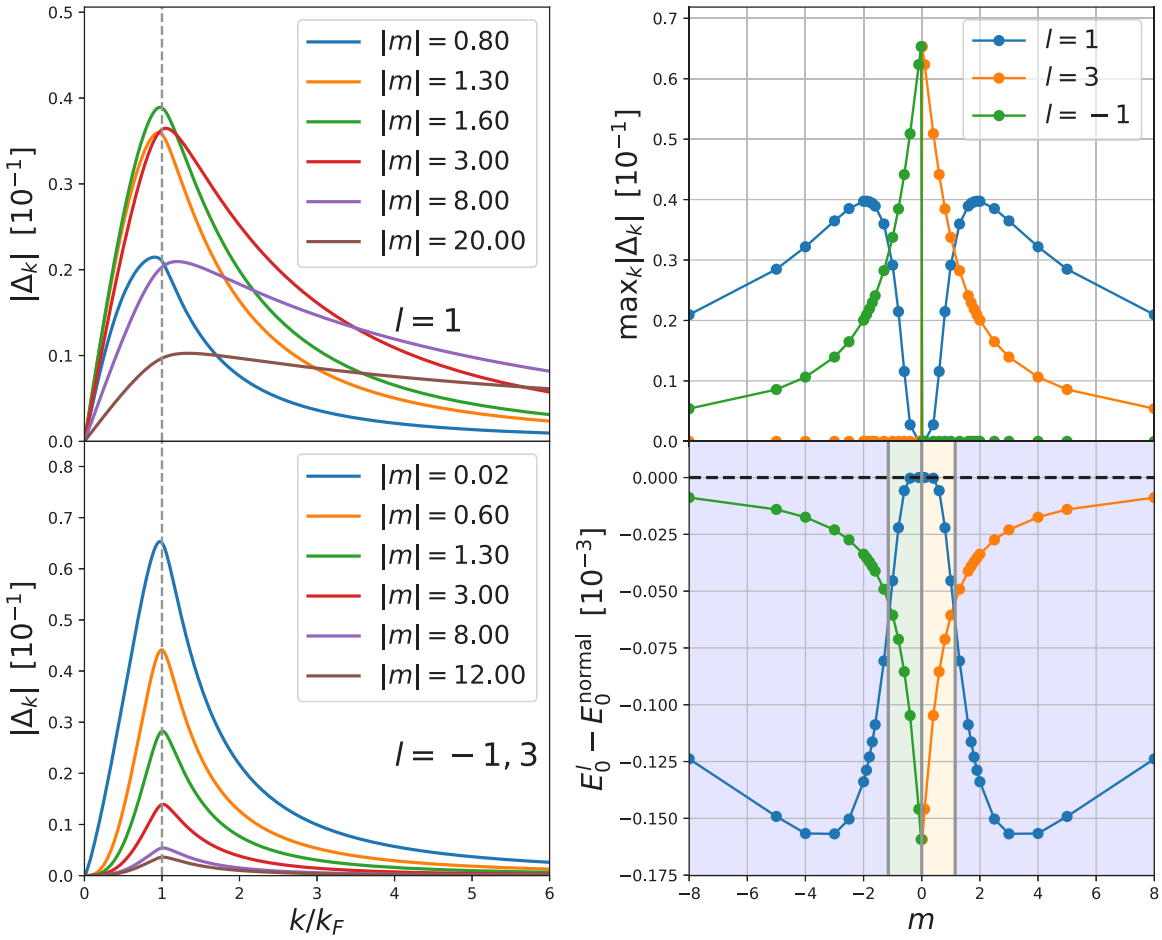

FIG. 1. The solutions of the self-consistent BCS problem. (Left column) Radial direction k-dependent pairing amplitude for various values of m. Channel $l = 1$ solution only depends on $|m|$, while $l = 3$ and $l = -1$ channel solutions are symmetric with the sign flip of m (see Appendix E 3). (Upper right) Dependence of the maximum of the pairing amplitude on m (always found at the Fermi level k_F). (Lower right) Total energy of the different pairing solutions compared to the normal state energy. Gray vertical lines denote the transition between different l channels. Color in the background corresponds to the energetically favorable channel at the given m. We identify $l = 3$ and -1 channels with an anti-Pfaffian and Pfaffian state, respectively, and $l = 1$ channel with a PH Pfaffian-like state.

identification seems plausible, although we do not have an explicit proof; we expect that the prediction of the phase diagram that follows from the theory, up to physical constants, depends solely on the unique parameter of the system, $l_B = \frac{1}{k_F}$, and thus the dimensionless parameter in Fig. 1 should represent LL mixing.

The LL mixing in experiments is of order 1, although it can be large as 4–8 [42,43], and with the above identification we may expect the anti-Pfaffian ($l = 3$) to be the dominant instability in the SLL from the phase diagram in Fig. 1, though the critical m [for the transition into the PH Pfaffian-like state ($l = 1$)], may be estimated to be $m_c = 1.2$, and thus the role and possibility for the development of a PH Pfaffian-like state, at sufficiently large LL mixing in a uniform system should not be underestimated or excluded.

We have confidence in our predictions, because the global features of the phase diagram in Fig. 1 are in agreement with numerical experiments in the SLL. (a) At $m = 0$, a Schrödinger cat superposition of Pfaffian and anti-Pfaffian is present as in Ref. [7], and depending on the sign of the mass for $m \neq 0$ we have Pfaffian or anti-Pfaffian. (b) The PH Pfaffian-like state is continuously connected to the excited composite FL state at $m = 0$ in an agreement with Ref. [13]. However, this does not mean that with an absolute certainty we can expect a PH Pfaffian-like state at large enough LL mixing in the SLL. This is because we do not possess the precise knowledge of the phenomenological parameter m^* as a function of the Dirac mass, m. The parameter m^* enters Eq. (60) and controls the effectiveness of the pair breaking due to the repulsive Coulomb interaction. We expect that for smaller values of Dirac mass, the parameter m^* is infinite and pairing is present, but, for some large m, the parameter m^* will become finite and an HLR-type of CFL will be established. As we do not know the precise value of m for which this drastic change will occur, we can not say beyond which large enough m the pairing scenario of Fig. 1 will not be realized.

V. DISCUSSION AND CONCLUSIONS

We showed that a complete DCF theory (introduced in Refs. [38,39]) may describe both the paired and FL state of the SLL and LLL, respectively, if we treat the parameter

m^* in (60) as a phenomenological long-distance parameter, which (in the scope of our treatment) is necessarily infinite in the paired states. The m^* is necessarily finite in the limit of large Dirac mass, m, (HLR theory) and in that region we should expect known results (no pairing). For small m, in the SLL, m^* must be infinite to allow for pairing of the (anti-)Pfaffian type consistent with numerics (see Fig. 1). But interestingly enough, we reveal (Fig. 1) a strong competition between an anti-Pfaffian and a PH Pfaffian-like state for intermediate Dirac mass m although we can not claim the absolute relevance of the PH Pfaffian-like state because we do not know the behavior of m^* in that region. However, it seems likely and the results of Fig. 1 are suggestive that a PH Pfaffian-like state [Eq. (19)] may play a role in experiments.

In this work, we discussed the effective Cooper pairing channel of the system at half-filling in the scope of the DCF theory with a mass term. The mass term of the DCF theory represents a term that breaks the particle-hole symmetry of electrons confined in an LL and represents an LL mixing. Solely on the basis of a gauge field description, we find for small Dirac mass an anti-Pfaffian or Pfaffian instability depending on the sign of the mass, consistent with numerical investigations of the SLL [7], while for large mass (LL mixing), irrespective of the mass sign, we find a PH Pfaffian-like instability.

ACKNOWLEDGMENTS

We would like to thank Vladimir Juričić and Michael Peterson for discussions. We also thank Nordita Institute for hospitality during the final stages of this work. This research was supported by the Ministry of Education, Science, and Technological Development of the Republic of Serbia under Project ON171017.

APPENDIX A: THE POLARIZATION TENSOR

The derivation of the polarization tensor $\Pi(\mathbf{k}, k_0)$ in the massive case, in the hydrodynamic approximation, can be done following and generalizing the procedure described in the massless case in Ref. [44]. We start from the fermion propagator in Eq. (28) as described in Ref. [45],

$$iS_F(x,y) = \theta(x^0-y^0)\int \frac{d^2p}{(2\pi)^2}\frac{1}{2p_0}(\gamma p + m)\theta(p^0-\mu)\exp\{-ip(x-y)\} - \theta(y^0-x^0)\int \frac{d^2p}{(2\pi)^2}\frac{1}{2p_0}$$
$$\times(\gamma p + m)\theta(\mu-p_0)\exp\{-ip(x-y)\} - \theta(y^0-x^0)\int \frac{d^2p}{(2\pi)^2}\frac{1}{2p_0}(\gamma p - m)\exp\{ip(x-y)\}, \quad \text{(A1)}$$

where $p_0 = \sqrt{\mathbf{p}^2+m^2}$, $px = p_0x^0 - \mathbf{px}$, and $\gamma p = \gamma^0 p_0 - \gamma\mathbf{p}$. Using the theta function representation,

$$\theta(x^0-y^0) = -\int \frac{d\omega}{2\pi i}\frac{\exp\{-i\omega(x^0-y^0)\}}{\omega+i\eta}, \quad \text{(A2)}$$

we arrive at

$$iS_F(x-y) = \int \frac{d\omega}{2\pi}\int \frac{d^2p}{(2\pi)^2}\exp\{-i\omega(x^0-y^0)+i\mathbf{p}(\mathbf{x}-\mathbf{y})\}$$
$$\times\left[i\gamma^0\frac{1}{\omega-p_0+i\eta(\theta(p_0-\mu)-\theta(\mu-p_0))}\Omega^-_{\mathbf{p}} + i\gamma^0\frac{1}{\omega+p_0-i\eta}\Omega^+_{\mathbf{p}}\right], \quad \text{(A3)}$$

where

$$\Omega^-_{\mathbf{p}} = \frac{1}{2}\left(1+\frac{\gamma^0 m}{p_0}-\frac{\gamma^0\gamma\mathbf{p}}{p_0}\right), \quad \text{(A4)}$$

and

$$\Omega^+_{\mathbf{p}} = \frac{1}{2}\left(1-\frac{\gamma^0 m}{p_0}+\frac{\gamma^0\gamma\mathbf{p}}{p_0}\right). \quad \text{(A5)}$$

To get the form of the fermion operator in Ref. [44], we can shift the frequency variable ω as $\omega \to \omega+\mu$. To find

$$\Pi^{\mu\nu} = -itr[\gamma^\mu S_F(x,y)\gamma^\nu S_F(y,x)], \quad \text{(A6)}$$

we need to generalize the trace calculations, frequency, and momentum integrals. The main approximation in the momentum integrals for the external momentum $\mathbf{k}$, $|\mathbf{k}| \ll k_F, \mu$, and internal momentum $\mathbf{q}$, $|\mathbf{q}| \sim k_F$ (constrained by the Fermi statistics inside integrals for $|\mathbf{k}| \ll k_F$) is

$$\theta(\sqrt{|\mathbf{q}+\mathbf{k}|^2+m^2}-\mu)$$
$$\approx \theta\left(\sqrt{|\mathbf{q}|^2+m^2}-\mu+|\mathbf{k}|\frac{|\mathbf{q}|}{\sqrt{|\mathbf{q}|^2+m^2}}\cos\phi\right)$$
$$\approx \theta(\sqrt{|\mathbf{q}|^2+m^2}-\mu)$$
$$+|\mathbf{k}|\frac{k_F}{\sqrt{k_F^2+m^2}}\delta(\sqrt{|\mathbf{q}|^2+m^2}-\mu)\cos\phi, \quad \text{(A7)}$$

where $k_F = \sqrt{\mu^2-m^2}$, and ϕ is the angle between vectors $\mathbf{k}$ and $\mathbf{q}$. Here an important difference with respect to the massless case is the appearance of the factor $\frac{k_F}{\sqrt{k_F^2+m^2}}$. A detailed analysis leads to a conclusion that to get $\Pi^{\mu\nu}$ in the massive case we have to rescale the external momenta $\mathbf{k}$ in the

massless case with a factor $\alpha_F = \frac{k_F}{\sqrt{k_F^2+m^2}}$, i.e., $\mathbf{k} \to \alpha_F \mathbf{k}$. In particular,

$$\Pi^{00}(k_0, \mathbf{k}) = \tilde{\Pi}^{00}(k_0, \alpha_F \mathbf{k}), \tag{A8}$$

$$\Pi^{0i}(k_0, \mathbf{k}) = \alpha_F \tilde{\Pi}^{0i}(k_0, \alpha_F \mathbf{k}) + \epsilon_{ji}\left(-\frac{ik_j m}{4\pi} - i\frac{k_j m}{2\mu^2}\tilde{\Pi}^{00}(k_0, \alpha_F \mathbf{k})\right), \tag{A9}$$

$$\Pi^{ij}(k_0, \mathbf{k}) = \alpha_F^2 \tilde{\Pi}^{ij}(k_0, \alpha_F \mathbf{k}), \tag{A10}$$

where by $\tilde{\Pi}^{\mu\nu}; \mu, \nu = 0, i, j$ we denoted the components of the polarization tensor in the massless case, and, furthermore, we can see the antisymmetric (Hall conductance) contribution in Π^{0i}, due to the presence of the mass term.

The components of the polarization tensor in the massless case, $\tilde{\Pi}^{\mu\nu}(k_0, \mathbf{k})$, can be found in Ref. [44], and they are

$$\begin{aligned}
\tilde{\Pi}^{00}(k_0, \mathbf{k}) &= \Pi_l(k_0, \mathbf{k}), \\
\tilde{\Pi}^{0i}(k_0, \mathbf{k}) &= k_0 \frac{k^i}{|\mathbf{k}|^2}\Pi_l(k_0, \mathbf{k}), \\
\tilde{\Pi}^{ij}(k_0, \mathbf{k}) &= \left(\delta^{ij} - \frac{k^i k^j}{|\mathbf{k}|^2}\right)\Pi_t(k_0, \mathbf{k}) + \frac{k^i k^j}{|\mathbf{k}|^2}\frac{k_0^2}{|\mathbf{k}|^2}\Pi_l(k_0, \mathbf{k}),
\end{aligned} \tag{A11}$$

where

$$\Pi_l(k_0, \mathbf{k}) = \frac{\mu}{2\pi}\left(\theta(k^2)\sqrt{\frac{k_0^2}{k^2}} - 1 - i\theta(-k^2)\sqrt{\frac{k_0^2}{-k^2}}\right), \tag{A12}$$

$$\Pi_t(k_0, \mathbf{k}) = \frac{\mu}{2\pi} - \frac{k^2}{|\mathbf{k}|^2}\Pi_l(k_0, \mathbf{k}), \tag{A13}$$

and $k^2 = k_0^2 - |\mathbf{k}|^2$.

The antisymmetric contribution in Eq. (A9) is expected from the Berry curvature contributions in the scope of the relativistic quantum mechanics [29], and here the Hall conductance can be recovered to be $\sigma_H = -\frac{1}{4\pi}\frac{m}{\sqrt{k_F^2+m^2}}$.

It is important to comment that due to the infinite Dirac sea, we have divergent contributions to the polarization tensor (when doing the calculation according to the definition). As discussed in the main text, the DCF theory as defined in Eq. (20) requires dimensional regularization in order to recover finite $\Pi^{\mu\nu}$. We used the version of the DCF theory given in Eq. (46) and the associated Pauli-Villars regularization to recover $\Pi^{\mu\nu}$.

APPENDIX B: THE PROPAGATOR OF THE GAUGE FIELD

To find $\bar{\mathcal{D}}^{-1}_{\mu\nu}$ defined in Eq. (31), we need to switch from Minkowski to Euclidean space-time. According to the definition of $\bar{\mathcal{D}}^{-1}_{\mu\nu}$, we need only to take into account the change in the fermion propagator, which amounts to taking $i\omega$ instead of ω at T(temperature) $= 0$ in the Fourier transform of the fermion propagator described in Eqs. (A3)–(A5). Thus we have to repeat the steps that we took to calculate $\Pi^{\mu\nu}$ taking into account this change. The components of $\bar{\mathcal{D}}^{-1}_{\mu\nu}$ are formally equal to the expressions in Eqs. (A8)–(A11) and (A13), i.e., $\bar{\mathcal{D}}^{-1}_{\mu\nu}(k_0, \mathbf{k}) = \Pi_{\mu\nu}(k_0, \mathbf{k})$, with $\Pi_l(k_0, \mathbf{k})$ equal to

$$\hat{\Pi}_l(k_0, \mathbf{k}) = \frac{\mu}{2\pi}\left(-1 + \frac{1}{\sqrt{1 - \frac{|\mathbf{k}|^2}{k_0^2}}}\right), \tag{B1}$$

where k_0 is purely imaginary.

In the transverse gauge, $\vec{\nabla}\mathbf{a} = 0$, and if we denote by $\alpha = \frac{2\pi e^2}{\epsilon_r}$, the Coulomb coupling constant, the inverse of the gauge field propagator is

$$\mathcal{D}^{-1}(k_0, \mathbf{k}) = \begin{bmatrix} \hat{\Pi}_{00} & \hat{\Pi}_{0T} \\ \hat{\Pi}_{0T} & \hat{\Pi}_{TT} \end{bmatrix}, \tag{B2}$$

where

$$\hat{\Pi}_{00} = \hat{\Pi}_l(k_0, \alpha_F \mathbf{k}), \tag{B3}$$

$$\hat{\Pi}_{0T} = -\frac{1}{4\pi}\frac{m}{\mu}|\mathbf{k}| - \frac{m}{2\mu^2}|\mathbf{k}|\hat{\Pi}_l(k_0, \alpha_F \mathbf{k}), \tag{B4}$$

$$\hat{\Pi}_{TT} = \frac{k_F^2}{2\pi\mu} - \frac{k_0^2 - \alpha_F^2|\mathbf{k}|^2}{|\mathbf{k}|^2}\hat{\Pi}_l(k_0, \alpha_F \mathbf{k}) + \alpha|\mathbf{k}|\frac{1}{(4\pi)^2}. \tag{B5}$$

Here we defined the transverse component of the gauge field to be $a_T = i\mathbf{k} \times \mathbf{a}(\mathbf{k})$ and it is understood that k_0 is purely imaginary.

APPENDIX C: THE EFFECTIVE COOPER CHANNEL AND POSSIBLE PAIRINGS

We can rewrite the Cooper channel interaction in Eq. (56), taking into account both possibilities for the sign of mass,

$$V_{st}^{\mathrm{BCS}} = -\frac{m}{|m|}\frac{2\pi}{8V}\sum_{\mathbf{k},\mathbf{p}} a_{\mathbf{k}}^\dagger a_{\mathbf{p}} a_{-\mathbf{k}}^\dagger a_{-\mathbf{p}} \frac{1}{E_{\mathbf{k}} \cdot E_{\mathbf{p}}|\mathbf{k}-\mathbf{p}|^2} \times \left\{-|\mathbf{p}|^2(m+E_k) - |\mathbf{k}|^2(m+E_p) + 4mk_-p_+ + \frac{(k_-p_+)^2}{|\mathbf{p}|^2|\mathbf{k}|^2}(E_k+E_p+2m)(E_k-m)(E_p-m)\right\}. \tag{C1}$$

We expect that in a self-consistent BCS equation the most important contribution will come from the region in which $\mathbf{k} \approx \mathbf{p}$, due to the denominator in the equation above. To explore this limiting behavior, we can divide terms in curly brackets as follows:

$$\left[-|\mathbf{p}|^2(m+E_k) - |\mathbf{k}|^2(m+E_p) + 2m(k_-p_+ + k_+p_-) + \frac{(E_k+E_p+2m)(E_k-m)(E_p-m)}{2|\mathbf{p}|^2|\mathbf{k}|^2}((k_-p_+)^2 + (k_+p_-)^2)\right] + \left[2m(k_-p_+ - k_+p_-) + \frac{(E_k+E_p+2m)(E_k-m)(E_p-m)}{2|\mathbf{p}|^2|\mathbf{k}|^2}((k_-p_+)^2 - (k_+p_-)^2)\right]. \tag{C2}$$

The first part in the square brackets is an even function of $(\theta_p - \theta_k)$ and as $\mathbf{k} \to \mathbf{p}$ the part is of the order of $(\theta_p - \theta_k)^2$. The second part is leading and dominant because in the same limit it is of the order of $(\theta_p - \theta_k)$. The Cooper channel can be cast in the following form:

$$V_{st}^{\rm BCS} = \frac{2\pi}{8V}\sum_{\mathbf{k},\mathbf{p}} a^\dagger_{\mathbf{k}} a_{\mathbf{p}} a^\dagger_{-\mathbf{k}} a_{-\mathbf{p}} \frac{1}{E_{\mathbf{k}}\cdot E_{\mathbf{p}}}\left\{-4|m||\mathbf{k}||\mathbf{p}|\frac{i\sin(\theta_p-\theta_k)}{|\mathbf{k}-\mathbf{p}|^2} - \frac{m}{|m|}(E_k+E_p+2m)(E_k-m)(E_p-m)\frac{i\sin 2(\theta_p-\theta_k)}{|\mathbf{k}-\mathbf{p}|^2}\right.$$
$$\left. + 4|m||\mathbf{k}||\mathbf{p}|\frac{(\lambda-1)}{|\mathbf{k}-\mathbf{p}|^2} - 4|m||\mathbf{k}||\mathbf{p}|\frac{\cos(\theta_p-\theta_k)-1}{|\mathbf{k}-\mathbf{p}|^2} - \frac{m}{|m|}(E_k+E_p+2m)(E_k-m)(E_p-m)\frac{\cos 2(\theta_p-\theta_k)-1}{|\mathbf{k}-\mathbf{p}|^2}\right\}, \tag{C3}$$

where $\lambda = \frac{|\mathbf{k}|^2+|\mathbf{p}|^2}{2|\mathbf{k}||\mathbf{p}|}$. The following analysis of the effective Cooper channel in Eq. (C3) is based on considerations similar to those described in the case of classical composite fermions Pfaffian pairing in Ref. [36].

For $m > 0$ and m large, the Cooper channel can be approximated as

$$V_{st}^{\rm BCS} \approx \frac{2\pi}{8V}\sum_{\mathbf{k},\mathbf{p}} a^\dagger_{\mathbf{k}} a_{\mathbf{p}} a^\dagger_{-\mathbf{k}} a_{-\mathbf{p}} \frac{1}{E_{\mathbf{k}}\cdot E_{\mathbf{p}}} - 2|m|\left\{\frac{i\sin(\theta_p-\theta_k)}{\lambda-\cos(\theta_p-\theta_k)} - 1\right\}. \tag{C4}$$

Thus, as previously discussed, the implied angular momentum pairing is $\Delta^*_{\mathbf{k}} \sim \langle a^\dagger_{\mathbf{k}} a^\dagger_{-\mathbf{k}}\rangle \sim e^{i\theta_{\mathbf{k}}}$, i.e., a PH Pfaffian-like pairing. For $m > 0$ and m small, the Cooper channel can be approximated as

$$V_{st}^{\rm BCS} \approx \frac{2\pi}{8V}\sum_{\mathbf{k},\mathbf{p}} a^\dagger_{\mathbf{k}} a_{\mathbf{p}} a^\dagger_{-\mathbf{k}} a_{-\mathbf{p}} \frac{1}{E_{\mathbf{k}}\cdot E_{\mathbf{p}}} - \frac{m}{|m|}(E_k+E_p+2m)(E_k-m)(E_p-m)\frac{\exp i2(\theta_p-\theta_k)-1}{|\mathbf{k}-\mathbf{p}|^2}. \tag{C5}$$

By doing the angular integration first in the implied BCS self-consistent equation, we find that the pairing $\Delta^*_{\mathbf{k}} \sim e^{i\theta_{\mathbf{k}}}$ is suppressed, and that $\Delta^*_{\mathbf{k}} \sim e^{i3\theta_{\mathbf{k}}}$ is the dominant pairing. The pairing in the same direction of PH Pfaffian, with angular momentum equal to 3, can be identified as an anti-Pfaffian instability. For $m < 0$ and $|m|$ small, the sign of the effective Cooper channel in Eq. (C5) is switched. This changes the chirality of the implied pairing, and we find that now $\Delta^*_{\mathbf{k}} \sim e^{-i\theta_{\mathbf{k}}}$ is the dominant pairing, which we can identify with a Pfaffian instability. For $m < 0$ and $|m|$ large, the effective channel is

$$V_{st}^{\rm BCS} \approx \frac{2\pi}{8V}\sum_{\mathbf{k},\mathbf{p}} a^\dagger_{\mathbf{k}} a_{\mathbf{p}} a^\dagger_{-\mathbf{k}} a_{-\mathbf{p}} \frac{1}{E_{\mathbf{k}}\cdot E_{\mathbf{p}}} - 2|m|\left\{\frac{i\sin(\theta_p-\theta_k)}{\lambda-\cos(\theta_p-\theta_k)} - \lambda\frac{(\exp i2(\theta_p-\theta_k)-1)}{\lambda-\cos(\theta_p-\theta_k)}\right\}, \tag{C6}$$

and we recover again a PH Pfaffian-like instability, $\Delta^*_{\mathbf{k}} \sim e^{i\theta_{\mathbf{k}}}$.

APPENDIX D: CLASSICAL HLR FERMIONS AT HALF-FILLING AND PAIRING INSTABILITIES

It is interesting to probe the large $|m|$ limit of the Lagrangian given by Eq. (46). In this limit and after redefinitions $a_\mu \to a_\mu + \frac{m}{|m|}A_\mu$, the Lagrangian becomes

$$\mathcal{L}_{\rm ccf} = \frac{m}{|m|}\frac{1}{8\pi}ada + \psi^\dagger\left(i\partial_0 + a_0 + \frac{m}{|m|}A_0\right)\psi$$
$$- \sum_{i=x,y}\frac{1}{2|m|}\psi^\dagger\left(i\partial_i + a_i + \frac{m}{|m|}A_i\right)^2\psi$$
$$+ \frac{\left(1-\frac{m}{|m|}\right)}{2}\frac{1}{4\pi}AdA. \tag{D1}$$

If $m > 0$, we have the usual Lagrangian of HLR (up to a Coulomb interaction term that we omitted), which, based on the mean-field approximation, leads to the description of composite fermion liquid (CFL). On the other hand, for $m < 0$, we have exactly the Lagrangian of Ref. [35], which in the same approximation describes anti-CFL, i.e., a Fermi liquid of composite holes.

The HLR theory ($m > 0$ case) is described by the following kinetic term of the Hamiltonian density:

$$\mathcal{K} = \frac{1}{2|m|}(-i\nabla + \mathbf{c})\psi^\dagger(i\nabla + \mathbf{c})\psi, \tag{D2}$$

where $\vec{c}$ represents the deviation from the uniform magnetic field configuration of the CS gauge field a_μ: $c_\mu = a_\mu + A_\mu$ such that

$$-\delta\rho_\psi = \frac{1}{4\pi}\nabla\times\mathbf{c}. \tag{D3}$$

In this nonrelativistic case, the effective statistical density-current interaction is given by

$$\tilde{V}_{\rm st} = -\frac{1}{2|m|}\mathbf{c}[\psi^\dagger(i\nabla\psi) - (i\nabla\psi^\dagger)\psi] \equiv \frac{\mathbf{cj}}{2|m|}. \tag{D4}$$

Using Eq. (D3), in parallel to Eqs. (48) and (8) in the relativistic case, we can express the interaction as

$$\tilde{V}_{\rm st} = \frac{1}{2|m|}\int d\mathbf{r}'\left[\frac{y-y'}{|\mathbf{r}-\mathbf{r}'|^2}j_x - \frac{x-x'}{|\mathbf{r}-\mathbf{r}'|^2}j_y\right]\delta\rho(\mathbf{r}'). \tag{D5}$$

If we introduce momentum space states,

$$\psi(\mathbf{r}) = \frac{1}{\sqrt{V}}\sum_{\mathbf{k}}\exp\{i\mathbf{kr}\}\,c_{\mathbf{k}}, \tag{D6}$$

$$\mathbf{j}(\mathbf{k}) = \frac{1}{\sqrt{V}}\int d\mathbf{r}\exp\{-i\mathbf{kr}\}\,\mathbf{j}(\mathbf{r})$$
$$= \frac{1}{\sqrt{V}}\sum_{\mathbf{q}}(2\mathbf{q}-\mathbf{k})\,c^\dagger_{\mathbf{q}}\,c_{\mathbf{k}+\mathbf{q}}. \tag{D7}$$

Thus

$$\int d\mathbf{r}\,\tilde{V}_{\rm st}(\mathbf{r}) = \frac{i\,V}{|m|}\sum_{\mathbf{q},\mathbf{p},\mathbf{l}} \frac{\mathbf{q}\times\mathbf{p}}{|\mathbf{q}|^2}\, c^\dagger_{\mathbf{p}}\, c_{\mathbf{p}-\mathbf{q}}\, c^\dagger_{\mathbf{l}}\, c_{\mathbf{l}+\mathbf{q}}. \tag{D8}$$

We get the BCS channel by taking $\mathbf{l} = -\mathbf{p}$. If we let $\mathbf{p} \to \mathbf{k}$ and $\mathbf{q} \to \mathbf{k} - \mathbf{p}$, we have

$$\sum_{\mathbf{k}} \tilde{V}_{\rm st}(\mathbf{k}) = \frac{-i\,V}{|m|}\sum_{\mathbf{k},\mathbf{p}} \frac{\mathbf{p}\times\mathbf{k}}{|\mathbf{p}-\mathbf{k}|^2}\, c^\dagger_{\mathbf{k}}\, c_{\mathbf{p}}\, c^\dagger_{-\mathbf{k}}\, c_{-\mathbf{p}}. \tag{D9}$$

Now we should note that

$$\mathbf{p}\times\mathbf{k} = \frac{p_+k_- - p_-k_+}{-2i}. \tag{D10}$$

Direct comparison of Eq. (D9) with Eq. (58) shows that a p wave of opposite chirality with respect to the one of PH Pfaffian, i.e., a Pfaffian p wave, is the statistical interaction implied BCS pairing instability of classical HLR CFs.

The diamagnetic term in Eq. (D2), i.e., the term $\sim \mathbf{c}^2\ \psi^\dagger\psi$ makes an interesting three-body interaction in the real space:

$$\int d\mathbf{r}_3\,\tilde{V}_{\rm st}(\mathbf{r}_3) \sim \int d\mathbf{r}_1 \int d\mathbf{r}_2 \int d\mathbf{r}_3 \frac{\mathbf{r}_1-\mathbf{r}_3}{|\mathbf{r}_1-\mathbf{r}_3|^2}\frac{\mathbf{r}_2-\mathbf{r}_3}{|\mathbf{r}_2-\mathbf{r}_3|^2} \times \delta\rho(\mathbf{r}_1)\delta\rho(\mathbf{r}_2)\delta\rho(\mathbf{r}_3), \tag{D11}$$

whose sign is fluctuating and this interaction represents a disordering factor.

We can easily repeat the analysis in the anti-CFL case and find that the current-density statistical interaction favors opposite chirality pairing with respect to the Pfaffian but of composite holes. This special pairing state of composite holes can be identified with an anti-Pfaffian [35]. However, again the additional, fluctuating sign three-body interaction, next to the attractive channel exists.

APPENDIX E: BCS SELF-CONSISTENT PROBLEM AND ITS SOLUTIONS

We start with the relevant parts of BCS mean-field theory and follow the notation of Ref. [25]. The effective Hamiltonian is

$$K_{\rm eff} = \sum_{\mathbf{k}} \left\{ \xi_k c^\dagger_{\mathbf{k}} c_{\mathbf{k}} + \frac{1}{2}\left(\Delta^* c_{-\mathbf{k}} c_{\mathbf{k}} + \Delta c^\dagger_{\mathbf{k}} c^\dagger_{-\mathbf{k}}\right)\right\}, \tag{E1}$$

and in our case $\xi_k = E_k - \mu$, with $E_k = \sqrt{|\mathbf{k}|^2 + m^2}$. The Bogoliubov transformation is

$$\alpha_{\mathbf{k}} = u_{\mathbf{k}} c_{\mathbf{k}} - v_{\mathbf{k}} c^\dagger_{-\mathbf{k}}, \tag{E2}$$

with

$$\begin{aligned} \frac{v_{\mathbf{k}}}{u_{\mathbf{k}}} &= \frac{-(\mathcal{E}_k - \xi_k)}{\Delta^*_{\mathbf{k}}}, \\ |u_{\mathbf{k}}|^2 &= \frac{1}{2}\left(1 + \frac{\xi_k}{\mathcal{E}_k}\right), \\ |v_{\mathbf{k}}|^2 &= \frac{1}{2}\left(1 - \frac{\xi_k}{\mathcal{E}_k}\right), \end{aligned} \tag{E3}$$

and $\mathcal{E}_k = \sqrt{\xi_k^2 + |\Delta_{\mathbf{k}}|^2}$.

On the other hand, if we start with a Cooper channel interaction and do the BCS mean-field decomposition with $b^\dagger_{\mathbf{k}} = c^\dagger_{\mathbf{k}} c^\dagger_{-\mathbf{k}}$,

$$\sum_{\mathbf{k},\mathbf{p}} V_{\mathbf{kp}}\, b^\dagger_{\mathbf{k}}\, b_{\mathbf{p}} = \sum_{\mathbf{k},\mathbf{p}} V_{\mathbf{kp}} \langle b^\dagger_{\mathbf{k}}\rangle b_{\mathbf{p}} + \sum_{\mathbf{k},\mathbf{p}} V_{\mathbf{kp}} b^\dagger_{\mathbf{k}} \langle b_{\mathbf{p}}\rangle - \sum_{\mathbf{k},\mathbf{p}} V_{\mathbf{kp}} \langle b^\dagger_{\mathbf{k}}\rangle \langle b_{\mathbf{p}}\rangle, \tag{E4}$$

and specify $u_{-\mathbf{k}} = u_{\mathbf{k}} = u^*_{\mathbf{k}}$ and $v_{-\mathbf{k}} = -v_{\mathbf{k}}$, then

$$\begin{aligned} \frac{\Delta^*_{\mathbf{p}}}{2} &= \sum_{\mathbf{k}} V_{\mathbf{kp}} \langle c^\dagger_{\mathbf{k}} c^\dagger_{-\mathbf{k}}\rangle \\ &= \sum_{\mathbf{k}} V_{\mathbf{kp}} \langle (u_{\mathbf{k}}\alpha^\dagger_{\mathbf{k}} + v^*_{\mathbf{k}}\alpha_{-\mathbf{k}})(-v^*_{\mathbf{k}}\alpha_{\mathbf{k}} + u_{\mathbf{k}}\alpha^\dagger_{-\mathbf{k}})\rangle, \end{aligned} \tag{E5}$$

i.e.,

$$\frac{\Delta^*_{\mathbf{p}}}{2} = \sum_{\mathbf{k}} V_{\mathbf{kp}} v^*_k u_k = \sum_{\mathbf{k}} V_{\mathbf{kp}}(-)\frac{\Delta^*_{\mathbf{k}}}{2\,\mathcal{E}_k}, \tag{E6}$$

and thus Eq. (64) in the main text.

1. BCS equation in polar coordinates $\mathbf{k} \to (k, \theta_k)$

We simplify the expression in Eq. (C3) to obtain

$$\begin{aligned} V_{\mathbf{kp}} = \frac{2\pi}{8V}\frac{1}{E_k\cdot E_p}\Bigg[&-4|m|kp\frac{i\sin(\theta_p-\theta_k)}{|\mathbf{k}-\mathbf{p}|^2} \\ &- \frac{m}{|m|}(E_k+E_p+2m)(E_k-m)(E_p-m) \\ &\times \frac{\exp\{i2(\theta_p-\theta_k)\}-1}{|\mathbf{k}-\mathbf{p}|^2}\Bigg]. \end{aligned} \tag{E7}$$

For a fixed angular momentum channel, $\Delta^*_{\mathbf{k}} = |\Delta_{\mathbf{k}}|e^{il\theta_k}$, we do first the integration over the angular variable, $\theta_k - \theta_p$, in Eq. (64) [or Eq. (E6) and after the change from sum to integral: $\sum_{\mathbf{k}} \to \frac{V}{(2\pi)^2}\int d\mathbf{k}$]. We use

$$I_m = \int_0^{2\pi} d\theta \frac{\sin m\theta \sin\theta}{\lambda - \cos\theta} = 2\pi(\lambda - \sqrt{\lambda^2-1})^m, \tag{E8}$$

$m = 1,\ 2,\ 3$, with $\lambda = \frac{k^2+p^2}{2kp}$, to get

$$V^l_{kp} = \frac{1}{2\pi}\int_0^{2\pi} d(\theta_k-\theta_p)e^{il(\theta_k-\theta_p)}V_{\mathbf{kp}}, \tag{E9}$$

for $l = 1,\ 3,\ -1$.

In particular, for $l = 1$ in (E9), we use (E8) to express the following integral:

$$\int_0^{2\pi} d(\theta_k-\theta_p)e^{i(\theta_k-\theta_p)}\frac{-i\sin(\theta_k-\theta_p)}{\lambda-\cos(\theta_k-\theta_p)} = I_1 \tag{E10}$$

and

$$\int_0^{2\pi} d(\theta_k-\theta_p)e^{i(\theta_k-\theta_p)}\frac{e^{-i2(\theta_k-\theta_p)}-1}{\lambda-\cos(\theta_k-\theta_p)}=\int_0^{2\pi} d(\theta_k-\theta_p)\frac{e^{-i(\theta_k-\theta_p)}-e^{i(\theta_k-\theta_p)}}{\lambda-\cos(\theta_k-\theta_p)}=0, \tag{E11}$$

for $l=3$ in (E9), we have

$$\int_0^{2\pi} d(\theta_k-\theta_p)e^{i3(\theta_k-\theta_p)}\frac{-i\sin(\theta_k-\theta_p)}{\lambda-\cos(\theta_k-\theta_p)}=I_3 \tag{E12}$$

and

$$\int_0^{2\pi} d(\theta_k-\theta_p)e^{i3(\theta_k-\theta_p)}\frac{e^{-i2(\theta_k-\theta_p)}-1}{\lambda-\cos(\theta_k-\theta_p)}=\int_0^{2\pi} d(\theta_k-\theta_p)e^{i2(\theta_k-\theta_p)}\frac{e^{-i(\theta_k-\theta_p)}-e^{i(\theta_k-\theta_p)}}{\lambda-\cos(\theta_k-\theta_p)}=2I_2, \tag{E13}$$

and similarly for $l=-1$. In this way, we can get the following expressions for V^l_{kp}, $l=1,\ 3,\ -1$:

$$V^1_{kp}=\frac{2\pi}{8\ E_p\ E_k}[-2|m|(\lambda-\sqrt{\lambda^2-1})], \tag{E14}$$

$$V^3_{kp}=\frac{2\pi}{8E_p\ E_k}\left[-2|m|(\lambda-\sqrt{\lambda^2-1})^3-\frac{m}{|m|}\frac{(E_p-m)(E_k-m)(E_p+E_k+2m)}{p\ k}(\lambda-\sqrt{\lambda^2-1})^2\right], \tag{E15}$$

and

$$V^{-1}_{kp}=\frac{2\pi}{8E_p\ E_k}\left[2|m|(\lambda-\sqrt{\lambda^2-1})+\frac{m}{|m|}\frac{(E_p-m)(E_k-m)(E_p+E_k+2m)}{p\ k}(\lambda-\sqrt{\lambda^2-1})^2\right]. \tag{E16}$$

Note that we take

$$\lambda-\sqrt{\lambda^2-1}=\begin{cases}\frac{k}{p}, & k<p\\ \frac{p}{k}, & p<k\end{cases}\equiv r_{pk} \tag{E17}$$

as $\sqrt{\lambda^2-1}=\sqrt{\frac{k^4+p^4+2k^2p^2}{4k^2p^2}-1}=\sqrt{\frac{k^4+p^4-2k^2p^2}{4k^2p^2}}=\frac{\sqrt{(k^2-p^2)^2}}{2kp}$. At this point, we choose $\sqrt{(k^2-p^2)^2}=|k^2-p^2|$, which then leads to Eq. (E17). Other choices lead to an unphysical V that does not decay to zero with large k and p and diverges at $k=0$ or $p=0$. The general expression for V in the three cases of interest $l=1,\ 3,\ -1$ is given by

$$V^l_{kp}=\frac{2\pi}{8E_p\ E_k}\left[-2\,\mathrm{sgn}(l)\,|m|\,r^{|l|}_{kp}-(1-\delta_{l,1})\mathrm{sgn}(l)\mathrm{sgn}(m)\frac{(E_p-m)(E_k-m)(E_p+E_k+2m)}{p\ k}r^2_{kp}\right]. \tag{E18}$$

where $\delta_{x,y}$ is the Kronecker delta, equal 1 when $x=y$ and otherwise 0. Finally, we need to solve

$$|\Delta_{\mathbf{k}}|=-\frac{1}{2\pi}\int_0^\infty dp\ p\ V^l_{kp}\frac{|\Delta_{\mathbf{p}}|}{\mathcal{E}_p}, \tag{E19}$$

with V^l_{kp} defined in Eq. (E18). Note that $|\Delta_{\mathbf{k}}|$ only depends on k.

2. Ground-state energy

For the BCS ground state $|\Omega\rangle$ for which $\alpha_{\mathbf{k}}|\Omega\rangle=0$, after a simple algebra, we have

$$\langle\Omega|K_{\mathrm{eff}}|\Omega\rangle=-\sum_{\mathbf{k}}\frac{\mathcal{E}_k-\xi_k}{2}. \tag{E20}$$

To make assessment of the implied ground-state energies we first note that

$$\langle b^\dagger_{\mathbf{k}}\rangle=-\frac{\Delta^*_{\mathbf{k}}}{2\ \mathcal{E}_k}, \tag{E21}$$

and thus

$$\begin{aligned}E_0&=\langle\Omega|K_{\mathrm{eff}}|\Omega\rangle-\sum_{\mathbf{k},\mathbf{p}}V_{\mathbf{kp}}\langle b^\dagger_{\mathbf{k}}\rangle\langle b_{\mathbf{k}}\rangle\\&=-\sum_{\mathbf{k}}\frac{\mathcal{E}_k-(E_k-\mu)}{2}-\sum_{\mathbf{k},\mathbf{p}}V_{\mathbf{kp}}\frac{\Delta^*_{\mathbf{k}}}{2\ \mathcal{E}_k}\frac{\Delta_{\mathbf{p}}}{2\ \mathcal{E}_p}.\end{aligned} \tag{E22}$$

In the second term (after the infinite volume limit), we need to integrate over θ_k and θ_p. Because $\Delta^*_{\mathbf{k}}\Delta_{\mathbf{p}}=|\Delta_{\mathbf{k}}||\Delta_{\mathbf{p}}|e^{il(\theta_k-\theta_p)}$, a change of variables, $\theta_+=\theta_k+\theta_p$ and $\theta_-=\theta_k-\theta_p$, is appropriate to apply. The function under integral $f(\theta_k,\theta_p)\sim e^{il(\theta_k-\theta_p)}V_{\mathbf{kp}}$ has a periodicity under translations for (multiples of) 2π of θ_k and of θ_p. After a short analysis of mappings, we can conclude

$$\begin{aligned}&\int_0^{2\pi}d\theta_k\int_0^{2\pi}d\theta_p f(\theta_k,\theta_p)\\&=\frac{1}{2}\int_0^{4\pi}d\theta_+\int_0^{2\pi}d\theta_- f(\theta_-)\\&=2\pi\int_0^{2\pi}d\theta_- f(\theta_-).\end{aligned} \tag{E23}$$

Therefore the ground-state energy density for a fixed angular momentum l instability, $\Delta^*_{\mathbf{k}} = |\Delta_{\mathbf{k}}|e^{il\theta_k}$, is

$$E_0^l = -\frac{1}{(2\pi)}\int dk\, k\frac{\mathcal{E}_k - (E_k-\mu)}{2} - \frac{1}{(2\pi)^2}\int_0^\infty dp\; p \times \int_0^\infty dk\; k\; V_{kp}^l \frac{|\Delta_{\mathbf{k}}|}{2\,\mathcal{E}_k}\frac{|\Delta_{\mathbf{p}}|}{2\,\mathcal{E}_p}, \tag{E24}$$

3. Proof of symmetry between $l = -1$ and 3 channels

The two pairing channels corresponding to $l = -1$ and 3 satisfy a symmetry relation

$$V_{kp}^{l=3}(m) = V_{kp}^{l=-1}(-m) \tag{E25}$$

and therefore the solutions for these two channels are equal up to a sign-flip of m. Here we present the proof of Eq. (E25).

First, we note that $E_k(m) = E_k(-m)$, as $E_k = \sqrt{k^2+m^2}$. Therefore E_k is an implicit function of $|m|$. For the sake of clarity, we introduce $A_{kp}(m) \equiv \frac{2\pi}{8E_kE_p}$ and $A_{kp}(m) = A_{kp}(-m)$. We also introduce $a \equiv E_k$ and $b \equiv E_p$. We focus here on the case $k < p$ but an analogous proof can be easily given for the case $k > p$,

$$V_{kp,k<p}^{l=3}(m) = A_{kp}(m)\Bigg[-2|m|\frac{k^3}{p^3} - \mathrm{sgn}(m)\frac{(a-m)(b-m)(a+b+2m)}{pk}\frac{k^2}{p^2}\Bigg]. \tag{E26}$$

We now separate the second term into parts which are even and odd with respect to m:

$$\begin{aligned}(a-m)(b-m)(a+b+2m) &= (ab-am-bm+m^2)(a+b+2m)\\ &= a^2b+b^2a+2mab-ma^2-mab-2m^2a-mab-mb^2-2m^2b+m^2a+m^2b+2m^3\\ &= a^2b+b^2a-m^2(a+b)-m(a^2+b^2-2m^2).\end{aligned} \tag{E27}$$

Now we perform a change of variables $\tilde{m} = -m$:

$$\begin{aligned}(a-m)(b-m)(a+b+2m) &= a^2b+b^2a-\tilde{m}^2(a+b)+\tilde{m}(a^2+b^2-2\tilde{m}^2)\\ &= (a-\tilde{m})(b-\tilde{m})(a+b+2\tilde{m})+2\tilde{m}(a^2+b^2-2\tilde{m}^2).\end{aligned} \tag{E28}$$

We now use $\mathrm{sgn}(x) = -\mathrm{sgn}(-x)$, and $\mathrm{sgn}(x)x = |x|$ to obtain

$$V_{kp,k<p}^{l=3}(-\tilde{m}) = A_{kp}(\tilde{m})\Bigg[-2|\tilde{m}|\frac{k^3}{p^3} + \mathrm{sgn}(\tilde{m})\frac{(a-\tilde{m})(b-\tilde{m})(a+b+2\tilde{m})}{pk}\frac{k^2}{p^2} + 2|\tilde{m}|\frac{a^2+b^2-2\tilde{m}^2}{kp}\frac{k^2}{p^2}\Bigg]. \tag{E29}$$

We rewrite the additional term using k, p, and $\tilde{m}$:

$$a^2+b^2-2\tilde{m}^2 = k^2+\tilde{m}^2+p^2+\tilde{m}^2-2\tilde{m}^2 = k^2+p^2 \tag{E30}$$

and

$$\frac{k^2+p^2}{kp}\frac{k^2}{p^2} = (k^2+p^2)\frac{k}{p^3} = \frac{k^3}{p^3}+\frac{k}{p}. \tag{E31}$$

The $\frac{k^3}{p^3}$ terms cancel and we finally obtain

$$V_{kp,k<p}^{l=3}(-\tilde{m}) = A_{kp}(\tilde{m})\Bigg[2|\tilde{m}|\frac{k}{p} + \mathrm{sgn}(\tilde{m})\frac{(a-\tilde{m})(b-\tilde{m})(a+b+2\tilde{m})}{pk}\frac{k^2}{p^2}\Bigg] = V_{kp,k<p}^{l=-1}(\tilde{m}). \tag{E32}$$

4. Numerical solution

We solve Eq. (E19) numerically, using the forward-substitution algorithm. We start from an initial guess for $|\Delta_k|$ (in practice $|\Delta_k| = 10^{-5}, \forall k$) and then recalculate it from the RHS of Eq. (E19) iteratively until it converges. We take as the criterion for convergence

$$\frac{\max_k\left|\Delta_k^{\mathrm{new}} - \Delta_k^{\mathrm{old}}\right|}{\max_k\left|\Delta_k^{\mathrm{new}}\right|} < 10^{-3}k_F. \tag{E33}$$

It takes 30–130 iterations to satisfy the convergence criterion. We keep $k_F = 1$ to set the unit.

We perform the integration on the RHS of Eq. (E19) using the trapezoid rule. The integrand function on the RHS is very sharply peaked around k_F. To properly resolve the integrand function, we discretize k using a logarithmic grid,

$$\tilde{k}_j = e^{a_{\min}+\frac{j}{N_k}(a_{\max}-a_{\min})}, \quad j \in [0, N_k) \tag{E34}$$

with $N_k = 500$, $a_{\min} = -30$, and $a_{\max} = 4$. The logarithmic grid is placed on both sides of k_F, to include all points given by

$$1 \pm \tilde{k}_j > 0.$$

We add the $k = 1$ point by hand. Therefore our grid can resolve peaks at k_F that have a width $\gtrsim e^{-30}$, which is near the limitation of double precision numeric type. The logarithmic grid is particularly important for the $l = 1$ case

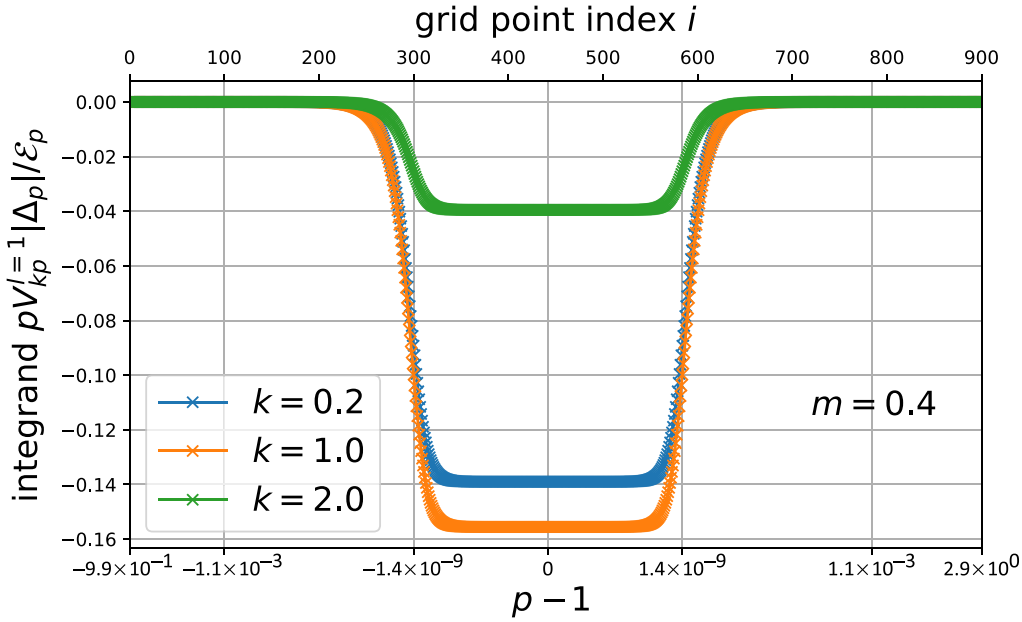

FIG. 2. Integrand function in the final iteration for $l=1$, $m=0.4$, and $k_F=1$. Examples are given for three different k. The sharp peak at k_F has a width $\sim 10^{-9}$ and is properly resolved using a logarithmic grid.

at low m, where the integrand is most sharply peaked. We illustrate our grid and the integrand function in Fig. 2. We have checked that the results do not depend on the numerical parameters.

[1] D. C. Tsui, H. L. Störmer, and A. C. Gossard, Phys. Rev. Lett. **48**, 1559 (1982).
[2] R. B. Laughlin, Phys. Rev. Lett. **50**, 1395 (1983).
[3] R. Willett, J. P. Eisenstein, H. L. Stormer, D. C. Tsui, A. C. Gossard, and J. H. English, Phys. Rev. Lett. **59**, 1776 (1987).
[4] G. Moore and N. Read, Nucl. Phys. B **360**, 362 (1991).
[5] S.-S. Lee, S. Ryu, C. Nayak, and M. P. A. Fisher, Phys. Rev. Lett. **99**, 236807 (2007).
[6] M. Levin, B. I. Halperin, and B. Rosenow, Phys. Rev. Lett. **99**, 236806 (2007).
[7] H. Wang, D. N. Sheng, and F. D. M. Haldane, Phys. Rev. B **80**, 241311(R) (2009).
[8] D. T. Son, Phys. Rev. X **5**, 031027 (2015).
[9] S. Kachru, M. Mulligan, G. Torroba, and H. Wang, Phys. Rev. B **92**, 235105 (2015).
[10] Z. Wang and S. Chakravarty, Phys. Rev. B **94**, 165138 (2016).
[11] M. V. Milovanović, Phys. Rev. B **95**, 235304 (2017).
[12] A. C. Balram, M. Barkeshli, and M. S. Rudner, Phys. Rev. B **98**, 035127 (2018).
[13] R. V. Mishmash, D. F. Mross, J. Alicea, and O. I. Motrunich, Phys. Rev. B **98**, 081107 (2018).
[14] P. T. Zucker and D. E. Feldman, Phys. Rev. Lett. **117**, 096802 (2016).
[15] M. Banerjee, M. Heiblum, V. Umansky, D. E. Feldman, Y. Oreg, and A. Stern, Nature **559**, 205 (2018).
[16] C. Wang, A. Vishwanath, and B. I. Halperin, Phys. Rev. B **98**, 045112 (2018).
[17] D. F. Mross, Y. Oreg, A. Stern, G. Margalit, and M. Heiblum, Phys. Rev. Lett. **121**, 026801 (2018).
[18] B. Lian and J. Wang, Phys. Rev. B **97**, 165124 (2018).
[19] B. I. Halperin, Journal Club for Condensed Matter Physics, December, 2017, https://www.condmatjclub.org.
[20] S. H. Simon, Phys. Rev. B **97**, 121406 (2018).
[21] D. E. Feldman, arXiv:1805.03204.
[22] T. Jolicoeur, Phys. Rev. Lett. **99**, 036805 (2007).
[23] M. Milovanovic and N. Read, Phys. Rev. B **53**, 13559 (1996).
[24] M. V. Milovanovic and T. Jolicoeur, Int. J. Mod. Phys. B **24**, 549 (2010).
[25] N. Read and D. Green, Phys. Rev. B **61**, 10267 (2000).
[26] A. Cappelli, L. S. Georgiev, and I. T. Todorov, Nucl. Phys. B **599**, 499 (2009).
[27] E. H. Rezayi and N. Read, Phys. Rev. Lett. **72**, 900 (1994).
[28] E. H. Rezayi and F. D. M. Haldane, Phys. Rev. Lett. **84**, 4685 (2000).
[29] A. C. Potter, M. Serbyn, and A. Vishwanath, Phys. Rev. X **6**, 031026 (2016).
[30] C. Wang, N. R. Cooper, B. I. Halperin, and A. Stern, Phys. Rev. X **7**, 031029 (2017).
[31] N. Read, Phys. Rev. Lett. **62**, 86 (1989).
[32] S.-C. Zhang, Int. J. Mod. Phys. B **6**, 25 (1992).
[33] B. I. Halperin, P. A. Lee, and N. Read, Phys. Rev. B **47**, 7312 (1993).
[34] F. Cai, Y. Yu, and Z. Wang, J. Phys.: Cond. Mat. **25**, 305601 (2013).
[35] M. Barkeshli, M. Mulligan, and M. P. A. Fisher, Phys. Rev. B **92**, 165125 (2015).
[36] M. Greiter, X. G. Wen, and F. Wilczek, Nucl. Phys. B **374**, 567 (1992).
[37] M. P. Zaletel, R. S. K. Mong, F. Pollmann, and E. H. Rezayi, Phys. Rev. B **91**, 045115 (2015).

[38] K. Prabhu and M. M. Roberts, arXiv:1709.02814.
[39] D. X. Nguyen, S. Golkar, M. M. Roberts, and D. T. Son, Phys. Rev. B **97**, 195314 (2018).
[40] A. C. Balram, Y.-H. Wu, G. J. Sreejith, A. Wojs, and J. K. Jain, Phys. Rev. Lett. **110**, 186801 (2013).
[41] S. Johri, Z. Papic, R. N. Bhatt, and P. Schmitteckert, Phys. Rev. B **89**, 115124 (2014).
[42] I. Sodemann and A. H. MacDonald, Phys. Rev. B **87**, 245425 (2013).
[43] S. Pu, M. Fremling, and J. K. Jain, Phys. Rev. B **98**, 075304 (2018).
[44] V. A. Miransky, G. W. Semenoff, I. A. Shovkovy, and L. C. R. Wijewardhana, Phys. Rev. D **64**, 025005 (2001).
[45] C. Manuel, Phys. Rev. D **53**, 5866 (1996).

Practical consequences of the Luttinger-Ward functional multivaluedness for cluster DMFT methods

J. Vučičević,[1,2] N. Wentzell,[1] M. Ferrero,[3,4] and O. Parcollet[1]

[1]*Institut de Physique Théorique (IPhT), CEA, CNRS, UMR 3681, 91191 Gif-sur-Yvette, France*

[2]*Scientific Computing Laboratory, Center for the Study of Complex Systems, Institute of Physics Belgrade, University of Belgrade, Pregrevica 118, 11080 Belgrade, Serbia*

[3]*Centre de Physique Théorique, Ecole Polytechnique,CNRS, Université Paris-Saclay, 91128 Palaiseau, France*

[4]*Collège de France, 11 place Marcelin Berthelot, 75005 Paris, France*

(Received 3 October 2017; revised manuscript received 7 February 2018; published 23 March 2018)

The Luttinger-Ward functional (LWF) has been a starting point for conserving approximations in many-body physics for 50 years. The recent discoveries of its multivaluedness and the associated divergence of the two-particle irreducible vertex function Γ have revealed an inherent limitation of this approach. Here we demonstrate how these undesirable properties of the LWF can lead to a failure of computational methods based on an approximation of the LWF. We apply the nested cluster scheme (NCS) to the Hubbard model and observe the existence of an additional stationary point of the self-consistent equations, associated with an unphysical branch of the LWF. In the strongly correlated regime, starting with the first divergence of Γ, this unphysical stationary point becomes attractive in the standard iterative technique used to solve DMFT. This leads to an incorrect solution, even in the large cluster size limit, for which we discuss diagnostics.

DOI: 10.1103/PhysRevB.97.125141

The Luttinger-Ward functional (LWF) Φ is a central object in the quantum many-body theory of strongly correlated fermionic systems. Φ [1] is defined as the interacting part of the Legendre transform of the free energy with respect to the bare propagator G_0 [2]. It is a functional of the full propagator G, formally equal to the sum of all vacuum skeleton diagrams [3,4]. Φ has been the basis of many approximations in the field over the last decades.

Dynamical mean-field theory (DMFT) [5,6] and its cluster extensions [7–10] are a class of Φ-derivable approximations with a systematic control parameter: the size N_c of the cluster. They interpolate between DMFT ($N_c = 1$) and the exact solution of the lattice model for $N_c = \infty$. Cluster methods allow to treat the Mott physics à la DMFT and to include short-range spatial correlations. They have led to significant progress in recent years, in particular on the Hubbard model [11–58]. Cluster DMFT methods are formulated in terms of one (or a few) auxiliary quantum impurity models in a noninteracting bath encoded in the bare propagator $\mathcal{G}$. The bath is determined self-consistently in such a way that the impurity Green function G^{imp} coincides with some (local) components of the Green function of the lattice model G^{latt}. This *representability* property, i.e., the possibility to find $\mathcal{G}$ for a given G^{imp} in a quantum impurity model lies at the very heart of DMFT methods [6,59].

Surprisingly, it was recently discovered [60–62] in simple strongly correlated models that the functional $\Phi[G]$ is in fact multivalued, i.e., has multiple branches. As a consequence, the relation $G[\mathcal{G}]$ cannot always be inverted in quantum impurity models as several $\mathcal{G}$ yield the same Green function G. This has deep consequences for numerical methods in some parameter regimes. The crossing of two branches of Φ leads to divergence of the two-particle irreducible vertex Γ [61,63–66] and therefore the breakdown of the parquet decomposition [65,67,68]. Moreover, at strong coupling, the bold diagrammatic series can converge to an incorrect result, as was checked explicitly using a bold quantum Monte Carlo algorithm [60]. Similar pathological behavior was observed in the context of GW-like approximations of Φ [69].

In this paper, we show that the multivaluedness of Φ has unexpected and severe consequences in certain cluster DMFT methods, and can potentially lead to incorrect results. Concretely, we study the *nested cluster* DMFT scheme (NCS) [5,52,70], which is an early example of the recently introduced self-energy embedding theory (SEET) [71–75]. NCS is a particularly interesting scheme since it addresses the main drawbacks of the most widely used cluster methods: cellular DMFT (CDMFT) [9] and the dynamical cluster approximation (DCA) [7]. It is a real-space cluster method which is translationally invariant (unlike CDMFT) and yields a continuous self-energy in reciprocal space (unlike DCA). In the classical limit, it reduces to the well-known Bethe-Kikuchi method of classical statistical physics [5,52].

We solve the NCS for the Hubbard model and compare it to benchmarks established with converged large DCA clusters. At weak to moderate couplings the scheme is stable and performs very well. Even at strong coupling, there is a physical solution, which is very close to the benchmarks already at moderate cluster size. However, (i) in the standard iterative method used to solve the DMFT equations, this solution is unstable towards an unphysical solution characterized by a noncausal Weiss field; (ii) as the cluster size increases, this stable unphysical solution converges to an incorrect result; and (iii) this occurs in the strong-coupling regime as delimited by the generalization of the divergences of the irreducible vertex observed in Refs. [61–65,76,77].

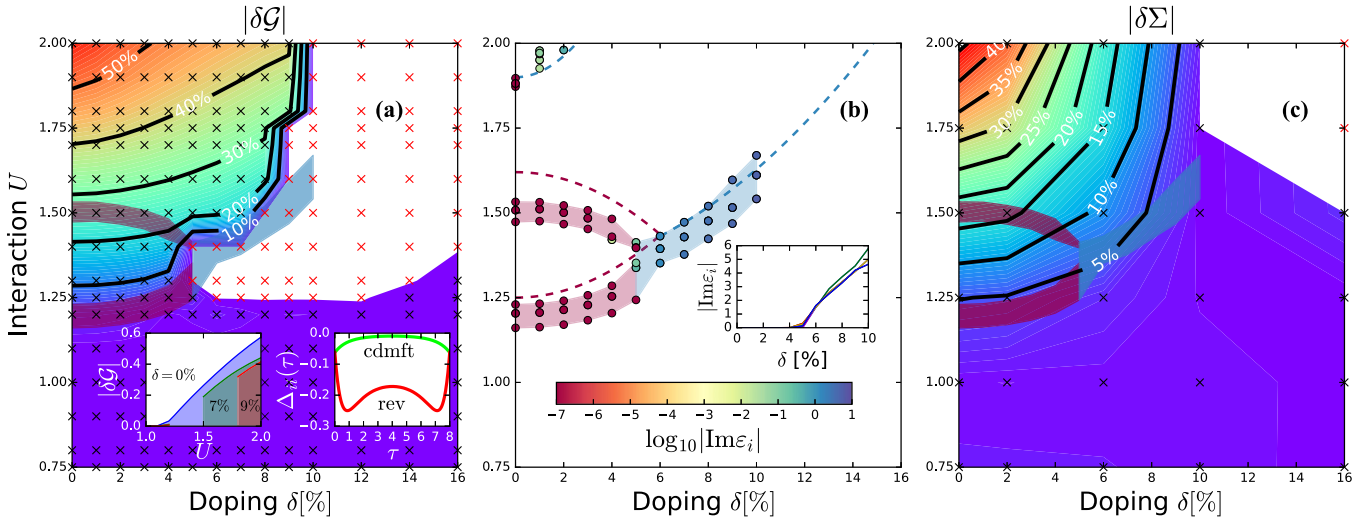

FIG. 1. For all panels, the temperature is $T/D = 0.125$. (a) Color plot of $|\delta\mathcal{G}| \equiv |\mathcal{G}_{00}^{\mathrm{cdmft}}(i\omega_0) - \mathcal{G}_{00}^{\mathrm{rev}}(i\omega_0)|/|\mathcal{G}_{00}^{\mathrm{cdmft}}(i\omega_0)|$; black crosses are data points, red crosses are points where the reverse impurity solver does not converge. (Left inset) Slices for fixed doping, showing discontinuity vs U for $\delta = 7\%$ and 9%. (Right inset) Hybridization (local) of $\mathcal{G}^{\mathrm{cdmft}}$ (top, green) and $\mathcal{G}^{\mathrm{rev}}$ (bottom, red), for $U = 2$ and $\delta = 0$ showing its causality violation. (b) Vertex divergences, where the real part of an eigenvalue ε_i of $\tilde{\chi}_c^{\Omega=0}$ crosses zero for single-site DMFT (dashed line) and 2×2 CDMFT (colored circles). Color encodes $\mathrm{Im}\,\varepsilon_i$ at the given point; colored stripes are guides for the eyes. (Inset) $\mathrm{Im}\,\varepsilon_i$ vs doping for the bottom two groups of circles for 2×2 CDMFT. (c) Color plot of $|\delta\Sigma| \equiv |\mathrm{Im}\,\Sigma_{00}^{\mathrm{cdmft}}(i\omega_0) - \mathrm{Im}\,\Sigma_{00}^{\mathrm{nested}}(i\omega_0)|/|\mathrm{Im}\,\Sigma_{00}^{\mathrm{cdmft}}(i\omega_0)|$, i.e., the difference between the imaginary part of the local self-energy for 2×2 NCS and the 2×2 CDMFT (the latter is close to the exact solution, see Appendix A 1 and Fig. 3).

We consider the Hubbard model on a square lattice:

$$H = -t \sum_{\langle ij\rangle\sigma} c_{i\sigma}^{\dagger} c_{j\sigma} - \mu \sum_{i\sigma} n_{i\sigma} + U \sum_{i} n_{i\uparrow} n_{i\downarrow}, \qquad (1)$$

where $c_{i\sigma}^{\dagger}$ creates a fermion with spin σ at site i. The density operator is $n_{i\sigma} = c_{i\sigma}^{\dagger} c_{i\sigma}$. The nearest-neighbor hopping amplitude is t, the on-site interaction U and the chemical potential μ. $D = 4t$ is the unit of energy. We use the CT-INT algorithm to solve the quantum impurity model [78,79].

Let us first address the representability issue of the Green function G by a Weiss field $\mathcal{G}$ in a cluster impurity model. We consider a 2×2 CDMFT calculation for $T/D = 0.125$ and various U and dopings δ, where it yields a quantitatively good solution as compared to converged large cluster DCA benchmarks (see Fig. 3). The CDMFT self-consistency equation reads [9] $G^{\mathrm{imp}}[\mathcal{G}] = G^{\mathrm{loc}}[\mathcal{G}]$ with

$$G^{\mathrm{loc}}[\mathcal{G}](i\omega_n) \equiv \sum_{k\in\mathrm{RBZ}} (i\omega_n + \mu - \hat{\epsilon}_k - \Sigma^{\mathrm{imp}}[\mathcal{G}](i\omega_n))^{-1},$$

where $\hat{\epsilon}_k$ is the dispersion over the superlattice of clusters, RBZ is the reduced Brillouin zone and Σ^{imp} (resp. G^{imp}) is the impurity cluster self-energy (respectively, Green function). The CDMFT equations are solved with the usual iterative technique for DMFT; given $\mathcal{G}^{(i)}$ at iteration i, the impurity model yields $\Sigma^{\mathrm{imp}}[\mathcal{G}^{(i)}]$ and the next iteration $\mathcal{G}^{(i+1)}$ is given by

$$\mathcal{G}^{(i+1)} = (G^{\mathrm{loc}}[\mathcal{G}^{(i)}]^{-1} + \Sigma^{\mathrm{imp}}[\mathcal{G}^{(i)}])^{-1}. \qquad (2)$$

Starting from the converged CDMFT solution G^{cdmft} we then implement a *reverse quantum impurity solver* [60]: we seek a bare propagator $\mathcal{G}^{\mathrm{rev}}$ of the cluster model such that $G^{\mathrm{imp}}[\mathcal{G}^{\mathrm{rev}}] = G^{\mathrm{cdmft}}$, with a similar iterative method as in Eq. (2) but with $G^{\mathrm{loc}}[\mathcal{G}^{(i)}]$ replaced by G^{cdmft}, which remains fixed in the calculation.

In Fig. 1(a), we present the relative difference between the local component of the converged CDMFT Weiss field $\mathcal{G}^{\mathrm{cdmft}}$ and the result of the reverse impurity solver $\mathcal{G}^{\mathrm{rev}}$. We observe three regions. At weak coupling, the reverse impurity solver yields $\mathcal{G}^{\mathrm{cdmft}}$ as naively expected. At strong coupling and high doping, the reverse solver does not converge. At strong coupling and low doping, $\mathcal{G}^{\mathrm{rev}}$ progressively deviates from $\mathcal{G}^{\mathrm{cdmft}}$, even though they both yield the exact same Green function G^{cdmft}. As soon as $\mathcal{G}^{\mathrm{rev}}$ is different from $\mathcal{G}^{\mathrm{cdmft}}$ it acquires a noncausal hybridization function Δ [80] as shown in the inset of Fig. 1(a). Indeed, $\Delta(\tau)$ is not concave over the full $[0,\beta]$ interval and therefore has a corresponding spectral function with negative parts. This calculation demonstrates the existence of multiple branches of Φ for the 2×2 impurity problem by exhibiting explicitly two $\mathcal{G}$ (and hence Σ) giving the same G, see also Refs. [60,61,63–65,77]. We will see below that a similar phenomenon occurs in NCS.

It is interesting to note that in the reverse impurity calculation at low doping $\delta < 5\%$, one first finds $\mathcal{G}^{\mathrm{rev}} = \mathcal{G}^{\mathrm{cdmft}}$ for small interactions $U < 1.25$ and then *continuously* switches to an unphysical solution for $\mathcal{G}$ as U is increased. This means that the physical branch of Φ crosses the unphysical branch. As has been discussed in the particle-hole symmetric case [61], this crossing has to be accompanied by a divergence of the corresponding two-particle irreducible vertex function Γ, since it is the second derivative of Φ with respect to G. We generalize the results of Refs. [63–65] to the doped case and map these divergences of Γ in the 2×2 CDMFT case, to obtain a characterization of the strong-coupling region, which is not linked to the details of an iterative algorithm. Given the two-particle propagator

$G^{\omega\omega'\Omega}_{2,\sigma\sigma',ijkl} = \frac{1}{\beta}\langle c^\dagger_{i,\sigma}(\omega)c_{j,\sigma}(\omega+\Omega)c^\dagger_{k,\sigma'}(\omega'+\Omega)c_{l,\sigma'}(\omega')\rangle$ and the single-particle Green function G, Γ can be calculated with the inverse Bethe-Salpeter equation

$$\Gamma^{\omega,\omega',\Omega}_{c,ijkl} = \beta^2\left[\left[\chi_0^\Omega\right]^{-1} - \left[\tilde{\chi}_c^\Omega\right]^{-1}\right]_{ij\omega,kl\omega'}, \tag{3}$$

where $\chi^{\omega\omega'\Omega}_{0,ijkl} = -G_{li}(i\omega)G_{jk}(i\omega+i\Omega)\beta\delta_{\omega,\omega'}$, and $\tilde{\chi}^{\omega\omega'\Omega}_{c,ijkl} = G^{\omega\omega'\Omega}_{2,\uparrow\uparrow,ijkl} + G^{\omega\omega'\Omega}_{2,\uparrow\downarrow,ijkl} - 2G_{ji}(\omega)G_{lk}(\omega')\beta\delta_{\Omega,0}$. The inverse is assumed to be in combined indices $(ij\omega)$ and $(lk\omega')$, where ω,ω' denote fermionic and Ω bosonic Matsubara frequencies. If $\tilde{\chi}_c(i\Omega)$ as a matrix has an eigenvalue $\varepsilon_i = 0$, it is singular and Γ diverges at the given $i\Omega$. While in single-site DMFT at particle-hole symmetry, the eigenvalues of $\tilde{\chi}_c(i\Omega = 0)$ are purely real by symmetry, it is no longer necessarily true here [65].

Figure 1(b) shows trajectories in the (δ,U) plane where the real part of an eigenvalue of $\tilde{\chi}_c$ crosses zero for single-site DMFT and 2×2 CDMFT. In single-site DMFT, at half-filling, there are three Γ divergences in the examined range of interaction, in agreement with Ref. [64]. As we go to finite doping, the divergence close to $U = 1.8$ disappears immediately as the corresponding eigenvalue acquires an imaginary part. However, the divergences close to $U = 1.2$ and 1.5 extend up to $\delta \simeq 5\%$ where they merge. For higher doping, the divergences disappear because the corresponding eigenvalues acquire an imaginary part. In CDMFT, the behavior is very similar except that each divergence is split into four, the two middle ones occurring simultaneously. Hence we conjecture (see also Refs. [61,63–65]) that the divergences in Γ are not an artifact of the single-site model but rather survive and multiply in the cluster impurity model. Finally, in the left inset of Fig. 1(a), we see that for $\delta \geqslant 6\%$, the unphysical solution appears discontinuously when U is increased, in agreement with the absence of a divergence in Γ.

Let us now turn to the NCS. It approximates Φ by $\Phi^{(L)}$, defined as its restriction to the set of real-space two particle irreducible (2PI) diagrams that involve lattice points lying within a box of shape $L\times L$. $\Phi^{(L)}$ can be expressed as a linear combination of the LWFs $\Phi_{L\times L}$ of a $L\times L$ cluster and the LWF of its subclusters, with appropriate weights that eliminate the double counting of diagrams. Each cluster LWF is associated to an impurity model, via the representability property. The lattice self-energy Σ^{latt} is therefore a linear combination of the self-energies of the impurities. This couples the impurity models together and the baths adjust so that, e.g., the impurity Green function is the same for every site of every cluster. This method was introduced for a two site cluster (a dimer) in Ref. [70], see also Refs. [5,52,81].

A priori, solving large nested clusters seems like a daunting task, requiring to solve a large number of coupled impurity problems, one for every subcluster of the $L\times L$ cluster. However, as shown in Appendix C 2, it is sufficient to solve only *four* coupled clusters since

$$\Phi^{(L)}[G] = \sum_i \Phi_{L\times L}\left[G|_{C_i^{L\times L}}\right] - \Phi_{L-1\times L}\left[G|_{C_i^{L-1\times L}}\right] - \Phi_{L\times L-1}\left[G|_{C_i^{L\times L-1}}\right] + \Phi_{L-1\times L-1}\left[G|_{C_i^{L-1\times L-1}}\right], \tag{4}$$

where $C_i^{n\times p}$ is the cluster of shape $n\times p$ whose bottom-left lattice point is i, and $G|_{C_i^{n\times p}}$ the restriction of the Green function to this cluster (i.e., the set $\{G_{lm}\}_{l,m\in C_i^{n\times p}}$). If we assume rotational invariance, the last two terms give the same contribution and the method can be solved using three coupled cluster impurity models. We present the full formalism for the NCS with several examples in Appendix C.

We solve the NCS using the standard iterative method of solution for DMFT equations as in Eq. (2). At weak coupling, the NCS yields a solution in excellent agreement with large DCA cluster benchmarks (see Fig. 3). However, at strong coupling the situation is more complex. First, in Fig. 1(c), we observe that the 2×2 NCS gives a poor result compared to CDMFT in the strong-coupling region delimited by the divergences of Γ discussed above. We then solve larger clusters $L = 2$, 3, 4, and 6 to examine the convergence of the method with the cluster size. We observe an unexpected and severe problem: *the nested cluster scheme converges for $L\to\infty$ but to an incorrect solution* even though formally $\Phi^{(L)} \xrightarrow{L\to\infty} \Phi$. In Fig. 2(a) and Appendix A 4 we show the momentum dependent self-energies obtained for $L = 4$ and 6; they are very close to each other, indicating convergence, but quite far from the benchmarks.

To gain further insight, we study the convergence of the $L = 4$ case at strong coupling iteration by iteration. In Fig. 2(b), we plot the difference between successive G_{loc} for $U/D = 1$ and $U/D = 2, \delta = 0$. At $U/D = 1$ convergence is roughly exponential until the level of Monte-Carlo noise is reached. However, for $U/D = 2$, we observe that the self-consistency is almost converged after three iterations [the green point on Fig. 2(b)] to an unstable solution before finally converging to another solution of the equation (red point). Remarkably, in Fig. 2(a), we see that this unstable (green) solution is almost perfectly on top of the benchmark, contrary to the stable (red) one.

Furthermore, we observe two pathologies of the stable (red) solution, which can be used as diagnostics in the absence of benchmarks. First, the inset of Fig. 2(b) shows the local hybridization function of both solutions (at the corner of the $L\times L$ cluster), Δ_{stable} and Δ_{unstable}. Δ_{stable} clearly violates causality at $U/D = 2$, similarly to the reverse impurity solver studied above, while Δ_{unstable} is fine. Moreover, we see in Fig. 2(c) that this effect appears as a function of U for $U > 1.2$, i.e., exactly when the solution deviates from the benchmark (or CDMFT in this case). Second, the Δ_{stable} bath does not decay in the large L limit at strong coupling ($U/D = 2$), contrary to $U/D = 1$, as illustrated in the inset of Fig. 2(a). Contrary to CDMFT or DCA, the NCS does not impose $\Delta = 0$ for every converged solution for $L\to\infty$, but only the weaker condition $\Sigma^{\text{latt}} = \Sigma^{\text{imp}} + \Delta$ (see Appendix A 4 and Fig. 8 for further discussion). For the physical solution, we conjecture that $\Delta\to 0$ for $L\to\infty$: the large cluster will be a Hubbard model with no bath. The unphysical solution converges on the other hand to a certain resummation of the bold diagrams series.

For CDMFT and DCA, the standard iterative method of solution is *iteratively causal* [7,9], i.e., one can prove that the bath stays causal at each iteration (and therefore at convergence). Hence the causality violation of the bath cannot occur and the solution stays on the physical branch. The NCS does

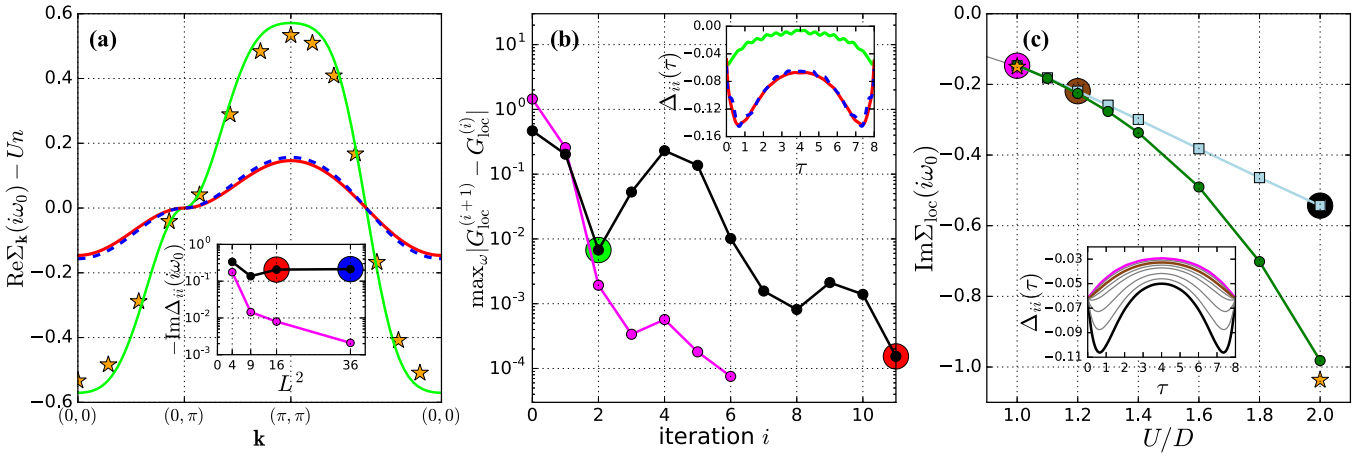

FIG. 2. (a) Real part of $\Sigma_{\mathbf{k}}(i\omega_0) - Un$ vs momentum $\mathbf{k}$, in NCS for $L = 4$ (solid line, red), $L = 6$ (dashed line, blue); unstable solution at the third iteration for $L = 4$ (solid line, green); the stars denote 98 sites DCA results. (Inset) Hybridization at the center of the $L \times L$ cluster at the first Matsubara frequency vs L for $U/D = 2$ (circles, black), and $U/D = 1$ (circles, magenta). (b) Norm of the difference of G_{loc} between iterations vs the iteration number i, for $L = 4$, $U/D = 2$ (circles, black), and $U/D = 1$ (circles, magenta). Green (resp. red) dot corresponds to the unstable (respectively, stable) solution, cf. text. (Inset) Hybridization at the corner of the $L \times L$ cluster vs τ for the unstable and the stable noncausal solution, with same convention as in (a). (c) Im $\Sigma_{\text{loc}}(i\omega_0)$ vs U/D for NCS $L = 2$ (square, blue online) and 2×2 CDMFT, (circle, green online). The star is 98 sites DCA. (Inset) Local hybridization for $L = 2$ vs τ.

not have this property, which, as we have seen, has drastic consequences on the stability of the physical solution in the iterative procedure. In the dimer case, NCS was already known to yield noncausal self-energies at low temperatures and strong coupling [5,70]. However, in previous works [52,82], this was simply interpreted as the signature of an insufficiently large cluster, i.e., a defect that the large L should cure.

To summarize, the nested cluster is a translationally invariant, real-space cluster method with a physical solution very close to numerically exact benchmarks already at moderate cluster sizes, both at weak and strong coupling. However, the multivaluedness of the LWF leads to an instability of the standard iterative procedure of solution in the strong-coupling region (as delimited by the divergence of the irreducible vertex Γ) towards an unphysical solution, even in the infinite cluster limit. This failure is signaled by causality violations of the hybridization function. All this points to the importance of distinguishing between a cluster method and the iterative procedure used to solve its equations. An important challenge is therefore to design new ways of solving the cluster DMFT equations that are guaranteed to stay on the physical branch of the LWF and stabilize the "hidden" physical solution, e.g., by implementing the "shifted-action" [83] proposal in this context. Alternatively, one can use cluster methods based on higher-order functionals (TRILEX [54,56,57], QUADRILEX [55]). We believe these are less likely to be multivalued, as it would require the existence of two systems with identical single-particle but also higher-order correlation functions, which is *a priori* harder to achieve. Moreover, going to higher-order functionals would correspond to adding more degrees of freedom to the solution, which in itself could remove the multivaluedness.

We are grateful to A. Georges and P. Thunström for useful insights and discussion. We further thank T. Schäfer and A. Toschi for critical reading of the manuscript. The DCA 98A and 50A data was provided by J. Leblanc. We thank Z. Mitrović Vučičević for figure editing. This work is supported by the FP7/ERC, under Grant Agreement No. 278472-MottMetals (J.V., N.W.) and by the Simons Foundation within the Many Electron Collaboration (N.W.). Part of this work was performed using HPC resources from GENCI-TGCC (Grant No. 2016-t2016056112). The CT-INT algorithm has been implemented using the TRIQS toolbox [84].

APPENDIX A: BENCHMARKS

In this section, we present results for various cluster DMFT methods applied to the two-dimensional square-lattice Hubbard model as introduced in the main text. We pay special attention to the nested cluster scheme (NCS), which is discussed in detail in Appendix C. Detailed summary of other cluster DMFT methods is provided in Appendix D.

We first present an extensive benchmark against exact results (Appendix A 1), which we use in the main text to determine the quality of solutions and to identify problematic regimes. We then address in particular the causality violations in the problematic region (subsection A 2). In Appendix A 3, we provide a comparison between two variants of the nested cluster scheme, differing in the nested quantity (self-energy versus cumulant). In Appendix A 4, we discuss the stable and unstable solution of the nested equations.

1. Comparison against exact results

In Fig. 3, we show the results of cluster DMFT methods for the Hubbard model, at various cluster sizes, in the four corners and the center of the phase diagram examined in the main text. The temperature is $T/D = 0.125$. At half-filling, $\text{Re}\,\Sigma_{\text{loc}}(i\omega_n) = U/2$ by symmetry, so we omit this data. The nonlocal part $\tilde{\Sigma}_{\mathbf{k}}(i\omega_n) = \Sigma_{\mathbf{k}}(i\omega_n) - \Sigma_{\text{loc}}(i\omega_n)$ we present at the lowest Matsubara frequency, along a triangular path enclosing the irreducible Brillouin zone. With stars we denote the best available result: at half-filling, we have DCA

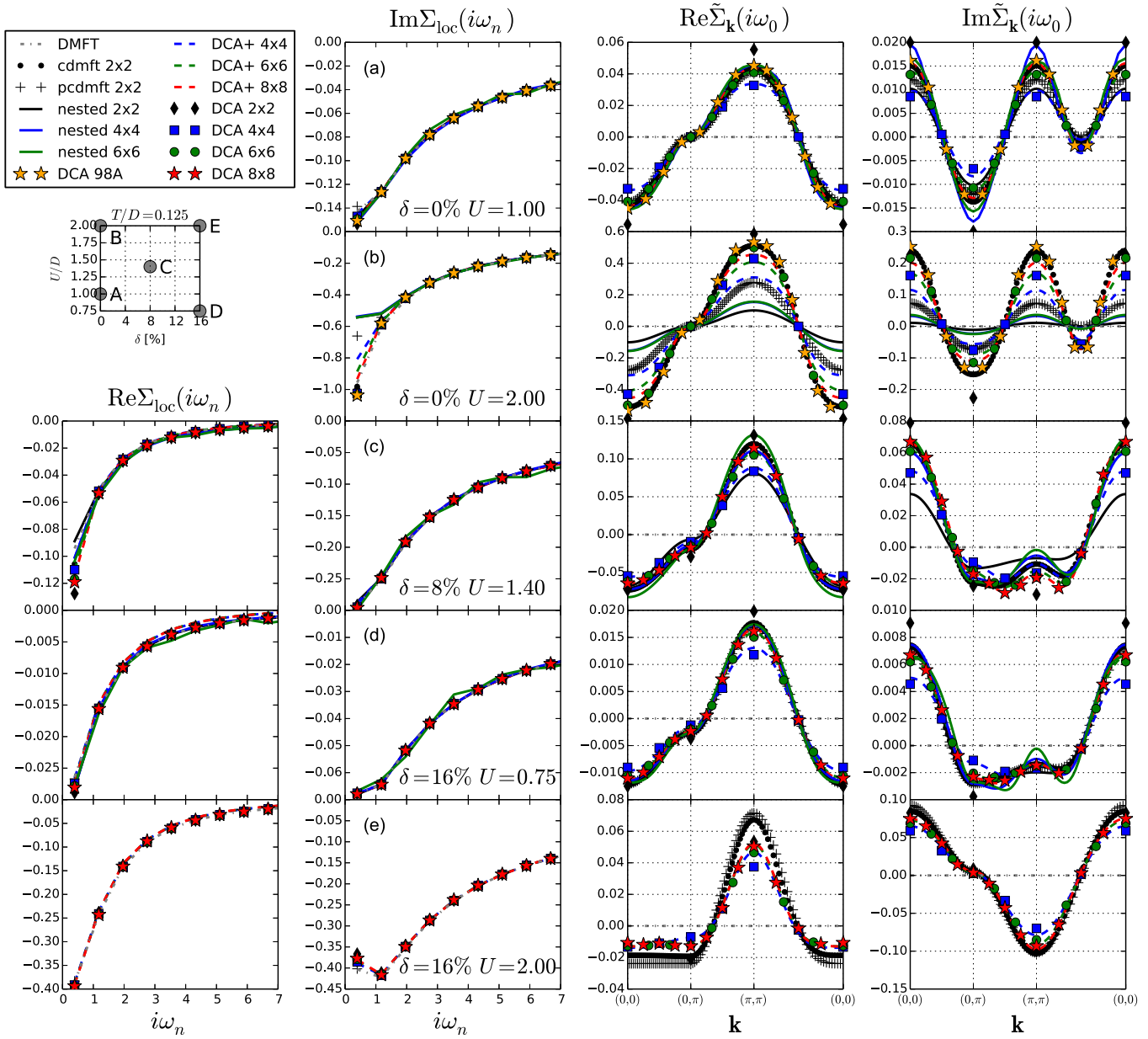

FIG. 3. Benchmark of DMFT and various cluster DMFT methods. Hubbard model square lattice, temperature $T/D = 0.125$. We present separately the local and the nonlocal parts of self-energy, $\tilde{\Sigma}_{\mathbf{k}} = \Sigma_{\mathbf{k}} - \Sigma_{\mathrm{loc}}$. Color denotes cluster size, symbols/line styles different methods. Stars denote the best available result. Agreement is excellent in all points except point B: NCS converges to a wrong solution, PCDMFT 2×2 is considerably worse than in other points, and DCA$^+$ converges very slowly with cluster size, while being a poor approximation at small cluster size. In other points, NCS 4×4 performs well, but at 6×6 amplification of statistical noise becomes a problem (see text for details).

$N_c = 98$, and away from half-filling, the biggest cluster is 8×8 ($N_c = 64$). These results are converged with respect to cluster size, and can be considered exact solutions of the Hubbard model.

The presented CDMFT result is the self-energy periodized by Eq. (D17) (in Appendix D 2 below). In DCA, we are showing only the values at coarse-grained wave vectors $\mathbf{K}$ (see Appendix D 4).

We first concentrate on the points other than point B. We see excellent agreement of all methods. The local part is captured correctly already at 2×2 cluster size. DCA typically overestimates the amount of $\mathbf{k}$ dependence at 2×2, then underestimates it at 4×4, and is mostly converged at 6×6. DCA$^+$ has a similar behavior (2×2 not shown for the sake of clarity). CDMFT and PCDMFT give almost the same result, and are on top of the benchmark except for the real nonlocal part in point E, where the overall shape is correct, but the amplitude is overestimated slightly; PCDMFT also noticeably misses the local imaginary part in point A. Nested cluster performs well, and at 4×4 cluster size is even more accurate than DCA around $\mathbf{k} = (0,0)$. In point E, it does not converge at any cluster size. Away from half-filling and at cluster size 6×6, statistical noise amplification in nested cluster becomes significant (see Appenidx C 1 b for details). It is particularly noticeable in the local part of self-energy at high Matsubara frequencies, in points C and D. Also in these points, there is a

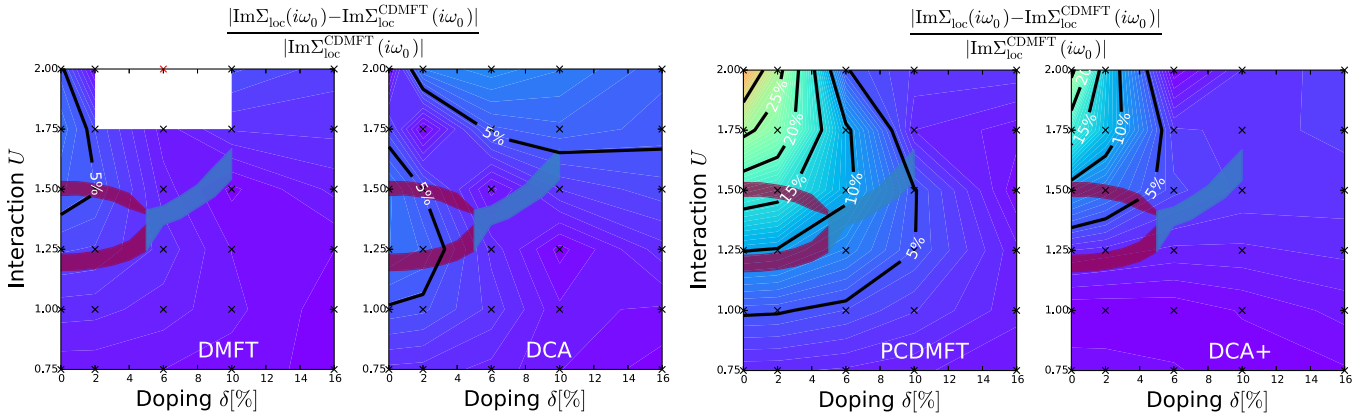

FIG. 4. Hubbard model, square lattice, temperature $T/D = 0.125$. Relative difference in $\mathrm{Im}\,\Sigma_{\mathrm{loc}}$ from the reference method (CDMFT 2×2). DCA, PCDMFT, and DCA$^+$ clusters are 2×2. The red and blue stripes are the Γ divergence trajectories from CDMFT 2×2 calculation [Fig. 1(b) in main text). In DCA and DMFT, performance is uniform across the phase diagram and appears unrelated to the divergence trajectories. In PCDMFT and DCA$^+$, the result is considerably poorer in the region roughly bounded by the divergence trajectories.

peaklike feature around $\mathbf{k} = (\pi,\pi)$ in the nonlocal imaginary part. It comes from the numerous long distance self-energy components, which are small and comparable to the statistical error bar. These fine details of the solution can not be perfectly converged due to the statistical noise.

Now we turn to point B. CDMFT 2×2 is, again, on top of the benchmark. DCA behaves no differently than in other points, and is almost converged at 6×6; the local part is correct already at 2×2. On the other hand, DCA$^+$ is not on top of the benchmark even at 8×8, and especially the local part is strongly underestimated: at 8×8, it is still worse than single-site DMFT. The nonlocal part is underestimated as well: the 6×6 calculation is comparable to DCA 4×4. PCDMFT, similarly, underestimates both the local and nonlocal part. Nested cluster converges to a wrong solution with respect to N_c: the local part is indistinguishable already between 2×2 and 4×4, and the nonlocal part between 4×4 and 6×6. The local part is underestimated by about 50%, and imaginary nonlocal part by almost an order of magnitude. The failure of PCDMFT, NCS, and DCA$^+$ in this particular point is strongly reminiscent of the failure of bold-diagrammatic QMC presented in Ref. [60], for the same model parameters: the self-energy obtained in these methods is more metallic and much more local than the exact solution. We note that the similar phenomenon can also be observed in the original DCA$^+$ paper [48]—in the strongly coupled regime, the $N_c = 16$ DCA$^+$ self-energy result is much more local and metallic than that of the DCA at the same cluster size.

In conclusion, in this phase diagram, the best performing 2×2 method is CDMFT. We take it as a reference method for benchmarking on a denser (δ,U) grid [Fig. 1(c) in the main text, and Fig. 4 below]. At 4×4 cluster size, in the points where it works, NCS does have an advantage over CDMFT and DCA. DCA 4×4 coarse-graining is still quite crude—due to symmetries of the lattice, it yields only six independent self-energy components; NCS at the same size yields ten independent self-energy components, and captures longer distance processes. In DCA, interpretation of the results in real space is problematic; NCS results can be looked at in both **r** and **k** space. CDMFT is also problematic at 4×4. At this size, both the translational symmetry and the homogeneity within a supercell are broken, and the periodization becomes even less straight-forward. Finally, we note that in pointB, even though NCS fails with forward substitution algorithm, there still appears to be a stationary point of the NCS equations (Fig. 2 in main text), which is in better agreement with the exact result than DCA at the same cluster size.

We finalize our analysis by a high-resolution benchmark of DMFT and 2×2 cluster methods (DCA, DCA$^+$, and PCDMFT), analogous to Fig. 1(c) in the main text. In Fig. 4, we present the deviation from the exact result of these methods. DMFT and DCA perform uniformly well across the phase diagram, and are at most $\approx$5% away from the correct result. No features can be associated with the Γ divergence trajectories. On the other hand, NCS, DCA$^+$ and PCDMFT all fail in similarly shaped regions around point B, but give good results in other regimes. In DCA$^+$ and PCDMFT the coincidence of the problematic region with the Γ-divergence trajectories is less conclusive, but we can similarly connect the failure with the noncausality of the hybridization function. It is, however, unclear whether a correct stationary point is present in these methods at all.

2. Causality properties

In this section, we analyze the causality properties of various quantities in the cluster methods presented above. Quantities like Green's functions, self-energies, and hybridization baths should have Lehmann spectral representation. The diagonal components of these quantities, should satisfy in real frequency

$$\mathrm{Im}X_{ii}(\omega) < 0, \tag{A1}$$

where X stands for G, Σ, $\mathcal{G}$, or Δ. This has implications for the shape of these objects in imaginary time:

$$X_{ii}(\tau) = \frac{1}{\pi}\int d\omega \frac{e^{-\tau\omega}}{1+e^{-\beta\omega}}\mathrm{Im}X_{ii}(\omega), \tag{A2a}$$

$$\partial_\tau^{2n} X_{ii}(\tau) = \frac{1}{\pi}\int d\omega \frac{\omega^{2n}e^{-\tau\omega}}{1+e^{-\beta\omega}}\mathrm{Im}X_{ii}(\omega). < 0, \quad n \in \mathbb{N} \tag{A2b}$$

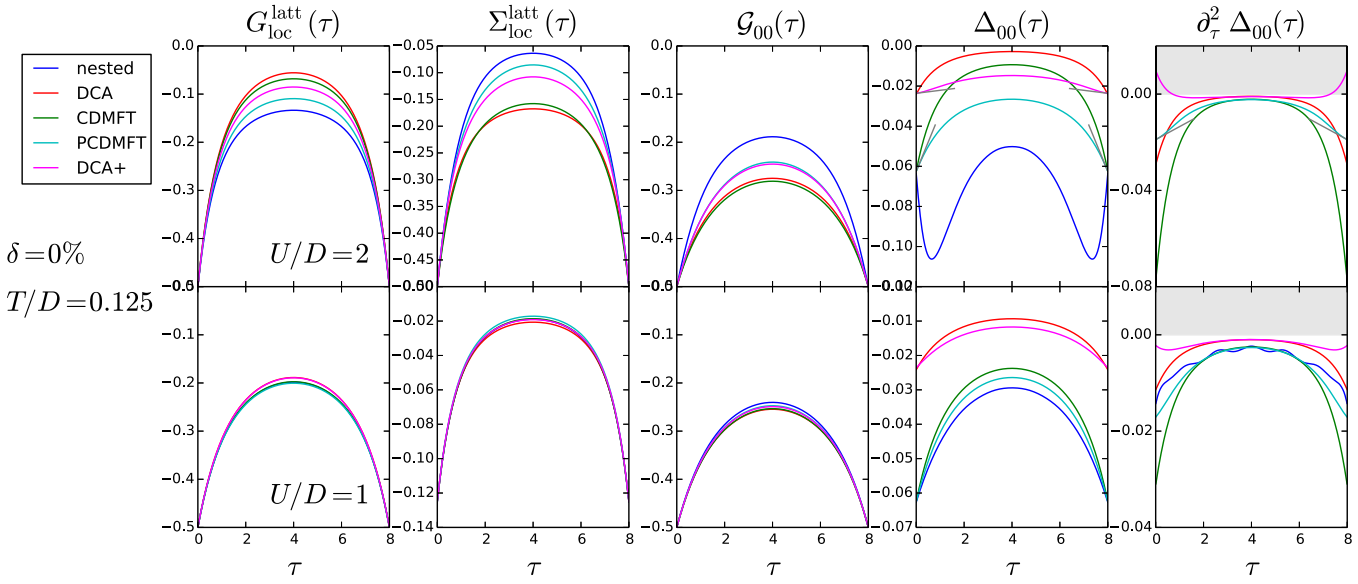

FIG. 5. Causality analysis of relevant quantities, in various cluster methods at 2×2 cluster size. Temperature $T/D = 0.125$, square lattice. At strong coupling, DCA$^+$ and NCS have pronounced inflection points in $\Delta(\tau)$, PCDMFT in the second derivative of $\Delta(\tau)$. Gray lines extrapolate the linear component close to $\tau = 0$ and β. Other quantities are all causal, including the bare propagator on the impurity. Increasing the cluster size in DCA$^+$ improves the causality in Δ, but not in NCS. In the upper right panel, NCS result is omitted for the sake of clarity [the noncausality is already obvious in $\Delta_{00}(\tau)$].

All even-order derivatives with respect to τ must be negative. This rules out the appearance of inflection points in $X_{ii}(\tau)$ and any of its even-order derivatives.

In Fig. 5, we present the results for the local G, Σ on the lattice, as well as the diagonal components of the bare propagator $\mathcal{G}$ and the hybridization function Δ on the impurity, all in imaginary time. All methods used are at 2×2 cluster size. In NCS we present the impurity quantities only for the biggest cluster. In all methods at 2×2, all the diagonal components of $\mathcal{G}$ and Δ are the same by symmetry (in DCA/DCA$^+$ this holds at any cluster size).

We see that all the quantities except the hybridization bath are causal. At $U/D = 1$, there is a slight violation of (A2b) in the second derivative of Δ in NCS, PCDMFT and DCA$^+$, but it is a tiny effect. In this regime, small fluctuations in the noncausal direction do not cause problems for these methods and the result is correct. However, it is clear that these methods do not impose causality on the hybridization function strictly, which then leads to problems at strong coupling. At $U/D = 2$, we see a strong violation of (A2b) in NCS, a clear inflection point in $\Delta(\tau)$ in DCA$^+$, and in PCDMFT there is an inflection point in $\partial^2_\tau \Delta(\tau)$. Here we observe a similar trend in DCA$^+$, NCS and PCDMFT: $\Delta_{00}(\tau \sim \beta/2)$ is generically overestimated (by absolute value) with respect to DCA and CDMFT, respectively (note that the difference in the bath between DCA/DCA$^+$ on one side and CDMFT/PCDMFT/NCS on the other is due to a different way of closing self-consistency in these two groups of methods: **k**-space versus **r**-space clusters; see Appendix D). The bigger $\Delta_{00}(\tau \sim \beta/2)$ translates to having a bigger bath at the low frequency—the observed noncausal bath is also bigger, and as we see in Fig. 2 in the main text, in NCS it does not even decay with increasing cluster size.

3. Cumulant versus self-energy nesting

In Fig. 6, we compare the two variants of the NCS: one embeds either the cumulant g, or the self-energy Σ (for details see Appendix C 4). The results are compared to a 50-site DCA calculation. The temperature is $T/D = 0.0625$ and the (hole) doping is 20%.

We present results for the simplest dimer calculation (2×1, see Appendix C 5 a), the double dimer $2 + 2$ [see Eq. (C42) and the corresponding section], and the 2×2 calculation (Appendix C 5 c). We see that the result is solid already at $2 + 2$, and is overall improved at 2×2. However, it is clearly not yet converged, and looking at the nonlocal part, the convergence is not monotonic. This is clearly expected at such small cluster size.

We observe that the cumulant variant performs slightly better, but the difference is almost negligible. We have checked that none of the features of the failure of NCS depend on the choice of the nested quantity (g or Σ). In the problematic region, the cumulant variant converges to almost exactly the same wrong solution as the self-energy variant.

4. Unstable and unphysical solutions

In Fig. 7, we present the self-energy for the apparently unstable (green line) and the stable solution (red line) in NCS 4×4, compared to the exact benchmark (from Fig. 3). We observe that the unstable solution is in excellent agreement with the exact benchmark, even better than DCA of the same size cluster. The stable solution on the other hand, is much more metallic and much more local. However, it does have the correct asymptotics and is apparently causal (see Appendix A 2).

Even in the large cluster limit, NCS does not guarantee $\Sigma^{\rm imp} \to \Sigma^{\rm latt}$, and therefore at large cluster size, a principal

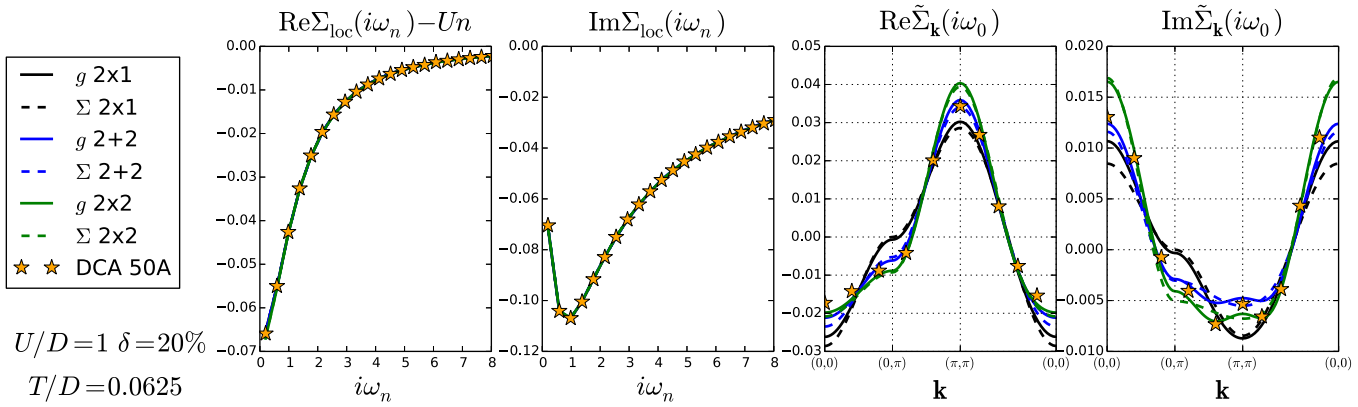

FIG. 6. Benchmark of the two variants of NCS (cumulant vs self-energy embedding) at small-cluster sizes. Stars denote the best available result (50-site DCA). The cumulant variant performs only slightly better. 2×2 calculation is already very close to the benchmark data.

solution is possible,

$$\Sigma^{\mathrm{imp},C}[\Delta^C] + \Delta^C \approx \mathcal{F}^C \Sigma^{\mathrm{latt}}[\Sigma^{\mathrm{imp}}], \tag{A3}$$

where $\mathcal{F}^C$ projects a lattice quantity onto impurity degrees of freedom of the cluster C. We check this explicitly in our unphysical solution in Fig. 8 and find excellent agreement.

APPENDIX B: VERTEX DIVERGENCES

The irreducible vertex function Γ_r contains all possible two-particle scattering processes that are two-particle irreducible [2,3,85] in the given channel r (see Fig. 9 for an illustration of the two-particle reducibility concept). The reducibility channels are particle-hole (ph), transverse particle-hole ($\overline{\mathrm{ph}}$), and particle-particle (pp), depending on which of the external indices remain connected after cutting two propagator lines [85]. Γ_{ph} in particular corresponds to the second-order functional derivative of the LWF:

$$\Gamma_{\mathrm{ph},\alpha\beta\gamma\delta} = \left.\frac{\delta\Sigma_{\delta\gamma}[G]}{\delta G_{\alpha\beta}}\right|_{G=G[G_0,\Sigma]} = \left.\frac{\delta^2\Phi[G]}{\delta G_{\alpha\beta}\delta G_{\gamma\delta}}\right|_{G=G[G_0,\Sigma]}. \tag{B1}$$

The greek indices combine the orbital and spin index and the imaginary time, e.g., $\alpha = (i_\alpha, \sigma_\alpha, \tau_\alpha)$. This relation is illustrated in Fig. 10 for diagrams of the second order.

The connection between Γ and Φ is the reason why Γ is sensitive to the multivaluedness of the LWF: it diverges along the lines in the phase diagram where two branches of the LWF cross [61] [see Fig. 1(a) in the main part]. However, note that also Γ_{pp} can diverge in some cases [63,64]. One can define the irreducible vertex function in the "charge" channel as $\Gamma_{\mathrm{c}} = \Gamma_{\mathrm{ph},\uparrow\uparrow\uparrow\uparrow} + \Gamma_{\mathrm{ph},\uparrow\uparrow\downarrow\downarrow}$ where we have omitted the time/frequency and orbital indices for clarity.

In this paper, we are interested in identifying divergences of Γ_{c}. It does not appear explicitly in the cluster DMFT equations, so we only need to calculate it at the end of the self-consistency loop. Note that due to the LWF construction of the methods, we calculate it only from the correlation functions on the impurity.

1. The Bethe-Salpeter equation

In general, Γ_{ph} can be calculated from the Green's function G and the four-point correlation function

$$\chi^{\omega\omega'\Omega}_{4,\sigma\sigma',ijkl} = \frac{1}{\beta}\langle c^\dagger_{i,\sigma}(\omega) c_{j,\sigma}(\omega+\Omega) c^\dagger_{k,\sigma'}(\omega'+\Omega) c_{l,\sigma'}(\omega')\rangle - G_{ji}(\omega)G_{lk}(\omega')\beta\delta_{\Omega,0} + \delta_{\sigma,\sigma'}G_{li}(\omega)G_{jk}(\omega+\Omega)\beta\delta_{\omega,\omega'}, \tag{B2}$$

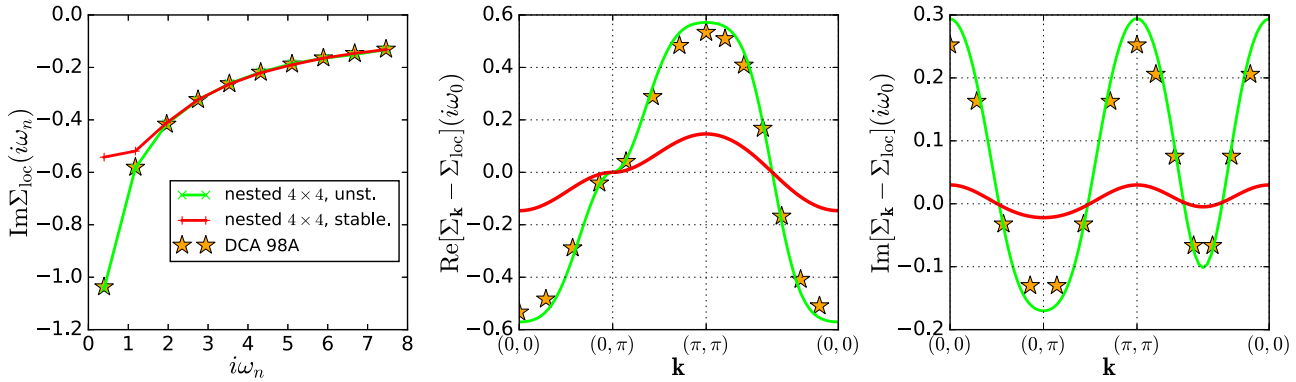

FIG. 7. Temperature $T/D = 0.125$, $U/D = 2$, $\delta = 0$, NCS 4×4. Red line: converged solution (stable, unphysical); green line: solution after 3 iterations (almost converged, physical, unstable); stars: DCA 98A (exact benchmark).

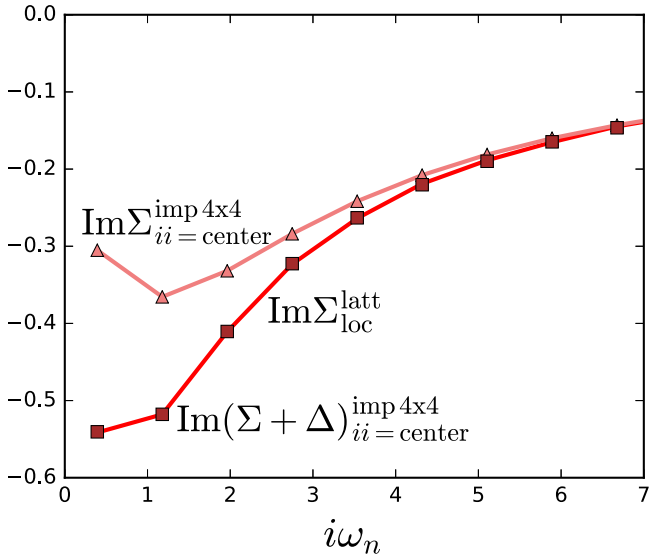

FIG. 8. Temperature $T/D = 0.125$, $U/D = 2$, $\delta = 0$, NCS 4×4. The unphysical solution retains a finite hybridization function even in the large cluster limit, such that $\Sigma^{\mathrm{latt}} = \Sigma^{\mathrm{imp}} + \Delta$. Quantities are presented at the center of the biggest cluster.

where we have assumed SU(2) symmetry and absence of spin-orbit interactions. First, we calculate the general χ_4, and then calculate the charge channel simply via

$$\chi_{4,\mathrm{c}} = \chi_{4,\uparrow\uparrow} + \chi_{4,\uparrow\downarrow}. \tag{B3}$$

From this object, one can obtain the full vertex function F_{c}, which contains *all* the possible two-particle scattering processes (including the reducible ones). It is identical to the four-point correlation function with amputated incoming/outgoing two-point propagators

$$F^{\omega\omega'\Omega}_{\mathrm{c},ijkl} = \sum_{mnop} G^{-1}_{mi}(\omega) G^{-1}_{ok}(\omega'+\Omega) \chi^{\omega\omega'\Omega}_{4,\mathrm{c},mnop} \times G^{-1}_{jn}(\omega+\Omega) G^{-1}_{lp}(\omega'). \tag{B4}$$

Γ_{c} is linked to F by the corresponding Bethe-Salpeter equation (BSE). The BSE can be understood as a Dyson Equation at the two-particle level [86], and it reads

$$F^{\omega\omega'\Omega}_{\mathrm{c},ijkl} = \Gamma^{\omega\omega'\Omega}_{\mathrm{c},ijkl} - \frac{1}{\beta} \sum_{\omega''} \sum_{mnop} \Gamma^{\omega\omega''\Omega}_{\mathrm{c},ijmn} G_{on}(\omega'') \times G_{mp}(\Omega+\omega'') F^{\omega''\omega'\Omega}_{\mathrm{c},opkl}. \tag{B5}$$

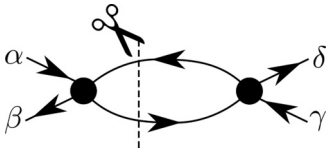

FIG. 9. Scattering diagrams can be classified according to their two-particle reducibility. If after cutting two Green's function lines, the diagram is separated into two vertex diagrams, with the external indices α and β in one and γ and δ in the other, the diagram is reducible in the ph channel.

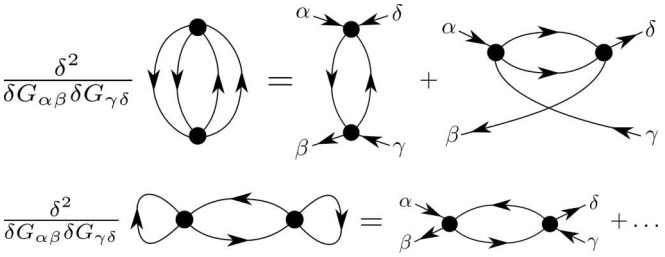

FIG. 10. (Top) Second-order functional derivative of the second-order contribution to Φ generates diagrams reducible in the pp and $\overline{\mathrm{ph}}$ channel. (Bottom) The ph-reducible diagrams can only be obtained by functional derivatives of nonskeleton vacuum diagrams which are not found in Φ.

The diagrammatic representation of BSE is presented in Fig. 11.

One can invert the BSE to obtain a closed expression for Γ. After rewriting the vertex quantities as matrices with respect to the properly grouped indices for a given transfer frequency Ω, $\hat{V}^{\Omega}_{(i,j,\omega),(l,k,\omega')} = V^{\omega\omega'\Omega}_{ijkl}$, the BSE becomes a matrix equation

$$\hat{F}^{\Omega}_{\mathrm{c}} = \hat{\Gamma}^{\Omega}_{\mathrm{c}} + \frac{1}{\beta^2} \hat{\Gamma}^{\Omega}_{\mathrm{c}} \hat{\chi}^{\Omega}_{0} \hat{F}^{\Omega}_{\mathrm{c}}, \tag{B6}$$

where

$$\chi^{\omega\omega'\Omega}_{0,ijkl} = -G_{li}(i\omega) G_{jk}(i\omega + i\Omega) \beta \delta_{\omega,\omega'}. \tag{B7}$$

A few algebraic steps then yield

$$\hat{\Gamma}^{\Omega}_{\mathrm{c}} = \beta^2 \left[\left[\hat{\chi}^{\Omega}_{0}\right]^{-1} - \left[\tilde{\chi}^{\Omega}_{\mathrm{c}}\right]^{-1} \right], \tag{B8}$$

where we have defined the so-called generalized susceptibility [85]

$$\tilde{\chi}_{\mathrm{c}} = \hat{\chi}_0 + \hat{\chi}_{4,\mathrm{c}}. \tag{B9}$$

The matrix $\hat{\chi}^{\Omega}_{0}$ is always invertible. This does not necessarily hold for the generalized susceptibility $\tilde{\chi}_{\mathrm{c}}$. As it approaches a singular matrix, Γ_{c} diverges.

While the analysis of Γ divergences can be performed for an arbitrary transfer frequency Ω, we here focus only on the $\Omega = 0$ case. $\tilde{\chi}^{\Omega=0}_{\mathrm{c}}$ is a symmetric matrix. In a single-site model at particle-hole symmetry, it is also purely real, which makes it Hermitian, and its eigenvalues purely real. In cluster-impurity models, and/or away from ph symmetry, it can have complex elements, and its eigenvalues are no longer necessarily real [65].

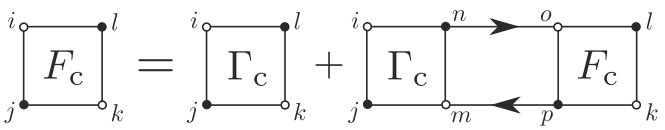

FIG. 11. Diagrammatic representation of the Bethe-Salpeter equation in the charge channel. Empty circles denote an ingoing connector of a vertex function, while black dots correspond to outgoing ones.

2. Eigenvalues and divergences

In this part, we present the procedure for determining the divergence trajectories of the irreducible vertex function, Γ_c. At a fixed temperature $T/D = 0.125$, in the (δ, U) phase diagram discussed in the main text, we determine trajectories $U^{d=1,2,3,\cdots}(\delta)$, where d indexes different divergences, counting from the low U ($U^d < U^{d'}$, $d < d'$).

From Eq. (B8), it is clear that $\Gamma_c^{\Omega=0}$ diverges when an eigenvalue of $\tilde{\chi}_c^{\Omega=0}$ goes through zero. The dimension of the matrix is $M = N_\omega \times N_c^2$, where N_ω is the number of fermionic frequencies stored, and N_c is the number of sites in the cluster. We start by solving the eigenproblem for $\tilde{\chi}_c^{\Omega=0}$. We fully diagonalize this matrix at each discrete value of U (U_l) at a fixed doping δ, and obtain a set of M eigenvectors and eigenvalues $\{(\mathbf{v}_i^l, \varepsilon_i^l)\}_{i\in[0,M)}$. In single-site DMFT, at the lowest U, the real part of all eigenvalues is positive ($\mathrm{Re}\varepsilon_i > 0$). Therefore, as we iterate over the interaction values U_l, it is straightforward to detect when the real part of an eigenvalue crosses zero—it is whenever a new eigenvalue with the negative real part appears. However, with this simple method, the error bar for $U^d(\delta)$ is given by the interaction step $U_{l+1} - U_l$. Furthermore, this method could potentially miss an event where between two U_l's two eigenvalues cross zero, one becoming negative, the other one positive. This is particularly important in CDMFT 2×2 where there are many negative eigenvalues present already at the lowest U. Furthermore, we would like to know the exact value of the imaginary part of the eigenvalue ($\mathrm{Im}\varepsilon_i$) when its real part is crossing zero—if it is nonzero ($\mathrm{Im}\varepsilon_i \neq 0$), $U^d(\delta)$ at that point does not correspond to an actual divergence of Γ.

One can do better by connecting the eigenvalues ε_i^l according to matching eigenvectors and then interpolating $\varepsilon_i^l \to \varepsilon_i(U)$. $U^d(\delta)$ is then defined by $\mathrm{Re}\varepsilon_i(U^d) = 0$. We start from the lowest U ($l = 0$), and for each eigenvector $\mathbf{v}_i^l$ we search for an eigenvector $\mathbf{v}_j^{l+1}$, such that $|\mathbf{v}_i^l \cdot \mathbf{v}_j^{l+1}|$ is maximal. After this is done for all eigenvectors $\mathbf{v}_i^l$, one proceeds with the next l until all the eigenvector/eigenvalue pairs are connected across the entire range of U. This procedure is, however, not entirely straightforward, especially when the step in U is big. The eigenbasis rotates with changing U, and in a given U step, different eigenvectors may "exchange." In the single-site DMFT calculation, we had to additionally require that ϵ_i^l is smooth to avoid getting eigenvalues mixed up. In CDMFT 2×2, the vector space is much bigger and we encountered no such problems. Note also that, as doping is changed, the eigenvectors change considerably, and we were unable to reliably connect the eigenvalues at the same U, but different values of doping.

In Fig. 12, we present the results from the single-site DMFT calculation. Here we have data at $\delta = 0{,}2\%{,}6\%$, 10%, and 16%. On the top left panel, results for $U^d(\delta)$ are presented with colored circles; the color represents the imaginary part of the eigenvalue crossing zero (color code is in the inset). The dashed lines are guides for the eye, and are also presented on Fig. 1(a) in the main text. The total count of negative eigenvalues as a function of U_l is given on the top right panel. We see that at $\delta = 0{,}2\%$, eigenvalues cross zero one by one. Then at $\delta = 6\%$ and 10%, we see that two eigenvalues cross zero in the same U step. In the bottom panels, we plot the interpolation $\epsilon_i(U)$ obtained after connecting the eigenvalues at different values of U. We present only the first two eigenvalues to cross zero in the examined range of U. We note that these eigenvalues are the highest valued ones at the lowest U. At $\delta = 16\%$, no eigenvalues have the real part cross zero, and instead we present the two mutually complex conjugate eigenvalues, which are the biggest ones at the lowest U, and thus apparently correspond to the two eigenvalues crossing zero at the lower δ's. We see that at low δ we have two separate eigenvalues which are purely real and cross zero at different values of U. Then at 6% doping, the two eigenvalues crossing zero are mutually complex conjugate, and cross zero at the same time, but with finite imaginary parts of opposite signs. As doping is further increased, the two eigenvalues remain mutually complex conjugate and have the real part grow towards positive values such that at $\delta = 16\%$ they no longer cross zero. The imaginary part grows with both doping and interaction.

In Fig. 13, we present the result from CDMFT 2×2. We show the result for the first eight eigenvalues to cross zero. These are separated in two groups of four (yielding $U^d(\delta)$ with $d = 1$–4 and $d = 5$–8), and each group apparently corresponds to one of the two eigenvalues crossing zero in single-site DMFT. At higher U, there is another group of four eigenvalues crossing zero ($d = 8$–11, not shown), apparently corresponding to the 3rd divergence in single-site DMFT. The two middle eigenvalues in all groups are mutually complex conjugate [the ones yielding $U^d(\delta)$ with $d = 2{,}3$, $d = 6{,}7$, and $d = 10{,}11$]. At $\delta = 3\%$, we see that the first two groups merge at around $U = 1.8$ ($d = 1$ with $d = 5$, 2 with $d = 6$, and so on). This point is denoted with the vertical gray dashed line. The merging of eigenvalues occurs at different U for various dopings, along the gray dashed line on the phase diagram in the inset. At $\delta = 8\%$, there are still eight eigenvalues crossing zero, but they have only three distinct real parts: first and last doubly degenerate and the middle one is four times degenerate. After merging, the imaginary part of the eigenvalues grows from zero, both with U and δ, similarly to the single-site DMFT case.

Note that we have performed the analogous analysis also in DCA, DCA$^+$, and PCDMFT. The overall picture is very similar. The only qualitative difference is the presence of additional crossings of zero at low U in DCA/DCA$^+$. These, however, occur with a very big imaginary part and do not correspond to singular behavior of Γ.

APPENDIX C: NESTED CLUSTER SCHEME

In this section, we present the fully general formalism of the self-energy embedding theory (SEET) and then focus on its application to infinite lattice systems (NCS). The main idea is to approximate the Luttinger-Ward functional Φ (LWF) by a sum of functionals, including counter terms to cancel double counting of diagrams. By now it is clear that combining different LW functionals is a very general approach, and can lead to a great variety of approximations. For example, one can rederive within the SEET framework also the GW+EDMFT method [75,87]. Moreover, CDMFT can be viewed as a special case of NCS, where no counter terms are needed in the construction of the LWF.

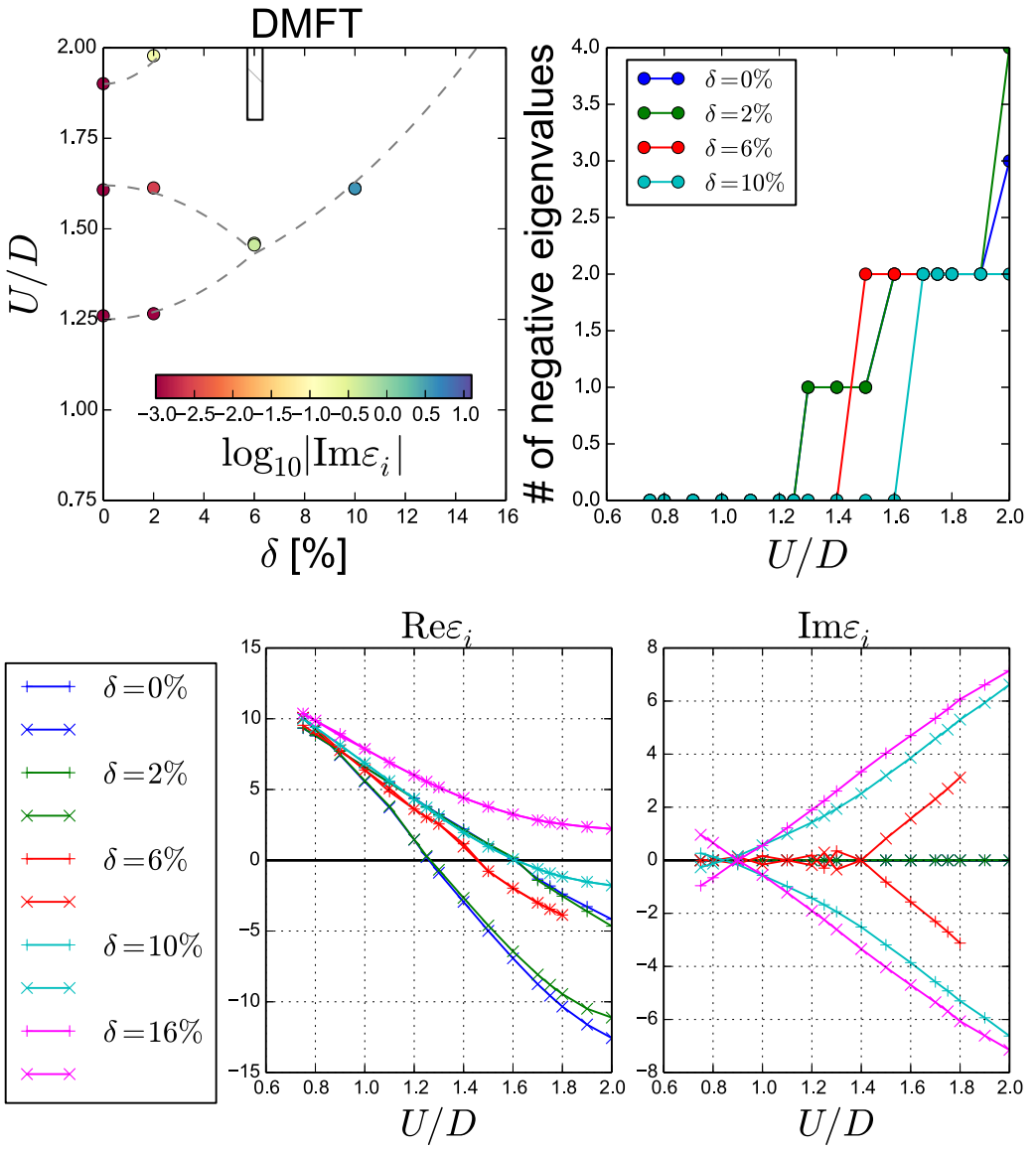

FIG. 12. Single-site DMFT calculation. Temperature $T/D = 0.125$, square lattice. Upper left: the colored points denote where the real part of an eigenvalue of $\tilde{\chi}_c(i\Omega = 0)$ crosses zero; the color denotes the imaginary part at that point, with respect to the color bar in the inset; gray dashed lines are eye-guides, used also in the Fig. 1 in the main text. Upper right: the number of negative eigenvalues; at $\delta > 5\%$ two eigenvalues cross zero at the same time. Bottom panels: evolution of the first two eigenvalues crossing zero, with U and δ. They remain purely real before becoming mutually complex conjugate. No eigenvalues cross zero at $\delta = 16\%$.

We develop a general algorithm to obtain NCS based LWF approximations and the corresponding self-energy expressions with no doubly counted diagrams, given a set of independent clusters one wishes to solve. Also, it was not clear previously whether pushing the cluster size will also increase the number of impurity problems one needs to solve. Here we prove that in the simplest scheme (square clusters), one needs to solve only three impurity problems, regardless of the cluster size.

1. General formulation

Consider a system with single-particle degrees of freedom $i \in \mathcal{L}$. At this point these may be lattice sites, or more general orbitals, and the system may or may not be infinite. The exact Luttinger-Ward functional depends on all the components of the Green's function

$$\Phi[G] \equiv \Phi[\{G_{ij}\}_{i,j\in\mathcal{L}}]. \tag{C1}$$

Consider now an approximation of the Luttinger-Ward functional, such that it is a sum of functionals, each depending on components of G that connect only a certain subset C of orbitals i, i.e., components of G within a "cluster" $C \subset \mathcal{L}$:

$$\Phi \approx \sum_{C\in\mathcal{C}} \Phi_C[G|_C] \tag{C2}$$

with

$$G|_C \equiv \{G_{ij}\}_{ij\in C}, \tag{C3}$$

where $|_C$ denotes the restriction of the orbital-space domain of the Green's function to the cluster C. It is assumed that the

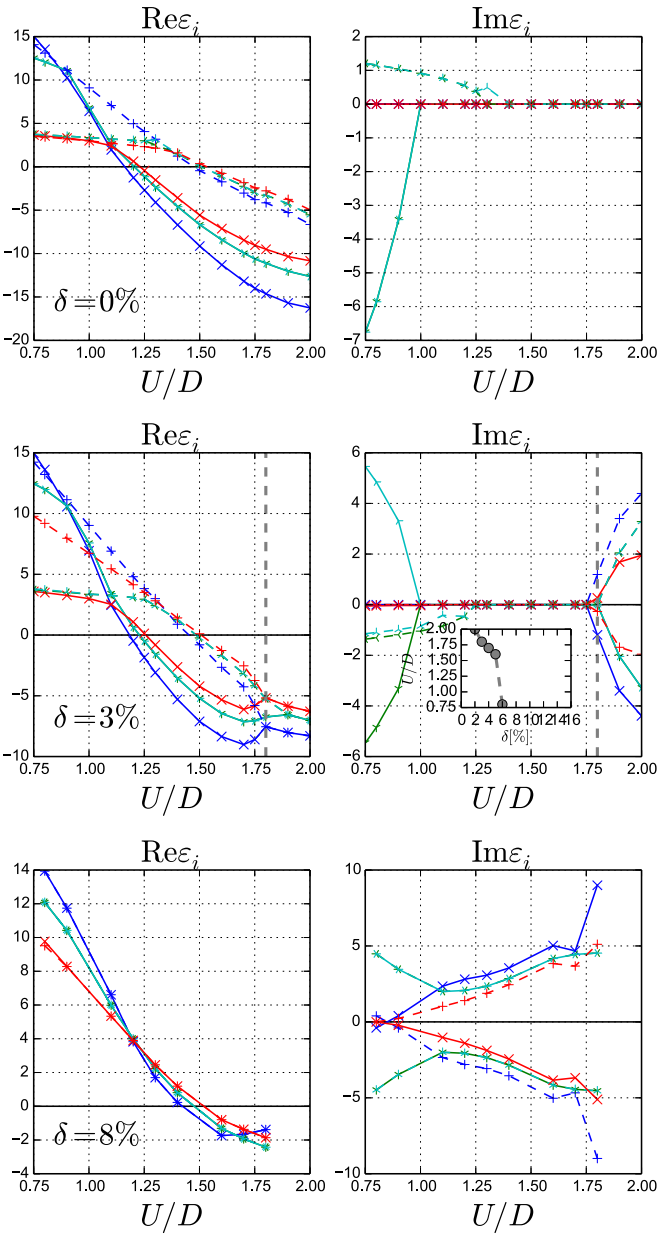

FIG. 13. 2x2 CDMFT calculation. Temperature $T/D = 0.125$, square lattice. Evolution of first eight eigenvalues to cross zero, with U and δ.

clusters are mutually independent,

$$C \nsubseteq C', \forall C, C' \in \mathcal{C},$$

and cover the entire system

$$\bigcup_{C \in \mathcal{C}} C = \mathcal{L}.$$

However, if any of the clusters are overlapping,

$$\exists C, C' \in \mathcal{C} : C \cap C' \neq \{\}, \tag{C4}$$

then we are double-counting diagrams constructed entirely from G components connecting the orbitals present in both C and C'. To avoid this, we need to add functional counter terms, each dependent only on G_{ij} within an overlap of clusters in $\mathcal{C}$.

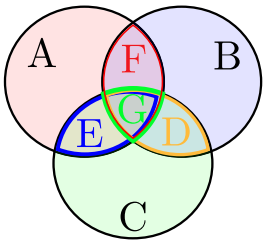

$$\mathcal{C} = \{\mathrm{A}, \mathrm{B}, \mathrm{C}\}$$
$$\mathcal{O} = \{\mathrm{D}, \mathrm{E}, \mathrm{F}, \mathrm{G}\}$$
$$\mathcal{U} = \{\mathrm{A}, \mathrm{D}, \mathrm{G}\}$$

FIG. 14. Illustration of reasoning in SEET. $\mathcal{C}$ sets of orbitals are chosen. $\mathcal{O}$ are all possible overlaps. $\mathcal{U}$ are sets independent by symmetry that one needs to solve in practice.

In general,

$$\Phi[G] \approx \sum_{C \in \mathcal{C}} \Phi_C[G|_C] + \sum_{C \in \mathcal{O}} p_C \, \Phi_C[G|_C] \tag{C5}$$

where $\mathcal{O}$ is the set of all possible overlaps between any number of nonidentical clusters in set $\mathcal{C}$, i.e.,

$$\mathcal{O} = \bigcup_{n \in [2, N_\mathcal{C}]} \left\{ \bigcap_{a=1}^{n} C_a \right\}_{C_a \in \mathcal{C}} \Big\backslash \mathcal{C},$$

which is ilustrated on Fig. 14. $N_\mathcal{C}$ is the size of the set $\mathcal{C}$. p_C are appropriately chosen integer prefactors, possibly negative or even zero.

We emphasize that NCS is defined only by the choice of $\mathcal{C}$; the set $\mathcal{O}$ and prefactors p_C are then determined uniquely by the requirement that no diagrams are counted more than once. We can rewrite more simply

$$\Phi[G] \approx \sum_{C \in \mathcal{C} \cup \mathcal{O}} p_C \Phi_C[G|_C], \tag{C6}$$

where $p_{C \in \mathcal{C}} = 1$. Hereinafter, summation $\sum_C$ is assumed to go over $\mathcal{C} \cup \mathcal{O}$ unless stated differently. Finally, the prefactors p_C must satisfy for each C

$$\sum_{\substack{C' \in \mathcal{C} \cup \mathcal{O} \\ C' \supseteq C}} p_{C'} = 1, \tag{C7}$$

which means that the contribution of diagrams that involve orbitals from a given cluster C are taken into account exactly once. In Appendix C 3, we present an algorithm to find p_C which satisfy this requirement.

a. Obtaining self-energy from the functional

Anticipating that the formalism will be used for the lattice systems below, and to avoid introducing new notation, here we assume that the system is a lattice, with lattice sites $\{i\}$. Note, however, that the considerations presented here are still fully general.

The self-energy is given by the functional derivative with respect to the Green's function

$$\Sigma_{\alpha\beta} = \sum_C p_C \left. \frac{\partial \Phi[\{G_{\gamma\delta}\}_{i_\gamma, i_\delta \in C}]}{\partial G_{\beta\alpha}} \right|_{G = G[G_0, \Sigma]}, \tag{C8}$$

where $\alpha,\beta,\ldots$ are combined indices defined in Appendix B. We can obtain it by solving a set of impurity problems

$$S^C = \sum_{IJ\in C,\sigma} \iint d\tau d\tau' c^+_{\sigma,I}(\tau)\left[-(\hat{\mathcal{G}}^C)^{-1}_\sigma\right]_{IJ}(\tau-\tau')c_{\sigma,J}(\tau') + U\sum_{I\in C}\int d\tau c^+_{\uparrow,I}(\tau)c^+_{\downarrow,I}(\tau)c_{\downarrow,I}(\tau)c_{\uparrow,I}(\tau) \quad \text{(C9)}$$

corresponding to each cluster C, under the condition that

$$G^{\mathrm{imp}\,C}_{IJ}(i\omega_n) = G^{\mathrm{latt}}_{i_{C,I}j_{C,J}}(i\omega_n), \quad \text{(C10)}$$

where $i_{C,I}$ is the mapping between the index I of a site within a cluster C and its index i within the lattice. The Green's function on the lattice is a matrix in site indices

$$\hat{G}^{\mathrm{latt}}(i\omega_n) = [(i\omega_n+\mu)\hat{I} - \hat{\Sigma}^{\mathrm{latt}}]^{-1} \quad \text{(C11)}$$

and the self-energy approximation on the lattice is given by

$$\Sigma^{\mathrm{latt}}_{ij} = \sum_{C\supseteq\{i,j\}} p_C\,\Sigma^{\mathrm{imp}\,C}_{I_{C,i}J_{C,j}}, \quad \text{(C12)}$$

where $I_{C,i}$ is the mapping between the site index on the lattice and in the cluster C, inverse of the previously defined $i_{C,I}$. Note that up to now we have not used any lattice symmetries. Therefore, this prescription can be used for solving (finite-size) disordered and inhomogenous lattice models (e.g., one could write down a cluster extension of real-space DMFT).

b. Application to lattice models

When there are symmetries in the system Hamiltonian, one should choose $\mathcal{C}$ in a way that does not artificially break those symmetries. For example, if there is translational symmetry on the lattice, clusters must be arranged uniformly across the entire lattice; if there is rotational symmetry, the arrangement must be the same along equivalent directions. A simple realization of a translationally and rotationally invariant set $\mathcal{C}$ for a square lattice would include 2×2 plaquettes on all possible positions on the lattice. On the contrary, if the plaquettes are only tiled over the system, with no overlaps (as is the case in CDMFT), the translational symmetry is artificially broken.

If translational, rotational, and mirror symmetry are present, the number of clusters one actually needs to solve is reduced—one solves only one cluster of each different shape and/or size. Due to translational invariance, the position of the cluster on the lattice does not make a difference, just its shape/size. Due to rotational symmetry, quantities on clusters of the same (nonsquare) shape, but different orientation, can be inferred one from another.

Translational symmetry also allows to rewrite the lattice quantities as functions of the real-space vector rather than matrices in site index. The self-consistency condition can be rewritten as

$$G^{\mathrm{imp}\,C}_{IJ}(i\omega_n) = G^{\mathrm{latt}}_{\mathbf{r}=\mathbf{r}_{i_{C,I}}-\mathbf{r}_{j_{C,J}}}(i\omega_n). \quad \text{(C13)}$$

The Green's function on the lattice, again, is calculated from the approximated self-energy

$$G^{\mathrm{latt}}_{\mathbf{r}} = \sum_{\mathbf{k}\in BZ} e^{-i\mathbf{k}\cdot\mathbf{r}}G^{\mathrm{latt}}_{\mathbf{k}} = \sum_{\mathbf{k}\in BZ}\frac{e^{-i\mathbf{k}\cdot\mathbf{r}}}{G^{-1}_{0,\mathbf{k}}(i\omega_n) - \Sigma^{\mathrm{latt}}_{\mathbf{k}}(i\omega_n)}, \quad \text{(C14)}$$

$$\Sigma^{\mathrm{latt}}_{\mathbf{k}} = \sum_{\mathbf{r}\in BL} e^{i\mathbf{k}\cdot\mathbf{r}}\Sigma^{\mathrm{latt}}_{\mathbf{r}}, \quad \text{(C15)}$$

which is given by a general expression

$$\Sigma^{\mathrm{latt}}_{\mathbf{r}} = \sum_{C\in\mathcal{U}}\sum_{IJ} a_{\mathbf{r},C,I,J}\,\Sigma^{\mathrm{imp}\,C}_{IJ}. \quad \text{(C16)}$$

The sum runs only over a set of clusters $\mathcal{U}\subset\mathcal{C}$ independent by lattice symmetry, as illustrated on Fig. 14. If both translational and rotational symmetries are present, $\mathcal{U}$ contains a single choice of a cluster, of each size and shape, and the sum over IJ accounts for all the shifts and rotations of the same cluster on the lattice. Note that $\sum_{CIJ} a_{\mathbf{r},C,I,J} = 1$ and $a_{\mathbf{r},C,I,J} \sim \delta_{\mathbf{r},\,\mathbf{r}_{i_{C,I}}-\mathbf{r}_{j_{C,J}}}$. Because some bonds on the cluster correspond to the same real-space vector and can have the same self-energy due to the symmetries of the cluster, one is free to choose which one to use, so $a_{\mathbf{r},C,I,J}$ is not uniquely defined. More importantly, $\sum_{CIJ}|a_{\mathbf{r},C,I,J}| \sim N_c$. This is a problematic property of the method and is the reason why the limit $N_c\to\infty$ does not guarantee the exact solution, and is the reason for an undesirable amplification of statistical noise when clusters are big.

Large-cluster limit. As cluster size increases, the difference in self-energy between different clusters becomes smaller, and the self-energy on the clusters becomes more uniform. On the other hand, the coefficients $a_{\mathbf{r},C,I,J}$ grow by absolute value roughly proportionally to N_c, while their total sum remains 1. This means that in the limit $N_c\to\infty$, an infinitesimal difference between the self-energies in different clusters and at different positions in the same cluster, all corresponding to the same real-space vector, can in principle be amplified such that

$$\Sigma^{\mathrm{latt}}_{\mathbf{r}=\mathbf{r}_{i_{C,I}}-\mathbf{r}_{j_{C,J}}} - \Sigma^{\mathrm{imp}\,C}_{IJ} \sim 1. \quad \text{(C17)}$$

Whether this happens or not depends on whether the coefficients $a_{\mathbf{r},C,I,J}$ grow more quickly than do decay the difference between clusters and the inhomogeneity within them. On the other hand, in the $N_c\to\infty$ limit, we have $G^{\mathrm{imp}}_0 \to G_0$, where G^{imp}_0 denotes the static part of the bare propagator on the impurity ($\mathcal{G} = [[G^{\mathrm{imp}}_0]^{-1} - \Delta]^{-1}$). So, if $\Sigma^{\mathrm{latt}} \neq \Sigma^{\mathrm{imp}}$, we must have a nonzero Δ to satisfy the self-consistency condition [recall Eq. (C10)]

$$\left[\left[G^{\mathrm{imp}}_0\right]^{-1} - \Delta - \Sigma^{\mathrm{imp}}\right]^{-1} = [[G_0]^{-1} - \Sigma^{\mathrm{latt}}]^{-1}. \quad \text{(C18)}$$

Because of this, NCS does not guarantee that in the $N_c\to\infty$ limit we arrive at the exact solution. A way of checking is to see whether the hybridization function falls off with increasing cluster size.

Amplification of noise. Having the property $\sum_{CIJ} a_{\mathbf{r},C,I,J} = 1$, when coefficients are large by absolute value, leads to amplification of QMC statistical error. The problem can be reduced by using symmetries of the clusters,

but may prove prohibitive at very large cluster sizes. On the other hand, an approximate solution not involving a stochastic impurity solver, can be safely pushed to bigger cluster sizes.

2. Square cluster case

For the special case that $\mathcal{C}$ contains all $L \times L$ square clusters of the lattice, the nested cluster approximation for Φ can be written down explicitly for arbitrary size L. It turns out that the only overlaps $C \in \mathcal{O}$ with $p_C \neq 0$ are the clusters of shape $L-1 \times L$, $L \times L-1$ and $L-1 \times L-1$, i.e., Φ is approximated by [Eq. (4) from the main text]

$$\Phi^{(L)} = \sum_i \Phi_{L\times L}\left[G|_{C_i^{L\times L}}\right] + \Phi_{L-1\times L-1}\left[G|_{C_i^{L-1\times L-1}}\right] - \Phi_{L-1\times L}\left[G|_{C_i^{L-1\times L}}\right] - \Phi_{L\times L-1}\left[G|_{C_i^{L\times L-1}}\right]. \quad \text{(C19)}$$

Here, $G|_C$ denotes the Green's function with the orbital-domain restricted to the sites within cluster C [recall Eq. (C3)]. The notation $C_i^{L_x\times L_y}$ denotes a rectangular cluster with width L_x and height L_y with its bottom left site sitting at lattice site i. In the following, we prove that $\Phi^{(L)}$ contains only the diagrams which can fit in a cluster $L \times L$, and counts each exactly once.

a. Proof of Eq. (4)

Let us consider any one diagram of Φ^{latt} in real space. This defines the (finite) set of lattice sites $D = \{\mathbf{i}\}$ contained in it. Denoting the coordinate as $\mathbf{i} = (\mathbf{i}_x, \mathbf{i}_y)$, we define

$$n = \max_{\mathbf{i}\in D}(\mathbf{i}_x) - \min_{\mathbf{i}\in D}(\mathbf{i}_x) + 1, \quad \text{(C20)}$$

$$p = \max_{\mathbf{i}\in D}(\mathbf{i}_y) - \min_{\mathbf{i}\in D}(\mathbf{i}_y) + 1. \quad \text{(C21)}$$

Then (n,p) is the shape of the smallest rectangular cluster containing the diagram (with $n = p = 1$ in the local case).

Let us first count the number of times the diagram appears in $\sum_i \Phi_{L_x\times L_y}[G|_{C_i^{L_x\times L_y}}]$. This count is identical to the number of ways to place a cluster of shape (n,p) into one of shape (L_x,L_y), i.e., $f(L_x+1-n)f(L_y+1-p)$, where $f(x) = x\theta(x)$ and θ is the Heaviside function. Therefore the number of times the diagram appears in $\Phi^{(L)}$, with proper weights, is given by

$$R = f(L+1-n)f(L+1-p) + f(L-n)f(L-p) - f(L-n)f(L+1-p) - f(L+1-n)f(L-p).$$

Whenever $n \leqslant L$ and $p \leqslant L$ we have (denoting $a \equiv L+1-n, b \equiv L+1-p$)

$$\begin{aligned} R &= (L+1-n)(L+1-p) + (L-n)(L-p) \\ &\quad - (L-n)(L+1-p) - (L+1-n)(L-p) \\ &= ab + (a-1)(b-1) - (a-1)b - a(b-1) \\ &= 1 \end{aligned}$$

while otherwise $R = 0$ by the definition of f. *QED.*

Note that even with the knowledge of p_C for all subclusters, one still needs to write down the expression for $\Sigma^{\text{latt}}[\Sigma^{\text{imp}}]$. We discuss the way this is done in the following sections, including nested schemes more general than the square cluster case discussed here.

3. Algorithm for self-energy coefficients

Deriving expressions for the self-energy when $\mathcal{C}$ clusters are taken to be bigger than 2×2 becomes very cumbersome, and should not be done by hand. Here we present a general algorithm for a uniform and rotationally invariant arrangement of solid rectangular clusters (solid meaning there are no sites missing in the rectangle; a more general algorithm can be devised, but we don't present it here). No symmetries are assumed in the beginning, and the first part of the algorithm gives the fully general expression for $\Sigma_{ij}^{\text{latt}}$ at a given choice of ij. In the second part, the symmetries of the lattice and the clusters are used to fully simplify the expressions.

The algorithm finds the subset of clusters and the corresponding coefficients p_C that appear in the expression Eq. (C12), for a given ij on the lattice. The prefactors p_C are determined so as to satisfy Eq. (C7). The algorithm finds all the clusters in $\mathcal{C}$ and their overlaps $\mathcal{O}$ containing the given two sites i and j ($i = j$ allowed), orders them by size, and then assigns the prefactors starting from biggest clusters, i.e., the ones in $\mathcal{C}$ for which we know $p_{C\in\mathcal{C}} = 1$. For the rest of the clusters C, the prefactors $p_{C'}$ of their superclusters $C' \supset C$ are taken into account to ensure that the contribution of C is taken exactly once. The procedure is "one pass" because the coefficients of smaller clusters cannot affect the coefficients for the bigger ones.

(1) Define the nested scheme by picking a set of independent rectangular clusters, defined by the size in each direction (L_x,L_y) (independent meaning no cluster can be fit into another). Note that the placement of these clusters on all possible positions on the lattice, with all possible orientations, constructs the set of clusters $\mathcal{C}$.

(2) For each pair of the lattice indices ij ("bond" if $i \neq j$ or "site" if $i = j$), perform the following (if you know there are symmetries, this part can be performed for only the independent bonds/sites).

(i) Determine all possible positions of all the clusters such that they contain the bond/site in question ij. These form a set of clusters defined by size and position (x,y,L_x,L_y), and the position is assumed to correspond to the left-bottom site of the cluster.

(ii) Determine all the overlaps between the clusters obtained in the previous step. Overlaps themselves form a set of clusters defined by size and position (x,y,L_x,L_y). Note that under present assumptions, any overlap of clusters from $\mathcal{O}$ is also an overlap of clusters in $\mathcal{C}$ ($C \cap C' \in \mathcal{O}, \forall C, C' \in \mathcal{O}$).

(iii) Group by shape all the clusters obtained in the previous two steps, independently of position and rotation, i.e., (x_1,y_1,L_x,L_y) goes together with (x_2,y_2,L_y,L_x).

(iv) Order the groups according to $N_c = L_xL_y$ [or $\max(L_x,L_y)$], from biggest to smallest clusters, and place them "left to right," so that no cluster contains a cluster to the left of it, but may or may not contain clusters to the right of it. Because clusters in the same group are of the same size, but different position and/or orientation, no cluster can contain a different cluster in the same group.

(v) Assign a prefactor $p(c)$ to each cluster c in each group.

(vi) For each group g, starting from biggest clusters (leftmost). (a) For each cluster c in the group g, do a weighted count of how many times it is contained in the clusters in the groups

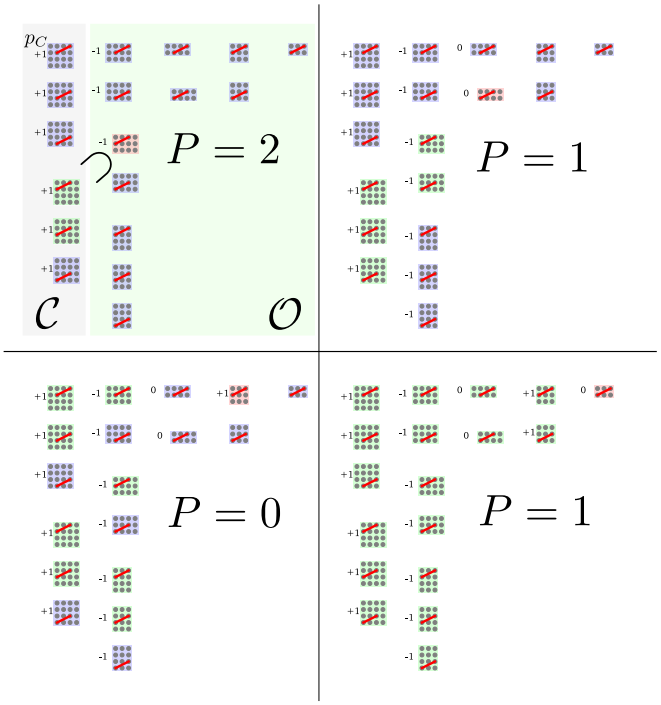

FIG. 15. Four snapshots of the algorithm for getting the self-energy coefficients; 4×4 nested scheme; coefficients are calculated for an ij bond (red line) corresponding to the real-space vector $\mathbf{r} = (2,1)$; clusters are sorted by size; the prefactors p_C are determined starting from the biggest clusters for which we know $p_C = 1$; the red cluster is the one for which p_C is determined at the given step; green clusters are the ones that contain the red cluster. See text for details.

left to it. Weighted means to take into account the prefactor of the cluster in which c is found to be contained. In other words, obtain the number $P = \sum_{c'} p(c')$, where the sum goes over all clusters c', which contain c. Then set the prefactor of c to be $p(c) = 1 - P$. This assures that the total contribution of the cluster c is 1. The coefficients of the smaller clusters, which are yet to change cannot affect this value. By construction, the clusters in $\mathcal{C}$ have $p(c) = 1$; they are not contained in any other clusters, so $P = 0$.

(vii) For the bond ij, the expression for self-energy is now

$$\Sigma_{ij} = \sum_c p(c) \Sigma^c_{I_{c,i}, J_{c,j}},$$

where c runs over all clusters in all groups, and $I_{c,i}$ and $J_{c,j}$ are determined trivially for each cluster c. The algorithm is visualized in Fig. 15.

a. Use of symmetries

When there are symmetries, we want to simplify the expression for self-energy by identifying identical contributions in the sum over clusters. First, if there is translational symmetry, clusters of the same shape but different position will have the same self-energy. If there is rotational symmetry, again, clusters of the same shape but different orientation must have the same $\hat{\Sigma}^C$. We therefore only solve clusters of different shape/size, and the sum over all C is replaced by the sum over independent clusters and a sum over the bonds IJ [recall

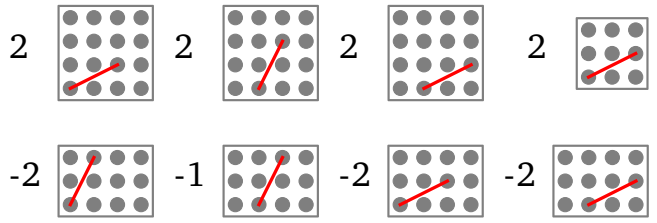

FIG. 16. After the use of symmetries, the result from the final step in Fig. 15 simplifies to what is shown in this figure. One needs to solve only three different clusters, and take into account a smaller number of bonds on each cluster, for a given real-space vector.

Eq. (C16)]. Second, $\Sigma^{\mathrm{imp}\,C}_{IJ}$ may not be the same for every IJ corresponding to the same real-space vector, but clusters will in general have some symmetries, and one is able to use them to simplify the expressions further. It is straightforward to identify groups of identical bonds/sites. Then, the sum over all IJ is replaced by a sum over only the independent bonds/sites IJ on a given cluster, and the prefactors are adjusted accordingly.

Recall now the self-consistency condition in the nested cluster scheme Eq. (C13). Unlike $\mathcal{G}^C$ and $\Sigma^{\mathrm{imp}\,C}$, when convergence is reached, $G^{\mathrm{imp}\,C}_{IJ}$ will be the same for any choice of IJ corresponding to the same real-space vector. We find it beneficial for the stability of the loop and the maximal level of convergence reached if this symmetry of $G^{\mathrm{imp}\,C}$ is imposed in each iteration, and if the cluster symmetries are imposed on $\mathcal{G}^C$ and $\Sigma^{\mathrm{imp}\,C}$. The simplification of the self-energy expression one obtains after using cluster symmetries is visualized in Fig. 16 (see caption).

4. Nesting the cumulant

Here we discuss a different variant of the nested cluster approximation, corresponding to cumulant embedding rather than self-energy embedding theory. The benchmark of this method in comparison with the self-energy nesting variant is presented in Fig. 6.

One can in principle define a functional Γ of the Green's function such that its derivative yields the cumulant, instead of self-energy

$$\hat{g} = \frac{\partial \Gamma[\hat{G}]}{\partial \hat{G}^{\mathsf{T}}}. \tag{C22}$$

The cumulant is the full-Green's function stripped of the bare hopping processes, so that

$$\hat{G}(i\omega_n) = \hat{g}(i\omega_n) + \hat{g}(i\omega_n)\,\hat{t}\,\hat{G}(i\omega_n), \tag{C23}$$

i.e.,

$$\hat{G}(i\omega_n) = [\hat{g}^{-1}(i\omega_n) - \hat{t}]^{-1}, \tag{C24}$$

where $\hat{t}$ is the hopping matrix. In $\mathbf{k}$ space,

$$G_{\mathbf{k}}(i\omega_n) = g_{\mathbf{k}}(i\omega_n) + g_{\mathbf{k}}(i\omega_n)\,\varepsilon_{\mathbf{k}}\,G_{\mathbf{k}}(i\omega_n) \tag{C25}$$

$$G_{\mathbf{k}}(i\omega_n) = \frac{1}{g^{-1}_{\mathbf{k}}(i\omega_n) - \varepsilon_{\mathbf{k}}}, \tag{C26}$$

which leads to the identity

$$\hat{g}(i\omega_n) = [(i\omega_n + \mu)\hat{I} - \hat{\Sigma}(i\omega_n)]^{-1} \tag{C27}$$

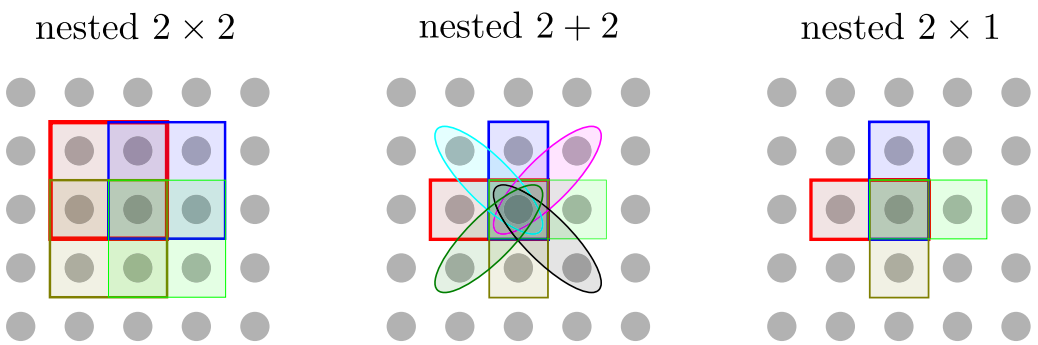

FIG. 17. Clusters contributing to the local self-energy in different kinds of simple nested schemes.

and the inverse is

$$\hat{\Sigma}(i\omega_n) = (i\omega_n + \mu)\hat{I} - \hat{g}^{-1}(i\omega_n). \tag{C28}$$

So, we can construct the cumulant on the lattice $g_{\mathbf{k}}$ from the cumulants on the impurities, the same way we did for the self-energy. The self-energy on the lattice can be obtained as

$$\Sigma^{\text{latt}}_{\mathbf{k}}(i\omega_n) = i\omega_n + \mu - \left(g^{\text{latt}}_{\mathbf{k}}(i\omega_n)\right)^{-1}, \tag{C29}$$

but this expression is ill-defined at high frequency, so it is important to avoid using it in the DMFT loop. Therefore, in each iteration, we construct G^{latt} directly from the cumulant using Eq. (C26), and calculate the self-energy only in the post-processing of the results.

We expect that the cumulant variant works better whenever the cumulant is shorter ranged than the self-energy. In practice, we find that the cumulant version does a slightly better job, but the difference is not big (see Appendix A 3).

5. Simple examples and summary of equations

a. 2 x 1

This example was originally presented in Ref. [70]. We rederive it only for pedagogical purposes.

For simplicity, we introduce a shorthand notation $i + x$ to denote the index of the nearest neighbor of the site i in the $+x$ direction, and similarly $i - x, i + y, \ldots$. Recall also the cluster notation $C_i^{2\times1} \equiv \{i, i + x\}$, $C_i^{1\times2} \equiv \{i, i + y\}$ and $C_i^{1\times1} \equiv \{i\}$.

Let us approximate LW functional such that it contains diagrams that involve at most two nearest-neighboring lattice sites

$$\mathcal{C} = \left\{C_i^{2\times1}\right\}_{\forall i} \cup \left\{C_i^{1\times2}\right\}_{\forall i}. \tag{C30}$$

This means we want to solve at most a two-site impurity problem. As for all possible overlaps of the clusters in $\mathcal{C}$, one can easily verify

$$\mathcal{O} = \{C \cap C'\}_{\forall C, C' \in \mathcal{C}} = \left\{C_i^{1\times1}\right\}_{\forall i}, \tag{C31}$$

which means we will need to take care of double counting. Each overlap cluster is contained in four clusters in $\mathcal{C}$,

$$\begin{aligned} C_i^{1\times1} &\subset C_i^{2\times1}, \quad C_i^{1\times1} \subset C_{i-x}^{2\times1}, \\ C_i^{1\times1} &\subset C_i^{1\times2}, \quad C_i^{1\times1} \subset C_{i-y}^{1\times2}, \end{aligned} \tag{C32}$$

which means that we are counting diagrams which involve only the local Green's function four times at each site. To have them taken into account only once, we need to subtract the DMFT functional (D1) three times at each site, i.e., $p_{C\in\mathcal{O}} = -3$,

$$\Phi \approx \sum_i \left(\Phi_2\left[G\big|_{C_i^{2\times1}}\right] + \Phi_2\left[G\big|_{C_i^{1\times2}}\right] - 3\Phi_1\left[G\big|_{C_i^{1\times1}}\right]\right). \tag{C33}$$

Now we write the clusters explicitly to perform the derivatives that yield the self-energy. The local component is given by

$$\begin{aligned} \Sigma_{ii} &= \frac{\partial}{\partial G_{ii}} \sum_l \left(\sum_{\delta\in\{x,y\}} \Phi_2[\{G_{l'm'}\}_{l'm'\in\{l,l+\delta\}}] - 3\Phi_1[G_{ll}] \right) \\ &= \sum_{\delta\in\{x,y,-x,-y\}} \frac{\partial\Phi_2[\{G_{lm}\}_{lm\in\{i,i+\delta\}}]}{\partial G_{ii}} - 3\frac{\partial\Phi_1[G_{ii}]}{\partial G_{ii}} \end{aligned} \tag{C34}$$

and the nearest-neighbor components (with $\delta = x, y$)

$$\begin{aligned} \Sigma_{i,i+\delta} &= \frac{\partial}{\partial G_{i+\delta,i}} \left(\sum_{l'} \sum_{\delta'\in\{x,y\}} \Phi_2[\{G_{lm}\}_{lm\in\{l',l'+\delta'\}}] \right. \\ &\qquad \left. - 3\sum_l \Phi_1[G_{ll}] \right) \\ &= \frac{\partial\Phi_2[\{G_{lm}\}_{lm\in\{i,i+\delta\}}]}{\partial G_{i+\delta,i}}. \end{aligned} \tag{C35}$$

When there is translational, mirror, and rotational symmetry, the contribution to the local part coming from four different nearest-neighbor pairs will be the same, and the self-energy on all nearest-neighbor bonds will be the same (see Fig. 17),

$$\Sigma^{\text{latt}}_{\mathbf{r}=(0,0)} = 4\Sigma^{\text{imp}\,2\times1}_{00} - 3\Sigma^{\text{imp}\,1\times1}_{00}, \quad \Sigma^{\text{latt}}_{\mathbf{r}=(0,1)} = \Sigma^{\text{imp}\,2\times1}_{01}, \tag{C36}$$

and the self-consistency is

$$G^{\text{imp}\,2\times1}_{00/11} = G^{\text{imp}\,1\times1}_{00} = G^{\text{latt}}_{\mathbf{r}=(0,0)}, \quad G^{\text{imp}\,2\times1}_{01/10} = G^{\text{latt}}_{\mathbf{r}=(1,0)}. \tag{C37}$$

b. Long-distance dimers

In this section, we present a nested cluster scheme where self-energy at an arbitrary real-space vector is approximated by the self-energy of a corresponding two-site impurity problem. The expression for Φ and Σ^{latt} can be worked out analytically.

Let us define $i + n_x + n_y$ to be the index of the lattice site at the real-space vector $\mathbf{r} = \mathbf{r}_i + n_x\mathbf{e}_x + n_y\mathbf{e}_y$. We can

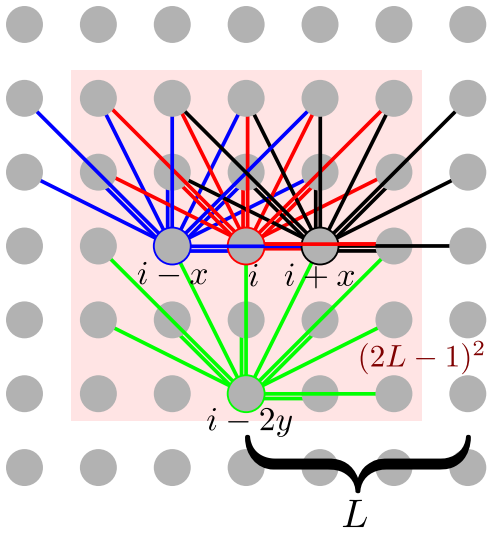

FIG. 18. Illustration of Eq. (C38). By placing the green set of dimers starting from each site, one covers all the dimers on the lattice, up to Manhattan distance $2(L-1)$. Each site is involved in $(2L-1)^2-1$ different dimers (red site goes with all the sites in the red square).

approximate the LW functional in such a way that it contains diagrams which involve at most two sites, but at a distance not bigger than $L-1$ in both directions (maximum Manhattan distance $2L-2$). We define the cluster notation $C_i^{(n_x,n_y)} \equiv \{i, i+n_x+n_y\}$. Analogously to Eq. (C33), one can prove the following approximation has no double counting:

$$\Phi \approx \sum_i \left(\sum_{\substack{n_x\in(-L,L)\\ n_y\in(0,L)}} + \sum_{\substack{n_x\in(0,L)\\ n_y=0}} \right) \Phi_2\left[\{G|_{C_i^{(n_x,n_y)}}\right] + (2-(2L-1)^2)\sum_i \Phi_1\left[G|_{C_i^{1\times1}}\right]. \tag{C38}$$

This is illustrated in Fig. 18. For example, the site with red outline is involved in dimers with all the sites within the red square, of which there are $(2L-1)^2-1$.

With translational/rotational/mirror symmetry, we get for the self-energy

$$\Sigma^{\text{latt}}_{\mathbf{r}=(0,0)} = \sum_{\substack{n_x\in(0,L)\\ n_y\in[0,n_x]}} m_{n_x,n_y}\Sigma_{00}^{\text{imp}\,(n_x,n_y)} + (2-(2L-1)^2)\Sigma_{00}^{\text{imp}\,1\times1},$$
$$\Sigma^{\text{latt}}_{\mathbf{r}=(n_x,n_y)} = \Sigma_{01}^{\text{imp}\,(n_x,n_y)}, \tag{C39}$$

where in the bottom row, $0<n_x<L, 0\leqslant n_y\leqslant n_x$. m_{n_x,n_y} is the multiplicity of the (nonzero) real-space vector $\mathbf{r}=n_x\mathbf{e}_x+n_y\mathbf{e}_y$

$$m_{n_x,n_y} = \begin{cases} 4, & n_x=0 \vee n_y=0 \vee n_x=n_y \\ 8, & \text{otherwise} \end{cases} \tag{C40}$$

and the self-consistency reads

$$G_{00/11}^{\text{imp}\,(n_x,n_y)} = G_{00}^{\text{imp}\,1\times1} = G^{\text{latt}}_{\mathbf{r}=(0,0)}, \quad G_{01/10}^{\text{imp}\,(n_x,n_y)} = G^{\text{latt}}_{\mathbf{r}=(n_x,n_y)}. \tag{C41}$$

The simplest example is the $2+2$ scheme corresponding to $L=2$, where we just take the dimer as in the previous example, and add the diagonal one $\{i, i+x, i+y\}$ (see Fig. 17):

$$\Sigma^{\text{latt}}_{\mathbf{r}=(0,0)} = 4\Sigma_{00}^{\text{imp}\,(0,1)} + 4\Sigma_{00}^{\text{imp}\,(1,1)} - 7\Sigma_{00}^{\text{imp}\,1\times1},$$
$$\Sigma^{\text{latt}}_{\mathbf{r}=(0,1)} = \Sigma_{01}^{\text{imp}\,(0,1)}, \tag{C42}$$
$$\Sigma^{\text{latt}}_{\mathbf{r}=(1,1)} = \Sigma_{01}^{\text{imp}\,(1,1)}.$$

Here we are solving three impurity problems: two of them two-site and one single-site.

c. 2 × 2

Here we discuss the special case of the square clusters scheme presented in Appendix C 2, with $L=2$. It corresponds to placing a square 2×2 cluster on all possible positions on the lattice. The Φ approximation is given by Eq. (4) with $L=2$.

We can write it more explicitly

$$\Phi^{(L=2)} = \sum_i \Phi_4[\{G_{lm}\}_{lm\in\{i,i+x,i+y,i+x+y\}}] - \sum_i \sum_{\delta\in\{x,y\}} \Phi_2[\{G_{lm}\}_{lm\in\{i,i+\delta\}}] + \sum_i \Phi_1[G_{ii}]. \tag{C43}$$

Now let us apply the derivative with respect to different components of the Green's function to get the expressions for self-energy:

$$\Sigma_{ii} = \frac{\partial}{\partial G_{ii}}\left[\sum_{l\in\{i,i-x,i-y,i-x-y\}} \Phi_4[\{G_{l'm'}\}_{l'm'\in\{l,l+x,l+y,l+x+y\}}] - \sum_{\delta\in\{x,y\}}\sum_{l\in\{i,i-\delta\}} \Phi_2[\{G_{l'm'}\}_{l'm'\in\{l,l+\delta\}}] + \Phi_1[\{G_{ii}\}]\right], \tag{C44}$$

$$\Sigma_{i,i+x} = \frac{\partial}{\partial G_{i+x,i}}\left[\sum_{l\in\{i,i-y\}} \Phi_4[\{G_{l'm'}\}_{l'm'\in\{l,l+x,l+y,l+x+y\}}] - \Phi_2[\{G_{lm}\}_{lm\in\{i,i+x\}}]\right].$$
$$\Sigma_{i,i+x+y} = \frac{\partial}{\partial G_{i+x+y,i}}\Phi_4[\{G_{lm}\}_{lm\in\{i,i+x,i+y,i+x+y\}}]. \tag{C45}$$

With full translational/rotational/mirror symmetry, clusters with same size and shape must give identical contributions to the self-energy. Following considerations analogous to Eqs. (C34) and (C35), we arrive at the final expression which connects the self energy on the lattice with the one in three different impurity problems (2×2, 2×1, and 1×1, see Fig. 17):

$$\Sigma^{\text{latt}}_{\mathbf{r}=(0,0)} = 4\Sigma_{00}^{\text{imp}\,2\times2} - 4\Sigma_{00}^{\text{imp}\,2\times1} + \Sigma_{00}^{\text{imp}\,1\times1},$$
$$\Sigma^{\text{latt}}_{\mathbf{r}=(1,0)} = 2\Sigma_{01}^{\text{imp}\,2\times2} - \Sigma_{01}^{\text{imp}\,2\times1},$$
$$\Sigma^{\text{latt}}_{\mathbf{r}=(1,1)} = \Sigma_{03}^{\text{imp}\,2\times2}, \tag{C46}$$

and the self-consistency condition is given by

$$G^{\mathrm{imp}\,2\times2}_{00/11/22/33} = G^{\mathrm{imp}\,2\times1}_{00/11} = G^{\mathrm{imp}\,1\times1}_{00} = G^{\mathrm{latt}}_{\mathbf{r}=(0,0)}, \quad G^{\mathrm{imp}\,2\times2}_{01/13/32/20/10/\ldots} = G^{\mathrm{imp}\,2\times1}_{01/10} = G^{\mathrm{latt}}_{\mathbf{r}=(0,1)}, \quad G^{\mathrm{imp}\,2\times2}_{03/30/12/21} = G^{\mathrm{latt}}_{\mathbf{r}=(1,1)}. \tag{C47}$$

d. 4 × 4

Using the algorithm (C 3) and lattice symmetries, we can now automatize the derivation of expressions for the self energy. Here we present as an example the expressions for the 4×4 nested scheme, where $\mathcal{C}$ contains all possible positions of a 4×4 cluster, and Φ approximation is given by Eq. (4) with $L = 4$.

6	7	8
3	4	5
0	1	2

12	13	14	15
8	9	10	11
4	5	6	7
0	1	2	3

8	9	10	11
4	5	6	7
0	1	2	3

$$\begin{aligned}
\Sigma^{\mathrm{latt}}_{\mathbf{r}=(0,0)} &= +4\Sigma^{\mathrm{imp}\,4\times4}_{00} + 8\Sigma^{\mathrm{imp}\,4\times4}_{11} + 4\Sigma^{\mathrm{imp}\,4\times4}_{55} - 8\Sigma^{\mathrm{imp}\,4\times3}_{00} - 4\Sigma^{\mathrm{imp}\,4\times3}_{44} + 4\Sigma^{\mathrm{imp}\,3\times3}_{00} - 8\Sigma^{\mathrm{imp}\,4\times3}_{11} \\
&\quad + 4\Sigma^{\mathrm{imp}\,3\times3}_{11} - 4\Sigma^{\mathrm{imp}\,4\times3}_{55} + \Sigma^{\mathrm{imp}\,3\times3}_{44}, \\
\Sigma^{\mathrm{latt}}_{\mathbf{r}=(1,0)} &= +4\Sigma^{\mathrm{imp}\,4\times4}_{01} + 4\Sigma^{\mathrm{imp}\,4\times4}_{15} + 2\Sigma^{\mathrm{imp}\,4\times4}_{12} + 2\Sigma^{\mathrm{imp}\,4\times4}_{56} - 4\Sigma^{\mathrm{imp}\,4\times3}_{01} - 2\Sigma^{\mathrm{imp}\,4\times3}_{45} \\
&\quad - 4\Sigma^{\mathrm{imp}\,4\times3}_{04} + 4\Sigma^{\mathrm{imp}\,3\times3}_{01} - 4\Sigma^{\mathrm{imp}\,4\times3}_{15} + 2\Sigma^{\mathrm{imp}\,3\times3}_{14} - 2\Sigma^{\mathrm{imp}\,4\times3}_{12} - \Sigma^{\mathrm{imp}\,4\times3}_{56}, \\
\Sigma^{\mathrm{latt}}_{\mathbf{r}=(1,1)} &= +2\Sigma^{\mathrm{imp}\,4\times4}_{05} + 4\Sigma^{\mathrm{imp}\,4\times4}_{16} + 2\Sigma^{\mathrm{imp}\,4\times4}_{14} + \Sigma^{\mathrm{imp}\,4\times4}_{5\,10} - 4\Sigma^{\mathrm{imp}\,4\times3}_{05} - 4\Sigma^{\mathrm{imp}\,4\times3}_{14} + 2\Sigma^{\mathrm{imp}\,3\times3}_{04} - 4\Sigma^{\mathrm{imp}\,4\times3}_{16} + 2\Sigma^{\mathrm{imp}\,3\times3}_{13}, \\
\Sigma^{\mathrm{latt}}_{\mathbf{r}=(2,0)} &= +4\Sigma^{\mathrm{imp}\,4\times4}_{02} + 4\Sigma^{\mathrm{imp}\,4\times4}_{19} - 4\Sigma^{\mathrm{imp}\,4\times3}_{02} - 2\Sigma^{\mathrm{imp}\,4\times3}_{46} - 2\Sigma^{\mathrm{imp}\,4\times3}_{08} + 2\Sigma^{\mathrm{imp}\,3\times3}_{02} - 2\Sigma^{\mathrm{imp}\,4\times3}_{19} + \Sigma^{\mathrm{imp}\,3\times3}_{17}, \\
\Sigma^{\mathrm{latt}}_{\mathbf{r}=(2,1)} &= +2\Sigma^{\mathrm{imp}\,4\times4}_{06} + 2\Sigma^{\mathrm{imp}\,4\times4}_{1\,10} + 2\Sigma^{\mathrm{imp}\,4\times4}_{17} - 2\Sigma^{\mathrm{imp}\,4\times3}_{06} - 2\Sigma^{\mathrm{imp}\,4\times3}_{17} - 2\Sigma^{\mathrm{imp}\,4\times3}_{09} + 2\Sigma^{\mathrm{imp}\,3\times3}_{05} - \Sigma^{\mathrm{imp}\,4\times3}_{1\,10}, \\
\Sigma^{\mathrm{latt}}_{\mathbf{r}=(2,2)} &= +2\Sigma^{\mathrm{imp}\,4\times4}_{0\,10} + 2\Sigma^{\mathrm{imp}\,4\times4}_{1\,11} - 4\Sigma^{\mathrm{imp}\,4\times3}_{0\,10} + \Sigma^{\mathrm{imp}\,3\times3}_{08}, \\
\Sigma^{\mathrm{latt}}_{\mathbf{r}=(3,0)} &= +2\Sigma^{\mathrm{imp}\,4\times4}_{03} + 2\Sigma^{\mathrm{imp}\,4\times4}_{1\,13} - 2\Sigma^{\mathrm{imp}\,4\times3}_{03} - \Sigma^{\mathrm{imp}\,4\times3}_{47}, \\
\Sigma^{\mathrm{latt}}_{\mathbf{r}=(3,1)} &= +2\Sigma^{\mathrm{imp}\,4\times4}_{07} + \Sigma^{\mathrm{imp}\,4\times4}_{1\,14} - 2\Sigma^{\mathrm{imp}\,4\times3}_{07}, \\
\Sigma^{\mathrm{latt}}_{\mathbf{r}=(3,2)} &= +2\Sigma^{\mathrm{imp}\,4\times4}_{0\,11} - \Sigma^{\mathrm{imp}\,4\times3}_{0\,11}, \\
\Sigma^{\mathrm{latt}}_{\mathbf{r}=(3,3)} &= +\Sigma^{\mathrm{imp}\,4\times4}_{0\,15}.
\end{aligned} \tag{C48}$$

In practice, we calculate self-energy for all vectors $\mathbf{r} = (x, y)$ such that $y \leqslant x$, up to $x = \max_C L_x(C) - 1$, and the rest is filled by lattice symmetry (analogously to Eq. (D17d) further below). In Eq. (C48), we have also used the symmetries of the clusters. The groups of equivalent bonds on all three clusters are given below in curly brackets (inversion symmetry $ij = ji$ is implicit):

3×3 :

6	7	8
3	4	5
0	1	2

{(0,0), (2,2), (6,6), (8,8)}; {(0,1), (0,3), (2,1), (2,5), (6,3), (6,7), (8,5), (8,7)};
{(0,2), (0,6), (2,8), (6,8)}; {(0,4), (2,4), (6,4), (8,4)}; {(0,5), (0,7), (2,3), (2,7), (6,1), (6,5), (8,1), (8,3)};
{(0,8), (2,6)}; {(1,1), (3,3), (5,5), (7,7)}; {(1,3), (1,5), (3,7), (5,7)};
{(1,4), (3,4), (5,4), (7,4)}; {(1,7), (3,5)}; {(4,4)}. (C49)

4×3 :

8	9	10	11
4	5	6	7
0	1	2	3

{(0,0), (3,3), (8,8), (11,11)}; {(0,1), (3,2), (8,9), (11,10)}; {(0,2), (3,1), (8,10), (11,9)};
{(0,4), (3,7), (8,4), (11,7)}; {(0,5), (3,6), (8,5), (11,6)}; {(0,6), (3,5), (8,6), (11,5)};
{(0,7), (3,4), (8,7), (11,4)}; {(0,8), (3,11)}; {(0,3), (8,11)}; {(0,9), (3,10), (8,1), (11,2)};
{(0,10), (3,9), (8,2), (11,1)}; {(0,11), (3,8)}; {(1,2), (9,10)}; {(1,1), (2,2), (9,9), (10,10)};
{(1,4), (2,7), (9,4), (10,7)}; {(1,5), (2,6), (9,5), (10,6)}; {(1,6), (2,5), (9,6), (10,5)};

{(1,7), (2,4), (9,7), (10,4)}; {(1,9), (2,10)}; {(1,10), (2,9)}; {(4,4), (7,7)}; {(4,5), (7,6)};
{(4,6), (7,5)}; {(4,7)}; {(5,5), (6,6)}; {(5,6)}. (C50)

4×4 :

12	13	14	15
8	9	10	11
4	5	6	7
0	1	2	3

{(0,0), (3,3), (12,12), (15,15)}; {(0,1), (0,4), (3,2), (3,7), (12,8), (12,13), (15,11), (15,14)};
{(0,2), (0,8), (3,1), (3,11), (12,4), (12,14), (15,7), (15,13)}; {(0,3), (0,12), (3,15), (12,15)};
{(0,5), (3,6), (12,9), (15,10)}; {(0,6), (0,9), (3,5), (3,10), (12,5), (12,10), (15,6), (15,9)};
{(0,7), (0,13), (3,4), (3,14), (12,1), (12,11), (15,2), (15,8)}; {(0,10), (3,9), (12,6), (15,5)};
{(0,11), (0,14), (3,8), (3,13), (12,2), (12,7), (15,1), (15,4)}; {(0,15), (3,12)};
{(1,1), (2,2), (4,4), (7,7), (8,8), (11,11), (13,13), (14,14)}; {(1,2), (4,8), (7,11), (13,14)};
{(1,4), (2,7), (8,13), (11,14)}; {(1,5), (2,6), (4,5), (7,6), (8,9), (11,10), (13,9), (14,10)};
{(1,6), (2,5), (4,9), (7,10), (8,5), (11,6), (13,10), (14,9)}; {(1,7), (2,4), (4,13), (7,14), (8,1), (11,2),
(13,11), (14,8)}; {(1,9), (2,10), (4,6), (7,5), (8,10), (11,9), (13,5), (14,6)};
{(1,10), (2,9), (4,10), (7,9), (8,6), (11,5), (13,6), (14,5)};
{(1,11), (2,8), (4,14), (7,13)}; {(1,13), (2,14), (4,7), (8,11)}; {(1,14), (2,13), (4,11), (7,8)};
{(5,5), (6,6), (9,9), (10,10)}; {(5,6), (5,9), (6,10), (9,10)}; {(5,10), (6,9)}. (C51)

APPENDIX D: CLUSTER DMFT METHODS

Here we summarize the (cluster) DMFT methods used in this paper.

The forward-substitution algorithm for the generic cluster DMFT scheme is presented in Fig. 19. Cluster DMFT methods differ in the cluster-impurity action, self-consistency condition, and the self-energy mapping $\Sigma^{\text{latt}}[\Sigma^{\text{imp}}]$—these properties we state for each method in the following sections. Where possible, we also state the LW functional approximation which leads to the given method.

1. Single-site DMFT

Single-site DMFT [5] is the limiting case of all cluster DMFT methods, corresponding to cluster size $N_c = 1$. It can be derived as the local approximation of the LW functional. While the exact LW functional depends on all components of the Green's function, in DMFT it depends only on the local components G_{ii}:

$$\Phi[\{G_{ij}\}_{\forall i,j}] \approx \Phi[\{G_{ii}\}_{\forall i}] = \sum_i \Phi[G_{ii}]. \tag{D1}$$

The second step is specific to local interactions, and is crucial to obtain a self-consistent scheme involving a single-site impurity problem.

The impurity action involves degrees of freedom of a single lattice site

$$S = \sum_\sigma \iint d\tau d\tau' c^+_\sigma(\tau)[-\mathcal{G}^{-1}_\sigma](\tau-\tau')c_\sigma(\tau') + U\int d\tau c^+_\uparrow(\tau)c^+_\downarrow(\tau)c_\downarrow(\tau)c_\uparrow(\tau). \tag{D2}$$

The self-consistency condition requires that the local Green's function on the lattice is the same as the one on the impurity,

$$G^{\text{imp}}(i\omega_n) = G^{\text{latt}}_{ii}(i\omega_n) \equiv \sum_{\mathbf{k}\in \text{BZ}} G^{\text{latt}}_{\mathbf{k}}(i\omega_n), \tag{D3}$$

where

$$G^{\text{latt}}_{\mathbf{k}}(i\omega_n) = \left(G^{-1}_{0,\mathbf{k}}(i\omega_n) - \Sigma^{\text{latt}}_{\mathbf{k}}(i\omega_n)\right)^{-1}. \tag{D4}$$

The self-energy approximation reads

$$\Sigma^{\text{latt}}_{\mathbf{k}}(i\omega_n) \approx \Sigma^{\text{imp}}(i\omega_n) \tag{D5}$$

as $\partial \sum_l \Phi[G_{ll}]/\partial G_{ij} \sim \delta_{ij}\partial\Phi[G_{ii}]/\partial G_{ii}$. The bare-propagator on the lattice

$$G_{0,\mathbf{k}}(i\omega_n) = \frac{1}{i\omega_n + \mu - \varepsilon_{\mathbf{k}}} \tag{D6}$$

is determined by the chemical potential μ and the bare dispersion $\varepsilon_{\mathbf{k}}$. On the square-lattice with only nearest-neighbor hopping, it is given by

$$\varepsilon_{\mathbf{k}} = -2t(\cos k_x + \cos k_y). \tag{D7}$$

2. Cellular DMFT (CDMFT)

Cellular DMFT rewrites the lattice problem in terms of supercells, as illustrated on Fig. 20 [9,11–26,88]. The lattice-site index is replaced by a double index: the index of the supercell and the index of the site within the supercell:

$$i \to (i,I), \quad G_{ij} \to G_{iI,jJ}.$$

We denote with $i,j,\ldots$ the index of the supercell, and with $I,J,\ldots$ the index of the site within the supercell. From here, the derivation proceeds just as in single-site DMFT—one may

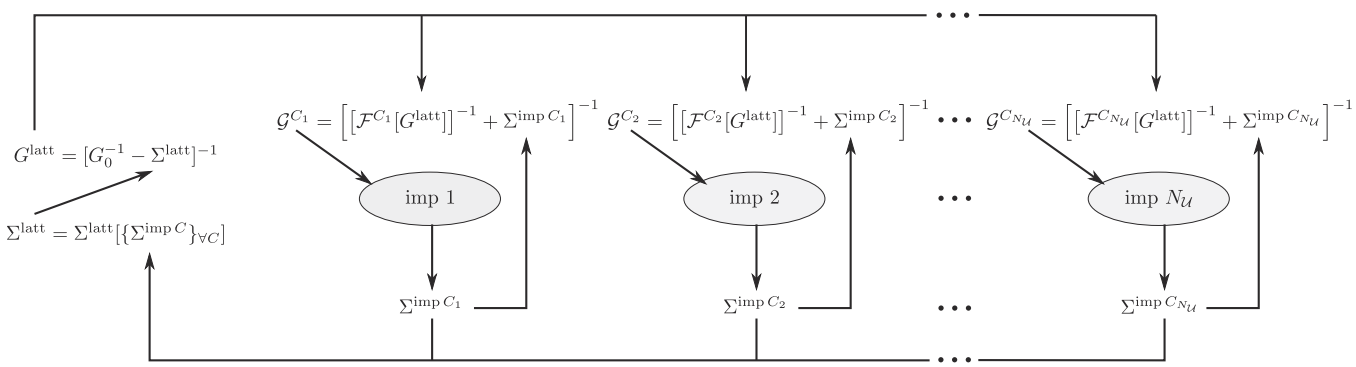

FIG. 19. Forward substitution solution of a generic cluster DMFT method. $N_\mathcal{U}$ is the number of independent impurity problems one needs to solve. In all methods except nested cluster, $N_\mathcal{U} = 1$. In nested cluster, it can be any number, but in the simplest scheme $N_\mathcal{U} = 3$ independently from the cluster size. The loop starts with an initial guess for Σ^{imp}. $\mathcal{F}^C[G^{\text{latt}}]$ project G^{latt} onto degrees of freedom of impurity C. Convergence is reached when $G^{\text{imp}\,C} = \mathcal{F}^C[G^{\text{latt}}]$ for each C.

view CDMFT as "single-supercell DMFT." The approximated LW functional then depends only on Green's function components within a single supercell

$$\Phi[\{\hat{G}_{ij}\}_{\forall i,j}] \approx \Phi[\{\hat{G}_{ii}\}_{\forall i}] = \sum_i \Phi[\hat{G}_{ii}], \tag{D8}$$

where with "hat" we denote matrix objects: $\hat{G}_{ij}$ is a matrix in the space of the I, J indices. Impurity action is given by

$$S = \sum_{IJ,\sigma} \iint d\tau d\tau' c^+_{\sigma,I}(\tau)\left[-\hat{\mathcal{G}}^{-1}_\sigma\right]_{IJ}(\tau - \tau')c_{\sigma,J}(\tau') + U\sum_I \int d\tau c^+_{\uparrow,I}(\tau)c^+_{\downarrow,I}(\tau)c_{\downarrow,I}(\tau)c_{\uparrow,I}(\tau) \tag{D9}$$

and the self-consistency condition reads

$$\hat{G}^{\text{imp}}(i\omega_n) = \hat{G}^{\text{latt}}_{ii}(i\omega_n) \equiv \sum_{\mathbf{k}\in\text{RBZ}} \hat{G}^{\text{latt}}_{\mathbf{k}}(i\omega_n), \tag{D10}$$

where RBZ stands for "reduced Brilloun zone." Note however, that in the derivation below we also rescale the lattice constant $a \to a/2$ so that no extra prefactors appear in the expressions,

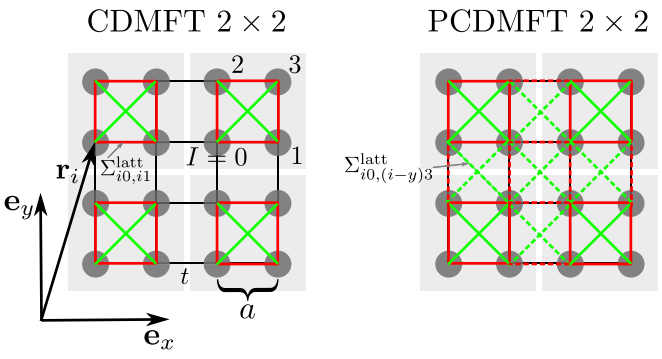

FIG. 20. Gray circles are lattice sites. Light gray squares are supercells. A site is denoted by the supercell index i and its index within the supercell I. In CDMFT, the self-energy is nonzero only between sites within a single supercell (green and red lines). In PCDMFT, it is copied by hand onto intercell bonds (dashed green and red lines). t is the hopping amplitude, a the lattice spacing, and $\mathbf{e}_{x,y}$ are the superlattice vectors.

and the RBZ extends from 0 to 2π along both axes. The lattice Dyson equation now involves a matrix inversion

$$\hat{G}^{\text{latt}}_{\mathbf{k}}(i\omega_n) = \left(\hat{G}^{-1}_{0,\mathbf{k}}(i\omega_n) - \hat{\Sigma}^{\text{latt}}_{\mathbf{k}}(i\omega_n)\right)^{-1}. \tag{D11}$$

The self-energy approximation is simply

$$\hat{\Sigma}^{\text{latt}}_{\mathbf{k}}(i\omega_n) \approx \hat{\Sigma}^{\text{imp}}(i\omega_n). \tag{D12}$$

Note that, physically, the self-energy is put exclusively on bonds *within* a supercell, and *not* on bonds between supercells. This artificially breaks the translational symmetry of the lattice.

The bare propagator and the dispersion need to be rewritten in the supercell language. Here we present the expressions in the simple 2×2 tiling ($\mathbf{e}_{x,y}/a \to 2\mathbf{e}_{x,y}/a$):

$$\hat{G}_{0,\mathbf{k}}(i\omega_n) = [(i\omega_n + \mu)\hat{I} - \hat{\varepsilon}_{\mathbf{k}}]^{-1}, \tag{D13}$$

$$\hat{\varepsilon}_{\mathbf{k}} = t \cdot \hat{u}_{\mathbf{k}}, \tag{D14}$$

$$\hat{u}_{\mathbf{k}} = \begin{bmatrix} & u(k_x) & u(k_y) & \\ u^*(k_x) & & & u(k_y) \\ u^*(k_y) & & & u(k_x) \\ & u^*(k_y) & u^*(k_x) & \end{bmatrix}, \tag{D15}$$

$$u(k) = 1 + e^{-ik}. \tag{D16}$$

The drawback of this approach is that no simple interpretation of the result in terms of the original, translationally invariant lattice is possible. To obtain a translationally invariant self-energy, which can be plotted in the original BZ requires a post-processing step, or "periodization." In the present case,

$$\Sigma^{\text{per}}_{\mathbf{r}=(0,0)} = \Sigma^{\text{imp}}_{00}, \tag{D17a}$$

$$\Sigma^{\text{per}}_{\mathbf{r}=(0,1)} = \Sigma^{\text{imp}}_{01}, \tag{D17b}$$

$$\Sigma^{\text{per}}_{\mathbf{r}=(1,1)} = \Sigma^{\text{imp}}_{03}. \tag{D17c}$$

The real-space vectors $\mathbf{r}$ are given in the basis of the original lattice vectors. The rest of the real-space vectors can be filled in by symmetry

$$\Sigma^{\text{per}}_{\mathbf{r}=(x,y)} = \Sigma^{\text{per}}_{\mathbf{r}=(\pm x,\pm y)} = \Sigma^{\text{per}}_{\mathbf{r}=(\pm y,\pm x)} \tag{D17d}$$

and then we can Fourier transform to $\mathbf{k}$ space:

$$\Sigma^{\text{per}}_{\mathbf{k}} = \sum_{\mathbf{r}} e^{i\mathbf{k}\cdot\mathbf{r}} \Sigma^{\text{per}}_{\mathbf{r}}. \tag{D17e}$$

Note that periodization is an *ad hoc* procedure that does not have a clear physical interpretation in terms of the LW approximation. Also, the physical quantity that is being periodized can be chosen arbitrarily, and different choices will in general lead to different results.

3. Periodized CDMFT (PCDMFT)

The idea of PCDMFT [6,8,49,50,52] is that the periodization should be performed in each DMFT iteration, and that the self-consistency should be closed using the translationally invariant Green's function, rather than the superlattice one. This scheme cannot be simply derived from an approximation of the LW functional. The impurity action remains the same as in CDMFT, Eq. (D9).

The idea of PCDMFT can be achieved either by placing the missing self-energies on the superlattice (see Fig. 20)

$$\begin{aligned}\hat{\Sigma}^{\text{latt}}_{\mathbf{k}}(i\omega_n) &\approx \Sigma^{\text{imp}}_{00}(i\omega_n)\hat{I} + \Sigma^{\text{imp}}_{01}(i\omega_n)\hat{u}_{\mathbf{k}} + \Sigma^{\text{imp}}_{03}(i\omega_n)\hat{w}_{\mathbf{k}} \\ &= \hat{\Sigma}^{\text{imp}}(i\omega_n) \circ (\hat{I} + \hat{u}_{\mathbf{k}} + \hat{w}_{\mathbf{k}}),\end{aligned} \tag{D18}$$

where $\circ$ denotes element-wise product, and

$$\hat{w}_{\mathbf{k}} = \begin{bmatrix} & & w_1(\mathbf{k}) \\ & w_2(\mathbf{k}) & \\ w_2^*(\mathbf{k}) & & \end{bmatrix}, \tag{D19}$$

$$w_1(\mathbf{k}) = 1 + e^{-ik_x} + e^{-ik_y} + e^{-i(k_x+k_y)}, \tag{D20}$$

$$w_2(\mathbf{k}) = 1 + e^{-ik_x} + e^{-ik_y} + e^{-i(k_x-k_y)}, \tag{D21}$$

or, equivalently, by periodizing the self-energy with Eq. (D17) and rewriting the self-consistency condition with

$$\hat{G}^{\text{imp}} = \begin{bmatrix} G^{\text{per}}_{\mathbf{r}=(0,0)} & G^{\text{per}}_{\mathbf{r}=(0,1)} & G^{\text{per}}_{\mathbf{r}=(0,1)} & G^{\text{per}}_{\mathbf{r}=(1,1)} \\ G^{\text{per}}_{\mathbf{r}=(0,1)} & G^{\text{per}}_{\mathbf{r}=(0,0)} & G^{\text{per}}_{\mathbf{r}=(1,1)} & G^{\text{per}}_{\mathbf{r}=(0,1)} \\ G^{\text{per}}_{\mathbf{r}=(0,1)} & G^{\text{per}}_{\mathbf{r}=(1,1)} & G^{\text{per}}_{\mathbf{r}=(0,0)} & G^{\text{per}}_{\mathbf{r}=(0,1)} \\ G^{\text{per}}_{\mathbf{r}=(1,1)} & G^{\text{per}}_{\mathbf{r}=(0,1)} & G^{\text{per}}_{\mathbf{r}=(0,1)} & G^{\text{per}}_{\mathbf{r}=(0,0)} \end{bmatrix}, \tag{D22}$$

where

$$G^{\text{per}}_{\mathbf{r}} = \sum_{\mathbf{k}\in BZ} e^{-i\mathbf{k}\cdot\mathbf{r}} G^{\text{per}}_{\mathbf{k}} = \sum_{\mathbf{k}\in BZ} \frac{e^{-i\mathbf{k}\cdot\mathbf{r}}}{G^{-1}_{0,\mathbf{k}}(i\omega_n) - \Sigma^{\text{per}}_{\mathbf{k}}(i\omega_n)}. \tag{D23}$$

The final result is the translationally invariant self-energy, which solves Eq. (D22).

Note there is another variant of PCDMFT method (proposed in Ref. [51]) where the self-energy is periodized with additional coefficients, so that it is rigorously causal. In the present case, this method would correspond to restoring translational invariance on the lattice the following way:

$$\hat{\Sigma}^{\text{latt}}_{\mathbf{k}}(i\omega_n) \approx \hat{\Sigma}^{\text{imp}}(i\omega_n) \circ \left(\hat{I} + \tfrac{1}{2}\hat{u}_{\mathbf{k}} + \tfrac{1}{4}\hat{w}_{\mathbf{k}}\right).$$

We observe that this method corrects the local part of self-energy in the difficult regime compared to regular PCDMFT, but the nonlocal part is strongly underestimated throughout the phase diagram (results not shown).

4. Dynamical cluster approximation (DCA)

In DCA [7,27–45] method, the conservation of momentum in LW diagrams is approximated by [27,33]

$$\mathbf{k}' - \mathbf{k} = \mathbf{q} \longrightarrow \mathbf{K}(\mathbf{k}') - \mathbf{K}(\mathbf{k}) = \mathbf{K}(\mathbf{q}), \tag{D24}$$

where $\mathbf{K}$ represents the "coarse-grained" BZ points, which is illustrated on Fig. 21. The coarse-grained BZ contains only a certain finite and discrete subset of wave vectors. The notation $\mathbf{K}(\mathbf{k})$ means "the coarse grained wave vector closest to the wave vector $\mathbf{k}$." Because of the relaxation of momentum conservation, the diagrams factorize: the LW functional still depends on all G components, but only through their sums:

$$\Phi[\{G_{\mathbf{k}}\}_{\forall\mathbf{k}}] \approx \Phi\left[\left\{\sum_{\mathbf{k}\in\mathcal{P}(\mathbf{K})} G_{\mathbf{k}}\right\}_{\forall\mathbf{K}}\right] \equiv \Phi[\{G_{\mathbf{K}}\}_{\forall\mathbf{K}}]. \tag{D25}$$

Here, $\mathcal{P}(\mathbf{K})$ is the set of fine-grain wave vectors $\mathbf{k}$ that are closest to the coarse-grained wave vector $\mathbf{K}$ (Voronoi patch [89] around $\mathbf{K}$). This approximation leads to a piecewise-constant self-energy in $\mathbf{k}$ space, because of

$$\frac{\partial\Phi[G_{\mathbf{K}}]}{\partial G_{\mathbf{k}}} = \frac{\partial\Phi[G_{\mathbf{K}}]}{\partial G_{\mathbf{K}}}\frac{\partial G_{\mathbf{K}}}{\partial G_{\mathbf{k}}} = \frac{\partial\Phi[G_{\mathbf{K}}]}{\partial G_{\mathbf{K}}}\delta_{\mathbf{k}\in\mathcal{P}(\mathbf{K})}. \tag{D26}$$

The impurity action is given by

$$\begin{aligned}S = &\sum_{\mathbf{K},\sigma}\iint d\tau d\tau' c^+_{\sigma,\mathbf{K}}(\tau)\left[-\mathcal{G}^{-1}_{\sigma,\mathbf{K}}(\tau-\tau')\right]c_{\sigma,\mathbf{K}}(\tau') \\ &+ U\sum_{\mathbf{K},\mathbf{K}',\mathbf{Q}}\int d\tau\, c^+_{\uparrow,\mathbf{K}+\mathbf{Q}}(\tau)c^+_{\downarrow,\mathbf{K}'-\mathbf{Q}}(\tau)c_{\downarrow,\mathbf{K}'}(\tau)c_{\uparrow,\mathbf{K}}(\tau),\end{aligned} \tag{D27}$$

and it corresponds to a finite cyclic cluster in real space $\mathbf{R}$.

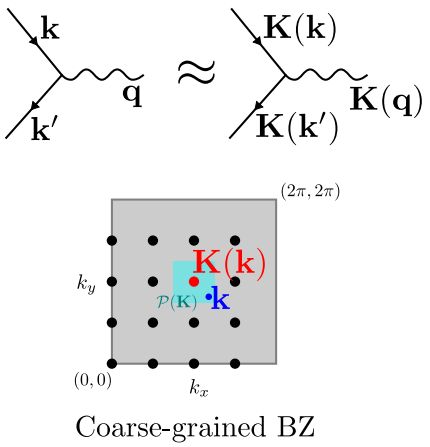

FIG. 21. DCA approximates momentum-conservation. Lattice self-energy at wave vector $\mathbf{k}$ is obtained from the impurity self-energy at the closest coarse grained wave vector $\mathbf{K}$. Therefore it is constant within each Voronoi patch $\mathcal{P}(\mathbf{K})$. The example presented is the 4×4 scheme.

Self-consistency condition reads

$$G^{\text{imp}}_{\mathbf{K}}(i\omega_n) = G^{\text{latt}}_{\mathbf{K}}(i\omega_n) \equiv \sum_{\mathbf{k}\in\mathcal{P}(\mathbf{K})} G^{\text{latt}}_{\mathbf{k}}(i\omega_n). \tag{D28}$$

As already mentioned, the self-energy on the lattice is simply

$$\Sigma^{\text{latt}}_{\mathbf{k}}(i\omega_n) = \Sigma^{\text{imp}}_{\mathbf{K}(\mathbf{k})}(i\omega_n). \tag{D29}$$

Note that more general coarse-graining schemes exist, and that $\mathcal{P}(\mathbf{K})$ does not necessarily present a Voronoi patch around the wave vector $\mathbf{K}$. Patches may have different shapes [29], and may even be interlaced [46]. In the present paper, we only use the simplest scheme where patches are Voronoi patches, and all have the same shape.

5. Continuous self-energy DCA (DCA$^+$)

DCA$^+$[46–48] aims at improving the interpretation of the impurity self-energy in terms of the self-energy on the lattice. A piecewise constant self-energy is strongly counter intuitive and hard to compare to other methods. It is a natural step to try and interpolate the coarse-grained self-energy to obtain a smooth self-energy on the lattice. However, this scheme does not have a clear derivation as a LW functional approximation. Furthermore, the interpolation can be done in various ways, and the method is not uniquely defined. In this paper we implement (and present here) the version of the method as proposed in the original paper, Ref. [48].

The impurity action is the same as in DCA, Eq. (D27).

The difference from DCA is the addition of a self-consistency condition that needs to be satisfied:

$$\Sigma^{\text{imp}}_{\mathbf{K}}(i\omega_n) = \Sigma^{\text{latt}}_{\mathbf{K}}(i\omega_n) \equiv \sum_{\mathbf{k}\in\mathcal{P}(\mathbf{K})} \Sigma^{\text{latt}}_{\mathbf{k}}(i\omega_n). \tag{D30}$$

Here, Σ^{latt} is a smooth function of $\mathbf{k}$. Note that for a given $\Sigma^{\text{imp}}_{\mathbf{K}}$, Σ^{latt} is not uniquely defined. This self-consistency condition imposes

$$\Sigma^{\text{latt}}_{\text{loc}} = \Sigma^{\text{imp}}_{\text{loc}}, \tag{D31}$$

but in general

$$\Sigma^{\text{latt}}_{\mathbf{k}=\mathbf{K}} \neq \Sigma^{\text{imp}}_{\mathbf{K}}. \tag{D32}$$

While a general interpolation of $\Sigma^{\text{imp}}_{\mathbf{K}}$ is unlikely to satisfy the condition (D30), a Bayesian approach can be employed to find the most probable interpolation that does satisfy it. The method used is Richardson-Lucy deconvolution, and it is performed with respect to an interpolation of $\Sigma^{\text{imp}}_{\mathbf{K}} \to \bar{\Sigma}^{\text{imp}}_{\mathbf{k}}$ such that

$$\bar{\Sigma}^{\text{imp}}_{\mathbf{k}=\mathbf{K}} = \Sigma^{\text{imp}}_{\mathbf{K}}. \tag{D33}$$

One starts from an initial guess for Σ^{latt} (say, $\Sigma^{\text{latt}}_{\mathbf{k}} = \bar{\Sigma}^{\text{imp}}_{\mathbf{k}}$), and iterates

$$\Sigma^{\text{latt}}_{\mathbf{k}} \leftarrow \Sigma^{\text{latt}}_{\mathbf{k}} \sum_{\mathbf{k}'\in\mathcal{P}(\mathbf{k})} \frac{\bar{\Sigma}^{\text{imp}}_{\mathbf{k}'}}{\sum_{\mathbf{k}''\in\mathcal{P}(\mathbf{k}')} \Sigma^{\text{latt}}_{\mathbf{k}''}} \tag{D34}$$

until convergence is reached. Here, $\mathcal{P}(\mathbf{k})$ denotes a patch of the same shape/size as the Voronoi patches of the coarse-grained BZ, but centered at the fine-grain wave vector $\mathbf{k}$. The final result has the property

$$\bar{\Sigma}^{\text{imp}}_{\mathbf{k}} = \sum_{\mathbf{k}'\in\mathcal{P}(\mathbf{k})} \Sigma^{\text{latt}}_{\mathbf{k}'}, \quad \forall \mathbf{k}, \tag{D35}$$

which satisfies a stronger requirement than necessary.

Note also that the actual interpolation is performed not on Σ^{imp}, but on an auxiliary quantity Ξ which is by construction more local than the self-energy. The method of interpolation proposed is the Wannier interpolation

$$\Xi_{\mathbf{K}}(i\omega_n) = \left(\Sigma^{\text{imp}}_{\mathbf{K}}(i\omega_n) - \text{sgn}(\omega_n) i\alpha\right)^{-1}, \tag{D36}$$

$$\Xi_{\mathbf{R}} = \sum_{\mathbf{K}} e^{-i\mathbf{K}\cdot\mathbf{R}} \Xi_{\mathbf{K}}, \tag{D37}$$

$$\bar{\Xi}_{\mathbf{k}} = \sum_{\mathbf{R}} e^{i\mathbf{k}\cdot\mathbf{R}} \Xi_{\mathbf{R}}, \tag{D38}$$

$$\bar{\Sigma}^{\text{imp}}_{\mathbf{k}}(i\omega_n) = \bar{\Xi}^{-1}_{\mathbf{k}}(i\omega_n) + \text{sgn}(\omega_n) i\alpha, \quad \alpha > 0. \tag{D39}$$

Note that $\bar{\Xi}_{\mathbf{k}}$ does not necessarily satisfy all the lattice symmetries. One way to restore lattice symmetries is to calculate it as

$$\bar{\Xi}_{\mathbf{k}} = \frac{1}{N_M} \sum_{\hat{M}} \sum_{\mathbf{R}} e^{i\mathbf{k}\cdot\hat{M}\mathbf{R}} \Xi_{\mathbf{R}}, \tag{D40}$$

where $\hat{M}$ runs over all the symmetry operations on the lattice, of which there are N_M. On the square lattice there are $N_M = 8$ operations ($\mathbf{R}_{x,y} \to \pm\mathbf{R}_{(x,y),(y,x)}$), which restore the eightfold symmetry in $\bar{\Xi}_{\mathbf{k}}$. Examples of different self-energy quantities appearing in DCA$^+$ are given in Fig. 22 and compared to the piecewise-constant interpolation that is used in standard DCA.

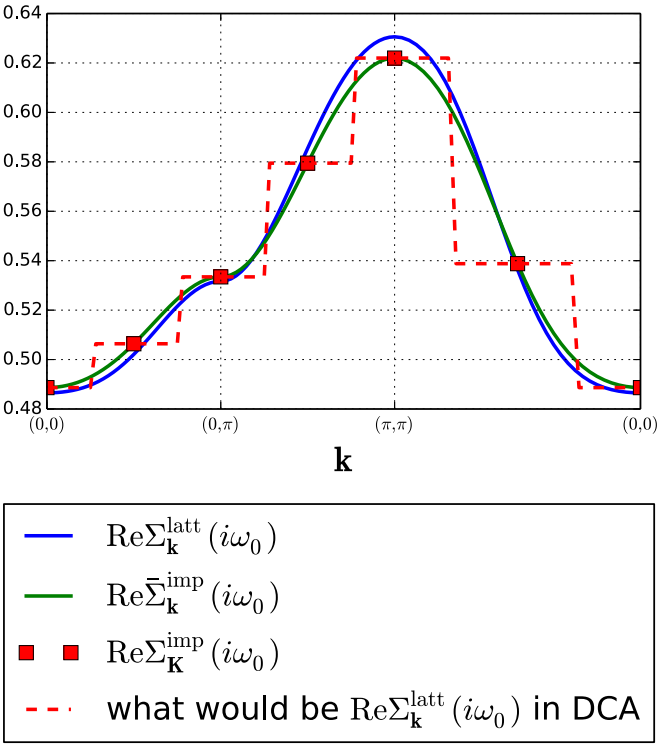

FIG. 22. Example of various quantities appearing in DCA$^+$. Parameters of the calculation: $U/D = 1.4$, $\delta = 8\%$, and $T/D = 0.125$.

[1] G. Baym and L. P. Kadanoff, Phys. Rev. **124**, 287 (1961).
[2] C. D. Dominicis and P. C. Martin, J. Math. Phys. **5**, 14 (1964).
[3] C. D. Dominicis and P. C. Martin, J. Math. Phys. **5**, 31 (1964).
[4] P. Nozieres, *Theory Of Interacting Fermi Systems (Advanced Books Classics)* (Westview Press, Boulder, Colorado, USA, 1997).
[5] A. Georges, G. Kotliar, W. Krauth, and M. J. Rozenberg, Rev. Mod. Phys. **68**, 13 (1996).
[6] G. Kotliar, S. Y. Savrasov, K. Haule, V. S. Oudovenko, O. Parcollet, and C. A. Marianetti, Rev. Mod. Phys. **78**, 865 (2006).
[7] M. H. Hettler, A. N. Tahvildar-Zadeh, M. Jarrell, T. Pruschke, and H. R. Krishnamurthy, Phys. Rev. B **58**, R7475 (1998).
[8] A. I. Lichtenstein and M. I. Katsnelson, Phys. Rev. B **62**, R9283 (2000).
[9] G. Kotliar, S. Y. Savrasov, G. Pálsson, and G. Biroli, Phys. Rev. Lett. **87**, 186401 (2001).
[10] T. A. Maier, M. Jarrell, T. Pruschke, and M. H. Hettler, Rev. Mod. Phys. **77**, 1027 (2005).
[11] M. Civelli, Phys. Rev. B **79**, 195113 (2009).
[12] M. Civelli, M. Capone, A. Georges, K. Haule, O. Parcollet, T. D. Stanescu, and G. Kotliar, Phys. Rev. Lett. **100**, 046402 (2008).
[13] M. Civelli, M. Capone, S. S. Kancharla, O. Parcollet, and G. Kotliar, Phys. Rev. Lett. **95**, 106402 (2005).
[14] L. De Leo, M. Civelli, and G. Kotliar, Phys. Rev. B **77**, 075107 (2008).
[15] S. S. Kancharla, B. Kyung, D. Sénéchal, M. Civelli, M. Capone, G. Kotliar, and A.-M. S. Tremblay, Phys. Rev. B **77**, 184516 (2008).
[16] B. Kyung, S. S. Kancharla, D. Sénéchal, A.-M. S. Tremblay, M. Civelli, and G. Kotliar, Phys. Rev. B **73**, 165114 (2006).
[17] B. Kyung, G. Kotliar, and A.-M. S. Tremblay, Phys. Rev. B **73**, 205106 (2006).
[18] S. Okamoto, D. Sénéchal, M. Civelli, and A.-M. S. Tremblay, Phys. Rev. B **82**, 180511 (2010).
[19] Ž. Osolin and R. Žitko, Phys. Rev. B **95**, 035107 (2017).
[20] O. Parcollet, G. Biroli, and G. Kotliar, Phys. Rev. Lett. **92**, 226402 (2004).
[21] H. Park, K. Haule, and G. Kotliar, Phys. Rev. Lett. **101**, 186403 (2008).
[22] S. Sakai, M. Civelli, and M. Imada, Phys. Rev. B **94**, 115130 (2016).
[23] G. Sordi, K. Haule, and A.-M. S. Tremblay, Phys. Rev. B **84**, 075161 (2011).
[24] G. Sordi, K. Haule, and A.-M. S. Tremblay, Phys. Rev. Lett. **104**, 226402 (2010).
[25] G. Sordi, P. Sémon, K. Haule, and A.-M. S. Tremblay, Phys. Rev. B **87**, 041101 (2013).
[26] Y. Z. Zhang and M. Imada, Phys. Rev. B **76**, 045108 (2007).
[27] K. Aryanpour, M. H. Hettler, and M. Jarrell, Phys. Rev. B **65**, 153102 (2002).
[28] H. T. Dang, X. Y. Xu, K.-S. Chen, Z. Y. Meng, and S. Wessel, Phys. Rev. B **91**, 155101 (2015).
[29] M. Ferrero, P. S. Cornaglia, L. De Leo, O. Parcollet, G. Kotliar, and A. Georges, Phys. Rev. B **80**, 064501 (2009).
[30] M. Ferrero, P. S. Cornaglia, L. De Leo, O. Parcollet, G. Kotliar, and A. Georges, Europhys. Lett. **85**, 57009 (2008).
[31] M. Ferrero, O. Parcollet, A. Georges, G. Kotliar, and D. N. Basov, Phys. Rev. B **82**, 054502 (2010).
[32] E. Gull, M. Ferrero, O. Parcollet, A. Georges, and A. J. Millis, Phys. Rev. B **82**, 155101 (2010).
[33] M. H. Hettler, M. Mukherjee, M. Jarrell, and H. R. Krishnamurthy, Phys. Rev. B **61**, 12739 (2000).
[34] C. Huscroft, M. Jarrell, T. Maier, S. Moukouri, and A. N. Tahvildarzadeh, Phys. Rev. Lett. **86**, 139 (2001).
[35] M. Jarrell, T. A. Maier, C. Huscroft, and S. Moukouri, Phys. Rev. B **64**, 195130 (2001).
[36] P. R. C. Kent, M. Jarrell, T. A. Maier, and T. Pruschke, Phys. Rev. B **72**, 060411 (2005).
[37] J. P. F. LeBlanc, A. E. Antipov, F. Becca, I. W. Bulik, G. K.-L. Chan, C.-M. Chung, Y. Deng, M. Ferrero, T. M. Henderson, C. A. Jiménez-Hoyos, E. Kozik, X.-W. Liu, A. J. Millis, N. V. Prokof'ev, M. Qin, G. E. Scuseria, H. Shi, B. V. Svistunov, L. F. Tocchio, I. S. Tupitsyn, S. R. White, S. Zhang, B.-X. Zheng, Z. Zhu, and E. Gull, (Simons Collaboration on the Many-Electron Problem) Phys. Rev. X **5**, 041041 (2015).
[38] A. Macridin, M. Jarrell, and T. A. Maier, Phys. Rev. B **70**, 113105 (2004).
[39] A. Macridin, M. Jarrell, T. Maier, P. R. C. Kent, and E. D'Azevedo, Phys. Rev. Lett. **97**, 036401 (2006).
[40] A. Macridin, M. Jarrell, T. Maier, and D. J. Scalapino, Phys. Rev. Lett. **99**, 237001 (2007).
[41] T. A. Maier, M. Jarrell, A. Macridin, and C. Slezak, Phys. Rev. Lett. **92**, 027005 (2004).
[42] T. A. Maier, M. Jarrell, T. C. Schulthess, P. R. C. Kent, and J. B. White, Phys. Rev. Lett. **95**, 237001 (2005).
[43] T. A. Maier, M. S. Jarrell, and D. J. Scalapino, Phys. Rev. Lett. **96**, 047005 (2006).
[44] T. A. Maier and D. J. Scalapino, Phys. Rev. B **84**, 180513 (2011).
[45] T. A. Maier, P. Staar, and D. J. Scalapino, arXiv:1507.06206.
[46] P. Staar, M. Jiang, U. R. Hähner, T. C. Schulthess, and T. A. Maier, Phys. Rev. B **93**, 165144 (2016).
[47] P. Staar, T. Maier, and T. C. Schulthess, Phys. Rev. B **89**, 195133 (2014).
[48] P. Staar, T. Maier, and T. C. Schulthess, Phys. Rev. B **88**, 115101 (2013).
[49] Q.-X. Li, R.-Q. He, and Z.-Y. Lu, Phys. Rev. B **92**, 155127 (2015).
[50] T. D. Stanescu and G. Kotliar, Phys. Rev. B **74**, 125110 (2006).
[51] G. Biroli and G. Kotliar, Phys. Rev. B **65**, 155112 (2002).
[52] G. Biroli, O. Parcollet, and G. Kotliar, Phys. Rev. B **69**, 205108 (2004).
[53] S. Sakai, G. Sangiovanni, M. Civelli, Y. Motome, K. Held, and M. Imada, Phys. Rev. B **85**, 035102 (2012).
[54] T. Ayral and O. Parcollet, Phys. Rev. B **93**, 235124 (2016).
[55] T. Ayral and O. Parcollet, Phys. Rev. B **94**, 075159 (2016).
[56] T. Ayral and O. Parcollet, Phys. Rev. B **92**, 115109 (2015).
[57] T. Ayral, J. Vucicevic, and O. Parcollet, Phys. Rev. Lett. **119**, 166401 (2017).
[58] J. Vučičević, T. Ayral, and O. Parcollet, Phys. Rev. B **96**, 104504 (2017).
[59] A. Georges, in *Lectures on the Physics of Highly Correlated Electron Systems VIII: Eighth Training Course in the Physics of Correlated Electron Systems and High-Tc Superconductors*, edited by A. Avella and F. Mancini, AIP Conf. Proc. No. 715 (AIP, New York, 2004), pp. 3–74.
[60] E. Kozik, M. Ferrero, and A. Georges, Phys. Rev. Lett. **114**, 156402 (2015).
[61] O. Gunnarsson, G. Rohringer, T. Schäfer, G. Sangiovanni, and A. Toschi, Phys. Rev. Lett. **119**, 056402 (2017).

[62] G. Rohringer, H. Hafermann, A. Toschi, A. A. Katanin, A. E. Antipov, M. I. Katsnelson, A. I. Lichtenstein, A. N. Rubtsov, and K. Held, arXiv:1705.00024.
[63] T. Schäfer, G. Rohringer, O. Gunnarsson, S. Ciuchi, G. Sangiovanni, and A. Toschi, Phys. Rev. Lett. **110**, 246405 (2013).
[64] T. Schäfer, S. Ciuchi, M. Wallerberger, P. Thunström, O. Gunnarsson, G. Sangiovanni, G. Rohringer, and A. Toschi, Phys. Rev. B **94**, 235108 (2016).
[65] O. Gunnarsson, T. Schäfer, J. P. F. LeBlanc, J. Merino, G. Sangiovanni, G. Rohringer, and A. Toschi, Phys. Rev. B **93**, 245102 (2016).
[66] T. Ribic, G. Rohringer, and K. Held, Phys. Rev. B **93**, 195105 (2016).
[67] O. Gunnarsson, T. Schäfer, J. P. F. LeBlanc, E. Gull, J. Merino, G. Sangiovanni, G. Rohringer, and A. Toschi, Phys. Rev. Lett. **114**, 236402 (2015).
[68] W. Wu, M. Ferrero, A. Georges, and E. Kozik, Phys. Rev. B **96**, 041105 (2017).
[69] F. Tandetzky, J. K. Dewhurst, S. Sharma, and E. K. U. Gross, Phys. Rev. B **92**, 115125 (2015).
[70] A. Schiller and K. Ingersent, Phys. Rev. Lett. **75**, 113 (1995).
[71] A. A. Kananenka, E. Gull, and D. Zgid, Phys. Rev. B **91**, 121111 (2015).
[72] T. N. Lan, A. Shee, J. Li, E. Gull, and D. Zgid, Phys. Rev. B **96**, 155106 (2017).
[73] T. N. Lan and D. Zgid, arXiv:1703.06981.
[74] M. Motta, D. M. Ceperley, G. K.-L. Chan, J. A. Gomez, E. Gull, S. Guo, C. Jimenez-Hoyos, T. N. Lan, J. Li, F. Ma, A. J. Millis, N. V. Prokof'ev, U. Ray, G. E. Scuseria, S. Sorella, E. M. Stoudenmire, Q. Sun, I. S. Tupitsyn, S. R. White, D. Zgid, and S. Zhang, Phys. Rev. X **7**, 031059 (2017).
[75] D. Zgid and E. Gull, New J. Phys. **19**, 023047 (2017).
[76] V. Janiš and V. Pokorný, Phys. Rev. B **90**, 045143 (2014).
[77] A. Stan, P. Romaniello, S. Rigamonti, L. Reining, and J. A. Berger, New J. Phys. **17**, 093045 (2015).
[78] A. I. Rubtsov and A. N. Lichtenstein, J. Exp. Theor. Phys. Lett. **80**, 61 (2004).
[79] E. Gull, A. J. Millis, A. I. Lichtenstein, A. N. Rubtsov, M. Troyer, and P. Werner, Rev. Mod. Phys. **83**, 349 (2011).
[80] The hybridization is Δ is defined by $\Delta(i\omega_n) \equiv i\omega_n + C - \mathcal{G}^{-1}$, where C is a constant such that $\Delta(i\omega_n) \xrightarrow{n\to\infty} 0$.
[81] T. Jabben, N. Grewe, and S. Schmitt, Phys. Rev. B **85**, 165122 (2012).
[82] S. Okamoto, A. J. Millis, H. Monien, and A. Fuhrmann, Phys. Rev. B **68**, 195121 (2003).
[83] R. Rossi, F. Werner, N. Prokof'ev, and B. Svistunov, Phys. Rev. B **93**, 161102 (2016).
[84] O. Parcollet, M. Ferrero, T. Ayral, H. Hafermann, P. Seth, and I. S. Krivenko, Comput. Phys. Commun. **196**, 398 (2015).
[85] G. Rohringer, A. Valli, and A. Toschi, Phys. Rev. B **86**, 125114 (2012).
[86] N. Bickers, in *Theoretical Methods for Strongly Correlated Electrons*, edited by D. Sènèchal, A.-M. Tremblay, and C. Bourbonnais, CRM Series in Mathematical Physics (Springer, New York, 2004), pp. 237–296.
[87] P. Sun and G. Kotliar, Phys. Rev. B **66**, 085120 (2002).
[88] D. Tanasković, K. Haule, G. Kotliar, and V. Dobrosavljević, Phys. Rev. B **84**, 115105 (2011).
[89] F. Aurenhammer, ACM Comput. Surv. **23**, 345 (1991).

Fierz Convergence Criterion: A Controlled Approach to Strongly Interacting Systems with Small Embedded Clusters

Thomas Ayral,[1,2] Jaksa Vučičević,[2,3] and Olivier Parcollet[2]
[1]Physics and Astronomy Department, Rutgers University, Piscataway, New Jersey 08854, USA
[2]Institut de Physique Théorique (IPhT), CEA, CNRS, UMR 3681, 91191 Gif-sur-Yvette, France
[3]Scientific Computing Laboratory, Center for the Study of Complex Systems, Institute of Physics Belgrade, University of Belgrade, Pregrevica 118, 11080 Belgrade, Serbia
(Received 5 June 2017; published 16 October 2017)

We present an embedded-cluster method, based on the triply irreducible local expansion formalism. It turns the Fierz ambiguity, inherent to approaches based on a bosonic decoupling of local fermionic interactions, into a convergence criterion. It is based on the approximation of the three-leg vertex by a coarse-grained vertex computed from a self-consistently determined cluster impurity model. The computed self-energies are, by construction, continuous functions of momentum. We show that, in three interaction and doping regimes of the two-dimensional Hubbard model, self-energies obtained with clusters of size four only are very close to numerically exact benchmark results. We show that the Fierz parameter, which parametrizes the freedom in the Hubbard-Stratonovich decoupling, can be used as a quality control parameter. By contrast, the GW + extended dynamical mean field theory approximation with four cluster sites is shown to yield good results only in the weak-coupling regime and for a particular decoupling. Finally, we show that the vertex has spatially nonlocal components only at low Matsubara frequencies.

DOI: 10.1103/PhysRevLett.119.166401

Two major approaches have been put forth to fathom the nature of high-temperature superconductivity. Spin fluctuation theory [1–8], inspired by the early experiments on cuprate compounds, is based on the introduction of phenomenological bosonic fluctuations coupled to the electrons. It belongs to a larger class of methods, including the fluctuation-exchange (FLEX) [9] and GW approximations [10,11], or the Eliashberg theory of superconductivity [12]. In the Hubbard model, these methods can formally be obtained by decoupling the electronic interactions with Hubbard-Stratonovich (HS) bosons carrying charge, spin, or pairing fluctuations. They are particularly well suited for describing long-range modes. However, they suffer from two main drawbacks: without an analog of Migdal's theorem for spin fluctuations they are quantitatively uncontrolled; worse, the results depend on the precise form of the bosonic fluctuations used to decouple the interaction term, an issue dubbed the "Fierz ambiguity" [13–18].

A second class of methods, following Anderson [19], puts primary emphasis on the fact that the undoped compounds are Mott insulators, where local physics plays a central role. Approaches like dynamical mean field theory (DMFT) [20] and its cluster extensions [21–25], which self-consistently map the lattice problem onto an effective problem describing a cluster of interacting atoms embedded in a noninteracting host, are tools of choice to examine Anderson's idea. Cluster DMFT has indeed been shown to give a consistent qualitative picture of cuprate physics, including pseudogap and superconducting phases [26–54]. Compared to fluctuation theories, it *a priori* comes with a control parameter, the size N_c of the embedded cluster. However, this is of limited practical use, since the convergence with N_c is nonmonotonic for small N_c [33], requiring large N_cs, which cannot be reached in interesting physical regimes due to the Monte Carlo negative sign problem. Thus, converged cluster DMFT results can only be obtained at high temperatures [55]. There, detailed studies [56–58] point to the importance of (possibly long-ranged) spin fluctuations, calling for a unification of both approaches. First steps in this direction have been accomplished by diagrammatic extensions of DMFT [59–80], and by the single-site triply irreducible local expansion (TRILEX) formalism [81,82], which interpolates between long-range and Mott physics and describes aspects of pseudogap physics and the d-wave superconducting dome [83].

In this Letter, we turn the Fierz ambiguity into a convergence criterion in the cluster extension of TRILEX. Like fluctuation approaches, cluster TRILEX is based on the introduction of bosonic degrees of freedom. Like cluster DMFT, it maps the corresponding electron-boson problem onto a cluster impurity problem. The latter is solved for its three-leg vertex, which is used as a cluster vertex correction to the self-energies. This approach improves on fluctuation approaches by endowing them with a control parameter, thus curing the absence of a Migdal theorem. In some parameter regimes, it can solve the cluster DMFT large-N_c stalemate by instead requiring minimal sensitivity to the Fierz parameter as a convergence criterion of the solution.

To illustrate the method, we focus on the two-dimensional Hubbard model, the simplest model to describe high-temperature superconductors. Its Hamiltonian reads

$$H = \sum_{ij\sigma} t_{ij} c^\dagger_{i\sigma} c_{j\sigma} + U \sum_i n_{i\uparrow} n_{i\downarrow}, \tag{1}$$

where $c^\dagger_{i\sigma}$ ($c_{i\sigma}$) creates (annihilates) an electron of spin σ at Bravais site $\mathbf{r}_i$, t_{ij} is the hopping matrix [with (next-)nearest-neighbor hopping t (t')], and U the local electronic repulsion. We set $t = -0.25$ and use $D \equiv 4|t|$ as the energy unit.

The first step of the TRILEX method consists in decoupling the interaction term with HS fields. There are several possible such decouplings. Here, we choose [84] to express the interaction in the charge and longitudinal spin channel ("Ising decoupling"), i.e., up to a density term

$$U n_{i\uparrow} n_{i\downarrow} = \frac{1}{2} U^{\mathrm{ch}} n_i n_i + \frac{1}{2} U^{\mathrm{sp}} s^z_i s^z_i, \tag{2}$$

with $n \equiv n_\uparrow + n_\downarrow$ and $s^z \equiv n_\uparrow - n_\downarrow$. This holds provided $U^{\mathrm{ch}} - U^{\mathrm{sp}} = U$, or, equivalently,

$$U^{\mathrm{ch}} = \alpha U, \qquad U^{\mathrm{sp}} = (\alpha - 1) U. \tag{3}$$

The Fierz parameter α materializes the freedom in choosing the charge-to-spin fluctuation ratio. The right-hand side of Eq. (2) is decoupled with a charge and a spin boson, resulting in an electron-boson coupling problem [81,82]. Its fermionic and bosonic interacting Green's functions are given by the Dyson equations:

$$G(\mathbf{k}, i\omega) = \frac{1}{i\omega + \mu - \varepsilon(\mathbf{k}) - \Sigma(\mathbf{k}, i\omega)}, \tag{4a}$$

$$W^\eta(\mathbf{q}, i\Omega) = \frac{U^\eta}{1 - U^\eta P^\eta(\mathbf{q}, i\Omega)}. \tag{4b}$$

$\varepsilon(\mathbf{k})$ is the Fourier transform of t_{ij} $\varepsilon(\mathbf{k}) = 2t[\cos(k_x) + \cos(k_y)] + 4t' \cos(k_x)\cos(k_y)$, μ the chemical potential, $\eta = \mathrm{ch}$, sp, and $i\omega$ ($i\Omega$) the fermionic (bosonic) Matsubara frequencies. The self-energy $\Sigma(\mathbf{k}, i\omega)$ and polarization $P^\eta(\mathbf{q}, i\Omega)$ are given by the exact Hedin expressions

$$\Sigma(\mathbf{k}, i\omega) = -\sum_\eta \sum_{\mathbf{q}, i\Omega} G(\mathbf{k} + \mathbf{q}, i\omega + i\Omega) \times W^\eta(\mathbf{q}, i\Omega) \Lambda^\eta_{\mathbf{kq}}(i\omega, i\Omega), \tag{5a}$$

$$P^\eta(\mathbf{q}, i\Omega) = 2 \sum_{\mathbf{k}, i\omega} G(\mathbf{k} + \mathbf{q}, i\omega + i\Omega) G(\mathbf{k}, i\omega) \Lambda^\eta_{\mathbf{kq}}(i\omega, i\Omega). \tag{5b}$$

$\Lambda^\eta_{\mathbf{kq}}(i\omega, i\Omega)$ is the interacting electron-boson vertex. TRILEX approximates it with a vertex computed from a self-consistent impurity model. In previous works [81,82], this impurity model contained a single site.

There are several ways to extend the TRILEX method to cluster impurity problems, like in DMFT. Here, we consider the analog of the dynamical cluster approximation (DCA [21,22,25]), and use periodic clusters so as not to break the lattice translational symmetry, at the price of discontinuities in the momentum dependence of the *vertex function*. Other cluster variants such as a real-space version, inspired from cellular DMFT [23,24], are also possible, but break translation invariance and require arbitrary reperiodization procedures.

We straighforwardly generalize the single-site impurity model of TRILEX to a cluster impurity model defined by the action

$$S_{\mathrm{imp}} \equiv \iint_{\tau\tau'} \sum_{ij\sigma} c^*_{i\sigma\tau} \{-[\mathcal{G}^{-1}]_{ij}(\tau - \tau')\} c_{j\sigma\tau'} + \frac{1}{2} \iint_{\tau\tau'} \sum_{ij} \{n_{i\tau} \mathcal{U}^{\mathrm{ch}}_{ij}(\tau - \tau') n_{j\tau'} + s^z_{i\tau} \mathcal{U}^{\mathrm{sp}}_{ij}(\tau - \tau') s^z_{j\tau'}\}. \tag{6}$$

The indices $i, j = 1, \ldots, N_c$ stand for the cluster positions $\mathbf{R}_i$, $\mathbf{R}_j$ (shown in Fig. 1 along with the cluster momenta $\{\mathbf{K}_i\}_{i=1\ldots N_c}$). $c^*_{i\sigma\tau}$ and $c_{i\sigma\tau}$ are conjugate Grassmann fields, τ denotes imaginary time. Since we have introduced a charge and a spin bosonic mode, the impurity action contains interactions in both channels [$\mathcal{U}^{\mathrm{ch}}(\tau)$ and $\mathcal{U}^{\mathrm{sp}}(\tau)$]. They are *a priori* retarded due to the nonlocal character of $P^\eta(\mathbf{q}, i\Omega)$

This impurity model is used to compute the cluster impurity vertex $\Lambda^\eta_{\mathrm{imp}}(\mathbf{K}, \mathbf{Q}; i\omega, i\Omega)$ with a continuous-time quantum Monte Carlo algorithm with a hybridization (interaction) expansion for $N_c = 1$ ($N_c = 2$, 4) (as described in Supplemental Material II.C [84]). Next, in the spirit of DCA, we want to use $\Lambda^\eta_{\mathrm{imp}}(\mathbf{K}, \mathbf{Q}; i\omega, i\Omega)$ to approximate the momentum dependence of the lattice vertex $\Lambda^\eta_{\mathbf{kq}}(i\omega, i\Omega)$ by a coarse-graining procedure. We recall that DCA consists in coarse-graining the cluster

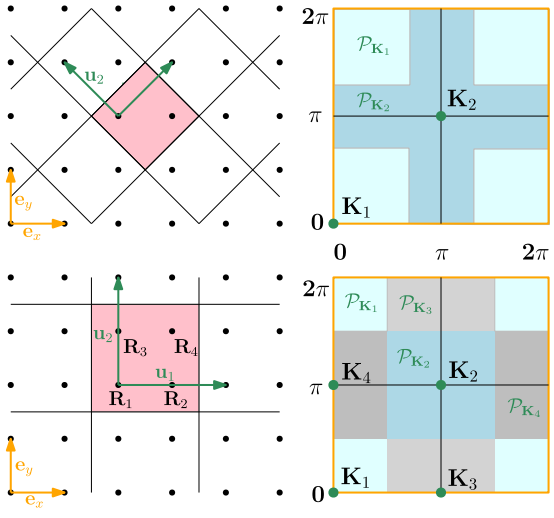

FIG. 1. Cluster geometry: real (left) and reciprocal (right) space, for $N_c = 2$ (top) and $N_c = 4$ (bottom). $\mathbf{e}_x$ and $\mathbf{e}_y$ ($\mathbf{u}_1$ and $\mathbf{u}_2$) are the unit vectors of the Bravais (super)lattice. The colored patches $\mathcal{P}_{\mathbf{K}_i}$ are of equal area.

self-energy as $\Sigma(\mathbf{k}, i\omega) \approx \sum_{\mathbf{K}} \theta_{\mathbf{K}}(\mathbf{k}) \Sigma_{\mathrm{imp}}(\mathbf{K}, i\omega)$, where $\Sigma_{\mathrm{imp}}(\mathbf{K}, i\omega)$ is the cluster impurity self-energy, and $\theta_{\mathbf{K}}(\mathbf{k}) = 1$ if $\mathbf{k}$ belongs to Brillouin-zone patch $\mathcal{P}_{\mathbf{K}}$, and vanishes otherwise. For the vertex function, the passage from $\Lambda^{\eta}_{\mathrm{imp}}(\mathbf{K}, \mathbf{Q}; i\omega, i\Omega)$ to an approximate lattice vertex $\Lambda^{\eta}_{\mathbf{k},\mathbf{q}}(i\omega, i\Omega)$ is not as straightforward. There are several possible coarse grainings for the vertex that reduce to single-site TRILEX for $N_c = 1$ and are exact in the $N_c = \infty$ limit, e.g.,

$$\Lambda^{\eta}_{\mathbf{kq}}(i\omega, i\Omega) \approx \sum_{\mathbf{K},\mathbf{Q}} \theta_{\mathbf{K}+\mathbf{Q}}(\mathbf{k}+\mathbf{q}) \theta_{\mathbf{Q}}(\mathbf{q}) \Lambda^{\eta}_{\mathrm{imp}}(\mathbf{K}, \mathbf{Q}; i\omega, i\Omega), \tag{7a}$$

$$\Lambda^{\eta}_{\mathbf{kq}}(i\omega, i\Omega) \approx \sum_{\mathbf{K},\mathbf{Q}} \theta_{\mathbf{K}}(\mathbf{k}) \theta_{\mathbf{K}+\mathbf{Q}}(\mathbf{k}+\mathbf{q}) \Lambda^{\eta}_{\mathrm{imp}}(\mathbf{K}, \mathbf{Q}; i\omega, i\Omega). \tag{7b}$$

We use a different coarse graining for Σ and for P: we substitute (7a) in (5a) [(7b) in (5b)] to compute $\Sigma(\mathbf{k}, i\omega)$ [$P^{\eta}(\mathbf{q}, i\Omega)$], whence

$$\Sigma(\mathbf{k}, i\omega) = -\sum_{\eta,\mathbf{K},\mathbf{Q}} \sum_{\mathbf{q},i\Omega} G^{\mathbf{K}+\mathbf{Q}}_{\mathbf{k}+\mathbf{q}}(i\omega + i\Omega) W^{\eta,\mathbf{Q}}_{\mathbf{q}}(i\Omega) \times \Lambda^{\eta}_{\mathrm{imp}}(\mathbf{K}, \mathbf{Q}; i\omega, i\Omega), \tag{8a}$$

$$P^{\eta}(\mathbf{q}, i\Omega) = 2\sum_{\mathbf{K},\mathbf{Q}} \sum_{\mathbf{k},i\omega} G^{\mathbf{K}+\mathbf{Q}}_{\mathbf{k}+\mathbf{q}}(i\omega + i\Omega) G^{\mathbf{K}}_{\mathbf{k}}(i\omega) \times \Lambda^{\eta}_{\mathrm{imp}}(\mathbf{K}, \mathbf{Q}; i\omega, i\Omega), \tag{8b}$$

with $X^{\mathbf{K}}_{\mathbf{k}}(i\omega) \equiv \theta_{\mathbf{K}}(\mathbf{k}) X(\mathbf{k}, i\omega)$ (for $X = G$ and W). As convolutions of continuous functions of $\mathbf{k}$ (G and W) with a piecewise-constant function (Λ), Σ and P are continuous in $\mathbf{k}$ by construction.

Finally, the cluster dynamical mean fields $\mathcal{G}_{ij}(\tau)$ and $\mathcal{U}^{\eta}_{ij}(\tau)$ are determined by imposing the following self-consistency conditions,

$$G_{\mathrm{imp}}(\mathbf{K}, i\omega)[\mathcal{G}, \mathcal{U}] = G_{\mathbf{K}}(i\omega), \tag{9a}$$

$$W^{\eta}_{\mathrm{imp}}(\mathbf{Q}, i\Omega)[\mathcal{G}, \mathcal{U}] = W^{\eta}_{\mathbf{Q}}(i\Omega). \tag{9b}$$

The left-hand sides are computed by solving the impurity model. The right-hand sides are the patch-averaged lattice Green's functions $G_{\mathbf{K}}(i\omega) \equiv \sum_{\mathbf{k}\in\mathcal{P}_{\mathbf{K}}} G(\mathbf{k}, i\omega)$ and $W^{\eta}_{\mathbf{Q}}(i\Omega) \equiv \sum_{\mathbf{q}\in\mathcal{P}_{\mathbf{Q}}} W^{\eta}(\mathbf{q}, i\Omega)$. The determination of $\mathcal{G}$ and $\mathcal{U}^{\eta}$ satisfying Eqs. (9a), (9b) is done by forward recursion (see Supplemental Material II.B, [84])

We have implemented this method and studied it in three physically distinct parameter regimes: (A) Weak-coupling regime at half-filling ($U/D = 0.5$, $\delta = 0\%$, $\beta D = 16$, $t' = 0$) at half-filling, (B) Intermediate-coupling regime at large doping ($U/D = 1$, $\delta = 20\%$, $\beta D = 16$, $t' = 0$) at large doping, (C) Strong-coupling regime at small doping ($U/D = 1.4$, $\delta = 4\%$, $\beta D = 8$, $t'/t = -0.3$) at small doping (the Mott transition occurs at $U_c/D \approx 1.5$ within plaquette cellular DMFT [89]). We solve at point A, B, C for different values of α.

In the absence of any approximation, every HS decoupling, hence every value of α, yields the same result: the exact solution does not depend on α. The cluster TRILEX approximation *a priori* breaks this property, but as N_c increases, we expect the α dependence to become weaker. We propose to use the weak α dependence for a given N_c, i.e., the existence of a plateau for at least a range α, as a (Fierz) convergence criterion. That this criterion is *sufficient* to establish convergence is an assumption, which we test here using exact benchmarks for points A, B, and C. Indeed, in these regimes, determinant quantum Monte Carlo (QMC) calculations and/or DCA can be converged and give a numerically exact solution of the Hubbard model, albeit at a significant numerical cost.

We start with point A. In Fig. 2, we show the self-energy $\Sigma(\mathbf{k}, i\omega_0)$ for cluster sizes of $N_c = 1$ (single-site), 2 (dimer), and 4 (plaquette) and for three different values of α. As expected, the dependence on α decreases with N_c. At $N_c = 4$, the self-energy is almost independent on α. The α dependence for $N_c = 1$, 2, 4 is further illustrated in Fig. 3: the $N_c = 4$ results show an extended plateau that is narrower or nonexistent for $N_c = 1$, 2.

The benchmarks, using numerically exact determinant QMC [90] computed with $N_c = 16 \times 16$ sites, are also presented on Figs. 2 and 3. We observe a very good

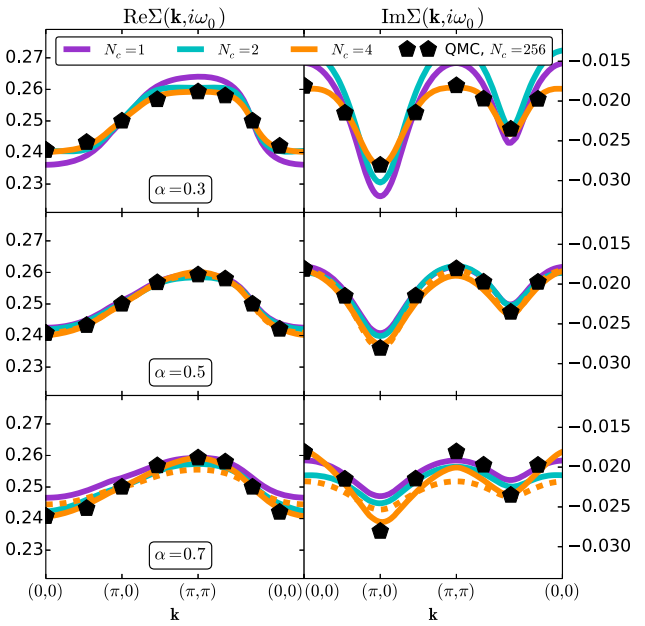

FIG. 2. Point A ($U/D = 0.5$, $\delta = 0\%$, $\beta D = 16$, $t' = 0$). $\mathrm{Re}\Sigma(\mathbf{k}, i\omega_0)$ (left) and $\mathrm{Im}\Sigma(\mathbf{k}, i\omega_0)$ (right) for $N_c = 1$, 2, 4 for various values of α (from top to bottom), along the path $(0,0) - (\pi,0) - (\pi,\pi) - (0,0)$. Solid lines: TRILEX. Dashed lines: GW + EDMFT ($N_c = 4$). Pentagons: determinant QMC (only a subset of $\mathbf{K}$ points is shown for better visibility).

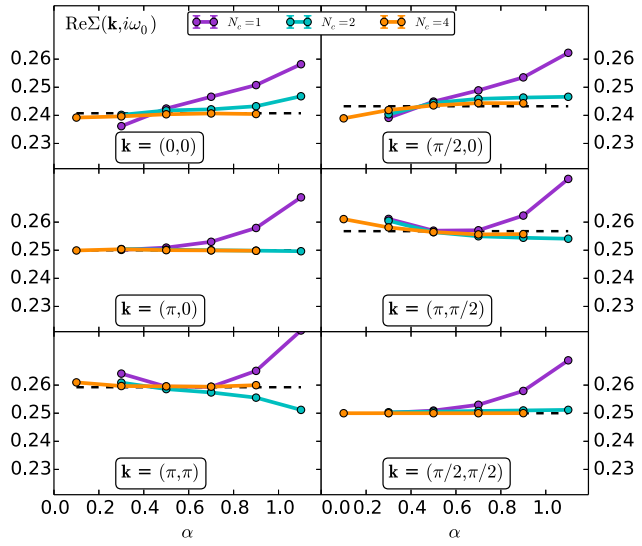

FIG. 3. Dependence of $\mathrm{Re}\Sigma(\mathbf{k}, i\omega_0)$ on α for different momenta (Point A: $U/D = 0.5$, $\delta = 0\%$, $\beta D = 16$, $t' = 0$). Black dashed lines: QMC.

agreement between $N_c = 4$ and the benchmark data, both for the real and imaginary parts of the self-energy, which validates the Fierz criterion in this regime. We also observe that for $\alpha = 0.5$, the results are in agreement with the converged values regardless of N_c. This can be understood by noticing that $\alpha = 0.5$ corresponds to the values of U^η used in the random phase approximation (RPA), which is correct to second order in U.

Moreover, we compare our results with the self-energy obtained by the $GW + \mathrm{EDMFT}$ [60–66] method for $N_c = 4$. $GW + \mathrm{EDMFT}$ can be regarded as a simplification of TRILEX where the vertex corrections are neglected in the nonlocal self-energy contribution. This explains why the $GW + \mathrm{EDMFT}$ results are, independently of α, quite close to the single-site TRILEX results: the vertex frequency and momentum dependences are weak in the low-U limit. Besides, they are different from the cluster TRILEX results and from the exact solution, except for the RPA value of α ($\alpha = 0.5$) where both methods give results close to the exact solution.

At point B (Fig. 4), the agreement between the benchmarks and the real and imaginary parts of the self-energy, for all values of α (with more important deviations for $\alpha = 0.3$), is very good for $N_c = 4$. Contrary to the weak-coupling limit, no value of α in the single-site case matches the exact solution. This points to the importance of nonlocal corrections to the three-leg vertex. This observation is further corroborated by looking at the $GW + \mathrm{EDMFT}$ curve. There, the agreement with the exact result is quite poor, while being similar to the single-site result, like in the weak-coupling limit (for $\alpha = 0.3$, a spin instability precludes convergence of $GW + \mathrm{EDMFT}$ and cluster TRILEX for $N_c = 2$). This discrepancy shows that as interactions are increased, the vertex frequency and momentum dependence play a more and more important role in the nonlocal self-energy, as discussed below. These conclusions are also valid for local observables (see Supplemental Material III.C [84]).

At the strong-coupling point C (Fig. 5), similarly to the previous regimes, the $N_c = 4$ self-energy is almost independent of α, and in good agreement with the converged

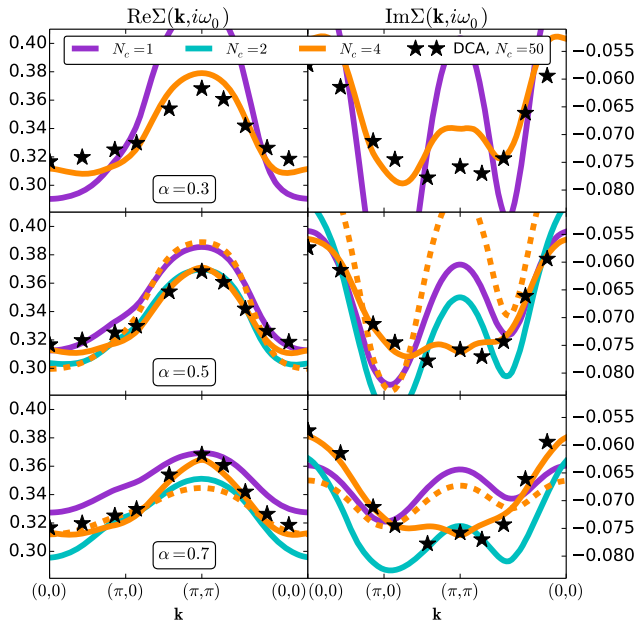

FIG. 4. $\Sigma(\mathbf{k}, i\omega_0)$ at point B ($U/D = 1$, $\delta = 20\%$, $\beta D = 16$, $t' = 0$). Same conventions as Fig. 2. Dashed lines: GW+EDMFT. Stars: DCA from Ref. [55].

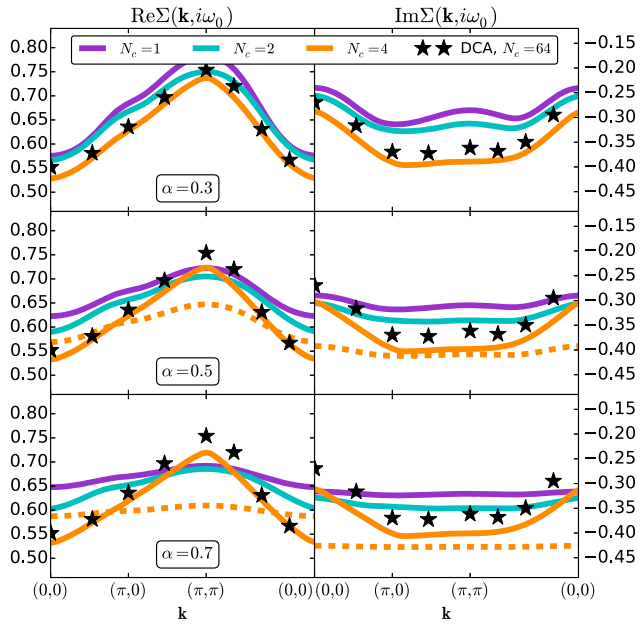

FIG. 5. $\Sigma(\mathbf{k}, i\omega_0)$ at point C ($U/D = 1.4$, $\delta = 4\%$, $\beta D = 8$, $t'/t = -0.3$). Same conventions as Fig. 2. Dashed lines: GW+EDMFT. Stars: DCA.

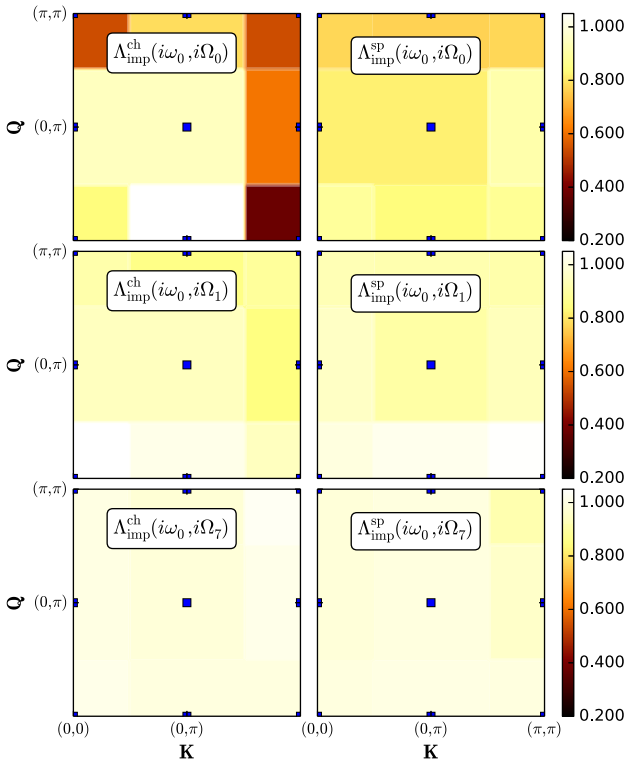

FIG. 6. Point B ($U/D = 1$, $\delta = 20\%$, $\beta D = 16$, $t' = 0$), $\alpha = 0.5$. Impurity vertex $\Lambda^{\eta}_{\mathrm{imp}}(\mathbf{K}, \mathbf{Q}; i\omega_0, i\Omega)$ at $\mathbf{K}, \mathbf{Q} \in [(0,0), (0,\pi), (\pi,\pi)]^2$ (the value is color coded in the square area surrounding each blue point) in the charge (left) and spin (right) channels, for increasing bosonic Matsubara frequency (from top to bottom).

(DCA) solution (especially for its real part). $GW +$ EDMFT at $N_c = 4$ is quite far from the exact result, as can be expected from the previous discussion.

Finally, we analyze the momentum and frequency dependence of the vertex, illustrated in Fig. 6. At low Matsubara frequencies, the vertex acquires a momentum dependence (especially in the charge channel), while it is essentially local at high frequencies. In other words, the largest deviations to locality occur at small frequencies only (see also Supplemental Material III.D [84]). The nonlocal components are smaller or much smaller than the local component, especially for large Matsubara frequencies. This gives an *a posteriori* explanation of the qualitatively good results of the single-site TRILEX approximation. More importantly, the fact that the momentum dependence is confined to low frequencies suggests optimizations for the vertex parametrization and computation.

In conclusion, we have presented a first implementation of the cluster extension of the TRILEX method. For a broad interaction and doping range of the two-dimensional Hubbard model, we obtain, for an embedded cluster with only four impurity sites, continuous self-energies in close agreement with the exact result obtained with comparatively expensive large-cluster lattice QMC and DCA calculations.

Cluster TRILEX is based on the computation and momentum coarse graining of the three-leg vertex function: it thus comes at a cost lower than cluster methods based on four-leg vertices [78,79], but it *a priori* suffers from the Fierz ambiguity. We have shown that this ambiguity can be turned into a practical advantage in two ways: First and foremost, we have shown that proximity to the exact solution coincides with stability with respect to the Fierz parameter α [91]. With this necessary condition, one can assess, at a given (possibly small) cluster size, the accuracy of the solution. Second, in some regimes, there exists a value of α for which accurate results can be reached for smaller cluster sizes. By allowing us to extract more information from smaller embedded TRILEX clusters, the Fierz convergence criterion paves the way to a controlled exploration of low-temperature phases such as superconducting phases, where cluster DMFT cannot be converged in practice.

We acknowledge useful discussions with M. Ferrero and A. Georges. We especially thank W. Wu for providing us determinant QMC numerical data for the benchmark results of point A and DCA data for point C, as well as J. LeBlanc for providing us the DCA data (from Ref. [55]) for point B. This work is supported by the FP7/ERC, under Grant Agreement No. 278472-MottMetals. Part of this work was performed using HPC resources from GENCI-TGCC (Grant No. 2016-t2016056112). Our implementation is based on the TRIQS toolbox [92].

[1] A. V. Chubukov, D. Pines, and J. Schmalian, *Superconductivity* (Springer, Berlin, Heidelberg, 2002), Chap. 22, p. 1349.
[2] F. Onufrieva and P. Pfeuty, Phys. Rev. Lett. **102**, 207003 (2009).
[3] M. A. Metlitski and S. Sachdev, Phys. Rev. B **82**, 075128 (2010).
[4] K. B. Efetov, H. Meier, and C. Pépin, Nat. Phys. **9**, 442 (2013).
[5] F. Onufrieva and P. Pfeuty, Phys. Rev. Lett. **109**, 257001 (2012).
[6] D. J. Scalapino, Rev. Mod. Phys. **84**, 1383 (2012).
[7] Y. Wang and A. Chubukov, Phys. Rev. B **90**, 035149 (2014).
[8] Y. Wang, A. Abanov, B. L. Altshuler, E. A. Yuzbashyan, and A. V. Chubukov, Phys. Rev. Lett. **117**, 157001 (2016).
[9] N. Bickers and D. Scalapino, Ann. Phys. (N.Y.) **193**, 206 (1989).
[10] L. Hedin, Phys. Rev. **139**, A796 (1965).
[11] L. Hedin, J. Phys. Condens. Matter **11**, 489 (1999).
[12] G. M. Eliashberg, Sov. Phys. JETP **11**, 696 (1960).
[13] J. Jaeckel and C. Wetterich, Phys. Rev. D **68**, 025020 (2003).
[14] T. Baier, E. Bick, and C. Wetterich, Phys. Rev. B **70**, 125111 (2004).
[15] L. Bartosch, H. Freire, J. J. R. Cardenas, and P. Kopietz, J. Phys. Condens. Matter **21**, 305602 (2009).
[16] K. Borejsza and N. Dupuis, Europhys. Lett. **63**, 722 (2003).

[17] K. Borejsza and N. Dupuis, Phys. Rev. B **69**, 085119 (2004).
[18] N. Dupuis, Phys. Rev. B **65**, 245118 (2002).
[19] P. W. Anderson, Science **235**, 1196 (1987).
[20] A. Georges, G. Kotliar, W. Krauth, and M. J. Rozenberg, Rev. Mod. Phys. **68**, 13 (1996).
[21] M. H. Hettler, A. N. Tahvildar-Zadeh, M. Jarrell, T. Pruschke, and H. R. Krishnamurthy, Phys. Rev. B **58**, R7475 (1998).
[22] M. H. Hettler, M. Mukherjee, M. Jarrell, and H. R. Krishnamurthy, Phys. Rev. B **61**, 12739 (2000).
[23] A. I. Lichtenstein and M. I. Katsnelson, Phys. Rev. B **62**, R9283 (2000).
[24] G. Kotliar, S. Y. Savrasov, G. Pálsson, and G. Biroli, Phys. Rev. Lett. **87**, 186401 (2001).
[25] T. A. Maier, M. Jarrell, T. Pruschke, and M. H. Hettler, Rev. Mod. Phys. **77**, 1027 (2005).
[26] B. Kyung, D. Sénéchal, and A.-M. S. Tremblay, Phys. Rev. B **80**, 205109 (2009).
[27] G. Sordi, P. Sémon, K. Haule, and A.-M. S. Tremblay, Phys. Rev. Lett. **108**, 216401 (2012).
[28] M. Civelli, M. Capone, A. Georges, K. Haule, O. Parcollet, T. D. Stanescu, and G. Kotliar, Phys. Rev. Lett. **100**, 046402 (2008).
[29] M. Ferrero, O. Parcollet, A. Georges, G. Kotliar, and D. N. Basov, Phys. Rev. B **82**, 054502 (2010).
[30] E. Gull, O. Parcollet, and A. J. Millis, Phys. Rev. Lett. **110**, 216405 (2013).
[31] A. Macridin, M. Jarrell, and T. A. Maier, Phys. Rev. B **70**, 113105 (2004).
[32] T. A. Maier, M. Jarrell, A. Macridin, and C. Slezak, Phys. Rev. Lett. **92**, 027005 (2004).
[33] T. A. Maier, M. Jarrell, T. C. Schulthess, P. R. C. Kent, and J. B. White, Phys. Rev. Lett. **95**, 237001 (2005).
[34] T. A. Maier, M. S. Jarrell, and D. J. Scalapino, Phys. Rev. Lett. **96**, 047005 (2006).
[35] E. Gull, M. Ferrero, O. Parcollet, A. Georges, and A. J. Millis, Phys. Rev. B **82**, 155101 (2010).
[36] S. X. Yang, H. Fotso, S. Q. Su, D. Galanakis, E. Khatami, J. H. She, J. Moreno, J. Zaanen, and M. Jarrell, Phys. Rev. Lett. **106**, 047004 (2011).
[37] A. Macridin and M. Jarrell, Phys. Rev. B **78**, 241101(R) (2008).
[38] A. Macridin, M. Jarrell, T. Maier, P. R. C. Kent, and E. D'Azevedo, Phys. Rev. Lett. **97**, 036401 (2006).
[39] M. Jarrell, T. A. Maier, C. Huscroft, and S. Moukouri, Phys. Rev. B **64**, 195130 (2001).
[40] O. Parcollet, G. Biroli, and G. Kotliar, Phys. Rev. Lett. **92**, 226402 (2004).
[41] P. Werner, E. Gull, O. Parcollet, and A. J. Millis, Phys. Rev. B **80**, 045120 (2009).
[42] G. Biroli, O. Parcollet, and G. Kotliar, Phys. Rev. B **69**, 205108 (2004).
[43] D. Bergeron, V. Hankevych, B. Kyung, and A.-M. S. Tremblay, Phys. Rev. B **84**, 085128 (2011).
[44] B. Kyung, V. Hankevych, A.-M. Daré, and A.-M. S. Tremblay, Phys. Rev. Lett. **93**, 147004 (2004).
[45] B. Kyung, S. S. Kancharla, D. Sénéchal, A.-M. S. Tremblay, M. Civelli, and G. Kotliar, Phys. Rev. B **73**, 165114 (2006).
[46] S. Okamoto, D. Sénéchal, M. Civelli, and A.-M. S. Tremblay, Phys. Rev. B **82**, 180511 (2010).
[47] G. Sordi, K. Haule, and A.-M. S. Tremblay, Phys. Rev. Lett. **104**, 226402 (2010).
[48] G. Sordi, P. Sémon, K. Haule, and A.-M. S. Tremblay, Sci. Rep. **2**, 547 (2012).
[49] M. Civelli, M. Capone, S. S. Kancharla, O. Parcollet, and G. Kotliar, Phys. Rev. Lett. **95**, 106402 (2005).
[50] M. Ferrero, P. S. Cornaglia, L. De Leo, O. Parcollet, G. Kotliar, and A. Georges, Europhys. Lett. **85**, 57009 (2009).
[51] M. Ferrero, P. S. Cornaglia, L. De Leo, O. Parcollet, G. Kotliar, and A. Georges, Phys. Rev. B **80**, 064501 (2009).
[52] E. Gull, O. Parcollet, P. Werner, and A. J. Millis, Phys. Rev. B **80**, 245102 (2009).
[53] X. Chen, J. P. F. LeBlanc, and E. Gull, Phys. Rev. Lett. **115**, 116402 (2015).
[54] X. Chen, J. P. F. LeBlanc, and E. Gull, Nat. Commun. **8**, 14986 (2017).
[55] J. P. F. LeBlanc *et al.*, Phys. Rev. X **5**, 041041 (2015).
[56] O. Gunnarsson, T. Schäfer, J. P. F. LeBlanc, E. Gull, J. Merino, G. Sangiovanni, G. Rohringer, and A. Toschi, Phys. Rev. Lett. **114**, 236402 (2015).
[57] O. Gunnarsson, T. Schäfer, J. P. F. LeBlanc, J. Merino, G. Sangiovanni, G. Rohringer, and A. Toschi, Phys. Rev. B **93**, 245102 (2016)..
[58] W. Wu, M. Ferrero, A. Georges, and E. Kozik, Phys. Rev. B **96**, 041105 (2017)..
[59] G. Rohringer, H. Hafermann, A. Toschi, A. A. Katanin, A. E. Antipov, M. I. Katsnelson, A. I. Lichtenstein, A. N. Rubtsov, and K. Held, arXiv:1705.00024.
[60] S. Biermann, F. Aryasetiawan, and A. Georges, Phys. Rev. Lett. **90**, 086402 (2003).
[61] P. Sun and G. Kotliar, Phys. Rev. B **66**, 085120 (2002).
[62] P. Sun and G. Kotliar, Phys. Rev. Lett. **92**, 196402 (2004).
[63] T. Ayral, P. Werner, and S. Biermann, Phys. Rev. Lett. **109**, 226401 (2012).
[64] T. Ayral, S. Biermann, and P. Werner, Phys. Rev. B **87**, 125149 (2013).
[65] S. Biermann, J. Phys. Condens. Matter **26**, 173202 (2014).
[66] T. Ayral, S. Biermann, P. Werner, and L. V. Boehnke, Phys. Rev. B **95**, 245130 (2017).
[67] A. N. Rubtsov, M. I. Katsnelson, and A. I. Lichtenstein, Phys. Rev. B **77**, 033101 (2008).
[68] A. Rubtsov, M. Katsnelson, and A. Lichtenstein, Ann. Phys. (Amsterdam) **327**, 1320 (2012).
[69] E. G. C. P. van Loon, A. I. Lichtenstein, M. I. Katsnelson, O. Parcollet, and H. Hafermann, Phys. Rev. B **90**, 235135 (2014).
[70] E. A. Stepanov, E. G. C. P. van Loon, A. A. Katanin, A. I. Lichtenstein, M. I. Katsnelson, and A. N. Rubtsov, Phys. Rev. B **93**, 045107 (2016).
[71] A. Toschi, A. A. Katanin, and K. Held, Phys. Rev. B **75**, 045118 (2007).
[72] A. A. Katanin, A. Toschi, and K. Held, Phys. Rev. B **80**, 075104 (2009).
[73] T. Schäfer, F. Geles, D. Rost, G. Rohringer, E. Arrigoni, K. Held, N. Blümer, M. Aichhorn, and A. Toschi, Phys. Rev. B **91**, 125109 (2015).

[74] A. Valli, T. Schäfer, P. Thunström, G. Rohringer, S. Andergassen, G. Sangiovanni, K. Held, and A. Toschi, Phys. Rev. B **91**, 115115 (2015).
[75] G. Li, N. Wentzell, P. Pudleiner, P. Thunström, and K. Held, Phys. Rev. B **93**, 165103 (2016).
[76] G. Rohringer and A. Toschi, Phys. Rev. B **94**, 125144 (2016).
[77] T. Ayral and O. Parcollet, Phys. Rev. B **94**, 075159 (2016).
[78] H. Hafermann, S. Brener, A. N. Rubtsov, M. I. Katsnelson, and A. I. Lichtenstein, JETP Lett. **86**, 677 (2008).
[79] C. Slezak, M. Jarrell, T. Maier, and J. Deisz, J. Phys. Condens. Matter **21**, 435604 (2009).
[80] S. X. Yang, H. Fotso, H. Hafermann, K. M. Tam, J. Moreno, T. Pruschke, and M. Jarrell, Phys. Rev. B **84**, 155106 (2011).
[81] T. Ayral and O. Parcollet, Phys. Rev. B **92**, 115109 (2015).
[82] T. Ayral and O. Parcollet, Phys. Rev. B **93**, 235124 (2016).
[83] J. Vučičević, T. Ayral, and O. Parcollet, Phys. Rev. B **96**, 104504 (2017).
[84] See Supplemental Material I at http://link.aps.org/supplemental/10.1103/PhysRevLett.119.166401 for another choice. The Supplemental Material includes Refs. [55,58,81–83,85–88].
[85] A. N. Rubtsov, V. V. Savkin, and A. I. Lichtenstein, Phys. Rev. B **72**, 035122 (2005).
[86] E. Gull, A. J. Millis, A. I. Lichtenstein, A. N. Rubtsov, M. Troyer, and P. Werner, Rev. Mod. Phys. **83**, 349 (2011).
[87] P. Staar, T. Maier, and T. C. Schulthess, Phys. Rev. B **88**, 115101 (2013).
[88] P. Staar, T. Maier, and T. C. Schulthess, Phys. Rev. B **89**, 195133 (2014).
[89] H. Park, K. Haule, and G. Kotliar, Phys. Rev. Lett. **101**, 186403 (2008).
[90] R. Blankenbecler, D. J. Scalapino, and R. L. Sugar, Phys. Rev. D **24**, 2278 (1981).
[91] This also holds for other HS decouplings; see Supplemental Material I [84].
[92] O. Parcollet, M. Ferrero, T. Ayral, H. Hafermann, P. Seth, and I. S. Krivenko, Comput. Phys. Commun. **196**, 398 (2015).

Supplemental Material for The Fierz convergence criterion: a controlled approach to strongly-interacting systems with small embedded clusters

Thomas Ayral,[1,2] Jaksa Vučičević,[2,3] and Olivier Parcollet[2]

[1] *Physics and Astronomy Department, Rutgers University, Piscataway, NJ 08854, USA*
[2] *Institut de Physique Théorique (IPhT), CEA, CNRS, UMR 3681, 91191 Gif-sur-Yvette, France*
[3] *Scientific Computing Laboratory, Center for the Study of Complex Systems, Institute of Physics Belgrade, University of Belgrade, Pregrevica 118, 11080 Belgrade, Serbia*

This Supplemental Material is organized as follows: in Section I, we show results corresponding to another decoupling than the Ising decoupling used in the main text, namely the Heisenberg decoupling. In Section II, we give the technical details relevant to the implementation of the cluster TRILEX method. Finally, in Section III, we give supplementary data to complement the figures and discussion of the main text.

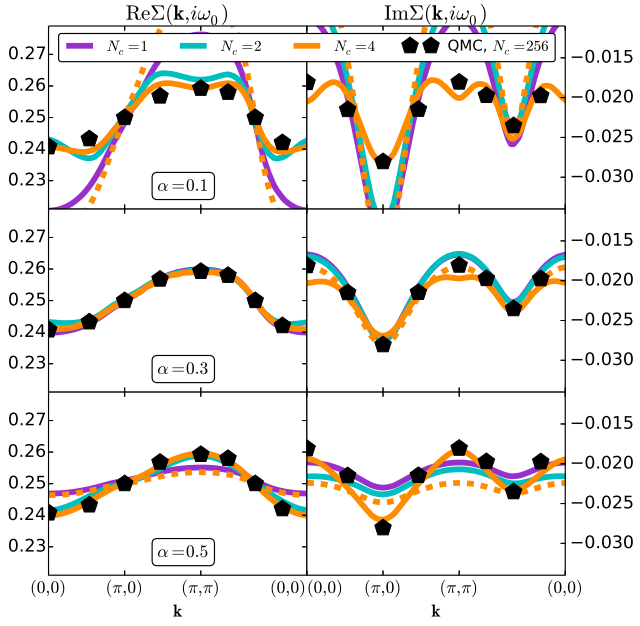

Figure S.1. Point A in the Heisenberg decoupling ($U/D = 0.5$, $\delta = 0\%$, $\beta D = 16$). $\mathrm{Re}\Sigma(\mathbf{k}, i\omega_0)$ (left column) and $\mathrm{Im}\Sigma(\mathbf{k}, i\omega_0)$ (right column) for $N_c = 1, 2, 4$ for various values of the Fierz parameter α (from top to bottom), along the path $(0,0) - (\pi,0) - (\pi,\pi) - (0,0)$. Solid lines: TRILEX. Dashed lines: GW+EDMFT ($N_c = 4$). Pentagons: determinant QMC ($N_c = 256$; only a small subset of $\mathbf{K}$ points is shown for a better visibility).

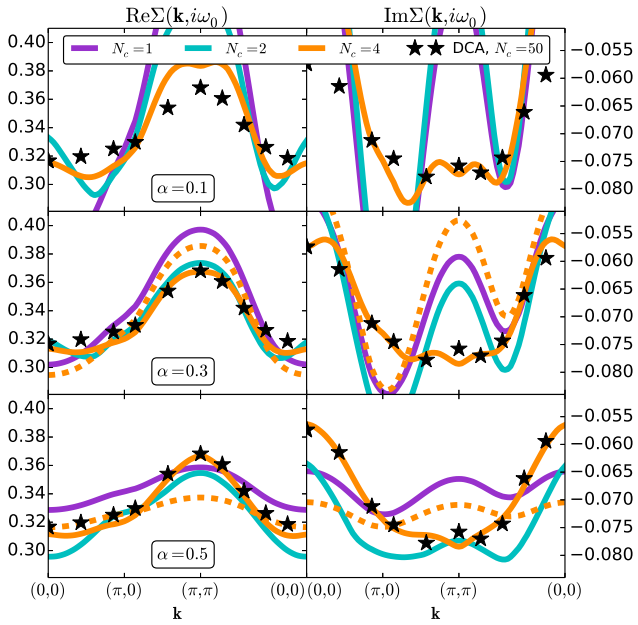

Figure S.2. Point B in the Heisenberg decoupling ($U/D = 1$, $\delta = 20\%$, $\beta D = 16$). Same conventions as Fig. S.1. Stars: DCA from Ref. 1, $N_c = 50$.

I. SELF-ENERGY IN THE HEISENBERG DECOUPLING: α AND N_c DEPENDENCE AND COMPARISON TO EXACT BENCHMARKS

In the main text, we have chosen to decouple the interaction with charge and longitudinal spin bosons (a decoupling sometimes called the "Ising" decoupling). One can alternatively use the "Heisenberg" decoupling, which consists in decomposing the interaction as follows (up to a density term):

$$U n_{i\uparrow} n_{i\downarrow} = \frac{1}{2} U^{\mathrm{ch}} n_i n_i + \frac{1}{2} U^{\mathrm{sp}} \left(s_i^x s_i^x + s_i^y s_i^y + s_i^z s_i^z \right) \quad (1)$$

where $s_i^I \equiv \sum_{\sigma\sigma'} c_{i\sigma}^\dagger \sigma^I_{\sigma\sigma'} c_{i\sigma'}$ (with σ^I the Pauli matrices). This equality holds whenever $U^{\mathrm{ch}} - 3U^{\mathrm{sp}} = U$, or in other words

$$U^{\mathrm{ch}} = (3\alpha - 1)U, \quad U^{\mathrm{sp}} = (\alpha - 2/3)U \quad (2)$$

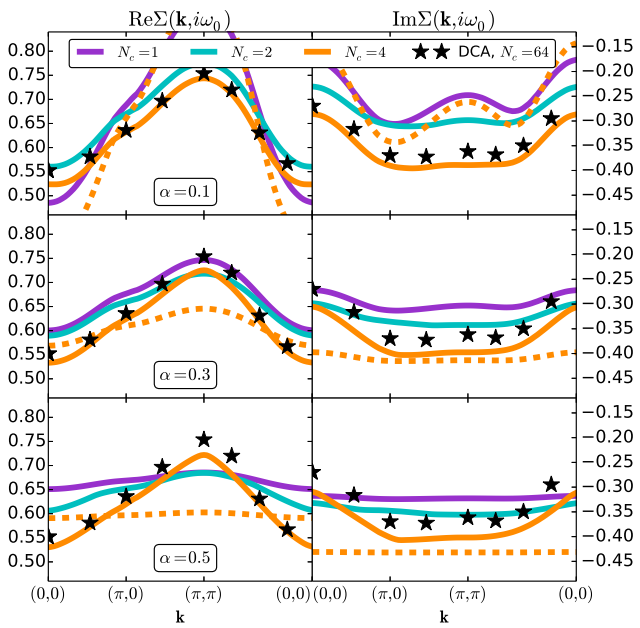

Figure S.3. Point C in the Heisenberg decoupling ($U/D = 1.4$, $\delta = 4\%$, $\beta D = 8$). Same conventions as Fig. S.1. Stars: DCA from Ref. 2, $N_c = 64$

This leads, after a Hubbard-Stratonovich transformation, to four bosonic modes, one in the charge channel and three in the spin channel (we refer the reader to [3] for more details and for the modified equations for the self-energy and impurity action).

In Figs (S.1-S.2-S.3), we show the self-energies obtained for the three characteristic points studied in the main text (A, B and C) for different values of the Fierz parameter α and cluster size N_c.

The observations with respect to α dependence are very similar to those made in the main text. This further underlines the main conclusion of the paper: even in this quite different decoupling, the results are similar to those obtained within the Ising decoupling of the main text.

II. TECHNICAL DETAILS OF CLUSTER TRILEX

A. Fourier conventions and patching details

1. Spatial Fourier transforms

$\mathbf{k}$ is a Brillouin zone momentum (black dots in Fig. S.4).

Direct transforms We define:

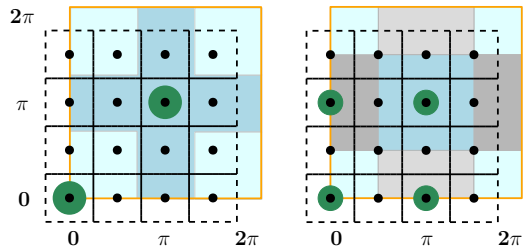

Figure S.4. Example of discretization of the Brillouin zone with $n_{\text{latt}} = n_k \times n_k$ $\mathbf{k}$ points (here $n_{\mathbf{k}} = 4$) for $N_c = 2$ (left panel) and $N_c = 4$ (right panel)

$$f_{\mathbf{k}} \equiv \sum_{i=1}^{n_{\text{latt}}} e^{-i\mathbf{k}\cdot\mathbf{r}_i} f_{\mathbf{r}_i} \tag{3}$$

Reciprocal transforms We define:

$$f_{\mathbf{r}} = \frac{1}{n_{\text{latt}}} \sum_{i=1}^{n_{\text{latt}}} e^{i\mathbf{k}_i\cdot\mathbf{r}} f_{\mathbf{k}} \tag{4}$$

2. Cluster Fourier transforms

$\mathbf{K}$ and $\mathbf{Q}$ are cluster momenta (green disks in Fig. S.4)

Direct transforms We define:

$$f_{\mathbf{K}} \equiv \frac{1}{N_c} \sum_{ij} e^{-i\mathbf{K}\cdot(\mathbf{R}_i - \mathbf{R}_j)} f_{ij} \tag{5}$$

$$g_{\mathbf{K},\mathbf{Q}} \equiv \frac{1}{N_c} \sum_{ijk} e^{-i\mathbf{K}\cdot(\mathbf{R}_i - \mathbf{R}_j) - i\mathbf{Q}\cdot(\mathbf{R}_k - \mathbf{R}_j)} g_{ijk} \tag{6}$$

with $i, j, k = 1 \dots N_c$.

Reciprocal transforms We define:

$$f_{ij} = \sum_{\mathbf{K}} e^{i\mathbf{K}\cdot(\mathbf{R}_i - \mathbf{R}_j)} f_{\mathbf{K}} \tag{7}$$

$$g_{ijk} = \sum_{\mathbf{KQ}} e^{i\mathbf{K}(\mathbf{R}_i - \mathbf{R}_j) + i\mathbf{Q}(\mathbf{R}_k - \mathbf{R}_j)} g_{\mathbf{K},\mathbf{Q}} \tag{8}$$

where $\sum_{\mathbf{K}} f_{\mathbf{K}}$ is shorthand for $\frac{1}{N_c}\sum_{i=1}^{N_c} f_{\mathbf{K}_i}$.

3. Temporal Fourier transforms

$i\omega$ (resp. $i\Omega$) denotes fermionic (resp. bosonic) Matsubara frequencies, and are shorthand for $i\omega_n = \frac{2n+1}{\beta}\pi$ (resp. $i\Omega_m = \frac{2m}{\beta}\pi$). β is the inverse temperature.

Direct transforms We define:

$$f_{i\omega} \equiv \int_0^\beta \mathrm{d}\tau e^{i\omega\tau} f_\tau \tag{9}$$

$$g_{i\omega,i\Omega} \equiv \iint_0^\beta \mathrm{d}\tau\mathrm{d}\tau' e^{i\omega\tau+i\Omega\tau'} g_{\tau,\tau'} \tag{10}$$

Reciprocal transforms We define:

$$f_\tau = \sum_{i\omega} e^{-i\omega\tau} f_{i\omega} \tag{11}$$

$$g_{\tau,\tau'} = \sum_{i\omega}\sum_{i\Omega} e^{-i\omega\tau-i\Omega\tau'} g_{i\omega,i\Omega} \tag{12}$$

Here, $\sum_{i\omega} f(i\omega)$ is shorthand for $\frac{1}{\beta}\sum_{n=-n_{\max}}^{n_{\max}-1} f(i\omega_n)$ (and $\sum_{i\Omega} f(i\Omega)$ for $\frac{1}{\beta}\sum_{m=-m_{\max}}^{m_{\max}} f(i\Omega_m)$).

4. *Patching and discretization*

In DCA, the $\mathbf{k}$ integrals can be replaced with integrals on the density of states, e.g.

$$\begin{aligned} G_{\mathbf{K}}(i\omega) &= \sum_{\mathbf{k}\in\mathcal{P}_{\mathbf{K}}} \frac{1}{i\omega+\mu-\varepsilon_{\mathbf{k}}-\Sigma_{\mathrm{imp}}(\mathbf{K},i\omega)} \\ &= \int_{-\infty}^{\infty} \mathrm{d}\varepsilon \frac{D_{\mathbf{K}}(\varepsilon)}{i\omega+\mu-\varepsilon-\Sigma_{\mathrm{imp}}(\mathbf{K},i\omega)} \end{aligned}$$

where $D_{\mathbf{K}}(\varepsilon) \equiv \sum_{\mathbf{k}\in\mathcal{P}_{\mathbf{K}}} \delta(\varepsilon-\varepsilon_{\mathbf{k}})$ is the noninteracting density of states of patch $\mathbf{K}$. This density of states can be precomputed once and for all for a given dispersion and patches with a very large number of $\mathbf{k}$ points to obtain a very good accuracy.

By contrast, in cluster TRILEX, the self-energy is a function of $\mathbf{k}$ instead of $\mathbf{K}$, forbidding this substitution and keeping the number of $\mathbf{k}$ points finite (this number is primarily limited by memory and computation time requirements, but it can be large due to the low cost of the computation of $\Sigma(\mathbf{k},i\omega)$: we typically discretize the Brillouin zone in $n_{\mathbf{k}}\times n_{\mathbf{k}}$ points, with $n_{\mathbf{k}}=32$).

This requires extra care when defining the theta functions $\theta_{\mathbf{K}}(\mathbf{k})$ defined in a loose way in the main text. $\theta_{\mathbf{K}}(\mathbf{k})$ is precisely defined as the overlap of the area surrounding a given $\mathbf{k}$ point with the patch $\mathcal{P}_{\mathbf{K}}$, divided by the total area surrounding the $\mathbf{k}$ point. This area is illustrated in Fig. S.4 for the case $n_{\mathbf{k}}=4$. For instance, the $\mathbf{k}$ point of coordinates $(1,1)$ has $\theta_{\mathbf{K}=(0,0)}(\mathbf{k})=1/4$, while that of coordinates $(1,2)$ has $\theta_{\mathbf{K}=(0,\pi)}(\mathbf{k})=1/2$. Correspondingly, $\sum_{\mathbf{k}\in\mathcal{P}_{\mathbf{K}}}$ is precisely defined as

$$f_{\mathbf{K}} = \sum_{\mathbf{k}\in\mathcal{P}_{\mathbf{K}}} f_{\mathbf{k}} = \frac{\sum_{i=1}^{n_{\mathbf{k}}\times n_{\mathbf{k}}} f(\mathbf{k}_i)\theta_{\mathbf{K}}(\mathbf{k}_i)}{\sum_{i=1}^{n_{\mathbf{k}}\times n_{\mathbf{k}}} \theta_{\mathbf{K}}(\mathbf{k}_i)} \tag{13}$$

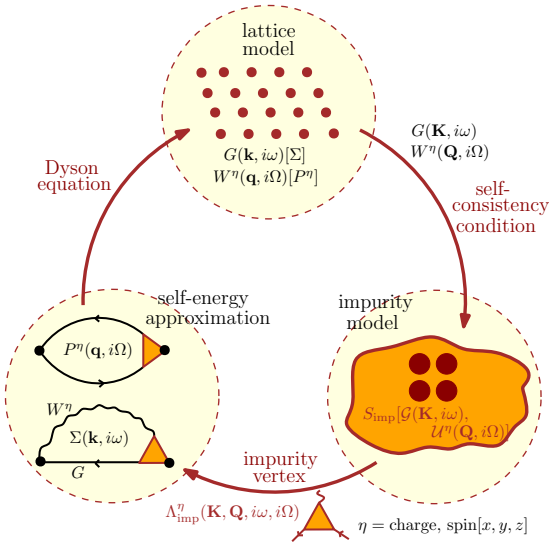

Figure S.5. The cluster TRILEX loop

B. Cluster TRILEX Loop

As in Refs 3–5, we solve the cluster TRILEX equations by forward recursion, with the following steps (illustrated in Fig. S.5):

1. Start with a guess $\Sigma(\mathbf{k},i\omega)$, $P^\eta(\mathbf{q},i\Omega)$
2. Compute $G(\mathbf{k},i\omega)$ and $W^\eta(\mathbf{q},i\Omega)$ (Eqs (4)) and then $G(\mathbf{K},i\omega)$ and $W^\eta(\mathbf{Q},i\Omega)$ (Eqs. (10))
3. Compute $\mathcal{G}(\mathbf{K},i\omega)$ and $\mathcal{U}^\eta(\mathbf{Q},i\Omega)$ by substituting Eqs (9) into the impurity Dyson equations, i.e

$$\mathcal{G}(\mathbf{K},i\omega) = \left[G^{-1}_{\mathbf{K}}(i\omega)+\Sigma_{\mathrm{imp}}(\mathbf{K},i\omega)\right]^{-1} \tag{14a}$$

$$\mathcal{U}^\eta(\mathbf{Q},i\Omega) = \left[\left[W^\eta_{\mathbf{Q}}\right]^{-1}(i\Omega)+P^\eta_{\mathrm{imp}}(\mathbf{Q},i\Omega)\right]^{-1} \tag{14b}$$

4. Solve the impurity model, Eq. (6), for its exact vertex $\Lambda^\eta_{\mathrm{imp}}(\mathbf{K},\mathbf{Q};i\omega,i\Omega)$ (see Section II C for more details).
5. Compute $\Sigma(\mathbf{k},i\omega)$ and $P^\eta(\mathbf{q},i\Omega)$ (Eqs (5))
6. Go back to step 2 until convergence of Σ and P^η.

As in Refs 4 and 5, and as justified in Ref. 3 for the single-site impurity case, in the equations presented in the main text and in the loop presented above, we have implicitly approximated the impurity's electron-boson vertex with the bare electron-boson vertex or, in other words, we have assumed the ζ function, introduced in Ref. 3, to be negligible.

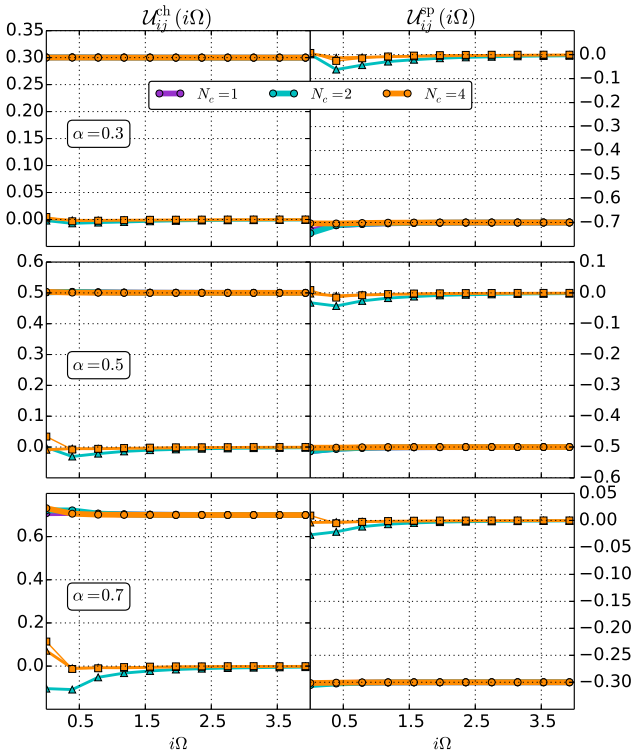

Figure S.6. Retarded interaction $\mathcal{U}^{\eta}_{ij}(i\Omega)$ in the charge (left column) and spin (right column) channels, for $\alpha = 0.3$ (top row), 0.5 (middle row), 0.7 (bottom row), at point B ($U/D = 1$, $\delta = 20\%$, $\beta D = 16$, $t' = 0$, Ising decoupling). Dots: local component ($i, j = 0, 0$). Triangles: nearest-neighbor component ($i, j = 0, 1$, for $N_c = 2$ and $N_c = 4$ only). Squares: next-nearest-neighbor component ($i, j = 0, 3$, for $N_c = 4$ only).

C. Solution of the Impurity Model

1. *Impurity solver*

The impurity model, defined by Eq. (6), is solved using a continuous-time quantum Monte-Carlo algorithm[6]. For $N_c = 1$, we refer the reader to Ref. 3 for details. For $N_c > 1$, contrary to the single-site case, the densities n^I_i are no longer good quantum numbers due to the intra-cluster hopping terms. This precludes the use of the hybridization expansion algorithms, which can be used with retarded interactions only if the operators involved in the retarded interactions are good quantum numbers, and in which only correlators between operators which are good quantum numbers can be easily measured. We therefore use an interaction-expansion (CT-INT) algorithm, described *e.g.* in Ref. 7. Here, for the measurement of the three-point function $\tilde{\chi}^{3,\sigma\sigma'}_{\rm imp}(i,j,k;\tau,\tau')$ (defined in Eq. (20) below), we use a straightforward operator-insertion method.

We observe that in all the parameter regimes studied in the main text (points A, B and C), the interactions $\mathcal{U}^I_{ij}(\tau)$ are static and local to a very good approximation:

$$\mathcal{U}^I_{ij}(\tau) \approx U^I \delta_{ij}\delta_\tau \tag{15}$$

This is illustrated in Fig. S.6 for point B. Thus, in practice, we do not have to use the retarded interactions. This simplifies the numerical computation since the dependence of the Monte-Carlo sign problem on CT-INT's density-shifting parameter $\alpha_\sigma(s)$ (see e.g. Eq. (145) of Ref. 7) is less simple than in the case of static interactions.

2. *Computation of $G_{\rm imp}(\mathbf{K}, i\omega)$ and $W_{\rm imp}(\mathbf{Q}, i\Omega)$*

$G_{\rm imp}(\mathbf{K}, i\omega)$ and $W_{\rm imp}(\mathbf{Q}, i\Omega)$ are obtained by computing the spatial and temporal Fourier transforms (defined in Section II A) $G_{\rm imp}(\mathbf{K}, i\omega)$ and $\chi^{\sigma\sigma'}_{\rm imp}(\mathbf{Q}, i\Omega)$ of the impurity's Green's function and density-density response functions:

$$G_{\rm imp}(i,j;\tau) \equiv -\langle T c_i(\tau) c^\dagger_j(0)\rangle_{\rm imp} \tag{16a}$$
$$\chi^{\sigma\sigma'}_{\rm imp}(i,j;\tau) \equiv \langle T n_{i\sigma}(\tau) n_{j\sigma'}(0)\rangle_{\rm imp} \tag{16b}$$

and by using the identity

$$W^{\eta}_{\rm imp}(\mathbf{Q}, i\Omega) = \mathcal{U}^{\eta}(\mathbf{Q}, i\Omega) - \mathcal{U}^{\eta}(\mathbf{Q}, i\Omega)\chi^{\eta,\rm conn}_{\rm imp}(\mathbf{Q}, i\Omega)\mathcal{U}^{\eta}(\mathbf{Q}, i\Omega) \tag{17}$$

where the passage from spin (σ, σ') to channel (η) indices is done using the expressions:

$$\chi^{\eta=\rm ch}_{\rm imp} \equiv 2(\chi^{\uparrow\uparrow}_{\rm imp} + \chi^{\uparrow\downarrow}_{\rm imp}) \tag{18a}$$
$$\chi^{\eta=\rm sp}_{\rm imp} \equiv 2(\chi^{\uparrow\uparrow}_{\rm imp} - \chi^{\uparrow\downarrow}_{\rm imp}) \tag{18b}$$

and the connected component is:

$$\chi^{\eta,\rm conn}_{\rm imp}(i,j;i\Omega) \equiv \chi^{\eta,\rm conn}_{\rm imp}(i,j;i\Omega) - \langle n^\eta_i\rangle\langle n^\eta_j\rangle\beta\delta_{i\Omega} \tag{19}$$

3. *Computation of the cluster vertex $\Lambda^{\eta}_{\rm imp}(\mathbf{K}, \mathbf{Q}; i\omega, i\Omega)$*

The computation of $\Lambda^{\eta}_{\rm imp}(\mathbf{K}, \mathbf{Q}; i\omega, i\Omega)$ is done by measuring the three-point function

$$\tilde{\chi}^{3,\sigma,\sigma'}_{\rm imp}(i,j,k;\tau,\tau') \equiv \langle T c_{i\sigma}(\tau) c^\dagger_{j\sigma}(0) n_{k\sigma'}(\tau')\rangle_{\rm imp} \tag{20}$$

The vertex, written in cluster coordinates $\mathbf{R}_i, \mathbf{R}_j, \mathbf{R}_k$, is then computed as:

$$\Lambda^{\eta}(i,j,k;i\omega,i\Omega) \equiv \sum_{pqr} G^{-1}_{\rm imp}(p,j;i\omega+i\Omega)G^{-1}_{\rm imp}(i,q;i\omega) \times \left[1-\mathcal{U}^{\eta}\chi^{\eta}_{\rm imp}\right]^{-1}(k,r;i\Omega)\tilde{\chi}^{3,\eta,\rm conn}_{\rm imp}(q,p,r;i\omega,i\Omega) \tag{21}$$

with the expression in the charge and spin channel:

$$\tilde{\chi}^{3,\eta=\rm ch}_{\rm imp} \equiv \tilde{\chi}^{3,\uparrow\uparrow}_{\rm imp} + \tilde{\chi}^{3,\uparrow\downarrow}_{\rm imp} \tag{22a}$$

$$\tilde{\chi}^{3,\eta=\rm sp}_{\rm imp} \equiv \tilde{\chi}^{3,\uparrow\uparrow}_{\rm imp} - \tilde{\chi}^{3,\uparrow\downarrow}_{\rm imp} \tag{22b}$$

and the connected component defined as:

$$\tilde{\chi}^{3,\eta,\rm conn}_{\rm imp}(i,j,k;i\omega,i\Omega) \equiv \tilde{\chi}^{3,\eta}_{\rm imp}(i,j,k;i\omega,i\Omega) + G_{\rm imp}(i,j;i\omega)n^{\eta}_{k}\beta\delta_{i\Omega} \tag{23}$$

$\Lambda^{\eta}(i,j,k;i\omega,i\Omega)$ is then Fourier-transformed to $\Lambda^{\eta}_{\rm imp}(\mathbf{K},\mathbf{Q};i\omega,i\Omega)$ (see Section II A, Eq. (6)).

In practice, instead of directly performing a temporal Fourier transform to compute $\tilde{\chi}^{3,\sigma\sigma'}_{\rm imp}(i,j,k;i\omega,i\Omega)$ from $\tilde{\chi}^{3,\sigma\sigma'}_{\rm imp}(i,j,k;\tau,\tau')$, we first compute the connected component $\tilde{\chi}^{3,\eta,\rm conn}_{\rm imp}(i,j,k;\tau,\tau')$ [defined in Eq. (23)], which is smooth and without discontinuities, perform a cubic spline interpolation of it, and then Fourier transform it to Matsubara frequencies. This allows us to use a small number (typically $n_\tau = n_{\tau'} = 100$) of τ,τ' points in the measurement.

D. Self-energy decomposition

In this section, we show that the coarse-grainings introduced for the vertex allow for a numerically convenient decomposition of Σ and P.

Following a procedure very similar to that described in section II.D.3 of Ref. 3, we decompose Eqs (5) as follows:

$$\Sigma(\mathbf{k},i\omega) = \Sigma_{\rm imp}(i,j=0,0;i\omega) - \sum_{\eta} m_{\eta} \sum_{\mathbf{K},\mathbf{Q}} \sum_{\mathbf{q},i\Omega} \tilde{G}^{\mathbf{K}+\mathbf{Q}}_{\mathbf{k}+\mathbf{q},i\omega+i\Omega}\tilde{W}^{\eta,\mathbf{Q}}_{\mathbf{q},i\Omega}\Lambda^{\eta}_{\rm imp}(\mathbf{K},\mathbf{Q};i\omega,i\Omega) \tag{24a}$$

$$P^{\eta}(\mathbf{q},i\Omega) = P^{\eta}_{\rm imp}(i,j=0,0;i\Omega) + 2\sum_{\mathbf{K},\mathbf{Q}} \sum_{\mathbf{k},i\omega} \tilde{G}^{\mathbf{K}+\mathbf{Q}}_{\mathbf{k}+\mathbf{q},i\omega+i\Omega}\tilde{G}^{\mathbf{K}}_{\mathbf{k},i\omega}\Lambda^{\eta}_{\rm imp}(\mathbf{K},\mathbf{Q};i\omega,i\Omega) \tag{24b}$$

where we have defined the nonlocal components:

$$\tilde{X}(\mathbf{k},i\omega) \equiv X(\mathbf{k},i\omega) - \sum_{\mathbf{k}} X(\mathbf{k},i\omega) \tag{25}$$

with $X = G$ or W.

Indeed, decomposing Eq. (5a) using Eq. (25), and expanding, one obtains four terms, two of which vanish. The two remaining terms are given in Eq. (24a). The first term is given by $\Sigma_{\rm imp}(00,i\omega)$:

$$-\sum_{\eta} m_{\eta} \sum_{\mathbf{K},\mathbf{Q}} \sum_{i\Omega} \left\{ \sum_{\mathbf{k}'} G_{i\omega+i\Omega}(\mathbf{k}')\theta_{\mathbf{K}+\mathbf{Q}}(\mathbf{k}') \right\} \times \left\{ \sum_{\mathbf{q}'} W_{i\Omega}(\mathbf{q}')\theta_{\mathbf{Q}}(\mathbf{q}') \right\} \Lambda^{\eta}_{\rm imp}(\mathbf{K},\mathbf{Q};i\omega,i\Omega) \tag{26}$$

$$= -\sum_{\eta} m_{\eta} \sum_{i\Omega} \sum_{\mathbf{q}'} \sum_{\mathbf{k}'} \{G_{i\omega+i\Omega}(\mathbf{k}'+\mathbf{q}')\}\{W_{i\Omega}(\mathbf{q}')\} \times \sum_{\mathbf{K}\mathbf{Q}} \theta_{\mathbf{K}+\mathbf{Q}}(\mathbf{k}'+\mathbf{q}')\theta_{\mathbf{Q}}(\mathbf{q}')\Lambda^{\eta}_{\rm imp}(\mathbf{K},\mathbf{Q};i\omega,i\Omega) \tag{27}$$

$$= -\sum_{\mathbf{k}'} \sum_{\eta} m_{\eta} \sum_{\mathbf{q}'} \sum_{i\Omega} G_{i\omega+i\Omega}(\mathbf{k}'+\mathbf{q}')W_{i\Omega}(\mathbf{q}')\Lambda^{\eta}_{\mathbf{k}',\mathbf{q}'}(i\omega,i\Omega)$$
$$= \sum_{\mathbf{k}'} \Sigma(\mathbf{k}',i\omega)$$
$$= \Sigma(\mathbf{R}=0,i\omega)$$
$$= \Sigma_{\rm imp}(0,0;i\omega) \tag{28}$$

A similar result holds for P.

In the second terms of Eqs (24a-24b), the summands decay fast for large Matsubara frequencies thanks to the fast decay of the nonlocal component $\tilde{G}(\mathbf{k},i\omega)$ and $\tilde{W}(\mathbf{q},i\Omega)$.

As in Ref. 3, we furthermore split Λ into a "regular part" $\Lambda^{\eta,\rm reg}$ which vanishes at large frequencies

$$\Lambda^{\eta,\rm reg}(i,j,k;i\omega,i\Omega) = \Lambda^{\eta}(i,j,k;i\omega,i\Omega) - l^{\eta}(i,j,k;i\Omega) \tag{29}$$

and a remainder $l^{\eta}(i\Omega)$ corresponding to the high-frequency asymptotics of the three-point function:

$$l^{\eta}(i,j,k;i\Omega) \equiv \sum_{p} \left[1-\mathcal{U}^{\eta}\chi^{\eta}\right]^{-1}(k,p;i\Omega)\delta_{ij} \tag{30}$$

The term containing $\Lambda^{\eta,\rm reg}(i,j,k;i\omega,i\Omega)$ has a quickly decaying summand thanks to $\tilde{G}$, $\tilde{W}$ *and* $\Lambda^{\rm reg}$. We compute it in Matsubara frequencies and real space after a fast Fourier transform of $\tilde{G}$ and $\tilde{W}$ (see Eq (4)). This is the bottleneck of the computation of the self-energy as it scales as $O(N^2_{\omega}N_k \log N_k N^2_c)$ (where N_ω is the number of Matsubara frequencies used and N_k the number of $\mathbf{k}$ points in the disctretized first Brillouin zone). The term containing $l^{\eta}(i,j,k;i\Omega)$ can be computed entirely in imaginary time and real space, with a computational complexity of $O(N_\omega \log N_\omega N_k \log N_k N^2_c)$.

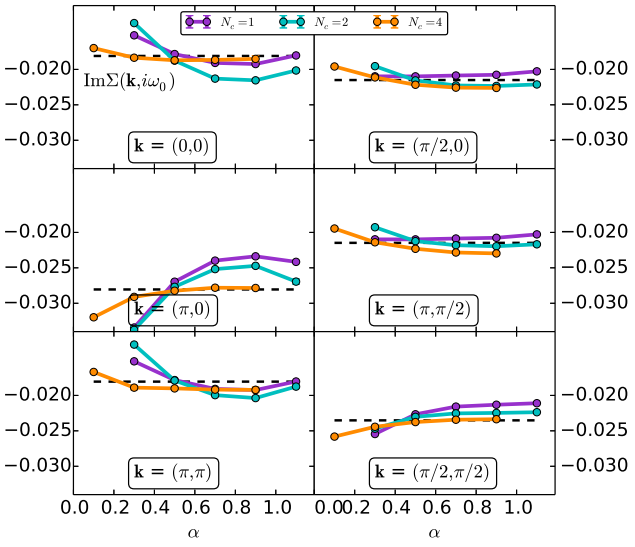

Figure S.7. Dependence of $\mathrm{Im}\Sigma(\mathbf{k}, i\omega_0)$ on the Fierz parameter α for different $\mathbf{k}$ points at point A ($U/D = 0.5$, $\delta = 0\%$, $\beta D = 16$, $t' = 0$, Ising decoupling).

III. SUPPLEMENTARY DATA

A. Additional data for the Fierz criterion: α-dependence of ImΣ

In Figure S.7, we complement the data of Fig. 3 of the main text by giving the data for the imaginary part. Similarly to the real part, the imaginary part shows plateaus for given ranges of α which are more pronounced for $N_c = 4$, which is the cluster size for which the self-energy is the closest to the exact benchmark result.

B. Continuity of the self-energy

In Fig. S.8, we show the lowest Matsubara component of the self-energy obtained in the dynamical cluster approximation (DCA) and the one obtained within cluster TRILEX, using Eq. (24a). While the DCA self-energy is piecewise constant in the Brillouin zone (with discontinuities at the patch edges), the cluster TRILEX self-energy is continuous by construction, similarly to what is achieved by the DCA$^+$ method[8, 9], but without arbitrary interpolation schemes.

C. Local components of ImG and ImΣ

In Fig. S.9, we display the local components G_{loc} and Σ_{imp} and compare them to benchmark results obtained

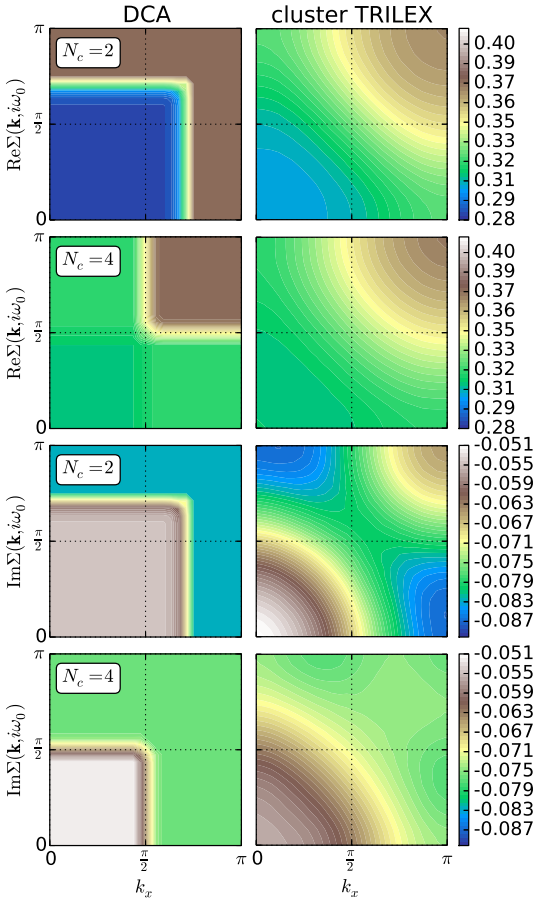

Figure S.8. $\Sigma(\mathbf{k}, i\omega_0)$ in the upper quadrant of the first Brillouin zone, at point B ($U/D = 1$, $\delta = 20\%$, $\beta D = 16$, $t' = 0$, $\alpha = 0.5$, Ising decoupling). *Left column*: DCA, *right column*: cluster TRILEX. *First two rows*: real part, *last two rows*: imaginary part. *Odd rows*: $N_c = 2$, *even rows*: $N_c = 4$.

with DCA ($N_c = 50$, Ref. 1). The $N_c = 4$ cluster TRILEX data is the closest to the benchmark data, irrespective of the value of α.

D. Vertex

1. *Momentum dependence of the vertex*

In Figures S.10 and S.11, we show the dependence of the vertex on the cluster momenta $\mathbf{K}$ and $\mathbf{Q}$ for points A and C (point B is shown in the main text).

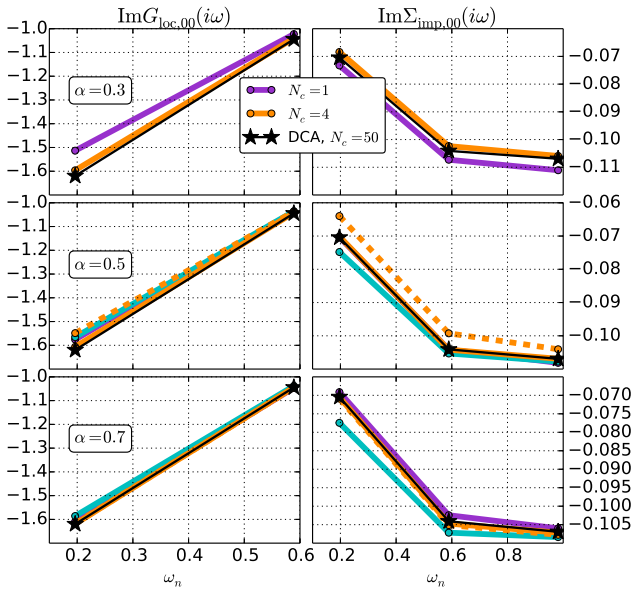

Figure S.9. (Point B: $U/D = 1$, $\delta = 20\%$, $\beta D = 16$, $t' = 0$, Ising decoupling). Imaginary part of the local components of G_{loc} (left column) and Σ_{imp} (right column) for for $\alpha = 0.3$ (top row), 0.5 (middle row), 0.7 (bottom row) and different N_c. Solid lines: TRILEX. Dashed lines: GW+EDMFT ($N_c = 4$). Black stars: DCA result from Ref. 1, $N_c = 50$.

2. *Cluster-site dependence of the vertex*

In Figures S.12, S.13 and S.14, we show all the inequivalent vertex components $\Lambda_{\mathrm{imp}}(i, j, k; i\omega, i\Omega)$ for the three regimes of parameters (respectively point A, B and C) studied in the main text. While the largest component is the local component $(i, j, k = 0, 0, 0)$, some nonlocal components are non-negligible.

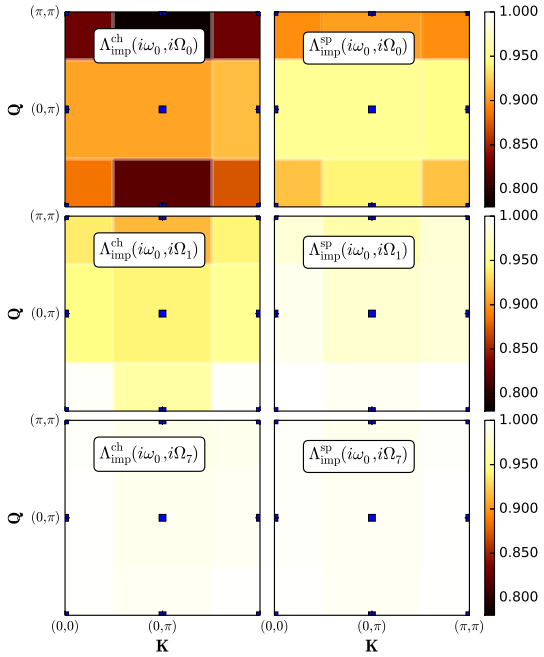

Figure S.10. Weak-coupling parameters (Point A, $U/D = 0.5$, $\delta = 0\%$, $\beta D = 16$, $t' = 0$, $\alpha = 0.5$, Ising decoupling). Same conventions as Fig. 6 of the main text.

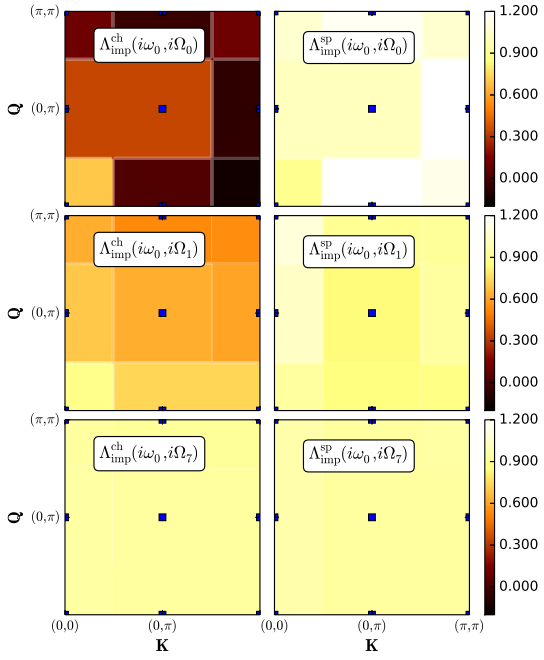

Figure S.11. Strong-coupling parameters (Point C, $U/D = 1.4$, $\delta = 4\%$, $\beta D = 8$, $t'/t = -0.3$, $\alpha = 0.5$, Ising decoupling). Same conventions as Fig. 6 of the main text.

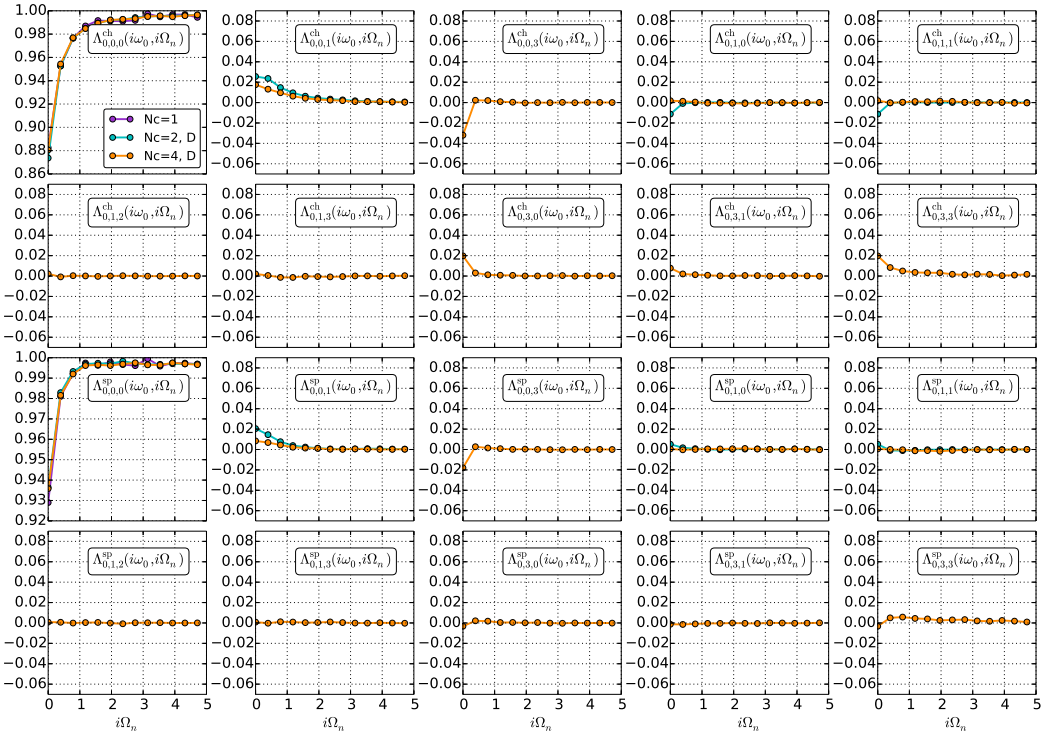

Figure S.12. Weak-coupling parameters (Point A, $U/D = 0.5$, $\delta = 0\%$, $\beta D = 16$, $t' = 0$), $\alpha = 0.5$, Ising decoupling. Impurity cluster vertex $\Lambda^{\eta}_{\mathrm{imp}}(i, j, k; i\omega, i\Omega)$ in the charge (first two rows) and spin (last two rows) channels, at fixed fermionic Matsubara frequency ω_0. See Fig 1 for a definition of the cluster coordinates $\mathbf{R}_i, \mathbf{R}_j$ and $\mathbf{R}_k$ denoted by the indices i, j, k.

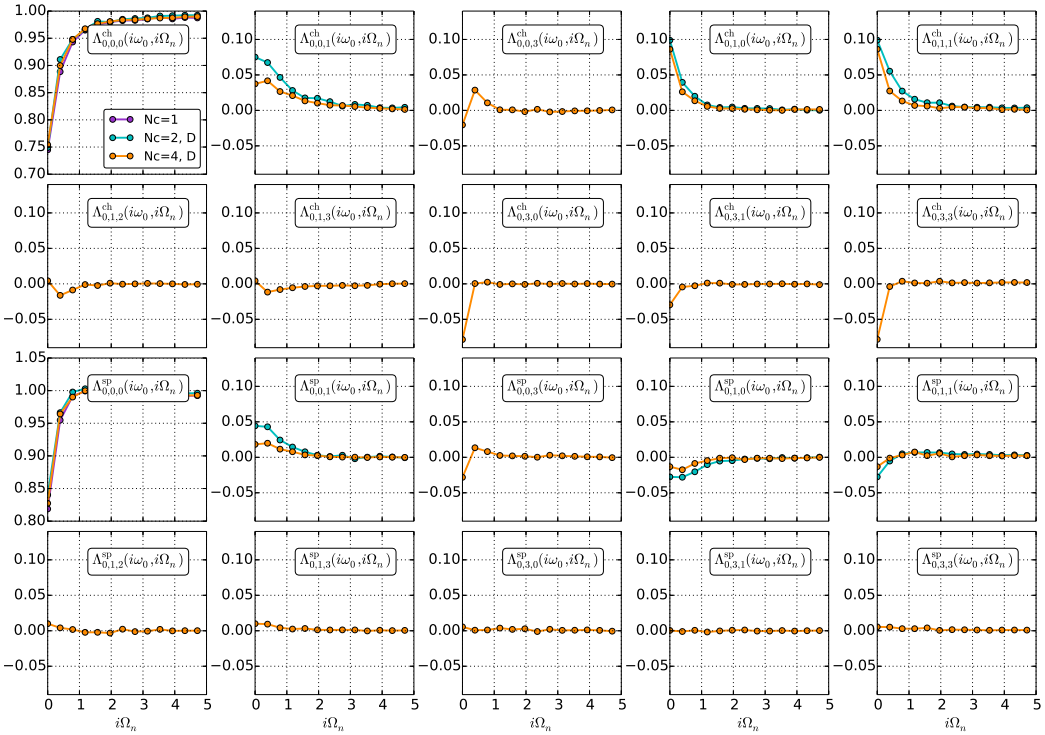

Figure S.13. Intermediate-coupling parameters (point B, $U/D = 1$, $\delta = 20\%$, $\beta D = 16$, $t' = 0$), $\alpha = 0.5$, Ising decoupling. Impurity cluster vertex $\Lambda^{\eta}_{\mathrm{imp}}(i, j, k; i\omega, i\Omega)$ in the charge and spin channels, at fixed fermionic Matsubara frequency ω_0.

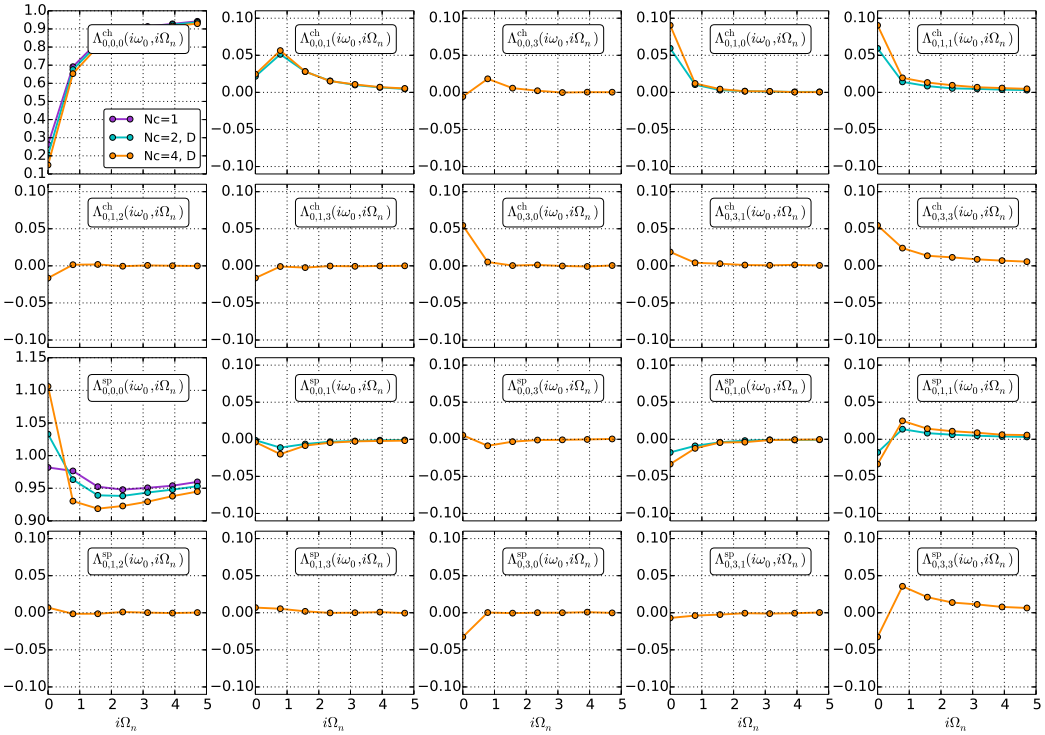

Figure S.14. Strong-coupling parameters (Point C, $U/D = 1.4$, $\delta = 4\%$, $\beta D = 8$, $t'/t = -0.3$), $\alpha = 0.5$, Ising decoupling. Impurity cluster vertex $\Lambda^{\eta}_{\mathrm{imp}}(i, j, k; i\omega, i\Omega)$ in the charge and spin channels, at fixed fermionic Matsubara frequency ω_0.

[1] J. P. F. LeBlanc, A. E. Antipov, F. Becca, I. W. Bulik, G. K.-L. Chan, C.-m. Chung, Y. Deng, M. Ferrero, T. M. Henderson, C. A. Jiménez-Hoyos, E. Kozik, X.-w. Liu, A. J. Millis, N. V. Prokof'ev, M. Qin, G. E. Scuseria, H. Shi, B. V. Svistunov, L. F. Tocchio, I. S. Tupitsyn, S. R. White, S. Zhang, B.-X. Zheng, Z. Zhu, and E. Gull, Physical Review X **5**, 041041 (2015).

[2] W. Wu, M. Ferrero, A. Georges, and E. Kozik, arXiv:1608.08402.

[3] T. Ayral and O. Parcollet, Physical Review B **93**, 235124 (2016).

[4] T. Ayral and O. Parcollet, Physical Review B **92**, 115109 (2015).

[5] J. Vučičević, T. Ayral, and O. Parcollet, arXiv:1705.08332.

[6] A. N. Rubtsov, V. V. Savkin, and A. I. Lichtenstein, Physical Review B **72**, 035122 (2005).

[7] E. Gull, A. J. Millis, A. I. Lichtenstein, A. N. Rubtsov, M. Troyer, and P. Werner, Reviews of Modern Physics **83**, 349 (2011).

[8] P. Staar, T. Maier, and T. C. Schulthess, Physical Review B **88**, 115101 (2013).

[9] P. Staar, T. Maier, and T. C. Schulthess, Physical Review B **89**, 195133 (2014).

PHYSICAL REVIEW B **96**, 104504 (2017)

TRILEX and GW+EDMFT approach to d-wave superconductivity in the Hubbard model

J. Vučičević,[1,2] T. Ayral,[1,3] and O. Parcollet[1]

[1]*Institut de Physique Théorique (IPhT), CEA, CNRS, UMR 3681, 91191 Gif-sur-Yvette, France*

[2]*Scientific Computing Laboratory, Center for the Study of Complex Systems, Institute of Physics Belgrade, University of Belgrade, Pregrevica 118, 11080 Belgrade, Serbia*

[3]*Department of Physics and Astronomy, Rutgers University, Piscataway, New Jersey 08854, USA*

(Received 23 May 2017; published 5 September 2017)

We generalize the recently introduced TRILEX approach (TRiply irreducible local EXpansion) to superconducting phases. The method treats simultaneously Mott and spin-fluctuation physics using an Eliashberg theory supplemented by local vertex corrections determined by a self-consistent quantum impurity model. We show that, in the two-dimensional Hubbard model, at strong coupling, TRILEX yields a d-wave superconducting dome as a function of doping. Contrary to the standard cluster dynamical mean field theory (DMFT) approaches, TRILEX can capture d-wave pairing using only a single-site effective impurity model. We also systematically explore the dependence of the superconducting temperature on the bare dispersion at weak coupling, which shows a clear link between strong antiferromagnetic (AF) correlations and the onset of superconductivity. We identify a combination of hopping amplitudes particularly favorable to superconductivity at intermediate doping. Finally, we study within GW+EDMFT the low-temperature d-wave superconducting phase at strong coupling in a region of parameter space with reduced AF fluctuations.

DOI: 10.1103/PhysRevB.96.104504

Strongly correlated electron systems such as high-temperature superconductors pose a difficult challenge to condensed-matter theory. One class of theoretical approaches for this problem focuses on the effect of long-range spin fluctuations [1–6]. They neglect vertex corrections in an Eliashberg-type approximation for the electronic self-energy and predict a d-wave superconducting order.

Another class of approaches focuses, following the seminal work of Anderson [7], on the fact that high-temperature superconductors are doped Mott insulators. In the recent years, progress has been made in this direction with cluster extensions [8–12] of dynamical mean field theory (DMFT) [13]. These methods have been shown to capture the essential aspects of cuprate physics, such as Mott insulating, pseudogap, and d-wave superconducting phases [14–39]. Cluster DMFT methods can be converged with respect to the cluster size at relatively high temperature [40,41], including in the pseudogap region [42], but not at lower temperatures and in particular in the superconducting phase.

Several approaches beyond cluster DMFT have been proposed recently [43–61]. In Refs. [62,63], the TRiply irreducible local EXpansion (TRILEX) approach was introduced. It consists in a local approximation of the electron-boson vertex extracted from a quantum impurity model with a self-consistently determined bath and interaction, in the spirit of DMFT. TRILEX interpolates between DMFT at strong interaction and the weak-coupling Eliashberg-type spin-fluctuation approximation at weak interaction. It is able to simultaneously describe Mott physics and the effect of long-range bosonic fluctuations. Hence, it unifies the two theoretical approaches mentioned above in the same formalism.

The main purpose of this paper is to study d-wave superconductivity in the Hubbard model within the single-site TRILEX approach. Contrary to DMFT, where d-wave superconducting correlations can by construction be captured only within multisite (cluster) impurity models, here we only need to solve a *single-site* impurity model. We also compare TRILEX to two simpler approaches, GW+EDMFT and GW, which can be viewed as further approximations of the electron-boson vertex in TRILEX. We show that TRILEX yields a d-wave superconducting dome at strong coupling.

We also study the dependence of the superconducting critical temperature T_c on the choice of the tight-binding parameters at weak coupling using the GW method. While T_c is enhanced by strong antiferromagnetic fluctuations, we find a region of parameter space where the superconducting transition occurs at a higher temperature than the antiferromagnetic instability of the method. At this point, we stabilize and study a superconducting solution below T_c within GW+EDMFT. We also identify a choice of dispersion where, at 16% doping, we have a pronounced maximum of T_c in the space of hopping parameters, which seems to persist even at strong coupling.

The paper is organized as follows: In Sec. I, we describe the Hubbard model studied in this paper. In Sec. II, we generalize the TRILEX equations to superconducting phases via the Nambu formalism, and discuss their simplifications GW and GW+EDMFT. In Sec. III, we describe the numerical methods and details used to solve the equations. In Sec. IV, we turn to the results. We first describe the phase diagram (Sec. IV A) within TRILEX and GW+EDMFT, and then focus on the weak-coupling regime (Sec. IV B) where, using the GW method, we scan the space of the nearest- and next-nearest-neighbor hopping parameters in search of dispersions with a weak antiferromagnetic instability where it is possible to reach a paramagnetic superconducting phase. The two dispersions which we thus identify are investigated in more detail at strong coupling with GW+EDMFT in Secs. IV C and IV D.

I. MODEL

We solve the Hubbard model on the square lattice with longer-range hoppings, defined by the Hamiltonian

$$H = \sum_{ij\sigma} t_{ij} c^\dagger_{i\sigma} c_{j\sigma} - \mu \sum_{i\sigma} n_{i\sigma} + U \sum_i n_{i\uparrow} n_{i\downarrow} \qquad (1)$$

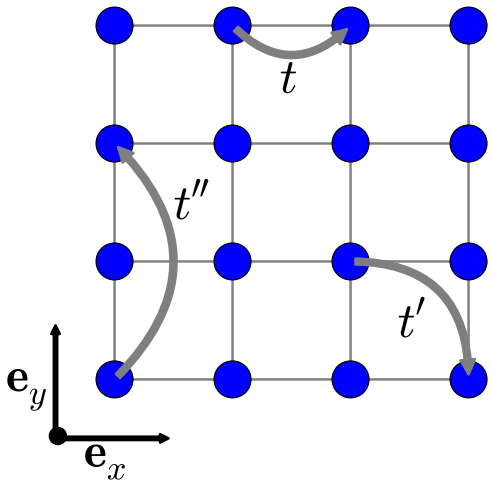

FIG. 1. Definition of the tight-binding parameters on the square lattice.

with i,j indexing lattice sites. $c^\dagger_{\sigma i}$ ($c_{\sigma i}$) denotes creation (annihilation) operators, $n_{\sigma i} = c^\dagger_{\sigma i} c_{\sigma i}$ the density operator, μ the chemical potential, and U the onsite Hubbard interaction. The hopping amplitudes, depicted on Fig. 1, are given by

$$t_{ij} = \begin{cases} t, & \mathbf{r}_i = \mathbf{r}_j \pm \mathbf{e}_{x,y} \\ t', & \mathbf{r}_i = \mathbf{r}_j \pm \mathbf{e}_x \pm \mathbf{e}_y \\ t'', & \mathbf{r}_i = \mathbf{r}_j \pm 2\mathbf{e}_{x,y} \\ 0, & \text{otherwise} \end{cases} \tag{2}$$

where $\mathbf{e}_{x,y}$ are the lattice vectors in the x and y directions. The bare dispersion is therefore

$$\varepsilon_{\mathbf{k}} = 2t(\cos k_x + \cos k_y) + 4t' \cos k_x \cos k_y + 2t''(\cos 2k_x + \cos 2k_y). \tag{3}$$

When $t' = t'' = 0$, the half-bandwidth is $D = 4|t|$, but nonzero t',t'' in general make the bandwidth larger. Hereinafter, we express all quantities in units of D, unless stated differently.

II. FORMALISM

The main goal of this paper is to study the superconducting (SC) phase of the two-dimensional Hubbard model within the TRILEX approach introduced in Refs. [62,63]. TRILEX is based on a bosonic decoupling of the interaction and a self-consistent approximation of the electron-boson vertex Λ with a quantum impurity model. The decoupling of the onsite interaction is done by an exact Hubbard-Stratonovich transformation, leading to a model of noninteracting electrons coupled to some auxiliary bosonic modes representing charge and spin fluctuations.

We also study two methods which can be regarded as simplifications of the TRILEX method, namely, GW+EDMFT [54–59] and GW [64,65]. In GW+EDMFT, vertex corrections are neglected in the nonlocal part of the self-energy and polarization. As both decay to zero, this additional approximation is negligible at very long distances. Due to the full treatment of the local vertex corrections, GW+EDMFT can capture the Mott transition, and we use it to obtain superconducting results in the doped Mott insulator regime. In the GW method, vertex corrections are neglected altogether, and the self-energy and polarization are entirely calculated from bold bubble diagrams. The GW equations do not require the solution of an auxiliary quantum impurity model and are therefore less costly to solve. This additional approximation is justified only at weak coupling (see, e.g., Ref. [57] for an illustration of its failure at large U), and there we use it to explore a large region of (t',t'',T,n_σ) parameter space (T denotes temperature, n_σ occupancy per spin).

Finally, let us stress that, in this paper, we use only *single-site* impurity models. Cluster extensions of TRILEX are discussed in our different work [66]. They naturally incorporate the effect of short-range antiferromagnetic exchange J and give a quantitative control on the accuracy of the solution.

A. Superconducting Hedin equations

In this section, we derive the Hedin equations [64,65,67] which give the self-energy and polarization as functions of the three-leg vertex function. The derivation holds in superconducting phases and is relevant for fluctuations not only in the charge channel [68], but also in the longitudinal and transversal spin channels.

1. Electron-boson action

The starting point of the TRILEX method, as described in Ref. [63], is the following electron-boson action:

$$S_{\text{eb}}[c,c^*,\phi] = c^*_\mu \left[-G_0^{-1}\right]_{\mu\nu} c_\nu + \tfrac{1}{2}\phi_\alpha \left[-W_0^{-1}\right]_{\alpha\beta}\phi_\beta + \lambda_{\mu\nu\alpha} c^*_\mu c_\nu \phi_\alpha, \tag{4}$$

where c^*_μ and c_ν are Grassmann fields describing fermionic degrees of freedom, while ϕ_α is a real bosonic field describing bosonic degrees of freedom. Indices μ,ν stand for space, time, spin, and possibly other (e.g., band) indices $\mu \equiv (\mathbf{r}_\mu,\tau_\mu,\sigma_\mu,\dots)$, where $\mathbf{r}_\mu$ denotes a site of the Bravais lattice, τ_μ denotes imaginary time, and σ_μ is a spin index ($\sigma_\mu \in \{\uparrow,\downarrow\}$). Indices α,β denote $\alpha \equiv (\mathbf{r}_\alpha,\tau_\alpha,I_\alpha,\dots)$, where I_α indexes the bosonic channels. Repeated indices are summed over. Summation $\sum_\mu$ is shorthand for $\sum_{\mathbf{r}\in\text{BL}} \sum_\sigma \int_0^\beta d\tau$. $G_{0,\mu\nu}$ (resp. $W_{0,\alpha\beta}$) is the noninteracting fermionic (resp. bosonic) propagator.

Action (4) can result from the exact Hubbard-Stratonovich decoupling of the Hubbard interaction of Eq. (1) with bosonic fields ϕ, but it can also simply describe an electron-phonon coupling problem.

In this work, we are interested in a generalization of TRILEX able to accommodate superconducting order. To this purpose, we rederive the TRILEX equations starting from a more general action, written in terms of Nambu four-component spinors. The departure from the usual two-component Nambu-spinor formalism is necessary to allow for spin-flip electron-boson coupling in the action. Such terms do appear in the Heisenberg decoupling of the Hubbard interaction (see Sec. II A 2).

We define a four-component Nambu-Grassmann spinor field as a column vector

$$\boldsymbol{\Psi}_i(\tau) \equiv \begin{bmatrix} c^*_{\uparrow i}(\tau) \\ c_{\downarrow i}(\tau) \\ c^*_{\downarrow i}(\tau) \\ c_{\uparrow i}(\tau) \end{bmatrix}, \tag{5}$$

where i stands for the lattice site $\mathbf{r}_i$. In combined indices, analogously to (4), a general electron-boson action can be written as

$$S^{\text{Nambu}}_{\text{eb}}[\boldsymbol{\Psi},\phi] = \tfrac{1}{2}\boldsymbol{\Psi}_u\left[-\boldsymbol{G}_0^{-1}\right]_{uv}\boldsymbol{\Psi}_v - \tfrac{1}{2}\phi_\alpha\left[W_0^{-1}\right]_{\alpha\beta}\phi_\beta + \tfrac{1}{2}\phi_\alpha\boldsymbol{\Psi}_u\boldsymbol{\lambda}_{uv\alpha}\boldsymbol{\Psi}_v, \tag{6}$$

where u,v is a combined index $u \equiv (\mathbf{r}_u,\tau_u,a_u,\dots)$, with $a,b,c,\ldots \in \{0,1,2,3\}$ a Nambu index comprising the spin degree of freedom. The sum is redefined to go over all Nambu indices $\sum_u \equiv \sum_{\mathbf{r}\in\text{BL}}\sum_a\int_0^\beta d\tau$. Bold symbols are used for Nambu-index-dependent quantities.

This action does *not* depend on the conjugate field of $\boldsymbol{\Psi}$ because $\boldsymbol{\Psi}_i$ already contains all the degrees of freedom of the action (4) at the site i. The partition function corresponding to the bare fermionic part of the action has the following form [69]:

$$\int \mathcal{D}[\boldsymbol{\Psi}]e^{\frac{1}{2}\boldsymbol{\Psi}_u\boldsymbol{A}_{uv}\boldsymbol{\Psi}_v} = (\det\boldsymbol{A})^{\frac{1}{2}}, \tag{7}$$

which is valid for any antisymmetric matrix $\boldsymbol{A}$. Due to the unusual form of the action (no conjugated fields), the right-hand side is not the determinant of $\boldsymbol{A}$, but its square root, i.e., the Pfaffian. We can redefine the propagators/correlation functions of interest as

$$\boldsymbol{G}_{uv} \equiv -\langle\boldsymbol{\Psi}_u\boldsymbol{\Psi}_v\rangle, \tag{8}$$

$$W_{\alpha\beta} \equiv -\langle(\phi_\alpha - \langle\phi_\alpha\rangle)(\phi_\beta - \langle\phi_\beta\rangle)\rangle, \tag{9}$$

$$\boldsymbol{\chi}^{3,\text{conn}}_{uv\alpha} \equiv \langle\boldsymbol{\Psi}_u\boldsymbol{\Psi}_v\phi_\alpha\rangle - \langle\boldsymbol{\Psi}_u\boldsymbol{\Psi}_v\rangle\langle\phi_\alpha\rangle. \tag{10}$$

The "conn" superscript denotes the connected part of the correlation function. The renormalized vertex is defined by

$$\boldsymbol{\Lambda}_{uv\alpha} \equiv [\boldsymbol{G}^{-1}]_{uw}[\boldsymbol{G}^{-1}]_{xv}[W^{-1}]_{\alpha\beta}\boldsymbol{\chi}^{3,\text{conn}}_{wx\beta}. \tag{11}$$

Actions (6) and (4) are physically equivalent, namely, their partition functions coincide:

$$Z = \int \mathcal{D}[\boldsymbol{\Psi},\phi]e^{-S^{\text{Nambu}}_{\text{eb}}[\boldsymbol{\Psi},\phi]} = \int \mathcal{D}[c,c^*,\phi]e^{-S_{\text{eb}}[c,c^*,\phi]} \tag{12}$$

for an appropriate choice of $\boldsymbol{G}_0$ and $\boldsymbol{\lambda}$. Yet, they are not formally identical to each other, i.e., one cannot reconstruct (6) from (4) by mere relabeling $c \to \boldsymbol{\Psi}$, $\mu\nu \to uv$ (note the absence of Grassmann conjugation and the additional prefactors in the Nambu action). Therefore, one must rederive the Hedin equations which connect the self-energy and polarization with the full propagators $\boldsymbol{G}$ and W and the renormalized vertex $\boldsymbol{\Lambda}$. We present the full derivation using equations of motion in Appendix A 2; here we just present the final result:

$$\boldsymbol{\Sigma}_{uv} = -\boldsymbol{\lambda}_{uw\alpha}\boldsymbol{G}_{wx}W_{\alpha\beta}\boldsymbol{\Lambda}_{xv\beta} + \tfrac{1}{2}\boldsymbol{\lambda}_{uv\alpha}W_{0,\alpha\beta}\langle\boldsymbol{\Psi}_y\boldsymbol{\lambda}_{yz\beta}\boldsymbol{\Psi}_z\rangle, \tag{13a}$$

$$P_{\alpha\beta} = \tfrac{1}{2}\boldsymbol{\lambda}_{uw,\alpha}\boldsymbol{G}_{xu}\boldsymbol{G}_{wv}\boldsymbol{\Lambda}_{vx,\beta}. \tag{13b}$$

Compared to the expressions in the normal case, there are extra factors $\frac{1}{2}$ in the Hartree term [second line in Eq. (13a)] and polarization [Eq. (13b)]. These factors come from the fact that with four-spinors, the summation over spin is performed twice. Note that the Hartree term can in principle have a frequency dependence if the bare electron-boson vertex has a dynamic part. On the other hand, the term beyond Hartree may as well contribute to the static part of the self-energy, if the bosonic propagator and the bare electron-boson vertex contain a static part. In all the calculations in this paper, the Hartree term is static and is the sole contributor the static part of self-energy. We will thus henceforth omit the Hartree term, as it can be absorbed in the chemical potential.

2. *Connection to the Hubbard model*

In this section, we specify the bare propagators and vertices such that action (6) corresponds to the Hubbard model (1). We then rewrite the Hedin equations under the assumption of spatial and temporal translational symmetry.

The Hubbard-Stratonovich transformation leading from Eq. (1) to an action of the form (4) relies on decomposing the Hubbard interaction as follows:

$$Un_{i\uparrow}n_{i\downarrow} = \frac{1}{2}\sum_I U^I n_i^I n_i^I \tag{14}$$

with $n_I \equiv \sum_{\sigma\sigma'}c^\dagger_\sigma\sigma^I_{\sigma\sigma'}c_{\sigma'}$, and I running within $\{0,z\}$ ("Ising decoupling") or $\{0,x,y,z\}$ ("Heisenberg decoupling") (σ^0 is the 2×2 identity matrix, $\sigma^{x/y/z}$ are the usual Pauli matrices). This identity is verified, up to a density term, whenever

$$U^{\text{ch}} - U^{\text{sp}} = U \tag{15a}$$

in the Ising decoupling, or

$$U^{\text{ch}} - 3U^{\text{sp}} = U \tag{15b}$$

in the Heisenberg decoupling. We have defined $U^{\text{ch}} \equiv U^0$ and $U^{\text{sp}} \equiv U^x = U^y = U^z$. Equations (15a) and (15b) leave a degree of freedom in the choice of U^{ch} and U^{sp}. Here, the choice $U^x = U^y = U^z$ stems from the isotropy of the Heisenberg decoupling (contrary to the Ising decoupling); it can describe SU(2) symmetry-broken phases. In the rest of the paper, we denote all quantities diagonal in the channel index with the channel as a superscript.

To make contact with the results of Ref. [70], for GW we will use the Ising decoupling with

$$U^{\text{ch}} = U/2, \quad U^{\text{sp}} = -U/2, \tag{16a}$$

while in TRILEX and GW+EDMFT (unless stated differently) we will use the Heisenberg decoupling with

$$U^{\text{ch}} = U/2, \quad U^{\text{sp}} = -U/6 \tag{16b}$$

because the antiferromagnetic (AF) instabilities discussed in Sec. III D, which violate the Mermin-Wagner theorem, are weaker in this scheme.

The equivalence of the action (6) with the Hubbard model is accomplished by setting

$$\boldsymbol{G}_{0,ij}(\tau) = \begin{bmatrix} 0 & 0 & 0 & -G_{0,ji}(-\tau) \\ 0 & 0 & G_{0,ij}(\tau) & 0 \\ 0 & -G_{0,ji}(-\tau) & 0 & 0 \\ G_{0,ij}(\tau) & 0 & 0 & 0 \end{bmatrix}, \tag{17a}$$

where i,j denote lattice sites, and

$$\begin{aligned} G_{0,ij}(\tau) &= \sum_{i\omega,\mathbf{k}} e^{-i[\omega\tau-(\mathbf{r}_i-\mathbf{r}_j)\cdot\mathbf{k}]} G_{0\mathbf{k}}(i\omega), \\ G_{0\mathbf{k}}(i\omega) &= \frac{1}{i\omega+\mu-\varepsilon_{\mathbf{k}}}. \end{aligned} \tag{17b}$$

The 4×4 matrices are written in Nambu indices. The bare vertex reads as

$$\boldsymbol{\lambda}_{uv\alpha} = \delta_{\mathbf{r}_u\mathbf{r}_\alpha}\delta_{\mathbf{r}_u\mathbf{r}_v}\delta_{\tau_u\tau_\alpha}\left[\boldsymbol{\delta}_{\tau_u,\tau_v}\cdot\boldsymbol{\lambda}^{I_\alpha}\right]_{a_u a_v} \tag{18a}$$

with

$$\boldsymbol{\delta}_{\tau_u,\tau_v} = \begin{bmatrix} \delta_{\tau_u,\tau_v^+} & & & \\ & \delta_{\tau_u^+,\tau_v} & & \\ & & \delta_{\tau_u,\tau_v^+} & \\ & & & \delta_{\tau_u^+,\tau_v} \end{bmatrix} \tag{18b}$$

and

$$\boldsymbol{\lambda}^I = \begin{bmatrix} & \sigma^I_{\uparrow\downarrow} & & \sigma^I_{\uparrow\uparrow} \\ -\sigma^I_{\uparrow\downarrow} & & -\sigma^I_{\downarrow\downarrow} & \\ & \sigma^I_{\downarrow\downarrow} & & \sigma^I_{\downarrow\uparrow} \\ -\sigma^I_{\uparrow\uparrow} & & -\sigma^I_{\downarrow\uparrow} & \end{bmatrix}. \tag{18c}$$

Thus, this vertex is local and static. The bare bosonic propagators are also local and static, as well as diagonal in the channel index:

$$W^I_{0,ij}(\tau) = \delta_{ij}\delta_\tau U^I. \tag{19}$$

Our Hubbard lattice Nambu action reads as (in explicit indices)

$$\begin{aligned} S^{\text{Nambu}}_{\text{eb}}[\boldsymbol{\Psi},\phi] &= \frac{1}{2}\sum_{i,j,a,b}\iint d\tau\, d\tau' \boldsymbol{\Psi}_{ia}(\tau)\left[-\boldsymbol{G}_0^{-1}\right]_{ia,jb}(\tau-\tau')\boldsymbol{\Psi}_{jb}(\tau') \\ &+ \frac{1}{2}\sum_i\sum_I\int d\tau\, \phi^I_i(\tau)[-(U^I)^{-1}]\phi^I_i(\tau) \\ &+ \frac{1}{2}\sum_i\sum_I\int d\tau\, \phi^I_i(\tau)\boldsymbol{\Psi}_{ia}(\tau)\boldsymbol{\lambda}^I_{ab}\boldsymbol{\Psi}_{ib}(\tau). \end{aligned} \tag{20}$$

3. *Translational invariance, singlet pairing, and SU(2) symmetry*

In this paper, we restrict ourselves to phases with no breaking of translational invariance. With translational invariance in time and space, the propagators depend on frequency and momentum, and are matrices only in the Nambu index. We rewrite the Hedin equations derived above in the special case of the Hubbard action

$$\begin{aligned} \boldsymbol{\Sigma}_{ab,\mathbf{k}}(i\omega) &= -\sum_{\mathbf{q},i\Omega}\sum_{c,d}\sum_I \boldsymbol{\lambda}^I_{ac}\boldsymbol{G}_{cd,\mathbf{k}+\mathbf{q}}(i\omega+i\Omega) \\ &\quad\times W^I_{\mathbf{q}}(i\Omega)\boldsymbol{\Lambda}^I_{db,\mathbf{kq}}(i\omega,i\Omega), \end{aligned} \tag{21a}$$

$$\begin{aligned} P^I_{\mathbf{q}}(i\Omega) &= \frac{1}{2}\sum_{\mathbf{k},i\omega}\sum_{a,b,c,d}\boldsymbol{\lambda}^I_{ac}\boldsymbol{G}_{ba,\mathbf{k}+\mathbf{q}}(i\omega+i\Omega) \\ &\quad\times \boldsymbol{G}_{cd,\mathbf{k}}(i\omega)\boldsymbol{\Lambda}^I_{db,\mathbf{kq}}(i\omega,i\Omega). \end{aligned} \tag{21b}$$

Similarly (see Appendix A 4 for details),

$$\begin{aligned} \boldsymbol{\Lambda}^I_{\mathbf{kq},ab}(i\omega,i\Omega) &= \sum_{cd}\left[\boldsymbol{G}^{-1}_{\mathbf{k}+\mathbf{q}}(i\omega+i\Omega)\right]_{ac}\left[\boldsymbol{G}^{-1}_{\mathbf{k}}(i\omega)\right]_{db} \\ &\quad\times\left[W^I_{\mathbf{q}}(i\Omega)\right]^{-1}\boldsymbol{\chi}^{3,\text{conn},I}_{\mathbf{kq},cd}(i\omega,i\Omega). \end{aligned} \tag{22}$$

Furthermore, we restrict ourselves to SU(2) symmetric phases, and allow only for singlet pairing, therefore,

$$\langle c^*_\uparrow(\tau)c^*_\uparrow(0)\rangle = \langle c^*_\downarrow(\tau)c^*_\downarrow(0)\rangle = 0. \tag{23}$$

We allow no emergent mixing of spin

$$\langle c^*_\uparrow(\tau)c_\downarrow(0)\rangle = \langle c^*_\downarrow(\tau)c_\uparrow(0)\rangle = 0. \tag{24}$$

These assumptions simplify the structure of the Green's function in Nambu space

$$\boldsymbol{G}_{\mathbf{k}}(i\omega) = \begin{bmatrix} & & -F_{\mathbf{k}}(i\omega) & -G^*_{\mathbf{k}}(i\omega) \\ & & G_{\mathbf{k}}(i\omega) & -F^*_{\mathbf{k}}(i\omega) \\ F_{\mathbf{k}}(i\omega) & -G^*_{\mathbf{k}}(i\omega) & & \\ G_{\mathbf{k}}(i\omega) & F^*_{\mathbf{k}}(i\omega) & & \end{bmatrix}, \tag{25}$$

where the normal and anomalous Green's functions read as

$$G_{ij}(\tau-\tau') \equiv -\langle c_{\uparrow i}(\tau)c^*_{\uparrow j}(\tau')\rangle, \tag{26}$$

$$F_{ij}(\tau-\tau') \equiv -\langle c^*_{\downarrow i}(\tau)c^*_{\uparrow j}(\tau')\rangle. \tag{27}$$

Under the present assumptions, $G_{\mathbf{k}}(\tau)$ is real, therefore, $G_{\mathbf{k}}(-i\omega) = G^*_{\mathbf{k}}(i\omega)$. Here, note that SU(2) symmetry and lattice inversion symmetry imply $F_{ij}(\tau) = F_{ij}(-\tau) = F_{ji}(\tau)$ [this can be proven by rotating $c_\sigma \to (-)^{\delta_{\uparrow,\sigma}}c_{\bar\sigma}$]. Therefore, if $F_{ij}(\tau)$ is real, $F_{\mathbf{k}}(i\omega)$ is also purely real. In this paper, we consider only purely real $F_{ij}(\tau)$.

Similarly, the block structure of the self-energy is given by

$$\boldsymbol{\Sigma}_{\mathbf{k}}(i\omega) = \begin{bmatrix} & & S^*_{\mathbf{k}}(i\omega) & \Sigma_{\mathbf{k}}(i\omega) \\ & & -\Sigma^*_{\mathbf{k}}(i\omega) & S_{\mathbf{k}}(i\omega) \\ -S^*_{\mathbf{k}}(i\omega) & \Sigma_{\mathbf{k}}(i\omega) & & \\ -\Sigma^*_{\mathbf{k}}(i\omega) & -S_{\mathbf{k}}(i\omega) & & \end{bmatrix}. \tag{28}$$

Σ and S are the normal and anomalous self-energies defined by the Nambu-Dyson equation

$$\boldsymbol{G}^{-1}_{\mathbf{k}}(i\omega) = \boldsymbol{G}^{-1}_{0,\mathbf{k}}(i\omega) - \boldsymbol{\Sigma}_{\mathbf{k}}(i\omega), \tag{29}$$

where the inverse is assumed to be the matrix inverse in Nambu indices. Componentwise, under the present assumptions, the

Nambu-Dyson equation reads as

$$G_{\mathbf{k}}(i\omega) = \frac{\left[G_{0\mathbf{k}}^{-1}(i\omega) - \Sigma_{\mathbf{k}}(i\omega)\right]^*}{\left|G_{0\mathbf{k}}^{-1}(i\omega) - \Sigma_{\mathbf{k}}(i\omega)\right|^2 + |S_{\mathbf{k}}(i\omega)|^2}, \quad (30a)$$

$$F_{\mathbf{k}}(i\omega) = \frac{-S_{\mathbf{k}}(i\omega)}{\left|G_{0\mathbf{k}}^{-1}(i\omega) - \Sigma_{\mathbf{k}}(i\omega)\right|^2 + |S_{\mathbf{k}}(i\omega)|^2}. \quad (30b)$$

Furthermore, due to SU(2) symmetry, the full bosonic propagator will be identical in the x, y, and z channels, so we define

$$\eta(I) = \begin{cases} \text{ch}, & I = 0 \\ \text{sp}, & I = x,y,z \end{cases} \quad (31)$$

and have $W^x = W^y = W^z = W^{\text{sp}}$, and similarly for the renormalized vertex. This will simplify the calculation of the self-energy in the Heisenberg decoupling scheme, as the contribution coming from x and y bosons is the same as the one coming from the z boson. The bosonic Dyson equation is then always solved in only two channels:

$$W_{\mathbf{q}}^{\eta}(i\Omega) = \frac{U^{\eta}}{1 - U^{\eta} P_{\mathbf{q}}^{\eta}(i\Omega)}. \quad (32)$$

B. TRILEX, GW+EDMFT, and GW equations

1. Single-site TRILEX approximation for d-wave superconductivity

The single-site TRILEX method consists in approximating the renormalized vertex by a local quantity, obtained from an effective single-site impurity model

$$\begin{aligned} &S_{\text{imp,eb}}^{\text{Nambu}}[\boldsymbol{\Psi},\phi] \\ &= \frac{1}{2}\iint d\tau\, d\tau' \boldsymbol{\Psi}_a(\tau)[-\boldsymbol{\mathcal{G}}^{-1}]_{a,b}(\tau-\tau')\boldsymbol{\Psi}_b(\tau') \\ &\quad + \frac{1}{2}\sum_I \iint d\tau\, d\tau' \phi^I(\tau)[-(\mathcal{U}^I)^{-1}](\tau-\tau')\phi^I(\tau') \\ &\quad + \frac{1}{2}\sum_I \int d\tau\, \phi^I(\tau)\boldsymbol{\Psi}_a(\tau)\boldsymbol{\lambda}_{ab}^I \boldsymbol{\Psi}_b(\tau). \end{aligned} \quad (33)$$

Solving the TRILEX equations amounts to finding $\boldsymbol{\mathcal{G}}(i\omega)$ and $\mathcal{U}(i\Omega)$ such that the full propagators in the effective impurity problem (33) coincide with the local components of the ones obtained on the lattice, namely, we want to satisfy

$$\sum_{\mathbf{k}} \boldsymbol{G}_{\mathbf{k}}(i\omega)[\boldsymbol{\mathcal{G}},\mathcal{U}] = \boldsymbol{G}_{\text{imp}}(i\omega)[\boldsymbol{\mathcal{G}},\mathcal{U}], \quad (34a)$$

$$\sum_{\mathbf{q}} W_{\mathbf{q}}^{\eta}(i\Omega)[\boldsymbol{\mathcal{G}},\mathcal{U}] = W_{\text{imp}}^{\eta}(i\Omega)[\boldsymbol{\mathcal{G}},\mathcal{U}], \quad (34b)$$

where the vertex of Eq. (21) is approximated by the impurity vertex

$$\boldsymbol{\Lambda}_{\mathbf{kq}} = \boldsymbol{\Lambda}_{\text{imp}}[\boldsymbol{\mathcal{G}},\mathcal{U}]. \quad (35)$$

In this paper, we allow only strictly d-wave superconducting pairing. Thus,

$$\sum_{\mathbf{k}} F_{\mathbf{k}}(i\omega) = 0, \quad (36)$$

which means that the anomalous components of the local Green's function $\boldsymbol{G}_{\text{loc}}$ will be zero. Therefore, at self-consistency [Eq. (34a)], the impurity's Green's function is normal and thus the anomalous components of the bare propagator on the impurity must vanish:

$$\boldsymbol{\mathcal{G}}_{02/20/13/31} = 0. \quad (37)$$

This means that the impurity problem will be identical to the one in the normal-phase calculations, which can be expressed in terms of the original Grassmann fields

$$\begin{aligned} &S_{\text{imp,eb}}[c^*,c,\phi] \\ &= \sum_{\sigma} \iint d\tau\, d\tau' c_{\sigma}^*(\tau)[-\mathcal{G}^{-1}](\tau-\tau')c_{\sigma}(\tau') \\ &\quad + \frac{1}{2}\sum_I \iint d\tau\, d\tau' \phi^I(\tau)[-(\mathcal{U}^I)^{-1}](\tau-\tau')\phi^I(\tau') \\ &\quad + \sum_{I,\sigma,\sigma'} \int d\tau\, \phi^I(\tau) c_{\sigma}^*(\tau)\lambda_{\sigma\sigma'}^I c_{\sigma'}(\tau), \end{aligned} \quad (38)$$

where the bare vertices (slim symbols denote the impurity quantities) are given by Pauli matrices $\lambda_{\sigma\sigma'}^I = \sigma_{\sigma\sigma'}^I$. After integrating out the bosonic degrees of freedom, one obtains an electron-electron action with retarded interactions:

$$\begin{aligned} S_{\text{imp,ee}}[c^*,c] &= \iint_{\tau,\tau'} \sum_{\sigma} c_{\sigma}^*(\tau)[-\mathcal{G}^{-1}(\tau-\tau')]c_{\sigma}(\tau') \\ &\quad + \frac{1}{2}\iint_{\tau\tau'} \sum_I n^I(\tau)\mathcal{U}^I(\tau-\tau')n^I(\tau'). \end{aligned} \quad (39)$$

This single-site impurity problem is solved using the numerically exact hybridization-expansion continuous-time quantum Monte Carlo (CTHYB or HYB-CTQMC [71,72]), employing the segment algorithm. The transverse spin-spin interaction term is dealt with in an interaction-expansion manner [73]. See Ref. [63] for details.

Under the present assumptions, the approximation for the renormalized vertex entering the Hedin equations (21) is

$$\begin{aligned} \boldsymbol{\Lambda}_{\mathbf{kq}}^I(i\omega,i\Omega) &\approx \boldsymbol{\Lambda}_{\text{imp}}^I(i\omega,i\Omega) \\ &= \boldsymbol{\lambda}^I \circ \begin{bmatrix} & \Lambda_{\text{imp}}^{\eta(I)} & & \Lambda_{\text{imp}}^{\eta(I)} \\ \left(\Lambda_{\text{imp}}^{\eta(I)}\right)^* & & \left(\Lambda_{\text{imp}}^{\eta(I)}\right)^* & \\ & \Lambda_{\text{imp}}^{\eta(I)} & & \Lambda_{\text{imp}}^{\eta(I)} \\ \left(\Lambda_{\text{imp}}^{\eta(I)}\right)^* & & \left(\Lambda_{\text{imp}}^{\eta(I)}\right)^* & \end{bmatrix} \\ &\quad \times (i\omega,i\Omega), \end{aligned} \quad (40)$$

where $\circ$ denotes the elementwise product $[A \circ B]_{ij} = A_{ij}B_{ij}$ (see Appendix A 5 for details).

We obtain $\Lambda_{\text{imp}}^{\eta}$ from the three-point correlation function on the impurity using

$$\begin{aligned} &\Lambda_{\text{imp}}^{\eta}(i\omega,i\Omega) \\ &\equiv \frac{\tilde{\chi}_{\text{imp}}^{3,\eta,\text{conn}}(i\omega,i\Omega)}{G_{\text{imp}}(i\omega)G_{\text{imp}}(i\omega+i\Omega)\left[1 - \mathcal{U}^{\eta}(i\Omega)\chi_{\text{imp}}^{\eta}(i\Omega)\right]}, \end{aligned} \quad (41)$$

where

$$\tilde{\chi}^{3,\eta,\mathrm{conn}}_{\mathrm{imp}}(i\omega,i\Omega) \equiv \iint_{\tau\tau'} e^{i\tau\omega+i\tau'\Omega} \tag{42}$$

$$(\langle c_\uparrow(\tau)c^*_\uparrow(0)n^\eta(\tau')\rangle_{\mathrm{imp}} + G_{\mathrm{imp}}(\tau)\langle n^\eta\rangle_{\mathrm{imp}}) \tag{43}$$

and

$$G_{\mathrm{imp}}(i\omega) \equiv -\int_0^\beta d\tau\, e^{i\tau\omega}\langle c_\uparrow(\tau)c^*_\uparrow(0)\rangle_{\mathrm{imp}}, \tag{44}$$

$$W^\eta_{\mathrm{imp}}(i\Omega) \equiv -\int_0^\beta d\tau\, e^{i\tau\Omega}\langle(\phi(\tau)-\langle\phi\rangle)(\phi(0)-\langle\phi\rangle)\rangle_{\mathrm{imp}} \tag{45}$$

$$= \mathcal{U}(i\Omega) - \mathcal{U}(i\Omega)\chi^\eta_{\mathrm{imp}}(i\Omega)\mathcal{U}(i\Omega), \tag{46}$$

$$\chi^\eta_{\mathrm{imp}}(i\Omega) \equiv \int_0^\beta d\tau\, e^{i\tau\Omega}\big(\langle n^\eta(\tau)n^\eta(0)\rangle_{\mathrm{imp}} - \langle n^\eta\rangle^2_{\mathrm{imp}}\big). \tag{47}$$

We can now write the final expressions for the self-energy and polarization:

$$\Sigma_{\mathbf{k}}(i\omega) = -\sum_\eta m_\eta \sum_{\mathbf{q},i\Omega} G_{\mathbf{k}+\mathbf{q}}(i\omega+i\Omega)W^\eta_{\mathbf{q}}(i\Omega)\Lambda^\eta_{\mathrm{imp}}(i\omega,i\Omega), \tag{48a}$$

$$S_{\mathbf{k}}(i\omega) = -\sum_\eta (-)^{p_\eta} m_\eta \sum_{\mathbf{q},i\Omega} F_{\mathbf{k}+\mathbf{q}}(i\omega+i\Omega) \times W^\eta_{\mathbf{q}}(i\Omega)\Lambda^\eta_{\mathrm{imp}}(i\omega,i\Omega), \tag{48b}$$

$$P^\eta_{\mathbf{q}}(i\Omega) = 2\sum_{\mathbf{k},i\omega} G_{\mathbf{k}+\mathbf{q}}(i\omega+i\Omega)G_{\mathbf{k}}(i\omega)\Lambda^\eta_{\mathrm{imp}}(i\omega,i\Omega) + (-)^{p_\eta}2\sum_{\mathbf{k},i\omega} F_{\mathbf{k}+\mathbf{q}}(i\omega+i\Omega)F_{\mathbf{k}}(i\omega)\Lambda^\eta_{\mathrm{imp}}(i\omega,i\Omega) \tag{48c}$$

with $p_{\mathrm{ch}} = 1$, $p_{\mathrm{sp}} = 0$, $m_{\mathrm{ch}} = 1$. These equations hold in both the Heisenberg ($m_{\mathrm{sp}} = 3$) and Ising ($m_{\mathrm{sp}} = 1$) decoupling schemes. In the expression for the polarization [Eq. (48c)], we have used lattice inversion symmetry and the symmetries of Λ and $\boldsymbol{G}$. Under the present assumptions, P is purely real (see Appendix A 3 for details).

2. GW+EDMFT

The GW+EDMFT approximation can be regarded as a simplified version of TRILEX where, in the calculation of the nonlocal ($\mathbf{r} \neq 0$) part of self-energy and polarization [second line of Eqs. (51a), (51b), and (51c) below], an additional approximation is made:

$$\Lambda^\eta_{\mathrm{imp}}(i\omega,i\Omega) \approx 1. \tag{49}$$

The efficiency is gained because one need not measure the three-point correlator $\tilde{\chi}^{3,\eta,\mathrm{conn}}$ in the impurity model. The local self-energy and polarization still have vertex corrections, but are identical to Σ and P on the impurity, which can be computed from only two-point correlators. Furthermore, the calculation of the nonlocal parts of the self-energy and polarization can now be performed in imaginary time, as opposed to the explicit summation over frequency needed in Eqs. (51a), (51b), and (51c).

3. GW

If we approximate the renormalized vertex by unity even in the calculation of the local part of self-energies, we obtain an approximation similar to the GW approximation, with the important difference that we are using a decoupling in both charge and spin channels, unlike the conventional GW approaches which are limited to the charge channel. This additional approximation eliminates the need for solving an impurity problem, as now even the local self-energy and polarization are calculated by the bubble diagrams (48a), (48b), and (48c), simplified by Eq. (49).

To summarize, the exact expressions for the self-energy and boson polarization are compared to the approximate ones in GW, EDMFT, GW+EDMFT, and TRILEX in Fig. 2.

4. Normal-phase calculation

In the normal phase, the further simplification is that $F_{\mathbf{k}}(i\omega) = 0$. Therefore, $S_{\mathbf{k}}(i\omega) = 0$ and the Dyson equation (30a) reduces to the familiar form

$$G_{\mathbf{k}}(i\omega) = \frac{1}{i\omega + \mu - \varepsilon_{\mathbf{k}} - \Sigma_{\mathbf{k}}(i\omega)}. \tag{50}$$

III. METHODS

A. Numerical implementation of the Hedin equations

As shown in Ref. [63], it is numerically advantageous to perform the computation in real space and to split the self-energy and polarization in the following way:

$$\Sigma_{\mathbf{r}}(i\omega) = \delta_{\mathbf{r}}\Sigma_{\mathrm{imp}}(i\omega) - \sum_\eta m_\eta \sum_{i\Omega} \tilde{G}_{\mathbf{r}}(i\omega+i\Omega) \times \tilde{W}^\eta_{\mathbf{r}}(i\Omega)\Lambda^\eta_{\mathrm{imp}}(i\omega,i\Omega), \tag{51a}$$

$$S_{\mathbf{r}}(i\omega) = -\sum_\eta (-)^{p_\eta} m_\eta \sum_{i\Omega} \tilde{F}_{\mathbf{r}}(i\omega+i\Omega) \times \tilde{W}_{\mathbf{r}}(i\Omega)\Lambda^\eta_{\mathrm{imp}}(i\omega,i\Omega), \tag{51b}$$

$$P^\eta_{\mathbf{r}}(i\Omega) = \delta_{\mathbf{r}}P^\eta_{\mathrm{imp}}(i\Omega) + 2\sum_{i\omega} \tilde{G}_{\mathbf{r}}(i\omega+i\Omega)\tilde{G}_{-\mathbf{r}}(i\omega) \times \Lambda^\eta_{\mathrm{imp}}(i\omega,i\Omega) + (-)^{p_\eta}2\sum_{i\omega} \tilde{F}_{\mathbf{r}}(i\omega+i\Omega) \times \tilde{F}_{-\mathbf{r}}(i\omega)\Lambda^\eta_{\mathrm{imp}}(i\omega,i\Omega), \tag{51c}$$

where $\tilde{X}_{\mathbf{r}}(i\omega) \equiv (1-\delta_{\mathbf{r}})X_{\mathbf{r}}(i\omega)$. In the presence of lattice inversion symmetry, $X_{\mathbf{r}} = X_{-\mathbf{r}}$. The impurity's self-energy and polarization are defined as

$$\Sigma_{\mathrm{imp}}(i\omega) \equiv \mathcal{G}^{-1}(i\omega) - G^{-1}_{\mathrm{imp}}(i\omega), \tag{52a}$$

$$P^\eta_{\mathrm{imp}}(i\Omega) \equiv [\mathcal{U}^\eta(i\Omega)]^{-1} - [W^\eta_{\mathrm{imp}}(i\Omega)]^{-1} = \frac{-\chi^\eta_{\mathrm{imp}}(i\Omega)}{1-\mathcal{U}^\eta\chi^\eta_{\mathrm{imp}}(i\Omega)}. \tag{52b}$$

B. Solution by forward recursion

In practice, the TRILEX, GW+EDMFT, and GW equations can be solved by forward recursion:

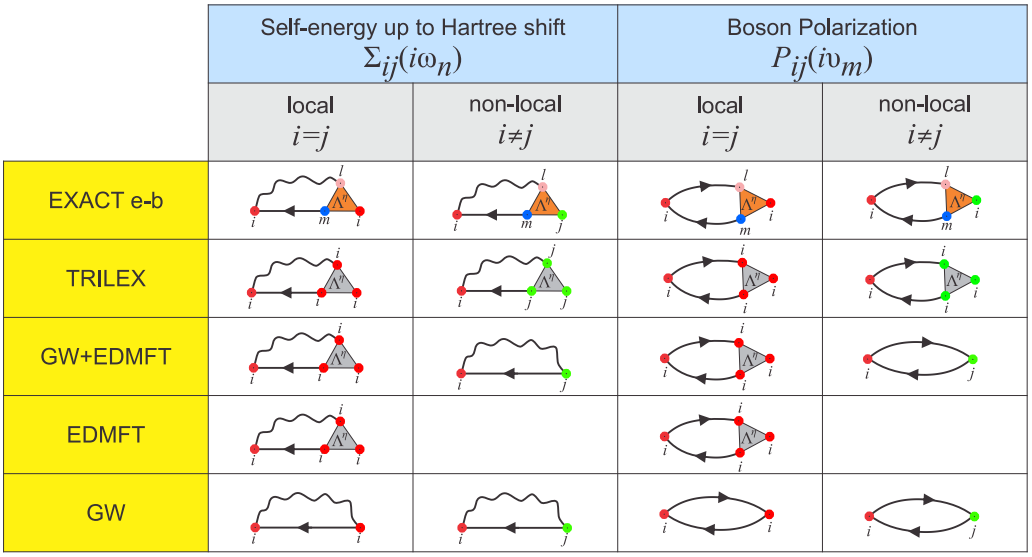

FIG. 2. Self-energy/polarization approximations in various methods based on a Hubbard-Stratonovich decoupling, compared to the exact expression. The renormalized electron-boson vertex is either approximated by a local dynamical quantity or by the bare vertex. Orange triangle denotes the exact renormalized vertex, with full spatial dependence; gray triangle denotes the local approximation of the vertex. Colored circles denote terminals of the propagators and the vertex and the (local) bare vertex at a given site; different colors denote different lattice sites $ijlm$. Internal site indices are summed over, but when the vertex is local, only a single term in the summation survives.

(1) Start with a given $\Sigma_{\mathbf{k}}(i\omega)$ and $P^{\eta}_{\mathbf{q}}(i\Omega)$, and (for SC phase only) $S_{\mathbf{k}}(i\omega)$ and (for TRILEX and GW+EDMFT only) $\Sigma_{\rm imp}(i\omega)$ and $P^{\eta}_{\rm imp}(i\Omega)$ (for instance set them to zero, or use EDMFT results).

(2) Compute the new $G_{\mathbf{k}}(i\omega)$ and $W^{\eta}_{\mathbf{q}}(i\Omega)$ and (for SC phase only) $F_{\mathbf{k}}(i\omega)$ from Eqs. (30a), (32), and (30b).

(3) (TRILEX/GW+EDMFT only) Impose the self-consistency conditions (34a) and (34b) by reversing the impurity Dyson equations (52a) and (52b), such that

$$\mathcal{G}(i\omega) = \left[\left\{\sum_{\mathbf{k}} G_{\mathbf{k}}(i\omega)\right\}^{-1} + \Sigma_{\rm imp}(i\omega)\right]^{-1}, \quad (53a)$$

$$\mathcal{U}^{\eta}(i\Omega) = \left[\left\{\sum_{\mathbf{q}} W^{\eta}_{\mathbf{q}}(i\Omega)\right\}^{-1} + P^{\eta}_{\rm imp}(i\Omega)\right]^{-1}. \quad (53b)$$

(4) (TRILEX/GW+EDMFT only) Solve the impurity model with the above bare fermionic and bosonic propagators: compute $G_{\rm imp}$, $\chi^{\eta}_{\rm imp}$, $\langle n^{\eta}\rangle_{\rm imp}$, and (for TRILEX only) $\tilde{\chi}^{3,\eta,\rm conn}$ and from them $\Sigma_{\rm imp}$ [Eq. (52a)], $P^{\eta}_{\rm imp}$ [Eq. (52b)], and (TRILEX only) $\Lambda^{\eta}_{\rm imp}$ [Eq. (41)].

(5) Compute $\Sigma_{\mathbf{k}}(i\omega)$ and $P^{\eta}_{\mathbf{q}}(i\Omega)$ and (for SC phase only) $S_{\mathbf{k}}(i\omega)$ with Eqs. (51a), (51c), and (51b).

(6) Go back to step 2 until convergence is reached.

C. Superconducting temperature T_c

In order to determine the superconducting transition temperature T_c, we solve a linearized gap equation (LGE). At $T = T_c$, the anomalous part of the self-energy S vanishes. Linearizing Eq. (30b) with respect to S and plugging it into Eq. (51b) leads to an implicit equation for T_c, featuring only the normal component of the Green's function

$$S_{\mathbf{r}}(i\omega) = -\sum_{\eta,i\Omega}(-)^{\delta_{\eta,\rm ch}} F_{\mathbf{r}}(i\omega + i\Omega) W^{\eta}_{\mathbf{r}}(i\Omega)\Lambda^{{\rm imp},\eta}(i\omega, i\Omega),$$

$$F_{\mathbf{k}}(i\omega_n) = -S_{\mathbf{k}}(i\omega_n)|G_{\mathbf{k}}(i\omega_n))|^2. \quad (54)$$

Using four-vector notation $k \equiv (\mathbf{k}, i\omega)$, we obtain

$$A_{kk'} \equiv \sum_{\eta={\rm ch,sp}} (-)^{p_\eta} m_\eta |G(k')|^2 W^{\eta}_{k-k'} \Lambda^{{\rm imp},\eta}_{k,k-k'}, \quad (55)$$

$$A_{kk'} S_{k'} = S_k. \quad (56)$$

This is an eigenvalue problem for S. In practice, it is more convenient to consider the spectrum of the operator A:

$$A_{kk'} S^{\lambda}_{k'} = \lambda S^{\lambda}_{k}. \quad (57)$$

The eigenvalues λ and the eigenvectors S^{λ}_{k} depend on the temperature T. The critical temperature T_c is therefore given by

$$\lambda_m(T_c) = 1,$$

where λ_m is the largest eigenvalue of A. In other words, $T = T_c$ when the first eigenvalue crosses 1. In addition, the symmetry of the superconducting instability is given by the k dependence of S for the corresponding eigenvector.

In practice, we first solve the normal-phase equations, and then solve the LGE (54) by forward substitution. Starting from an initial simple $d_{x^2-y^2}$-wave form

$$S_{\mathbf{k}}(i\omega_n) = (\delta_{n,0} + \delta_{n,-1})(\cos k_x - \cos k_y), \quad (58)$$

we use the power method [74] to compute the leading eigenvalue of the operator A. We do this in a select range of temperature for the given parameters (U, n, t, t', t'') and monitor the leading eigenvalue $\lambda_m(T)$. If we observe a T_c [$\lambda_m(T) > 1$)], we can then use the eigenvector S as an initial guess to

stabilize the superconducting solution using the algorithm from Sec. III B. We have also examined other irreducible representations of the symmetry group and found that this d-wave representation is the one with highest T_c, in agreement with Refs. [75,76].

D. AF instability

As documented in Refs. [62,63], the TRILEX equations present an instability towards antiferromagnetism below some temperature T_{AF} (see also Refs. [70,75]). The antiferromagnetic susceptibility χ^{sp} is related to the propagator of the boson in the spin channel via

$$W^{\mathrm{sp}}_{\mathbf{q}}(i\Omega) = U^{\mathrm{sp}} - U^{\mathrm{sp}}\chi^{\mathrm{sp}}_{\mathbf{q}}(i\Omega)U^{\mathrm{sp}}.$$

They both diverge at $T = T_{\mathrm{AF}}$ because the polarization becomes too large [the denominator in (32) vanishes]. This instability, which is an artifact of the approximation for the two-dimensional Hubbard model, violates the Mermin-Wagner theorem. For many values of t',t'', this AF instability prevents us from reaching the superconducting temperature T_c.

This AF instability also exists in conventional cluster DMFT methods (cellular DMFT, DCA) [21,77,78]. Yet, in most works, it is simply ignored by enforcing a paramagnetic solution (by symmetrizing up- and down-spin components). In TRILEX, however, we do not have this possibility. Indeed, the antiferromagnetic susceptibility directly enters the equations (via W), and its divergence makes it impossible to stabilize a paramagnetic solution of the TRILEX equations at a temperature lower than T_{AF}. For a precise definition of T_{AF} in the present context, see Appendix C.

In the following, we circumvent this issue in two ways: either by extrapolating the temperature dependence of the eigenvalue of the linearized gap equation to low temperatures, despite the AF instability (Sec. IV A, with tight-binding values t',t'' relevant for cuprate physics), or, in Sec. IV B, by finding other values of t',t'', where the Fermi surface shape is qualitatively similar to the cuprate case, but where the AF instability occurs at a temperature lower than T_c.

IV. RESULTS AND DISCUSSION

A. Phase diagram

First, using the linearized-gap equation (LGE) method described in Sec. III C, we compute the SC phase boundary from high temperature, for $t' = -0.2t$, $t'' = 0$, a physically relevant case for the physics of cuprates. We set $U/D = 4$ in order to be above the Mott transition threshold at half-filling (we recall that for the square lattice, $U_c/D \approx 2.4$ within single-site DMFT [49]). The results are presented on Fig. 3.

The top panel presents the largest eigenvalue of the LGE as a function of temperature, for TRILEX and GW+EDMFT. The calculation becomes unstable due to AF instability before we can observe $\lambda_m > 1$. The extrapolation of λ_m towards low temperature is not straightforward. We use an empirical law

$$\lambda_m(T) \approx a\exp(bT^{\gamma} + cT^{2\gamma}) \tag{59}$$

to fit the data and extrapolate to lower temperature. This form can be shown (see Appendix C) to provide a very good fit to similar computations in the Dynamical Cluster

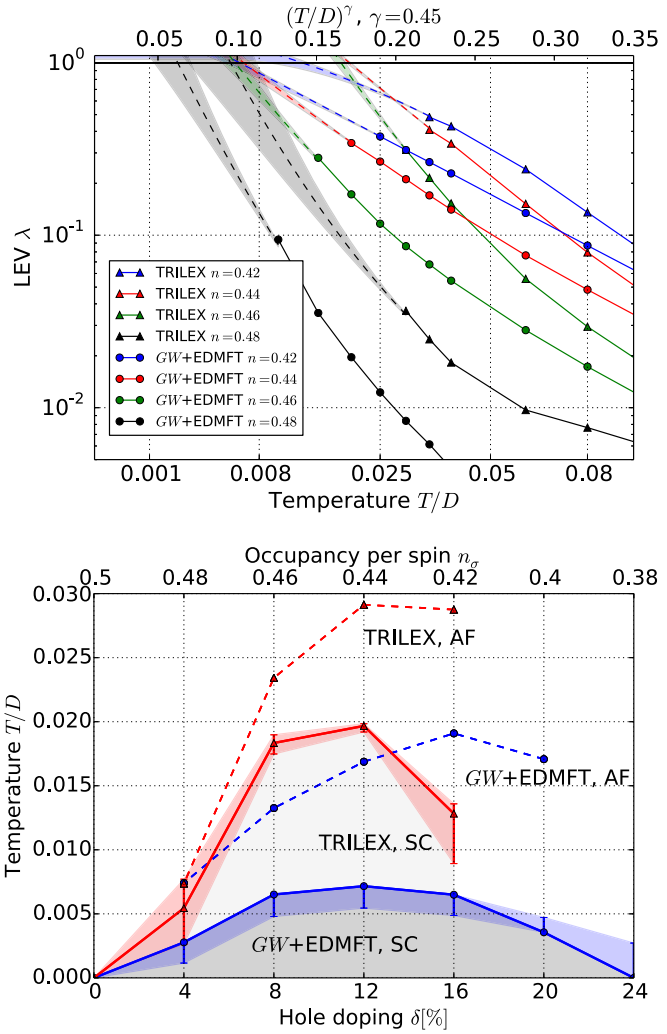

FIG. 3. Top panel: the leading eigenvalue of the linearized gap equation in TRILEX and GW+EDMFT. Bottom panel: SC critical temperature in both methods for $U/D = 4$, $(t',t'') = (-0.2t,0)$. The dashed lines represent the AF instability (see text).

Approximation (DCA) and DCA$^+$ methods, from the data of Refs. [22,77]. We perform the fit and extrapolation with $\gamma = 0.3$ for GW+EDMFT and $\gamma = 0.45$ for TRILEX, and get the result for T_c reported with solid lines on the bottom panel. The error bars shown are obtained by fitting and extrapolating with γ varied in the window 0.3–0.6. The error bars coming from the uncertainty of the fit for a fixed γ and a detailed discussion of the fitting procedure can be found in Appendix C. The dashed lines denote the temperature of the antiferromagnetic instability, below which no stable paramagnetic calculation can be made.

For all values of γ, the raw data at high temperature for both methods indicate a similar dome shape for T_c vs δ, where δ is the percentage of hole doping: $\delta[\%] = (1 - 2n_\sigma) \times 100$ ($n_\sigma = \frac{1}{2}$ corresponds to half-filling). The fact that T_c vanishes at zero δ can be checked directly, but we cannot exclude that it vanishes at a finite, small value of δ. The optimal doping in both methods is found to be around 12%. At half-filling, both methods recover a Mott insulating state, and $\lambda_m(T)$ is found to be very small. We observe that TRILEX has a higher T_c

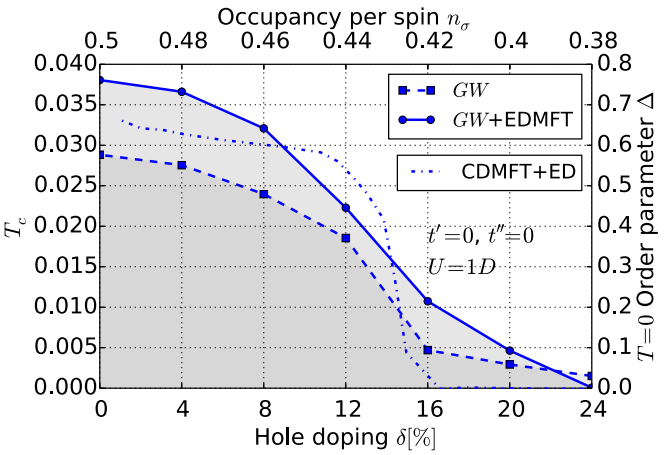

FIG. 4. Comparison of $T_c(\delta)$ in GW and GW+EDMFT methods at weak coupling $U/D = 1$, $t' = t'' = 0$. The dotted line is the order parameter Δ at $T = 0$ from a 2×2 CDMFT+ED calculation, replotted from Ref. [78] (scale on the right).

than GW+EDMFT, showing that the effects of the renormalization of the electron-boson vertex are non-negligible in this regime.

These results for $T_c(\delta)$ are qualitatively comparable to the results of cluster DMFT methods, e.g., the four-site CDMFT + ED computation of Refs. [78–80] or the eight-site DCA results of Ref. [81]. In particular, Ref. [79] reports a $T_c/D \approx 0.0125$ at doping $\delta = 13\%$ in a doped Mott insulator, which falls halfway between the TRILEX and GW+EDMFT results. Furthermore, the optimal doping in Ref. [78] seems to coincide with our result, while in Ref. [79] it is somewhat bigger (around 20%). We emphasize, however, that here we solve only a *single-site* quantum impurity problem, and obtain the d-wave order, which is not possible in single-site DMFT due to symmetry reasons.

Let us now turn to the weak-coupling regime ($U/D = 1$). We present in Fig. 4 the SC temperature in the GW and GW+EDMFT approximations within the Ising decoupling [for the $\lambda(T)$ plot, see Appendix C]. Both methods give similar results, which justifies using the faster GW at weak coupling. In contrast to the larger-U case, one does not obtain the dome versus doping due to the absence of Mott insulator at $\delta = 0$.

We compare our results with the order parameter at $T = 0$ obtained from a 2×2 CDMFT+ED calculation [78]. The general trend observed is similar: optimal doping is zero, and there is a quick reduction of T_c between 12% and 16% doping.

As for the value of T_c, we compare to the result presented in Ref. [77]. Here, a DCA$^+$ calculation with a 52-site cluster impurity, at $U/D = 1, t' = t'' = 0, \delta = 10\%$, predicts $T_c/D \approx 0.06$. With the same parameters, GW gives $T_c/D \approx 0.21$, GW+EDMFT gives $T_c/D \approx 0.27$, hence overestimating T_c.

B. Weak coupling

As explained in Sec. III D, in order to study the SC phase itself, we need to identify a dispersion for which T_c is above T_{AF}. To achieve this, we first scan a large set of parameters t', t'' with the GW approximation at weak coupling.

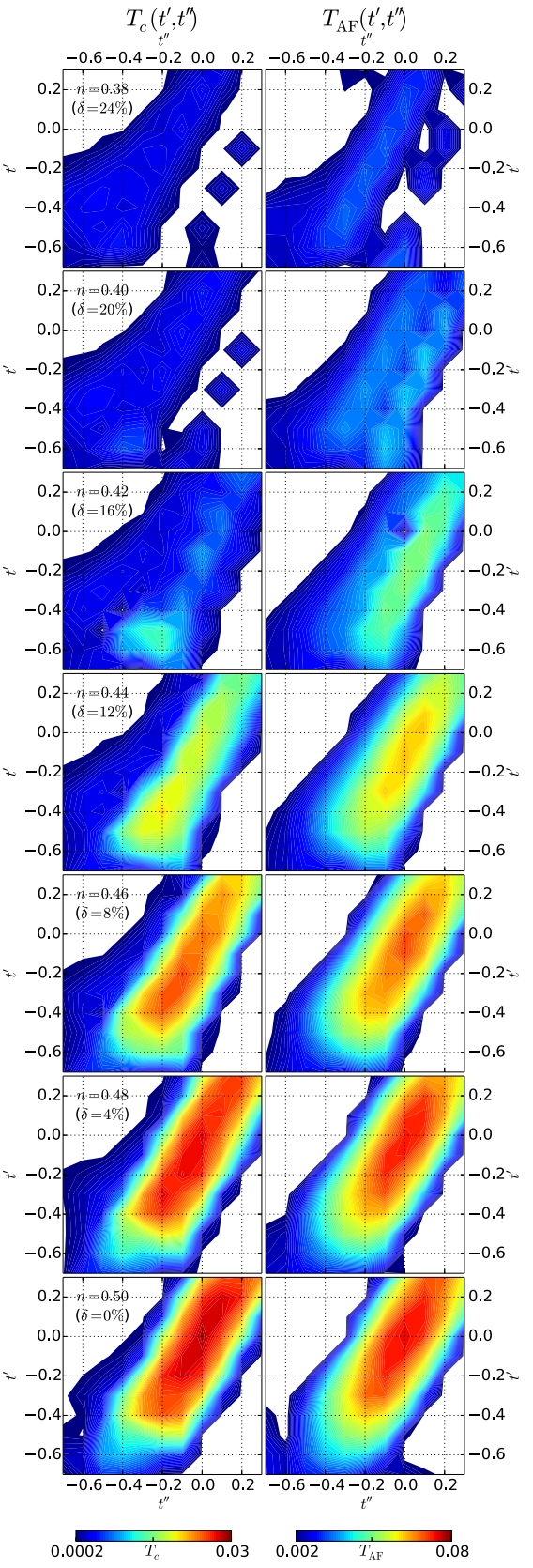

FIG. 5. GW calculation of d-wave T_c (left panels) and T_{AF} (right panels) at $U/D = 1$, $t = -1.0$, for different values of n, as functions of (t',t''). t' and t'' are sampled between (and including) -0.7 and 0.3 with the step 0.1. n is taken between (and including) 0.38 and 0.5 (i.e., the half-filling) with the step 0.02.

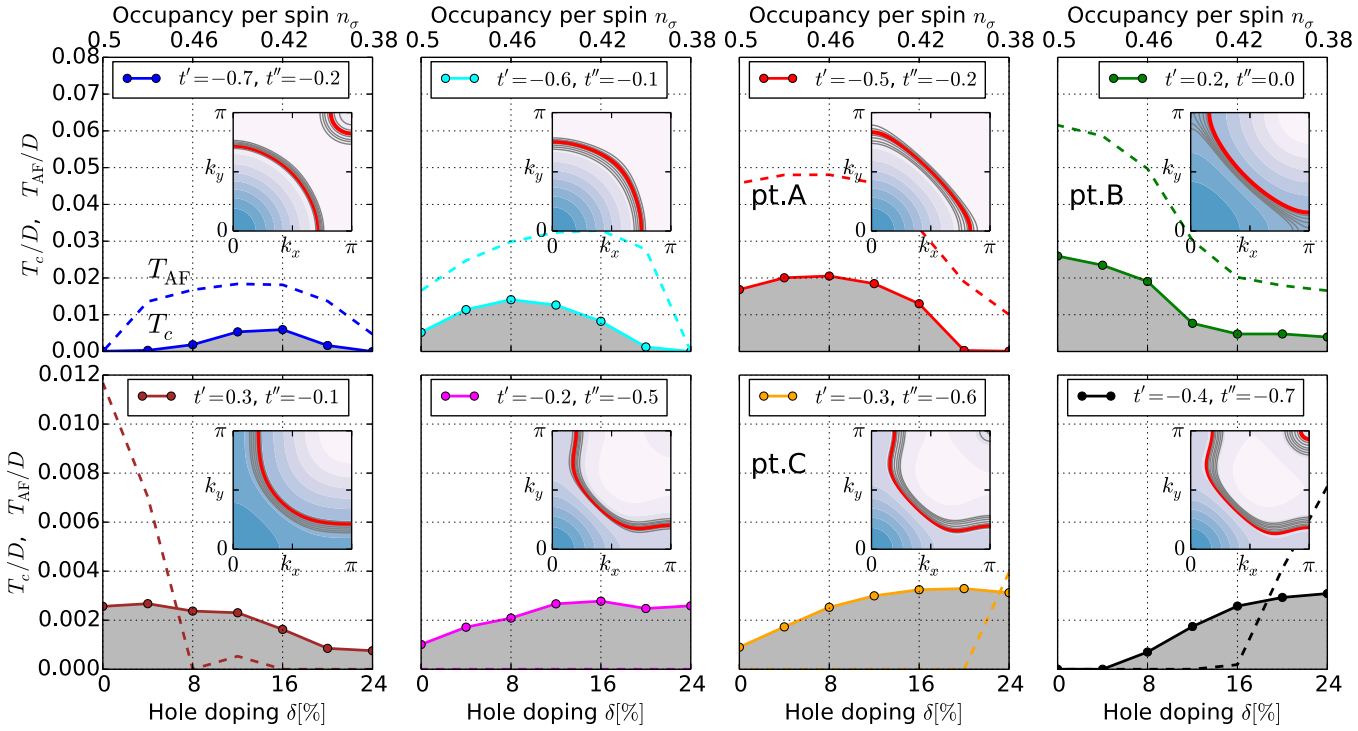

FIG. 6. GW calculations at $U/D = 1$, $t = -1$. Dashed lines denote T_{AF}, full lines T_c. Inset: color map for $\varepsilon_{\mathbf{k}}$. Gray contours denote bare Fermi surfaces at examined values of doping. The red line corresponds to the Fermi surface with maximum T_c.

Indeed, at weak coupling, we can approximate TRILEX by GW, which is faster to compute (there is no quantum impurity model to solve). We look for a (t',t'') point for which not only $T_{AF} > T_c$, but also the shape of the Fermi surface is qualitatively compatible with cuprates. We find a whole region of parameters where this is satisfied, and then use these parameters in a strong-coupling computation with GW+EDMFT and TRILEX. Whether a weak-coupling computation is a reliable guide in the search for t',t'' with maximal T_c at strong coupling remains open and would require a systematic exploration with cluster methods. However, at least in one example (shown below), this assumption will provide us with an appropriate choice of hopping amplitudes that allows us to stabilize a superconducting solution in the doped Mott insulator regime.

Figure 5 presents the computation of the AF instability (T_{AF}) and the SC instability (T_c) in GW, for $U/D = 1$ and various t',t'' ($t = -1.0$ is held fixed) and various dopings. The temperature is taken from 0.2 down to the lowest accessible temperature, but not below 0.01 in cases where the extrapolation of $\lambda(T)$ yielded no finite T_c. The temperature step depends on T (smaller step at lower T; see Appendix C for an example of raw data).

The first observation is that the region of high T_c broadly coincides with the region of high T_{AF}. This is expected as in GW the attractive interaction comes from the spin boson, and a high-valued and sharply peaked W^{sp} is clearly necessary for satisfying the gap equation (54) with $\lambda = 1$. However, the maximum of T_c with respect to (t',t'') at a fixed n does not coincide with the maximum of T_{AF}, thus indicating that there are factors other than sharpness (criticality) of the spin boson which contribute to the height of T_c. While the maximum of T_{AF} is found rather close to $t' = t'' = 0$ at all dopings, the maximum in T_c starts from $(t',t'') = (-0.6, -0.4)$ at $n = 0.38$ and gradually moves as n is increased. It is only at half-filling that the two maxima are found to coincide. Furthermore, while at around $t' = t'' = 0$ and $t' \approx t''$ one sees $T_{AF} > T_c$, this trend is gradually reversed as t'' is made more and more negative, such that around $t' \approx t'' + 0.4$ one usually sees a finite T_c in the absence of a finite T_{AF}.

In Fig. 6, we plot T_{AF} and T_c vs doping for different values of t',t''. The corresponding dispersion (color map) and Fermi surfaces (gray contours; red for the maximal T_c) are presented in the insets.

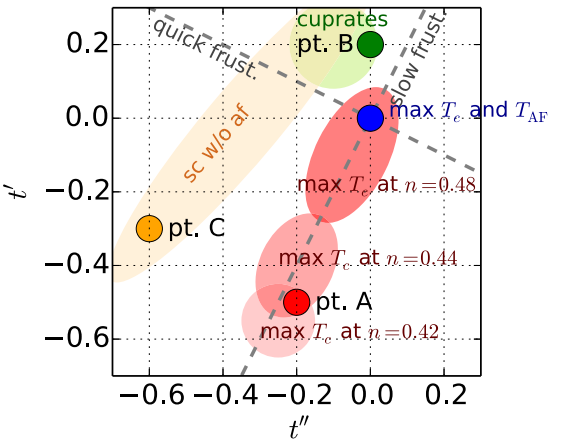

FIG. 7. Sketch of the GW phase diagram at $U/D = 1$, $t = -1.0$ based on Fig. 5. Points A, B, and C are of special interest, and are further studied at strong coupling.

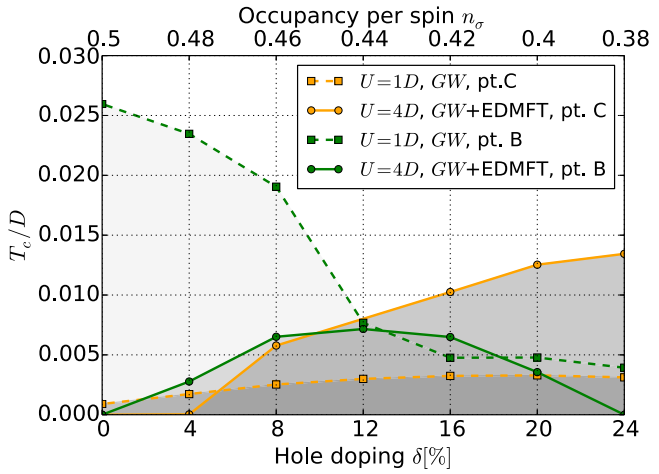

FIG. 8. T_c for dispersions B and C at weak and strong couplings.

Finally, in Fig. 7, we summarize the observations from Fig. 5. The blue dot denotes the global maximum of T_c and T_{AF}. The dashed gray lines denote the directions of the slowest and quickest decay of antiferromagnetism. The red ellipses denote the regions of maximal T_c, at various dopings. The yellow region is where one finds little antiferromagnetism, but still a sizable T_c. The green region corresponds to dispersions relevant for cuprates [82]. The points A, B, and C are the dispersions that we focus on and for which we perform TRILEX and GW+EDMFT computations. Point B is most relevant for the cuprates, and was analyzed in Fig. 3. Point C has $T_{\mathrm{AF}} < T_c$ which allows us to converge a superconducting solution at both weak and strong coupling. We analyze it in the next subsection. Point A is where we observe a maximal T_c at 16% doping, and we focus on it in Sec. IV D.

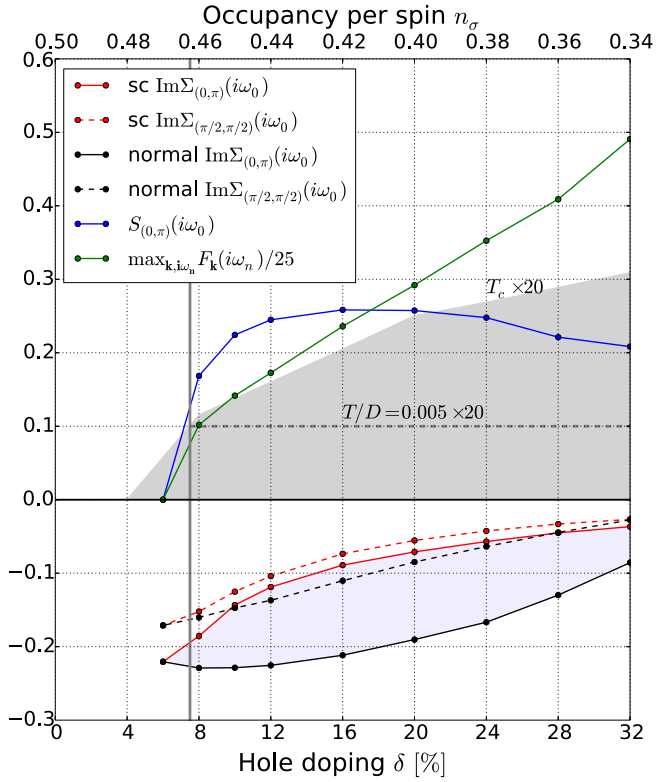

FIG. 9. Evolution of various quantities within the superconducting dome at dispersion point C, using GW+EDMFT, $U/D=4$, $T=0.005D$. The T_c, as obtained from $\lambda_m(T)$, is denoted by the gray area. Quantities are scaled to fit the same plot. The gray dashed horizontal line denotes the temperature at which the data are taken, relative to the (scaled) T_c. The vertical full line denotes the end of the superconducting dome at the temperature denoted by the dashed horizontal line, i.e., denotes the doping where all the anomalous quantities are expected to go to zero.

C. Nature of the superconducting phase at strong coupling

In this section, we study the dispersion C $(t,t',t'')=(-1,-0.3,-0.6)$. In Fig. 6, we have determined that *at weak coupling* $(U/D=1)$, the superconducting temperature T_c is larger than the AF temperature: we can therefore reach the

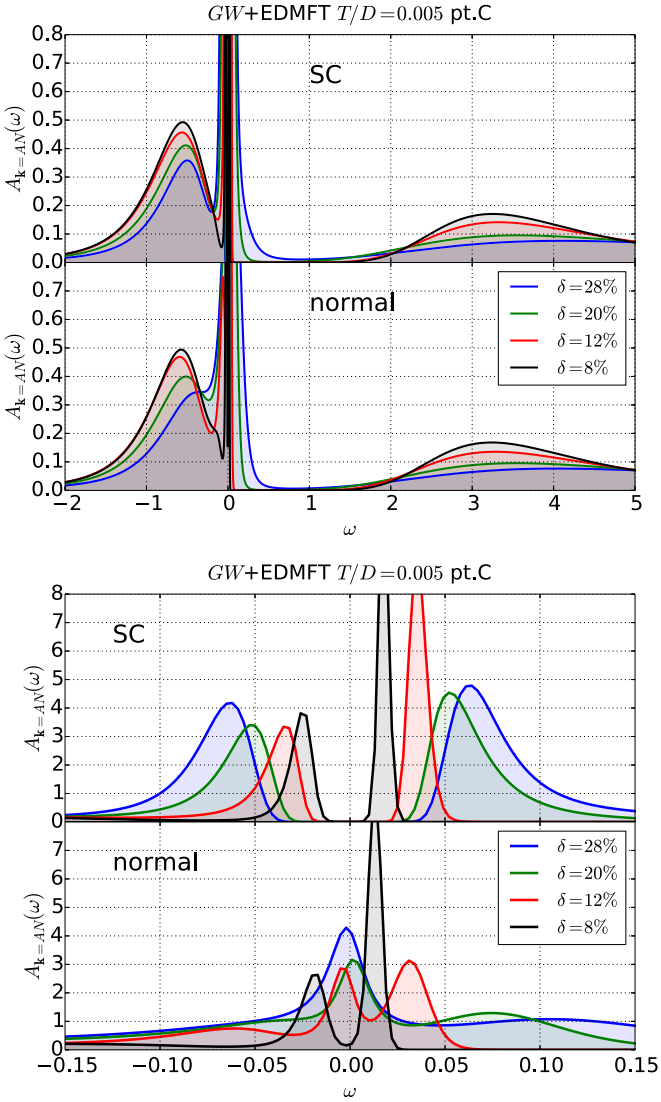

FIG. 10. Top panel: spectral function versus frequency, at the antinodal wave vector, defined by $n_{\mathbf{k}_{\mathrm{AN}}=[\pi,k_x(\mathrm{AN})]}=0.5$, obtained by maximum entropy method [83] from $G_{\mathbf{k}}(i\omega_n)$. $U/D=4$, $T/D=0.005$ for doping $\delta=8\%$, 12%, 20%, 28%. Bottom panel: zoom-in at low frequencies.

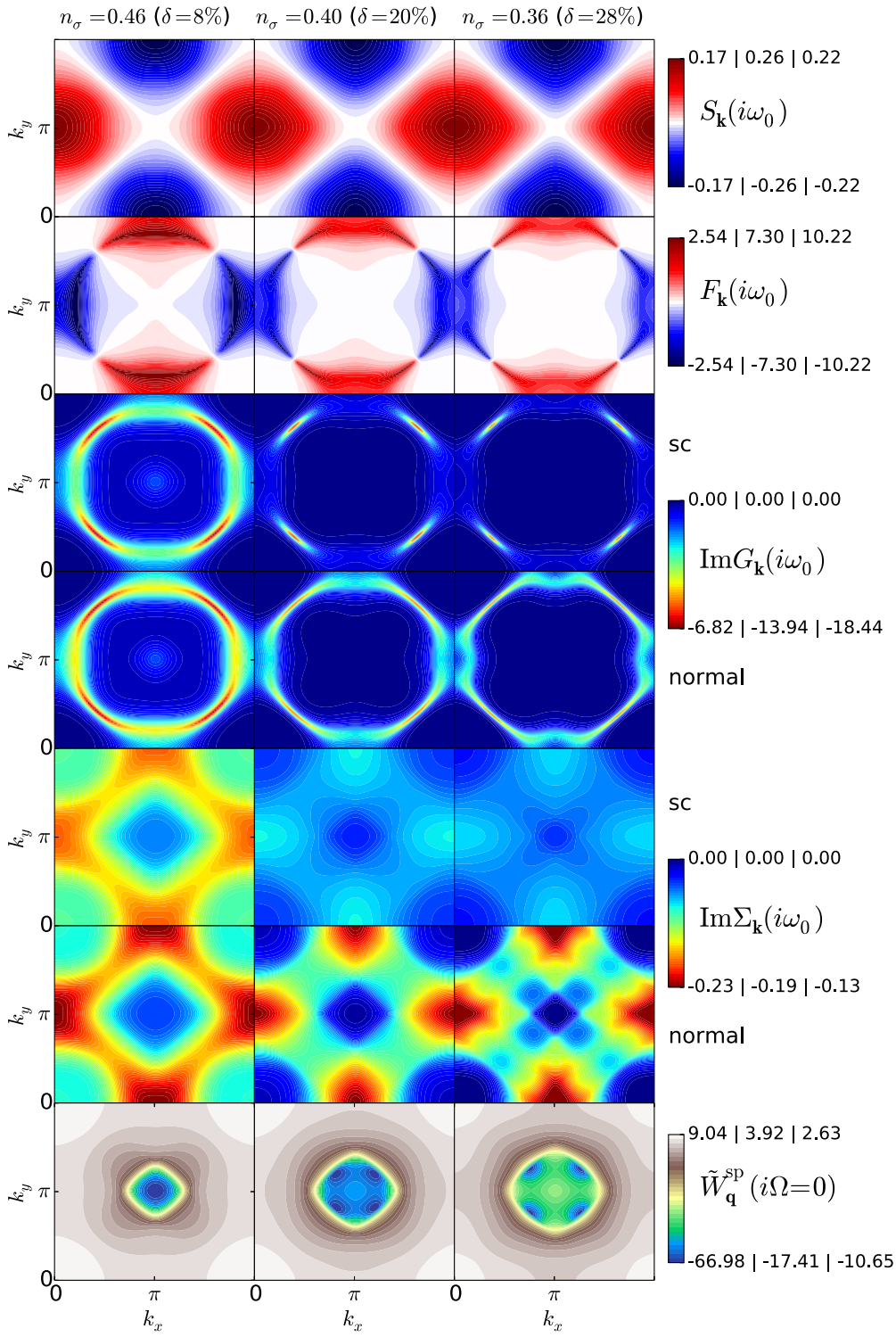

FIG. 11. Color plots of various quantities in the first Brillouin zone, at lowest Matsubara frequency. GW+EDMFT calculation at point C dispersion, $U/D = 4$. Temperature is below T_c, $T/D = 0.005$. All plots correspond to the superconducting phase unless stated differently. The three numbers defining the color-bar range correspond to three columns (different dopings) in the figure.

superconducting phase numerically (see Appendix D). It turns out that at strong coupling, the AF instability is also absent. This allows us to stabilize superconducting solutions in the doped Mott insulator regime. We also perform a calculation restricted to the normal phase for all parameters in order to compare results to the ones in the SC phase. For simplicity, in this section we will present only GW+EDMFT results for $U/D = 4$.

In Fig. 8, we show the superconducting temperatures at $U/D = 1$ and 4. Contrary to point B, in point C strong coupling seems to strongly enhance superconductivity. Also, the SC dome extends to higher dopings.

In Fig. 9, we show the results for the both the anomalous self-energy and Green's function, as well as the imaginary part of the normal self-energy, in both the normal phase and superconducting solution, antinodal and nodal regions.

The imaginary part of the normal self-energy is larger at antinodes than at nodes and is growing when approaching the Mott insulator. When going from the normal phase to the SC phase, the imaginary part of the self-energy is strongly reduced at the antinode and weakly reduced at the node. The difference between the normal and SC solutions (light blue area) is roughly proportional to the anomalous self-energy in the SC phase (blue line). Note that we observe a similar phenomenon even at weak coupling (see Appendix D).

In Fig. 10, we plot the spectral function at the antinodes at low temperature, in the normal and in the superconducting phases. At low doping, we observe at low energy a pseudogap in the normal phase and the superconducting gap in the SC phase. The result obtained here is qualitatively different to the one obtained using eight-site DCA cluster by Gull *et al.* [18,81]. In the cluster computations, the superconducting gap is smaller than the pseudogap, i.e., the quasiparticle peak at the edge of the SC gap appears within the pseudogap. It is not the case here. Also, we do not see any "peak-dip-hump" structure. Note that we are, however, using different parameters (for the hoppings t',t'', the interaction U and the doping δ). It is not clear at this stage whether these qualitative differences are due to this different parameter regime or to an artifact of the single-site TRILEX method, e.g., the lack of local singlet physics in a single-site impurity model. Further investigations with cluster-TRILEX methods are necessary in the SC phase.

In Fig. 11, we plot various quantities at the lowest Matsubara frequency, as a function of $\mathbf{k}$. In the first two rows we compare the anomalous self-energy and the pairing amplitude. Both are clearly of d-wave symmetry. The pairing amplitude has a different order of magnitude (see Appendix A 6 for an illustration of the dependence between F, G, Σ, and S). In the third and fourth rows, we show the imaginary part of the Green's function in the SC and normal phases. Due to the absence of long-lived quasiparticles in this sector, the maximum of $F_{\mathbf{k}}$ is moved towards the nodes, and does not coincide with the maximum of $S_{\mathbf{k}}$. At small doping, the Fermi surface in both cases becomes less sharp and more featureless, due to proximity to the Mott insulator. In the next two rows we show the imaginary part of the normal self-energy. In the superconducting phase, $\mathrm{Im}\Sigma_{\mathbf{k}}$ is strongly reduced in only antinodal regions, and thus flattened (made more local). In the last row, we show the nonlocal part of the propagator for the spin boson. At large doping, we observe a splitting of resonance at (π,π) which corresponds to incommensurate AF correlations (see, e.g., Ref. [84] for a similar phenomenon). Having that the Green's function at around $\mathbf{k} = (0,0)$ is quite featureless, and that the boson is sharply peaked at zero frequency, the shape of the spin boson around $\mathbf{q} = (\pi,\pi)$ is similar to the self-energy at around $\mathbf{k} = (\pi,\pi)$. This pattern is observed at all three dopings.

D. Strong coupling T_c at point A

At weak coupling, we have observed in Sec. IV B that the dispersion point A $[(t,t',t'') = (-1, -0.5, -0.2)]$ presents

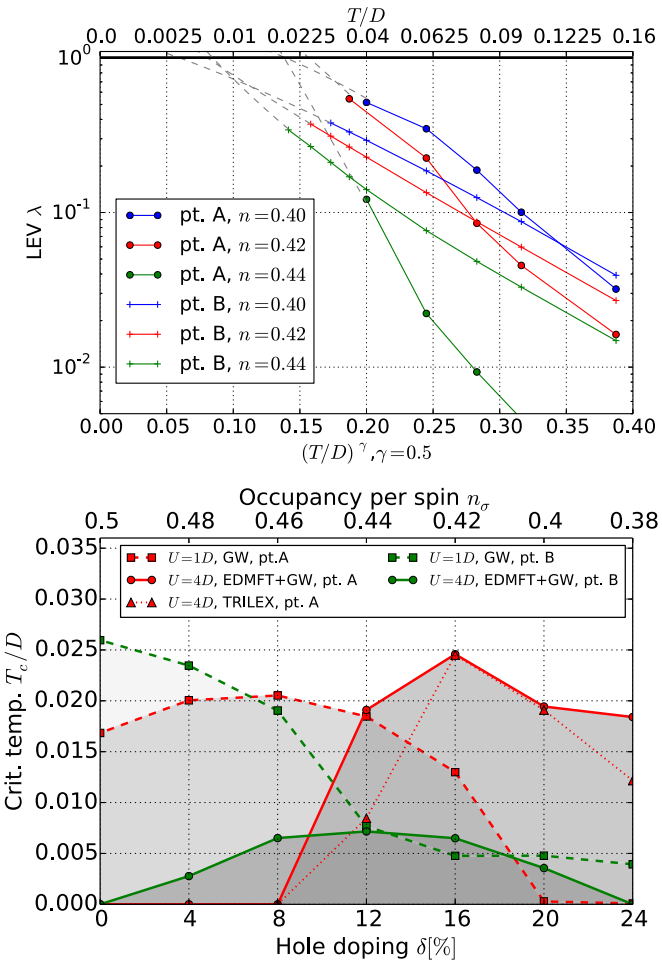

FIG. 12. Top panel: evolution of the LGE leading eigenvalue λ_m with temperature at points A and B, in a GW+EDMFT calculation. Bottom panel: the extrapolated T_c in both cases, including a TRILEX calculation at point A.

a pronounced maximum in $T_c(t',t'')$ at 16% doping (see Fig. 5). Here, we investigate that point at strong coupling using GW+EDMFT and TRILEX and find that also at $U/D = 4$, the T_c is substantially higher than in points B and C (see Fig. 12). Here, T_c is below T_{AF} and the result is again based on extrapolation of λ. The proposed fitting function in this case does not perform as well and the extrapolation is less reliable, but GW+EDMFT and TRILEX are in better agreement than in the case of point B. A further investigation using cluster methods is necessary since, apart from Refs. [76,80,85], little systematic exploration of $T_c(t',t'')$ has been performed.

V. CONCLUSION

In this work, we have generalized the TRILEX equations and their simplifications GW+EDMFT and GW to the case of paramagnetic superconducting phases, using the Nambu formalism. We also generalized the corresponding Hedin equations. We have then investigated within TRILEX, GW+EDMFT, and GW the doping-temperature phase diagram of the two-dimensional single-band Hubbard model with various choices of hopping parameters. In the case

of a bare dispersion relevant for cuprates, in the doped Mott insulator regime, both TRILEX and GW+EDMFT yield a superconducting dome of $d_{x^2-y^2}$-wave symmetry, in qualitative agreement with earlier cluster DMFT calculations. Let us emphasize that this was obtained at the low cost of solving a *single-site* impurity model. At weak coupling, we have performed a systematic scan of tight-binding parameter space within the GW approximation. We have identified the region of parameter space where superconductivity emerges at temperatures higher than antiferromagnetism. With one of those dispersions, we studied the properties of the superconducting phase at strong coupling with GW+EDMFT. We also addressed the question of the optimal dispersion for superconductivity in the Hubbard model at weak coupling. At 16% doping, we identify a candidate dispersion for the highest d wave T_c, which remains to be investigated in detail at strong coupling (e.g., with cluster DMFT methods).

The next step will be to solve in the SC phase the recently developed cluster TRILEX methods [66]. Indeed, the single-site TRILEX method contains essentially an Eliashberg-type equation with a decoupling boson, and a local vertex (computed from the self-consistent impurity model) which has no anomalous components. The importance of anomalous vertex components and the effect of local singlet physics (present in cluster methods) is an important open question. Note that the framework developed in this paper can also be used to study more general pairings and decoupling schemes in TRILEX, e.g., the effect of bosonic fluctuations in the particle-particle (i.e., superconducting) channel.

Finally, let us emphasize that the question of superconductivity in multiorbital systems like iron-based superconductors is another natural application of the TRILEX method, in particular in view of the strong AF fluctuations in these compounds. In this multiorbital case, being able to describe the SC phase without having to solve clusters (which are numerically very expensive within multiorbital cluster DMFT [86,87]) could prove to be very valuable.

ACKNOWLEDGMENTS

We thank M. Kitatani for useful insights and discussion. This work is supported by the FP7/ERC, under Grant Agreement No. 278472-MottMetals. Part of this work was performed using HPC resources from GENCI-TGCC (Grant No. 2016-t2016056112). The CT-HYB algorithm has been implemented using the TRIQS toolbox [88].

APPENDIX A: DETAILS OF DERIVATIONS

1. Relation between χ^3 and $\tilde{\chi}^3$

Let us define the following correlation functions:

$$\chi^3_{uv\alpha} \equiv \langle \Psi_u \Psi_v \phi_\alpha \rangle, \tag{A1a}$$

$$\chi^{3,\mathrm{disc}}_{uv\alpha}(\tau) \equiv \langle \Psi_u \Psi_v \rangle \langle \phi_\alpha \rangle, \tag{A1b}$$

$$\tilde{\chi}^3_{uv\alpha} \equiv \langle \Psi_u \Psi_v (\Psi_x \boldsymbol{\lambda}_{xw\alpha} \Psi_w) \rangle, \tag{A1c}$$

$$\tilde{\chi}^{3,\mathrm{disc}}_{uv\alpha}(\tau) \equiv \langle \Psi_u \Psi_v \rangle \langle \Psi_x \boldsymbol{\lambda}_{xw\alpha} \Psi_w \rangle, \tag{A1d}$$

$$\tilde{\chi}^{3,\mathrm{conn}}_{uv\alpha} \equiv \tilde{\chi}^3_{uv\alpha} - \tilde{\chi}^{3,\mathrm{disc}}_{uv\alpha}. \tag{A1e}$$

In this section, we derive useful relations between these quantities.

Let us introduce source fields in the electron-boson action [Eq. (6)]:

$$S^{\mathrm{Nambu}}_{\mathrm{eb}}[\Psi,\phi] = -\tfrac{1}{2}\Psi_u \left[\boldsymbol{G}_0^{-1} - \boldsymbol{F}\right]_{uv} \Psi_v - \tfrac{1}{2}\phi_\alpha \left[W_0^{-1}\right]_{\alpha\beta}\phi_\beta + \tfrac{1}{2}\phi_\alpha \Psi_u \boldsymbol{\lambda}_{uv\alpha} \Psi_v - H_\alpha \phi_\alpha. \tag{A2}$$

We may now write

$$\boldsymbol{\chi}^3_{uv\alpha} = -\frac{2}{Z}\frac{\partial^2 Z}{\partial \boldsymbol{F}_{uv}\partial H_\alpha}\bigg|_{\boldsymbol{F},H=0}, \tag{A3}$$

$$\boldsymbol{\chi}^{3,\mathrm{disc}}_{uv\alpha} = -\frac{2}{Z^2}\frac{\partial Z}{\partial \boldsymbol{F}_{uv}}\bigg|_{\boldsymbol{F},H=0}\frac{\partial Z}{\partial H_\alpha}\bigg|_{\boldsymbol{F},H=0}. \tag{A4}$$

Let us now integrate out the bosonic degrees of freedom in Eq. (A2). We obtain

$$Z = \int \mathcal{D}[\Psi] e^{-S^{\mathrm{Nambu}}_{\mathrm{ee}}[\Psi]} \tag{A5}$$

with

$$S^{\mathrm{Nambu}}_{\mathrm{ee}}[\Psi] = \frac{1}{2}\Psi_u[-\boldsymbol{G}_0^{-1} + \boldsymbol{F}]_{uv}\Psi_v + \frac{1}{2}W_{0,\alpha\beta} \times \left(H_\alpha - \frac{\Psi_u \boldsymbol{\lambda}_{uv\alpha}\Psi_v}{2}\right)\left(H_\beta - \frac{\Psi_x \boldsymbol{\lambda}_{xw\beta}\Psi_w}{2}\right). \tag{A6}$$

We now perform the derivatives of Eqs. (A3) and (A4) using the new expression (A5), yielding

$$\boldsymbol{\chi}^3_{uv\alpha} = -2\left\langle \frac{1}{2}\Psi_u\Psi_v \frac{1}{2}W_{0\alpha\beta}(-2)\frac{\Psi_x \boldsymbol{\lambda}_{xw\beta}\Psi_w}{2}\right\rangle, \tag{A7}$$

$$\boldsymbol{\chi}^{3,\mathrm{disc}}_{uv\alpha} = -2\left\langle \frac{1}{2}\Psi_u\Psi_v\right\rangle\left\langle \frac{1}{2}W_{0,\alpha\beta}(-2)\frac{\Psi_x \boldsymbol{\lambda}_{xw\beta}\Psi_w}{2}\right\rangle. \tag{A8}$$

Thus, we have, for the full correlator, as well as for the connected and disconnected parts,

$$\boldsymbol{\chi}^3_{uv\alpha} = \tfrac{1}{2}W_{0,\alpha\beta}\tilde{\boldsymbol{\chi}}^3_{uv\beta}. \tag{A9}$$

2. Derivation of Hedin equations from equations of motion

In this section, we derive the Hedin equations of the main text using the Dyson-Schwinger equation-of-motion technique [69] already used in Ref. [63].

a. Equation of motion for the self-energy

Since the functional integral of a total derivative vanishes

$$\int \mathcal{D}[\Psi]\frac{\partial(f[\Psi]g[\Psi])}{\partial \Psi_x} = 0 \tag{A10}$$

for any f and g, we have

$$-(-)^{\deg f}\int \mathcal{D}[\Psi] f[\Psi]\frac{\partial g[\Psi]}{\partial \Psi_x} = \int \mathcal{D}[\Psi]\left(\frac{\partial f[\Psi]}{\partial \Psi_x}\right) g[\Psi], \tag{A11}$$

which comes directly from the Leibniz derivation rule for Grassmann variables. deg f denotes the degree of the polynomial f in the variable Ψ. Let us now assume $f[\Psi] = e^{-S_0[\Psi]} = e^{\frac{1}{2}\Psi_u \boldsymbol{G}^{-1}_{0,uv}\Psi_v}$ and $g[\Psi] = h[\Psi]e^{-V[\Psi]}$, with h containing an odd

number of Grassmann fields. f has an infinite number of terms, but all are products of an even number of $\mathbf{\Psi}$ fields. We obtain

$$-\int \mathcal{D}\left\{\frac{\partial h}{\partial \mathbf{\Psi}_x} - h\left(-\frac{\partial V}{\partial \mathbf{\Psi}_x}\right)\right\} e^{-(S_0+V)} = \left[\boldsymbol{G}_0^{-1}\right]_{xw} \int \mathcal{D}[\mathbf{\Psi}]\mathbf{\Psi}_w h e^{-(S_0+V)}.$$

On the left-hand side we have again used the Leibniz rule with $\deg h$ assumed to be odd, hence, the extra minus sign. On the right-hand side similarly, $\deg \mathbf{\Psi} = 1$, and $\boldsymbol{G}^{-1}_{0,uv} = -\boldsymbol{G}^{-1}_{0,vu}$, so the $\frac{1}{2}$ prefactor is canceled. Both integrals are now averages with respect to the action $S = S_0 + V$, namely,

$$\left\langle \frac{\partial h}{\partial \mathbf{\Psi}_x} + h[\mathbf{\Psi}]\frac{\partial V}{\partial \mathbf{\Psi}_x}\right\rangle = -\left[\boldsymbol{G}_0^{-1}\right]_{xw}\langle \mathbf{\Psi}_w h[\mathbf{\Psi}]\rangle. \tag{A12}$$

Let us now consider the case when $h \equiv \mathbf{\Psi}_v$, and V is the interacting part of the electron-electron action (A6), with the source field H set to zero, i.e., $V \equiv \frac{1}{8}[W_0]_{\alpha\beta}(\mathbf{\Psi}_u \boldsymbol{\lambda}_{uw\alpha}\mathbf{\Psi}_w)(\mathbf{\Psi}_y \boldsymbol{\lambda}_{yz\beta}\mathbf{\Psi}_z)$. We get

$$\delta_{xv} + \tfrac{1}{8}[W_0]_{\alpha\beta}\boldsymbol{\lambda}_{xw\alpha}\cdot 4\langle \mathbf{\Psi}_v\mathbf{\Psi}_w(\mathbf{\Psi}_y\boldsymbol{\lambda}_{yz\beta}\mathbf{\Psi}_z)\rangle \tag{A13}$$

$$= -\left[\boldsymbol{G}_0^{-1}\right]_{xw}\langle \mathbf{\Psi}_w\mathbf{\Psi}_v\rangle. \tag{A14}$$

Multiplying both sides by $\boldsymbol{G}_0$ and using Eqs. (A1a) and (A9),

$$\begin{aligned}\boldsymbol{G}_{uv} &= \boldsymbol{G}_{0,uv} - \tfrac{1}{2}\boldsymbol{G}_{0,ux}W_{0,\alpha\beta}\boldsymbol{\lambda}_{xw\alpha}\tilde{\boldsymbol{\chi}}^3_{wv\beta}\\ &= \boldsymbol{G}_{0,uv} - \boldsymbol{G}_{0,ux}\boldsymbol{\lambda}_{xw\alpha}\boldsymbol{\chi}^3_{wv\alpha}\\ &= \boldsymbol{G}_{0,uv} - \boldsymbol{G}_{0,ux}\boldsymbol{\lambda}_{xw\alpha}\left(\boldsymbol{\chi}^{3,\mathrm{conn}}_{wv\alpha} + \tfrac{1}{2}W_{0,\alpha\beta}\tilde{\boldsymbol{\chi}}^{3,\mathrm{disc}}_{wv\alpha}\right)\\ &= \boldsymbol{G}_{0,uv} - \boldsymbol{G}_{0,ux}\boldsymbol{\lambda}_{xw\alpha}\boldsymbol{G}_{wy}W_{\alpha\beta}\boldsymbol{\Lambda}_{yz\beta}\boldsymbol{G}_{zv}\\ &\quad - \boldsymbol{G}_{0,ux}\boldsymbol{\lambda}_{xw\alpha}\tfrac{1}{2}W_{0,\alpha\beta}\langle \mathbf{\Psi}_y\boldsymbol{\lambda}_{yz\beta}\mathbf{\Psi}_z\rangle(-\boldsymbol{G}_{wv}).\end{aligned} \tag{A15}$$

Since the self-energy is defined as

$$\boldsymbol{G}_{uv} = \boldsymbol{G}_{0,uv} + \boldsymbol{G}_{0,ux}\boldsymbol{\Sigma}_{xw}\boldsymbol{G}_{wv}, \tag{A16}$$

we obtain

$$\boldsymbol{\Sigma}_{uv} = -\boldsymbol{\lambda}_{uw\alpha}\boldsymbol{G}_{wx}W_{\alpha\beta}\boldsymbol{\Lambda}_{xv\beta} + \boldsymbol{\lambda}_{uv\alpha}\tfrac{1}{2}W_{0,\alpha\beta}\langle \mathbf{\Psi}_y\boldsymbol{\lambda}_{yz\beta}\mathbf{\Psi}_z\rangle. \tag{A17}$$

The second term is the Hartree term (note the $\frac{1}{2}$ factor). The Fock term is included in the first term.

b. Equation of motion for the polarization

Real fields ϕ commute with the derivative, so the Leibniz rule is simpler. Analogously to Eq. (A11),

$$-\int \mathcal{D}[\phi,\mathbf{\Psi}]f[\phi,\mathbf{\Psi}]\frac{\partial g[\phi,\mathbf{\Psi}]}{\partial \phi_\gamma} = \int \mathcal{D}[\phi,\mathbf{\Psi}]\left(\frac{\partial f[\phi,\mathbf{\Psi}]}{\partial \phi_\gamma}\right) g[\phi,\mathbf{\Psi}]. \tag{A18}$$

Similarly to Eq. (A12), by taking $f[\phi,\mathbf{\Psi}] = e^{-S_0[\mathbf{\Psi},\phi]}$, where S_0 is the noninteracting part of the electron-boson action (4), and $V[\mathbf{\Psi},\phi] = \frac{1}{2}\mathbf{\Psi}_u\boldsymbol{\lambda}_{uv\delta}\mathbf{\Psi}_v\phi_\delta$, one has

$$\left\langle \frac{\partial h}{\partial \phi_\gamma} - \frac{1}{2}\mathbf{\Psi}_u\boldsymbol{\lambda}_{uv\gamma}\mathbf{\Psi}_v h[\phi]\right\rangle = -\left[W_0^{-1}\right]_{\gamma\beta}\langle \phi_\beta h[\phi]\rangle. \tag{A19}$$

Again, note the minus sign in the left-hand side [to be compared with Eq. (A12)] coming from the bosonic nature of the field ϕ. For $h \equiv \phi_\alpha - \langle\phi_\alpha\rangle$,

$$\begin{aligned}\delta_{\gamma\alpha} - \tfrac{1}{2}\boldsymbol{\lambda}_{uv\gamma}\langle \mathbf{\Psi}_u\mathbf{\Psi}_v(\phi_\alpha - \langle\phi_\alpha\rangle)\rangle\\ = -\left[W_0^{-1}\right]_{\gamma\beta}\langle(\phi_\beta - \langle\phi_\beta\rangle)(\phi_\alpha - \langle\phi_\alpha\rangle)\rangle.\end{aligned}$$

Multiplying by W_0 and using Eqs. (10) and (11), we obtain

$$\begin{aligned}W_{\delta\alpha} &= W_{0,\delta\alpha} + W_{0,\delta\gamma}\tfrac{1}{2}\boldsymbol{\lambda}_{uv\gamma}\boldsymbol{\chi}^{3,\mathrm{conn}}_{vu\alpha}\\ &= W_{0,\delta\alpha} + W_{0,\delta\gamma}\tfrac{1}{2}\boldsymbol{\lambda}_{uv\gamma}\boldsymbol{G}_{vx}\boldsymbol{G}_{wu}\boldsymbol{\Lambda}_{xw,\beta}W_{\beta\alpha}.\end{aligned}$$

With the definition of P as

$$W_{\delta\alpha} = W_{0,\delta\alpha} + W_{0,\delta\gamma}P_{\gamma\beta}W_{\beta\alpha}, \tag{A20}$$

we identify

$$P_{\gamma\beta} = \tfrac{1}{2}\boldsymbol{\lambda}_{uv\gamma}\boldsymbol{G}_{vx}\boldsymbol{G}_{wu}\boldsymbol{\Lambda}_{xw\beta}. \tag{A21}$$

Note the extra prefactor $\frac{1}{2}$ compared to the normal-case expression.

3. Proof that P is real

In the derivation of Eq. (48c) we have used the symmetries of G, F, and Λ. It turns out that the imaginary part of Λ does not play a role in the summation and that the polarization is strictly real.

The renormalized vertex has the following symmetries [63]:

$$\Lambda(i\omega, -i\Omega) = \Lambda(i\omega - i\Omega, i\Omega), \tag{A22a}$$

$$\Lambda^*(i\omega, -i\Omega) = \Lambda(-i\omega, i\Omega). \tag{A22b}$$

Under the present assumptions, all components of the Green's function (G and F) have the property

$$X_{\mathbf{k}}(-i\omega) = X^*_{\mathbf{k}}(i\omega),$$
$$X_{\mathbf{k}}(i\omega) = X_{-\mathbf{k}}(i\omega).$$

Therefore,

$$\begin{aligned}&\sum_{\mathbf{k},i\omega} X_{\mathbf{k}}(i\omega)X_{\mathbf{k}+\mathbf{q}}(i\omega + i\Omega)\Lambda(i\omega, i\Omega)\\ &= \sum_{\mathbf{k},i\omega} X_{\mathbf{k}}(-i\omega)X_{\mathbf{k}+\mathbf{q}}(-i\omega + i\Omega)\Lambda(-i\omega, i\Omega)\\ &= \sum_{\mathbf{k},i\omega} X_{\mathbf{k}}(-i\omega)X_{\mathbf{k}+\mathbf{q}}(-i\omega + i\Omega)\Lambda^*(i\omega, -i\Omega)\\ &= \sum_{\mathbf{k},i\omega} X_{\mathbf{k}}(-i\omega)X_{\mathbf{k}+\mathbf{q}}(-i\omega + i\Omega)\Lambda^*(i\omega - i\Omega, i\Omega)\\ &= \sum_{\mathbf{k},i\omega'} X_{\mathbf{k}}(-i\omega' - i\Omega)X_{\mathbf{k}+\mathbf{q}}(-i\omega')\Lambda^*(i\omega', i\Omega)\\ &= \sum_{\mathbf{k},i\omega'} X^*_{\mathbf{k}}(i\omega' + i\Omega)X^*_{\mathbf{k}+\mathbf{q}}(i\omega')\Lambda^*(i\omega', i\Omega)\end{aligned} \tag{A23}$$

$$= \left[\sum_{\mathbf{k}',i\omega'} X_{-\mathbf{k}'-\mathbf{q}}(i\omega' + i\Omega)X_{-\mathbf{k}'}(i\omega')\Lambda(i\omega', i\Omega)\right]^*$$

$$= \left[\sum_{\mathbf{k}',i\omega'} X_{\mathbf{k}'+\mathbf{q}}(i\omega' + i\Omega)X_{\mathbf{k}'}(i\omega')\Lambda(i\omega', i\Omega)\right]^*, \tag{A24}$$

which proves that the polarization is real. In the derivation of the first term in Eq. (48c), we have used the equality between Eqs. (A23) and (A24). Then, for any real valued F, we furthermore have $F_{\mathbf{k}}(i\omega) = F_{\mathbf{k}}(-i\omega)$, which gives us

$$\sum_{\mathbf{k},i\omega} F_{\mathbf{k}}(i\omega)F_{\mathbf{k}+\mathbf{q}}(i\omega+i\Omega)\Lambda(i\omega,i\Omega) = \sum_{\mathbf{k},i\omega} F_{\mathbf{k}+\mathbf{q}}(i\omega+i\Omega)F_{\mathbf{k}}(i\omega)\Lambda^*(i\omega,i\Omega) = \sum_{\mathbf{k},i\omega} F_{\mathbf{k}+\mathbf{q}}(i\omega+i\Omega)F_{\mathbf{k}}(i\omega)\mathrm{Re}\Lambda(i\omega,i\Omega), \tag{A25}$$

which is what we use in the derivation of the second term in Eq. (48c).

4. Fourier transforms: Hedin equations with translational symmetry

Here, we derive Eq. (22). A completely analogous derivation can be used for Eqs. (21). For the sake of clarity, we omit the spatial indices, as the spatial Fourier transform (FT) is completely analogous to the temporal FT:

$$\begin{aligned}\boldsymbol{\Lambda}_{uv\alpha} &= [\boldsymbol{G}^{-1}]_{uw}[\boldsymbol{G}^{-1}]_{xv}[W^{-1}]_{\alpha\beta}\boldsymbol{\chi}^{3,\mathrm{conn}}_{wx\beta} = \sum_{\omega,\omega',\omega'',\Omega,\Omega'} e^{i\omega(\tau_u-\tau_w)}[\boldsymbol{G}^{-1}(i\omega)]_{a_ua_w} \\ &\quad\times e^{i\omega'(\tau_x-\tau_v)}[\boldsymbol{G}^{-1}(i\omega')]_{a_xa_v}e^{i\Omega(\tau_\alpha-\tau_\beta)}(W^{I_\alpha}(i\Omega))^{-1}e^{i\omega''(\tau_w-\tau_x)+i\Omega'(\tau_\beta-\tau_x)}\boldsymbol{\chi}^{3,\mathrm{conn},I_\alpha}_{a_wa_x}(i\omega'',i\Omega') \\ &= \sum_{\omega,\omega',\omega'',\Omega,\Omega'} e^{i\omega\tau_u-i\omega'\tau_v+i\Omega\tau_\alpha}e^{i\tau_x(\omega'-\omega''-\Omega')}e^{i\tau_w(\omega''-\omega)}e^{i\tau_\beta(\Omega'-\Omega)} \\ &\quad\times[\boldsymbol{G}^{-1}(i\omega)]_{a_ua_w}[\boldsymbol{G}^{-1}(i\omega')]_{a_xa_v}(W^{I_\alpha}(i\Omega))^{-1}\boldsymbol{\chi}^{3,\mathrm{conn},I_\alpha}_{a_wa_x}(i\omega'',i\Omega').\end{aligned} \tag{A26}$$

Applying the (implicit) integration over times produces Kronecker delta functions at $\omega'' = \omega$, $\omega' = \omega + \Omega$, and $\Omega = \Omega'$. Therefore,

$$\sum_{\omega\Omega} e^{i\omega(\tau_u-\tau_v)+i\Omega(\tau_\alpha-\tau_v)}\boldsymbol{\Lambda}^{I_\alpha}_{a_ua_v}(\omega,\Omega) = \sum_{\omega\Omega} e^{i\omega(\tau_u-\tau_v)+i\Omega(\tau_\alpha-\tau_v)}[\boldsymbol{G}^{-1}(i\omega'+\Omega)]_{a_ua_w}[\boldsymbol{G}^{-1}(i\omega')]_{a_xa_v}(W^{I_\alpha}(i\Omega))^{-1}\boldsymbol{\chi}^{3,\mathrm{conn},I_\alpha}_{a_wa_x}(i\omega,i\Omega). \tag{A27}$$

We now reinstate the momentum indices, and obtain Eq. (22) by identifying the summands on both sides of the equation:

$$\boldsymbol{\Lambda}^{I}_{\mathbf{kq},ab}(i\omega,i\Omega) = \left[\boldsymbol{G}^{-1}_{\mathbf{k}+\mathbf{q}}(i\omega+\Omega)\right]_{ac}\left[\boldsymbol{G}^{-1}_{\mathbf{k}}(i\omega)\right]_{db}\left(W^{I}_{\mathbf{q}}(i\Omega)\right)^{-1}\boldsymbol{\chi}^{3,\mathrm{conn},I}_{\mathbf{kq},cd}(i\omega,i\Omega). \tag{A28}$$

Here, summation over c,d is implicit.

5. $\boldsymbol{\Lambda}_{\mathrm{imp}}$ from $\boldsymbol{\Lambda}_{\mathrm{imp}}$

Here, we prove Eq. (40). In the Hubbard model we have

$$\sum_{yz}\boldsymbol{\Psi}_y\boldsymbol{\lambda}_{yz\beta}\boldsymbol{\Psi}_z = 2n^{I_\beta}_{i_\beta}(\tau_\beta). \tag{A29}$$

On the impurity (33), where we have no anomalous components,

$$\boldsymbol{\chi}^{3,I}_{\mathrm{imp}}(\tau,\tau') = \int_{\tau''}\mathcal{U}^I(\tau'-\tau'')\begin{bmatrix}\langle c^*_\downarrow(\tau)c_\downarrow(0)n^I(\tau'')\rangle & \langle c^*_\uparrow(\tau)c_\downarrow(0)n^I(\tau'')\rangle & \langle c^*_\uparrow(\tau)c_\uparrow(0)n^I(\tau'')\rangle \\ \langle c_\downarrow(\tau)c^*_\uparrow(0)n^I(\tau'')\rangle & \langle c_\downarrow(\tau)c^*_\downarrow(0)n^I(\tau'')\rangle & \langle c^*_\downarrow(\tau)c_\uparrow(0)n^I(\tau'')\rangle \\ \langle c_\uparrow(\tau)c^*_\uparrow(0)n^I(\tau'')\rangle & \langle c_\uparrow(\tau)c^*_\downarrow(0)n^I(\tau'')\rangle & \end{bmatrix}. \tag{A30}$$

The $\frac{1}{2}$ prefactor in (A9) cancels the prefactor 2 in (A29). If we define

$$\tilde{\chi}^{3,I=0,z}_{\mathrm{imp}}(\tau,\tau') \equiv \langle c_\uparrow(\tau)c^*_\uparrow(0)n^I(\tau')\rangle = \tfrac{1}{2}\tilde{\boldsymbol{\chi}}^{3,I}_{\mathrm{imp},30}(\tau,\tau'), \quad \tilde{\chi}^{3,I=x,y}_{\mathrm{imp}}(\tau,\tau') \equiv \langle c_\uparrow(\tau)c^*_\downarrow(0)n^I(\tau')\rangle = \tfrac{1}{2}\tilde{\boldsymbol{\chi}}^{3,I}_{\mathrm{imp},32}(\tau,\tau'),$$

we can rewrite

$$\boldsymbol{\chi}^{3,I=0,z}_{\mathrm{imp}}(i\omega,i\Omega) = \mathcal{U}^I(i\Omega)\begin{bmatrix} & & \left(-\tilde{\chi}^{3,I}_{\mathrm{imp}}\right)^* \\ & \pm\left(-\tilde{\chi}^{3,I}_{\mathrm{imp}}\right)^* & \pm\tilde{\chi}^{3,I}_{\mathrm{imp}} \\ \tilde{\chi}^{3,I}_{\mathrm{imp}} & & \end{bmatrix}(i\omega,i\Omega), \tag{A31a}$$

$$\boldsymbol{\chi}^{3,I=x,y}_{\rm imp}(i\omega,i\Omega) = (-i)^{\delta_{I,y}}\mathcal{U}^I(i\Omega)\begin{bmatrix} \pm\tilde{\chi}^{3,I}_{\rm imp} & & \pm\left(-\tilde{\chi}^{3,I}_{\rm imp}\right)^* & \\ & \left(-\tilde{\chi}^{3,I}_{\rm imp}\right)^* & & \tilde{\chi}^{3,I}_{\rm imp} \end{bmatrix}(i\omega,i\Omega). \tag{A31b}$$

More compactly,

$$\boldsymbol{\chi}^{3,I}_{\rm imp}(i\omega,i\Omega) = \mathcal{U}^I(i\Omega)(\boldsymbol{\lambda}^I)^{\mathsf{T}} \circ \begin{bmatrix} \tilde{\chi}^{3,I}_{\rm imp} & \left(\tilde{\chi}^{3,I}_{\rm imp}\right)^* & \tilde{\chi}^{3,I}_{\rm imp} & \left(\tilde{\chi}^{3,I}_{\rm imp}\right)^* \\ \tilde{\chi}^{3,I}_{\rm imp} & \left(\tilde{\chi}^{3,I}_{\rm imp}\right)^* & \tilde{\chi}^{3,I}_{\rm imp} & \left(\tilde{\chi}^{3,I}_{\rm imp}\right)^* \end{bmatrix}(i\omega,i\Omega), \tag{A32}$$

where $\boldsymbol{\lambda}^I$ and $\circ$ have been defined in main text. For $I = 0,z$, we have used

$$\begin{aligned}\int_{\tau,\tau',\tau''} e^{i\omega(\tau-\tau')+i\Omega(\tau''-\tau')}\langle c^*_\uparrow(\tau)c_\uparrow(\tau')n^I(\tau'')\rangle &= -\int_{\tau,\tau',\tau''} e^{i\omega(\tau-\tau')+i\Omega(\tau''-\tau')}\langle c_\uparrow(\tau')c^*_\uparrow(\tau)n^I(\tau'')\rangle \\ = -\int_{\tau,\tau',\tau''} e^{-i\omega(\tau'-\tau)+i\Omega(\tau''-\tau+\tau-\tau')}\langle c_\uparrow(\tau')c^*_\uparrow(\tau)n^I(\tau'')\rangle &= -\int_{\tau,\tau',\tau''} e^{-i(\omega+\Omega)(\tau'-\tau)+i\Omega(\tau''-\tau)}\langle c_\uparrow(\tau')c^*_\uparrow(\tau)n^I(\tau'')\rangle \\ = -\tilde{\chi}^{3,I}_{\rm imp}(-i\omega-i\Omega,i\Omega) = -\tilde{\chi}^{3,I}_{\rm imp}(-i\omega,-i\Omega) &= -(\tilde{\chi}^{3,I}_{\rm imp}(i\omega,i\Omega))^*\end{aligned} \tag{A33}$$

and

$$\langle c^*_\uparrow(\tau)c_\uparrow(0)[n_\uparrow(\tau')\pm n_\downarrow(\tau')]\rangle = \pm\langle c^*_\downarrow(\tau)c_\downarrow(0)[n_\uparrow(\tau')\pm n_\downarrow(\tau')]\rangle \tag{A34}$$

and similar considerations for $I = x,y$. Expressions completely analogous to (A31a) and (A31b) hold for the connected part of $\boldsymbol{\chi}^3$. Plugging these in Eq. (22) together with Eq. (A9),

$$\boldsymbol{G}^{-1}_{\rm imp}(i\omega) = \begin{bmatrix} & -\left(G^{-1}_{\rm imp}\right)^* & G^{-1}_{\rm imp} \\ G^{-1}_{\rm imp} & & \\ -\left(G^{-1}_{\rm imp}\right)^* & & \end{bmatrix}(i\omega) \tag{A35}$$

and

$$\langle c_\uparrow(\tau)c^*_\uparrow(0)[n_\uparrow(\tau')-n_\downarrow(\tau')]\rangle = \langle c_\uparrow(\tau)c^*_\downarrow(0)c^*_\uparrow(\tau')c_\downarrow(\tau')\rangle \tag{A36}$$

immediately yields Eq. (40). Equation (A36) holds in presence of SU(2) symmetry. It can be proven by applying a $\pi/2$ rotation around the y axis ($n^z \to -n^x, n^x \to n^z, n^y \to n^y$), i.e., $c_\sigma \to [\exp(-\frac{i}{2}\frac{\pi}{2}\sigma^y)]_{\sigma,\sigma'}c_{\sigma'} = \frac{1}{\sqrt{2}}(c_\sigma + (-)^{\delta_{\sigma,\uparrow}}c_{\bar\sigma})$:

$$\begin{aligned}&\langle c_\uparrow(\tau)c^*_\uparrow(0)[n_\uparrow(\tau')-n_\downarrow(\tau')]\rangle \\ &= \tfrac{1}{2}\langle[c_\uparrow(\tau)-c_\downarrow(\tau)][c^*_\uparrow(0)-c^*_\downarrow(0)] \\ &\quad\times[-c^*_\uparrow(\tau')c_\downarrow(\tau')-c^*_\downarrow(\tau')c_\uparrow(\tau')]\rangle \\ &= \tfrac{1}{2}[\langle[-c_\downarrow(\tau)c^*_\uparrow(0)][-c^*_\downarrow(\tau')c_\uparrow(\tau')]\rangle \\ &\quad+\langle[-c_\uparrow(\tau)c^*_\downarrow(0)][-c^*_\uparrow(\tau')c_\downarrow(\tau')]\rangle]\end{aligned} \tag{A37}$$

and then rotating the operators of the first term on the right-hand side by π around the y axis $\{c_\sigma \to [\exp(-\frac{i}{2}\pi\sigma^y)]_{\sigma,\sigma'}c_{\sigma'} = (-)^{\delta_{\uparrow,\sigma}}c_{\bar\sigma}\}$.

6. Relation between S, F, Σ, and G

Here, we emphasize that the order of magnitude of the anomalous self-energy S and that of the pairing amplitude F are not the same, as illustrated on Fig. 13. The pairing amplitude has a strongly nonmonotonous dependence on the anomalous self-energy. At a given normal self-energy, there is a "sweet spot" where a small anomalous self-energy

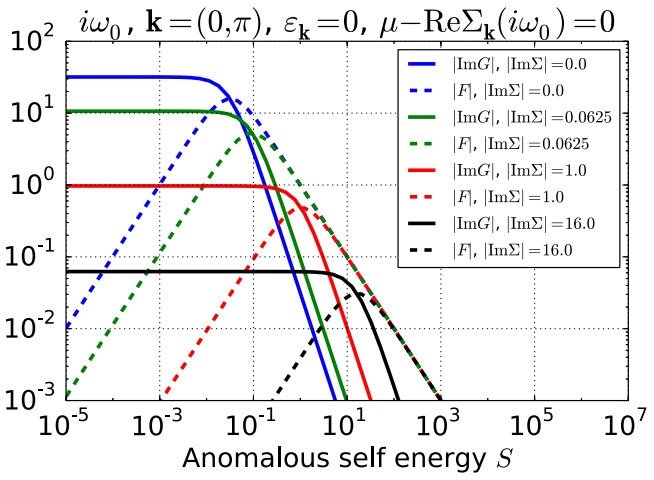

FIG. 13. The anomalous Green's function (or pairing amplitude F) and the normal Green's function G as functions of the anomalous self-energy S at various values of fixed normal self-energy Σ. All quantities are taken at the lowest Matsubara frequency $i\omega_0$, at the antinodal wave vector $\mathbf{k} = (0,\pi)$, assuming particle-hole symmetry [$\epsilon_{\mathbf{k}=(0,\pi)} = 0$ and $\mu - \mathrm{Re}\Sigma_{\mathbf{k}=(0,\pi)}(i\omega_n) = 0$]. The antinode in this case is precisely at the Fermi surface.

produces a very strong superconducting pairing. As soon as the anomalous self-energy starts gapping out the Green's function, this affects also the pairing amplitude as no pairing is possible in the absence of long-lived quasiparticles. In general, strong superconducting gap and normal self-energy diminish both the Green's function and the pairing amplitude.

APPENDIX B: NUMERICAL DETAILS

The numerical parameters in our calculations include the following:

(i) The number of **k** points in the first Brillouin zone, discretized as a grid $N_k \times N_k$; we take it to be temperature dependent, growing as temperature is lowered, to be able to capture increasingly sharp Fermi surface, and gain extra precision when the spin boson is nearly critical:

T	N_k
0.06+	32
0.03–0.06	48
0.005–0.03	64
0–0.005	96

(ii) The cutoff frequency $i\omega_{\max}$ for the Green's functions, and the frequency above which the data are replaced by the high-frequency tail fit $i\omega_{\text{fit}}$. Throughout the paper we use $i\omega_{\text{fit}} = 14.0$ and $i\omega_{\max} = 30$. The actual number of Matsubara frequencies taken is therefore temperature dependent.

(iii) The number of τ points is taken simply as the number of frequencies times 3.

(iv) The mixing ratio for the polarization between iterations; in GW we take $P^{\text{old}} : P^{\text{new}} = 0.95 : 0.05$. In GW+EDMFT and TRILEX, we use $P^{\text{old}} : P^{\text{new}} = 0.7 : 0.3$.

(v) Number of iterations performed and the level of convergence reached; in GW we start from the non-interacting solution, and perform up to 70 iterations. In the superconducting phase, we perform 150 iterations. In GW+EDMFT and TRILEX, we start from DMFT solution at the highest temperature, and then use the GW+EDMFT solution as the initial guess at lower temperature, and perform up to 30 iterations. In all cases, we reach convergence level $\max_{i\omega_n} |G^{\text{loc,new}}(i\omega_n) - G^{\text{loc,old}}(i\omega_n)| \lesssim 10^{-3}$.

(vi) The parameter γ used in the LEV extrapolation; in GW for Fig. 5 we use $\gamma = 0.5$.

APPENDIX C: EXTRAPOLATION OF THE LOWEST EIGENVALUE

Because of the AF instability in the methods used in this paper, there is a need for extrapolating the results for the leading eigenvalue [LEV, $\lambda(T)$] in the linearized gap equation (LGE) to lower temperatures. In Fig. 14 we show some examples of this procedure. The $\lambda(T)$ results are contrasted with $\max_{\mathbf{q},i\nu_m} U^{\text{sp}} P^{\text{sp}}_{\mathbf{q}}(i\nu_m)$ which is shown to approach 1 at finite temperature. Below this temperature, a stable calculation is not possible. For the precise definition of T_{AF} shown in figures in Secs. IV B and IV A, we follow Ref. [70], and identify it with the condition $\max_{\mathbf{q},i\nu_m} U^{\text{sp}} P^{\text{sp}}_{\mathbf{q}}(i\nu_m) = 0.99$ (this value is denoted with a horizontal black line in the bottom two panels of Fig. 14).

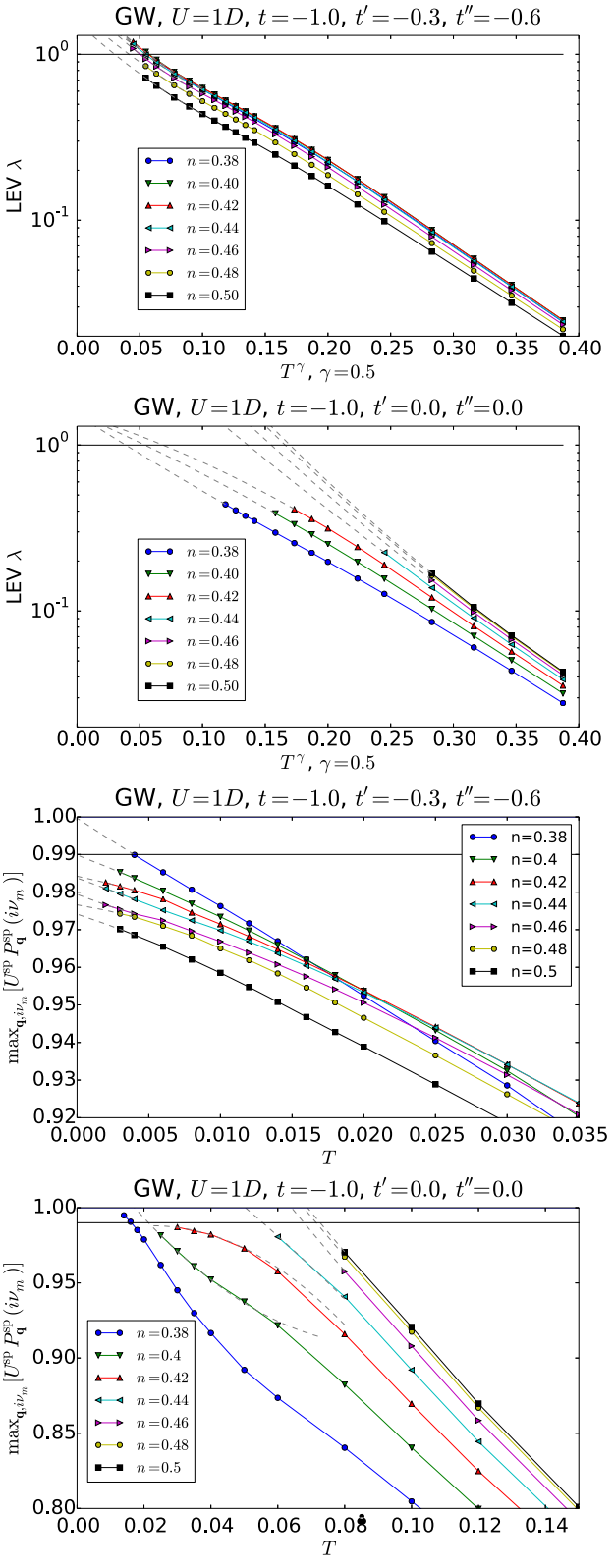

FIG. 14. Extrapolation of $\lambda(T)$ (see text).

The LEV $\lambda(T)$ is found to follow a simple law and we perform a parabola fit

$$\log \lambda(T) \approx a + bT^{\gamma} + cT^{2\gamma} \equiv f(T,\hat{\theta}), \qquad \text{(C1)}$$

with $\hat{\theta} = a,b,c$, to extrapolate it to lower temperatures.

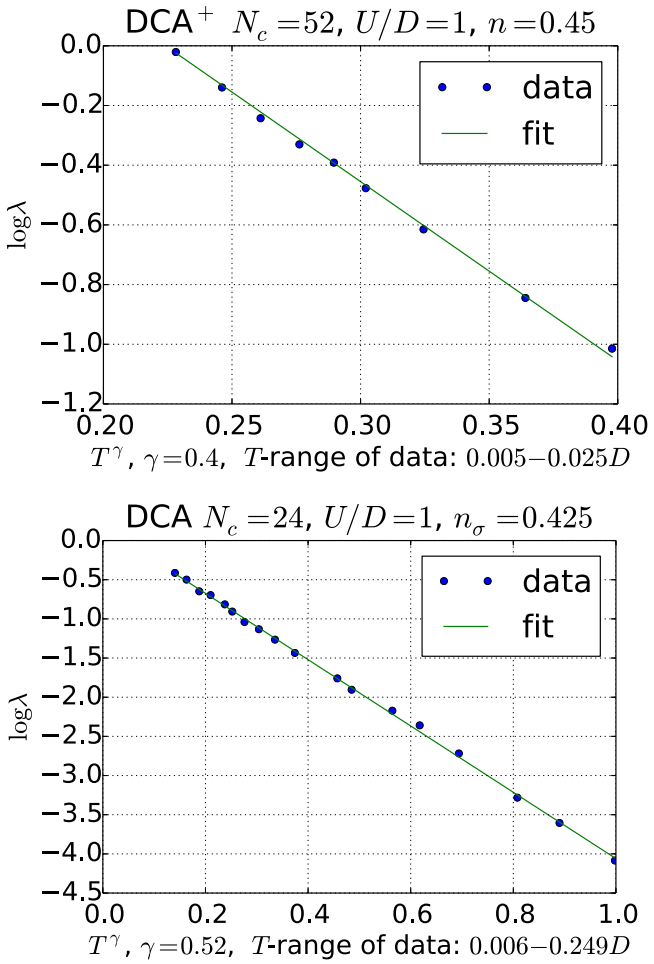

FIG. 15. In DCA and DCA$^+$, one observes a behavior very similar to what is seen in GW. Data are replotted from Refs. [22,77] and fitted to the phenomenological form (C1) with $c=0$. See text for a more detailed discussion.

Interestingly, a similar $\lambda(T)$ behavior is observed in DCA and DCA$^+$ calculations (see Fig. 15). The fact that the general temperature-dependent behavior of the LEV (as found in the LGE) is captured correctly with respect to DCA indicates that the leading contribution to $\Gamma^{pp}_{\sigma\bar{\sigma}}$, and therefore the superconducting glue, is indeed bosoniclike, dominated by the random-phase-approximation–like processes. Otherwise, one would expect a slower decay of $\lambda(T)$ with temperature in DCA than observed in GW, as here the decay is determined primarily by the gradual decondensation of the spin boson. This notion has been investigated thoroughly in Ref. [89] where the authors have found both the spin-spin correlation and the pp-irreducible vertex from a full DCA calculation to be in excellent agreement with simple random-phase-approximation estimates.

In the main text (Sec. III C), we have estimated the error bar on the extrapolation of the lowest eigenvalue by varying the parameter γ (see Fig. 3). Here, we give a method to determine the prediction interval for the extrapolation at fixed γ. We choose the parameters corresponding to point B (Fig. 7) to illustrate this method.

Following standard statistics (see, e.g., Ref. [90], Sec. 13.8.1), we proceed as follows:

(i) For a given doping n, we carry out a least-squares fit of the N data points (T_i,λ_i) to Eq. (C1): this yields optimal least-square parameters $\hat{\theta}=a^*,b^*,c^*$.

(ii) For a given temperature T_0 (not necessarily in the same range as the data points), the prediction interval at $100(1-\alpha)\%$ is given by the two extremal values

$$f_{\alpha,\pm}(T_0)=f(T_0,\hat{\theta})\pm\overline{\sigma}t_{\alpha/2,N-3}\sqrt{1+v_0^t[V^tV]^{-1}v_0},$$

where $\overline{\sigma}$ is the empirical variance

$$\overline{\sigma}=\frac{1}{N-3}\sum_{i=1}^{N}(\log\lambda_i-f(T_i,\hat{\theta}))^2,$$

$t_{\alpha,k}$ is defined as

$$\int_{t_{\alpha,N}}^{\infty}P_N(t)dt=\alpha,$$

where $P_N(t)$ is the probability density function of the Student distribution function. V is the $N\times 3$ matrix

$$V_{ij}=\left.\frac{\partial f}{\partial\theta_j}\right|_{T=T_i}$$

and v_0 the column vector:

$$v_{0j}=\left.\frac{\partial f}{\partial\theta_j}\right|_{T=T_0}.$$

The corresponding prediction intervals (at 68%) are shown in the upper panel of Fig. 16. They are used to compute the error bars shown in the lower panel of the same figure.

Especially in GW+EDMFT, the fit is found to be of high quality and as the extrapolation is not carried far away from the range of data points, the prediction intervals are found to be small. In TRILEX, the fit is of poorer quality and the prediction intervals are comparable to the uncertainty due to free parameter γ.

APPENDIX D: SUPERCONDUCTING PHASE AT WEAK COUPLING

Here, we compare the results of the below-T_c calculation: GW at weak coupling (Fig. 17) vs GW+EDMFT at strong coupling (Fig. 9), at the same dispersion, point C. We observe that in the weak-coupling case, the normal self-energy remains constant with doping, while at strong coupling it grows by a factor of about 5 in a similar range of doping, as Mott insulating phase at half-filling is approached. In the normal phase and at weak coupling, the self-energy becomes smaller as half-filling is approached, while the trend is the opposite at strong coupling. On the other hand, the onset of the anomalous self-energy in the antinodal regions also seems to reduce the normal self-energy in these regions, therefore making the normal-self energy more local. This seems to be a generic feature, not only associated with the doped Mott insulator regime. It is particularly interesting that the reduction in ImΣ seems proportional to S in both cases.

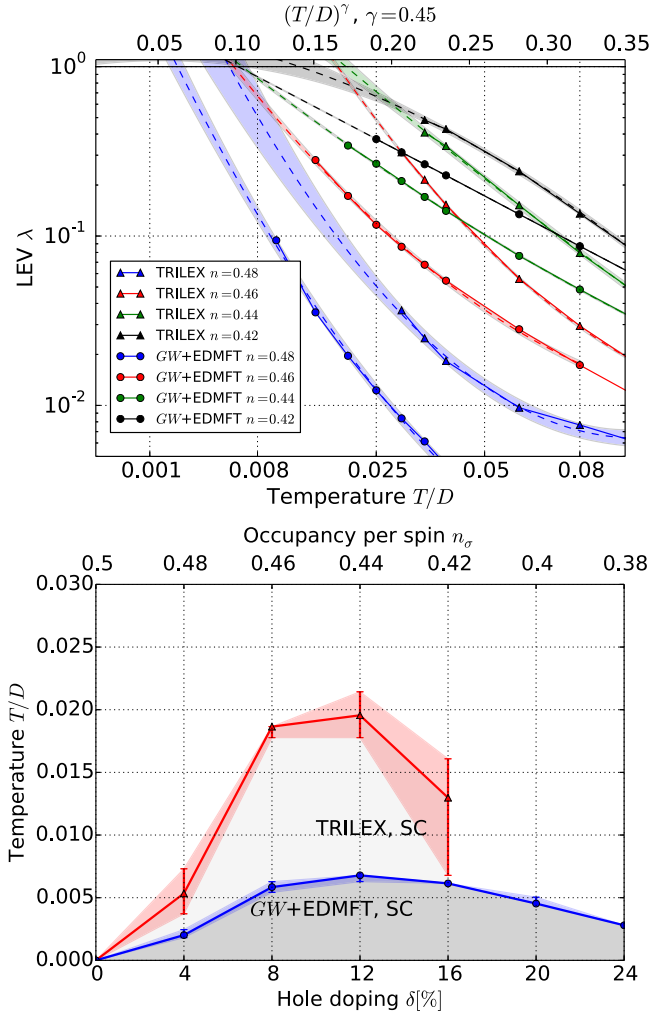

FIG. 16. Error bars determined by standard Bayesian statistics method at a fixed $\gamma = 0.45$.

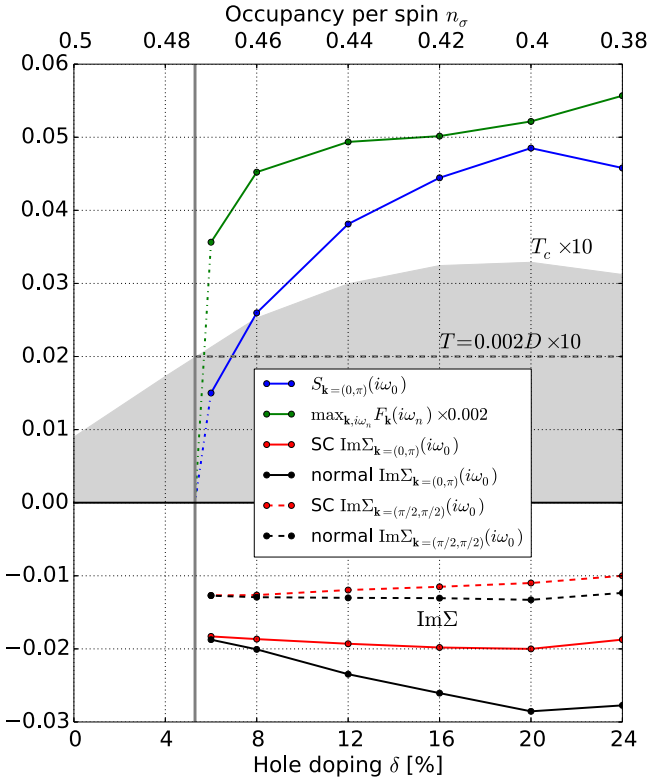

FIG. 17. Evolution of various quantities within the superconducting dome at dispersion point C, GW calculation, $U/D = 1$, $T/D = 0.002$. The T_c, as obtained from $\lambda_m(T)$, is denoted by the gray area. Quantities are scaled to fit the same plot. The gray dashed horizontal line denotes the temperature at which the data are taken, relative to the (scaled) T_c. The vertical full line denotes the end of the superconducting dome at the temperature denoted by the dashed horizontal line, i.e., denotes the doping where all the anomalous quantities are expected to go to zero.

[1] A. V. Chubukov, D. Pines, and J. Schmalian, *Superconductivity* (Springer, Berlin, 2002), Chap. 22, pp. 1349–1413.
[2] K. B. Efetov, H. Meier, and C. Pépin, Nat. Phys. **9**, 442 (2013).
[3] Y. Wang and A. Chubukov, Phys. Rev. B **90**, 035149 (2014).
[4] M. A. Metlitski and S. Sachdev, Phys. Rev. B **82**, 075128 (2010).
[5] F. Onufrieva and P. Pfeuty, Phys. Rev. Lett. **102**, 207003 (2009).
[6] F. Onufrieva and P. Pfeuty, Phys. Rev. Lett. **109**, 257001 (2012).
[7] P. W. Anderson, Science **235**, 1196 (1987).
[8] M. H. Hettler, A. N. Tahvildar-Zadeh, M. Jarrell, T. Pruschke, and H. R. Krishnamurthy, Phys. Rev. B **58**, R7475 (1998).
[9] M. H. Hettler, M. Mukherjee, M. Jarrell, and H. R. Krishnamurthy, Phys. Rev. B **61**, 12739 (2000).
[10] A. I. Lichtenstein and M. I. Katsnelson, Phys. Rev. B **62**, R9283(R) (2000).
[11] G. Kotliar, S. Y. Savrasov, G. Pálsson, and G. Biroli, Phys. Rev. Lett. **87**, 186401 (2001).
[12] T. A. Maier, M. Jarrell, T. Pruschke, and M. H. Hettler, Rev. Mod. Phys. **77**, 1027 (2005).
[13] A. Georges, G. Kotliar, W. Krauth, and M. J. Rozenberg, Rev. Mod. Phys. **68**, 13 (1996).
[14] B. Kyung, D. Sénéchal, and A.-M. S. Tremblay, Phys. Rev. B **80**, 205109 (2009).
[15] G. Sordi, P. Sémon, K. Haule, and A.-M. S. Tremblay, Sci. Rep. **2**, 547 (2012).
[16] M. Civelli, M. Capone, A. Georges, K. Haule, O. Parcollet, T. D. Stanescu, and G. Kotliar, Phys. Rev. Lett. **100**, 046402 (2008).
[17] M. Ferrero, O. Parcollet, A. Georges, G. Kotliar, and D. N. Basov, Phys. Rev. B **82**, 054502 (2010).
[18] E. Gull, O. Parcollet, and A. J. Millis, Phys. Rev. Lett. **110**, 216405 (2013).
[19] A. Macridin, M. Jarrell, and T. A. Maier, Phys. Rev. B **70**, 113105 (2004).
[20] T. A. Maier, M. Jarrell, A. Macridin, and C. Slezak, Phys. Rev. Lett. **92**, 027005 (2004).
[21] T. A. Maier, M. Jarrell, T. C. Schulthess, P. R. C. Kent, and J. B. White, Phys. Rev. Lett. **95**, 237001 (2005).

[22] T. A. Maier, M. S. Jarrell, and D. J. Scalapino, Phys. Rev. Lett. **96**, 047005 (2006).
[23] E. Gull, M. Ferrero, O. Parcollet, A. Georges, and A. J. Millis, Phys. Rev. B **82**, 155101 (2010).
[24] S. X. Yang, H. Fotso, S. Q. Su, D. Galanakis, E. Khatami, J. H. She, J. Moreno, J. Zaanen, and M. Jarrell, Phys. Rev. Lett. **106**, 047004 (2011).
[25] A. Macridin and M. Jarrell, Phys. Rev. B **78**, 241101(R) (2008).
[26] A. Macridin, M. Jarrell, T. Maier, P. R. C. Kent, and E. D'Azevedo, Phys. Rev. Lett. **97**, 036401 (2006).
[27] M. Jarrell, T. A. Maier, C. Huscroft, and S. Moukouri, Phys. Rev. B **64**, 195130 (2001).
[28] D. Bergeron, V. Hankevych, B. Kyung, and A.-M. S. Tremblay, Phys. Rev. B **84**, 085128 (2011).
[29] B. Kyung, V. Hankevych, A.-M. Daré, and A.-M. S. Tremblay, Phys. Rev. Lett. **93**, 147004 (2004).
[30] B. Kyung, S. S. Kancharla, D. Sénéchal, A.-M. S. Tremblay, M. Civelli, and G. Kotliar, Phys. Rev. B **73**, 165114 (2006).
[31] S. Okamoto, D. Sénéchal, M. Civelli, and A.-M. S. Tremblay, Phys. Rev. B **82**, 180511 (2010).
[32] G. Sordi, K. Haule, and A.-M. S. Tremblay, Phys. Rev. Lett. **104**, 226402 (2010).
[33] M. Civelli, M. Capone, S. S. Kancharla, O. Parcollet, and G. Kotliar, Phys. Rev. Lett. **95**, 106402 (2005).
[34] O. Parcollet, G. Biroli, and G. Kotliar, Phys. Rev. Lett. **92**, 226402 (2004).
[35] M. Ferrero, P. S. Cornaglia, L. De Leo, O. Parcollet, G. Kotliar, and A. Georges, Europhys. Lett. **85**, 57009 (2008).
[36] M. Ferrero, P. S. Cornaglia, L. De Leo, O. Parcollet, G. Kotliar, and A. Georges, Phys. Rev. B **80**, 064501 (2009).
[37] E. Gull, O. Parcollet, P. Werner, and A. J. Millis, Phys. Rev. B **80**, 245102 (2009).
[38] X. Chen, J. P. F. LeBlanc, and E. Gull, Phys. Rev. Lett. **115**, 116402 (2015).
[39] X. Chen, J. P. F. LeBlanc, and E. Gull, Nat. Commun. **8**, 14986 (2017)
[40] J. P. F. LeBlanc, A. E. Antipov, F. Becca, I. W. Bulik, G. K.-L. Chan, C.-M. Chung, Y. Deng, M. Ferrero, T. M. Henderson, C. A. Jiménez-Hoyos *et al.* (Simons Collaboration on the Many-Electron Problem), Phys. Rev. X **5**, 041041 (2015).
[41] E. Koch, G. Sangiovanni, and O. Gunnarsson, Phys. Rev. B **78**, 115102 (2008).
[42] W. Wu, M. Ferrero, A. Georges, and E. Kozik, Phys. Rev. B **96**, 041105 (2017).
[43] A. N. Rubtsov, M. I. Katsnelson, and A. I. Lichtenstein, Phys. Rev. B **77**, 033101 (2008).
[44] A. N. Rubtsov, M. I. Katsnelson, and A. I. Lichtenstein, Ann. Phys. (NY) **327**, 1320 (2012).
[45] E. G. C. P. van Loon, A. I. Lichtenstein, M. I. Katsnelson, O. Parcollet, and H. Hafermann, Phys. Rev. B **90**, 235135 (2014).
[46] E. A. Stepanov, E. G. C. P. van Loon, A. A. Katanin, A. I. Lichtenstein, M. I. Katsnelson, and A. N. Rubtsov, Phys. Rev. B **93**, 045107 (2016).
[47] A. Toschi, A. A. Katanin, and K. Held, Phys. Rev. B **75**, 045118 (2007).
[48] A. A. Katanin, A. Toschi, and K. Held, Phys. Rev. B **80**, 075104 (2009).
[49] T. Schäfer, F. Geles, D. Rost, G. Rohringer, E. Arrigoni, K. Held, N. Blümer, M. Aichhorn, and A. Toschi, Phys. Rev. B **91**, 125109 (2015).
[50] A. Valli, T. Schäfer, P. Thunström, G. Rohringer, S. Andergassen, G. Sangiovanni, K. Held, and A. Toschi, Phys. Rev. B **91**, 115115 (2015).
[51] G. Li, N. Wentzell, P. Pudleiner, P. Thunström, and K. Held, Phys. Rev. B **93**, 165103 (2016).
[52] G. Rohringer and A. Toschi, Phys. Rev. B **94**, 125144 (2016).
[53] T. Ayral and O. Parcollet, Phys. Rev. B **94**, 075159 (2016).
[54] S. Biermann, F. Aryasetiawan, and A. Georges, Phys. Rev. Lett. **90**, 086402 (2003).
[55] P. Sun and G. Kotliar, Phys. Rev. B **66**, 085120 (2002).
[56] P. Sun and G. Kotliar, Phys. Rev. Lett. **92**, 196402 (2004).
[57] T. Ayral, P. Werner, and S. Biermann, Phys. Rev. Lett. **109**, 226401 (2012).
[58] T. Ayral, S. Biermann, and P. Werner, Phys. Rev. B **87**, 125149 (2013).
[59] S. Biermann, J. Phys.: Condens. Matter **26**, 173202 (2014).
[60] T. Ayral, S. Biermann, P. Werner, and L. V. Boehnke, Phys. Rev. B **95**, 245130 (2017).
[61] G. Rohringer, H. Hafermann, A. Toschi, A. A. Katanin, A. E. Antipov, M. I. Katsnelson, A. I. Lichtenstein, A. N. Rubtsov, and K. Held, arXiv:1705.00024.
[62] T. Ayral and O. Parcollet, Phys. Rev. B **92**, 115109 (2015).
[63] T. Ayral and O. Parcollet, Phys. Rev. B **93**, 235124 (2016).
[64] L. Hedin, Phys. Rev. **139**, A796 (1965).
[65] L. Hedin, J. Phys.: Condens. Matter **11**, R489 (1999).
[66] T. Ayral, J. Vučičević, and O. Parcollet, arXiv:1706.01388.
[67] F. Aryasetiawan and S. Biermann, Phys. Rev. Lett. **100**, 116402 (2008).
[68] A. Linscheid and F. Essenberger, arXiv:1503.00970v1.
[69] J. Zinn-Justin, *Quantum Field Theory and Critical Phenomena*, 4th ed. (Oxford University Press, Oxford, 2002).
[70] M. Kitatani, N. Tsuji, and H. Aoki, Phys. Rev. B **92**, 085104 (2015).
[71] P. Werner, A. Comanac, L. de Medici, M. Troyer, and A. J. Millis, Phys. Rev. Lett. **97**, 076405 (2006).
[72] P. Werner and A. J. Millis, Phys. Rev. B **75**, 085108 (2007).
[73] J. Otsuki, Phys. Rev. B **87**, 125102 (2013).
[74] R. V. Mises and H. Pollaczek-Geiringer, J. Appl. Math. Mech./Z. Angew. Math. Mech. **9**, 152 (1929).
[75] J. Otsuki, H. Hafermann, and A. I. Lichtenstein, Phys. Rev. B **90**, 235132 (2014).
[76] A. T. Rømer, A. Kreisel, I. Eremin, M. A. Malakhov, T. A. Maier, P. J. Hirschfeld, and B. M. Andersen, Phys. Rev. B **92**, 104505 (2015).
[77] P. Staar, T. Maier, and T. C. Schulthess, Phys. Rev. B **89**, 195133 (2014).
[78] M. Capone and G. Kotliar, Phys. Rev. B **74**, 054513 (2006).
[79] S. Sakai, M. Civelli, and M. Imada, Phys. Rev. B **94**, 115130 (2016).
[80] S. S. Kancharla, B. Kyung, D. Sénéchal, M. Civelli, M. Capone, G. Kotliar, and A.-M. S. Tremblay, Phys. Rev. B **77**, 184516 (2008).
[81] E. Gull and A. J. Millis, Phys. Rev. B **91**, 085116 (2015).
[82] E. Pavarini, I. Dasgupta, T. Saha-Dasgupta, O. Jepsen, and O. K. Andersen, Phys. Rev. Lett. **87**, 047003 (2001).
[83] R. K. Bryan, Eur. Biophys. J. **18**, 165 (1990).
[84] F. Onufrieva and P. Pfeuty, Phys. Rev. B **65**, 054515 (2002).

[85] K.-S. Chen, Z. Y. Meng, S.-X. Yang, T. Pruschke, J. Moreno, and M. Jarrell, Phys. Rev. B **88**, 245110 (2013).
[86] Y. Nomura, S. Sakai, and R. Arita, Phys. Rev. B **91**, 235107 (2015).
[87] P. Sémon, K. Haule, and G. Kotliar, Phys. Rev. B **95**, 195115 (2017).
[88] O. Parcollet, M. Ferrero, T. Ayral, H. Hafermann, P. Seth, and I. S. Krivenko, Comput. Phys. Commun. **196**, 398 (2015).
[89] T. A. Maier, P. Staar, and D. J. Scalapino, arXiv:1507.06206.
[90] T. P. Ryan, in *Modern Regression Methods*, edited by W. A. Shewhart and S. S. Wilks, Wiley Series in Probability and Statistics (Wiley, New York, 1997).

Anderson localization effects near the Mott metal-insulator transition

Helena Bragança,[1] M. C. O. Aguiar,[1] J. Vučičević,[2] D. Tanasković,[2] and V. Dobrosavljević[3]
[1]*Departamento de Física, Universidade Federal de Minas Gerais, Belo Horizonte, MG, Brazil*
[2]*Scientific Computing Laboratory, Institute of Physics Belgrade, University of Belgrade, Pregrevica 118, 11080 Belgrade, Serbia*
[3]*Department of Physics and National High Magnetic Field Laboratory, Florida State University, Tallahassee, Florida 32306, USA*
(Received 15 July 2015; published 24 September 2015)

The interplay between Mott and Anderson routes to localization in disordered interacting systems gives rise to different transitions and transport regimes. Here, we investigate the phase diagram at finite temperatures using dynamical mean-field theory combined with typical medium theory, which is an effective theory of the Mott-Anderson metal-insulator transition. We mainly focus on the properties of the coexistence region associated with the Mott phase transition. For weak disorder, the coexistence region is found to be similar to that in the clean case. However, as we increase disorder, Anderson localization effects are responsible for shrinking the coexistence region, and at sufficiently strong disorder (approximately equal to twice the bare bandwidth) it drastically narrows, the critical temperature T_c abruptly goes to zero, and we observe a phase transition in the absence of a coexistence of the metallic and insulating phases. In this regime, the effects of interaction and disorder are found to be of comparable importance for charge localization.

DOI: 10.1103/PhysRevB.92.125143 PACS number(s): 71.27.+a, 71.30.+h, 71.55.−i, 71.10.Hf

I. INTRODUCTION

The Mott mechanism of localization [1] is an emergent phenomenon in which a large local Coulomb repulsion suppresses double occupation, which prevents charge transport in a half-filled system. Strongly correlated electron materials, such as transition-metal oxides [2–5] and some organic salts [6–10], exhibit a Mott metal-insulator transition due to the effectively strong Coulomb repulsion that exists between electrons occupying a narrow valence band. Below the critical temperature T_c, this transition is of first-order and one observes a region where metal and insulator coexist [4–6,8].

The presence of disorder also leads to localization of electron wave functions, a phenomenon known as Anderson localization [11,12]. In this case, the energetic mismatch between neighboring sites prevents charge transport in the lattice. These two mechanisms of localization—Mott and Anderson—combine in nontrivial ways, sometimes reducing, sometimes enhancing each other's effects. Recently, the interplay between interaction and disorder has received much attention, mainly through three different perspectives. First, due to the investigation of the many-body localization [13], a novel paradigm arose for understanding localization in disordered and interacting quantum systems at nonzero temperature. Second, very recently, models of disordered and interacting systems have been simulated with cold atoms in optical lattices [14,15]. Finally, the disorder and the effective interaction strength can be systematically tuned by doping [3,5,9,16,17], or even x-ray irradiation [10,18].

Over the past few decades, considerable progress has been made in the description of strongly correlated materials and the Mott metal-insulator transition (MIT) through dynamical mean-field theory (DMFT) [19]. In this method, a lattice model of interacting electrons is mapped to the Anderson impurity model with a conduction bath that needs to be calculated self-consistently. To describe disorder, the simplest treatment is within the coherent potential approximation (CPA) [20]. The CPA can be easily combined with the DMFT [21–28] by considering an ensemble of impurities surrounded by an average bath, which is the same for each electron. This approach thus does not describe the spatial fluctuations associated with the Anderson localization. Near the Anderson transition, the distribution of the local density of states (DOS) changes from Gaussian to log-normal [29,30], implying that its arithmetic average value does not provide a proper description of the system. The typical medium theory (TMT) [31] provides a simple method that can effectively describe the Anderson localization. The central quantity in TMT is the typical density of states, defined as the geometric average of the local DOS [32], which plays the role of the order parameter for the Anderson localization. The TMT method was carefully tested for the noninteracting system [31,33,34], and it was successfully applied to the interacting case within the TMT-DMFT approach [35], elucidating the full nonmagnetic phase diagram for the disordered half-filled Hubbard model and the precise nature of the Mott-Anderson critical point [36]. The TMT-DMFT approach also allows for a spin-dependence analysis of the DOS, which enables one to include the effects of long-range magnetic order in disordered and interacting systems [37].

In this paper, we perform a TMT-DMFT calculation at finite temperatures. We explore the entire nonmagnetic phase diagram, with a particular focus on the effects of disorder on the Mott metal-insulator coexistence region. We carefully compare the TMT-DMFT and CPA-DMFT results with the goal of precisely determining the Anderson localization effects, described only within the former method. We find that the TMT-DMFT coexistence region is at comparatively lower values of the interaction U, while the critical temperature T_c is higher than in CPA-DMFT. The width of the coexistence region, however, quickly decreases with disorder. At disorder strength $W \sim 2B$, where B is the bandwidth in the clean noninteracting system, TMT-DMFT predicts T_c to abruptly go to zero, as opposed to the CPA-DMFT solution, where the coexistence region asymptotically shrinks to a single point as disorder is increased to infinity. In the regime $W \gtrsim 2B$, the MIT takes place at $U \approx W$, which causes Anderson and Mott mechanisms to become equally important for the properties of the system.

The paper is organized as follows. In Sec. II we briefly present the TMT-DMFT method for the solution of the disordered Hubbard model, and the (U,W) phase diagram is shown is Sec. III. Sections IV and V show details of the metal-insulator transition in the presence of weak, moderate, and strong disorder. Section VI contains conclusions.

II. TMT-DMFT METHOD

We consider the Hubbard model with random site energies, given by the Hamiltonian

$$H = -t \sum_{\langle ij\rangle\sigma} (c^{\dagger}_{i\sigma} c_{j\sigma} + \text{H.c.}) + U \sum_{i} n_{i\uparrow} n_{i\downarrow} + \sum_{i\sigma} (\varepsilon_i - \mu) n_{i\sigma},$$

where $c^{\dagger}_{i\sigma}$ ($c_{i\sigma}$) creates (destroys) an electron with spin σ on site i, $n_{i\sigma} = c^{\dagger}_{i\sigma} c_{i\sigma}$, t is the hopping amplitude for nearest-neighbor sites, U is the on-site repulsion, and ε_i is the random on-site energy, which follows a uniform distribution $P(\varepsilon)$ of width W, centered in $\varepsilon_i = 0$. We study the half-filled particle-hole symmetric lattice by setting the chemical potential μ equal to $U/2$. In general, transition-metal oxides and organic salts described by the Hubbard model can exhibit both antiferromagnetic and paramagnetic Mott insulating phases. In this work, we focus on the paramagnetic solution, which is present even at zero temperature in frustrated lattices.

Within TMT-DMFT, the lattice model describing a disordered correlated system is mapped onto an ensemble of single-impurity problems, corresponding to sites with different values of the on-site energy, each being embedded in a typical effective medium that needs to be calculated self-consistently. The TMT-DMFT self-consistent procedure can be summarized as follows [31,36]: By considering an initial guess for the (typical) bath $\Delta(\omega)$ surrounding the impurities, we solve an ensemble of impurity problems, which give us local Green's functions $G(\omega,\varepsilon_i)$ from which local spectra $\rho(\omega,\varepsilon_i) = -\frac{1}{\pi}\text{Im}G(\omega,\varepsilon_i)$ are obtained. The typical DOS is then calculated by the geometric average of the local spectra,

$$\rho_{\text{typ}}(\omega) = \exp\left[\int d\varepsilon\, P(\varepsilon) \ln \rho(\omega,\varepsilon)\right],$$

and the typical Green's function is obtained through the Hilbert transform, $G_{\text{typ}}(\omega) = \int_{-\infty}^{\infty} d\omega \frac{\rho_{\text{typ}}(\omega')}{\omega-\omega'}$. For lattices with semicircular DOS, $\rho_0(\omega) = \frac{4}{\pi B}\sqrt{1-(\frac{2\omega}{B})^2}$, in the clean non-interacting limit (Bethe lattice with infinite coordination number), the self-consistent loop is closed by calculating a new bath according to $\Delta(\omega) = t^2 G_{\text{typ}}(\omega)$. To solve the single-impurity problems, in this work we use the iterative perturbation theory (IPT) on the real axis [38,39]. In this case, we do not need analytic continuation. This is an important advantage of this method since the TMT self-consistency relation is based on the local DOS.

III. PHASE DIAGRAM

Figure 1 presents the TMT-DMFT phase diagram of the disordered Hubbard model obtained at a small temperature, $T = 0.008$. Here and throughout the paper, we define the noninteracting bandwidth $B = 4t$ as the unit of energy. In the phase diagram, the black and pink circles correspond to the metallic and the insulating spinodal lines of the first-order Mott phase transition; these two lines delimit the metal-insulator coexistence region. The green triangles indicate a transition between a metal and a Mott insulator in the absence of a well-defined coexistence region (see Sec. V for details), while the blue stars indicate a transition between a metal and a correlated Anderson insulator. Finally, the red squares correspond to a crossover between the two insulators, which takes place at $W \approx U$.

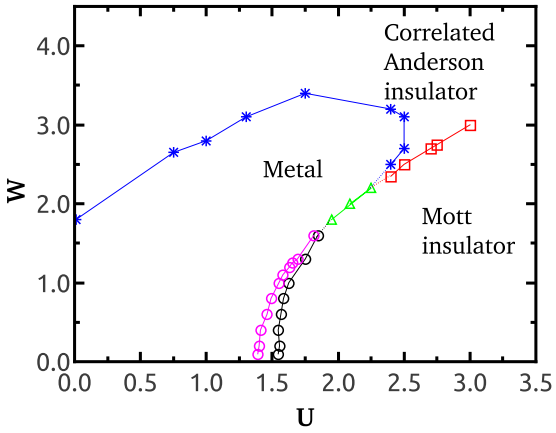

FIG. 1. (Color online) (U,W) phase diagram obtained within TMT-DMFT for the disordered Hubbard model at $T = 0.008$. The description of the different symbols/colors used is given in the text.

To differentiate the phases and build the phase diagram, we have analyzed the behavior of the typical DOS at the Fermi level [$\rho_{\text{typ}}(0)$], the frequency-integrated typical DOS (N), and the site occupation as a function of the on-site energy. As an example, these quantities are presented in Fig. 2 for the particular case of $U = 1.75$ and $T = 0.008$. For this set of parameters, as disorder W increases, the system goes from the Mott insulator to the Anderson insulator, crossing an intermediate metallic phase (see Ref. [40], for example, for a discussion about the presence of an intermediate metallic phase when disorder increases). The Mott insulator is characterized by a gap in the typical DOS [$\rho_{\text{typ}}(0) = 0$] and a finite frequency-integrated typical-DOS N [see panel (a)], as well as a single occupation of all sites [see panel (b)]. The metallic phase, on the other hand, features a quasiparticle peak in the typical DOS, nonzero integrated DOS N, and a variable site occupation n_i. Finally, the correlated Anderson insulator shows a vanishing typical DOS, indicating that all the states are localized and as such do not contribute with spectral weight to the typical DOS [31,35]. For this reason, the frequency-integrated typical DOS goes to zero when the system approaches the Anderson insulator, and thus it can be used as an order parameter that signalizes this transition. Furthermore, within the TMT-DMFT, the Anderson insulating phase corresponds to a two-fluid phase [36]: it consists of empty and doubly occupied sites, characteristic of noninteracting Anderson insulators, as well as singly occupied sites, characterizing Mott localized states [see the results for $W = 4$ in panel (b)].

We find good agreement between our diagram and others known in the literature at $T = 0$ [35,36]. The most relevant effects of finite but small temperature are over the Mott

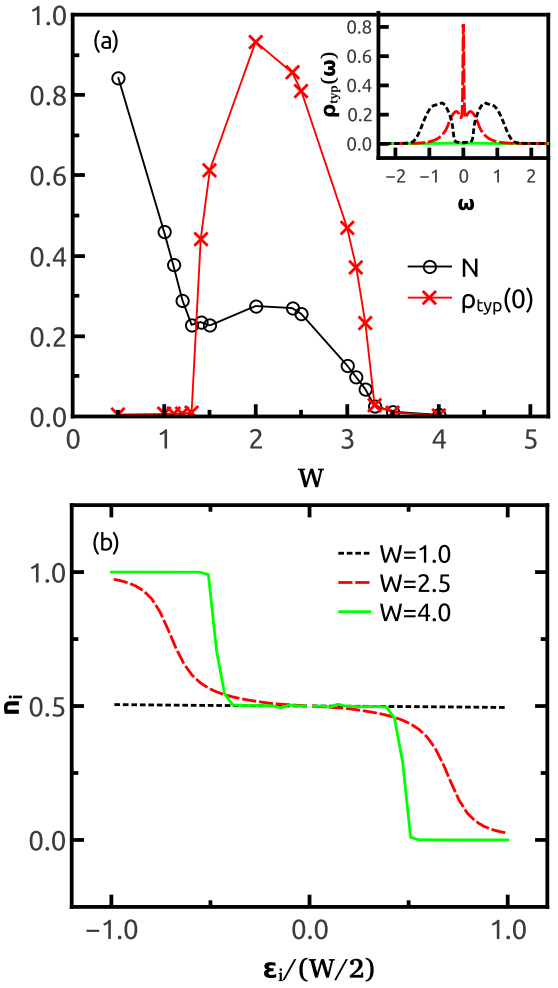

FIG. 2. (Color online) TMT-DMFT results for $U = 1.75$ and $T = 0.008$. According to the phase diagram of Fig. 1, as disorder W increases, the system goes from the Mott insulating phase to the metallic phase and finally to the Anderson insulating phase. These transitions are identified (and the phase diagram is built) by looking at the behavior of the quantities shown in the two panels of the present figure: (a) frequency-integrated typical DOS, N, and typical DOS at the Fermi level, $\rho_{\rm typ}(0)$, as a function of W, and (b) site occupation per spin as a function of the site energy, normalized by the disorder distribution width, W. The inset shows an example of the typical DOS in the metallic phase (red long-dashed line), as well as in the Mott (black dashed line) and the Anderson (green solid line) insulating phases.

coexistence region, which spans a smaller range of U in comparison with the $T = 0$ case. The real axis IPT impurity solver makes it possible to solve TMT-DMFT equations for a broad range of parameters and several temperatures. In the following, we concentrate on the range of parameters near the phase transition, and, in particular, near the coexistence region of metallic and insulating solutions.

IV. MOTT TRANSITION FOR WEAK AND MODERATE DISORDER $W < 2B$

In this section, we analyze the coexistence region for weak and moderate disorder, which corresponds to

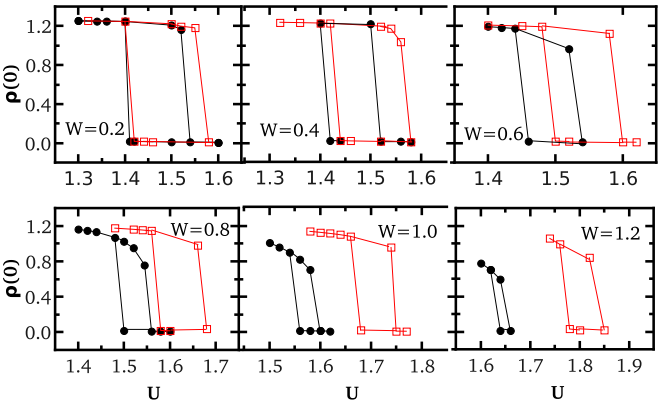

FIG. 3. (Color online) Hysteresis curves for the DOS at the Fermi level obtained by increasing and decreasing U at a fixed temperature $T = 0.01$. The curves enclose the coexistence region. The open squares were obtained within CPA-DMFT, while the filled circles correspond to TMT-DMFT results.

$W < W^*$, $W^* \approx 1.7$. At this regime, the critical U for the Mott transition is greater than the disorder strength. Although the phase transition described within TMT-DMFT is qualitatively similar to that of CPA-DMFT, some Anderson localization effects are already observed.

A. Coexistence region

To obtain the coexistence region within CPA-DMFT or TMT-DMFT for a fixed temperature $T < T_c$, we start from a metallic initial bath and increase U to find U_{c2}, which corresponds to the interaction value at which $\rho(0)$ goes to zero, indicating the disappearance of the quasiparticle peak in the DOS. Alternatively, when starting from an insulator, by decreasing U we find U_{c1}, where $\rho(0)$ becomes finite, indicating the closure of the gap at the Fermi level. This procedure allows us to obtain hysteresis curves of $\rho(0)$ as a function of U, which enclose the coexistence region (see Fig. 3 for examples of these hysteresis curves). For a given W, we can repeat this procedure for different temperatures and determine the two spinodal lines, $U_{c1}(T)$ and $U_{c2}(T)$, defining the coexistence region. The temperature at which the two spinodal lines merge gives the critical temperature, T_c, which corresponds to a second order critical end point.

Figure 4 shows the coexistence region obtained as described above for the clean case ($W = 0$) and for a disordered system ($W = 0.8$), both within TMT-DMFT and CPA-DMFT. According to our results, when disorder is added to the system, the critical U at which the transition occurs increases in comparison with the clean case. This happens because the general effect of disorder is to broaden the bands, as shown in Fig. 5, when the CPA-DMFT calculation is performed inside both the metallic and the insulating phases. Another general effect of disorder seen in the results of Fig. 4 is that the temperature of the second-order critical point decreases with disorder, in agreement with previous CPA-DMFT calculations [26]. These general consequences of disorder do not depend on the inclusion of Anderson localization effects, since they are observed even within the CPA-DMFT approach.

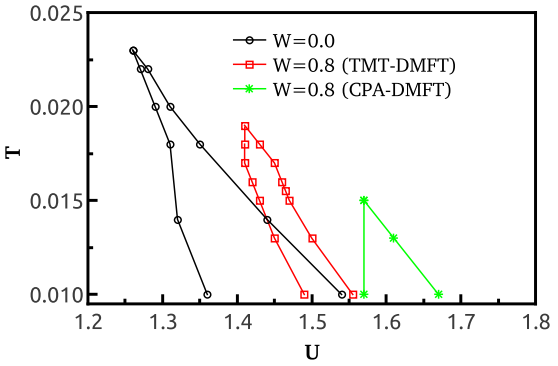

FIG. 4. (Color online) Spinodal lines enclosing the coexistence region for the clean system ($W = 0$) and the disordered case ($W = 0.8$) obtained within both TMT-DMFT and CPA-DMFT.

To carefully study the effects of Anderson localization, we compare the results obtained within TMT-DMFT with those of CPA-DMFT. As can be seen in Fig. 4 for $W = 0.8$, the critical U at which the transition occurs is smaller within TMT-DMFT than within CPA-DMFT. Moreover, a narrower coexistence region is observed within the former. To understand these results, one should consider that the wave-function localization starts at the band edges and that localized states do not contribute with spectral weight to the typical DOS. For these reasons, in the presence of Anderson localization, narrower bands are observed in comparison with CPA-DMFT results, both in the metallic and the insulating phase, as can be seen in Fig. 6. This is the opposite effect to that described in the previous paragraph regarding the effects of adding disorder to a clean system. As a consequence, the coexistence region within TMT-DMFT is seen in between that of a clean system and that obtained within CPA-DMFT for the same value of disorder.

From the TMT-DMFT and the CPA-DMFT hysteresis curves shown in Fig. 3, we see that the Anderson localization effects over the coexistence region become more important as the disorder increases. As W approaches $W^* \approx 1.7$, the width of the TMT-DMFT coexistence region vanishes, and we were not able to observe the hysteresis even at the lowest temperatures $T = 0.005$ (see Sec. V). In contrast, in the CPA-DMFT solution [26], the coexistence region with finite small T_c is observed even for very large W.

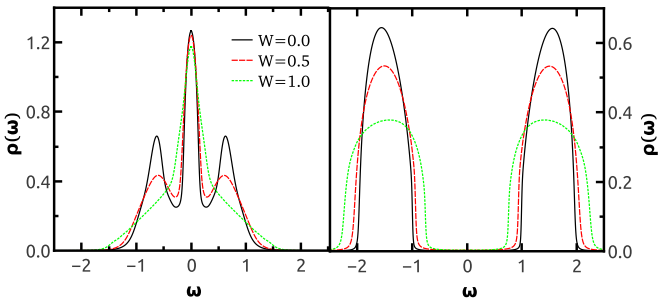

FIG. 5. (Color online) Average DOS obtained within CPA-DMFT for different values of disorder at fixed temperature $T = 0.01$. Disorder broadens the bands in both the metallic (left panel, for $U = 1$) and the insulating (right panel, for $U = 3$) phase.

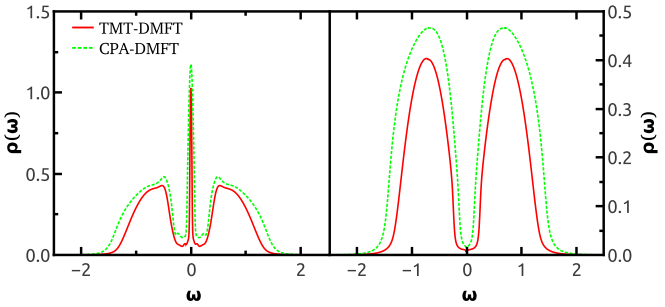

FIG. 6. (Color online) Typical (TMT-DMFT) and average (CPA-DMFT) values of the DOS as a function of frequency showing that Anderson localization effects start at the band edges, since both localized and extended states contribute to the average DOS, while only extended ones contribute to the typical DOS. The left panel shows results for $U = 1.5$, while those in the right panel are for $U = 1.6$, both at $T = 0.01$.

B. Crossover regime and the critical temperature T_c

As seen in Fig. 3, the coexistence region shrinks as disorder increases, making it difficult to obtain the critical temperature T_c from the merging of the two spinodal lines. One alternative is to determine T_c from the results obtained above it, that is, in the crossover region between metal and insulator. This was shown to be possible in the clean case, and in the present work we extend this analysis to the disordered system.

The quantum Widom line (QWL) associated with the Mott transition is defined in Refs. [41–44] in analogy with the classical Widom line [45] as the instability (crossover) line above the critical end point (U_c, T_c). It starts at the critical end point and goes to higher temperatures (above the coexistence region) as a continuation of the first-order phase-transition line. It is associated with the (zero-temperature) quantum critical point, which is masked by the coexistence region in the case of the Mott transition. The QWL can be defined from the free-energy functional $F_L[G(i\omega_n)]$, and it can be used to determine T_c from the behavior at higher temperatures, as explained (for the clean case) in Refs. [41,42]. With the objective of applying the QWL analysis to obtain T_c in the disordered case, here we review this procedure.

The Landau free-energy functional of the Hubbard model as a functional of $G(i\omega_n)$ is given by

$$F_L[G(i\omega_n)] = -Tt^2 \sum_n G^2(i\omega_n) + F_{\rm imp}[G(i\omega_n)],$$

where the first term represents the energy needed to form the bath around a given site, and the second term describes the energy of the electron at the impurity level surrounded by the bath, that is, the free energy of the single-impurity problem. The DMFT (TMT-DMFT) equations are obtained by minimizing $F_L[G(i\omega_n)]$ with respect to $G(i\omega_n)$.

The curvature λ of the above free-energy functional with respect to U is finite and minimal along the crossover line and is zero at the second-order critical point. This curvature can be identified with the convergence rate of the iterative DMFT calculation [41,42], that is, $\lambda(U,T)$ corresponds to the slope of the convergence rate $\ln\{\mathrm{Im}[G^{(\mathrm{it})}(0) - G^{(\mathrm{it}-1)}(0)]\}$ as a function of the step "it" of the iterative calculation. Repeating

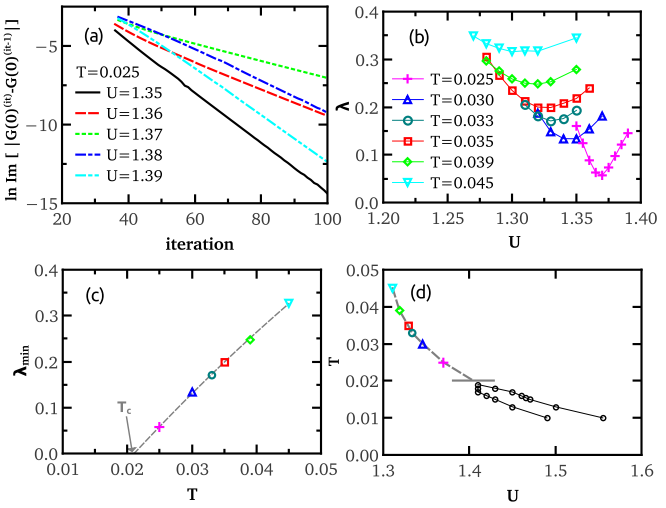

FIG. 7. (Color online) QWL analysis for the disordered system with $W = 0.8$ described by TMT-DMFT. See the text for the explanation of the results in each panel.

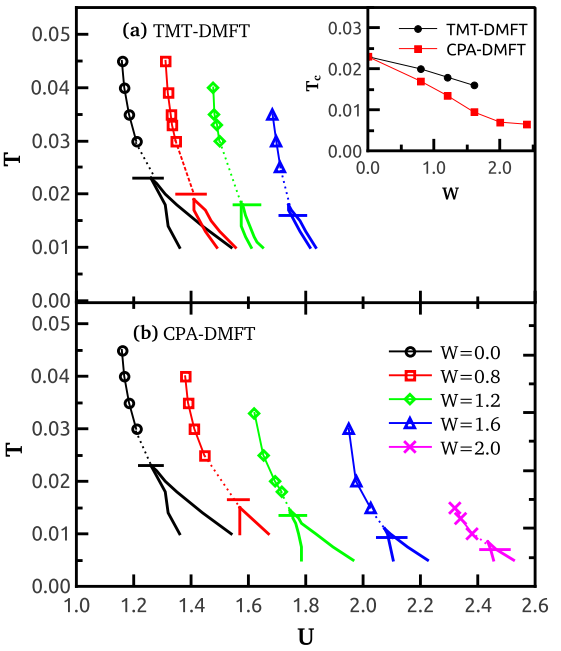

FIG. 8. (Color online) QWL and coexistence regions obtained within TMT-DMFT (a) and CPA-DMFT (b) for different values of disorder (CPA-DMFT coexistence regions for $W \geqslant 1.2$ were obtained from Ref. [26]). The horizontal lines represent T_c obtained from the corresponding QWL, calculated as exemplified in Fig. 7 (c). The inset shows these T_c values as a function of disorder.

the calculation for different values of T, we obtain the curve $\lambda_{\min} = \lambda(T)|_{U^*}$, where U^* is the point at which λ is minimum for a given T. This line can be extrapolated, to $\lambda_{\min}|_{T=T_c} = 0$, since the curvature of the free-energy functional is zero at the second-order critical point.

The procedure is illustrated in Fig. 7 for the disordered system with $W = 0.8$. For each value of U, we obtain the free-energy curvature λ from the convergence rate of the typical Green's function through the iterative steps, as presented in (a) for $T = 0.025$. For a fixed temperature and different values of U, we obtain the corresponding $\lambda(U)|_T$ curve. Repeating this procedure for different temperatures, we obtain the set of curves $\lambda(U)|_T$ presented in Fig. 7(b). The minima $\lambda_{\min}$ of these curves are shown in panel (c), and we obtain T_c as the temperature at which $\lambda_{\min} = 0$. Finally, panel (d) shows the crossover line obtained from data in panel (b), T_c obtained through the QWL analysis (gray horizontal line), and the two spinodal lines. We conclude that the T_c calculated from the QWL analysis coincides with the T_c obtained from the merging of the two spinodal lines that define the coexistence region.

In Fig. 8, we show the QWL and the critical temperatures obtained from them as we vary the system disorder, both within TMT-DMFT and CPA-DMFT. For disorder strengths $W \gtrsim 1.6$, we find a nonlinear behavior of the TMT-DMFT convergence rate as a function of the iteration step; we were thus unable to use the QWL analysis discussed above to evaluate T_c for very large disorder. For $W < 1.7$, both methods predict that T_c decreases when W increases [see also the inset in Fig. 8(a)]. The critical temperature T_c is higher within TMT-DMFT than within CPA-DMFT, although the coexistence region becomes (very) narrow in the presence of Anderson localization effects (TMT-DMFT results). However, T_c always remains finite within CPA-DMFT even for very large disorder strength [26], whereas we do not observe the coexistence region for $W \gtrsim 1.7$ in TMT-DMFT (see the next section). Our numerical TMT-DMFT solution indicates that T_c abruptly drops to zero as the coexistence region disappears for $W \approx 1.7$.

V. MOTT-ANDERSON TRANSITION FOR STRONG DISORDER $W \gtrsim 2B$

Within the TMT-DMFT calculation, as we increase disorder, the value of the critical U becomes closer to the disorder width W. For $U \sim W \sim 2B$ both Mott and Anderson routes to localization become equally relevant, and it becomes the most difficult to precisely understand the mechanism of the MIT. In Fig. 9, we show the results for $W = 2.0$ at $T = 0.01$. The transition is seen to take place at $U \approx 2.09$. Moreover, if we look at the results for the typical DOS at the Fermi level when U increases, as well as when U decreases [see panel (a)], we observe no hysteresis, even if we decrease the temperature down to $T = 0.005$, in contrast to the results shown in Fig. 3. Since $\rho_{\text{typ}}(0)$ becomes zero, the system certainly goes through a MIT—but to what type of insulator does the system go?

To answer this question, we first look at the frequency-integrated typical DOS N, which can be considered an order parameter in the case of the Anderson transition, as discussed in the beginning of the paper. As can be seen in Fig. 9(a), N becomes very small but is still finite when $\rho_{\text{typ}}(0) \to 0$, suggesting that the transition is *not* of the Anderson type. The nature of the transition can finally be confirmed by analyzing the occupation number per spin n_i as a function of the site energy close to the transition, which can be seen in panel (b). As U increases toward the MIT, all sites become singly occupied, which is a characteristic of the Mott insulator. Although of the Mott type, the Hubbard subbands are strongly

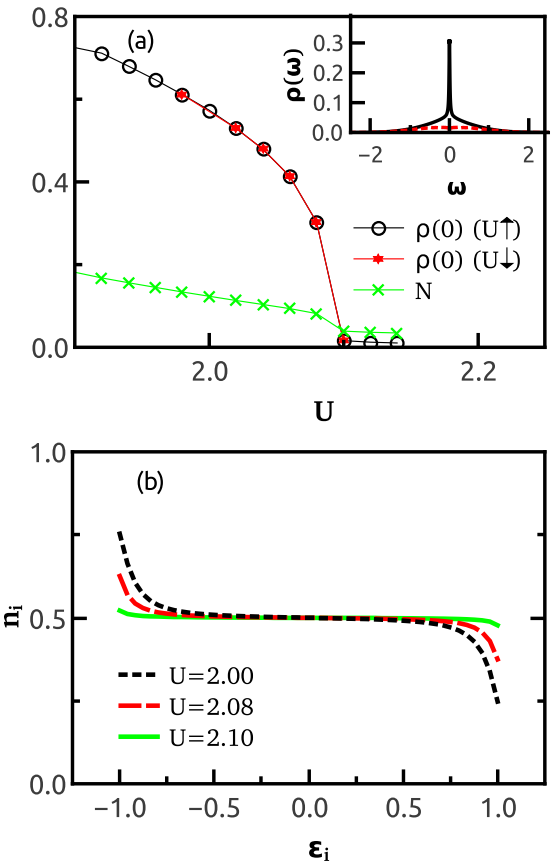

FIG. 9. (Color online) Results obtained within TMT-DMFT for $W = 2.0$ at $T = 0.01$. Panel (a) presents the typical DOS at the Fermi level obtained by increasing U (black circles) and decreasing U (red stars); no coexistence region is observed. In the same panel, we can also see the frequency-integrated typical DOS N as a function of U. The inset shows the typical DOS as a function of frequency for $U = 2.08$ (black solid line) and $U = 2.10$ (red dashed line). Finally, panel (b) presents the occupation number per spin as a function of the site energy as the transition is approached.

reduced for this value of W, as can be seen in the DOS presented in the inset, which is consistent with our expectation that both Mott and Anderson routes to localization are relevant in this regime of $U \approx W$.

Interestingly, our analysis of Fig. 9 suggests that for $W = 2.0$ there exists a transition between a metal and a Mott insulator in the *absence* of a coexistence region. Indeed, according to the phase diagram (Fig. 1), the same behavior is observed in a small range around $U \approx W \approx 2$. According to Figs. 3 and 8, TMT-DMFT predicts that the coexistence region will become (very) narrow when the system is in the $U < W$ regime and disorder increases. When the system enters the $U \sim W$ regime, the two spinodal lines seem to merge and no coexistence is observed, suggesting that T_c abruptly goes to zero due to the Anderson localization effects. Our results are in general agreement with the $T = 0$ phase diagram of Ref. [35] while presenting a much more detailed analysis of the MIT with the vanishing coexistence region.

For $W \gtrsim 2.3$, one can find a direct crossover between the two insulators, Mott and correlated Anderson, without an intermediate metallic phase; this crossover is represented by red squares in our diagram of Fig. 1. To distinguish between the two insulators, we have looked at the occupation number as a function of site energy, as exemplified in Fig. 2. Our results show that when $W < U$, all the sites are singly occupied, characterizing a Mott insulator; when $W > U$, on the other hand, there are sites with energy larger than $U/2$, which are empty, sites with energy smaller than $-U/2$, which have double occupancy, and also sites occupied with one electron, characterizing the two-fluid behavior of the correlated Anderson insulator. According to these results, as might have been expected from the two-fluid picture of the Mott-Anderson insulator [36], the crossover between the two insulators is seen to take place at $W \approx U$.

VI. CONCLUSIONS

In this work, we studied Mott and Anderson routes to localization by using a combination of dynamical mean-field theory (DMFT) and typical medium theory (TMT) to solve the disordered Hubbard model. According to our TMT-DMFT results, Anderson localization has important effects near the Mott transition, especially on the coexistence region of metallic and insulating phases that exists below a critical temperature T_c. In the presence of small and moderate disorder W, the TMT-DMFT transition is qualitatively similar to that in the CPA-DMFT case (which does not describe localization due to disorder), and the main precursors of Anderson localization are seen in the narrowing of the coexistence region in comparison with CPA-DMFT. As the disorder increases further, for $W \gtrsim 2B$ (where B is the bandwidth for $U = W = 0$), the transition occurs at $U \approx W$ and our results indicate that Anderson and Mott routes to localization become equally important. The critical temperature T_c abruptly goes to zero for $W = W^* \approx 1.7B$. For $1.7B < W \sim U < 2.3B$, the typical DOS at the metal-insulator transition is strongly reduced, but the states are nearly half-filled irrespective of the on-site energy, indicating dominantly Mott character of the MIT, although no coexistence region is observed. For even larger disorder, $W > 2.3$, there is a crossover between the Mott and the correlated Anderson insulator.

The observation of a Mott transition without a coexistence region suggests that the nature of the transition has changed from first to second order as disorder increases. For the clean system, it has been shown [41] that at T just above T_c the resistivity as a function of temperature shows a scaling behavior that is compatible with an assumption of quantum criticality. In other words, despite the presence of a coexistence region between the metallic and the Mott insulating phases at small temperatures, at intermediate temperatures the system seems to be controlled by a hidden quantum critical point. Very recently, an experimental work on κ-organics confirmed the presence of this quantum critical regime at intermediate temperatures [44]. In this respect, it will be very important to compare the TMT-DMFT phase diagram and charge transport with the experiments on disordered correlated systems. Preliminary results [46] on introducing disorder by x-ray irradiation show that U_c indeed increases with disorder while T_c also decreases and seems to vanish at some finite disorder.

ACKNOWLEDGMENTS

We acknowledge the HPC facility at Florida State University and CENAPAD-SP, where part of the results were obtained. This work was supported by the Brazilian agencies CNPq, FAPEMIG, and Capes (H.B. and M.C.O.A.), by the Ministry of Education, Science, and Technological Development of the Republic of Serbia under Project No. ON171017 (J.V. and D.T.), and by the NSF, Grants No. DMR-1005751 and No. DMR-1410132 (V.D.).

[1] N. F. Mott, *Metal-Insulator Transitions* (Taylor and Francis, London, 1974).
[2] M. Imada, A. Fujimori, and Y. Tokura, Rev. Mod. Phys. **70**, 1039 (1998).
[3] D. B. McWhan, T. M. Rice, and J. P. Remeika, Phys. Rev. Lett. **23**, 1384 (1969); D. B. McWhan, A. Menth, J. P. Remeika, W. F. Brinkman, and T. M. Rice, Phys. Rev. B **7**, 1920 (1973).
[4] P. Limelette, A. Georges, D. Jérome, P. Wzietek, P. Metcalf, and J. M. Honig, Science **302**, 89 (2003).
[5] S. Lupi, L. Baldassarre, B. Mansart, A. Perucchi, A. Barinov, P. Dudin, E. Papalazarou, F. Rodolakis, J.-P. Rueff, J.-P. Itié, S. Ravy, D. Nicoletti, P. Postorino, P. Hansmann, N. Parragh, A. Toschi, T. Saha-Dasgupta, O. K. Andersen, G. Sangiovanni, K. Held, and M. Marsi, Nat. Commun. **1**, 105 (2010).
[6] F. Kagawa, K. Miyagawa, and K. Kanoda, Nature (London) **436**, 534 (2005).
[7] J. Merino, M. Dumm, N. Drichko, M. Dressel, and R. H. McKenzie, Phys. Rev. Lett. **100**, 086404 (2008).
[8] P. Limelette, P. Wzietek, S. Florens, A. Georges, T. A. Costi, C. Pasquier, D. Jérome, C. Mézière, and P. Batail, Phys. Rev. Lett. **91**, 016401 (2003).
[9] M. Dumm, D. Faltermeier, N. Drichko, M. Dressel, C. Mézière, and P. Batail, Phys. Rev. B **79**, 195106 (2009).
[10] T. Sasaki, Crystals **2**, 374 (2012).
[11] P. W. Anderson, Phys. Rev. **109**, 1492 (1958).
[12] P. A. Lee and T. V. Ramakrishnan, Rev. Mod. Phys. **57**, 287 (1985).
[13] D. M. Basko, I. L. Aleiner, and B. L. Altshuler, Ann. Phys. (N.Y.) **321**, 1126 (2006).
[14] S. Murmann, A. Bergschneider, V. M. Klinkhamer, G. Zurn, T. Lompe, and S. Jochim, Phys. Rev. Lett. **114**, 080402 (2015).
[15] S. S. Kondov, W. R. McGehee, W. Xu, and B. DeMarco, Phys. Rev. Lett. **114**, 083002 (2015).
[16] Y. Sekine, H. Takahashi, N. Môri, T. Matsumoto, and T. Kosaka, Physica B **237-238**, 148 (1997).
[17] M. Matsuura, H. Hiraka, K. Yamada, and Y. Endoh, J. Phys. Soc. Jpn. **69**, 1503 (2000).
[18] J. G. Analytis, A. Ardavan, S. J. Blundell, R. L. Owen, E. F. Garman, C. Jeynes, and B. J. Powell, Phys. Rev. Lett. **96**, 177002 (2006).
[19] A. Georges, G. Kotliar, W. Krauth, and M. J. Rozenberg, Rev. Mod. Phys. **68**, 13 (1996).
[20] E. N. Economou, *Green's Functions in Quantum Physics*, 3rd ed. (Springer, Berlin, 2005).
[21] V. Janiš and D. Vollhardt, Phys. Rev. B **46**, 15712 (1992).
[22] M. Ulmke, V. Janiš, and D. Vollhardt, Phys. Rev. B **51**, 10411 (1995).
[23] M. S. Laad, L. Craco, and E. Müller-Hartmann, Phys. Rev. B **64**, 195114 (2001).
[24] K. Byczuk, M. Ulmke, and D. Vollhardt, Phys. Rev. Lett. **90**, 196403 (2003).
[25] K. Byczuk, W. Hofstetter, and D. Vollhardt, Phys. Rev. B **69**, 045112 (2004).
[26] M. C. O. Aguiar, V. Dobrosavljević, E. Abrahams, and G. Kotliar, Phys. Rev. B **71**, 205115 (2005).
[27] M. M. Radonjić, D. Tanasković, V. Dobrosavljević, and K. Haule, Phys. Rev. B **81**, 075118 (2010).
[28] A. I. Poteryaev, S. L. Skornyakov, A. S. Belozerov, and V. I. Anisimov, Phys. Rev. B **91**, 195141 (2015).
[29] G. Schubert, J. Schleede, K. Byczuk, H. Fehske, and D. Vollhardt, Phys. Rev. B **81**, 155106 (2010).
[30] S. Mahmoudian and V. Dobrosavljević, arXiv:1503.00420.
[31] V. Dobrosavljević, A. A. Pastor, and B. K. Nikolic, Europhys. Lett. **62**, 76 (2003).
[32] M. Janssen, Phys. Rep. **295**, 1 (1998).
[33] C. E. Ekuma, H. Terletska, Z.-Y. Meng, J. Moreno, M. Jarrell, S. Mahmoudian, and V. Dobrosavljevic, J. Phys.: Condens. Matter **26**, 274209 (2014).
[34] C. E. Ekuma, H. Terletska, K.-M. Tam, Z.-Y. Meng, J. Moreno, and M. Jarrell, Phys. Rev. B **89**, 081107(R) (2014).
[35] K. Byczuk, W. Hofstetter, and D. Vollhardt, Phys. Rev. Lett. **94**, 056404 (2005).
[36] M. C. O. Aguiar, V. Dobrosavljević, E. Abrahams, and G. Kotliar, Phys. Rev. Lett. **102**, 156402 (2009).
[37] K. Byczuk, W. Hofstetter, and D. Vollhardt, Phys. Rev. Lett. **102**, 146403 (2009).
[38] H. Kajueter and G. Kotliar, Phys. Rev. Lett. **77**, 131 (1996).
[39] M. Potthoff, T. Wegner, and W. Nolting, Phys. Rev. B **55**, 16132 (1997).
[40] D. Heidarian and N. Trivedi, Phys. Rev. Lett. **93**, 126401 (2004).
[41] H. Terletska, J. Vučičević, D. Tanasković, and V. Dobrosavljević, Phys. Rev. Lett. **107**, 026401 (2011).
[42] J. Vučičević, H. Terletska, D. Tanasković, and V. Dobrosavljević, Phys. Rev. B **88**, 075143 (2013).
[43] J. Vučičević, D. Tanasković, M. J.. Rozenberg, and V. Dobrosavljević, Phys. Rev. Lett. **114**, 246402 (2015).
[44] T. Furukawa, K. Miyagawa, H. Taniguchi, R. Kato, and K. Kanoda, Nat. Phys. **11**, 221 (2015).
[45] G. G. Simeoni, T. Bryk, F. A. Gorelli, M. Krisch, G. Ruocco, M. Santoro, and T. Scopigno, Nat. Phys. **6**, 503 (2010).
[46] K. Kanoda (private communication).

Bad-Metal Behavior Reveals Mott Quantum Criticality in Doped Hubbard Models

J. Vučičević,[1] D. Tanasković,[1] M. J. Rozenberg,[2] and V. Dobrosavljević[3]
[1]Scientific Computing Laboratory, Institute of Physics Belgrade, University of Belgrade, Pregrevica 118, 11080 Belgrade, Serbia
[2]Laboratoire de Physique des Solides, CNRS-UMR8502, Université de Paris-Sud, Orsay 91405, France and Departamento de Física, FCEN, Universidad de Buenos Aires, Ciudad Universitaria Pabellón I, (1428) Buenos Aires, Argentina
[3]Department of Physics and National High Magnetic Field Laboratory, Florida State University, Tallahassee, Florida 32306, USA
(Received 26 December 2014; published 18 June 2015)

Bad-metal (BM) behavior featuring linear temperature dependence of the resistivity extending to well above the Mott-Ioffe-Regel (MIR) limit is often viewed as one of the key unresolved signatures of strong correlation. Here we associate the BM behavior with the Mott quantum criticality by examining a fully frustrated Hubbard model where all long-range magnetic orders are suppressed, and the Mott problem can be rigorously solved through dynamical mean-field theory. We show that for the doped Mott insulator regime, the coexistence dome and the associated first-order Mott metal-insulator transition are confined to extremely low temperatures, while clear signatures of Mott quantum criticality emerge across much of the phase diagram. Remarkable scaling behavior is identified for the entire family of resistivity curves, with a quantum critical region covering the entire BM regime, providing not only insight, but also quantitative understanding around the MIR limit, in agreement with the available experiments.

DOI: 10.1103/PhysRevLett.114.246402 PACS numbers: 71.27.+a, 71.30.+h

Metallic transport inconsistent with Fermi liquid theory has been observed in many different systems; it is often linked to quantum criticality around some ordering phase transition [1,2]. Such behavior is notable near quantum critical points in good conductors, for example in heavy fermion compounds [3,4]. In several other classes of materials, however, much more dramatic departures from conventional metallic behavior are clearly observed, where resistivity still rises linearly with temperature, but it reaches paradoxically large values, well past the Mott-Ioffe-Regel (MIR) limit [5,6]. This bad-metal (BM) behavior [7] was first identified in the heyday of high-temperature superconductivity, in materials such as $La_{2-x}Sr_xCuO_4$ [8]. While the specific copper-oxide family and related high-T_c materials remain ill-understood and marred with controversy, it soon became clear that BM behavior is a much more general feature [6] of materials close to the Mott metal-insulator transition (MIT) [9]. Indeed, it has been clearly identified also in various oxides [10,11], organic Mott systems [12–14], as well as more recently discovered families of iron pnictides [15]. Despite years of speculation and debate, so far its clear physical interpretation has not been established.

To gain reliable insight into the origin of BM behavior, it is useful to examine an exactly solvable model system, where one can suppress all possible effects associated with the approach to some broken symmetry phase, or those specific to low dimensions and a given lattice structure. This can be achieved by focusing on the maximally frustrated Hubbard model, where an exact solution can be obtained by solving dynamical mean-field theory (DMFT) equations [16] in the paramagnetic phase. Although various aspects of the DMFT equation have been studied for more than twenty years, only very recent work [17,18] established how to identify the quantum critical (QC) behavior associated with the interaction-driven Mott transition at half-filling.

Here we present a large-scale computational study across the entire phase diagram, showing that qualitatively different transport behavior is found in doped Mott insulators. Our study reveals a clear and quantitative connection between BM phenomenology and the signatures of Mott quantum criticality, including the characteristic mirror symmetry [19] of the relevant scaling function. We demonstrate that the associated QC region, featuring linear temperature dependence of resistivity around the MIR limit, corresponds to a fully incoherent transport regime. In contrast, the coherent Fermi liquid (FL) regime and even the resilient-quasiparticle regime [20,21] do emerge at lower temperature, but here the resistivity remains well below the MIR limit. Our results provide strong evidence that bad-metallic behavior represents a universal feature of high-temperature transport close to the Mott transition, presenting intriguing parallels with recent ideas based on holographic duality [22,23].

Phase diagram.—We consider a single-band Hubbard model defined by the Hamiltonian

$$H = -t\sum_{\langle i,j\rangle,\sigma}(c^\dagger_{i\sigma}c_{j\sigma} + \text{H.c.}) + U\sum_i n_{i\uparrow}n_{i\downarrow} - \mu\sum_{i,\sigma}c^\dagger_{i\sigma}c_{i\sigma},$$

where t stands for the nearest-neighbor hopping amplitude, U is the on-site interaction, and μ denotes the chemical potential. The creation and annihilation operators for spin orientation σ are denoted by $c^\dagger_\sigma$ and c_σ, and $n_{i\sigma} = c^\dagger_{i\sigma}c_{i\sigma}$. We solve the DMFT equations using the continuous-time quantum Monte Carlo (CTQMC) algorithm for the impurity solver [24–26]. We focus on the paramagnetic solution which is a physically justified assumption for frustrated lattices. We

use the semielliptic bare density of states and set the half-bandwidth $D = 1$ as the unit of energy. This corresponds to the infinitely dimensional Bethe lattice, as well as the fully connected lattice with random hopping amplitudes [16].

At half-filling, strong enough on-site interaction U opens a spectral gap at the Fermi level and produces the Mott insulating state [16]. The Mott insulator can also be destroyed by adding electrons to the system, i.e., raising the chemical potential μ. When μ reaches the upper Hubbard band, the system is once again conducting [20]. In both cases, at low temperature the transition is of the first order, and features a pronounced jump in the value of resistivity and other quantities [27]. Around the first-order transition line, a small coexistence region is present, where both metallic and insulating phases are locally stable. Our calculations show (see the Supplemental Material, Secs. I and II [28]) that the critical end-point temperature $T_c(U)$ for the doping-driven transition rapidly drops with increasing interaction, and at $U = 4$ it already is less than 10% of that at half-filling. This is illustrated in Fig. 1(a). At the critical end-point (red dots), the two solutions merge, and above it no true distinction between the phases exists; only a rapid crossover is observed upon variation of U or μ. Previous work [17,18] examined the vicinity of the interaction-driven MIT at half-filling; here we analyze the broad finite temperature crossover region between the half-filled Mott insulator and the doped Fermi liquid state [27,34–36]. This bad-metal regime, displaying very different transport behavior than that found at half-filling, is the main focus of this work.

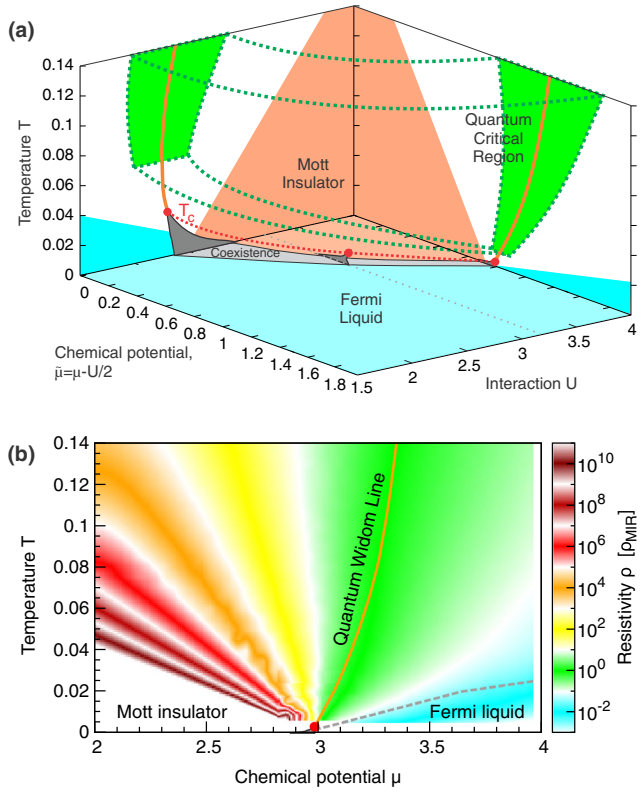

FIG. 1 (color online). (a) Phase diagram of the maximally frustrated Hubbard model. The quantum critical scaling is observed in the green region which extends to lower temperatures as T_c (red dots) is reduced. (b) Color plot of the resistivity in the (μ, T) plane for $U = 4$. The quantum Widom line (see text) passes through the crossover region where the resistivity is around the MIR limit. The coexistence region (gray) is barely visible on the scale of this plot.

In Fig. 1(b), we color-code the resistivity in the (μ, T) plane, calculated for $U = 4$. The resistivity is given in units of the Mott-Ioffe-Regel limit ρ_{MIR} which is defined as the highest possible resistivity in a Boltzmann semiclassical metal, corresponding to the scattering length of one lattice spacing. Numerical value for ρ_{MIR} is taken consistently with Ref. [21]. At $\mu = U/2$, the system is half-filled. At approximately $\mu = U - D = 3$, the Fermi level enters the upper Hubbard band, and a first-order doping-driven MIT is observed at temperatures below $T_c = 0.003D$. While the chemical potential is within the gap, a clear activation behavior, $\rho \sim e^{E_g/T}$, is found at low temperatures. On the metallic side of the MIT, due to the strong electron-electron scattering, the resistivity grows rapidly with temperature, and typical Fermi-liquid behavior is observed only below rather low coherence temperature T_{FL} (denoted with the gray dashed line).

Quantum critical scaling.—In the standard scenario for quantum criticality [1,9], the system undergoes a zero-temperature phase transition at a critical value of some control parameter $g = g_c$, and within a V-shaped finite temperature region, physical quantities display scaling behavior of the form $A(g, T) = A_c(T)F[T/(g - g_c)^{z\nu}]$. Mott MIT is a first-order phase transition [37], but the corresponding coexistence region is confined to extremely low temperatures, and at temperatures sufficiently above the critical end-point T_c, the quantum effects are expected to set in [1], and restore the QC behavior.

To test the QC scaling hypothesis in the case of a Mott transition, one must first identify the appropriate $g_c(T)$ instability trajectory [17,18] which enters the argument of the scaling function (for illustration, see the Supplemental Material, Fig. 2 [28]). $g_c(T)$ marks, on the phase diagram, a trajectory where the system is least stable (i.e., is found in equal proximity to both the metal and the insulator), and is therefore most prone to fluctuations. The relevant thermodynamic stability is most easily determined from the curvature λ of the free energy functional $\mathcal{F}[G(i\omega_n)]$ near its global minimum; this can be numerically determined by monitoring the convergence rate in the DMFT self-consistency loop [17]. Having in mind the analogy of this definition with the standard Widom crossover line for classical liquid-gas transitions [38], we refer to the instability line as the "quantum Widom line" (QWL) [18].

We carried out a careful λ analysis for the doped Mott insulator (see the Supplemental Material, Sec. III [28]), and we display the resulting QWL trajectory $\mu^*(T)$ as an orange line in all plots [throughout this Letter, an asterisk in the superscript indicates physical quantities evaluated along the

QWL; e.g., $\rho^*(T)$ is resistivity calculated at temperature T at $\mu = \mu^*(T)$]. The QC region (green) spreads above the critical end point (red points and dotted line) and quickly extends to much lower temperatures as T_c is reduced [Fig. 1(a)]. The QWL, separating the metallicalike and the insulatinglike behavior, marks the center of the corresponding QC region, where the resistivity curves are expected to display the scaling behavior of the form

$$\rho(\mu, T) = \rho^*(T) F[T/T_0(d\mu)]. \quad (1)$$

Here the parameter T_0 should assume power-law dependence on the deviation from the QWL: $T_0(d\mu) \sim d\mu^{z\nu}$, with $d\mu = \mu - \mu^*(T)$.

To check validity of the scaling hypothesis, Eq. (1), we calculate the resistivity along the lines parallel to the QWL, as shown in Fig. 2(a). We find that, for the doped Mott insulator, the resistivity shows very weak temperature dependence along the QWL. In particular, above $T = 0.08$, it follows the line of constant resistivity *which coincides* with the MIR limit, $\rho^*(T > 0.08) = \rho_{\mathrm{MIR}}$ (in contrast to the behavior previously established at half-filling [17,18], where $\rho \gg \rho_{\mathrm{MIR}}$ along the QWL). In fact, all curves converge *precisely* to the MIR limit at high temperatures, suggesting its fundamental role in characterizing the metal-insulator crossover for doped Mott insulators. The curves also display the characteristic bifurcation upon reducing temperature, and a clear change in trend upon crossing the QWL. The scaling analysis confirms that all the curves indeed display fundamentally the same functional dependence on temperature, and that they all can be collapsed onto two distinct branches of the corresponding scaling function [Fig. 2(b)]. The scaling exponent has been estimated to be $z\nu \approx 1.35 \pm 0.1$ for both branches of the scaling function, which display mirror symmetry [17,19] over almost two decades in T/T_0, and the scaling covers more than 3 orders of magnitude in resistivity.

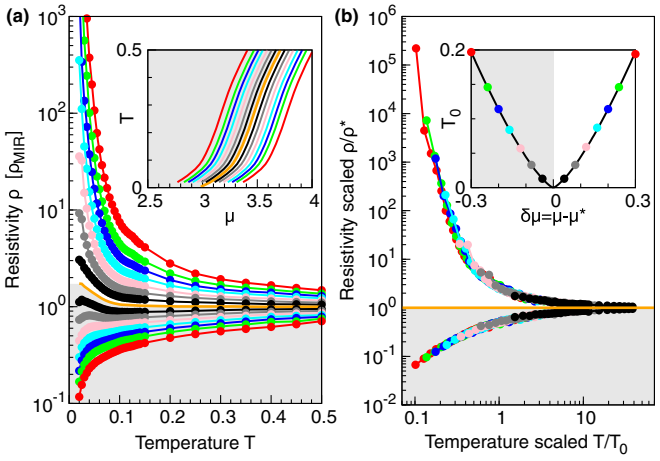

FIG. 2 (color online). (a) Family of resistivity curves calculated along lines parallel to the QWL (orange). (b) Upon rescaling the temperature with adequately chosen parameter T_0, the resistivity curves collapse and reveal mirror symmetry of metalliclike and insulatinglike behavior around the QWL. T_0 depends on the distance from the QWL as $T_0(d\mu) \sim d\mu^{z\nu}$, with $z\nu \approx 1.35$.

Bad-metal behavior.—We demonstrated the emergence of clearly defined quantum critical behavior through an analysis of the (μ, T) phase diagram, with $d\mu = \mu - \mu^*$ as the scaling parameter. From the experimental point of view, it is, however, crucial to identify the corresponding QC region in the (δ, T) plane and understand its implications for the form of the resistivity curves for fixed level of doping $\rho(T)|_\delta$. By performing a careful calculation of the $\delta(\mu, T)$ dependence (see the Supplemental Material, Fig. 4 [28]), it is straightforward to replot our phase diagram and resistivity curves in the (δ, T) plane. Remarkably, we find that the quantum critical scaling region covers a broad range of temperatures and dopings, and almost perfectly matches the region of the well-known bad-metal transport [21,39], characterized by the absence of long-lived quasiparticles and linear $\rho(T)|_\delta$ curves. We first analyze the (δ, T) phase diagram in detail, and then establish a connection between the slope of $\rho(T)|_\delta$ curves in the bad-metal regime and the QC scaling exponent νz.

In Fig. 3(a), we show the phase diagram of the doped Mott insulator. At $T = 0$, the Mott insulator phase is found exclusively at zero doping. At low enough temperature and finite doping, characteristic Fermi liquid behavior is always observed. Here, the resistivity is quadratic in temperature, while a clear Drude peak is observed at low frequencies in optical conductivity and density of states (see the Supplemental Material, Fig. 5 [28]). The coherence temperature T_{FL} is found to be proportional to the amount of doping δ, however, with a small prefactor of about 0.1, in agreement with Refs. [20,21]. In a certain temperature range above T_{FL}, a Drude peak is still present as well as the quasiparticle resonance in the single-particle density of states, but the resistivity no longer follows the FL T^2 dependence. This corresponds to the resilient-quasiparticle (RQP) transport regime, which was carefully examined in Ref. [21]. At even higher temperatures, the temperature-dependent resistivity at fixed doping $\rho(T)|_\delta$ enters a prolonged linear regime [see Fig. 3(b)] [40], which is accompanied by the eventual disappearance of the Drude peak around the MIR limit. This behavior is usually referred to as the bad-metal regime [21]. The resistivity is comparable to the MIR limit throughout the BM region, and the QWL (as determined from our thermodynamic analysis) passes through its middle.

The region of linear $\rho(T)|_\delta$ dependence is found to be completely encompassed by the QC scaling region between the dashed lines on Fig. 3(a) (see the Supplemental Material, Sec. VI [28]). We therefore expect that the emergence of the linear T dependence of the resistivity, as well as the doping dependence of its slope, should be directly related to the precise form of the corresponding scaling function. Indeed, at high temperature and close

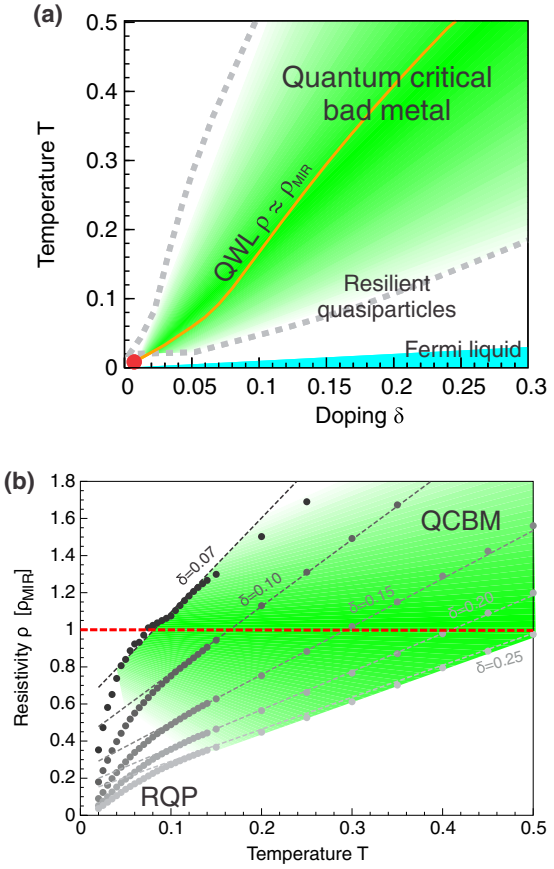

FIG. 3 (color online). (a) DMFT phase diagram of the doped Mott insulator on a frustrated lattice. The bad-metal (green) region matches perfectly the region of quantum critical scaling. (b) The bad-metal regime features linear temperature dependence of resistivity with the slope roughly proportional to an inverse power law of doping which we find to be a consequence of underlying quantum criticality.

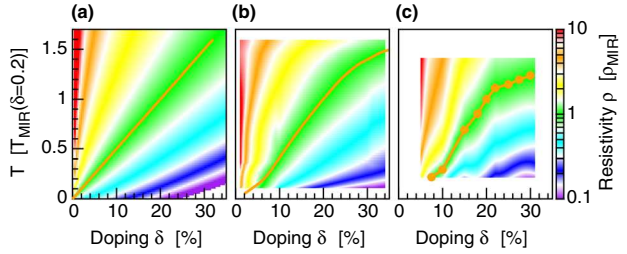

FIG. 4 (color online). Resistivity given by (a) the semianalytical formula obtained from the scaling hypothesis, (b) DMFT result, and (c) the experimental result on cuprate $La_{2-x}Sr_xCuO_4$ samples from Ref. [8].

to the QWL, the argument of the scaling function $x = d\mu/T^{1/z\nu}$ is always small, and the scaling function can be linearized, viz., $\tilde{F}(x) \approx 1 + Ax + \cdots$. We find that the coefficient A has the numerical value $A \approx -0.74$. The functional form for $\rho(T)|_\delta$ close to the QWL is then directly determined by the behavior of the scaling parameter $x(T)|_\delta$. We find that $x(T)|_\delta$ is a linear function in a wide range of temperatures around $T^*(\delta)$. Then, close to the QWL, the resistivity is well approximated by a linear function of the form

$$\rho(T)|_\delta \approx \rho^*(\delta)\left\{1 + A\frac{\partial x}{\partial T}\Big|_{\delta,T=T^*(\delta)}[T - T^*(\delta)]\right\}. \quad (2)$$

Furthermore, the slope of the scaling argument at the QWL can be expressed as $(\partial x/\partial T)|_{\delta,T=T^*(\delta)} = \{\chi^*(\delta)(dT^*/d\delta)\times [T^*(\delta)]^{1/z\nu}\}^{-1}$, where $\chi^*(\delta) = (\partial\delta/\partial\mu)|_{T=T^*(\delta)}$. Here, we observe that the charge compressibility is nearly constant along the QWL, $\chi^*(\delta) \approx \chi^* = 0.33$ (see the Supplemental Material, Fig. 6 [28]), which may be interpreted as another manifestation of the quantum critical behavior we identified. $T^*(\delta)$ is approximately a linear function $T^*(\delta) \approx K_0 + K\delta$, where $K \approx 2$ and K_0 is small. In Fig. 3(b), we compare the approximation stated in Eq. (2) with the DMFT result and find excellent agreement.

Finally, noting that for $\delta > 5\%$, $\rho^*(\delta) = \rho_{\rm MIR}$, we arrive at the central result of this Letter,

$$\rho_{\rm QCBM}(T)|_\delta \approx \rho_{\rm MIR}[1 + C\delta^{-1/z\nu}(T - K\delta)]. \quad (3)$$

In the quantum critical bad-metal regime, the resistivity has a linear temperature dependence with the slope decreasing as a power $-1/z\nu$ of doping. This demonstrates a direct connection of the universal high-temperature behavior in the bad-metal regime with the (zero-temperature) quantum phase transition. The MIR limit of the resistivity is reached at temperature roughly proportional to the amount of doping, $T^*(\delta) \propto \delta$, since the doping level sets the main energy scale in the problem. The result of this simplified scaling formula is color-plotted in Fig. 4(a) (with $C = 0.69$, $K = 1.97$, and $z\nu = 1.35$) and shown to capture the features of the full DMFT solution at high temperatures.

Discussion.—Sufficiently systematic experimental studies of doped Mott insulators, covering an appreciable range of doping and temperature, remain relatively scarce. Still, approximately linear temperature dependence of the resistivity at high temperatures with a slope that decreases with doping has been observed, most notably in the seminal work of Takagi *et al.* [8] on $La_{2-x}Sr_xCuO_4$. To make a qualitative comparison with our theory and to highlight a universal link of bad-metal behavior and quantum criticality associated with the Mott metal-insulator transition, in Fig. 4 we color code the reported experimental data; here the temperature is shown in units of $T_{\rm MIR}$ at 20% doping and the resistivity is given in units of $\rho_{\rm MIR}$, which in this material is estimated as 1.7 mΩ cm. The experimental results presented in Fig. 4(c) cover the temperature range of 150–1000 K at 5% to 30% doping. Here one observes a striking similarity between DMFT theory and the experiment, as already noted in early studies [39–41]. We established this result by focusing on an exactly solvable model, where all ordering tendencies are suppressed, and single-site DMFT becomes exact. Real materials, of course,

exist in finite (low) dimensions where systematic corrections to DMFT need to be included [42–45]. In many cases [46–48], these nonlocal corrections prove significant only at sufficiently low temperatures. Then our findings should be even quantitatively accurate in the high-temperature incoherent regime, as in the very recent experiments on organic materials [49] for the case of half-filling.

We thank E. Abrahams, H. Alloul, S. Hartnoll, N. Hussey, K. Kanoda, A. Schofield, Q. Si, J. Schmalian and M. Vojta for useful discussions. J. V. and D. T. acknowledge support from the Serbian Ministry of Education, Science and Technological Development under Project No. ON171017. V. D. was supported by the NSF, Grants No. DMR-1005751 and No. DMR-1410132. Numerical simulations were run on the AEGIS e-Infrastructure, supported in part by FP7 projects EGI-InSPIRE and PRACE-3IP. J. V., D. T., and M. J. R. acknowledge support from the bilateral French-Serbian PHC Pavle Savic 2012-2013 grant.

[1] S. Sachdev, *Quantum Phase Transitions* (Cambridge University Press, Cambridge, England, 1999).
[2] H. v. Löhneysen, A. Rosch, M. Vojta, and P. Wölfle, Rev. Mod. Phys. **79**, 1015 (2007).
[3] G. R. Stewart, Rev. Mod. Phys. **56**, 755 (1984).
[4] G. R. Stewart, Rev. Mod. Phys. **73**, 797 (2001).
[5] O. Gunnarsson, M. Calandra, and J. E. Han, Rev. Mod. Phys. **75**, 1085 (2003).
[6] N. E. Hussey, K. Takenaka, and H. Takagi, Philos. Mag. **84**, 2847 (2004).
[7] V. J. Emery and S. A. Kivelson, Phys. Rev. Lett. **74**, 3253 (1995).
[8] H. Takagi, B. Batlogg, H. L. Kao, J. Kwo, R. J. Cava, J. J. Krajewski, and W. F. Peck, Phys. Rev. Lett. **69**, 2975 (1992).
[9] V. Dobrosavljević, N. Trivedi, and J. M. Valles, Jr., *Conductor-Insulator Quantum Phase Transitions* (Oxford University Press, New York, 2012).
[10] M. M. Qazilbash, K. S. Burch, D. Whisler, D. Shrekenhamer, B. G. Chae, H. T. Kim, and D. N. Basov, Phys. Rev. B **74**, 205118 (2006).
[11] A. W. Tyler, A. P. Mackenzie, S. NishiZaki, and Y. Maeno, Phys. Rev. B **58**, R10107 (1998).
[12] P. Limelette, P. Wzietek, S. Florens, A. Georges, T. A. Costi, C. Pasquier, D. Jérome, C. Mézière, and P. Batail, Phys. Rev. Lett. **91**, 016401 (2003).
[13] F. Kagawa, K. Miyagawa, and K. Kanoda, Nature (London) **436**, 534 (2005).
[14] J. Merino, M. Dumm, N. Drichko, M. Dressel, and R. H. McKenzie, Phys. Rev. Lett. **100**, 086404 (2008).
[15] M. M. Qazilbash, J. J. Hamlin, R. E. Baumbach, L. Zhang, D. J. Singh, M. B. Maple, and D. N. Basov, Nat. Phys. **5**, 647 (2009).
[16] A. Georges, G. Kotliar, W. Krauth, and M. J. Rozenberg, Rev. Mod. Phys. **68**, 13 (1996).
[17] H. Terletska, J. Vučičević, D. Tanasković, and V. Dobrosavljević, Phys. Rev. Lett. **107**, 026401 (2011).
[18] J. Vučičević, H. Terletska, D. Tanasković, and V. Dobrosavljević, Phys. Rev. B **88**, 075143 (2013).
[19] V. Dobrosavljević, E. Abrahams, E. Miranda, and S. Chakravarty, Phys. Rev. Lett. **79**, 455 (1997).
[20] A. Camjayi, R. Chitra, and M. J. Rozenberg, Phys. Rev. B **73**, 041103 (2006).
[21] X. Deng, J. Mravlje, R. Žitko, M. Ferrero, G. Kotliar, and A. Georges, Phys. Rev. Lett. **110**, 086401 (2013).
[22] A. Donos and S. A. Hartnoll, Nat. Phys. **9**, 649 (2013).
[23] S. Hartnol, arXiv:1405.3651.
[24] P. Werner, A. Comanac, L. de Medici, M. Troyer, and A. J. Millis, Phys. Rev. Lett. **97**, 076405 (2006).
[25] K. Haule, Phys. Rev. B **75**, 155113 (2007).
[26] E. Gull, A. J. Millis, A. I. Lichtenstein, A. N. Rubtsov, M. Troyer, and P. Werner, Rev. Mod. Phys. **83**, 349 (2011).
[27] G. Kotliar, S. Murthy, and M. J. Rozenberg, Phys. Rev. Lett. **89**, 046401 (2002).
[28] See Supplemental Material at http://link.aps.org/supplemental/10.1103/PhysRevLett.114.246402, which includes Refs. [29–33], for numerical details, determination of T_c and quantum Widom line, and scaling analysis.
[29] D. S. Fisher, G. Kotliar, and G. Moeller, Phys. Rev. B **52**, 17112 (1995).
[30] M. J. Rozenberg, R. Chitra, and G. Kotliar, Phys. Rev. Lett. **83**, 3498 (1999).
[31] M. J. Case and V. Dobrosavljević, Phys. Rev. Lett. **99**, 147204 (2007).
[32] M. Jarrell and J. E. Gubernatis, Phys. Rep. **269**, 133 (1996).
[33] A. W. Sandvik, Phys. Rev. B **57**, 10287 (1998).
[34] R. Žitko, D. Hansen, E. Perepelitsky, J. Mravlje, A. Georges, and B. S. Shastry, Phys. Rev. B **88**, 235132 (2013).
[35] P. Werner and A. J. Millis, Phys. Rev. B **75**, 085108 (2007).
[36] A. Amaricci, G. Sordi, and M. J. Rozenberg, Phys. Rev. Lett. **101**, 146403 (2008).
[37] P. Nozières, Eur. Phys. J. B **6**, 447 (1998).
[38] G. G. Simeoni, T. Bryk, F. A. Gorelli, M. Krisch, G. Ruocco, M. Santoro, and T. Scopigno, Nat. Phys. **6**, 503 (2010).
[39] T. Pruschke, D. L. Cox, and M. Jarrell, Phys. Rev. B **47**, 3553 (1993).
[40] M. Jarrell and T. Pruschke, Phys. Rev. B **49**, 1458 (1994).
[41] The high-temperature slope of the resistivity curves is estimated to be proportional to δ^{-1} in Ref. [40]. However, only four doping levels were considered and having in mind the uncertainty of the analytical continuation, it is difficult to distinguish this value from our slope $\delta^{-1/z\nu} = \delta^{-1/1.35}$. Our numerical data are in agreement with high precision CTQMC data from Ref. [21].
[42] T. Maier, M. Jarrell, T. Pruschke, and M. H. Hettler, Rev. Mod. Phys. **77**, 1027 (2005).
[43] G. Kotliar, S. Y. Savrasov, K. Haule, V. S. Oudovenko, O. Parcollet, and C. A. Marianetti, Rev. Mod. Phys. **78**, 865 (2006).
[44] G. Sordi, P. Sémon, K. Haule, and A.-M. S. Tremblay, Phys. Rev. B **87**, 041101 (2013).
[45] E. Gull, O. Parcollet, and A. J. Millis, Phys. Rev. Lett. **110**, 216405 (2013).
[46] A. Georges, Ann. Phys. (Berlin) **523**, 672 (2011).
[47] D. Tanasković, K. Haule, G. Kotliar, and V. Dobrosavljević, Phys. Rev. B **84**, 115105 (2011).
[48] J. Kokalj and R. H. McKenzie, Phys. Rev. Lett. **110**, 206402 (2013).
[49] T. Furukawa, K. Miyagawa, H. Taniguchi, R. Kato, and K. Kanoda, Nat. Phys. **11**, 221 (2015).

Supplementary Information: Bad-metal behavior reveals Mott quantum criticality in doped Hubbard models

J. Vučičević,[1] D. Tanasković,[1] M. J. Rozenberg,[2] and V. Dobrosavljević[3]

[1] *Scientific Computing Laboratory, Institute of Physics Belgrade, University of Belgrade, Pregrevica 118, 11080 Belgrade, Serbia.*
[2] *Laboratoire de Physique des Solides, CNRS-UMR8502, Université de Paris-Sud, Orsay 91405, France.*
[3] *Department of Physics and National High Magnetic Field Laboratory, Florida State University, Tallahassee, Florida 32306, USA.*

I. NUMERICAL DETAILS: THE DMFT LOOP AND THE IMPURITY SOLVER

We have used the CTQMC impurity solver as implemented by K. Haule in Ref. 1. We have used $4-6\times10^9$ Monte Carlo steps. When $T>0.14$, the high frequency tail was calculated from the atomic limit and Hubbard-I approximation was used otherwise. At high temperatures, 10-15 DMFT iterations were usually sufficient to reach the self-consistent solution with the accuracy $|G^i(i\omega_0)-G^{i-1}(i\omega_0)|\approx10^{-4}$, where $\omega_0=\frac{1}{2}\pi T$. In the coexistence region, we used a larger number of DMFT iterations (up to 30) to test the stability of the obtained solution.

II. DETERMINATION OF T_c

T_c from the position of the spinodals

The first order phase transition is most easily observed by looking at the occupation number. At very low temperature, while the chemical potential is within the spectral gap, filling is roughly a constant, i.e. $n(\mu)\approx0.5$. When the chemical potential reaches the upper Hubbard band, a quasi particle peak forms abruptly at its lower edge causing an immediate transfer of spectral weight from the lower Hubbard band to the vicinity of the Fermi level [2, 3]. This is observed as a jump in the occupancy from nearly half-filling to around 2-3% doping. An insulating solution is not possible when μ is in the upper Hubbard band, hence its bottom edge determines the insulating (right) spinodal. However, a metallic solution is possible even when μ is in the gap. This type of state features an in-gap quasi-particle peak [4] and is observed in the coexistence region. The lowest value of the chemical potential at which the quasi particle peak can survive constitutes the metallic (left) spinodal. The disappearance of the QP peak at the metallic spinodal is also abrupt, and occurs at finite doping. Therefore, there is a range of doping that is not achievable locally at any value of the chemical potential, but only globally through phase separation. With increasing temperature, the forbidden doping range shrinks and disappear together with the hysteresis loop, precisely at T_c [5, 6]. Note also, that the range of forbidden doping vanishes at $T=0$ as well, where a metallic solution is possible even at infinitesimal doping [2], although in this case particle-hole symmetry is broken and $\mu\neq U/2$. In Supplementary Figure 1a,b we show the hysteresis curves of the occupancy for two values of interaction U. The position of spinodals and the width of the coexistence region are easily determined from the jumps in $n(\mu)$. We considered the lowest temperature at which no coexistence is observed to be the critical temperature. Note also that due to the numerical error of the CTQMC, some unphysical doping is observed in the insulating state at the lowest temperatures. We were not able to obtain physically meaningful results below $T\approx0.0015$ and this is the lowest temperature at which we have found the method to be reliable. The numerical error from the CTQMC becomes significant at low temperature and a precise assessment of T_c's lower than ≈0.002 proves very difficult. The coexistence regions at the two values of U are shown in Supplementary Figure 1c and d. The $T=0$ position of the left spinodal is taken from the ED calculation found in [4] and seems to fit well our finite temperature results.

T_c from the charge compressibility

The alternative way of determining T_c is by looking at the uniform charge susceptibility $\chi=\frac{\partial n}{\partial\mu}$. Precisely at the critical point, χ is divergent and above T_c, there is a line of maxima in $\chi(\mu)|_T$. Furthermore, it can be shown [7] that close to the critical point $\chi^{-1}\sim\frac{T-T_c}{a+b(T-T_c)}$. This is useful as one can extrapolate the values of $\chi^{-1}_{\max}(T)$ to lower temperatures and see where it goes to zero. However, such method is of inferior accuracy compared to the direct observation of the coexistence, and we use it only for cross-checking of our results. In Fig. 1e we show such calculation in the case of $U=3.2$.

T_c from the λ analysis

In Supplementary Figure 1f we plot the values of λ along the instability line (see the next Section). Close to the the critical point, it is very difficult to make a precise estimate of the DMFT convergence rate, as high con-

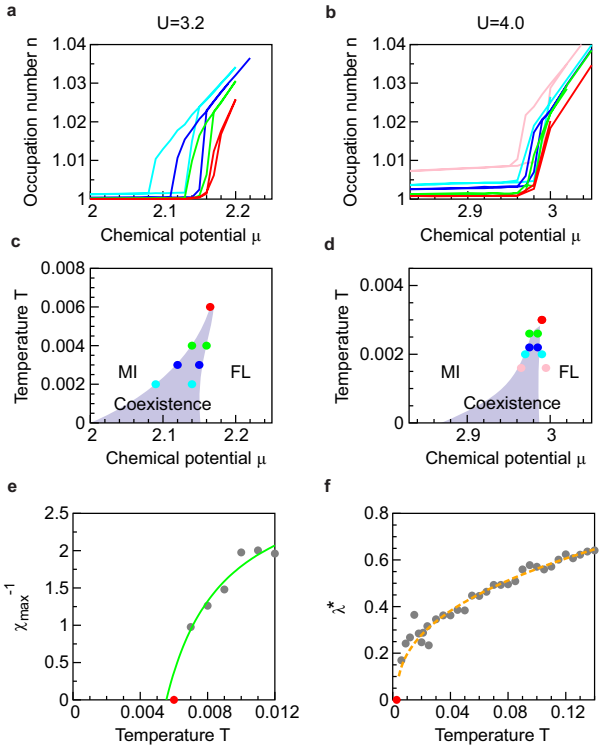

Figure 1: **Coexistence region of the first-order doping-driven Mott metal-insulator transition can be determined in different ways.** (a),(b),(c),(d) The position of spinodals can be determined from the jumps in the occupation number. In the coexistence region, two types of solution are possible, depending on the initial guess in the DMFT procedure. This is observed as a hysteresis loop in the occupation number and other quantities. (e),(f) Precisely at the critical point, physical quantities often have extremal values (zero or infinity). By extrapolating such quantities from higher temperatures, one can estimate the critical temperature. (e) The maxima of the inverse charge compressibility with respect to the chemical potential can be extrapolated to obtain a good estimate for T_c. (f) The values of λ along the instability line $\mu^*(T)$ become scattered and overestimated close to the critical point, due to numerical error from the CTQMC. This makes it unpractical to to use extrapolation of λ^* for estimation of T_c.

vergence is not achievable at all. The low temperature values are therefore much more scattered and systematically overestimated. Although in principle one could estimate T_c from higher temperatures by extrapolating $\lambda^*(T) \equiv \lambda(\mu^*(T), T)$, the numerical noise makes such a method very impractical. Further difficulty lies in the possibility of $\lambda^*(T)$ changing trend before going to zero, which introduces additional systematic error to the estimate of T_c.

III. QUANTUM WIDOM LINE AND THE λ ANALYSIS

In our previous work [8], we have discussed a possible generalization of the Widom line (originally defined in the context of classical liquid-gas transitions [9]), to strictly zero-temperature (quantum) phase transitions (see Supplementary Fig. 2). The most natural way of defining such a quantum Widom line is by looking at the free-energy landscape around the ground state of the system, as it is well defined in all physical models. Regardless of the specifics of the phase transition, precisely at the critical point, the free energy minimum is flat, i.e. its curvature λ is zero. At higher temperatures, this leads to a line of minima in λ with respect to the parameter that is driving the transition (at half-filling we had $\frac{\partial \lambda}{\partial U}\big|_T = 0$). It is at those minima that the fluctuations are most pronounced - the system is "equally close" to the two competing phases and thus the least stable. Now we utilize this concept in the case of doping-driven Mott transition, and at each temperature search for the minimum value of λ with respect to the chemical potential.

In practice, we calculate λ by monitoring the convergence rate of the iterative DMFT procedure [10]. Given the model parameters, the free energy functional $\mathcal{F}_{U,T,\mu}[G(i\omega_n)]$ yields a smooth manifold in the Hilbert space of the Green's functions. Being Taylor expandable, the local environment of any free-energy minimum has to be parabolic. Thus, in the advanced stage of the DMFT procedure, i.e. close to the self-consistent solution, a steady, exponential convergence should be observed. The curvature λ is then directly related to the exponent of

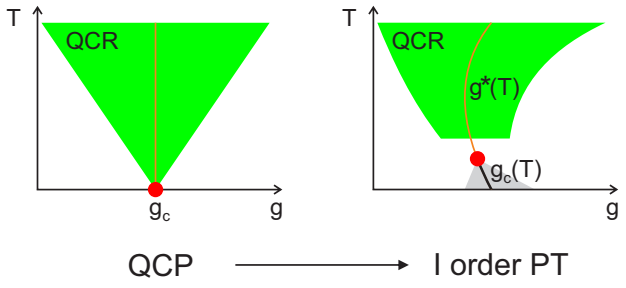

Figure 2: **Standard QCP scenario is modified in the case of the Mott MIT.** At low temperature, the Mott MIT is of (weakly) first order character, and features a coexistence region (gray) where both phases are locally stable. However, at temperatures sufficiently above the (very low) critical temperature T_c, the QC scaling holds (green). The critical transition-driving parameter g_c is replaced by a more general, temperature dependent quantity. Below T_c this is the line of first order transition $g_c(T)$ where the two states are equally favorable. Above T_c it is the line of "maximal instability" of the ground state (see text), or the quantum Widom line $g^*(T)$.

the functional dependence of the difference between the consecutive solutions versus the iteration index. When determining the convergence rate, however, it is not always sufficient to look at the Green's function in only the lowest Matsubara frequency, and one must use the generalized Raileigh-Ritz (RR) formula [11]

$$\lambda_i = 1 - \sum_n \frac{|G_n^{i+1} - G_n^i||G_n^i - G_n^{i-1}|}{|G_n^{i+1} - G_n^i|^2}, \qquad (1)$$

where i stands for the iteration index, and ideally, $\lambda = \lim_{i\to\infty} \lambda_i$. However, the highest achievable level of convergence is determined by the amount of statistical noise in the CTQMC result, and when it is reached, $G(i\omega_n)$ just fluctuates around the self-consistent solution, and no further convergence is observed. Especially near the critical point, CTQMC error becomes substantial and a high convergence can not be reached at all. Here, typically only a few iterations are available for the estimation of λ as most of the parabolic region is below the level of numerical noise, and one must look carefully for the range of iterations in which a steady exponential convergence is observed.

The result presented with gray dots in Fig. 3a is obtained by employing the RR formula from equation (1) at each iteration i, and then taking the average over the set of 5 consecutive iterations that shows the least variance, i.e. the one corresponding to the period of the steadiest exponential convergence.

Away from half-filling, however, there are additional difficulties. Namely, $G(i\omega_n)$ is complex, which means that it has additional degrees of freedom as compared to its purely imaginary analogue at particle-hole symmetry. Thus, the fluctuations encountered in the convergence rate of $G(i\omega_n)$ are more severe, and the λ-analysis is harder to perform compared to the half-filled case. This is why the data points presented with gray dots in Fig. 3 exhibit considerable scattering, but the overall trend is still rather obvious. In all of the calculations regarding the quantum critical (QC) scaling analysis, we use the smooth fit (orange dashed line) as the instability line and denote it with $\mu^*(T)$. Note that no other smoothing has been performed on the data, and all the minima are estimated automatically from the raw λ results. Although there are considerable error bars on each $\mu^*(T)$ value, the high resolution in temperature increases the certainty of the result.

It is interesting that $\mu^*(T)$ is very close to the line of maxima of the second derivative of the occupation number versus the chemical potential, $\left.\frac{\partial^2 n}{\partial \mu^2}\right|_T = \max$. This is the place where $n(\mu)$ changes trend, and as expected, the instability line separates the metallic-like and insulating-like behavior on the phase diagram. Also note that $\mu^*(T)$ roughly follows an iso-resistive curve and so the resistivity does not change considerably along the instability line. At $T > 0.08$ ρ^* is found to be constant and equal to the Mott-Ioffe-Regel (MIR) limit. Above $T = 0.14$, λ-analysis can not give reliable results as the minimum in $\lambda(\mu)|_T$ becomes very shallow, i.e. of depth comparable to the level of numerical noise. Throughout the paper we extrapolate the instability line to high temperatures $T > 0.14$ by imposing the criterion $\rho^* = \rho_{\mathrm{MIR}}$. Also note that at very low temperature, the actual form of $\rho(\mu^*(T), T)$ depends strongly on the precise values of $\mu^*(T)$ because, in this region, the resistivity changes rapidly with the chemical potential.

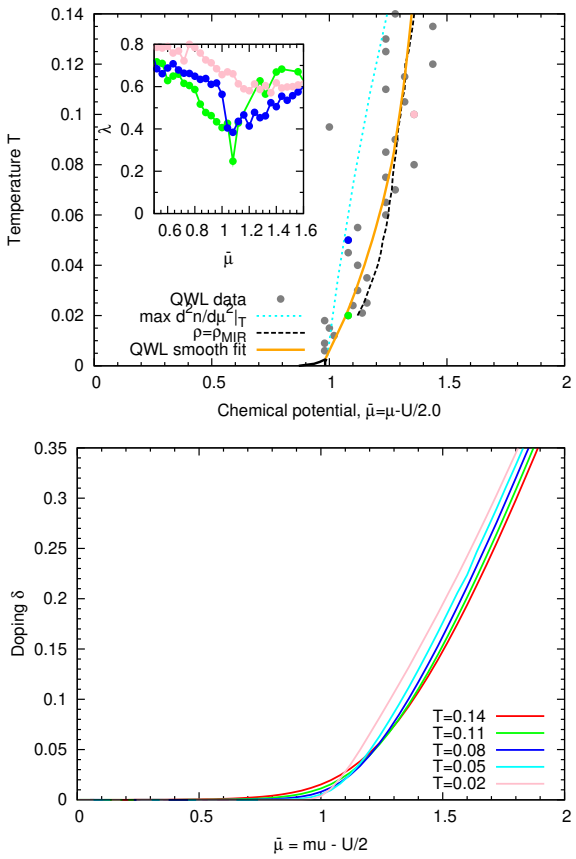

Figure 3: **The instability line $\mu^*(T)$ (orange dashed) corresponds to the minima in $\lambda(\mu)|_T$, which is related to the convergence rate of the DMFT loop.** (a) The precision of λ results is limited by the statistical noise in CTQMC. However, the minima in $\lambda(\mu)|_T$ are still clearly present, and $\mu^*(T)$ can be determined with satisfactory accuracy. At high temperature, QWL is found to coincide with the iso-resistive curve of the MIR limit (black dashed), which is then used to extrapolate the QWL to temperatures above $T = 0.14$, where λ-analysis is no longer reliable. (b) The QWL is also very close to the point where occupancy $n(\mu)|_T$ changes trend, i.e. has a maximum of the second derivative. The line of maxima in $d^2n/d\mu^2|_T$ can also be considered a crossover line between metallic and insulating behavior (light blue dotted line on panel (a)).

IV. ANALYTICAL CONTINUATION AND CALCULATION OF RESISTIVITY

The straightforward application of the maximum entropy method (MEM) [12, 13] for analytical continuation of the Green's function can in some cases lead to unphysical results. In the metallic phase, this method tends to overestimate the height of the quasi-particle (QP) peak in the single-particle energy spectrum given by $-\frac{1}{\pi}\mathrm{Im}G(\omega+i0^+)$. Sometimes in those cases, the imaginary part of the self-energy falsely goes to zero at several frequencies (usually two or four), yielding an unphysical vanishing DC resistivity. Given the analytically continued Green's function on the real axis, the self-energy is obtained from the DMFT self-consistency condition

$$\Sigma(\omega) = \omega + \mu - G^{-1}(\omega) - t^2 G(\omega), \tag{2}$$

and the imaginary part of the above equation reads

$$\mathrm{Im}\Sigma(\omega) = \mathrm{Im}G(\omega)(|G(\omega)|^{-2} - t^2). \tag{3}$$

It is immediately obvious that $|G(\omega)| = 1/t$ yields $\mathrm{Im}\Sigma(\omega) = 0$, at any frequency. When there is an unphysical excess of QP weight, precisely this is seen, usually at the edges of the QP peak. This makes the conductivity integral divergent and the DC resistivity exactly zero.

We find that much better results are obtained by performing MEM on the spectral function

$$A(\varepsilon, i\omega_n) = \frac{1}{i\omega_n + \mu - \varepsilon - \Sigma(i\omega_n)}. \tag{4}$$

The self-energy is then easily extracted from the real-axis result

$$\Sigma(\varepsilon;\omega) = \omega + \mu - \varepsilon - A^{-1}(\varepsilon, \omega). \tag{5}$$

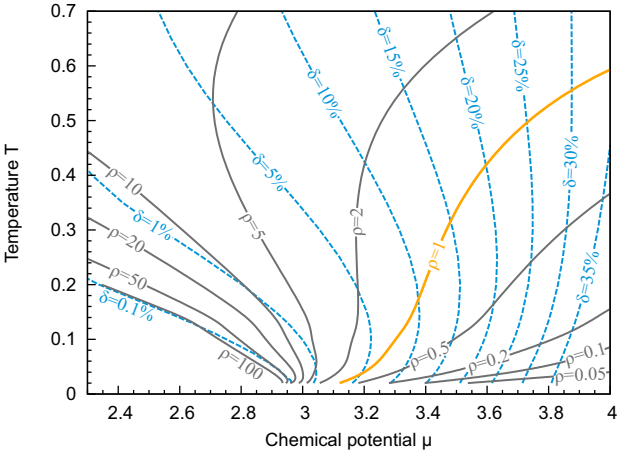

Figure 4: **Lines of constant doping intersect with the QWL (orange), along which the resistivity is equal to the MIR limit ρ_{MIR}.**

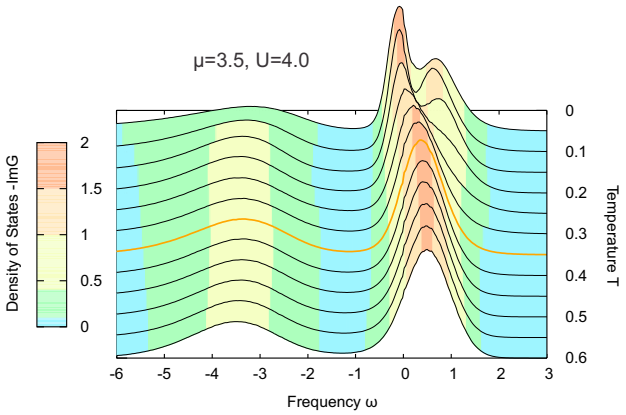

Figure 5: **Evolution of the density of states with increasing temperature.** At low temperature there is a clear quasiparticle peak in the density of states. The quasiparticle peak gradually disappears in the bad metal regime which is centered around the QWL. The orange line is the density of states at the QWL. The data are shown for the fixed chemical potential $\mu = 3.5$ and $U = 4$, which corresponds to roughly 15 % doping.

This procedure should in principle yield the same self-energy for any value of ε, but in practice this is not found to be the case. However, a good estimate of $\Sigma(\omega)$ is obtained by averaging the results of each continuation, i.e.

$$\Sigma(\omega) = \frac{1}{N}\sum_{i=1}^{N}\Sigma(\varepsilon_i;\omega). \tag{6}$$

Similarly, one could first calculate the Green's function

$$G(\omega) = \int d\varepsilon \rho_0(\varepsilon) A(\varepsilon, \omega) \tag{7}$$

and then get the self-energy from the DMFT self-consistency. In practice, we have used 40 values of ε, equally spaced within the energy range of the non-interacting band, and found that the systematic and numerical error of MEM gets canceled by the averaging. We have found that in this approach, physically meaningful solutions are always obtained, results are more consistent and have less numerical noise, but at the expense of performing a much larger number of analytical continuations. Where available, we cross-checked our results with the findings in Ref. 14 where the analytical continuation is performed via Pade approximant on the high-precision CTQMC data, and found very good agreement.

Given the self-energy on the real axis $\Sigma(\omega)$, the optical conductivity of the system can be calculated using the Kubo formula [2]

$$\sigma(\omega) = \sigma_o \iint d\varepsilon d\nu \Phi(\varepsilon) A(\varepsilon,\nu) A(\varepsilon,\nu+\omega) \frac{f(\nu) - f(\nu+\omega)}{\omega}, \tag{8}$$

where $A(\varepsilon,\nu) = -(1/\pi)\mathrm{Im}(\varepsilon+\mu-\nu-\Sigma(\varepsilon))^{-1}$, f denotes the Fermi function, $\Phi(\varepsilon) = \Phi(0)[1-(\varepsilon/D)^2]^{3/2}$, and $\sigma_o = 2\pi e^2/\hbar$. We present the resistivity results in the units of $\rho_{\mathrm{MIR}} = \hbar D/e^2\Phi(0)$, consistently with Ref. 14. We have calculated the resistivity $\rho_{\mathrm{DC}} = \sigma^{-1}(\omega \to 0)$ in the whole (μ, T) plane. In Supplementary Figure 4 we show the lines of constant resistivity and constant doping in the (μ, T) plane. An example of the evolution of the density of states with temperature is shown in Supplementary Figure 5.

V. CHARGE COMPRESSIBILITY

The QWL is defined in purely thermodynamic terms, from the free energy functional, and as such can be examined for any model. In fact, it does not even require the presence of a first order transition line with finite T_c. It is therefore important to explore physical properties other than the resistivity along and near the QWL. It is striking that the charge compressibility is nearly constant along the QWL, and has intermediate value between the one in almost incompressible Mott insulator and Fermi liquid, see Fig. 6.

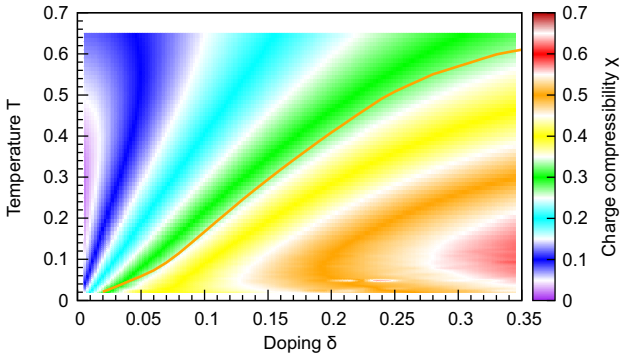

Figure 6: **Color plot of the charge compressibility has the "fan-like" form, as generally expected for quantum criticality.** The compressibility is approximately constant along the QWL.

VI. BOUNDARIES OF THE QC SCALING REGION

Around the quantum Widom line the resistivity is well approximated by a function of only one argument, such that

$$\rho(\mu, T) = \rho^*(T) F\left(\frac{T}{d\mu^{z\nu}}\right), \tag{9}$$

where $\rho^*(T) = \rho(\mu^*(T), T)$ is the resistivity along the QWL. This behavior, typical for the quantum criticality, is shown in Fig. 2 in the Main Text, where the resistivity curves are collapsed on the metallic and insulating branch. The explicit form of the scaling function can be obtained from an equivalent scaling equation

$$\rho(\mu, T) = \rho^*(T) \tilde{F}\left(\frac{d\mu}{T^{1/z\nu}}\right). \tag{10}$$

with the advantage of $\tilde{F}(x)$ being a smooth analytical function in x. Then, the scaling function $\tilde{F}(x)$ can be obtained by plotting the DMFT resistivity data versus the argument $x = \frac{d\mu}{T^{1/z\nu}}$ and performing a numerical fit. This is shown in Supplementary Figure 7a. $\tilde{F}(x)$ is approximately linear on the logarithmic scale which implies that $\tilde{F}(x) \approx 10^{Bx}$, where $B \approx -0.33$. This analytical form is consistent with the mirror symmetry of the scaling formula near the QWL, $\tilde{F}(x) = 1/\tilde{F}(-x)$. We can see that the scaling region goes beyond the mirror symmetry of the scaled resistivity curves, especially on the metallic side of the QC region.

The scaling region can be estimated from the color plot of the relative error $r = |\rho_{DMFT} - 10^{Bx}|/\rho_{DMFT}$, which is shown in Supplementary Figure 7b. The boundaries of the QC scaling region defined by $r < 10\%$ are shown with gray dashed lines and correspond to the values $x_{\min} = -1.0$ and $x_{\max} = 1.5$. Note that they coincide with the $\mu = 3.0$ line (red dashed; it corresponds to chemical potential being at the lower edge of the upper Hubbard band), and the knee-like feature in $\rho(T)|_\delta$ curves (blue dashed; it corresponds to the boundary of the linear resistivity bad metal region). It is obvious from this plot that the QC scaling region completely matches the region of typically bad metallic temperature dependence of the resistivity.

The boundaries of the QC scaling region can alternatively be estimated simply by looking at Fig. 7a and observing the maximum and minimum values of x for which the DMFT results fall on a single well defined curve. This yields $x_{\min} = -1.0$ and $x_{\max} = 1.5$. These lines are also shown in Fig. 7b (gray dashed) and are in good agreement with the independent estimate based on relative error r.

Finally, the region of mirror-symmetry can be estimated by plotting the DMFT resistivity data $|\log \frac{\rho}{\rho^*}|$ as a function of $y = T/d\mu^{z\nu}$ (shown in Fig. 7c) and observing the lowest y at which the two branches of data are found to coincide. This analysis yields $y_{\min} = 1 = |x_{\min/\max}|^{-1}$, in agreement with other approaches.

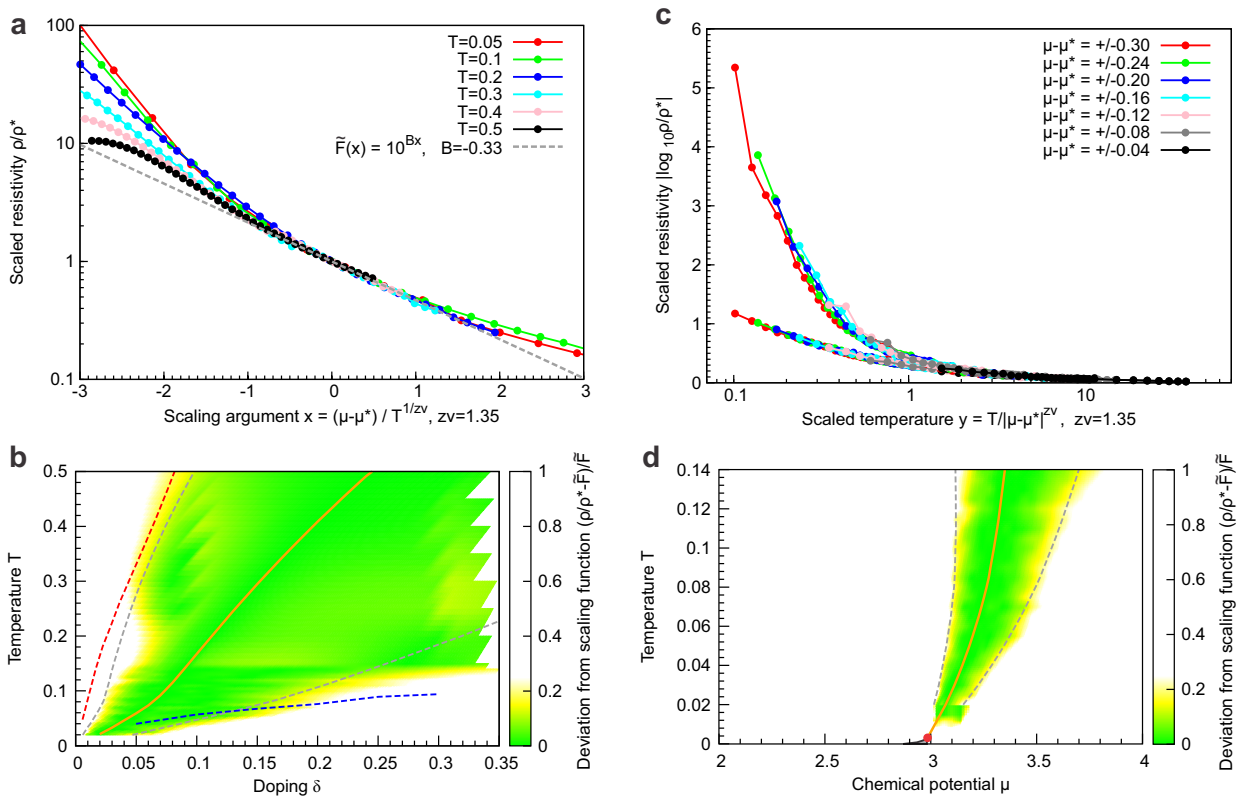

Figure 7: **The extent of the scaling region.** (a) The DMFT data are plotted as a function of the scaling argument x to obtain a fit for the scaling function. The range of x where DMFT data points fall on a single, well defined curve can be used as an estimate of the scaling region. (b) Between $x = -1.0$ and $x = 1.5$ (gray dashed lines), the relative error of the scaling formula is below 10%. The boundaries of the scaling region coincide with the $\mu = 3.0$ line (dashed red) and the knee-like feature in resistivity $\rho(T)|_\delta$ which marks the boundary of the linear resistivity bad metal region (blue line). (c) The mirror symmetry is found where the two branches of $|\log F(y)|$ coincide. (d) The scaling region in the $\mu - T$ plane; the scaling is valid for $T \gtrsim 4T_c$.

[1] K. Haule, Phys. Rev. B **75**, 155113 (2007).
[2] A. Georges, G. Kotliar, W. Krauth, and M. J. Rozenberg, Rev. Mod. Phys. **68**, 13 (1996).
[3] R. Žitko, D. Hansen, E. Perepelitsky, J. Mravlje, and A. Georges, Phys. Rev. B **88**, 235132 (2013).
[4] D. S. Fisher, G. Kotliar, and G. Moeller, Phys. Rev. B **52**, 17112 (1995).
[5] G. Kotliar, S. Murthy, and M. J. Rozenberg, Phys. Rev. Lett. **89**, 046401 (2002).
[6] P. Werner and A. J. Millis, Phys. Rev. B **75**, 085108 (2007).
[7] M. J. Rozenberg, R. Chitra, and G. Kotliar, Phys. Rev. Lett. **83**, 3498 (1999).
[8] J. Vučičević, H. Terletska, D. Tanasković, and D. Dobrosavljević, Phys. Rev. B **88**, 075143 (2013).
[9] G. G. Simeoni, T. Bryk, F. A. Gorelli, M. Krisch, G. Ruocco, M. Santoro, and T. Scopigno, Nature Physics **6**, 503 (2010).
[10] H. Terletska, J. Vučičević, D. Tanasković, and V. Dobrosavljević, Phys. Rev. Lett. **107**, 026401 (2011).
[11] M. J. Case and V. Dobrosavljević, Phys. Rev. Lett. **99**, 147204 (2007).
[12] M. Jarrell and J. E. Gubernatis, Physics Reports **269**, 133 (1996).
[13] A. W. Sandvik, Phys. Rev. B **57**, 10287 (1998).
[14] X. Deng, J. Mravlje, R. Žitko, M. Ferrero, G. Kotliar, and A. Georges, Phys. Rev. Lett. **110**, 086401 (2013).

Finite-temperature crossover and the quantum Widom line near the Mott transition

J. Vučičević,[1] H. Terletska,[2] D. Tanasković,[1] and V. Dobrosavljević[3]
[1]*Scientific Computing Laboratory, Institute of Physics Belgrade, University of Belgrade, Pregrevica 118, 11080 Belgrade, Serbia*
[2]*Condensed Matter Physics and Materials Science Department, Brookhaven National Laboratory, Upton, New York 11973, USA*
[3]*Department of Physics and National High Magnetic Field Laboratory, Florida State University, Tallahassee, Florida 32306, USA*
(Received 4 June 2013; published 28 August 2013)

The experimentally established phase diagram of the half-filled Hubbard model features the existence of three distinct finite-temperature regimes, separated by extended crossover regions. A number of crossover lines can be defined to span those regions, which we explore in quantitative detail within the framework of dynamical mean-field theory. Most significantly, the high-temperature crossover between the bad metal and Mott-insulator regimes displays a number of phenomena marking the gradual development of the Mott insulating state. We discuss the quantum critical scaling behavior found in this regime, and propose methods to facilitate its possible experimental observation. We also introduce the concept of *quantum Widom lines* and present a detailed discussion that highlights its physical meaning when used in the context of quantum-phase transitions.

DOI: 10.1103/PhysRevB.88.075143 PACS number(s): 71.30.+h, 71.27.+a

I. INTRODUCTION

Strongly correlated materials exhibit a variety of phases whose properties often lack a complete microscopic understanding.[1] The most interesting new aspect of this class of materials is a possibility to tune the system through two or more different ground states separated by quantum critical points (QCPs).[2] Such QCPs are often difficult to directly approach and investigate, not only because they reside at $T = 0$, but also because various additional instabilities and orders emerge in their immediate vicinity. Nevertheless, understanding them is of chief importance, because they often control rather extended finite-temperature quantum critical regions displaying universal properties and featuring scaling behavior of all quantities.

Quantum critical points have been experimentally identified and studied in several classes of physical systems, ranging from heavy fermion metals[3,4] to conventional[5] and even high-temperature superconductors.[6] In most of these, however, the QCP is obtained when quantum fluctuations become sufficiently strong to suppress an appropriate ordering temperature—for magnetic, structural, or superconducting order—down to $T = 0$. When this happens, then concepts familiar from the very successful theory of classical critical phenomena can be utilized and naturally extended to a quantum regime.[2] Indeed, most conventional theoretical approaches follow the Landau theory paradigm[7] and examine the impact of thermal and quantum fluctuations of appropriate order parameters, as describing the corresponding patterns of spontaneous symmetry breaking.

Should most exotic phenomena, then, be regarded as manifestations of some form of (static or fluctuating) order, as Slater speculated even in the 1930's,[8] or should fundamentally different classes of quantum-phase transitions exist? The first viewpoint was at the origin of the Hertz (weak coupling) approach[9,10] to quantum criticality, which, despite its formal elegance, resulted in only modest successes. The latter, however, was at the core of pioneering ideas of Mott[11] and Anderson,[12] who provided a complementary perspective. According to their views, strong electronic correlations are able destroy the metallic state even in the absence of any ordering, leading to the formation of the Mott insulating state. The existence of broad classes of Mott insulators is, of course, beyond the doubt at this time. And while most order antiferromagnetically at low temperature, they indeed remain robustly insulating (gaps often in the electron volt range) even well above the corresponding Néel temperature.[13–15]

The nature of the phase transition between the metallic and the insulating phase—the Mott transition—has, in contrast, remained highly controversial and subject to much debate. Because the two phases share the same symmetries, the clear distinction between them is apparent only at $T = 0$. Should a direct and *continuous* transition between a paramagnetic metal and a paramagnetic Mott insulator exist at $T = 0$, it would represent the most obvious example of a QCP outside the Landau paradigm, unrelated to any mechanism of spontaneous symmetry breaking. Unfortunately, in most familiar situations, the Mott metal-insulator transition is also accompanied by simultaneous magnetic, charge, structural, or orbital ordering, considerably complicating the situation and fogging the issues, both from the theoretical and the experimental perspective.

Still, it is a well established experimental fact that in all known cases, the characteristic temperature scale T_c, below which many of such "intervening" phases are found, is quite small, as compared to both basic competing energy scales: the Fermi energy E_F measuring the quantum fluctuations, and the Coulomb repulsion U that opposes the electron motion. As a result, a very sharp crossover between metallic and insulating behavior is observed even at $T \gg T_c$, for all physical quantities. The key issue thus remains: What is the main physical mechanism controlling this finite-temperature metal-insulator crossover? Should it be viewed as a quantum critical regime dominated by appropriate order-parameter fluctuations, or is it, as postulated by Mott and Anderson, a dynamical phenomenon not directly related to any ordering tendency.

To clearly and precisely address this question, one must (1) suppress all ordering tendencies, at least in the relevant temperature range, and (2) understand and describe the remaining physical processes controlling the resulting finite-temperature

crossovers, and the corresponding quantum critical region, if one exists. From the theoretical point of view, this ambitious goal is generally very difficult to achieve, at least for realistic model systems. The task is hard, because standard perturbative approaches, which are so well suited to describe Fermi-surface instabilities and the associated competing orders, are quite incapable in describing the Mott physics. The situation, however, improved with the development of dynamical mean-field theory (DMFT) method,[16] which capitalizes on performing a local approximation for appropriate self-energies and vertex functions, yet which provides a completely nonperturbative description of strong correlation effects. Its physical content is most clearly revealed by focusing at the "maximally frustrated Hubbard model" (MFHM)[16,17] with long-range and frustrating intersite hopping (see below), where the DMFT approximation becomes exact.

The MFHM, because it is maximally frustrated, displays no magnetic or any other kind of long-range order across its phase diagram. It does display, however, a precisely defined Mott metal-insulator transition at low temperature, precisely in the fashion anticipated by the early ideas of Mott and Anderson. It has been studied by many authors, ever since the beginning of the DMFT era some 20 years ago,[18] yet, surprisingly, some of its basic features have remained ill understood and even confusing. Most studies focused on characterizing the low-temperature behavior, where a strongly correlated Fermi liquid (FL) forms on the metallic side of the Mott transition.[18] At low temperatures, this FL phase is separated from the Mott insulator by an intervening phase coexistence region (see Fig. 1), and the associated first-order transition line (FOTL) terminating at the critical end point (CEP) at $T = T_c$.[19] The behavior in the immediate vicinity of the CEP has attracted much recent attention[20,21] but, unsurprisingly (as any other finite-temperature CEP), it display scaling behavior of the standard classical liquid-gas (Ising) universality class.[19] Indeed, several experiment reporting transport in this regime have successfully been interpreted[22] using these classical models.

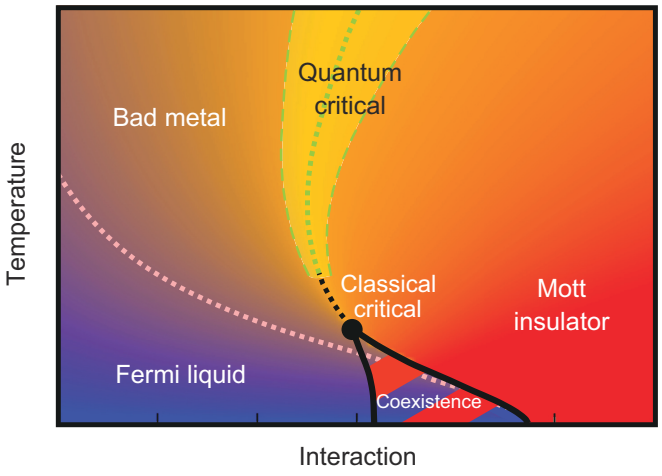

FIG. 1. (Color online) Phase diagram of the half-filled maximally frustrated Hubbard model. The background is an actual color map of the resistivity obtained using the IPT impurity solver (see the text): Blue, small resistivity; red, large resistivity.

But what about the supercritical ($T \gg T_c$) behavior? Its rough features have been investigated by many authors,[16] who identified several regimes and complicated crossovers connected to them, but no simple and plausible physical picture has emerged. Most importantly, almost no one has attempted to interpret the features of this high-temperature regime in terms of ideas or concepts of quantum criticality.[2] The complication, of course, comes from the presence of the coexistence dome at $T < T_c$, which confuses the issues, and, at least at first glance, makes the situation seem incompatible with the standard paradigm of quantum criticality.

Our very recent work,[17] however, provided a new perspective. It made two key observations. (1) The characteristic temperature scale of the coexistence dome $T_c \ll E_F, U$: The physics associated with it should, at $T \gg T_c$, be little affected by its presence, and thus behave just as if $T_c \approx 0$, and an actual QCP would exist separating the two phases. (2) To reveal the possible quantum critical scaling associated with the proposed "hidden" QCP, one must follow a judiciously chosen trajectory (sometimes called the "Widom line"[23,24]), as in almost any standard critical phenomenon. This work also demonstrated[17] remarkable scaling of the resistivity curves, displaying all features expected of quantum criticality. The resistivity around this line exhibits a characteristic "fan-shaped" form, surprisingly similar to experimental findings in several systems,[1,20,21,25–27] reflecting gradual crossover from metallic to insulating transport. The scaling behavior in this high-temperature crossover regime was thus argued to encapsulate the universal features of finite-temperature transport near the metal-insulator transition.

The work of Ref. 17 focused on behavior close to the "instability line" and the associated quantum critical scaling regime around it. It should be noted, however, that several other finite-temperature crossover lines have been discussed by other authors[16,24,28–30] to characterize the metal-insulator region. The exact relationship between these different ideas and approaches—for the same model—thus remained an open and rather confusing issue that needs to be carefully investigated and understood. This important task is the chief subject of this paper, where we present a detailed and very precise characterization of all the crossover regimes across the entire phase diagram for the maximally frustrated Hubbard model at half filling, within the paramagnetic solution of dynamical mean-field theory. We carefully characterize the relevant crossover lines employing all the various proposed criteria used for their definitions. Two fundamentally distinct crossover regions are identified: one referring to the thermal destruction of long-lived quasiparticles and the other to the gradual opening of the Mott gap. The instability line, as previously determined from a thermodynamic analysis,[17] belongs to the latter region, and is found to lie very near to the line of inflection points in the resistivity curves $\log \rho(U)$. The scaling of resistivity curves found around both of these lines is analyzed and discussed from the perspective of hidden quantum criticality and its experimental observation. In the end, we outline the generalized concept of the Widom lines, and argue that they gain a new fundamental meaning in the context of quantum-phase transitions, which opens an avenue to put our results into a more general theoretical framework.

II. PHASE DIAGRAM

We consider a single band Hubbard model at half filling,

$$H = -t \sum_{\langle i,j\rangle\sigma} (c^\dagger_{i\sigma} c_{j\sigma} + \text{H.c.}) + U \sum_i n_{i\uparrow} n_{i\downarrow}, \qquad (1)$$

where $c^\dagger_{i\sigma}$ and $c_{i\sigma}$ are the electron creation and annihilation operators, $n_{i\sigma} = c^\dagger_{i\sigma} c_{i\sigma}$, t is the nearest-neighbor hopping amplitude, and U is the repulsion between two electrons on the same site. We use a semicircular density of states, and the corresponding half bandwidth $D = 2t$ is set to be our energy unit. We focus on the paramagnetic DMFT solution, which is formally exact in the limit of large coordination number, including the maximally frustrated Hubbard model.[16,17] The DMFT provides a unique theoretical framework, as it works well in the entire range of model parameters, thus treating all the relevant phases and regimes on an equal footing. It is, however, most reliable at high temperatures,[31–34] when the correlations are more local, and this is precisely the regime of primary interest of this paper. To solve the DMFT equations we utilize both the iterated perturbation theory[16] (IPT) and the numerically exact continuous time quantum Monte Carlo (CTQMC).[35,36] The results obtained with these two methods are found to be in very good agreement. In this section we concentrate on IPT results, which cover the entire phase diagram and do not suffer from numerical noise. Figures in the rest of the paper are the QMC results.

The phase diagram in the U-T plane is shown in Fig. 1. The DMFT solution reproduces the three regimes found close to the metal-insulator transition (MIT): Fermi liquid, bad metal, and Mott insulator, in qualitative agreement with experiments on various Mott systems.[16] We begin their characterization by first analyzing the behavior of the resistivity in the relevant range of parameters.

The DMFT expression for the calculation of DC resistivity, $\rho = 1/\sigma(\omega \to 0)$, is given by[16]

$$\sigma = \pi\sigma_0 \int_{-\infty}^{+\infty} d\varepsilon v^2(\varepsilon) D^0(\varepsilon) \int_{-\infty}^{+\infty} \left(-\frac{df}{d\omega} A^2(\varepsilon,\omega) \right), \quad (2)$$

where $A(\varepsilon,w) = -\frac{1}{\pi}\text{Im}\, G(\varepsilon,w)$, $v(\varepsilon) = \sqrt{(4t^2-\varepsilon^2)/3}$. $D^0(\varepsilon) = \frac{1}{2\pi t^2}\sqrt{4t^2-\varepsilon^2}$ is the noninteracting density of states (DOS), and f is the Fermi function. The calculation of resistivity from the IPT results is straightforward as this method is defined on the real axis. To calculate the resistivity from the QMC results, one first needs to perform the analytical continuation, which we carry out using the maximum entropy method.[37]

Our quantitative IPT results are replotted in Fig. 2, where the value of resistivity is color coded, with white stripes separating the consecutive orders of magnitude between 10^{-3} and 10^{13}. In this plot, as well as in the rest of the paper, the resistivity is given in the units of ρ_{Mott}, the maximal metallic resistivity in the semiclassical Boltzmann theory, defined as the resistivity of the system when the scattering length is equal to one lattice spacing.[38,39] At zero temperature, the metallic resistivity vanishes, while the Mott insulator has an infinite resistivity. With increasing temperature, the difference between the two states becomes less and less pronounced. (Between the spinodals, both metallic and insulating solutions

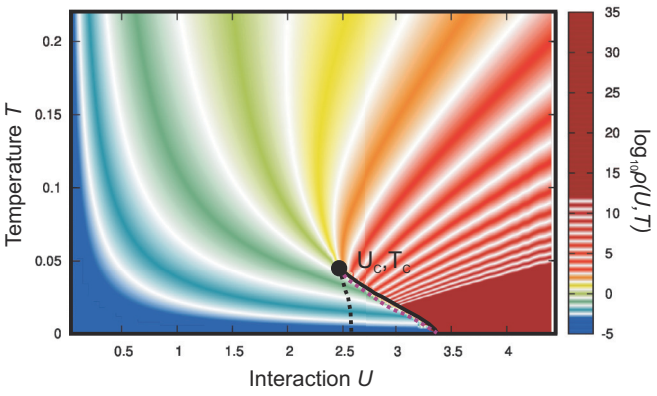

FIG. 2. (Color online) Resistivity (in units of ρ_{Mott}) calculated in the entire U-T plane. The white stripes follow the lines of equal resistivity and separate the orders of magnitude in the resistivity. Spinodals are denoted with thick black lines, and the first-order phase transition line is dashed.

are possible, but in this plot only the metallic resistivity is shown.) In the intermediate correlation, $U < U_c$, high-temperature, $T > T_c$, regime, the resistivity is comparable or even larger than ρ_{Mott}, but it still (weakly) increases with temperature, which is characteristic for the "bad metal" regime observed in several Mott systems.[38]

It is remarkable how this way of presenting the data immediately creates the familiar "fan-shape" structure, generally expected for quantum criticality.[2] At high temperatures all the white constant-resistivity stripes seem to converge almost to the same point $U \sim U_c$. The perfect convergence, however, is interrupted by the emergence of the coexistence done at $T < T_c$, but such behavior is exactly what one expects for "avoided quantum criticality,"[30] consistent with the physical picture proposed in Ref. 17.

Different regions of the phase diagram are also distinguished by the qualitatively different form for the temperature dependence of the resistivity. To make this behavior even more apparent, we follow a commonly used procedure to display the data around QCPs, compute the logarithmic derivative of resistivity with respect to the temperature, i.e., the "effective exponent"[40,41]

$$\beta(T,U) = d\log\rho(U,T)/d\log T, \qquad (3)$$

which is presented in color-coded form in Fig. 3.

On the metallic side, at the lowest temperatures, one finds a typical metallic dependence of the form $\rho \sim T^2$ and here we have $\beta = 2$ (white). Far from the transition, this regime survives up to relatively high temperatures, but eventually the temperature dependence of the resistivity starts gradually slowing down, displaying behavior sometimes described as "marginal Fermi-liquid" transport (green, $\beta \sim 1$). Closer to the transition, this is preceded by an increase in the effective exponent (red), which is a reflection of the existence of the critical end point in which β diverges (yellow). Very close to the transition, a maximum of the resistivity is reached at some temperature (pink) and the trend of the resistivity increase is then reversed. On the other side of the phase diagram, deep in the Mott insulator, one finds typical activation curves which exhibit the exponential drop in the resistivity with increasing

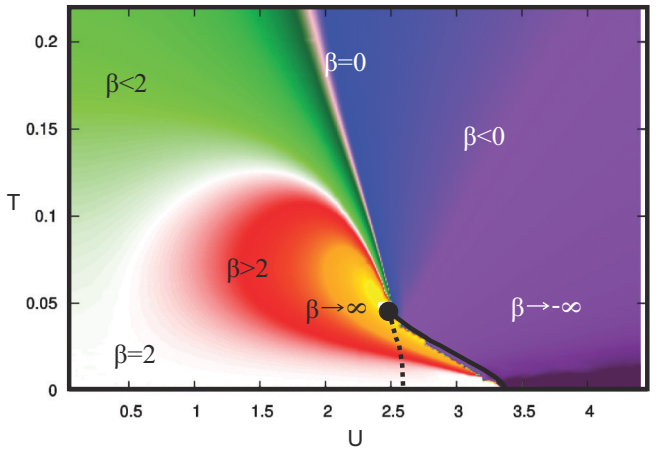

FIG. 3. (Color online) The effective resistivity exponent ($\beta = d\log\rho/d\log T$) calculated in the entire U-T plane illustrates the different transport regimes (see the text).

temperature, due to the gap in the excitation spectrum (black and purple). However, just above the coexistence dome, one finds an intermediate regime, where the behavior is generally insulating because the resistivity decreases with temperature, but the gap is not yet fully open, and the temperature dependence deviates from exponential (blue). This region is sometimes referred to as the "bad insulator."

III. CROSSOVER LINES

In the previous section we have characterized the different regimes in the vicinity of the Mott MIT: Fermi liquid, bad metal, and Mott insulator. However, apart from the coexistence region, the properties of the system change continuously in the entire phase diagram. The lines separating the different regimes are thus a matter of convention and many definitions can be found in literature proposing the criteria for their distinction.

In Fig. 4 we present the lines corresponding to various definitions of a crossover line between the Fermi-liquid and the bad metal regimes. The definition of each line is illustrated on a smaller panel on the right, where the corresponding feature in the resistivity and other relevant quantities is marked with the dots of the same color. The dark blue line (a) is defined by $\rho = 0.1\rho_{\rm Mott}$ and it roughly corresponds to the Fermi coherence temperature $T_{\rm FL}$ (the temperature above which the temperature dependence of resistivity is no longer quadratic). The corresponding small panel (a) shows the resistivity as a function of temperature, plotted for three different values of U. The dotted horizontal line marks $\rho = 0.1\rho_{\rm Mott}$. The arrow denotes the direction of increase of U. The light blue line (b) corresponds to the inflection point of the resistivity, $d^2\rho(\omega=0)/dT^2 = 0$, and the green line (c) is determined as the inflection point of the spectral density at the Fermi level with respect to the temperature, $d^2A(\omega=0)/dT^2 = 0$. These are illustrated on smaller panels (b) and (c) where the dc resistivity and $A(\omega=0)$ are plotted versus the temperature, for three different values of U. The inflection points are marked with the dots of color corresponding to the (b) and (c) lines on the main panel. The additional two dotted lines are (d) the quasiparticle weight at zero temperature defined by $Z = [1 - d\,\mathrm{Im}\,\Sigma(i\omega_n)/d\omega_n|_{\omega_n\to 0}]^{-1}$ and (e) the zero temperature local spin susceptibility χ. Both quantities are divided by 10 to fit in the temperature range of the plot and to be more easily compared to the crossover lines. It is evident that the coherence temperature is roughly proportional to the quasiparticle weight at zero temperature, but with the prefactor 0.1, $T_{\rm FL}(U) \sim 0.1Z(U)$. As compared with the doped Hubbard model,[42,43] $T_{\rm FL}$ is higher but still distinct from the temperature corresponding to $\rho_{\rm Mott}$, in agreement with the experiments on organic materials.[39,44,45] The quasiparticle weight Z is weakly temperature dependent and the Drude peak in the opticalal conductivity is still pronounced for $\rho \lesssim \rho_{\rm Mott}$.[46]

In contrast with these lines, one can also define the lines separating the bad metal from the (bad) Mott insulator. In Fig. 5, we present several criteria for their definition. In analogy to line (a) of Fig. 4, one can use the resistivity to distinguish between the two regimes. The dark blue line (a) plotted here connects the points where the resistivity is equal

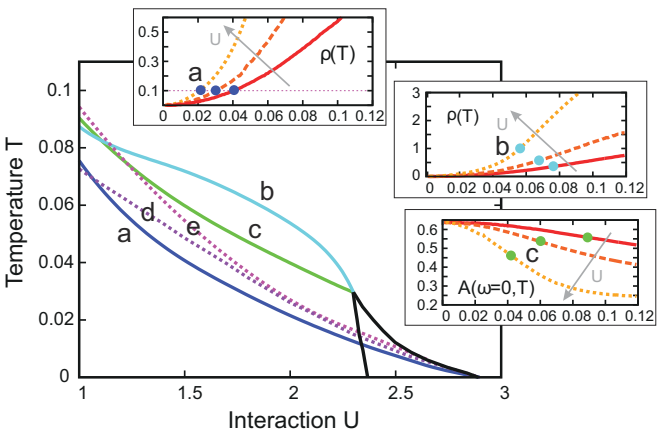

FIG. 4. (Color online) Various definitions for the crossover lines between the Fermi liquid and the bad metal. The meaning of each definition is illustrated on a smaller panel to the right. The results are obtained with the QMC.

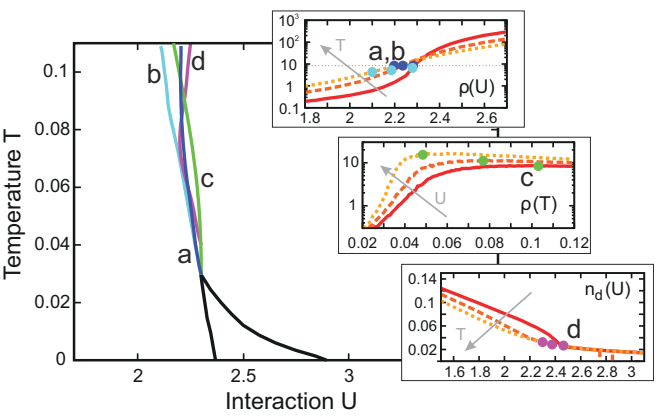

FIG. 5. (Color online) Various definitions for the crossover lines between the bad metal and the Mott insulator. The meaning of each definition is illustrated on a smaller panel to the right. The results are obtained with the QMC.

to the one found precisely at the critical end point, which we estimate to be roughly $10\rho_{\text{Mott}}$. The light blue line (b) marks the inflection point of logarithmic resistivity as a function of U [$\partial^2 \log \rho(U,T)/\partial U^2 = 0$]. It is a well pronounced feature up to high temperatures, and it is a direct consequence of the discontinuity across the FOTL at $T < T_c$. These two are illustrated on the small panel to the right, where $\log \rho(U)$ is plotted at three different temperatures. The dark blue dots are the intersections of these lines with the dotted, $10\rho_{\text{Mott}}$ line. The inflection points are marked with the light blue dots, and are found at slightly lower values of U. Another natural definition for the crossover is the $\beta = 0$ line (c), as it marks the place where the trend of resistivity growth is reversed. At its right-hand side, the resistivity decreases with temperature, which is a sign of insulating behavior. This is illustrated on the corresponding small panel, where $\log \rho(T)$ is plotted for three different values of U and the maxima are marked with the green dots. The double occupancy n_d has an obvious change in trend on crossing line (d). Here, the second derivative $\partial^2 n_d/\partial U^2$ has a sharp maximum, and separates the two distinct regimes of $n_d(U)$, both almost linear but with different slopes. This is apparent on the small panel (d), where double occupancy is plotted as a function of U at various temperatures.

It is striking that these lines almost coincide, in sharp contrast to what is seen in Fig. 4. Although the opening of the gap is very gradual, it is possible to pinpoint the boundary between the two regimes and actually divide the supercritical part of the phase diagram into metallic and insulatinglike regions. In the following section we present an overview of the instability line, another definition for a metal-insulator crossover line, and explain how it helps reveal a very peculiar property of the Hubbard model, which is very suggestive when it comes to interpreting the Mott MIT in terms of quantum-phase transitions.

IV. INSTABILITY LINE AND QUANTUM CRITICAL SCALING

It is a well established phenomenon that in the vicinity of quantum critical points, at finite temperatures, physical observables display a characteristic quantum critical scaling.[2] A very good example of this is the transport in high-mobility two-dimensional electron gases, in particular, in metal-oxide-semiconductor field-effect transistors (MOSFETs).[1] There is overwhelming evidence that they exhibit a zero temperature metal-insulator transition at a critical concentration of charge carriers.[25] It is experimentally observed in these systems that the value of resistivity at finite temperatures above the quantum critical point ($n_c, T = 0$) is a function of only $\delta n = n - n_c$ and T, which is considered a hallmark of quantum criticality. As shown in Fig. 6(a), [47] the resistivity curves collapse onto two branches: The resistivity is first divided by the "separatrix" $\rho_c(T) = \rho(n_c, T)$ which weakly depends on the temperature, and then the temperature is scaled by $T_o(\delta n) = |\delta n|^{\nu z}$, yielding

$$\rho(\delta n, T) = \rho_c(T) f(\delta n T^{-1/\nu z}). \quad (4)$$

The mechanism behind the physical picture of MOSFETs is still elusive,[27] but a similar physical picture is seen is various spin systems, where the physics is well understood.[2]

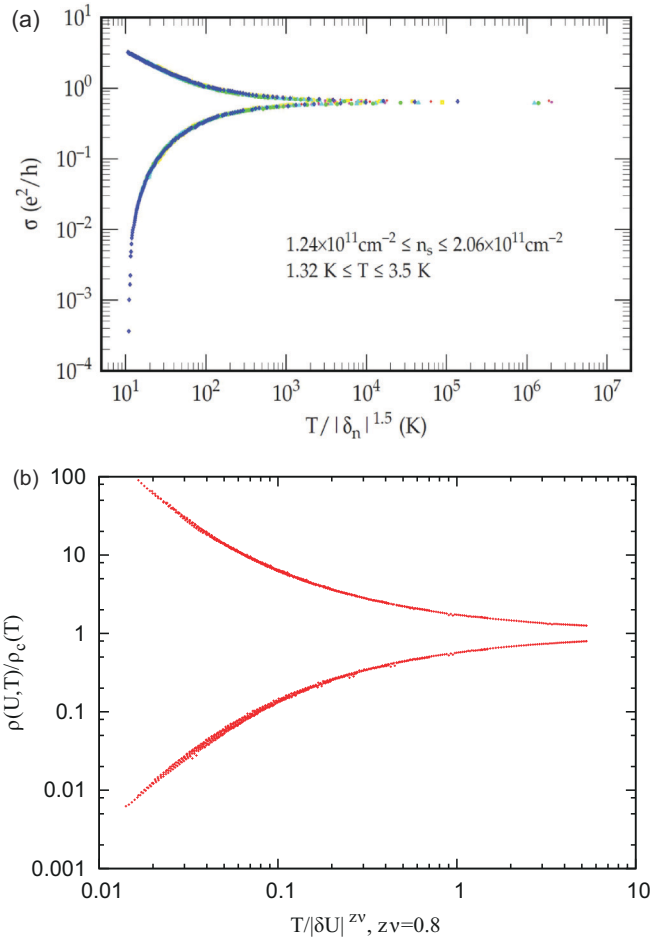

FIG. 6. (Color online) (a) Experimental results: Conductivity scaling in high-mobility Si MOSFETs presents a textbook example of quantum critical scaling (taken from Ref. 47). (b) DMFT QMC results: Resistivity scaling strongly reminiscent of what is seen in MOSFETs. After dividing $\rho(U,T)$ with the value of resistivity on the instability line $\rho_c(T)$ (see the text) and then rescaling the temperature with an appropriately chosen parameter $T_0(\delta U)$, the resistivity curves collapse onto two branches.

When there is a well defined order parameter, the separatrix corresponds to the line of zero symmetry-breaking field, which is trivially a straight vertical line emanating from the quantum critical point.

Although our model does feature a FOTL, the critical temperature is actually very low ($T_c \approx 0.03$), which makes it reasonable to pursue a description of its supercritical region from the perspective of quantum criticality. This is the approach that we have taken in a recent work,[17] where we have shown that in the Hubbard model, a quantum critical scaling of the resistivity curves does indeed hold [Fig. 6(b)]. There is an obvious analogy between the interaction U in our model and the carrier density n in MOSFETs, but it was not immediately clear what line $U_c(T)$ should correspond to the separatrix in our model. The phase transition in the Hubbard model does not break any symmetries and the first-order transition line is curved, which indicated that U_c has possibly a nontrivial temperature dependence.

A. The instability line

Starting from the thermodynamic arguments,[19,48] we have defined the instability line $U^*(T)$ as the line which corresponds to the minimum curvature of the free-energy functional $\mathcal{F}[G(i\omega_n)]$ with respect to U.[49] Above T_c the system has a unique ground state which corresponds to the minimum of $\mathcal{F}[G(i\omega_n)]$. In this minimum, the curvature of $\mathcal{F}[G(i\omega_n)]$ is determined by the lowest eigenvalue λ of the fluctuation matrix

$$M_{mn} = \frac{1}{2Tt^2} \left. \frac{\partial^2 \mathcal{F}[G]}{\partial G(i\omega_m)\partial G(i\omega_n)} \right|_{G=G_{\mathrm{DMFT}}}, \tag{5}$$

where $\delta G(i\omega_n) \equiv G(i\omega_n) - G_{\mathrm{DMFT}}(i\omega_n)$, and G_{DMFT} is the self-consistent solution of the DMFT equations. As explained in detail in the Supplemental Material of Ref. 17, λ can be obtained by monitoring the rate of convergence in the DMFT iteration loop. Close to the self-consistent solution, the difference between the consecutive solutions drops exponentially, with an exponent proportional to λ. We have

$$\mathbf{G}^{(n+1)} - \mathbf{G}^{(n)} = \delta\mathbf{G}^{(n)} = e^{-n\lambda}\mathbf{G}_\lambda(i\omega_n), \tag{6}$$

where $\mathbf{G}_\lambda$ is the eigenvector of $\hat{M}$ corresponding to its lowest eigenvalue λ.

The curvature λ is actually a very general quantity that describes the response of the system to an infinitesimal external perturbation, which may be a time-dependent field of an arbitrary form. As such, λ is very important in describing a thermodynamical state close to the Mott MIT, since it has a fundamentally dynamic nature. Indeed, λ vanishes precisely at the critical end point, as the free-energy functional becomes flat around G_{DMFT}. This is directly connected to the critical slowing down of dynamics, which manifests as the vanishing of a characteristic frequency scale. Above T_c, λ is related to the local stability of a given thermodynamic state and has a minimum precisely where the system is the least stable, or where its proximity to either competing phase is equal. Therefore, the instability line which connects the minima of λ vs U is the closest analogy to the lines of the zero symmetry-breaking field in systems with an order parameter.

The instability line is presented in Fig. 1 and indeed it represents a boundary between a metallic and insulating transport. It lies among the other crossover lines from Fig. 5 (see also Sec. V). Its physical meaning is illustrated in Fig. 7. The middle column shows the DOS along the instability line for three different temperatures. While the DOS at the Fermi level is strongly suppressed, the gap is not yet fully open. The left column shows the density of states in the metallic phase following a trajectory parallel to the instability line: There is a clear quasiparticle peak at low temperatures, which gradually disappears as the bad metal region is reached by increasing the temperature. At larger U (right column) the system is in the insulating phase with a fully open Mott gap, featuring activated transport.

B. Free-energy calculation

To further illustrate the physical meaning of the instability line, we explore the free-energy landscape in the Hilbert space of Green's functions. For this we closely follow the procedure described in Ref. 49. The iterative self-consistency procedure used to solve the DMFT equations converges towards a local

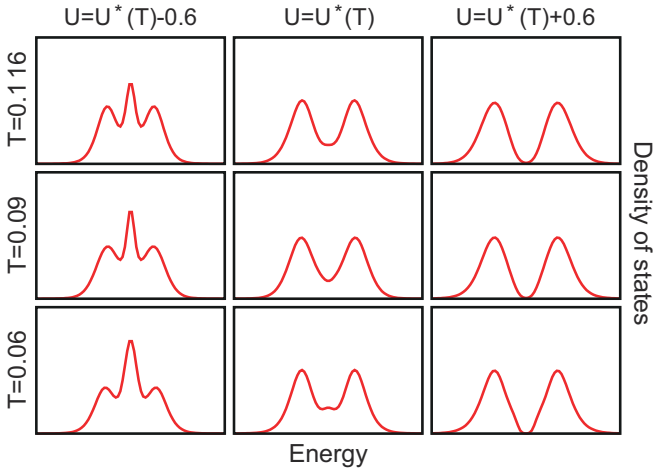

FIG. 7. (Color online) Density of states (QMC results) along the instability line $U^*(T)$ (middle column), and along the parallel trajectory for smaller (left column) and larger U (right column).

minimum of the corresponding Ginzburg-Landau free-energy functional $\mathcal{F}[\mathbf{G}]$, which, in the Hilbert space of the Matsubara Green's functions $G(i\omega_n)$, takes the form

$$\begin{aligned}\mathcal{F}[\mathbf{G}] &= \mathcal{F}_{\mathrm{imp}}[\mathbf{G}] + \mathcal{F}_{\mathrm{bath}}[\mathbf{G}] \\ &= \mathcal{F}_{\mathrm{imp}}[\mathbf{G}] - t^2 T \sum_n G^2(i\omega_n),\end{aligned} \tag{7}$$

where the first term is the free energy of the impurity site in the presence of the Weiss field $\Delta = t^2\mathbf{G}$, while the second term is the energy cost of forming the Weiss field around a given site.

The DMFT self-consistency condition, typically reached via an iterative procedure, is then regarded as a saddle-point equation derived from the extremum condition of such a Ginzburg-Landau functional. The physical DMFT solution corresponds to the local stationary point of $\mathcal{F}[\mathbf{G}]$, where a gradient vector $\mathbf{g} = \partial\mathcal{F}[\mathbf{G}]/\partial\mathbf{G}$ becomes zero. However, in the coexistence region below T_c, two such local minima are found. They correspond to physical solutions (metallic $\mathbf{G}_M$ and insulating $\mathbf{G}_I$), and are separated by an unstable solution (a local maximum or a saddle point).

We can visualize the shape of the infinitely dimensional free-energy surface by calculating $F[\mathbf{G}]$ along a single direction going through the self-consistent $\mathbf{G}_{\mathrm{DMFT}}$. Below T_c, we do this along the direction connecting the two solutions, which can be parametrized as $\mathbf{G}(l) = (1-l)\mathbf{G}_M - l\mathbf{G}_I$. Above T_c, where there is only one solution, we follow the eigenvector $\mathbf{G}_\lambda$ with $\mathbf{G}(l) = \mathbf{G}_{\mathrm{DMFT}} + l\mathbf{G}_\lambda$. The relative change of the free energy is calculated[49] as an integral $\Delta\mathcal{F}(l) = \mathcal{F}[\mathbf{G}(l)] - \mathcal{F}[\mathbf{G}_{M/\mathrm{DMFT}}] = t^2 T \int_0^l dl' \mathbf{e}_l \cdot \mathbf{g}[\mathbf{G}(l')]$, where $\mathbf{e}_l$ is the unit vector of the followed direction [$\mathbf{e}_l = (\mathbf{G}_M - \mathbf{G}_I)/|\mathbf{G}_M - \mathbf{G}_I|$ below T_c and $\mathbf{e}_l = \mathbf{G}_\lambda/|\mathbf{G}_\lambda|$ above T_c]. The gradient vector takes the form $\mathbf{g} = \mathbf{G}_{\mathrm{imp}}(\mathbf{G}) - \mathbf{G}$, with $\mathbf{G}_{\mathrm{imp}}(\mathbf{G})$ the output of the impurity solver used in the DMFT procedure, and $\mathbf{G}$ is the input–effective medium (hybridization bath) Green's function.

Figure 8(a) shows the free-energy landscape around $\mathbf{G}_{\mathrm{DMFT}}$, precisely at the instability line. The curvature of the global minimum vanishes as one approaches T_c, which is consistent with eigenvalue λ being zero at this point. Below T_c there are two minima and the instability line is no longer well defined,

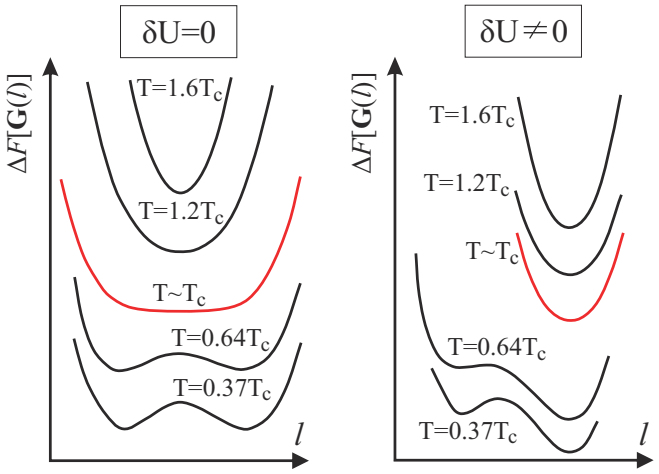

FIG. 8. (Color online) Free-energy landscape (IPT results): (a) Along the "zero field" line ($\delta U = 0$). At $T > T_c$, the curvature of the free energy increases with temperature, and it is zero at $T = T_c$. Below T_c, at the first-order transition line, metallic and insulating solutions have the same free energy. (b) Along the "finite field" line ($\delta U = -0.05$). At $T > T_c$, the curvature of the free energy is greater than in the "zero field" case. In the coexistence region one of the minima is energetically favored. Note that the spacing between $\Delta\mathcal{F}$ curves for different temperatures is arbitrary.

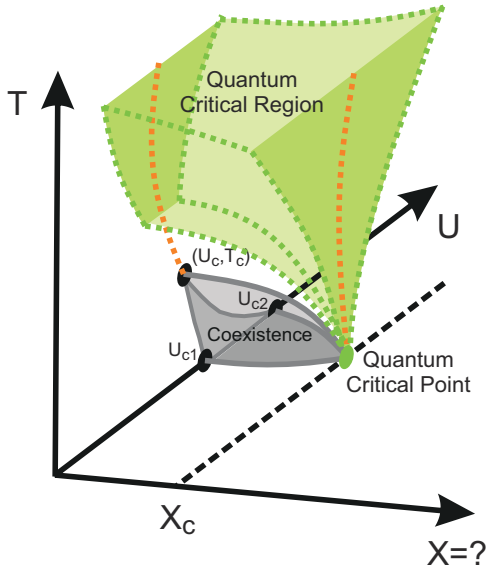

FIG. 9. (Color online) Possible phase diagram of a generalized Hubbard model. The observed scaling (valid in the green region) may be due to a quantum critical point that is unreachable by the simple two-parameter half-filled Hubbard model. An additional, third parameter (here marked with X) could drive T_c to zero at some critical value, and extend the region of validity of the scaling formula in the U-T plane.

but it is logically continued to the line of the first-order phase transition, where two possible solutions are of the same energy. On Fig. 8(b), we move along a parallel trajectory, defined by $\delta U \neq 0$. It is immediately obvious that λ never reaches zero and that in the coexistence region one of the solutions is energetically favored. This physical picture is common to various models. For example, it is seen in the Ising model in an external field, where the analogy is between the strength of the magnetic field and δU in our case.

C. Quantum critical scaling

While the instability line is determined from the free-energy analysis, a novel physical perspective is obtained by looking at the transport properties in its vicinity. We have demonstrated[17] that around this line, all resistivity curves can be collapsed onto two branches: We first divide each resistivity curve by the resistivity along the instability line (the "separatrix") $\rho_c(T) = \rho(T,\delta U = 0)$, and then rescale the temperature for each curve with an appropriately chosen parameter $T_0(\delta U)$ to collapse the data onto two branches [Fig. 6(b)]. The family of resistivity curves displays characteristic quantum critical scaling of the form

$$\rho(T,\delta U) = \rho_c(T) f(T/T_o(\delta U)), \tag{8}$$

with $T_o(\delta U) \sim |\delta U|^{z\nu}$. The scaling parameter T_o displays power-law scaling with the same exponents for both scaling branches and falls sharply as $U \to U^*$, which is consistent with the quantum critical scenario. The resistivity scaling holds in the temperature range roughly between $2T_c$ and $4T_c$, as depicted in Fig. 1. We estimate the exponent $z\nu$ to be around 0.6 when IPT is used to solve the DMFT equations. The scaling procedure with the data obtained with the CTQMC impurity solver gives a slightly larger critical exponent with an error bar due to numerical noise of the data and due to the analytical continuation.

We emphasize the difference in the proposed quantum critical scaling and classical scaling in the immediate vicinity of the critical end point (classical critical region in Fig. 1). It has been already carefully studied theoretically,[19,50] and even observed in experiments,[20] revealing the classical Ising scaling in this regime. In contrast, the scaling parameter in our formula is T rather than $|T - T_c|$ and the value of the exponent does not fit any of the known universality classes. The scaling region in our analysis is significantly broader and the collapse of the resistivity curves is observed in a large temperature region above the critical end point.

A stringent test of the proposed quantum critical transport scenario would be on systems with reduced critical temperature T_c. Figure 9 presents a schematic phase diagram with an additional parameter driving T_c to zero at some critical value X_c and merging U_{c1}, U_{c2}, and U_c into a single, quantum critical point. If this were the case, the quantum critical region would extend down to zero temperature. For a simple half-filled Hubbard model, the critical temperature can be reduced, e.g., by the disorder[51] or particle-hole asymmetry, but still remains finite. Therefore, other models should be considered, also away from half filling,[52,53] which have a significantly reduced coexistence region and where the proposed scaling may give a more direct evidence of the quantum criticality. In some of these models the coexistence region was not even detected, and then the eigenvalue analysis can also be used as an ultimate test for its existence. It would be also very interesting to explore a possible quantum critical scaling in the external electric field within the nonlinear I-V regime,[5] similar as in the experiments on Si MOSFETs.[54] This seems especially important in light

of the recent discovery of devices displaying novel resistive switching in narrow gap Mott insulators.[55] Finally, the concept of the instability line above the quantum critical point, which is based on the thermodynamic analysis, is very general and can be applied to other physical systems (e.g., interacting spins in an external field), and the scaling analysis can be tested on physical quantities other than the resistivity.

V. SCALING AROUND THE INFLECTION-POINT LINE

As stated in the previous section, the curvature λ must be directly related to an appropriate relaxation rate of a system perturbed away from the equilibrium, a quantity that in principle should be possible to measure on any system. However, it is currently very hard to make such measurements on the Mott systems and precisely determine the instability line. Our calculations, however, show that it lies just among the crossover lines that separate the bad metal and the Mott insulator, so it might not be necessary to know its exact position to observe quantum criticality. In the following, we present a scaling analysis that can be performed around the resistivity inflection-point line (or any of the other crossover lines) to test the scaling hypothesis. As it turns out, the scaling is a robust feature, not particularly sensitive to the choice of $U_c(T)$, as already tested in experiments on various organic Mott systems.[56]

We first observe that the resistivity curves display almost a perfect mirror symmetry when plotted on the log scale [Fig. 6(b)]. This puts a strong constraint on the functional form of the scaling function f (as we show below) and also indicates that the resistivity curve along the inflection-point line, $\partial \log \rho(U)/\partial U = 0$, could also serve as the separatrix. The mirror symmetry requires that

$$f(y) = 1/f(-y). \tag{9}$$

For the above to be satisfied, the function f must be of the form

$$f(y) = e^{h(y)}, \tag{10}$$

where h is an antisymmetric function of y. It is clear that $f(0) = 1$ and therefore $h(0) = 0$. h must also be smooth, so it can be represented as a Taylor series with only odd terms,

$$h(y) = ay + by^3 + \cdots. \tag{11}$$

In our calculations, it turns out that only the linear term is significant, and here we show how this can be tested. First we make a substitution of variables $T/\delta U^{z\nu} \to \delta U T^{-1/z\nu}$ and then take the logarithm of both sides of the scaling formula to obtain

$$\log\left(\frac{\rho(U_c(T)+\delta U,T)}{\rho(U_c(T),T)}\right) = \log\left(f(\delta U T^{-1/z\nu})\right). \tag{12}$$

If the mirror symmetry is satisfied, then

$$\log\left(\frac{\rho(U_c(T)+\delta U,T)}{\rho(U_c(T),T)}\right) = h(\delta U T^{-1/z\nu}), \tag{13}$$

which means that the precise form of $h(y)$ can be deduced by plotting the left-hand side of the above equation as a function of $y = \delta U T^{-1/z\nu}$ and then making a fit of a polynomial curve to the data. This is possible because in the region where the scaling formula is valid, all the data points should collapse onto a single curve. To test whether $h(y)$ is truly antisymmetric, it is convenient to first split it into symmetric and antisymmetric parts, $h(y) = h_s(y) + h_a(y)$, where $h_s(y) = \frac{1}{2}[h(y) + h(-y)]$ and $h_a(y) = \frac{1}{2}[h(y) - h(-y)]$. If the resistivity is mirror symmetric, h_s should be 0 and h_a should be equal to h. In Fig. 10 we plot these functions around the inflection-point line and find h_s to be negligible. Also, it is easily seen that $h(y)$ is purely linear in the region where the data points perfectly collapse on a single curve.

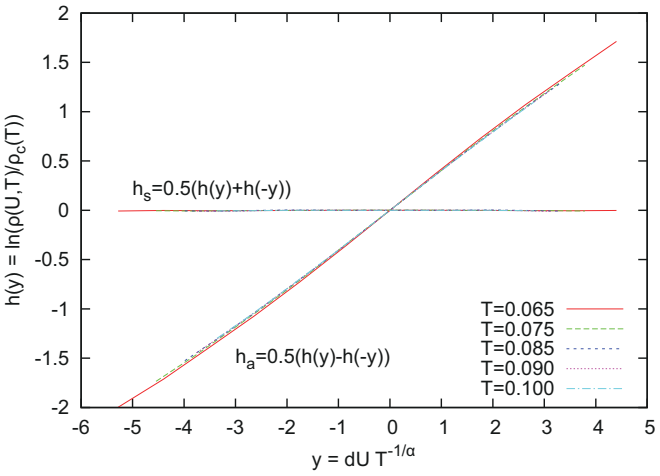

FIG. 10. (Color online) The symmetric and asymmetric part of the scaling function, h_s and h_a, at various temperatures. The small value of $h_s(y)$ shows that the mirror symmetry of resistivity curves is present. The $h_a(y)$ curves collapse around the inflection-point line, which shows that the exponent, $z\nu = 0.953$, is well evaluated. Fitting a third-order polynomial to $h_a(y)$ in the range where these curves collapse can reveal the exact form of the scaling formula. In our calculations only the linear term is significant.

Now it is clear that there are two conditions that $U_c(T)$ has to satisfy for the scaling with mirror symmetry to be possible. First, if we take the partial derivative over U at both sides of the equation, we get

$$\frac{\partial \log \rho(U,T)}{\partial U} = aT^{-\frac{1}{z\nu}} + b\delta U^2 T^{-\frac{3}{z\nu}} + \cdots. \tag{14}$$

If $h(y)$ is a linear function, then only the first term in the above equation remains, which means that the logarithm of resistivity is a linear function of U in the entire region in which the scaling formula holds. Even if there are higher terms in $h(y)$, the above has to be true at least close to U_c (small δU), where the linear term is dominant in any case. This imposes a constraint on $U_c(T)$, such that it has to be in a region where the second derivative of logarithmic resistivity is zero, or at least small,

$$\frac{\partial^2 \log \rho(U,T)}{\partial U^2} \approx 0. \tag{15}$$

This derivative is color coded in the (U,T) plane in Fig. 11 so that yellow color corresponds to a small absolute value. As it is readily verified, the above condition is not fulfilled anywhere exactly [except precisely at the log $\rho(U)$ inflection-point line by its definition], but all of the crossover lines lie in the region where this condition is approximately satisfied. There is an additional requirement for $U_c(T)$ which is not in

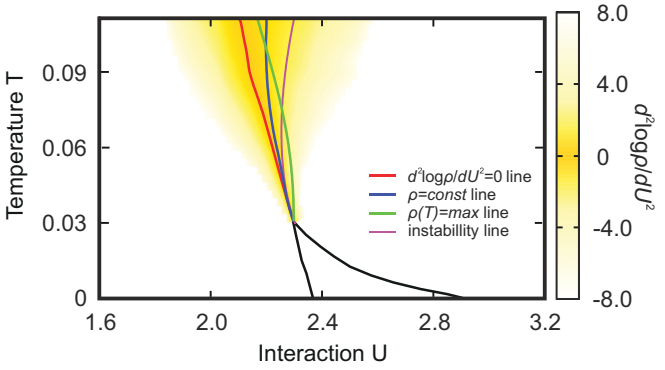

FIG. 11. (Color online) The instability line lies among the other crossover lines. $\log \rho(U)$ is linear in this crossover region, which allows for the scaling formula to be valid.

any way implied by definition of any of the crossover lines. Namely, the first derivative of the logarithmic resistivity has to be decreasing along $U_c(T)$ as a power law of temperature. This can be shown by taking the limit $\delta U \to 0$ in Eq. (14),

$$\left.\frac{\partial \log \rho(U,T)}{\partial U}\right|_{U_c} \propto T^{-\frac{1}{z\nu}}. \tag{16}$$

The above holds regardless of the value of the cubic (or any higher) term coefficient. One can even use this to give a good assessment of the exponent $z\nu$, by fitting such an experimental (or theoretical) curve to a power law as shown in Fig. 12. As it is seen here, the derivative Eq. (16) calculated along the inflection-point line fits well to a power-law curve of exponent -0.95, but only above roughly $2T_c$. The same analysis of the IPT results yields a slightly lower value of $z\nu = 0.63$.

Finally, an estimate of how well the scaling works can be made by comparing the value of resistivity obtained by the scaling formula and the one measured in experiment or, as it

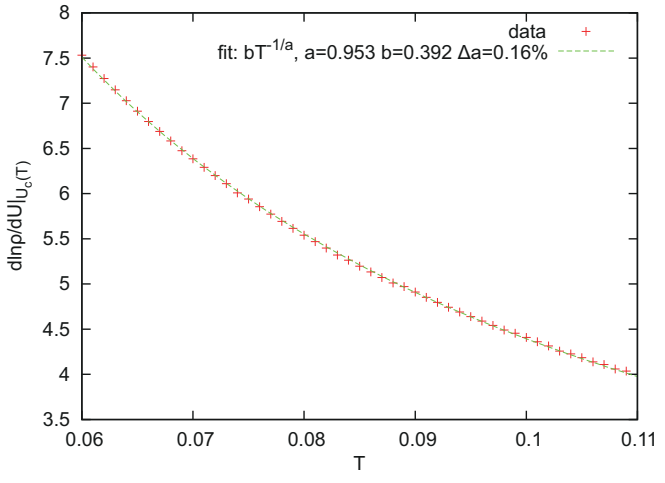

FIG. 12. (Color online) The derivative of resistivity with respect to U $[\partial\rho(U,T)/\partial U|_{U_{\rm infl}}]$ along the inflection-point line. Above roughly $2T_c$, it fits well to a power-law curve of exponent -0.95. This can be used to evaluate the value of the scaling formula exponent. At lower temperatures the decrease in resistivity is faster, and the behavior deviates from the power law, and the scaling formula fails at temperatures below $2T_c$.

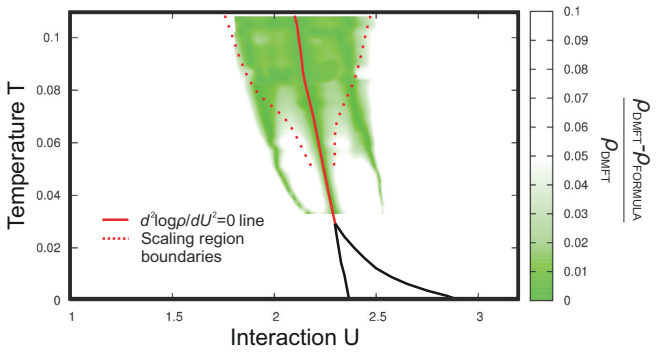

FIG. 13. (Color online) Relative error of the scaling formula color coded in the U-T plane. The dotted lines are the boundary of the scaling region. The two green filaments below $2T_c$ are where the scaling formula intersects with the actual DMFT result.

is in our case, calculated from the DMFT solution. In Fig. 13 it is shown how the scaling formula works within the 5% error bar in a large region, for the inflection-point line. This result is qualitatively the same for the other crossover lines. It is important to note that in the case of the instability line (and all the other crossover lines other than the inflection-point line), one is able to improve the quality of scaling by using different exponents $z\nu$ depending on $\mathrm{sgn}(\delta U)$, and that way compensate for the lack of exact mirror symmetry. Also, when only the linear term in $h(y)$ is used, slightly lowering the value of $z\nu$ obtained from the power-law fitting procedure typically broadens the region of validity of such a scaling formula.

In conclusion, the $\log \rho(U)$ inflection-point line is easily observable in experiment and our calculations show that it lies very close to the instability line. The analysis presented here indicates that the quantum critical scaling previously found to hold around the instability line should also be observable around the inflection-point line. We show that the scaling formula that is valid around this line displays almost a perfect mirror symmetry of resistivity curves. In general, mirror symmetry, or "duality," should not be considered a necessary ingredient for a quantum critical scaling. In fact, we find that the scaling is of better quality around the instability line, although it is slightly less symmetric.

It is also very important to examine how the resistivity changes along the separatrix, and our results are presented in Fig. 14. In this crossover region, the resistivity far exceeds the Mott limit and is only weakly dependent on temperature. We find that along the instability line, the resistivity is roughly a linear, increasing function of T. Along the inflection-point line and $\rho(T) = \max$ lines, the resistivity is slowly decreasing. We note that these results, however, must be model specific. Above the critical end point, the resistivity is strongly dependent on U, and a small change in the shape or position of these lines can cause a significant change in the temperature dependences of resistivity presented in Fig. 14.

VI. WIDOM LINES

The notion of a crossover line is very general and different physical motivations can be used for its precise definition. The concept of the Widom crossover line is, however, more strict and relies on one fundamental principle.

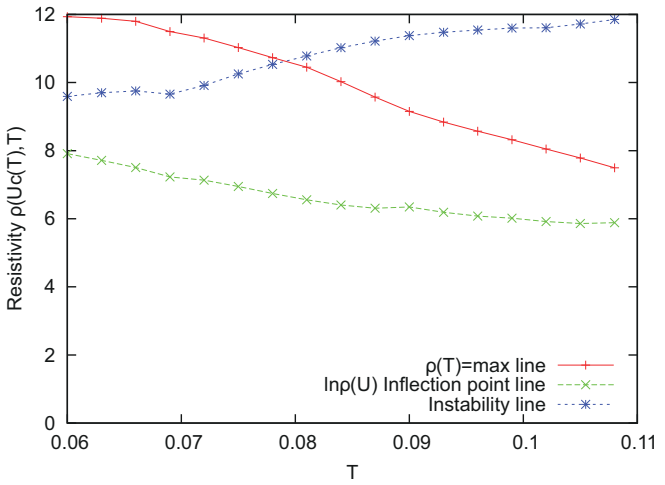

FIG. 14. (Color online) Resistivity (in units of ρ_{Mott}) along the crossover lines is weakly dependent on temperature and much larger than the Mott limit.

The Widom line was originally defined in the context of liquid-gas phase transition,[57] and as the line connecting the maxima of the isobaric specific heat as a function of pressure ($\partial C_p/\partial p = 0$), above T_c. It was conceived as a logical continuation of the first-order phase transition line to supercritical temperatures. C_p is divergent along the first-order transition line, which directly causes the maxima in C_p present above the critical temperature. This concept is easily generalized to include all the lines that mark features directly caused by nonanalyticities due to a phase transition.[58] As such, a Widom line can be defined for any quantity that exhibits either a divergence or a discontinuity because of a phase transition, and thus a maximum or an inflection point above T_c.

Very recently,[23] in the supercritical region of an argon liquid-gas phase diagram, an unexpected nonanalyticity has been found in sound velocity dispersion curves, precisely at the Widom line. The authors give a new depth and physical meaning to the concept, by observing that there is no single supercritical fluid phase, and that the Widom line actually separates two regimes of fluidlike and gaslike dynamical behavior. This finding makes it clear that the Widom lines should not be exclusively connected with the thermodynamics of the system. The changes in transport that follow certain features in thermodynamic quantities can also be used for making a meaningful and possibly even equivalent definition of the Widom line. The significance of this concept was recognized once more[24,59] in the context of hole-doped high-T_c superconductors, where the characteristic temperature T^* of the pseudogap phase is shown to correspond to the Widom line arising above a first-order transition at critical doping.

In the above sense, we emphasize that the quantum critical scaling observed in our model can also be easily connected with the concept of Widom lines, giving them new physical importance in the context of quantum-phase transitions. One can immediately recognize that the log $\rho(U)$ inflection-point line and the instability line both qualify as generalized Widom lines—they emanate from the critical end point, separate regions of metallic and insulating behavior, and mark features that are directly caused by nonanalyticities due to the phase transition. The quality of the scaling and the close proximity of these two lines may even indicate a profound connection between them. As the proposed physical concept may well surpass the scope of the Hubbard model and Mott physics, a definition of the instability line can be very useful. Contrary to the inflection-point line, it is based on a purely thermodynamical quantity, i.e., the free energy, and can be defined for an arbitrary model. It does not require the presence of the finite-temperature critical point (which makes a conceptual difference with the work[24,59] on hole-doped cuprates) and can be used to introduce the Widom line concept to exclusively zero temperature quantum-phase transitions.

VII. CONCLUSIONS

In this paper we carefully investigated the finite-temperature crossover behavior around the Mott transition, with the goal to provide both theoretical insight and experimental guidance for the search for quantum criticality in this regime. To obtain quantitative and reliable results that allow direct comparison with experiments, we performed these studies within the framework of single-site dynamical mean-field theory. From the conceptual point of view, this approach offers an immediate advantage—it is physically very clear what kinds of mechanisms and processes are captured by such a theory, and which are not. Most importantly, such an approach explicitly excludes all mechanisms directly or indirectly associated with any ordering tendencies, in agreement with the physical pictures for the Mott transition introduced by early pioneering ideas of Mott and Anderson.

More specifically, we focused on a single band half-filled Hubbard model, which, within DMFT, maps to solving a Kondo-Anderson magnetic impurity model in a self-consistently determined bath. The formation of the heavy Fermi liquid on the metallic side of the Mott transition is described as a formation of a Kondo-like singlet in the ground state, similarly as in the early work of Brinkmann and Rice.[60] In contrast to the Brinkmann-Rice theory, the DMFT approach is able to quantitatively and accurately describe the thermal destruction of such a correlated Fermi liquid, and the resulting coherence-incoherence crossover. The possibility to systematically and quantitatively describe this incoherent regime is especially important to properly characterize the high-temperature crossover behavior above the coexistence dome, where we obtained clear and precise signatures of quantum critical behavior. Our results show remarkable agreement with several experimental systems,[56] but future experiments should provide even more precise tests for our predictions. We expect that close enough to the quantum critical point all quantities should display appropriate scaling behaviors. Our work has, so far, focused mostly on the transport properties, and sufficiently detailed results for thermodynamic and other quantities are not available at this time to permit a scaling analysis. The investigation of these interesting questions is beyond the scope of the present work, and is left for future studies.

We should mention that ideas closely related to ours have also been discussed in a series of papers by Senthil

and collaborators,[61–63] who also seek a description of Mott quantum criticality unrelated to any ordering phenomena. This approach, however, focuses on capturing the possible effects of gapless "spinon" excitations, which may exist on the insulating side of the Mott transition, but only in the presence of sufficient and specific magnetic frustration, preventing the familiar antiferromagnetic order. Because of their gapless nature, they should remain long lived (e.g., well defined) only at the lowest temperatures, inducing long-range spatial correlations in the proposed spin liquid. The corresponding theory, therefore, focuses on long-distance spatial fluctuations, which, as in ordinary critical phenomena, are tackled by appropriate renormalization-group methods. In contrast to our DMFT approach, this theory implicitly disregards the strongly incoherent Kondo-like processes, which may play a dominant role at sufficiently high temperatures.

The key physical question thus remains: What is the crossover temperature T_{nonlocal} below which the nonlocal effects ignored by DMFT become significant? This important question can, in principle, be investigated by computing systematic nonlocal corrections to single-site DMFT, a research direction already investigated by several authors.[31–33,64] The recent work already provides some evidence that for a Hubbard model on a square lattice the nonlocal corrections are very small well above the coexistence dome (at $T \gg T_c$)[64] and are essentially negligible for a frustrated triangular lattice.[33] On the experimental side, the possible role of nonlocal effects such as spinons can be investigated by systematic studies of a series of materials with varying degrees of magnetic frustration. Such studies are accessible in organic Mott systems,[14,15] where $T_c \sim 10$–20 K, while the magnetic frustration may be varied using different crystal lattices. In some cases the magnetic ordering is completely suppressed on the insulating side,[65] while in others it remains.[66] If robust signatures of quantum criticality in transport are observed at $T \gg T_c$ in all of these materials, this finding would provide strong support for the "local quantum criticality" scenario we proposed that is based on the DMFT approach.

ACKNOWLEDGMENTS

We thank A. Georges, K. Kanoda, G. Kotliar, M. Rozenberg, G. Sordi, and J. M. Tremblay for useful discussions. The authors thank K. Haule for the usage of his CTQMC code. J.V. and D.T. acknowledge support from the Serbian Ministry of Education and Science under Project No. ON171017. V.D. was supported by the National High Magnetic Field Laboratory and the NSF Grant No. DMR-1005751, and H.T. by the DOE BES CMCSN Grant No. DE-AC02-98CH10886. Numerical simulations were run on the AEGIS e-Infrastructure, supported in part by FP7 Projects EGI-InSPIRE, PRACE-1IP, and HP-SEE.

[1] V. Dobrosavljević, N. Trivedi, and J. M. Valles, Jr., *Conductor-Insulator Quantum Phase Transitions* (Oxford University Press, Oxford, UK, 2012).
[2] S. Sachdev, *Quantum Phase Transitions* (Cambridge University Press, Cambridge, UK, 1999).
[3] G. R. Stewart, Rev. Mod. Phys. **56**, 755 (1984).
[4] H. v. Löhneysen, A. Rosch, M. Vojta, and P. Wölfle, Rev. Mod. Phys. **79**, 1015 (2007).
[5] S. Sondhi, S. Girvin, J. Carini, and D. Shahar, Rev. Mod. Phys. **69**, 315 (1997).
[6] C. Panagopoulos and V. Dobrosavljević, Phys. Rev. B **72**, 014536 (2005).
[7] L. D. Landau, Sov. Phys. JETP **3**, 920 (1957).
[8] J. C. Slater, Rev. Mod. Phys. **6**, 209 (1934).
[9] J. A. Hertz, Phys. Rev. B **14**, 1165 (1976).
[10] A. J. Millis, Phys. Rev. B **48**, 7183 (1993).
[11] N. F. Mott, Proc. R. Soc. London, Ser. A **197**, 269 (1949).
[12] P. W. Anderson, Rev. Mod. Phys. **50**, 191 (1978).
[13] M. Imada, A. Fujimori, and Y. Tokura, Rev. Mod. Phys. **70**, 1039 (1998).
[14] K. Kanoda and R. Kato, Annu. Rev. Condens. Matter Phys. **2**, 167 (2011).
[15] B. J. Powell and R. H. McKenzie, Rep. Prog. Phys. **74**, 056501 (2011).
[16] A. Georges, G. Kotliar, W. Krauth, and M. J. Rozenberg, Rev. Mod. Phys. **68**, 13 (1996).
[17] H. Terletska, J. Vučičević, D. Tanasković, and V. Dobrosavljević, Phys. Rev. Lett. **107**, 026401 (2011).
[18] M. J. Rozenberg, X. Y. Zhang, and G. Kotliar, Phys. Rev. Lett. **69**, 1236 (1992).
[19] G. Kotliar, E. Lange, and M. J. Rozenberg, Phys. Rev. Lett. **84**, 5180 (2000).
[20] P. Limelette, A. Georges, D. Jérome, P. Wzietek, P. Metcalf, and J. M. Honig, Science **302**, 89 (2003).
[21] F. Kagawa, K. Miyagawa, and K. Kanoda, Nature (London) **436**, 534 (2005).
[22] S. Papanikolaou, R. M. Fernandes, E. Fradkin, P. W. Phillips, J. Schmalian, and R. Sknepnek, Phys. Rev. Lett. **100**, 026408 (2008).
[23] G. G. Simeoni, T. Bryk, F. A. Gorelli, M. Krisch, G. Ruocco, M. Santoro, and T. Scopigno, Nat. Phys. **6**, 503 (2010).
[24] G. Sordi, P. Sémon, and A.-M. S. Tremblay, Sci. Rep. **2**, 547 (2012).
[25] E. Abrahams, S. V. Kravchenko, and M. P. Sarachik, Rev. Mod. Phys. **73**, 251 (2001).
[26] V. Dobrosavljević, E. Abrahams, E. Miranda, and S. Chakravarty, Phys. Rev. Lett. **79**, 455 (1997).
[27] M. M. Radonjić, D. Tanasković, V. Dobrosavljević, K. Haule, and G. Kotliar, Phys. Rev. B **85**, 085133 (2012).
[28] T. Pruschke, D. L. Cox, and M. Jarrell, Phys. Rev. B **47**, 3553 (1993).
[29] M. J. Rozenberg, G. Kotliar, H. Kajueter, G. A. Thomas, D. H. Rapkine, J. M. Honig, and P. Metcalf, Phys. Rev. Lett. **75**, 105 (1995).
[30] K. Haule and G. Kotliar, Phys. Rev. B **76**, 092503 (2007).
[31] A. Georges, Ann. Phys. **523**, 672 (2011).
[32] D. Tanasković, K. Haule, G. Kotliar, and V. Dobrosavljević, Phys. Rev. B **84**, 115105 (2011).
[33] A. Liebsch, H. Ishida, and J. Merino, Phys. Rev. B **79**, 195108 (2009).

[34]J. Kokalj and R. H. McKenzie, Phys. Rev. Lett. **110**, 206402 (2013).
[35]P. Werner, A. Comanac, L. de Medici, M. Troyer, and A. J. Millis, Phys. Rev. Lett. **97**, 076405 (2006).
[36]K. Haule, Phys. Rev. B **75**, 155113 (2007).
[37]M. Jarrell and J. E. Gubernatis, Phys. Rep. **269**, 133 (1996).
[38]N. E. Hussey, K. Takenaka, and H. Takagi, Philos. Mag. **84**, 2847 (2004).
[39]J. Merino and R. H. McKenzie, Phys. Rev. B **61**, 7996 (2000).
[40]R. A. Cooper, Y. Wang, B. Vignolle, O. J. Lipscombe, S. M. Hayden, Y. Tanabe, T. Adachi, Y. Koike, M. Nohara, H. Takagi *et al.*, Science **323**, 603 (2009).
[41]P. Gegenwart, Q. Si, and F. Steglich, Nat. Phys. **4**, 186 (2008).
[42]X. Deng, J. Mravlje, R. Žitko, M. Ferrero, G. Kotliar, and A. Georges, Phys. Rev. Lett. **110**, 086401 (2013).
[43]W. Xu, K. Haule, and G. Kotliar, arXiv:1304.7486.
[44]P. Limelette, P. Wzietek, S. Florens, A. Georges, T. A. Costi, C. Pasquier, D. Jérome, C. Mézière, and P. Batail, Phys. Rev. Lett. **91**, 016401 (2003).
[45]J. Merino, M. Dumm, N. Drichko, M. Dressel, and R. H. McKenzie, Phys. Rev. Lett. **100**, 086404 (2008).
[46]M. M. Radonjić, D. Tanasković, V. Dobrosavljević, and K. Haule, Phys. Rev. B **81**, 075118 (2010).
[47]D. Popović, A. B. Fowler, and S. Washburn, Phys. Rev. Lett. **79**, 1543 (1997).
[48]J. H. Mooij, Phys. Status Solidi A **17**, 521 (1973).
[49]G. Moeller, V. Dobrosavljević, and A. E. Ruckenstein, Phys. Rev. B **59**, 6846 (1999).
[50]P. Sémon and A.-M. S. Tremblay, Phys. Rev. B **85**, 201101(R) (2012).
[51]M. C. O. Aguiar, V. Dobrosavljević, E. Abrahams, and G. Kotliar, Phys. Rev. B **71**, 205115 (2005).
[52]G. Sordi, A. Amaricci, and M. J. Rozenberg, Phys. Rev. B **80**, 035129 (2009).
[53]A. Amaricci, A. Camjayi, K. Haule, G. Kotliar, D. Tanasković, and V. Dobrosavljević, Phys. Rev. B **82**, 155102 (2010).
[54]S. V. Kravchenko, D. Simonian, M. P. Sarachik, W. Mason, and J. E. Furneaux, Phys. Rev. Lett. **77**, 4938 (1996).
[55]V. Guiot, L. Cario, E. Janod, B. Corraze, V. T. Phuoc, M. Rozenberg, P. Stoliar, T. Cren, and D. Roditchev, Nat. Commun. **4**, 1722 (2013).
[56]K. Kanoda (private communication).
[57]B. Widom, in *Phase Transitions and Critical Phenomena*, edited by C. Domb and M. S. Green (Academic, New York, 1972), Vol. 2.
[58]L. Xu, P. Kumar, S. V. Buldyrev, S.-H. Chen, P. H. Poole, F. Sciortino, and H. E. Stanley, Proc. Natl. Acad. Sci. USA **102**, 16558 (2005).
[59]G. Sordi, P. Sémon, K. Haule, and A.-M. S. Tremblay, Phys. Rev. B **87**, 041101 (2013).
[60]W. F. Brinkman and T. M. Rice, Phys. Rev. B **2**, 4302 (1970).
[61]T. Senthil, Phys. Rev. B **78**, 035103 (2008).
[62]T. Senthil, Phys. Rev. B **78**, 045109 (2008).
[63]W. Witczak-Krempa, P. Ghaemi, T. Senthil, and Y. B. Kim, Phys. Rev. B **86**, 245102 (2012).
[64]H. Park, K. Haule, and G. Kotliar, Phys. Rev. Lett. **101**, 186403 (2008).
[65]Y. Shimizu, K. Miyagawa, K. Kanoda, M. Maesato, and G. Saito, Phys. Rev. Lett. **91**, 107001 (2003).
[66]K. Miyagawa, A. Kawamoto, Y. Nakazawa, and K. Kanoda, Phys. Rev. Lett. **75**, 1174 (1995).

d-wave superconductivity on the honeycomb bilayer

J. Vučičević,[1] M. O. Goerbig,[2] and M. V. Milovanović[1]

[1]*Scientific Computing Laboratory, Institute of Physics Belgrade, University of Belgrade, Pregrevica 118, 11080 Belgrade, Serbia*

[2]*Laboratoire de Physique des Solides, Université Paris-Sud, CNRS UMR 8502, F-91405 Orsay Cedex, France*

(Received 19 February 2012; revised manuscript received 1 August 2012; published 7 December 2012)

We introduce a microscopic model on the honeycomb bilayer, which in the small-momentum limit captures the usual (quadratic dispersion in the kinetic term) description of bilayer graphene. In the limit of strong interlayer hopping it reduces to an effective honeycomb monolayer model with also third-neighbor hopping. We study interaction effects in this effective model, focusing on possible superconducting instabilities. We find $d_{x^2-y^2}$ superconductivity in the strong-coupling limit of an effective tJ-model-like description that gradually transforms into $d+id$ time-reversal symmetry-breaking superconductivity at weak couplings. In this limit the small-momentum order-parameter expansion is $(k_x+ik_y)^2$ [or $(k_x-ik_y)^2$] in both valleys of the effective low-energy description. The relevance of our model and investigation for the physics of bilayer graphene is also discussed.

DOI: 10.1103/PhysRevB.86.214505 PACS number(s): 74.20.Mn, 74.20.Rp, 74.70.Wz, 73.20.At

I. INTRODUCTION

Interaction effects are expected to be important for the physics of bilayer graphene and may cause a formation of correlated many-body phases.[1,2] This needs to be contrasted to intrinsic monolayer graphene, in which a vanishing density of states at the Dirac points suppresses the influence of electronic correlations.[2,3] Recent experiments on suspended bilayer graphene,[4–7] which is free of substrate effects, reveal a gapped state at and around the charge neutrality point. The state may be of topological origin[8] due to the observed[4,6] conductance of the order of e^2/h and may exhibit an anomalous quantum Hall effect, i.e., a quantum Hall effect at zero magnetic field. In the most recent experiment on high mobility samples, from Ref. 7, a completely insulating behavior was found.

From the theory point of view, several proposals were given[9–19] for the existence of gapped (and gapless) phases at the charge neutrality point, including those that break the time-reversal symmetry. Most of them are based on the particle-hole (excitonic) binding, which is the most natural assumption in the understanding of a gapped phase at the charge neutrality point. These theories assume a quadratic dispersion of the electrons in the low-energy effective description,[20] and direct hopping between two sublattices in different layers that leads to the linear dispersion ("triagonal warping") is neglected. This assumption is justified if the chemical potential is not exactly situated at the charge neutrality point.

To explore additional possibilities for gapped phases in the presence of a finite chemical potential, we discuss here superconducting instabilities, especially with an eye on the possibility of topological (fully gapped) superconductivity on the honeycomb bilayer. Bilayer graphene may be potentially also viewed as a strongly correlated system with a possibility to support a layered antiferromagnetic state,[13,14] similar to the Mott physics of high T_c superconductors. The existence of a layered antiferromagnetic state is supported by the most recent experiment with high quality samples,[7] which feature completely insulating behavior at the charge neutrality point.

There is, so far, no systematic study of superconducting instabilities in the presence of electron-electron and electron-phonon interactions on the honeycomb bilayer at finite doping (see, however, Ref. 21 for fermions in the presence of weak electron-electron interactions only at zero chemical potential). To address this question, we study in the present paper a microscopic model of a single effective honeycomb monolayer with reduced nearest-neighbor hopping and third-neighbor hopping, in addition to intersite attractive interactions. The kinetic term of the effective model is obtained by integrating out the "high-energy" degrees of freedom from the direct interlayer hopping (i.e., assuming strong interlayer hopping in the honeycomb bilayer), and the intersite superexchange interaction originates from the Hubbard on-site repulsion. This model is to a certain degree biased to antiferromagnetism and d-wave superconductivity but preserves the usual low-energy description of the bilayer graphene.[20] Moreover, in contrast to the usual low-energy model of bilayer graphene, the present model accounts for the lattice symmetry of the original model (the honeycomb bilayer) that may be relevant for the symmetry of the superconducting order parameters.

Our primary interest here is to find the most probable symmetry of a superconducting instability on the honeycomb bilayer together with an understanding of its nature, i.e., whether this instability is topological. We also aim at an understanding of the change in the superconducting order parameter and correlations as we go from a monolayer to a few-layer honeycomb lattice. The mean-field solution of the introduced model yields a time-reversal symmetry-breaking $d+id$-wave superconducting state at weak coupling, which continuously transforms into a $d_{x^2-y^2}$-wave type with increasing interaction. Near $3/8$ and $5/8$ filling of the π bands, i.e., near the Van Hove singularity in the density of states, the Cooper pairing becomes much stronger. Our conclusion is that the $d+id$ superconducting instability is the leading superconducting instability of the honeycomb bilayer with strong interlayer hopping at finite doping, and the same instability may be present in the bilayer graphene at finite doping. However, due to the presumed smallness of the coupling constant and order parameter, as well as strong quantum fluctuations in two dimensions, it may be difficult to detect this order experimentally in today's graphene samples.

The remaining part of the paper is organized as follows. In Sec. II we define our effective two-band model on an effective

honeycomb lattice with third-nearest-neighbor hopping. The model is then, in Sec. III, solved by a Bogoliubov-de Gennes (BdG) transformation for a singlet bond-pairing order parameter, and we discuss the relevant symmetries. Section IV presents the phase diagram obtained from a numerical solution of the BdG equations. In Sec. V, the relevance for the physics of the bilayer graphene is discussed, and our main conclusions are presented in Sec. VI. Two appendices summarize analytically obtained solutions in the weak-coupling BCS limit.

II. MODEL

The honeycomb bilayer lattice consists of two Bernal stacked honeycomb lattices, each consisting of two triangular sublattices as illustrated in Fig. 1 such that the unit cell contains four lattice sites. The Hamiltonian of free electrons on such a lattice is given by

$$\begin{aligned} H_0 = &-t\sum_{\vec{j},\sigma}\sum_{\vec{u}}(a^{\dagger}_{1,\vec{j},\sigma}b_{1,\vec{j}+\vec{u},\sigma}+a^{\dagger}_{2,\vec{j},\sigma}b_{2,\vec{j}-\vec{u},\sigma}+\text{H.c.})\\ &-t_{\perp}\sum_{\vec{j},\sigma}(a^{\dagger}_{1,\vec{j},\sigma}a_{2,\vec{j},\sigma}+\text{H.c.})\\ &-\mu\sum_{i,\vec{j}}(a^{\dagger}_{i,\vec{j},\sigma}a_{i,\vec{j},\sigma}+b^{\dagger}_{i,\vec{j},\sigma}b_{i,\vec{j},\sigma}). \end{aligned} \tag{1}$$

Here, the index $i = 1,2$ denotes the layer and $\vec{j}$ enumerates primitive cells. The sum runs over $\vec{u} = \vec{u}_0, \vec{u}_1, \vec{u}_2$, where

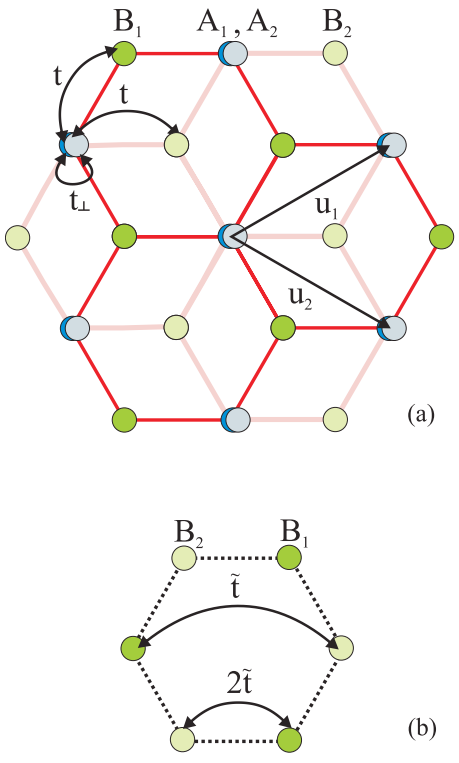

FIG. 1. (Color online) (a) View of Bernal stacked honeycomb lattices 1 and 2 with corresponding sublattice sites A1, B1 and A2, B2, respectively. (b) Model reduced to a monolayer model with the third-neighbor hopping $\tilde{t} \equiv t^2/t_{\perp}$ and the nearest-neighbor hopping $2\tilde{t}$ (see the text).

$\vec{u}_1 = a(\frac{3}{2}, \frac{\sqrt{3}}{2})$ and $\vec{u}_2 = a(\frac{3}{2}, -\frac{\sqrt{3}}{2})$ are the primitive vectors of the lattice, and $\vec{u}_0 = (0, 0)$ is an auxiliary vector for denoting the hopping between sites in the same primitive cell. The norm of these vectors is $|\vec{u}| = \sqrt{3}a$, in terms of the distance a between neighboring sites in each layer, and t is the associated hopping energy, whereas $t_{\perp}$ denotes the interlayer hopping energy between A sites in two different layers. The finite chemical potential μ takes into account doping, either due to the electric-field effect or to chemically active adatoms. The operators $a^{\dagger}_{i,\vec{n},\sigma}(a_{i,\vec{n},\sigma})$ represent electron creation (annihilation) on the sublattice site A_i of the layer i with spin $\sigma = \uparrow, \downarrow$, and $b^{\dagger}_{i,\vec{n},\sigma}(b_{i,\vec{n},\sigma})$ represent those for electrons on the sublattice site B_i. μ is the chemical potential. We use units such that $\hbar = 1$.

By introducing the Fourier transforms $a_{i,\vec{k},\sigma} = \sum_{\vec{j}} a_{i,\vec{j},\sigma}\exp(i\vec{k}\cdot\vec{j})$ and $b_{i,\vec{k},\sigma} = \sum_{\vec{j}} b_{i,\vec{j},\sigma}\exp(i\vec{k}\cdot\vec{j})$, and diagonalizing the Hamiltonian one obtains the spectrum

$$E^{\pm}_{\alpha}(\vec{k}) = \pm\left[(-1)^{\alpha}\frac{t_{\perp}}{2} + \sqrt{\frac{t_{\perp}^2}{4} + t^2|\gamma_{\vec{k}}|^2}\right], \tag{2}$$

where $\alpha = 1,2$, and $\pm$ denote four different branches of dispersion and

$$\gamma_{\vec{k}} = \sum_{\vec{u}} e^{i\vec{k}\cdot\vec{u}} = 1 + e^{i\vec{k}\cdot\vec{u}_1} + e^{i\vec{k}\cdot\vec{u}_2}. \tag{3}$$

In their original work,[20] McCann and Falko showed that the four-band model may be simplified to an effective two-band model if one considers energies much smaller than $t_{\perp}$. In momentum space, the Hamiltonian in Eq. (1) becomes

$$H_0 = \sum_{\sigma}\int_{\text{BZ}}\frac{d^2\vec{k}}{(2\pi)^2} \tag{4}$$

$$\begin{aligned} \{&-t(\gamma_{\vec{k}}a^{\dagger}_{1,\sigma,\vec{k}}b_{1,\sigma,\vec{k}} + \gamma^{*}_{\vec{k}}a^{\dagger}_{2,\sigma,\vec{k}}b_{2,\sigma,\vec{k}} + \text{H.c.})\\ &-t_{\perp}(a^{\dagger}_{1,\sigma,\vec{k}}a_{2,\sigma,\vec{k}} + \text{H.c.}) - \mu(a^{\dagger}_{1,\sigma,\vec{k}}a_{1,\sigma,\vec{k}} + a^{\dagger}_{2,\sigma,\vec{k}}a_{2,\sigma,\vec{k}}\\ &+b^{\dagger}_{1,\sigma,\vec{k}}b_{1,\sigma,\vec{k}} + b^{\dagger}_{2,\sigma,\vec{k}}b_{2,\sigma,\vec{k}})\}. \end{aligned} \tag{5}$$

If we introduce the spinor

$$\Psi_{\sigma}(\vec{k}) = (a_{1,\sigma,\vec{k}}, a_{2,\sigma,\vec{k}}, b_{2,\sigma,\vec{k}}, b_{1,\sigma,\vec{k}})^{T}, \tag{6}$$

the Hamiltonian can be expressed as a 4×4 matrix:

$$H_0(\vec{k}) = \sum_{\sigma}\Psi^{\dagger}_{\sigma}(\vec{k})\begin{bmatrix} -\mu & -t_{\perp} & 0 & -t\gamma_{\vec{k}} \\ -t_{\perp} & -\mu & -t\gamma^{*}_{\vec{k}} & 0 \\ 0 & -t\gamma_{\vec{k}} & -\mu & 0 \\ -t\gamma^{*}_{\vec{k}} & 0 & 0 & -\mu \end{bmatrix}\Psi_{\sigma}(\vec{k}). \tag{7}$$

One may further define 2×2 matrices $H_{11} = -\mu I + t_{\perp}\sigma_x$, $H_{22} = -\mu I$, and $H_{12} = -t(\text{Re}\,\gamma_{\vec{k}}\sigma_x + \text{Im}\,\gamma_{\vec{k}}\sigma_y) = H_{21}$, such that the eigenvalue equation can be written in the following form ($\vec{k}$ indices are implied):

$$\begin{bmatrix} H_{11} & H_{12} \\ H_{21} & H_{22} \end{bmatrix}\begin{bmatrix} \Psi_1 \\ \Psi_2 \end{bmatrix} = E\begin{bmatrix} \Psi_1 \\ \Psi_2 \end{bmatrix}, \tag{8}$$

from which we obtain

$$\{H_{22} - H_{21}(H_{11} - E)^{-1}H_{12}\}\Psi_2 = E\Psi_2. \tag{9}$$

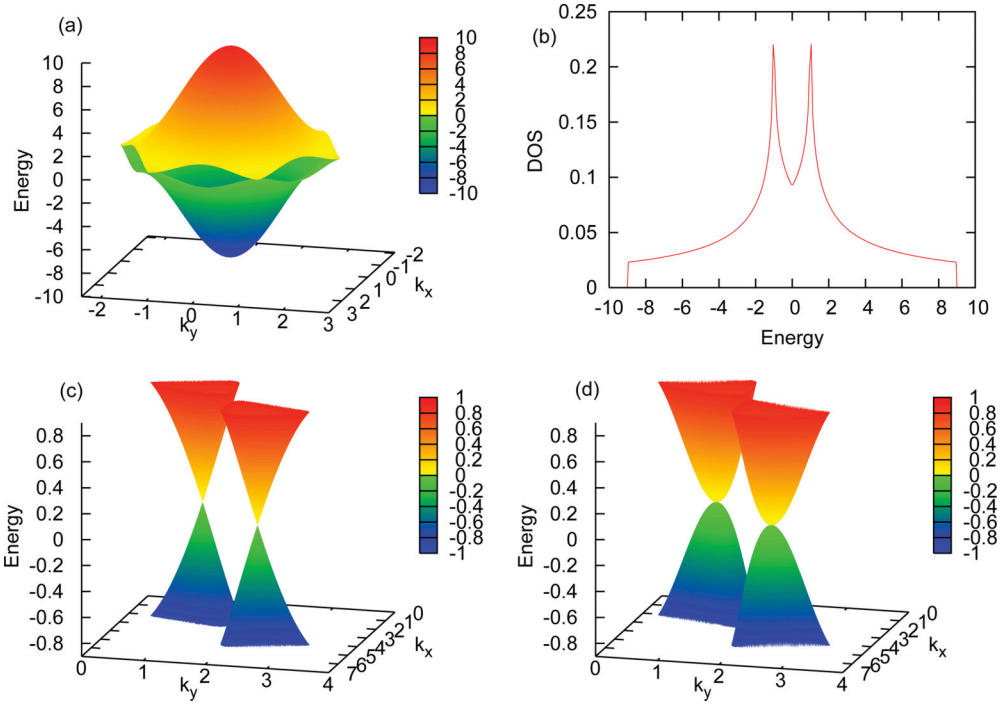

FIG. 2. (Color online) (a) Noninteracting dispersion and (b) density of states of the projected monolayer model. (c) Linear dispersion in the vicinity of the K points in the graphene monolayer in comparison to (d) quadratic dispersion in our model. We use $\tilde{t} = t^2/t_\perp$ for the unit of energy.

If we assume $t_\perp$ to be the largest-energy scale and consider the low-energy limit ($E \ll t_\perp$), Eq. (9) becomes

$$H_{\text{eff}}\Psi_2 \equiv \begin{bmatrix} -\mu & \frac{t^2}{t_\perp}\gamma_{\vec{k}}^2 \\ \frac{t^2}{t_\perp}\gamma_{\vec{k}}^{*2} & -\mu \end{bmatrix} \Psi_2 = E\Psi_2, \qquad (10)$$

with $\Psi_2(\vec{k}) = (b_{2,\sigma,\vec{k}}, b_{1,\sigma,\vec{k}})^T$.

The two-band model described by the Hamiltonian in Eq. (10) is also valid in the limit[20] where $E \ll t_\perp \ll t$. For energies larger than $t_\perp$, one needs to take into account the other two bands which overlap in energy with those considered in Eq. (10). In the following sections we use the simplified two-band model at even larger energies, up to the Van Hove singularity. Formally, this amounts to increasing artificially (with respect to the graphene bilayer) the interlayer hopping $t_\perp$ such that it becomes the largest-energy scale, $t_\perp \gg t$. In that limit Eq. (10) becomes the exact description of the honeycomb bilayer for $E, t \ll t_\perp$ and for the wave vectors of the whole Brillouin zone. We will adopt that model in the following.

The Hamiltonian in Eq. (10) corresponds, in real space, to a single-layer honeycomb lattice with nearest-neighbor and third-neighbor hoppings. Whereas the effective hopping amplitude of the latter is given by $t^2/t_\perp$, the effective nearest-neighbor hopping is twice as large.[23] This means that due to the strong interlayer hopping the complete low-energy physics is projected onto the B1 and B2 sublattices, which themselves form a hexagonal lattice (see Fig. 1).

As mentioned above, the model is equivalent to the graphene bilayer in the small-momentum limit, i.e., for $t^2/t_\perp|ka|^2 \sim \mu \ll t^2/t_\perp$, and reproduces correctly the finite density of states (DOS) at $E = 0$ of bilayer graphene (Fig. 2). Finally, the Hamiltonian in Eq. (10) does not take into account direct hopping between the B1 and B2 sublattices, which may, though, easily be accounted for by adding $-t'\gamma_{\vec{k}}^*$ to the off-diagonal matrix elements, where $t' \simeq 0.3$ eV is the associated hopping amplitude. This term yields the so-called trigonal warping close to the charge neutrality point, which consists of a splitting of the parabolic band-contact point into four linear Dirac points.[20] However, these Dirac points are present only at very low energies, for chemical potentials $|\mu|$ in the meV range, such that the parabolic band approximation becomes valid even at low dopings. Since we are interested, here, in moderate doping, we neglect this additional term and use the effective band the model in Eq. (10) in the following sections.

Since we consider the effective hopping $t^2/t_\perp$ to be small, and if there is a significant on-site repulsion U, spin-singlet bonds between B1 and B2 sites are expected to form due to superexchange processes. Therefore, we apply the $t - J$ model but relax the requirement of the model that double occupation of sites is excluded. We justify this by our primary aim: to find the most probable symmetry of the superconducting instability. As we will be working in the mean-field approximation, we just assume an effective nearest-neighbor attractive interaction between electrons on B1 and B2 sublattices, and in doing this we favor spin-singlet bond formation. The spin-singlet formation directly follows from the mean-field approach to the $t - J$ model.[22] If the attractive interaction is not too strong, it can be simply added to Hamiltonian Eq. (10), with the help of the term

$$H_I = -J \sum_{\vec{j},\vec{u}} \sum_{\sigma} b^\dagger_{1,\vec{j},\sigma} b_{1,\vec{j},\sigma} b^\dagger_{2,\vec{j}+\vec{u},-\sigma} b_{2,\vec{j}+\vec{u},-\sigma}, \qquad (11)$$

where $J > 0$. Now we apply the BCS ansatz by introducing the superconducting order parameter as a three component complex vector:

$$\Delta \equiv (\Delta_{\vec{u}_0}, \Delta_{\vec{u}_1}, \Delta_{\vec{u}_2}),$$

where the components are defined by

$$\Delta_{\vec{u}} = \frac{1}{\sqrt{2}} \langle b_{1,\vec{j},\uparrow} b_{2,\vec{j}+\vec{u},\downarrow} - b_{1,\vec{j},\downarrow} b_{2,\vec{j}+\vec{u},\uparrow} \rangle \tag{12}$$

and correspond to the spin-singlet pairing amplitudes of three inequivalent pairs of nearest neighbors. The interaction part H_I in the mean-field approximation becomes

$$H_{\mathrm{BCS}} = \sqrt{2} J \sum_{\vec{j},\vec{u}} \Delta_{\vec{u}} (b^\dagger_{1,\vec{u},\uparrow} b^\dagger_{2,\vec{j}+\vec{u},\downarrow} - b^\dagger_{1,\vec{j},\downarrow} b^\dagger_{2,\vec{j}+\vec{u},\uparrow}) + \mathrm{H.c.} + 2N \sum_{\vec{u}} J |\Delta_{\vec{u}}|^2, \tag{13}$$

where N is the number of unit cells.

III. BOGOLIUBOV-DE GENNES ANALYSIS AND PAIRING SYMMETRIES

The complete BCS Hamiltonian in momentum space is given by

$$H = -\frac{t^2}{t_\perp} \sum_{\vec{k},\sigma} \left(\gamma^2_{\vec{k}} b^\dagger_{2,\vec{k}\sigma} b_{1,\vec{k}\sigma} + \mathrm{H.c.} \right) + \sqrt{2} J \sum_{\vec{k}} \left[\sum_{\vec{u}} \Delta_{\vec{u}} e^{i\vec{k}\cdot\vec{u}} (b^\dagger_{2,\vec{k}\uparrow} b^\dagger_{1,-\vec{k}\downarrow} - b^\dagger_{2,\vec{k}\downarrow} b^\dagger_{1,-\vec{k}\uparrow}) + \mathrm{H.c.} \right] - \mu \sum_{\vec{k},\sigma} (b^\dagger_{1,\vec{k}\sigma} b_{1,\vec{k}\sigma} + b^\dagger_{2,\vec{k}\sigma} b_{2,\vec{k}\sigma}). \tag{14}$$

Similar to the case of the honeycomb monolayer,[22] we can make our description much more transparent if we apply the following transformation that diagonalizes the kinetic part of the above Hamiltonian:

$$\begin{bmatrix} b_{2,\vec{k}\sigma} \\ b_{1,\vec{k}\sigma} \end{bmatrix} = \frac{1}{\sqrt{2}} \begin{bmatrix} d_{\vec{k}\sigma} + c_{\vec{k}\sigma} \\ e^{-i2\varphi_{\vec{k}}} (d_{\vec{k}\sigma} - c_{\vec{k}\sigma}) \end{bmatrix}, \tag{15}$$

where $\varphi_{\vec{k}} = \arg(\gamma_{\vec{k}})$.

In this basis, where $c_{\vec{k}\sigma}$ and $d_{\vec{k}\sigma}$ represent the electron states in the upper and lower band, respectively, the Hamiltonian transforms into

$$H = \sum_{\vec{k}} \left\{ \sum_{\sigma} (\tilde{t}\epsilon_{\vec{k}} - \mu) c^\dagger_{\vec{k}\sigma} c_{\vec{k}\sigma} + \sum_{\sigma} (-\tilde{t}\epsilon_{\vec{k}} - \mu) d^\dagger_{\vec{k}\sigma} d_{\vec{k}\sigma} + \sqrt{2} J \left[\sum_{\vec{u}} \Delta_{\vec{u}} \cos(\vec{k}\cdot\vec{u} - 2\varphi_{\vec{k}}) (d^\dagger_{\vec{k}\uparrow} d^\dagger_{-\vec{k}\downarrow} - c^\dagger_{\vec{k}\uparrow} c^\dagger_{-\vec{k}\downarrow}) + \sum_{\vec{u}} i \Delta_{\vec{u}} \sin(\vec{k}\cdot\vec{u} - 2\varphi_{\vec{k}}) (c^\dagger_{\vec{k}\uparrow} d^\dagger_{-\vec{k}\downarrow} - d^\dagger_{\vec{k}\uparrow} c^\dagger_{-\vec{k}\downarrow}) \right] + \mathrm{H.c.} \right\}. \tag{16}$$

Here $\tilde{t} \equiv t^2/t_\perp$ and $\epsilon_{\vec{k}} \equiv |\gamma_{\vec{k}}|^2$. The eigenvalues are given by

$$E_{\vec{k}} = \pm \sqrt{(\tilde{t}\epsilon_{\vec{k}})^2 + \mu^2 + 2J^2(|S_{\vec{k}}|^2 + |C_{\vec{k}}|^2) \pm 2\sqrt{A}}, \tag{17}$$

where $C_{\vec{k}} = \sum_{\vec{u}} \Delta_{\vec{u}} \cos(\vec{k}\cdot\vec{u} - 2\varphi_{\vec{k}})$, $S_{\vec{k}} = \sum_{\vec{u}} \Delta_{\vec{u}} \sin(\vec{k}\cdot\vec{u} - 2\varphi_{\vec{k}})$, and

$$A = (\mu^2 + 2J^2|S_{\vec{k}}|^2)\tilde{t}^2\epsilon^2_{\vec{k}} + 4J^4(\mathrm{Re}C_{\vec{k}}\mathrm{Im}S_{\vec{k}} - \mathrm{Im}C_{\vec{k}}\mathrm{Re}S_{\vec{k}})^2. \tag{18}$$

If all $\Delta_{\vec{u}}$ are purely real, i.e., there is no time-reversal symmetry breaking, then the second term in A is zero and the expression for the dispersion simplifies to

$$E_{\vec{k}} = \pm \sqrt{\left(\tilde{t}\epsilon_{\vec{k}} \pm \sqrt{\mu^2 + 2J^2 S^2_{\vec{k}}}\right)^2 + 2J^2 C^2_{\vec{k}}}. \tag{19}$$

In this case $S_{\vec{k}}$ only renormalizes the chemical potential, whereas $C_{\vec{k}}$ plays the main role in the description of the superconducting order parameter. A comparison between the Bogoliubov energy dispersion in Eq. (19) and the usual BCS expression shows that $C_{\vec{k}}$ can be identified with the gap function. However, this name may be misleading because $C_{\vec{k}}$ does not describe the gap, as in the example in Eq. (22) below.

The symmetry analysis of the order parameter on a honeycomb lattice[22] yields the basis vectors which correspond to s, $d_{x^2-y^2}$, and d_{xy} waves, respectively:

$$\Delta = \begin{cases} \Delta\,(1, & 1, & 1) \\ \Delta\,(2, & -1, & -1) \\ \Delta\,(0, & 1, & -1) \end{cases}. \tag{20}$$

The function $C_{\vec{k}}$ corresponding to these symmetries is shown in Fig. 3, in comparison with the monolayer case. The last two possibilities belong to a two-dimensional (2D) subspace of irreducible representation of permutation group $\mathcal{S}_3$.[24] This means that any superposition of these two order parameters, which we may identify with the $d_{x^2-y^2}$ [$(2,-1,-1)$ of Eq. (20) and permutations] and d_{xy} [$(0,1,-1)$ of Eq. (20) and permutations] solutions of d-wave superconductivity, is possible from a symmetry point of view. In spite of this principle possibility, the precise realization of a particular order parameter is a question of energy calculations. One notices that the spatial

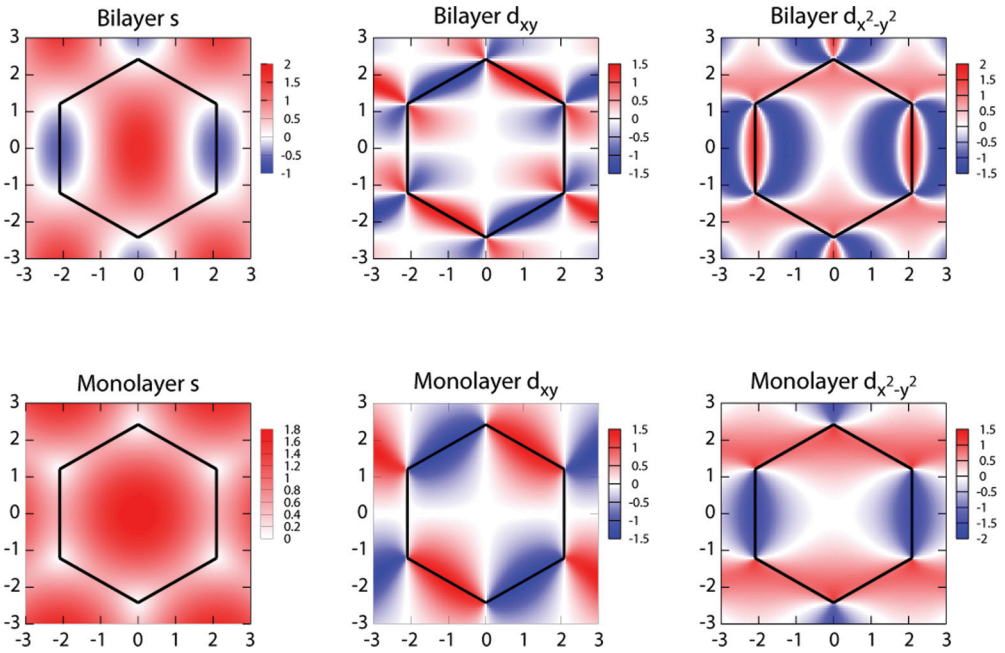

FIG. 3. (Color online) C_k in the first Brillouin zone calculated for three possible symmetries on monolayer and projected bilayer lattices.

point symmetry of the underlying honeycomb lattice is C_{3v}, which includes $2\pi/3$ rotations, whereas a transformation from $d_{x^2-y^2}$ to d_{xy} involves $\pi/4$ rotations. The order parameters thus have a different symmetry than the underlying lattice, as one may also see in Fig. 3, such that the two order parameters do not represent degenerate ground states. Indeed we find, within the BCS mean-field theory, that the $d_{x^2-y^2}$ solution has a lower energy than the d_{xy} solution.

This finding needs to be contrasted to the case of p-wave superconductivity on the square lattice.[31] In the latter case, superpositions of the p_x and p_y solutions are also permitted by the symmetry of the order parameter, but both solutions are related to each other by $\pi/2$ rotations that respect the point symmetry of the underlying (square) lattice. The p_x and p_y solutions are therefore degenerate.

The above arguments indicate that the C_{3v} symmetry of the honeycomb lattice is dynamically broken, only through interactions, via the formation of a $d_{x^2-y^2}$ order parameter. This is similar to the findings of Poletti *et al.* in the context of superfluidity of spinless fermions with nearest-neighbor attraction.[24] Also in this case, the C_{3v} symmetry is dynamically broken. Notice finally that in the small-J limit, i.e., at weak coupling or in the low-energy limit, the BdG system recovers the symmetry of the C_{3v} group but has also an (emergent) continuous rotational symmetry that will lead to a $d_{x^2-y^2} \pm i\sqrt{3}\, d_{xy}$ instability (see Appendix A).

In the case of an s-wave order parameter with $\Delta = \Delta\,(1,1,1)$, a small-wave-vector expansion ($|\vec{q}|a \ll 1$) around the K points yields

$$C_{\vec{K}_\pm+\vec{q}} \approx \mp\frac{\sqrt{3}}{2} q_y a\Delta, \qquad S_{\vec{K}_\pm+\vec{q}} \approx +\frac{\sqrt{3}}{2} q_x a\Delta. \tag{21}$$

Thus both couplings are nonzero and no simple effective picture emerges by looking at the Hamiltonian in Eq. (16). The lower excitation energy branch can be approximated in the small-momentum limit as

$$\begin{aligned} E_{\vec{q}} &\simeq \sqrt{\mu^2 - 2\mu\tilde{t}\epsilon_{\vec{K}_\pm+\vec{q}} + \tfrac{3}{2}J^2(|\vec{q}|a)^2\Delta^2} \\ &\simeq \sqrt{\mu^2 - \tfrac{3}{2}[3\mu\tilde{t} - (J\Delta)^2](|\vec{q}|a)^2}, \end{aligned} \tag{22}$$

where we have used $\epsilon_{\vec{K}_\pm+\vec{q}} \simeq 9(|\vec{q}|a)^2/4$.

If the coupling strengths are such that $E_{\vec{q}}$ has a minimum at $q = 0$, that is for $(J\Delta)^2 > 3\mu\tilde{t}$, a special superconducting instability may be realized (if other possibilities, order parameters, have higher free energy).[25] In the absence of trigonal warping at very low doping, we obtain a time-reversal invariant superconducting instability with two kinds of Cooper pairs with $p_x + ip_y$ and $p_x - ip_y$ pairings. Due to the forms of $C_{\vec{k}}$ and $S_{\vec{k}}$ in the above Hamiltonian in the small-momentum limit, p-wave Cooper pairings are expected. For a sufficiently large chemical potential, one can neglect $S_{\vec{k}}$ in Eq. (19) and the system may be unstable towards a p_y gapless superconductor, with gap minima on the Fermi surface, i.e., on a circle.

For $\Delta = \Delta(2,-1,-1)$, the small-momentum expansion around the K points yields

$$\begin{aligned} C_{\vec{K}_\pm+\vec{q}}(d_{x^2-y^2}) &\approx -3\frac{(q_x^2 - q_y^2)}{|\vec{q}|^2}\Delta, \\ S_{\vec{K}_\pm+\vec{q}}(d_{x^2-y^2}) &\approx \mp 6\frac{q_x q_y}{|\vec{q}|^2}\Delta \end{aligned} \tag{23}$$

and for $\Delta = \Delta(0,1,-1)$

$$\begin{aligned} C_{\vec{K}_\pm+\vec{q}}(d_{xy}) &\approx 2\sqrt{3}\frac{q_x q_y}{|\vec{q}|^2}\Delta, \\ S_{\vec{K}_\pm+\vec{q}}(d_{xy}) &\approx \mp\sqrt{3}\frac{(q_x^2 - q_y^2)}{|\vec{q}|^2}\Delta. \end{aligned} \tag{24}$$

The gap function $C_{\vec{k}}$ thus clearly shows the $d_{x^2-y^2}$ and the d_{xy} symmetry in Eqs. (23) and (24), respectively.

Notice that one may superpose two waves in the manner

$$C_{\vec{k}}(d \pm id) = C_{\vec{k}}(d_{x^2-y^2}) \pm i\sqrt{3}C_{\vec{k}}(d_{xy}) \tag{25}$$

and

$$S_{\vec{k}}(d \pm id) = S_{\vec{k}}(d_{x^2-y^2}) \pm i\sqrt{3}S_{\vec{k}}(d_{xy}), \tag{26}$$

which is identified with the $d + id$-wave superconducting phase in the following. In the small-wave-vector limit, the combined forms of $C_{\vec{k}}$,

$$C_{\vec{K}_\pm+\vec{q}}(d + id) \approx \mp iS_{\vec{K}_\pm+\vec{q}} \approx 3(q_x + iq_y)^2/|\vec{q}|^2 \tag{27}$$

and

$$C_{\vec{K}_\pm+\vec{q}}(d - id) \approx \pm iS_{\vec{K}_\pm+\vec{q}} \approx 3(q_x - iq_y)^2/|\vec{q}|^2, \tag{28}$$

restore the rotational symmetry—they are indeed eigenstates of rotation in two dimensions with the value of angular momentum equal to 2. Thus a fixed complex combination in real space, either $d_{x^2-y^2} + i\sqrt{3}\, d_{xy}$ or $d_{x^2-y^2} - i\sqrt{3}\, d_{xy}$, leads to the same form of the expansion in small momenta at both valley points, either Eq. (27) or Eq. (28). Because it is the same irrespective of the valley K or K' one obtains a solution that spontaneously breaks time-reversal symmetry. Thus we can identify the solution with the broken time-reversal symmetry $d + id$ state. Something similar happens in the monolayer case, but the d-wave symmetry is recognized as a global dependence of the order parameter on the $\vec{k}$ vector in the Brillouin zone around the central Γ point (see Ref. 26) and p-wave behavior around $\vec{K}_\pm$ points.[27] In the bilayer case the time-reversal symmetry breaking d-wave order parameter emerges as a property of the low-energy small-momentum effective description around the K points, as shown above.

IV. PHASE DIAGRAM

We have found the ground state of our model Hamiltonian for a broad range of J and μ by minimizing the free energy. At zero temperature, as a function of the order parameter, it is given by

$$F = -\sum_{\vec{k}\in \mathrm{IBZ}} \sum_{\alpha=\pm1} E_{\vec{k},\alpha} + 2NJ \sum_{\vec{u}} |\Delta_{\vec{u}}|^2, \tag{29}$$

where the first sum is over all wave vectors $\vec{k}$ in the first Brillouin zone and two Bogoliubov bands with positive energies. The ground state is defined as a global minimum of the free energy in the order-parameter space. In the present study, we concentrate on superconducting order parameters in a variational approach, and thus we cannot exclude that other correlated (nonsuperconducting) phases may have an even lower energy. In the mean-field approach, superconducting ground states are expected even for infinitesimal positive values of J.

The order-parameter space is six-dimensional, because it is defined by three complex numbers. However, adding the same phase to all three complex parameters does not modify the physical state, so one can always make one of the parameters purely real (we set $\Delta_{d_{x^2-y^2}}$ real) and reduce the order-parameter space dimensionality to 5. We used the amoeba numerical method[28] to directly minimize the free energy. Five-dimensional minimization often reveals more than one local minimum, but we were always able to identify the lowest-lying state to a satisfying level of certainty. However, for small values of J, the local free-energy minima are extremely shallow, with energies only slightly lower than the free energy of the normal state. Such features in the free-energy landscape are completely clouded by numerical noise due to the discretization of the first Brillouin zone. Our numerical calculations are therefore limited to higher values of J, which give a solution with the amplitude of the order parameter larger than 10^{-4}. This is marked by the dashed lines in Fig. 4.

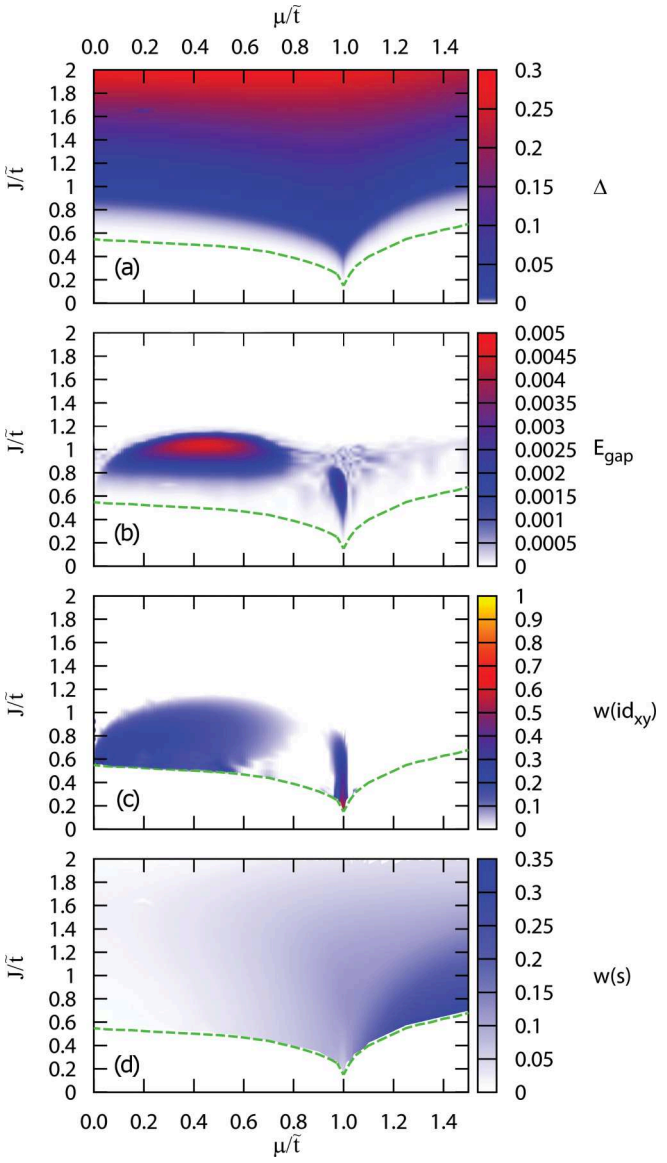

FIG. 4. (Color online) (a) Order-parameter amplitude Δ in the (μ, J) parameter space, obtained by a minimization of the free energy, (b) single-particle excitation gap, (c) contribution of id_{xy}, and (d) s-wave component in the ground-state order parameter. The green dashed line marks where Δ drops below 10^{-4}. Below this line, our numerics is not reliable. We use $\tilde{t} = t^2/t_\perp$ for the unit of energy.

Our results are shown on Fig. 4, where the relevant quantities are represented by color in the (μ, J) plane. The amplitude of the order parameter is shown in Fig. 5(a).

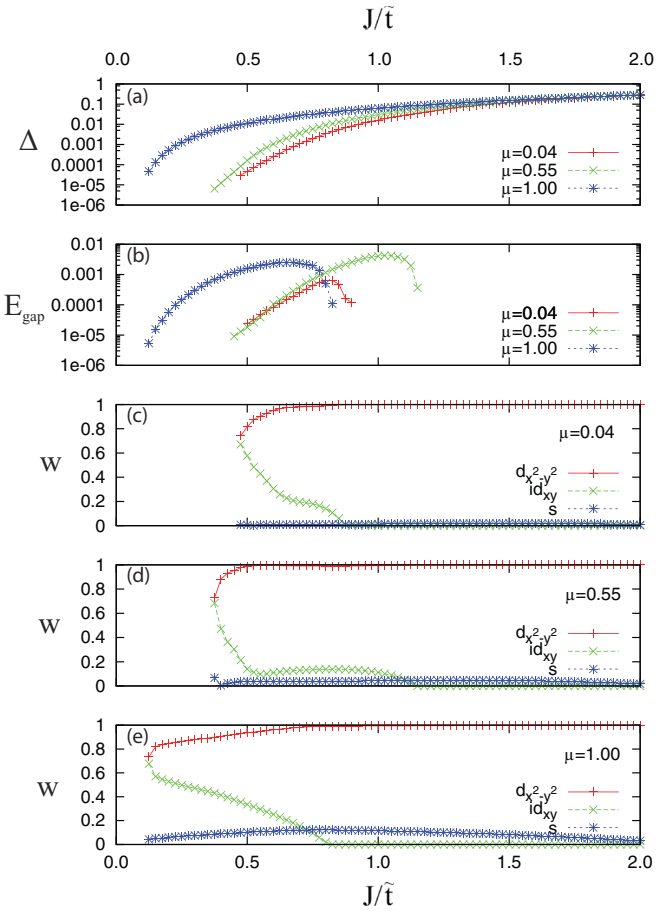

FIG. 5. (Color online) (a) Order-parameter amplitude Δ and (b) single-particle excitation gap as a function of J, for $\mu = 0.04, 0.55, 1$. (c–e) The contributions of three relevant symmetry components. The $d_{x^2-y^2}$ component is the dominant one for large J. The contribution of id_{xy} increases with decreasing J until the two contributions are equal and we find a pure $d+id$-wave symmetry. We use $\tilde{t} = t^2/t_\perp$ for the unit of energy. The data are plotted only above the value for the coupling J which is numerically significant, as mentioned in the text (see also the dashed green line in Fig. 4).

Upon small to moderate doping, the SC instability increases and becomes particularly favorable at the filling 5/8, which corresponds to the chemical potential $\mu/\tilde{t} = 1$, and the Van Hove singularity in the noninteracting DOS. For further doping the SC instability decreases. This gives to Fig. 4(a) roughly the look of the inverse DOS of Fig. 2(b). The gap in the single-particle excitations is shown in Fig. 4(b). It is particularly pronounced in the case of strong mixing of $d_{x^2-y^2}$ and id_{xy} symmetry components, as we can see from Fig. 4(c). The contribution of different pairing symmetries is defined by the ratio w of different components of Δ, where

$$\mathbf{\Delta} = \Delta_s \hat{e}_s + i\Delta_{is}\hat{e}_s + \Delta_{d_{xy}}\hat{e}_{d_{xy}} + i\Delta_{id_{xy}}\hat{e}_{d_{xy}} + \Delta_{d_{x^2-y^2}}\hat{e}_{d_{x^2-y^2}}, \tag{30}$$

with $\hat{e}_s = (1,1,1)/\sqrt{3}$, $\hat{e}_{d_{xy}} = (0,1,-1)/\sqrt{2}$, and $\hat{e}_{d_{x^2-y^2}} = (2,-1,-1)/\sqrt{6}$. Figure 4(c) shows the ratio $w(id_{xy}) = |\Delta_{id_{xy}}|/|\Delta|$, and Fig. 4(d) shows the ratio $w(s) = |\Delta_s|/|\Delta|$. The contributions of is and d_{xy} components are negligible in all cases, and $d_{x^2-y^2}$ is the dominant component.

The numerical results are, for clarity, also shown in Fig. 5 for three chosen values of the chemical potential, $\mu/\tilde{t} = 0.04, 0.55, 1$. Figure 5(a) shows a sudden increase in the pairing amplitude with the increasing interaction J (note the logarithmic scale on the y axis). For small J, the pairing amplitude is much larger for $\mu/\tilde{t} = 1$, i.e., at the Van Hove singularity, and in this case the single-particle excitation gap is also larger due to the strong mixing of $d_{x^2-y^2}$ and id_{xy} symmetries. Contributions of relevant components are compared in Figs. 5(c)–5(e). At higher values of J one has a pure $d_{x^2-y^2}$ symmetry, whereas a mixture of $d_{x^2-y^2}$ and id_{xy} symmetries is found at lower values of J. The contribution of id_{xy} symmetry increases with decreasing J, and almost pure $d+id$ symmetries are usually found at the lowest accessible values of J.

Our numerical calculations were performed on processors with 8 GB of RAM, which limited the number of $\vec{k}$ points in the first Brillouin zone to 4000×4000, but we checked that results do not differ qualitatively even with a much sparser 2000×2000 $\vec{k}$ grid. A much denser and probably a nonuniform discretization of the first Brillouin zone would be needed to probe the weak-coupling behavior of our model, that is for values of J below the dashed lines in Fig. 4. Notice, however, that the system in the small-J limit may be treated analytically within the weak-coupling limit, the results of which are presented in Appendices A and B, for the cases of finite and zero chemical potential, respectively.

In this weak-coupling regime and at finite chemical potential, we find that the $d+id$ superconducting order parameter yields the lowest mean-field energy, when compared to order parameters that respect time-reversal symmetry (Appendix A), in agreement with our numerical results for larger values of J. In the weak-coupling limit, in the symmetry-protected subspace of $d_{x^2-y^2}$ and d_{xy} order parameters the complex combination $d_{x^2-y^2} + i\sqrt{3}d_{xy}$ leads to a fully gapped system with no nodes at the Fermi surface. This means that the gap is proportional to $|C_{\vec{k}}| = \text{const}$, and maximum gain in the energy for this superconducting instability is obtained. Notice that this topological instability is in line with a theorem for the BCS description, according to which a time-reversal symmetry-broken 2D superconducting state has a lower free energy, as compared to time-reversal symmetric ones, when confronted with two-dimensional representations of the superconducting order parameter.[31] Indeed, as mentioned after Eq. (20), the $d_{x^2-y^2}$ and d_{xy} components of the order parameter $\mathbf{\Delta}$ form a two-dimensional irreducible representation of the symmetry group of the honeycomb lattice. Although the theorem of Ref. 31 was derived for a single band, it is expected also to apply to the present case at finite doping when the higher Bogoliubov band is irrelevant for the superconducting instability. This instability occurs at any strength of attractive interaction at finite doping since the gap opens as

$$J\Delta \propto \exp\left[-\frac{8\pi}{\sqrt{3}}\frac{1}{\rho(\mu)J}\right] \tag{31}$$

(see Appendix A), in terms of the DOS $\rho(E_F)$ at the Fermi level E_F. This is simply the BCS expression with the pairing potential equal to J.

Finally, we notice that the weak-coupling analysis yields a different picture at zero doping (Appendix B), where a time-reversal-symmetric superconducting order parameter (with any real combination of $d_{x^2-y^2}$ and d_{xy}) is energetically favored.

V. POSSIBLE RELEVANCE FOR BILAYER GRAPHENE

In the following we will discuss the possible relevance of our model for the physics of bilayer graphene. With an estimate[1,29] for the Coulomb on-site repulsion, $U \sim 10$ eV, intralayer nearest-neighbor hopping,[30] $t \sim 3$ eV, and interlayer hopping,[30] $t_\perp \sim 0.4$ eV, bilayer graphene may have a tendency to develop strongly correlated electron phases. Notice that, although similar energy scales are found in monolayer graphene, the latter is to great accuracy described in terms of (quasi-)free electrons because of a vanishing DOS at the Fermi level, in the absence of intensive doping.[1–3] In contrast, electronic correlations are much more efficient in bilayer graphene as a consequence of the finite DOS even at the band-contact points. This finite DOS may also be invoked when considering screening. Whereas screening is highly inefficient in monolayer graphene, and one needs then to take into account the long-range nature of the electronic interaction potential, the screening properties in bilayer graphene are similar to those in usual 2D electron systems with a parabolic band dispersion, albeit with a rather small band mass ($\sim 0.05 m_0$, in terms of the bare electron mass). In this sense, an approach based on the Hubbard model, as used here excluding nearest- and further-neighbor interactions, is better justified in bilayer than in monolayer graphene. However, this remains a strong approximation, as in the case of 2D electrons in GaAs heterostructures, and numerical calculations indicate that longer-range terms remain relevant also in bilayer graphene.[29]

Generally, the interplay between a strong on-site repulsion U and the hopping terms t and $t_\perp$ leads to antiferromagnetic Heisenberg-type exchange interactions, $J \sim t^2/U \sim 1$ eV between nearest neighbors in the same layer and $J_\perp \sim t_\perp^2/U \sim 16$ meV between nearest neighbors in opposite layers. Although clear evidence for antiferromagnetism is lacking in bilayer graphene, the quadratic dispersion of juxtaposed conduction and valence bands (together with the nonzero density of states) favor antiferromagnetic fluctuations.[32] Because the low-energy electrons move preferentially on the B1 and B2 sublattice sites, one needs to estimate an effective exchange interaction between them that may be obtained from a perturbative expansion, $J_{\text{eff}} \sim J^2 J_\perp / t_\perp^2 \sim t^4/U^3 \sim 100$ meV.

Remember that the effective hopping parameter in the projected honeycomb lattice (between the B1 and B2 sites) is a more subtle issue because it is derived in the limit where $t_\perp \gg t$, in contrast to the natural order in bilayer graphene. In order to make a comparison between our effective model and that of bilayer graphene, in view of the correlated phases we consider, it is therefore more appropriate to define the effective hopping indirectly from the value of J_{eff} and U, $J_{\text{eff}} \sim t_{\text{eff}}^2/U$, which yields a value of $t_{\text{eff}} \sim 1$ eV that should replace the value $\tilde{t}$ in the previous sections.

Therefore modeled with two effective parameters, J_{eff} and t_{eff}, bilayer graphene may be compared with the effective honeycomb lattice considered in our paper and the corresponding $t-J$ model. The main feature of bilayer graphene appears to be that $J_{\text{eff}} \sim 0.1 t_{\text{eff}} \ll t_{\text{eff}}$, and in considering the relevance of our model we should confine ourselves to weak couplings and small or moderate dopings; because we simplified the high-momentum physics of the bilayer (by considering the large $t_\perp$ limit) we should confine ourselves to lower dopings. First one sees from Fig. 4 that the gaps are in the meV range (2 to 5 meV for the maximal gaps) if one considers the energy scale $t_{\text{eff}} \sim J \sim 1$ eV. Thus our results indicate very small energy scales that are unlikely to be resolved in today's graphene samples. Furthermore we should use t_{eff} and J_{eff} for t and J for the exponent in the weak-coupling analysis in Appendix A. Because we estimate $t_{\text{eff}}/J_{\text{eff}} \sim 10$, the weak-coupling analysis yields an exponential suppression and gaps below 1 meV, in agreement with our numerical findings shown in Fig. 4.

VI. CONCLUSIONS

We presented an analysis of a model of a honeycomb bilayer with attractive interactions that (1) supports $d+id$ superconductivity with the canonical effective (low-momentum) description $\sim(k_x+ik_y)^2$ at both valley points and (2) transforms at moderate and strong couplings into $d_{x^2-y^2}$ superconductivity. The implied tJ model may be relevant for future investigations of such a complex and intriguing system as the graphene bilayer. We discussed the possibility of a superconducting instability in this framework and concluded that $d+id$ is the leading superconducting instability in the case of the graphene bilayer at moderate dopings and low-energy scales.

We would like to point also to the difference between the monolayer and bilayer case that follows from the symmetry analysis of the simple model with attractive interactions and the ensuing short-range order parameter on both lattices. In the effective description around $\vec{K}$ points an s wave and p wave are found[22,26] in the monolayer case, and a p wave and d wave are found in the bilayer case. The bilayer honeycomb lattice appears at moderate dopings as yet another stage on which time-reversal symmetry-breaking d-wave superconductivity may appear (see Refs. 22,33–37 for moderately doped monolayer) and may be driven by similar physics as in the case of predicted instabilities at special (very high) dopings of a honeycomb monolayer.[38,39] In the case we presented, the canonical[40] low momentum description, $\sim(k_x+ik_y)^2$, holds due to the quadratically dispersing Dirac electrons.

ACKNOWLEDGMENTS

We thank A. M. Black-Schaffer, M. Civelli, M. Franz, and Y. Hatsugai for useful discussions. Furthermore, we thank D. Tanasković for support and his implication at the early stage of this project. J. V. and M. V. M. are supported by the Serbian Ministry of Education and Science under Project No. ON171017, and M. O. G. is supported by the ANR (Agence Nationale de la

Recherche) project NANOSIM GRAPHENE under Grant No. ANR-09-NANO-016. The authors acknowledge financial support from the bilateral MES-CNRS 2011/12 program. This research was funded in part by the NSF under Grant No. NSF PHY05-51164; M. V. M. and M. O. G. acknowledge the hospitality of the Kavli Institute for Theoretical Physics, University of California, Santa Barbara. Numerical simulations were run on the AEGIS e-Infrastructure, supported in part by FP7 projects EGI-InSPIRE, PRACE-1IP, and HP-SEE.

APPENDIX A: WEAK-COUPLING ANALYTICAL SOLUTION AT FINITE CHEMICAL POTENTIAL

Here, we present briefly the weak-coupling analysis of superconducting order in the effective bilayer model. In order to simplify the notation, we use the letter t to denote the effective hopping $\tilde{t}$. The DOS at the Fermi level, $\rho(E_F)$, is on the order of the inverse hopping parameter $1/t$. Notice that if only a parabolic band is taken into account it remains fixed at its $E_F = 0$ value, but corrections to the parabolic approximation immediately yield a contribution that varies linearly with the Fermi level, in agreement with the DOS plotted in Fig. 2(b).

In the case when $\Delta = \Delta(1,1,1)$, a weak-coupling BCS analysis that takes into account only electrons in the lower Bogoliubov band gives

$$J\Delta = \sqrt{2tE_c}\exp\left(-24\sqrt{3}\pi\frac{t}{\mu\rho(E_F)J}\right), \tag{A1}$$

with E_c as an energy cutoff around the Fermi value, for the solution, and

$$\frac{\delta E^p_{\rm MF}}{N} = -(J\Delta)^2\frac{\mu\rho(E_F)}{t}\frac{1}{4\sqrt{3}\pi}, \tag{A2}$$

for the gain in the mean-field energy, $\delta E_{\rm MF}$, by the pairing instability.

The weak-coupling BCS analysis in the case of electron doping ($\mu > 0$) for $d_{x^2-y^2}$ and $d_{x^2-y^2} + i\sqrt{3}\, d_{xy}$ gives

$$J\Delta_d = \frac{\sqrt{2}}{3}E_c\exp\left(-\frac{8\pi}{\sqrt{3}}\frac{1}{\rho(E_F)J} + \frac{1}{2}\right), \tag{A3}$$

for the solution which we denoted by $\Delta = \Delta_d$, and

$$J\Delta = \sqrt{\frac{2}{3}}E_c\exp\left(-\frac{8\pi}{\sqrt{3}}\frac{1}{\rho(E_F)J} + \frac{1}{2}\right), \tag{A4}$$

in the case of the d_{xy} wave. For the energy gain one obtains

$$\frac{\delta E_{\rm MF}(d_{x^2-y^2})}{N} = \frac{\delta E_{\rm MF}(d_{xy})}{N} = -(J\Delta_d)^2\rho(E_F)\frac{3\sqrt{3}}{4\pi}, \tag{A5}$$

and for a $d_{x^2-y^2} + i\sqrt{3}\, d_{xy}$ wave one finds

$$\frac{\delta E^d_{\rm MF}}{N} = -(J\Delta_d)^2\rho(E_F)\frac{3\sqrt{3}}{2\pi}. \tag{A6}$$

Because of its twice lower mean-field energy, the $d_{x^2-y^2} + i\sqrt{3}d_{xy}$ time-reversal symmetry-breaking instability, which we call in short the d wave, is more likely than $d_{x^2-y^2}$- and d_{xy}-wave order parameters. In the large-doping limit, the energy minimization is also much more efficient for the d wave than the p_y wave, as seen in the small value of the ratio

$$\frac{\delta E^p_{\rm MF}}{\delta E^d_{\rm MF}} = \frac{\mu}{2E_c}\exp\left[-\frac{2\pi\times 8}{\sqrt{3}}\frac{1}{\rho(E_F)J}\left(\frac{9t}{2\mu}-1\right)\right], \tag{A7}$$

for $\mu < \frac{9t}{2}$. The most natural choice for E_c is to be of the order of μ as a first energy scale when we start from the smallest one, i.e., J. The time-reversal symmetry-breaking d-wave solution of our BCS mean-field Hamiltonian is also expected from a theorem proved in Ref. 31. The theorem was derived for 2D one-band models that reveal both time-reversal symmetry and a point symmetry described by the dihedral group D_n [or the O(2) rotation symmetry in the case of continuum models]. It states that generally a time-reversal symmetry-breaking superconducting state has a lower free energy than time-reversal symmetric ones if one is confronted with a 2D representation of the symmetry group. In the case of weak coupling that we consider here, i.e., $J \ll \mu$, and $\mu > 0$ (electron doping), we have an effective one-band theory of electrons to which the theorem can be applied. Also, the dispersion of the complex d-wave order parameter is more complicated in our case (than in Ref. 31), as can be seen in Eqs. (17) and (18). But in the weak-coupling limit the J^4 term can be neglected in Eq. (18), and we obtain expressions that are reminiscent of those of Ref. 31.

In the following we investigate more closely an effective low-energy description of the d-wave instability, in the case of high electron doping, and discuss only the lower-energy Bogoliubov band. Therefore our effective Hamiltonian is

$$H_e = \sum_{\vec{k}\sigma}(t\epsilon_{\vec{k}} - \mu)c^\dagger_{\vec{k}\sigma}c_{\vec{k}\sigma} + \sum_{\vec{k}}(\Delta_{\vec{k}}c^\dagger_{\vec{k}\uparrow}c^\dagger_{-\vec{k}\downarrow} + \text{H.c.}), \tag{A8}$$

where $\Delta_{\vec{k}} \sim (k_x - ik_y)^2/|k|^2$. In the weak-coupling BCS analysis it can be easily shown that the Hamiltonian is completely equivalent to the one with $\Delta_{\vec{k}} \sim (k_x - ik_y)^2$, because both Hamiltonians have an effective description on a Fermi circle defined by $t\epsilon_{\vec{k}} = \mu$. With this adjustment we have exactly the form of the BCS Hamiltonian studied in Ref. 40 on time-reversal symmetry-breaking superconductors in two dimensions. In the so-called weak-pairing case for finite $\mu > 0$ that we want to study, the minimum of Bogoliubov excitations moves to finite values of $\vec{k}$, $t\epsilon_{\vec{k}} = \mu$, i.e., to the Fermi surface of free particles. The Cooper pair wave function $g(\vec{r})$ may be a nonuniversal function of $|\vec{r}|$ where $\vec{r}$ is the relative coordinate of the pair. On the other hand, the dependence of the function on the angle of vector $\vec{r}$ is fixed and can easily be derived in the Bogoliubov formalism to be $g(|\vec{r}|) \propto \frac{\bar{z}}{z} \propto (x - iy)^2$ where $z = x + iy$ is the two-dimensional complex coordinate. Thus the relative angular momentum of the Cooper pair is $l = -2$. The weak-pairing phase is topological, gapped in the bulk because $\mu > 0$, and possesses a doublet of spin-1/2 Dirac edge modes.[40] In our case, because of the fermion doubling on the honeycomb lattice and the existence of the two $\vec{K}$ points (valleys) [and because around each one we have the same effective description given by the

Hamiltonian in Eq. (16)], we expect four Dirac modes on the edge.

APPENDIX B: WEAK-COUPLING ANALYTICAL SOLUTION AT ZERO CHEMICAL POTENTIAL

In the weak-coupling limit at $\mu = 0$, when both Bogoliubov bands are taken into account we find for $d_{x^2-y^2}$ symmetry

$$J\Delta^d = \frac{E_c}{3}\exp\left(-\frac{\frac{8}{3J} - 11c}{2c}\right), \tag{B1}$$

with $c \equiv \frac{1}{2\pi\sqrt{3}}\frac{1}{t}$, for the solution, and

$$\frac{\delta E_{\mathrm{MF}}^{d_{x^2-y^2}}}{N} = -\frac{9}{2}c\,(J\Delta^d)^2, \tag{B2}$$

for the energy gain. On the other hand, for $d + id$ symmetry we find

$$J\Delta^{d+id} = \frac{\sqrt{2}E_c}{3}\exp\left(-\frac{\frac{8}{3J} - 5c}{2c}\right), \tag{B3}$$

and

$$\frac{\delta E_{\mathrm{MF}}^{d+id}}{N} = -9c\,(J\Delta^{d+id})^2. \tag{B4}$$

Because

$$\frac{\delta E_{\mathrm{MF}}^{d+id}}{\delta E_{\mathrm{MF}}^{d_{x^2-y^2}}} = \frac{\delta E_{\mathrm{MF}}^{d+id}}{\delta E_{\mathrm{MF}}^{d_{xy}}} = 4e^{-6}, \tag{B5}$$

any real combination of $d_{x^2-y^2}$ and d_{xy} waves is more likely than the $d + id$ wave.

[1] A. H. Castro Neto, F. Guinea, N. M. R. Peres, K. S. Novoselov, and A. K. Geim, Rev. Mod. Phys. **81**, 109 (2009).
[2] V. N. Kotov, B. Uchoa, V. M. Peirera, A. H. Castro Neto, and F. Guinea, Rev. Mod. Phys. **84**, 1067 (2012).
[3] M. O. Goerbig, Rev. Mod. Phys. **83**, 1193 (2011).
[4] J. Martin, B. E. Feldman, R. T. Weitz, M. T. Allen, and A. Yacoby, Phys. Rev. Lett. **105**, 256806 (2010).
[5] R. T. Weitz, M. T. Allen, B. E. Feldman, J. Martin, and A. Yacoby, Science **330**, 812 (2010).
[6] F. Freitag, J. Trbovic, M. Weiss, and C. Schönenberger, Phys. Rev. Lett. **108**, 076602 (2012).
[7] J. Velasco, Jr., L. Jing, W. Bao, Y. Lee, P. Kratz, V. Aji, M. Bockrath, C. N. Lau, C. Varma, R. Stillwell, D. Smirnov, F. Zhang, J. Jung, and A. H. MacDonald, Nature Nanotech. **7**, 156 (2012).
[8] X.-L. Qi and S.-C. Zhang, Rev. Mod. Phys. **83**, 1057 (2011).
[9] H. Min, G. Borghi, M. Polini, and A. H. MacDonald, Phys. Rev. B **77**, 041407(R) (2008).
[10] R. Nandkishore and L. Levitov, Phys. Rev. Lett. **104**, 156803 (2010); Phys. Rev. B **82**, 115124 (2010).
[11] F. Zhang, H. Min, M. Polini, and A. H. MacDonald, Phys. Rev. B **81**, 041402(R) (2010).
[12] O. Vafek and K. Yang, Phys. Rev. B **81**, 041401(R) (2010).
[13] F. Zhang, J. Jung, G. A. Fiete, Q. Niu, and A. H. MacDonald, Phys. Rev. Lett. **106**, 156801 (2011).
[14] J. Jung, F. Zhang, and A. H. MacDonald, Phys. Rev. B **83**, 115408 (2011).
[15] Y. Lemonik, I. L. Aleiner, C. Toke, and V. I. Falko, Phys. Rev. B **82**, 201408 (2010).
[16] F. Zhang and A. H. MacDonald, Phys. Rev. Lett. **108**, 186804 (2012).
[17] R. E. Throckmorton and O. Vafek, Phys. Rev. B **86**, 115447 (2012).
[18] M. Kharitonov, arXiv:1109.1553.
[19] M. M. Scherer, S. Uebelacker, and C. Honercamp, Phys. Rev. B **85**, 235408 (2012).
[20] E. McCann and V. I. Falko, Phys. Rev. Lett. **96**, 086805 (2006).
[21] O. Vafek, Phys. Rev. B **82**, 205106 (2010).
[22] A. M. Black-Schaffer and S. Doniach, Phys. Rev. B **75**, 134512 (2007).
[23] C. Bena and L. Simon, Phys. Rev. B **83**, 115404 (2011).
[24] D. Poletti, C. Miniatura, and B. Gremaud, Europhys. Lett. **93**, 37008 (2011).
[25] Notice that other symmetries of the superconducting order parameter are indeed energetically favored at higher doping, as is shown in the weak-coupling analysis presented in Appendix A.
[26] J. Linder, A. M. Black-Schaffer, T. Yokoyama, S. Doniach, and A. Sudbo, Phys. Rev. B **80**, 094522 (2009).
[27] B. Uchoa and A. H. Castro Neto, Phys. Rev. Lett. **98**, 146801 (2007).
[28] *Numerical Recipes: The Art of Scientific Computing* (Cambridge University Press, Cambridge, 2007).
[29] T. O. Wehling, E. Sasioglu, C. Friedrich, A. I. Lichtenstein, M. I. Katsnelson, and S. Blugel, Phys. Rev. Lett. **106**, 236805 (2011).
[30] K. Zou, X. Hong, and J. Zhu, Phys. Rev. B **84**, 085408 (2011), and references therein.
[31] M. Cheng, K. Sun, V. Galitski, and S. Das Sarma, Phys. Rev. B **81**, 024504 (2010).
[32] A. H. MacDonald, J. Jung, and F. Zhang, Phys. Scr. **146**, 014012 (2012).
[33] G. Baskaran, Phys. Rev. B **65**, 212505 (2002).
[34] C. Honerkamp, Phys. Rev. Lett. **100**, 146404 (2008).
[35] S. Pathak, V. B. Shenoy, and G. Baskaran, Phys. Rev. B **81**, 085431 (2010).
[36] F. M. D. Pellegrino, G. G. N. Angilella, and R. Pucci, Eur. Phys. J. B **76**, 469 (2010).
[37] Z.-C. Gu, H.-C. Jiang, D. N. Sheng, H. Yao, L. Balents, and X.-G. Wen, arXiv:1110.1183.
[38] R. Nandkishore, L. Levitov, and A. Chubukov, Nature Phys. **8**, 158 (2012).
[39] M. Kiesel, Ch. Platt, W. Hanke, D. A. Abanin, and R. Thomale, Phys. Rev. B **86**, 020507(R) (2012).
[40] N. Read and D. Green, Phys. Rev. B **61**, 10267 (2000).

Quantum Critical Transport near the Mott Transition

H. Terletska,[1] J. Vučičević,[2] D. Tanasković,[2] and V. Dobrosavljević[1]

[1]*Department of Physics and National High Magnetic Field Laboratory, Florida State University, Tallahassee, Florida 32306, USA*
[2]*Scientific Computing Laboratory, Institute of Physics Belgrade, University of Belgrade, Pregrevica 118, 11080 Belgrade, Serbia*

(Received 26 January 2011; published 5 July 2011)

We perform a systematic study of incoherent transport in the high temperature crossover region of the half filled one-band Hubbard model. We demonstrate that the family of resistivity curves displays characteristic quantum critical scaling of the form $\rho(T, \delta U) = \rho_c(T) f(T/T_0(\delta U))$, with $T_0(\delta U) \sim |\delta U|^{z\nu}$, and $\rho_c(T) \sim T$. The corresponding β function displays a "strong coupling" form $\beta \sim \ln(\rho_c/\rho)$, reflecting the peculiar mirror symmetry of the scaling curves. This behavior, which is surprisingly similar to some experimental findings, indicates that Mott quantum criticality may be acting as the fundamental mechanism behind the unusual transport phenomena in many systems near the metal-insulator transition.

DOI: 10.1103/PhysRevLett.107.026401 PACS numbers: 71.27.+a, 71.30.+h

Many systems close to the metal-insulator transition (MIT) often display surprisingly similar transport features in the high temperature regime [1–3]. Here, the family of resistivity curves typically assumes a characteristic "fan-shaped" form [see Fig. 1(a)], reflecting a gradual crossover from metallic to insulating transport. At the highest temperatures the resistivity depends only weakly on the control parameter (concentration of charge carriers [1] or pressure [2,3]), while as T is lowered, the system seems to "make up its mind" and rapidly converges towards either a metallic or an insulating state. Since temperature acts as a natural cutoff scale for the metal-insulator transition, such behavior is precisely what one expects for quantum criticality [4]. In some cases [1], the entire family of curves displays beautiful scaling behavior, with a remarkable "mirror symmetry" of the relevant scaling functions [4]. But under which microscopic conditions should one expect such scaling phenomenology? What is the corresponding driving force for the transitions? Despite recent progress, such basic physics questions remain the subject of much ongoing controversy and debate.

The phenomenon of disordered-driven Anderson localization of noninteracting electrons is at present rather well understood based on the scaling formulation [5] and is generally viewed as an example of a $T = 0$ quantum phase transition. On the other hand, a considerable number of recent experiments [1] provide compelling evidence that strong correlation effects—some form of Mott localization—may be the dominant mechanism [6]. Should one expect similar or very different transport phenomenology in the Mott picture? Is the paradigm of quantum criticality even a useful language to describe high temperature transport around the Mott point? These issues are notoriously difficult to address, because conventional Fermi liquid concepts simply cannot be utilized in the relevant high temperature incoherent regime. In this Letter, we answer this question in the framework of dynamical mean-field theory (DMFT) [7], the only theoretical method that is most reliable precisely at high temperatures.

Model and DMFT solution.—We consider a single-band Hubbard model at half filling

$$H = -\sum_{\langle i,j\rangle\sigma} t_{ij}(c^\dagger_{i\sigma}c_{j\sigma} + \text{c.c.}) + \sum_i U n_{i\uparrow}n_{i\downarrow}, \qquad (1)$$

where $c^\dagger_{i\sigma}$ and $c_{i\sigma}$ are the electron creation and annihilation operators, respectively, $n_{i\sigma} = c^\dagger_{i\sigma}c_{i\sigma}$, t_{ij} is the hopping amplitude, and U is the repulsion between two electrons on the same site. We use a semicircular density of states, and the corresponding half-bandwidth D is set to be our energy unit. We focus on the paramagnetic DMFT

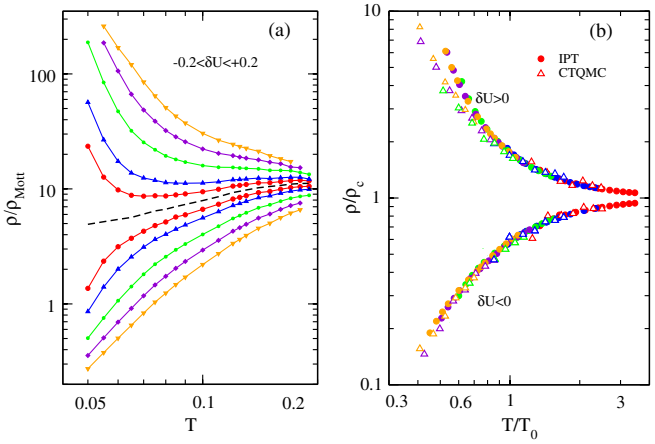

FIG. 1 (color online). (a) DMFT resistivity curves as a function of temperature along different trajectories $-0.2 \le \delta U \le +0.2$ with respect to the instability line $\delta U = 0$ (black dashed line; see the text). Data are obtained by using IPT impurity solver. (b) Resistivity scaling; essentially identical scaling functions are found from CTQMC (open symbols) and from IPT (closed symbols).

solution, which is formally exact in the limit of large coordination. Here the Hubbard model maps onto an effective Anderson impurity model supplemented by a self-consistency condition [7]. To solve the DMFT equations we use the iterated perturbation theory (IPT) [7] and cross-check our results with numerically exact continuous time quantum Monte Carlo (CTQMC) calculations [8,9]. We find, in agreement with previous work [10], that after appropriate energy rescaling (see below), the two methods produce qualitatively and even quantitatively identical results in the incoherent crossover region that we examine.

It is well known that at very low temperatures $T < T_c \sim 0.03$, this model features a first-order metal-insulator transition terminating at the critical end point T_c (Fig. 2), very similar to the familiar liquid-gas transition [10]. For $T > T_c$, however, different crossover regimes have been tentatively identified [7,11], but they have not been studied in any appreciable detail. The fact that the first-order coexistence region is restricted to such very low temperatures provides strong motivation to examine the high temperature crossover region from the perspective of "hidden quantum criticality." In other words, the presence of a coexistence dome at $T < T_c \ll 1$, an effect with a very small energy scale, is not likely to influence the behavior at much higher temperatures $T \gg T_c$. In this high temperature regime smooth crossover is found, which may display behavior consistent with the presence of a "hidden" quantum critical (QC) point at $T = 0$. To test this idea, we utilize standard scaling methods appropriate for quantum

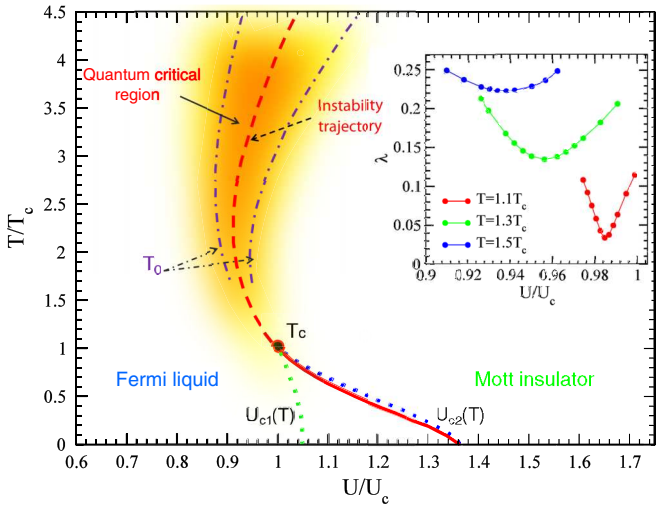

FIG. 2 (color online). DMFT phase diagram of the fully frustrated half filled Hubbard model, with a shaded region showing where quantum critical-like scaling is found. Metallic $U_{c2}(T)$ and insulating $U_{c1}(T)$ spinodals (dotted lines) are found at $T < T_c$; the corresponding first-order phase transition is shown by a thick solid line. The thick dashed line, which extends at $T > T_c$, shows the instability trajectory $U^\star(T)$, and the crossover temperature T_0 delimits the QC region (dash-dotted lines). The inset shows examples of eigenvalue curves at three different temperatures, with pronounced minima at $U^\star(T)$ determining the instability trajectory.

criticality and compute the resistivity curves along judiciously chosen trajectories respecting the symmetries of the problem.

Instability trajectory formalism.—Previous work has already recognized [10] that, in order to reveal the proper scaling behavior close to the critical end point, one has to follow a set of trajectories parallel to "zero field" trajectory $U^*(T)$. We thus expect $\delta U \equiv U - U^\star(T)$ to play the role of the scaling variable corresponding to a symmetry-breaking field favoring one of the two competing (metal vs insulator) phases. By analogy [10,12] to the familiar liquid-gas transition, we determine the precise location of such an "instability trajectory" by examining the curvature of the corresponding free energy functional [13]. This curvature vanishes at T_c and is finite and minimal at $T > T_c$, along this instability line. Consequently, as in Refs. [10,13,14], our problem is recast as an eigenvalue analysis of the corresponding free energy functional $\mathcal{F}[G(iw_n)]$ for which the DMFT Green's function solution $G_{\mathrm{DMFT}}(iw_n)$ represents a local extremum and can be regarded as a vector in an appropriate Hilbert space.

The free energy near such an extremum can be written as $\mathcal{F}[G(iw_n)] = \mathcal{F}_0 + Tt^2 \sum_{m,n} \delta G(i\omega_m) M_{mn} \delta G(i\omega_n) + \cdots$, where

$$M_{mn} = \frac{1}{2Tt^2} \frac{\partial^2 \mathcal{F}[G]}{\partial G(i\omega_m) \partial G(i\omega_n)} \Bigg|_{G=G_{\mathrm{DMFT}}} \qquad (2)$$

and $\delta G(i\omega_n) \equiv G(i\omega_n) - G_{\mathrm{DMFT}}(i\omega_n)$. The curvature of the free energy functional is determined by the lowest eigenvalue λ of the fluctuation matrix M. As explained in Ref. [15], λ can be obtained from the iterative solution of DMFT equations. The difference of the Green's functions in iterations n and $n+1$ of the DMFT self-consistency loop is given by

$$\delta G^{(n+1)}(i\omega_n) - \delta G^{(n)}(i\omega_n) = e^{-n\lambda} \delta G^{(0)}(i\omega_n), \qquad (3)$$

and therefore λ determines the rate of convergence of the Green function to its solution.

An example of our calculations is shown in the inset in Fig. 2, where the eigenvalues at several temperatures are plotted as a function of interaction U/U_c. The minima of these curves define the locus of the instability trajectory $U^\star(T)$, which terminates at the critical end point (U_c, T_c), as shown in Fig. 2. Note that the immediate vicinity $T \approx T_c$ of the critical end point has been carefully studied theoretically [10] and even observed in experiments [2], revealing classical Ising scaling (since one has a finite temperature critical point) of transport in this regime. In our study, we examine the crossover behavior at much higher temperatures $T \gg T_c$, displaying very different behavior: precisely what is expected in presence of quantum criticality.

Resistivity calculation.—To reveal quantum critical scaling, we calculate the temperature dependence of the resistivity along a set of trajectories parallel to our instability trajectory [fixed $\delta U = U - U^\star(T)$]. Resistivity was calculated by using standard DMFT procedures [7], with

the maximum entropy method [16] utilized to analytically continue CTQMC data to the real axis. The resistivity results are shown in Fig. 1, where in panel (a) IPT resistivity data for $\delta U = 0, \pm 0.025, \pm 0.05, \pm 0.1, \pm 0.15, \pm 0.2$ in the temperature range of $T \approx 0.07$–0.2 are presented (CTQMC data are not shown for the sake of clarity of the figure). The resistivity is given in units of ρ_{Mott}, maximal resistivity according to the Boltzmann quasiclassical theory of transport [17]. The family of resistivity curves above ($\delta U > 0$) the "separatrix" $\rho_c(T)$ (dashed line, corresponding to $\delta U = 0$) has an insulatinglike behavior, while metallic dependence is obtained for $\delta U < 0$.

Scaling analysis.—According to what is generally expected for quantum criticality, our family of curves should satisfy the following scaling relation:

$$\rho(T, \delta U) = \rho_c(T) f(T/T_0(\delta U)). \tag{4}$$

We thus first divide each resistivity curve by the separatrix $\rho_c(T) = \rho(T, \delta U = 0)$ and then rescale the temperature, for each curve, with an appropriately chosen parameter $T_0(\delta U)$ to collapse our data onto two branches [Fig. 1(b)]. Note that this unbiased analysis does not assume any specific form of $T_0(\delta U)$: It is determined for each curve simply to obtain optimum collapse of the data [18]. This puts us in a position to perform a stringent test of our scaling hypothesis: True quantum criticality corresponds to $T_0(\delta U)$, which vanishes at $\delta U = 0$ and displays power-law scaling with the same exponents for both scaling branches. As seen in Fig. 3(a), T_0 falls sharply as $U = U^\star$ is approached, consistent with the QC scenario but opposite to what is expected in a "classical" phase transition. The inset in Fig. 3(a) with log-log scale shows clearly a power-law behavior of $T_0 = c|\delta U|^{z\nu}$, with the estimated power $(z\nu)^{\mathrm{IPT}}_{\delta U<0} = 0.56 \pm 0.01$ for the "metallic " side and $(z\nu)^{\mathrm{IPT}}_{\delta U>0} = 0.57 \pm 0.01$ for an insulating branch.

We also find [Fig. 3(b)] a very unusual form of our critical resistivity $\rho_c(T)$, corresponding to the instability trajectory. Its values largely exceeds the Mott limit, yet it displays metalliclike but non-Fermi liquidlike temperature dependence $\rho_c(T) \sim T$. Such puzzling behavior, while inconsistent with any conventional transport mechanism, has been observed in several strongly correlated materials close to the Mott transition [17,20]. Our results thus suggest that it represents a generic feature of Mott quantum criticality.

β function and mirror symmetry of scaled curves.—To specify the scaling behavior even more precisely, we compute the corresponding β function [4] $\beta(g) = \frac{d\ln g}{d\ln T}$, with $g = \rho_c/\rho$ being the inverse resistivity scaling function. Remarkably [Fig. 4(a)], it displays a nearly linear dependence on $\ln g$ and is continuous through $\delta U = 0$ indicating precisely the same form of the scaling function on both sides of the transition—another feature exactly of the form expected for genuine quantum criticality. This functional form is very natural for the insulating transport, as it is obtained even for simple activated behavior $\rho(T) \sim e^{-E_g/T}$. The fact that the same functional form persists well into the metallic side is a surprise, especially since it covers almost an order of magnitude for the resistivity ratio. Such a behavior has been interpreted [4] to reflect the "strong coupling" nature of the critical point, which presumably is governed by the same physical processes that dominate the insulator. This points to the fact that our QC behavior has a strong coupling, i.e., nonperturbative character.

The fact that the β function assumes this logarithmic form on both sides of the transition is mathematically equivalent [4] to stating that the two branches of the corresponding scaling functions display "mirror symmetry" over the same resistivity range. Indeed, we find that transport in this QC region exhibits a surprisingly developed reflection symmetry [dashed vertical lines of Fig. 4(a) mark its boundaries]. Such a symmetry is clearly seen in Fig. 4(b), where the resistivity ρ/ρ_c (for $\delta U > 0$) and conductivity $\sigma/\sigma_c = \rho_c/\rho$ ($\delta U < 0$) can be mapped onto each other by reflection with $\frac{\rho(\delta U)}{\rho_c} = \frac{\sigma(-\delta U)}{\sigma_c}$ [21].

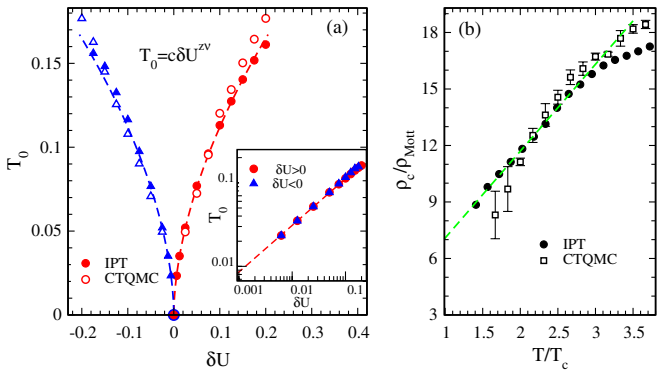

FIG. 3 (color online). (a) Scaling parameter $T_0(\delta U)$ as a function of control parameter $\delta U = U - U^\star$; the inset illustrates power-law dependence of scaling parameter $T_0 = c|\delta U|^{z\nu}$. (b) Resistivity $\rho_c(T)$ of the separatrix. Excellent agreement is found between IPT (closed symbols) and CTQMC (open symbols) results.

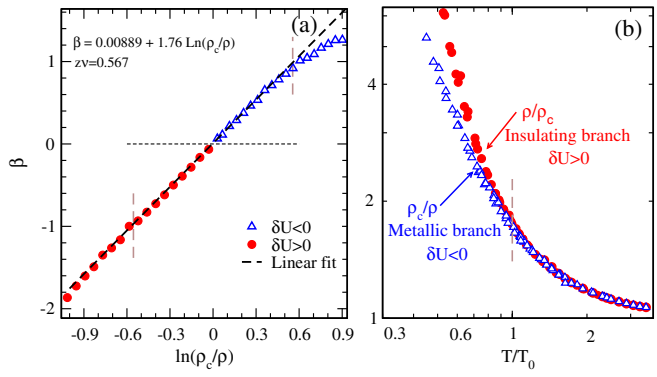

FIG. 4 (color online). (a) The β function shows linear in $\ln(\rho_c/\rho)$ behavior close to the transition. Open symbols are for the metallic branch ($\delta U < 0$), and closed ones are for the insulating side ($\delta U > 0$); vertical dashed lines indicate the region where mirror symmetry of curves is found. (b) Reflection symmetry of scaled curves close to the transition.

Note that $T/T_0 = 1$ sets the boundary of the quantum critical region, over which the reflection symmetry of scaled curves is observed. It is depicted by dash-dotted crossover lines T_0 in the phase diagram of Fig. 2 [15].

These remarkable features of the β function, and associated reflection symmetry, have been observed earlier in experimental [1,21] and theoretical [4] studies, which tentatively associated this with disorder-dominated MITs. Speculation that $\beta \sim \ln g$ reveals disorder as the fundamental driving force for MIT presumably reflects the fact that, historically, it has first been recognized for Anderson transitions [5]. Our work, however, shows that such behavior can be found even in the absence of disorder—in interaction-driven MITs. This finding calls for rethinking of basic physical processes that can drive the MIT.

Conclusions.—We have presented a careful and detailed study of incoherent transport in the high temperature crossover regime above the critical end point T_c of a single-band Hubbard model. Our analysis revealed a so-far overlooked scaling behavior of the resistivity curves, which we interpreted as evidence of hidden Mott quantum criticality. Precisely locating the proposed QC point in our model is hindered by presence of the low temperature coexistence dome, which limits our quantum critical scaling to the region well above T_c. Regarding the nature of transport in the QC regime, we found that the critical resistivity well exceeds the Mott limit, and yet it—surprisingly—assumes a metallic form, in dramatic contrast to conventional MIT scenarios. These features, together with large amounts of entropy characterizing this entire regime [22], prove surprisingly reminiscent of the ''holographic duality'' scenario [23,24] for a yet-unspecified QC point. Interestingly, the holographic duality picture has—so far—been discussed mostly in the context of quantum criticality in correlated metals (e.g., $T = 0$ magnetic transitions in heavy fermion compounds). Ours is the first work proposing that the same physical picture could apply to quantum criticality found at the MIT.

We believe that our results provide a significant new perspective on QC around the Mott transition and a deeper understanding of an apparent universality in the high temperature crossover regime. Our method traces a clear avenue for further searches for QC scaling, which are likely to be found in many other regimes and models.

In particular, it would be interesting to study a corresponding critical regime by going beyond the single-site DMFT analysis. It was shown in Ref. [19] that inclusion of spatial fluctuations does not significantly modify the high temperature crossover region in the half filled Hubbard model. Consequently, we expect our main findings to persist. An even more stringent test of our ideas should be provided in models where the critical end point T_c can be significantly reduced. This may include studies of the Mott transition away from half filling [25] or in systems with frustrations [6,26]. In such situations the proposed scaling regime should extend to much lower temperatures, perhaps revealing more direct evidence of the—so far—hidden Mott QC point. Our ideas should also be tested by performing more detailed transport experiments in the relevant incoherent regime, a task that may be easily accessible in various organic Mott systems [3], where T_c is sufficiently below room temperature.

The authors thank K. Haule for the usage of his CTQMC code and M. Jarrell for the use of his maximum entropy code for analytical continuation of the CTQMC data. This work was supported by the National High Magnetic Field Laboratory and the NSF through Grants No. DMR-0542026 and No. DMR-1005751 (H. T. and V. D.) and Serbian Ministry of Science under Project No. ON171017 (J. V. and D. T.). D. T. acknowledges support from the NATO Science for Peace and Security Programme Grant No. EAP.RIG.983235. Numerical simulations were run on the AEGIS e-Infrastructure, supported in part by FP7 projects EGI-InSPIRE, PRACE-1IP, and HP-SEE.

[1] E. Abrahams *et al.*, Rev. Mod. Phys. **73**, 251 (2001).
[2] P. Limelette *et al.*, Science **302**, 89 (2003).
[3] F. Kagawa *et al.*, Nature (London) **436**, 534 (2005).
[4] V. Dobrosavljević *et al.*, Phys. Rev. Lett. **79**, 455 (1997).
[5] E. Abrahams *et al.*, Phys. Rev. Lett. **42**, 673 (1979).
[6] A. Camjayi *et al.*, Nature Phys. **4**, 932 (2008).
[7] A. Georges *et al.*, Rev. Mod. Phys. **68**, 13 (1996).
[8] P. Werner *et al.*, Phys. Rev. Lett. **97**, 076405 (2006).
[9] K. Haule, Phys. Rev. B **75**, 155113 (2007).
[10] G. Kotliar *et al.*, Phys. Rev. Lett. **84**, 5180 (2000).
[11] M. J. Rozenberg *et al.*, Phys. Rev. Lett. **75**, 105 (1995).
[12] J. H. Mooij, Phys. Status Solidi A **17**, 521 (1973).
[13] G. Moeller, V. Dobrosavljevic, and A. E. Ruckenstein, Phys. Rev. B **59**, 6846 (1999).
[14] M. J. Case and V. Dobrosavljević, Phys. Rev. Lett. **99**, 147204 (2007).
[15] See supplemental material at http://link.aps.org/supplemental/10.1103/PhysRevLett.107.026401 for eigenvalue analysis and scaling procedure.
[16] M. Jarrell and J. E. Gubernatis, Phys. Rep. **269**, 133 (1996).
[17] N. E. Hussey *et al.*, Philos. Mag. **84**, 2847 (2004).
[18] Other criteria have also been employed to identify a MIT crossover line. Reference [19] used the flatness of the lowest Matsubara points of the self-energy; Refs. [7,11] used the inflection point of the resistivity curves. We have not reveal any apparent scaling behavior following these trajectories.
[19] H. Park, K. Haule, and G. Kotliar, Phys. Rev. Lett. **101**, 186403 (2008).
[20] B. J. Powell and R. H. McKenzie, J. Phys. Condens. Matter **18**, R827 (2006).
[21] D. Simonian, S. V. Kravchenko, and M. P. Sarachik, Phys. Rev. B **55**, R13 421 (1997).
[22] L. De Leo *et al.*, Phys. Rev. A **83**, 023606 (2011).
[23] S. Sachdev, Phys. Rev. Lett. **105**, 151602 (2010).
[24] J. McGreevy, Physics **3**, 83 (2010).
[25] G. Sordi, A. Amaricci, and M. J. Rozenberg, Phys. Rev. B **80**, 035129 (2009).
[26] M. Eckstein *et al.*, Phys. Rev. B **75**, 125103 (2007).

Quantum Critical Transport Near the Mott Transition: Supplementary Notes

H. Terletska,[1] J. Vučičević,[2] D. Tanasković,[2] and V. Dobrosavljević[1]

[1] *Department of Physics and National High Magnetic Field Laboratory, Florida State University, Tallahassee, Florida 32306, USA.*

[2] *Scientific Computing Laboratory, Institute of Physics Belgrade, University of Belgrade, Pregrevica 118, 11080 Belgrade, Serbia.*

PACS numbers: 71.27.+a,71.30.+h

EIGENVALUE ANALYSIS OF THE FREE ENERGY CURVATURE

Here we present in detail the procedure that we use to determine the minimum curvature of the free energy functional for a given temperature. For simplicity we concentrate on the Bethe lattice. The Ginzburg-Landau free energy functional $F(\vec{G})$ in the Hilbert space of the Matsubara Green's functions $\vec{G} \equiv G(i\omega_n)$ is given by [1–3]

$$\begin{aligned} F(\vec{G}) &= -Tt^2\vec{G}^2 + F_{imp}(\vec{G}) \\ &= -Tt^2 \sum_n G^2(i\omega_n) + F_{imp}(\vec{G}), \end{aligned} \tag{1}$$

where the first term is the energy cost of forming the Weiss field $\vec{\Delta} = t^2\vec{G}$ around a given site, while the second term is the free energy of an electron at this site in the presence of the Weiss field.

Close to a local extremum $\vec{G}_0$, we can Taylor expand $F(\vec{G})$ in terms of deviation from this point $\delta\vec{G} = \vec{G} - \vec{G}_0$:

$$\begin{aligned} F(\vec{G}) &= F(\vec{G}_0) + Tt^2 \sum_{mn} \delta G(i\omega_m) M_{mn} \delta G(i\omega_n) + \dots \\ &= F(\vec{G}_0) + Tt^2\, \delta\vec{G}\hat{M}\delta\vec{G} + \dots \end{aligned} \tag{2}$$

where

$$M_{mn} = \frac{1}{2Tt^2} \frac{\partial^2 F(\vec{G})}{\partial G(i\omega_n)\partial G(i\omega_m)}\bigg|_{\vec{G}=\vec{G}_0}. \tag{3}$$

We introduce a gradient function

$$\vec{g}(\vec{G}) \equiv \frac{1}{2Tt^2}\frac{\partial F(\vec{G})}{\partial \vec{G}} = \hat{M}\delta\vec{G} \tag{4}$$

and define an iteration-substitution procedure by

$$\delta\vec{G}^{(n+1)} = \delta\vec{G}^{(n)} - \vec{g}(\vec{G}^{(n)}), \tag{5}$$

which gives the minimum of the free energy as the iteration step $n \to \infty$. In the case of the free energy functional given by Eq. (1), we have

$$\vec{g}(\vec{G}) = \vec{G}_{imp}(\vec{G}) - \vec{G}, \tag{6}$$

and in the iterative procedure the Green's function converges to the minimum of the free energy which is at the same time also a self-consistent solution of the DMFT equations, given by the relation $G_{imp}(i\omega_n) = G(i\omega_n)$.

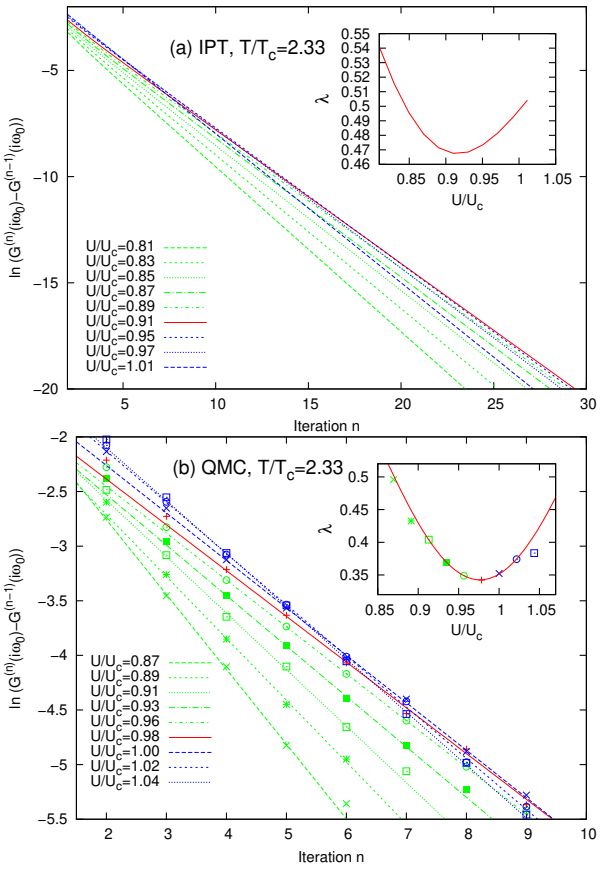

Figure 1: Convergence rate in the iterative solution of DMFT equations at $T/T_c = 2.33$ using IPT impurity solver, panel (a), and CTQMC impurity solver, panel (b). The dashed lines in panel (b) are linear fits to the data. The insets are the corresponding eigenvalues determined by the slopes from the main panels.

The curvature of the free energy for interaction U and temperature T can be obtained as follows. The eigenbasis $\vec{G}_\alpha$ and eigenvalues λ_α of matrix $\hat{M}$ are defined by

$$\hat{M}\vec{G}_\alpha = \lambda_\alpha \vec{G}_\alpha. \tag{7}$$

We can expand $\delta\vec{G}^{(n)}$ as

$$\delta\vec{G}^{(n)} = \sum_\alpha a_\alpha^{(n)} \vec{G}_\alpha \tag{8}$$

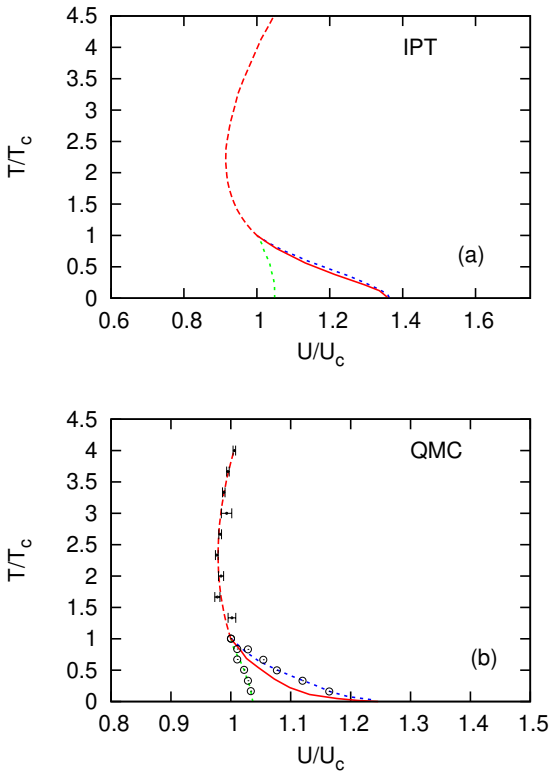

Figure 2: Phase diagram obtained with IPT, panel (a), and CTQMC, panel (b). Temperature and interaction are scaled by their values at the critical endpoint ($T_c^{IPT} = 0.046$, $T_c^{QMC} = 0.03$ and $U_c^{IPT} = 2.472$, $U_c^{QMC} = 2.3$). Red dashed line is the instability line $U^*(T)$, full red line is the line of the first order MIT, and green and blue dotted lines are left and right spinodals.

where $a_\alpha^{(n)}$ are the coefficients of $\delta\vec{G}^{(n)}$ in the eigenvalue basis. Substituting into Eq. (5), one obtains

$$\delta\vec{G}^{(n)} = \sum_\alpha e^{-nB_\alpha} a_\alpha^{(0)} \vec{G}_\alpha, \tag{9}$$

where

$$B_\alpha = -\ln(1-\lambda_\alpha). \tag{10}$$

For large n the term with lowest $B_\alpha = B_{\alpha_0}$, which corresponds to the lowest eigenvalue $\lambda_{\alpha_0} \equiv \lambda$, is dominant

$$\delta\vec{G}^{(n)} = e^{-nB_{\alpha_0}} a_{\alpha_0}^{(0)} \vec{G}_{\alpha_0}, \quad n \gg 1. \tag{11}$$

Here α_0 is the coefficient corresponding to the Green function with the lowest eigenvalue λ. Now it is obvious that through iterations, the solution $\vec{G}$ approaches to $\vec{G}_0$ exponentially along a direction defined by the eigenvector of $\hat{M}$ corresponding to its minimal eigenvalue λ. The coefficient B_{α_0} and the corresponding eigenvalue λ are then obtained from the slope in the iterative relation

$$\ln\left[G(i\omega_n)^{(n+1)} - G(i\omega_n)^{(n)}\right] = const - nB_{\alpha_0}, \tag{12}$$

which follows from Eq. (9).

In practice, to obtain λ (and thus the curvature of free energy), we monitor DMFT loop convergence rate, $G(i\omega_o)^{(n+1)} - G(i\omega_o)^{(n)}$, in as many iterations as possible and then linearly fit $\ln\left(G(i\omega_o)^{(n+1)} - G(i\omega_o)^{(n)}\right)$ versus iteration index n. Here $\omega_o = \pi T$ is the lowest Matsubara frequency. For small λ, $B_{\alpha_0} \approx \lambda$. We repeat this procedure for different values of U at the same temperature T to determine $U^*(T)$ in which $\lambda(U)|_T$ is minimal. It takes few iterations of the DMFT loop to enter into the linear regime given by Eq. (12).

With IPT impurity solver, we can use data from several tens of iterations to determine the slope B_{α_0}, Fig. 1(a). The solution with CTQMC impurity solver has a statistical error and the number of iterations is limited before the difference $|G(i\omega_o)^{(n+1)} - G(i\omega_o)^{(n)}|$ becomes too small and acquires a large relative statistical error. Nevertheless, we were able to determine rather precisely the eigenvalue λ and the interaction $U^*(T)$ for which it becomes minimal, Fig. 1(b). The "instability line" corresponding to the minimum curvature of the free energy is shown in Fig. 2(a) (IPT phase diagram), and Fig. 2(b) (CTQMC phase diagram). Error bars in Fig. 2(b) are estimates of the uncertainty in the position of the instability line.

DETAILS OF THE SCALING PROCEDURE

The resistivity $\rho(T, \delta U)$ is calculated along the lines parallel to the instability line $U^*(T)$. Here $\delta U = U - U^*(T)$. The resistivity is fist divided by its value $\rho_c(T)$ at $\delta U = 0$, Fig. 3(a). Then for each δU the temperature axis is scaled by T_0 where the scaling parameter T_0 is chosen to collapse the data onto two branches: insulating-like for $\delta U > 0$ and metallic-like for $\delta U < 0$. The scaling was done in such a way that data were collapsed on the lowest curves with $\delta U = \pm 0.025$ as shown in Fig. 3(b). The scaling parameter T_0 has a power law form $T_0 = c|\delta U|^{z\nu}$, where the prefactor c depends on this referent value of U.

Our data exhibit a reflection symmetry which is seen in Fig. 4(a), where the resistivity ρ/ρ_c (for $\delta U > 0$) and conductivity $\sigma/\sigma_c = \rho_c/\rho$ ($\delta U < 0$) can be mapped onto each other by reflection with $\frac{\rho(\delta U)}{\rho_c} = \frac{\rho_c(-\delta U)}{\rho}$.

The standard estimate for the scale (prefactor) of the crossover temperature is obtained by requiring that the scaling variable $x = T/T_0 = 1$ at the point where the scaling function changes its functional form; in our case this corresponds to the temperature below which the mirror symmetry of the scaling curves no longer holds. Before rescaling the prefactor, this is found at $x^* = T_{sc}/T_o = 0.052$. Our final form of scaled data is shown in Fig. 4(b), where T/T_0 - axis is rescaled by $x^* = T_{sc}/T_o$ so that $T/T_o = 1$ sets the *boundary of the quantum critical region*. The scaling parameter T_0 as function of δU is shown in Fig. 5(a) (before rescaling

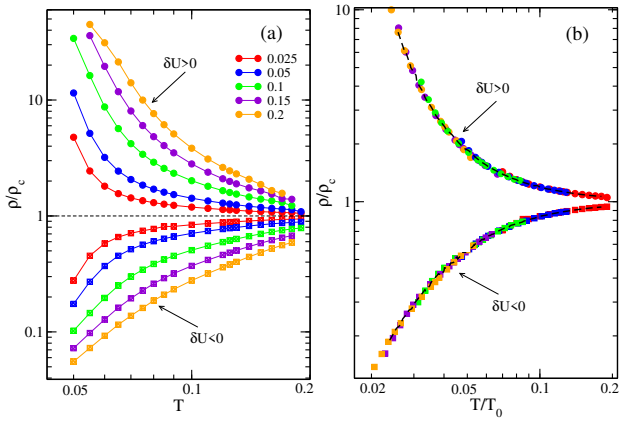

Figure 3: (a) Resistivity as function of temperature for $\delta U = \pm 0.025, 0.05, 0.1, 0.15, 0.2$. (b) By scaling the data along $T-$axis by T_0 data are collapsed onto two branches. Data are collapsed on the lowest $\delta U = \pm 0.025$ curves.

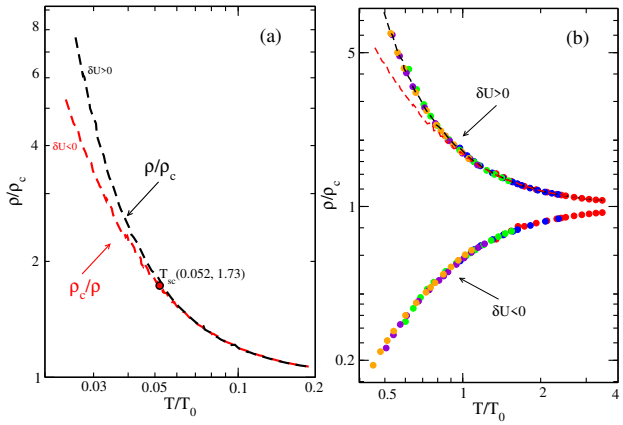

Figure 4: (a) Total scaled data (for clarity shown by single branches) exhibit reflection symmetry for $T \geq T_{sc}$. (b) T/T_0-axis is rescaled by T_{sc} in such a way that $T/T_o = 1$ set the boundary of quantum critical region over which the reflection symmetry of scaled curves is observed.

with x^*) and in Fig. 5(b) (after rescaling with x^*). The corresponding values for c and $z\nu$ from the power law fit are also given.

We can now plot the crossover temperature T_0 setting the boundary of QC region on our phase diagram. $T = T_0$ condition is equivalent to

$$T_0 = c|\delta U(T_o)|^{\nu z} = c\delta|U - U^\star(T_o)|^{z\nu}, \qquad (13)$$

where $U^\star(T_o)$ is value of U at temperature $T = T_o$, along the instability line. This equation implicitly defines the crossover line $T_o(U)$. Alternatively, we can invert this dependence to describe the same crossover line as $U_0(T)$ that takes the form

$$U_o^{\pm}(T) = U^\star(T) \pm (T/c)^{1/z\nu}. \qquad (14)$$

As we can see from this expression, the crossover line approaches the instability line at low T and diverges away

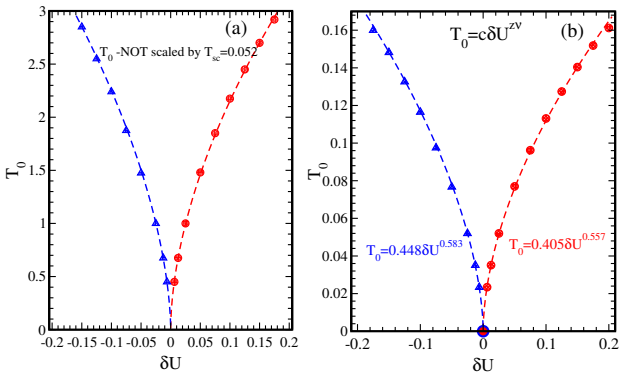

Figure 5: (a) Scaling temperature T_0 vs. δU obtained from scaling procedure shown on Fig. 4(a). (b) T_0 vs. δU after rescaling by T_{sc}. The boundary of the quantum critical region is now given by condition $T/T_o = 1$.

from it at high T. The phase diagram including the instability line and the crossover temperature T_0 is shown on Fig. 6.

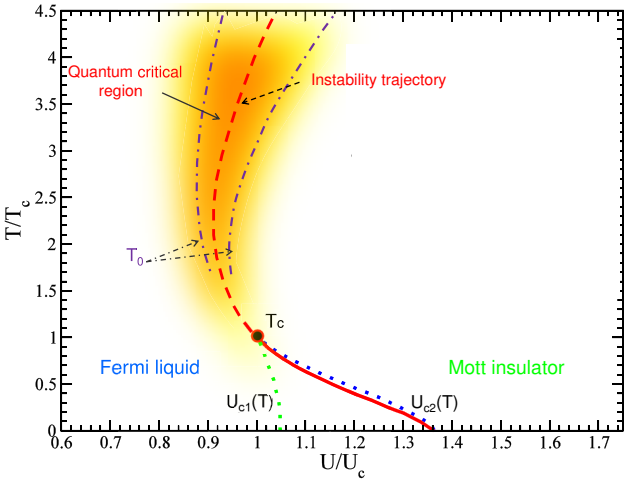

Figure 6: (Color online) DMFT phase diagram of the fully frustrated half-filled Hubbard model. The thick dashed line, which extends at $T > T_c$ shows the "instability trajectory" $U^*(T)$, and the crossover temperature T_o delimits the QC region (dash-dotted lines).

[1] A. Georges, G. Kotliar, W. Krauth, and M. J. Rozenberg, Rev. Mod. Phys. **68**, 13 (1996).

[2] G. Moeller, V. Dobrosavljević, and A. E. Ruckenstein, Phys. Rev. B **59**, 6846 (1999).

[3] G. Kotliar, E. Lange and M. J. Rozenberg, Phys. Rev. Lett. **48**, 5180 (2000).